Transactions of the ASME® Journal of Turbomachinery

Published Quarterly by The American Society of Mechanical Engineers

VOLUME 116 • NUMBER 4 • OCTOBER 1994

Technical Editor, **T. H. OKIISHI (1998)**
Associate Technical Editors
Aeromechanical Interaction
R. E. KIELB (1996)
Gas Turbine
C. J. RUSSO (1995)
Heat Transfer
M. G. DUNN (1996)
Nuclear Engineering
H. H. CHUNG (1996)
Power
P. H. GILSON (1996)
Turbomachinery
N. A. CUMPSTY (1995)

BOARD ON COMMUNICATIONS
Chairman and Vice-President
R. D. ROCKE

Members-at-Large
T. BARLOW, N. H. CHAO, A. ERDMAN,
G. JOHNSON, L. KEER, W. MORGAN,
E. M. PATTON, S. PATULSKI, R. E. REDER,
S. ROHDE, R. SHAH, F. WHITE,
J. WHITEHEAD

OFFICERS OF THE ASME
President, **P. J. TORPEY**
Executive Director
D. L. BELDEN
Treasurer
R. A. BENNETT

PUBLISHING STAFF
Mng. Dir., Publ.,
CHARLES W. BEARDSLEY
Managing Editor,
CORNELIA MONAHAN
Sr. Production Editor,
VALERIE WINTERS
Production Assistant,
MARISOL ANDINO

Transactions of the ASME, Journal of Turbomachinery (ISSN 0889-504X) is published quarterly (Jan., Apr., July, Oct.) for $150.00 per year by The American Society of Mechanical Engineers, 345 East 47th Street, New York, NY 10017. Second class postage paid at New York, NY and additional mailing offices. POSTMASTER: Send address change to Transactions of the ASME, Journal of Turbomachinery, c/o THE AMERICAN SOCIETY OF MECHANICAL ENGINEERS, 22 Law Drive, Box 2300, Fairfield, NJ 07007-2300.
CHANGES OF ADDRESS must be received at Society headquarters seven weeks before they are to be effective. Please send old label and new address.
PRICES: To members, $40.00, annually; to nonmembers, $150.00.
Add $24.00 for postage to countries outside the United States and Canada.

STATEMENT from By-Laws. The Society shall not be responsible for statements or opinions advanced in papers or . . . printed in its publications (B7.1, Par. 3).
COPYRIGHT © **1994** by The American Society of Mechanical Engineers. Authorization to photocopy material for internal or personal use under circumstances not falling within the fair use provisions of the Copyright Act is granted by ASME to libraries and other users registered with the Copyright Clearance Center (CCC) Transactional Reporting Service provided that the base fee of $3.00 per article is paid directly to CCC, 27 Congress St., Salem, MA 01970. Request for special permission or bulk copying should be addressed to Reprints/Permission Department.

INDEXED by Applied Mechanics Reviews and Engineering Information, Inc.
Canadian Goods & Services
Tax Registration #126148048

TECHNICAL PAPERS

(Contents Continued on p. 569)

Downloaded 01 Jun 2010 to 171.66.16.52. Redistribution subject to ASME license or copyright; see http://www.asme.org/terms/Terms_Use.cfm

(Contents Continued)

ANNOUNCEMENTS

M. J. Hartmann Memorial Session Paper

NASA/GE Fan and Compressor Research Accomplishments

L. H. Smith, Jr.
GE Aircraft Engines,
Cincinnati, OH 45215

Fan and compressor research projects carried out at GE Aircraft Engines under NASA sponsorship are described in this paper. Four 1400-fps-tip-speed rotors designed with different airfoil shapes were found to have comparable stall lines but different efficiency trends. A stator placed behind one of these affected its performance somewhat. Adjustments of variable camber inlet guide vanes placed ahead of a 1500 fps stage were found to affect its pumping capability without much affecting its stall line. For the Quiet Engine Program (QEP), two 1160-fps fans and one 1550-fps fan were tested. Development of the high-speed fan revealed the effects on performance of airfoil shape and part-span shroud blockage. The 950-fps variable-pitch fan for the Quiet Clean Short-haul Experimental Engine (QCSEE) demonstrated reverse thrust capabilities and a novel method of avoiding large core inlet pressure losses during reverse thrust operation. The 1350-fps Energy Efficient Engine (E^3) fan demonstrated excellent performance with a novel quarter-stage arrangement that eliminated the need for interspool bleed while giving good dirt removal potential. The E^3 compressor program employed Low Speed Research Compressor tests to identify the most appropriate blading type. High-speed rig tests and engine tests were then used to develop this 23:1-spool-pressure-ratio compressor. Research on casing boundary layer control through bleeding and blowing led to the discovery that irregular casing geometries usually give stall line enhancements even without auxiliary air circuits. Some of the resulting casing treatment research is reported herein. Instances in which NASA-sponsored research has affected GE Aircraft Engine products are pointed out.

1 Introduction

When the National Advisory Committee for Aeronautics (NACA) became NASA in 1958, their large in-house effort on compressors was terminated. By the mid-1960s it was concluded that further air-breathing-engine compressor research was needed, and that this should involve not only a re-start of Lewis Lab in-house efforts but should also include direct participation by the engine companies. Consequently, in late 1964, a Request for Proposal was issued for seven tasks of compressor aerodynamic research. GE Aircraft Engines submitted bids on three of these and subsequently won contracts for two. This work was followed by many other contractual efforts, almost all of which are discussed herein.

This paper is organized into three main topics. The first subject is transonic rotors and fan-type stages. Multistage compressors are discussed second, and end-wall boundary layer control (mostly casing treatment research) is the final topic.

2 Fan Stages

2.1 Blade Shapes for 1400 fps Rotors. A set of four rotors was designed as a vehicle for experimental evaluation of the use of blade camber line shape to minimize blade element losses. All four rotors had some overall characteristics in common as listed below:

1. Corrected tip speed, 1400 ft/sec (427 m/s).
2. Inlet hub-tip radius ratio, 0.50.
3. Inlet tip diameter, 36.5 in. (927 mm).
4. Corrected airflow, 215.5 lb/sec (97.8 kg/s).
5. Corrected airflow/annulus area, 39.6 lb/sec-ft^2 (193.1 kg/s-m^2).
6. Tip solidity, 1.3 with chord radially constant.
7. Number of blades, 44.

Two levels of loading resulted in differences in some of the overall design characteristics as listed in Table 1. The annulus flowpaths are shown in Fig. 1.

NASA multiple-circular-arc blade shapes were employed in which the camber line consists of two circular arcs that are mutually tangent at the point where they join. This point is directly across the flow passage from the leading edge of the adjacent blade that forms the other side of the flow passage. The front arc is identified as the supersonic arc, and the rear arc is identified as the subsonic arc. The term camber ratio refers to the ratio of the camber of the supersonic arc to the total camber. The camber ratios employed are shown in Fig. 2. Rotor 2D was made up entirely of double-circular-arc airfoils, as were the inner portions of the other rotors. Incidence angles for the outboard sections were set to give zero suction surface incidence for double-circular-arc profiles, and these

---

Contributed by the International Gas Turbine Institute and presented at the 38th International Gas Turbine and Aeroengine Congress and Exposition, Cincinnati, Ohio, May 24–27, 1993. Manuscript received at ASME Headquarters March 17, 1993. Paper No. 93-GT-315. Associate Technical Editor: H. Lukas.

Table 1 Design properties of 1400 fps rotors

	Rotor 1B	Rotors 2
Rotor tip diffusion factor	0.35	0.45
Total-pressure ratio, radially constant	1.60	1.76
Rotor blade aspect ratio	2.5	2.4
Rotor tip axial velocity ratio	0.91	0.91
Rotor tip relative Mach number	1.43	1.45
Tip blade element camber ratio	1 level	3 levels
Mass averaged rotor adiabatic efficiency,%	85.8	83.7

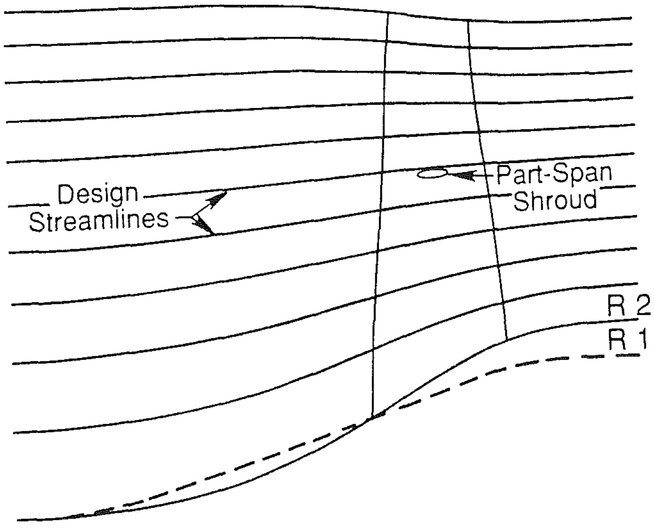

Fig. 1 Design flowfield for 1400 fps rotors 2

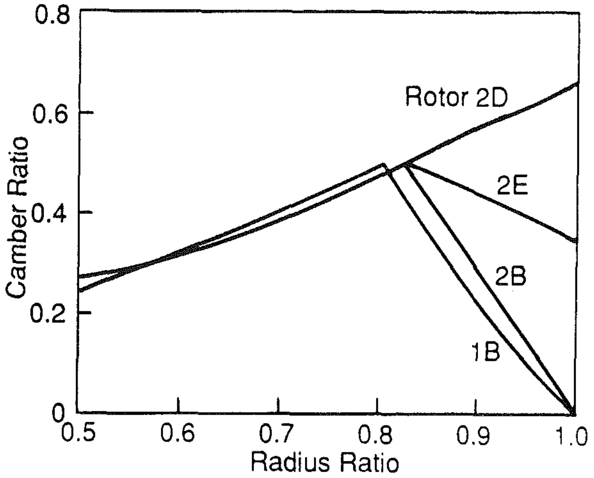

Fig. 2 Radial variation of design ratio of supersonic to total blade camber

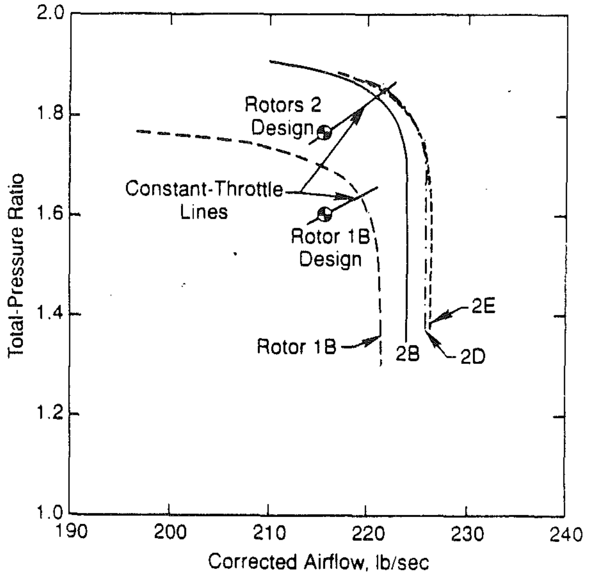

Fig. 3 Design-speed pumping characteristics

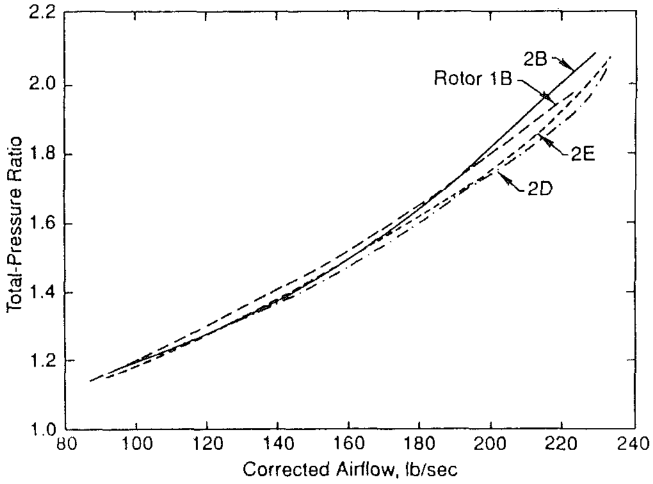

Fig. 4 Stall lines of 1400 fps rotors

same incidences were used for the multiple-circular-arc profiles also. Incidences near the hub were set somewhat lower. Deviation angles were obtained from Carter's rule with rational adjustments for change in radius and change in axial velocity across the blade row and empirical adjustments from experience. Throat areas were examined and found to be adequate, perhaps excessive in some cases. At the tip the throat area exceeded that needed to pass the flow (assuming a normal shock at inlet Mach number) by 4 percent for Rotor 1B and 15 percent for Rotor 2D with the other rotors being intermediate. Further design details are given in [1].

Design-speed pumping characteristics are shown in Fig. 3. It is seen that all rotors pumped high. Some of this occurred because the design inlet annulus blockage was assumed to be 2 percent, which is probably too high, with the rest explained by excessive throat and unique-incidence allowances. Figure 4 compares the stall lines. It is interesting to note that, despite

Nomenclature

P = static pressure

SM = stall margin = $\dfrac{(\text{pressure ratio/airflow})_{\text{stall}}}{(\text{pressure ratio/airflow})_{\text{operating line}}} - 1$

W = relative velocity

ρ = static density

Subscript

1 = rotor inlet

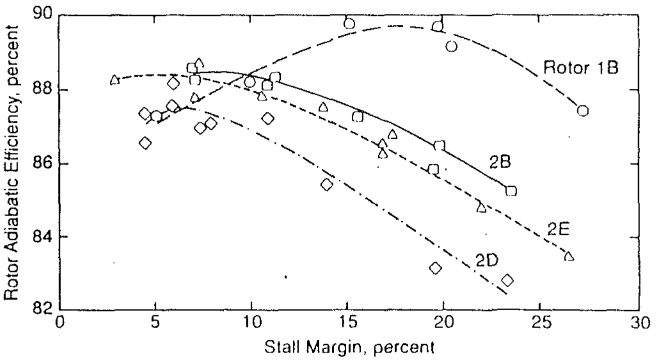

Fig. 5 Rotor efficiency versus distance from stall line at 100 percent speed

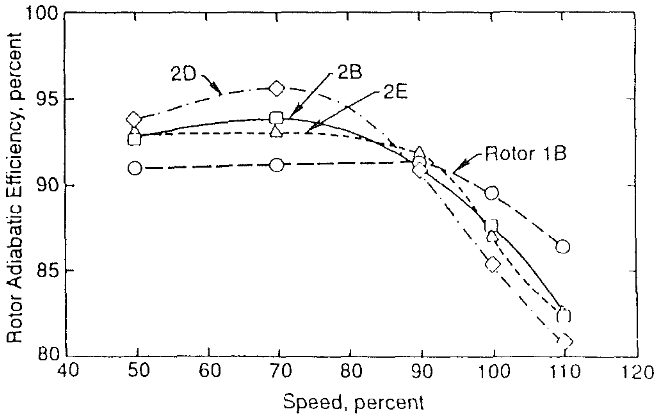

Fig. 6 Efficiencies along constant-throttle lines having 15 percent stall margin at 100 percent speed

the fact that Rotor 1B had less camber and less annulus contraction because it was designed for a lower pressure ratio, its stall line is the best at part speed and second best at high speed. This shows that camber increases are not always helpful in raising a stall line. Futhermore, as shown in Fig. 5 where design speed efficiency is plotted versus distance from each actual stall line, the lower loaded Rotor 1B clearly has an efficiency advantage at the larger stall margin values where engine fans must operate. To explore this further, a simulated fixed-nozzle sea-level-static operating line was drawn on each of the four performance maps, located such that the stall margin at design speed was 15 percent. The results are shown on Fig. 6, where the tradeoff between high-speed and low-speed performance is evident. Detailed performance data are given in [2–5] where actual blade shapes are also shown, and more extensive performance comparisons are given in [6].

This test series was completed just as the original CF6 engine fan was being designed, and although the CF6 was not constrained to use multiple-circular-arc airfoils, there is a distinct resemblance between it and Rotor 1B. This program also influenced the design of the TF34 fan.

2.2 1400 fps Stage Test. A stator was designed for Rotor 1B described above. Actually, the stator was designed specifically to match a higher speed rotor design described in Section 2.3, but the stator inlet air angles were very similar for both stages. The flowpath is the same as that to be described later in Fig. 7 expect that the inlet guide vanes were not installed.

The presence of the stator did affect the performance of Rotor 1B. The rotor efficiency near the design point was reduced by 1.3 points, and the design speed stalling airflow was reduced by 4.4 percent. The stall pressure ratio was also reduced by 1.4 percent, so the stall line was improved by 3.0 percent. Detailed inspection of the measurements showed that a flow deterioration in the rotor hub region was responsible for these effects. As Fig. 7 shows, when the stator was added, the convex hub curvature near the rotor trailing edge was greatly reduced. Therefore the axial velocity did not accelerate as much across the rotor near the hub, and the loading parameters and losses were increased there. The movement of flow away from the hub tended to unload the tip, and hence the tip rotating stall was delayed to a lower airflow. The stator performed about as expected, and the flow in its hub region did not deteriorate drastically as the rotor was throttled to stall. The peak efficiency at design speed was 85 percent at a pressure ratio of 1.65 with 18 percent stall margin. The detailed performance of this stage is given in [7].

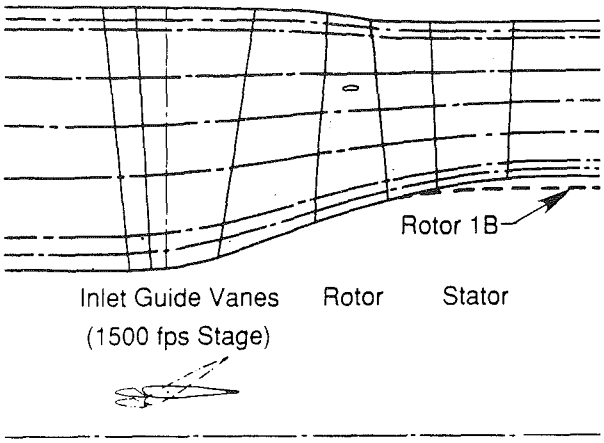

Fig. 7 1500 fps stage flowpath

2.3 1500 fps Stage. This stage was designed to have somewhat higher values of pressure ratio and specific airflow than the 1400 fps stage, but otherwise have similar properties and to use the same annulus. It also included variable camber inlet guide vanes, as it might be considered to be the first stage of a multistage fan for supersonic engine application. Design properties of the two stages are given in Table 2. Rotor 1B had been tested when the stage designs were conducted, so the 1400 fps stage design point was selected to match test experience. The 1500 fps stage design airflow was chosen to match that measured when the 1400 fps rotor ran at 1500 fps, and the pressure ratio was selected to produce very nearly the same stator inlet air angles along the span for both stages. This could be accomplished by designing the 1500 fps rotor to have an exit total-pressure distribution that was approximately constant from tip to hub.

Multiple-circular-arc airfoils were not used for the 1500 fps rotor. Unique incidence concepts were employed to shape the outboard sections, with mild negative camber being employed in the forward part of the airfoil to reduce the suction surface Mach number at the tip from 1.57 to 1.48 at the passage mouth. Passage throat areas were set to have 5 percent margin assuming a relative total-pressure loss equivalent to a normal shock at upstream Mach number for each streamline. Deviation angles were obtained by the same method used for the 1400 fps rotors but with updated empirical adjustments.

For the stator vane, the design vector diagrams for the 1500 fps stage were employed. Double-circular-arc airfoils were selected for the outer half of the vane. A custom-tailored airfoil section was developed for the hub to obtain lower suction surface Mach numbers than produced by a double-circular-arc hub section. The vane sections between the tailored hub and double-circular-arc pitchline sections were selected to form a smooth transition.

Figure 7 shows the flowpath. Each inlet guide vane was made up of two pieces. The forward piece was attached to a ring at each end. These rings were recessed into the inner and outer

Table 2 Design properties of 1400 and 1500 fps stages

	1400 fps Stage	1500 fps Stage
Rotor inlet corrected tip speed, ft/sec (m/sec)	1400 (427)	1500 (457)
Stage inlet corrected airflow, lb/sec (kg/sec)	219.4 (99.5)	226.0 (102.5)
Rotor inlet corrected airflow/annulus area, lb/sec-ft^2 (kg/sec-m^2)	40.3 (196.5)	41.6 (203.2)
Stage total-pressure ratio	1.62	1.66
Stage adiabatic efficiency, %	87.3	85.4
Number of inlet guide vanes	0	24
Inlet guide vane exit flow angle, deg		0
Rotor inlet tip relative Mach number	1.41	1.53
Rotor tip diffusion factor	0.382	0.368
Rotor tip solidity	1.3	1.4
Number of rotor blades	44	44
Stator inlet hub absolute Mach number	0.684	0.766
Stator exit flow angle, deg	0	0
Stator hub diffusion factor	0.474	0.435
Stator hub solidity	2.16	2.16
Stator aspect ratio	2.07	2.07
Number of stator vanes	46	46

casings, and ball bearing were provided to allow the rings to rotate slightly around the compressor centerline as the aft piece stagger was varied. Although mechanically complex, this arrangement gave excellent cascade properties at all settings. The airfoils were shaped to impart no swirl at the stage design point. Full design details for the 1500 fps stage are given in [8].

The performance map for the 1500 fps stage is given in Fig. 8 for three combinations of inlet guide vane and stator vane settings. The reduction in flow pumping at speed as the vanes are closed is clearly evident. Only small improvements in the map stall line can be inferred with vane closure, and stage efficiencies are generally lower at the larger closures, but these effects are minor in importance compared with the flow pumping changes that permit favorable stage rematching in multistage compressors at off-design operating conditions.

The 1500 fps stage was also tested with the inlet guide vanes removed. At design speed the stall line was improved by about 4 percent when the inlet guide vanes were removed and about 1 percent at 90 percent speed. All stalls are believed to have initiated at the rotor tip. The efficiency improved about 1 point by removing the inlet guide vane loss source.

Much more detailed information is given in [9–11]. This includes tests with tip-radial and circumferential inlet total-pressure distortions for all of the stages described above. Some of the distortion results will be reported in Section 4 when discussing casing treatment effects.

2.4 Quiet Engine Program Fans. This program was a major NASA contracted effort aimed at reduction of engine noise. It commenced in the late 1960s and ran through the early 1970s, and it involved engine tests that incorporated noise reduction and noise suppression features. Since fans are a prominent noise source, three alternative fans were designed, built, and tested on the component stand, and two of these were tested in engines. Since blade speed reduction is one way to reduce source noise, two of the fans had low blade speeds but consequently had rather high blade aerodynamic loading levels to produce the required pressure ratio. In the third fan the opposite approach was taken: high speed was employed to keep aerodynamic loadings low. Design properties of the three fans are given in Table 3.

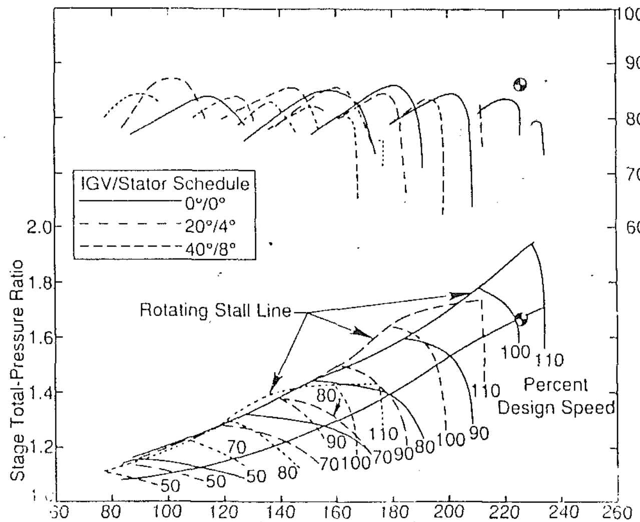

Fig. 8 1500 fps stage performance map

Flowpaths of the three fans are shown in Fig. 9. The large axial spacings between the rotor and stator bladings were specified to minimize interaction noise. The relatively large hub radii and relatively low aspect ratios of Fans A and B (compared to contemporary practice) were specified to cope with the large aerodynamic loadings. Fan A employed a tip shroud. Fan C employed a part-span shroud, but its aspect ratio was also low looking toward the possibility of an unshrouded production version, possibly employing composite blades.

Blade shapes employed in the rotor designs varied with blade height. In the tip regions, where the relative Mach number is supersonic, the profiles were tailored to prevent excessive shock losses and to minimize diffusion losses. In the hub regions, profiles similar to double-circular-arc airfoils were used.

The bypass duct outlet guide vanes for all fans and the core duct outlet guide vanes for Fan A operate at moderate conditions of inlet Mach number and diffusion factor. The profile selected for these vane rows was a modified NACA 65 series *thickness distribution on a circular arc meanline.* The core duct outlet guide vanes for Fan B and Fan C operate in relatively high inlet-Mach-number environments, when considering the turning requirements and diffusion factor levels. Accordingly, tandem vane rows were designed. Further design details are given in [13].

Fan A Performance. Fan A performed well. At design speed on an operating line through the design point it achieved a bypass pressure ratio of 1.52 with 12.4 percent stall margin at 1.3 percent high airflow with an efficiency of 88.3 percent. The core stream pressure ratio was 1.36 at its design airflow with an efficiency of 83.1 percent. Peak bypass efficiencies were over 88 percent at all lower speeds and peak core stream efficiencies were 85 percent at speeds of 90 percent and below.

Test detailed are given in [14]. These include data for bypass ratio excursions from 4.7 to 13 at 90 percent speed, detailed pressure, temperature, and flow angle traverses, and inlet distortion test results.

Table 3 Design properties of Quiet Engine fan stages

	Fan A	Fan B	Fan C
Corected rotor tip speed, ft/sec (m/sec)	1160 (354)	1160 (354)	1550 (472)
Inlet hub/tip radius ratio	0.465	0.465	0.360
Inlet tip diameter, in(m)	73.35 (1.863)	73.35 (1.863)	68.30 (1.735)
Corrected airflow, lb/sec (kg/sec)	950 (430.9)	950 (430.9)	915 (415.0)
Corrected airflow/ annulus area, lb/sec-ft^2 (kg/sec-m^2)	41.3 (201.7)	41.3 (201.7)	41.3 (201.7)
Bypass total-pressure ratio	1.50	1.50	1.60
Core stream total pressure ratio	1.32	1.43	1.49
Bypass ratio	5.6	5.4	5.0
Bypass adiabatic efficiency, %	86.5	87.0	84.2
Rotor inlet tip relative Mach number	1.20	1.20	1.52
Rotor aspect ratio	2.32	1.71	2.09
Rotor solidity: OD	1.45	1.30	1.40
ID	2.50	2.16	2.45
Number of rotor blades	40	26	26
Number of outer OGVs	90	60	60
Number of inner OGVs	90	60	60

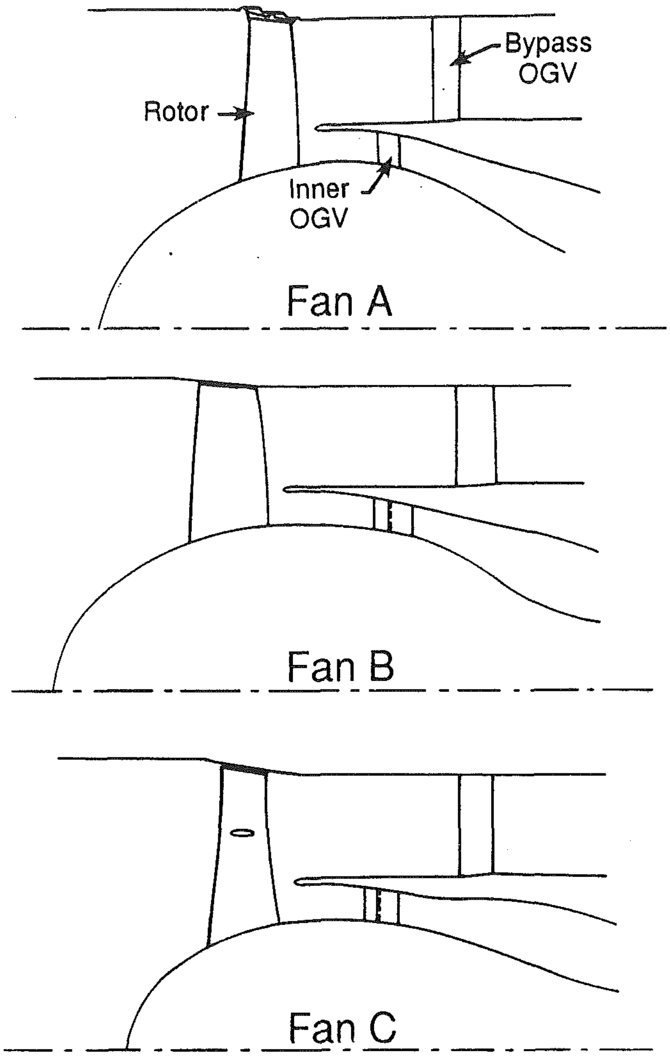

Fig. 9 Quiet Engine fan flowpaths

Fan B Performance. Fan B was not as efficient as Fan A. At design speed on an operating line through the design point it achieved a bypass pressure ratio of 1.52 with 19.5 percent stall margin at 1.7 percent high airflow with an efficiency of 86.9 percent. The design core stream pressure ratio of 1.43 was attained at design airflow, but the efficiency was only 77.0 percent. The peak bypass efficiency was 87.5 percent, and the peak core stream efficiency did not quite reach 80 percent. At speeds from 85 to 95 percent, throttling was limited by rotor blade vibratory stress rather than stall.

Measurements indicate that the 1.4 point poorer efficiency of the bypass portion of Fan B compared to Fan A resulted mainly from higher losses in the outer 25 percent span and, to a lesser extent, the inner 15 percent of the bypass outlet guide vanes. Reasons for this are believed to be the larger axial length of Fan B together with the lower blade and vane numbers (large circumferential spacings) that could cause endwall effects to penetrate further from the wall. The higher rotor tip solidity of Fan A could also have had a beneficial effect. Losses associated with the rotating tip shrouds of Rotor A were not large.

The disappointing performance of the core stream resulted from a combination of poor rotor airfoil design, large axial spacing between rotor and outlet guide vanes, and high aerodynamic loadings. The rotor hub airfoils were 9 percent thick, nearly double-circular-arc profiles placed on a hub that was convex inside the blade row. This must have led to increased boundary layer thickness from corner stall, because traverses taken at rotor exit showed a secondary flow pattern that extended over nearly all of the core stream. Losses were high in the tandem outlet guide vanes, particularly in the inner half span, even after the aft portions had been closed 6 deg to yield the quoted 77 percent efficiency. Modern designs guided by design tools not then available would be expected to perform much better. Detailed test results for Fan B are given in [15].

Fan C Performance. Fan C underwent three builds, between which the rotor was modified. During tests of the first build it was determined that the design intent rotor oblique shock pattern was not attained at design speed. The test vehicle was equipped with 10 Kulite transducers mounted in the casing over the rotor tips to determine the time-varying static pressure field caused by the passage of the rotor blades. These indicated a strong normal shock standing in front of the passage, an unstarted mode of operation. The bypass efficiency was about 79 percent at design speed and below. However, at 105 percent speed, an efficiency of 82 percent was recorded. On-test observations of the over-the-rotor high-response pressure pickups showed a definite discontinuity in the shock pattern as corrected speed was gradually increased from 100 to 105 percent. Stabilized steady-state readings were recorded at corrected speeds of 100, 101.8, 102.8, 103.6, and 105 percent at constant discharge valve settings. At corrected speeds of 100 and 101.8 percent the shock patterns were qualitatively similar. The 103.6 and 105 percent corrected speed shock patterns were also qualitatively similar with the desired oblique shock at passage inlet. At 102.8 percent corrected speed the shock pattern alternated between a pattern that was qualitatively similar to that observed at 101.8 percent and that observed at 103.6 percent corrected

Table 4 Design properties of QCSEE fan stages

	UTW Fan	OTW Fan
Corrected tip speed, ft/sec (m/sec)	1005 (306)	1175 (358)
Inlet hub/tip radius ratio	0.444	0.419
Inlet tip diameter, in(m)	71.00 (1.803)	71.00 (1.803)
Corrected airflow, lb/sec (kg/sec)	900 (408)	900 (408)
Corrected airflow/annulus area lb/sec-ft^2 (kg/sec-m^2)	40.8 (199)	39.8 (194)
Bypass total-pressure ratio	1.34	1.36
Core stream total-pressure ratio	1.23	1.43
Bypass ratio	11.3	9.9
Bypass adiabatic efficiency,%	88	88
Rotor inlet tip relative Mach number	1.13	1.22
Rotor solidity: OD	0.95	1.3
ID	0.98	2.2
Number of rotor blades	18	28
Number of outer vane-frame vanes	33	33
Number of inner OGVs	96	156

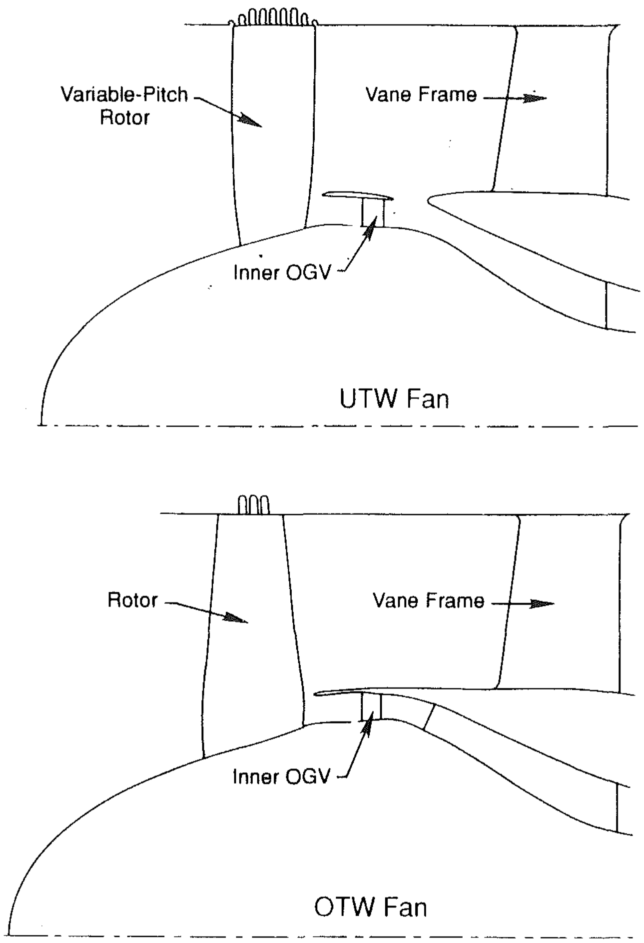

Fig. 10 QCSEE fan flowpaths

speed. The period of the alternations was on the order of seconds, with the flow appearing steady between alternations. The change from one shock pattern to the other, irrespective of direction, appeared to be discontinuous.

In an attempt to achieve started flow at a lower speed, the blades were modified outboard of the shroud by opening the throat and decreasing the passage mouth area so as to reduce the internal contraction of the passage an average of 3 percent. This was tested as Build 2. The flow remained unstarted at 100 percent, with only slight efficiency improvements noted.

The final Build 3 configuration was obtained by removing the part-span shroud and twisting the blade tip closed somewhat more than that needed for the larger untwist from static to running conditions. This enabled the flow to start smoothly and gradually, and large efficiency improvements were measured at all speeds below 105 percent speed. At design speed on an operating line through the design point it achieved a bypass pressure ratio of 1.61 at 0.7 percent high airflow with an efficiency of 83.9 percent. The core stream pressure ratio was 1.54 at its design airflow with an efficiency of 82.3 percent. The peak bypass efficiency at design speed was 85 percent at 1.68 pressure ratio. At speeds lower than design, bypass efficiencies were generally lower, peaking between 83 and 84 percent in the 60–90 percent speed range. For this third build, with the rotor part-span shrouds removed, throttling was generally limited by vibratory stress, but adequate margin for development engine operation was demonstrated. The core stream efficiencies were around 84 percent at speeds lower than design.

Examination of the spanwise efficiency distributions for the three builds at design speed indicated that the efficiency improvement had all occurred at the middle third of the span where the part-span shrouds had been. The original design had been carried out without tailoring the blade shapes to match the flowfield of the shroud (we did not start that until 1974), and the shroud blockage had unfortunately been placed just where the cascade throat occurred without the shroud. The local internal contraction was therefore too excessive to be overcome by only modifying the tip as had been tried in Build 2.

This lesson concerning the adverse effects of excessive internal contraction on high-speed fans was learned during 1971 while the first full-scale F101 fan for the B1 bomber was being fabricated. Even though that fan did not have part-span shrouds, we designers realized that it did have excessive internal contraction, and at some costs to our budgets, schedules, and reputations we did get the design properly modified before it was (successfully) tested.

The Fan C development program, including rotor tip shock patterns, is described in [16]. Because Fan C without a part-span shroud encountered stall flutter over a wide speed range, it was considered to be an ideal design for flutter research. Consequently, NASA sponsored such research employing a 21-in. (54-cm) dia scale model of Fan C, and it was extensively tested. That work was reported in [17].

2.5 QCSEE Fans. The Quiet Clean Short-haul Experimental Engine (QCSEE) program was a second major NASA-contracted effort aimed at developing propulsion technology for aircraft that could operate from small airports using some form of powered lift. Studies identified promising blown flap systems with the jet passing either under or over the wing, and engines to accomplish this were built. These engines have low fan pressure ratios and high bypass ratios. Design properties of the fans evaluated are given in Table 4. Flowpaths of the two fans are given in Fig. 10.

Under-the-Wing (*UTW*) *Fan.* The unique layout of this fan was conceived to reduce core inlet flow pressure losses during reverse-pitch operation that would otherwise occur in the inner outlet guide vanes of a conventional fan, while keeping engine length short and avoiding variable auxiliary inlets. The island over the inner outlet guide vanes has a vortex sheet shed from it because of the flow angle discontinuity at its trailing edge. A somewhat similar island has been successfully employed in the CF6-6 engine for other reasons [18].

The QCSEE engines had variable fan nozzles, allowing independent optimization of takeoff and cruise performance. Studies indicated that at takeoff the UTW fan blade pitch should be opened 2 deg and the nozzle opened to produce a pressure ratio of 1.27 at 950 fps (289 m/s) corrected tip speed with a corrected airflow of 99.3 percent design, while at max cruise the blade pitch should be closed 2 deg and the nozzle closed to produce a pressure ratio of 1.34 at a tip speed of 1063 fps (324 m/s), also at 99.3 percent design airflow.

The rotor blade solidity was kept less than unity so that the fan could be reversed through flat pitch as is done with propellers. Reversal in the other direction would not require this solidity restriction and would result in positive rather than negative camber during reverse operation, but concern about thrust surges followed by abrupt blade stall and recovery in reverse during aircraft braking led us to a design that kept the flat-pitch option open. The solidity restriction did limit the core supercharging pressure ratio and resulted in rather high airfoil aerodynamic loadings in the bypass stream. Circumferential-groove casing treatment was employed to help out. Design details are given in [19].

A 20-in. (50.8-cm) scale model of the UTW fan was built and tested at forward pitch and with both kinds of reverse pitch. At design speed and pitch setting the fan pumped 5.5 percent low in airflow on an operating line through the design point. The bypass efficiency was 86 percent. The design airflow was attained at a lower back pressure, indicating that the low flow was a consequence of inadequate trailing-edge camber. In retrospect this is not surprising because the combination of low solidity, transonic Mach numbers, and high loading pushed the design toward hooked-trailing-edge profiles, and the designers were reluctant to overdo this, knowing that low flow could be made up by opening the pitch angle. The objective stall line was met, and stall margins of 20 percent at takeoff and 15 percent at maximum cruise were estimated. The inner outlet guide vane exit pressure ratio slightly exceeded the objective value, and the deduced efficiency of 85 percent was better than expected.

Scale model reverse-pitch operation with reversal through stall yielded fan efficiencies around 50 percent and an estimate that the engine objective reverse thrust would be met. Reversal through flat pitch with its negative camber gave efficiencies around 35 percent and roughly half of the objective reverse thrust. Full details of the 20-in. scale model tests are given in [20].

Some fan performance data up to 95 percent speed were obtained during the engine tests. Scale model airflows were slightly exceeded in the engine, bypass efficiencies were about the same, but core-stream pressure ratios were noticeably higher in the engine at comparable efficiencies. These data are presented in [21]. Engine tests did not achieve the objective reverse thrust at any pitch-angle setting [21]. Subsequent tests of the engine at the NASA Lewis Research Center did achieve objective reverse thrust when the variable fan nozzle was replaced with a fixed conical nozzle that had better inlet recovery with reverse flow. Transient reversals through stall with the variable nozzle were also demonstrated. All of the engine tests were static; the effects of forward speed were not simulated. The Lewis tests are reported in [22].

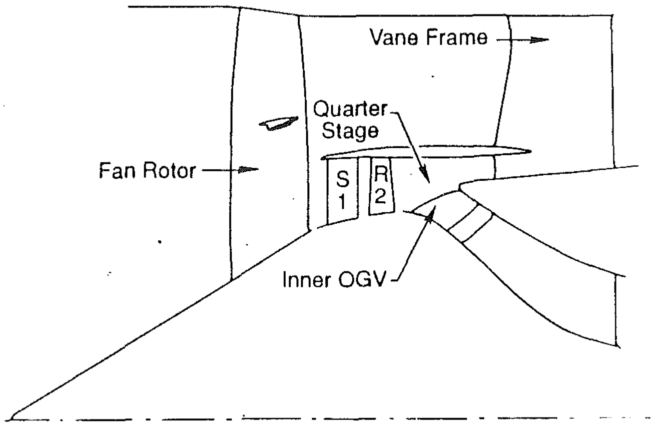

Fig. 11 E^3 fan flowpath

Over-the-Wing (*OTW*) *Fan.* The unusual feature in this fixed-pitch fan is its relatively high core-stream total-pressure ratio combined with a low-bypass pressure ratio. To achieve this the rotor hub turned the flow 16 deg past the axial direction, and the inner outlet guide vane hub inlet Mach number was 0.81. In retrospect we could have gone further, but the poor core-stream performance of Quiet Engine Program Fan B discussed previously kept us cautious. Design details are presented in [23].

There was no component rig test of this fan—only engine tests—so the stall line was not determined. At design speed on an operating line near the design point the airflow was 3.0 percent high at a bypass pressure ratio of 1.38 with an efficiency of 87.2 percent. There were no rakes at the inner outlet guide vane exit, only at core engine inlet. There the measured pressure ratio was 3.4 percent higher than predicted and the efficiency was as predicted. Further test details are given in [24].

2.6 E^3 Fan. The Energy Efficient Engine (E^3) program was a third major contracted effort aimed at the demonstration of component technologies necessary to achieve higher thermodynamic and propulsion efficiencies as well as environmental improvements in future subsonic turbofan engines. These technology advancements were focused on providing at least a 12 percent reduction in specific fuel consumption and at least a 5 percent reduction in direct operating cost as compared to the then-current most fuel-efficient commercial engines.

Studies done in the mid-1970s had indicated that such an engine should have at maximum climb an overall pressure ratio around 38 with a bypass pressure ratio of 1.65 and a bypass ratio near 7. The engine should also be capable of 20 percent thrust growth without major alterations. A compressor pressure ratio of 23 on one spool was accepted as a technology challenge (see Section 3), leaving a corestream pressure ratio of 1.67 for the low-pressure spool. Although this could possibly have been accomplished in a single stage, the growth studies indicated a need for a corestream pressure ratio around 2.0, which was not considered feasible in a single stage with other constraints. The arrangement shown in Fig. 11 was identified as the best solution. If properly proportioned it could provide high efficiency, would not need an interspool bleed valve, and would be an excellent device for preventing dirt from entering the core engine. And with a speed increase and blade shape changes only, it could produce a bypass pressure ratio of 1.75 and a core-stream pressure ratio of 2.05 needed for a growth engine. Design properties are given in Table 5 at the maximum climb design point. Blade shapes were all custom tailored using the best available techniques. The design is described in detail in [25].

A full-scale component test was conducted. The design airflow and bypass pressure ratio were attained at 97.5 percent corrected speed with a bypass efficiency of 88.6 percent. Be-

Table 5 Design properties of E^3 fan

Corrected tip speed, ft/sec (m/s)	1350 (412)
Inlet hub/tip radius ratio	0.342
Inlet tip diameter, in (m)	83.00 (2.108)
Corrected airflow, lb/sec (kg/sec)	1419 (643.6)
Corrected airflow/annulus area lb/sec-ft^2 (kg/sec-m^2)	42.8 (209)
Bypass total-pressure ratio	1.65
Core stream total-pressure ratio	1.67
Bypass ratio	6.8
Quarter stage bypass ratio	0.74
Bypass adiabatic efficiency, %	87.9
Core stream adiabatic efficiency, %	88.5
Rotor inlet tip relative Mach number	1.41
Number of rotor blades	32, 56
Number of vane-frame vanes	34
Number of inner stator vanes	60, 64

cause of power limitations the fan could not be stalled at 100 percent speed, but at 90 percent speed it exhibited 25 percent stall margin above the sea-level-static operating line. Flutter was not observed at any speed. The bypass efficiency peaked at 90 percent between the sea-level-static and cruise operating lines at 90 percent speed and all lower speeds.

The core stream also performed well. At 97.8 percent speed it met the design airflow and pressure ratio with an efficiency of 89.2 percent. Its efficiency was between 89 and 90 percent all along the cruise operating line for engine-matched bypass ratios. It is believed that this efficiency would have been even higher if the inner outlet guide vanes, which had been leaned somewhat to aid in directing the flow radially inward toward the core engine, had been leaned even more, because relatively high losses were measured near the inner wall. Bypass ratio excursions from 4 to 13 were demonstrated by varying the core-stream discharge valve. The quarter-stage stall line exceeded its goal substantially.

Radial distributions of properties were close to design intent in both streams. The part-span shroud loss was found to be 0.3–0.5 point in bypass efficiency.

Further test details are given in [26]. The aero design and performance test results are also summarized in [27]. A recent analysis of the fan rotor blade using a Navier–Stokes code is given in [28].

3 Compressor Research and Development

In the early 1970s, the demise of the American supersonic transport project and an oil supply crisis caused increased attention to be focused on subsonic engines designed for low energy consumption. The need for a suitable advanced compressor for such engines led NASA in early 1975 to request proposals from industry to conduct studies aimed at identifying optimum core compressor configurations for turbofan engines of the 1980s time period. GE Aircraft Engines carried out one such study, and the results strongly influenced the subsequent design of the GE E^3 compressor. Also, a program of experimental aerodynamic research on compressor rear stages was undertaken; this influenced the detailed design of the E^3 compressor. These three efforts will be described in the following subsections.

3.1 Compressor Preliminary Design Study. Engine preliminary design studies underway at the time had identified two different promising engine architectures [29]. In the first, the core compressor was driven by a single-stage turbine, which limited the compressor pressure ratio to about 14. In the second, a more efficient two-stage turbine was employed, which did not limit the compressor pressure ratio. It was visualized that the fan hub could produce a pressure ratio of 1.67, so if the compressor could produce 23, the desired overall pressure ratio 38 could be obtained without the need for booster stages and a variable interspool bleed valve. The compressor preliminary design studies therefore undertook to optimize both compressor types.

There are many parameters to consider when designing a compressor to produce a given pressure ratio. Those evaluated were number of stages, average aspect ratio, average solidity, flow per unit inlet annulus area, exit Mach number, average stator exit flow angle, inlet radius ratio, and flowpath shape. Appropriate values for tip clearances, axial gaps, surface finishes, blading thicknesses, and exit diffuser losses were also specified. Output quantities included the rotative speed required to produce adequate stall margin, efficiency (including the exit diffuser), weight, length, cost and erosion life. Constraints were applied on minimum inlet hub radius and maximum last-stage physical rim speed. The method used to predict compressor stage stall pressure ratio (actually used to predict the rotative speed required to achieve adequate stall margin) was similar to the method described by Koch [30], and the method used to predict efficiency potential was that described by Koch and Smith [31].

Compressor properties also influenced other engine components. For example, high-pressure turbine weight, cost, efficiency, and cooling flows are influenced by compressor rotative speed, and installation weight, cost, and drag are influenced by engine length. These and other features were included in economic studies that yielded overall engine installed weight, fuel usage, initial cost, and direct operating cost deltas.

Initial optimizations were done for a series of 14:1-pressure-ratio compressors and again for a series of 23:1-pressure-ratio machines. In each series the design parameters were grouped to produce three compressor types: a conservative loading compressor (properties like those of the CF6), a nominal loading compressor (like the CFM56) and a maximum loading compressor. Also, to find the effects of the individual independent parameters, the 14:1 nominal loading compressor was re-analyzed while each parameter was changed individually from its conservative loading value to its maximum loading value. In general, the results of these initial optimizations showed that the conservative loading compressors, although having the highest efficiencies, were not quite as attractive as the nominal loading designs because of the other factors considered. The engines with maximum loading compressors were less attractive because of their poor compressor efficiencies. The findings of the one-parameter variation studies showed the following trends:

1 Best efficiency is obtained when core compressors are designed with:

(*a*) Medium average aspect ratios (1.3–2.0)
(*b*) Medium average solidities (1.2–1.5)
(*c*) Medium-to-high reactions (0.5–0.7)
(*d*) Low exit Mach number ($\approx$ 0.28)
(*e*) Low inlet flow/annulus area (35 lb/sec-ft^2) (171 kg/s-m^2)
(*f*) Low inlet radius ratio (i.e., minimum practical value within physical and structural constraints)

2 High blade speed does not penalize performance until front stage tip Mach number is greater than about 1.4.

3 High rpm can increase turbine efficiency, often without reducing compressor efficiency.

4 Fewer stages are less expensive but not necessarily lighter,

and need not involve an efficiency penalty provided that tip speed does not become excessive.

5 Medium-to-high rear radius ratio can be beneficial, provided that it helps maintain the front stage relative tip Mach number below the level at which high shock losses are encountered.

Based on these findings, further studies were done to refine pressure-ratio-23 compressors with 9 and 11 stages (it was observed that a nearly optimum pressure-ratio-14 compressor could be obtained by removing the first stage of an optimum 23:1-pressure-ratio compressor). These refinements included complete vector diagram and preliminary blade shape specifications, as well as off-design operation performance estimates and more detailed mechanical design studies. At the end, although the 11-stage compressor efficiency was estimated to be 0.7 point higher, the economic studies indicated that the engines containing the 9- and 11-stage compressors were virtually equal. On that evidence a 10-stage compressor was identified and recommended. This became known as the AMAC compressor, an acronym for the project title, which was "Advanced Multistage Axial-Flow Core Compressor."

Full details of this study are given in [32].

3.2 Compressor Rear Stage Research. When the preliminary design study described above was carried out, it was assumed that current compressor aerodynamic technology would be improved by the time a new engine went into service. Specifically, it was assumed that end-wall losses would be reduced by 15 percent at constant clearance (clearance reductions were also foreseen). In order to learn how to achieve this loss reduction, NASA sponsored a research program to be carried out in the General Electric four-stage Low Speed Research Compressor (LSRC). The way in which this multistage facility is used to achieve loss reductions is described by Wisler [33]. Actually, most of the NASA-sponsored research carried out under this program is included in [33].

At the time this work was started in 1976, preliminary vector diagrams for the ten-stage AMAC compressor discussed above had been identified, so basic rear-stage dimensionless parameters such as flow coefficient, pressure coefficient, reaction, solidity levels, etc., were known. This permitted the design of the baseline LSRC configuration known as Stage A. At that time GE employed, for rotor blades with moderately high subsonic Mach numbers, airfoils with double-circular-arc thickness distributions on modified circular-arc meanlines. We had learned from previous F101/CFM56 compressor research that meanline modifications in the rotor hub region should provide reduced curvature toward the trailing edge, and this feature was embodied in the AMAC design. The lower Mach numbers of the AMAC stators allowed them to employ circular-arc meanlines with modified 65-series thickness distributions. When designing Stage A, airfoil meanlines were tailored so that at low speed the suction surface velocity distributions had (very nearly) the same shapes as those of corresponding airfoils in the seventh stage of the high-speed AMAC compressor, calculated using the same computer code. This is the basic philosophy employed in low-speed modeling. Obviously this cannot be done when the high-speed flow contains shocks. But for subsonic multistage compressor stages it is believed that viscous loss mechanisms—particularly near the end walls—can be adequately modeled at low speed by this method.

Rotor B, Stator B, and Stator C were candidate designs for reducing endwall losses relative to the baseline Stage A. Rotor B was designed to the same set of vector diagrams as Rotor A, but used a type of meanline in the tip region that unloaded the leading edge and loaded the trailing edge relative to Rotor A. Detailed measurements had indicated that very small blade wakes are present in the tip region of rotors similar in design to Rotor A. (The first documentation of this was by Fessler and Hartmann [34].) This region should, therefore, be able to take higher trailing-edge loading without undue risk of separation. That would reduce maximum surface Mach numbers and, perhaps, tip clearance losses. The modification to the tip region was blended into the pitchline so that Rotor A and Rotor B were identical from the pitchline to the hub.

Stator B embodied blade sections twisted closed locally in the endwall regions similar to those used in a highly loaded single stage that had rather good performance for its loading level [35]. Different vector diagrams were calculated to account for the high values of swirl angle near the end walls. The appearance of Stator B is quite different from that of Stator A because of the twist gradients and because the vane was stacked at 30 percent chord from the leading edge in order to reduce an unfavorable leading-edge lean angle.

Stator C embodied airfoil sections near the endwall that have reduced trailing edge loading and increased leading-edge loading relative to Stator A. These airfoils were designed to the same vector diagrams as Stator A. Details of these designs are given in [36].

The different designs were tested as four-stage groups of identical stages. The Rotor B–Stator A combination was found to have virtually the same peak efficiency as Stage A, but the range of high-efficiency operation was greater and the efficiency was improved 0.3 point at the design point. Stator B tested with Rotor A was an even greater success. In addition to having an increased range of high-efficiency operation, it had a higher peak efficiency and a 0.4–0.5 point efficiency increase at the design point compared to Stage A. Also, its peak pressure rise before stall was 3.2 percent higher. The gains found individually for Rotor B and Stator B did not turn out to be additive, however; the Rotor B–Stator B combination performance was very similar to that of Rotor A–Stator B, perhaps very slightly poorer. Stator C, when tested with Rotor A, was no better than Stator A, perhaps slightly worse. Details of these tests are given in [37–39], with highlights given in [33].

Based on results obtained from these tests, a third rotor, Rotor C, was designed to run with Stator B. It differed from the earlier rotors in two ways: The tip airfoil shape was tailored to cancel tip-clearance-vortex-induced velocity pertubations partially, and also the blade twist was increased to strengthen the flow in the hub region. The effect on overall performance parameters was favorable but small [40, 33]. The overall program is summarized in [41].

3.3 Evolution of the E^3 Compressor. The prospect of achieving a successful engine compressor having a pressure ratio of 23 on a single spool was recognized as very challenging. The highest pressure ratio previously successfully employed was 17 in the TF39 and CF6-6 engines. Stage mismatching difficulties in a multistage compressor at part-load tend to be proportional to the design point overall density ratio, which is about 25 percent higher at 23:1 pressure ratio. This implied that a large fraction of the overall density ratio would have to be produced by stages governed by variable stators. GE correlations and off-design analysis indicated that it should be possible to operate with variability only in the inlet guide vanes and first four stators, but stator 5 and stator 6 were also made variable for development and risk reduction purposes. In addition, provision was made for bleed for use during starting, although most GE aircraft engines have not needed this.

As the E^3 design evolved, some relatively small changes to the AMAC configuration were made; see Table 6. The flowpath of the E^3 compressor is shown in Fig. 12.

In the spring of 1978, during the blading detailed design phase, results from the LSRC program described in Section 3.2 were coming in, indicating that the Stage A-type design that was being employed could be improved upon. Although some concern was expressed, the decision was taken to employ the Rotor B and Stator B modifications in the E^3 design.

Several rig tests and engine tests were scheduled and employed in the compressor development process. The first rig test evaluated the inlet gooseneck and employed the first six stages only. Certain flow weaknesses were uncovered, and blading modifications were made before the first ten-stage test. Also, fear of inadequate low-speed stall margin led to the employment of contingency high-flow rear rotors in the first ten-stage test. As it turned out, the forward stage modifications worked as expected and the rear stages pumped too high; the low-speed stall margin goal was met or exceeded but high-speed stall margin was low. In the second ten-stage build, the front stages were further refined and the original-design rear rotors were employed to achieve a better balance between front and rear block pumping. Test results confirmed that this was achieved. The configuration specified for the engine employed no further changes in the front stages, but additional rear stage tuning was done to lower the pumping a bit more. Complete details of the initial design as well as the modifications leading up to the engine compressor are given in [42].

Table 6 Core compressor design properties

	AMAC	E^3
Total-pressure ratio	23	23
Number of stages	10	10
Corrected tip speed, ft/sec (m/sec)	1540 (469)	1495 (456)
Inlet hub/tip radius ratio	0.496	0.503
Corrected airflow/ annulus area, lb/sec-ft^2 (kg/sec-m^2)	36.5 (178)	38.0 (186)
Rotor 10 exit hub speed, ft/sec (m/sec)	1175 (358)	1157 (353)
Rotor 10 exit radius ratio	0.930	0.931
OGV exit Mach number	0.26	0.30
Number of blades and vanes	1956	1672
Average aspect ratio	1.72	1.48
Average pitchline solidity	1.40	1.36
Adiabatic efficiency, %	86.0	85.7
Stall margin potential, %	18	25

The engine compressor was tested first in a core engine and later in a full turbofan engine known by the acronym ICLS (for Integrated Core/Low Spool). Since data were obtained only near the operating line during these tests, the engine compressor was subsequently tested in the rig to obtain its complete performance map, which is presented in Fig. 13. The efficiencies shown have not been adjusted for interstage instrumentation drag nor the fact that the compressor contained two variable stator rows that could have been fixed because their variability was not exercised during the mapping. The fully adjusted peak adiabatic efficiency for the core engine test was 86.1 percent, which corresponds to a polytropic efficiency of 90.4 percent.

The efficiencies for the rig test are lower than those of the engine tests for two reasons: Reynolds number and clearance. At high speeds the rig was run about 1/3 atmosphere inlet pressure and with refrigerated inlet temperature, which lowered the Reynolds number to about 40 percent of the engine value. More significantly, the lower inlet temperatures plus wear and tear on the hardware caused the rig to run with substantially larger clearances.

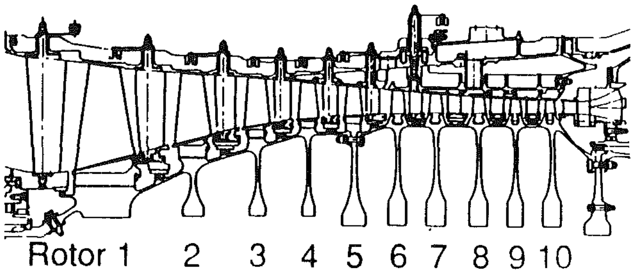

Fig. 12 E^3 compressor cross section

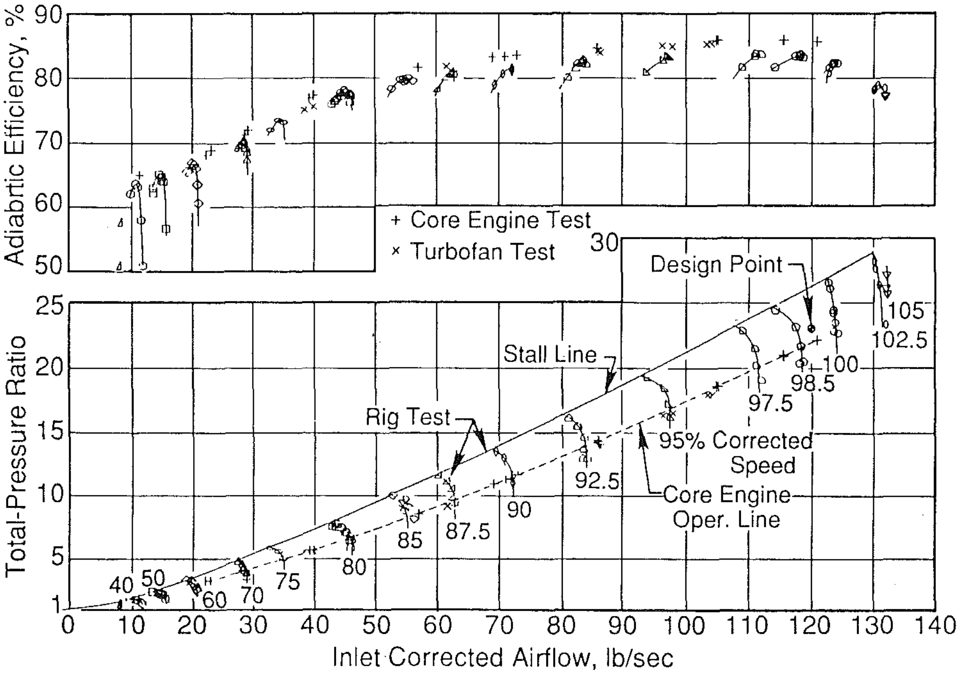

Fig. 13 E^3 compressor performance map

It is believed that the demonstrated stall pressure ratio of almost 29 is a world record for a single-spool compressor. Rapid starting of both engines without bleed was demonstrated.

References [43–45] describe tests in the core engine, turbofan engine, and rig. During this final rig test the compressor was intentionally held in stall for several seconds at speeds up to 98.5 percent while surge and rotating stall data were recorded with dynamic instrumentation. Analyses of these data are given in [46].

The success of the E^3 compressor led to its selection for use (scaled) in the GE90 engine.

4 Casing Boundary Layer Control Research

4.1 Initial Test Series. One of the original seven tasks of work requested in 1964 involved research on blowing and bleeding at the tip of an isolated high-aspect-ratio rotor. The rotor had a corrected tip speed of 1120 ft/sec (341 m/s) and a corrected airflow/annulus area of 39.5 lb/sec-ft^2 (193 kg/s-m^2) to produce a tip relative inlet Mach number of 1.2. The design total-pressure ratio was 1.47, radially constant. The tip solidity was unity, and the 1.77-in. (45-mm) chord was radially constant. The hub/tip radius ratio was 0.5, there were 60 double-circular-arc blades of aspect ratio 4.5, and there was a part-span shroud at 60.5 percent span. The shroud was roughly elliptical in cross section, with a length (parallel to the local blade chord) of 43 percent of the blade chord, and a thickness of 19 percent of the shroud length. The shroud's major axis was aligned with the local design streamline meridional flow angle. The average tip clearance at design speed was 1.5 percent chord.

The blowing insert contained three rows of tapered, converging-area holes. These holes were oriented so as to direct the blowing flow radially inward at a 20 deg angle from a cylindrical surface and also to impart 30 deg of counterswirl. The length of the holes was about equal to the blade chord. The first two rows of holes discharged forward of the rotor's leading edge, while the third row discharged over the rotor tip. The area of the holes was set so that, with an assumed flow coefficient of 0.92, approximately 4 percent of design airflow would be passed with the holes just choked.

The bleed insert was made of 0.062-in. (1.6-mm) hexagonal honeycomb material extending from just aft of the rotor's leading edge to just aft of the trailing edge. The center lines of the honeycomb cells were tilted 70 deg from radial in the tangential direction in order to recover better the energy of the tangential component of the flow at the tip of the rotor. The length of the cells was about-half of the blade chord. The available bleed flow area was sized so that up to 4 percent of the compressor design airflow could be extracted. Both inserts were surrounded on the outside by a large plenum manifold.

With a plain casing and no inlet distortion, throttling was limited at all speeds by rotating stall. With an array of three hot-wire anemometers it was determined that the rotating stall was initiated at the part-spans shroud rather than at the tip. When a boundary layer trip of 17 percent chord radial extent was added to the casing 5.3 chords ahead of the rotor, the stall line on the map was not affected, giving added evidence that stall was not being initiated at the tip. This was a distressing finding for a research program that was supported to evaluate the effects of casing blowing and bleeding on stall inception. However, it turned out that the rotor did become tip critical when a 54 percent solidity tip-radial distortion screen covering the outer 40 percent of the annulus area was employed at the 5.3-chord upstream location. This caused a substantial lowering of the stall line, and all of the casing treatments were evaluated with that screen present.

Both blowing and bleeding were found to improve the stall line significantly, with the maximum benefits coming at or near the maximum blow/bleed flow rates. But the unexpected finding was that there was a substantial stall line improvement compared to the plain casing configuration even when there was no air being blown or bled. This finding in 1967 led NASA to initiate extensive research on casing treatments, both in-house and with contractors, aimed at understanding this phenomenon and identifying geometries that maximize the stall line benefit while minimizing the efficiency penalty.

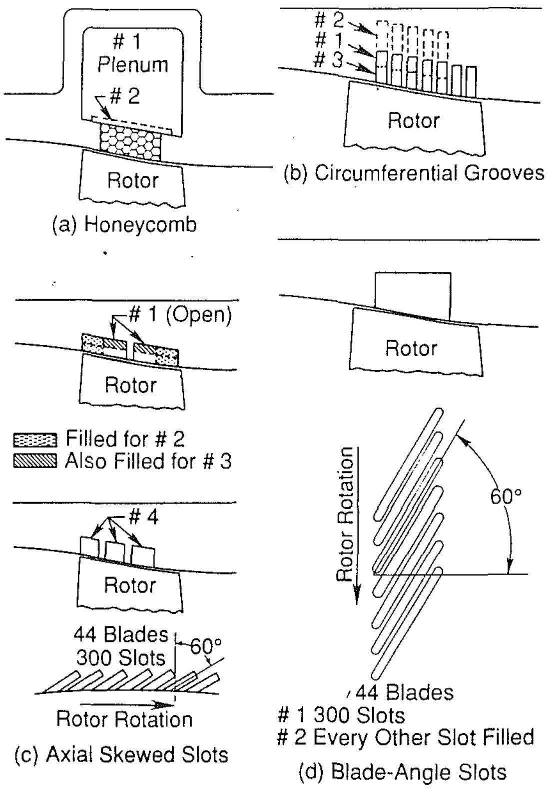

(a) Honeycomb

(b) Circumferential Grooves

(c) Axial Skewed Slots

(d) Blade-Angle Slots

Fig. 14 Casing Treatments for 1400 fps stage

The initial test series is described in [47–52]. Further tests were carried out in the same rig to evaluate the effects of blocking off some of the blow holes with outer bands, extending the honeycomb forward, reducing the size of the plenum, adding circumferential or axial baffles in the smaller plenum, and two other inserts with radial holes. Some observations were:

1 For the tapered-hole configuration, recirculation appeared to be a necessity for stall line improvement, and the amount of the improvement was directly related to the recirculation. With all holes banded off there was no improvement.

2 The plenum volume around the honeycomb could be made quite small with no change in the stall line improvement, but when the plenum volume was zero, no improvement was obtained.

3 The baffles reduced the improvement.

4 The radial-hole inserts gave no improvement.

More detailed results of these further tests are reported in [53].

4.2 Higher Speed Stage Tests. The research described above occurred while tests of the 1400- and 1500-fps stages described in Sections 2.2 and 2.3 were being planned, and consequently those tests were expanded to include casing treatment research. The treatments tested are described in Fig. 14. The honeycomb insert had 0.125-in. (3.2-mm) hexagonal cells tilted 70 deg from radial in the same direction as described in Section 4.1.

All of the treatments were tested in the 1400-fps stage without inlet guide vanes. The results at design speed are summarized in Table 7. The distortion screens were located one rotor di-

Table 7 1400 fps stage casing treatment effects at design speed

Casing Treatment	Undistorted Inflow Stall Marg.,%	Undistorted Inflow Peak Eff.,%	Tip-Radial Distortion Stall Marg.,%	Tip-Radial Distortion Peak Eff.,%	Circumferential Distortion Stall Marg.,%	Circumferential Distortion Peak Eff.,%
Plain Casing	21.3	85.0	3.5	80.0	9.0	80.0
Honeycomb #1	27.7	83.2	15.0	79.7		
Honeycomb #2	29.0	84.3	11.7	79.6		
Circumferential Grooves #1	26.4	84.9	9.5	80.8		
Circumferential Grooves #2	27.8	85.3	8.4	81.3		
Circumferential Grooves #3	25.6	85.0	10.8	80.8		
Axial Skewed Slots #1	26.0	83.0	16.3	79.3		
Axial Skewed Slots #2	29.0	83.9			14.0	82.8
Axial Skewed Slots #3	26.7	84.4	9.4	79.5		
Axial Skewed Slots #4	25.5	83.3	14.1	79.6		
Blade-Angle Slots #1	26.2	84.2	14.6	78.9		
Blade-Angle Slots #2	25.8	84.5	12.0	79.0		

ameter upstream of the rotor leading edge in a cylindrical annulus extension and had 54 percent solidity. The tip-radial screen covered the outer 40 percent of the annulus area, and the circumferential screen covered 90 deg of circumference from hub to tip. A full-annulus support screen with 17 percent solidity was in place for all tests. The operating line above which stall margin was measured passes through the stage design point.

Table 7 indicates that all of the treatments gave worthwhile stall margin improvements with efficiency penalties generally less than 2 points.[1]

The circumferential groove treatments gave no measurable efficiency penalties. Efficiencies with distortion present are difficult to measure accurately (particularly with circumferential distortions), so the indicated increases may not be real. The only configuration that employed a plenum (Honeycomb #1) was not noticeably better than the others for this test stage even though a plenum had been found to be essential during the further tests of the rotor of Section 4.1.

The 1500-fps stage was tested only with the Blade-Angle Slot #1 treatment, but it was tested both with and without inlet guide vanes installed. Results at design speed are summarized in Table 8. Significant stall margin gains from treatment were found in all cases without excessive efficiency penalties. With a plain casing and undistorted inflow, the inlet guide vanes hurt stall margin, but not with distortion present. Apparently the thickening of the casing boundary layer caused by the inlet guide vanes hurt this tip-critical rotor, but that effect was overwhelmed by the inflow distortions when they were added. It had been expected that the inlet guide vanes would help stall margin with circumferential distortion present by straightening the flow into the rotor. But flow angle measurements at rotor inlet for the near-stall operating points showed little difference in the swirl pattern with and without the inlet guide vanes. Apparently the inlet guide vanes were far enough forward that the swirl could re-establish itself with only a 90 deg distortion (see Fig. 7). More details of this research, including results at 70 and 90 percent speeds, are given in [11].

Table 8 1500 fps stage casing treatment and inlet guide vane effects at design speed

Configuration	Undistorted Inflow Stall Marg.,%	Undistorted Inflow Peak Eff.,%	Tip-Radial Distortion Stall Marg.,%	Tip-Radial Distortion Peak Eff.,%	Circumferential Distortion Stall Marg.,%	Circumferential Distortion Peak Eff.,%
No Inlet Guide Vanes, Plain Casing	18.2	84.5	1.7	77.4	8.1	82.4
No Inlet Guide Vanes, Blade-Angle Slots #1	36.0	82.6	14.6	76.8	18.5	81.0
With Inlet Guide Vanes, Plain Casing	12.9	83.7	3.6	78.0	7.7	80.0
With Inlet Guide Vanes, Blade-Angle Slots #1	32.0	82.7	16.0	77.0	15.4	80.9

4.3 Flow Details With Casing Treatments.

By 1971, casing treatments of various kinds had been found to be effective in delaying stall, but there was little knowledge about how they worked. So General Electric proposed a research program employing its large 60-in. (1.524-m)-dia Low Speed Research Compressor. Existing blades with 4.58-in. (116-mm) chord would be used; this was sufficiently large so that detailed measurements could be taken in casing treatment cavities, and the transparent casing construction would permit tuft studies. NASA supported such an approach, but there was a potential problem: All casing treatment demonstrations until then had been done with transonic rotors, and if compressibility effects, such as cavity resonances, were critical to success, then low-speed research would be of little value. So the program was structured to have an early demonstration of stall line improvement, and if that did not happen the work could be stopped without much cost. As it turned out, each of the treatments tried gave about the same stall line improvement and efficiency loss as it had yielded in previous high-speed tests, so cavity resonance was quickly eliminated as a major factor.

The single-stage test geometry is described in Table 9. These airfoils are the same as the LAR airfoils described in [54], but the solidity was increased.

The main casing treatment configurations investigated were:

1 Circumferential grooves resembling the forward five #1 grooves in Fig. 14(*b*).

2 Axial skewed slots resembling the #2 configuration in Fig. 14(*c*).

3 Wide blade-angle slots resembling the #1 slots in Fig. 14(*d*) except the slot angle was 53.5 deg, there were 40 percent fewer slots per blade, and an axial partition existed near mid-chord as with the axial skewed slots.

Other variations of these were also investigated.

Numerous static pressure taps were included on and in the treatments and on two rotor blades. Hot-film anemometers and tufts were also employed to discern the cavity flow patterns. Some significant findings were:

1 Casing treatments often increase rotor and stage pressure rises at the stalling flow rate of the untreated stage, as if incipient separations are being suppressed.

2 Casing treatments increase annulus wall pressure gradients in the trailing-edge region, as if wall stall effects are being suppressed.

3 Pressure-surface pressures on the rotor blades close to the tips are substantially higher in the presence of axial skewed slot or blade-angle slot treatments than with a plain casing and may be higher than the free-stream relative total pressure. This is seen in Fig. 15 for the slotted treatments.

---

[1] Tabulated efficiencies with casing treatment and undistorted inflow have been adjusted downward by 0.2 to 0.4 point to account for spurious indicated improvements in hub-element efficiencies.

Table 9 Blade Geometry for low-speed research compressor casing treatment phenomena investigation

	Inlet Guide Vanes		Rotor		Stator	
Number of blades	40	40	54	54	53	53
Radius ratio	0.7	1.0	0.7	1.0	0.7	1.0
Camber, deg.			41.7	23.1	32.6	31.6
Stagger, deg.	13.2	21.9	16.4	43.4	29.9	41.5
Solidity	1.5	1.5	1.88	1.31	1.85	1.30
Thickness/ chord	0.1	0.1	0.13	0.045	0.04	0.12
Aspect ratio			1.96	1.96	1.94	1.94
Tip clearance/ chord				0.016		

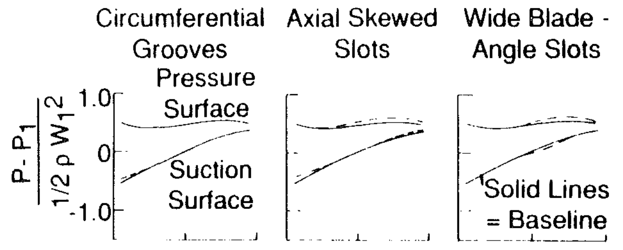

(a) 17% Span from Tip

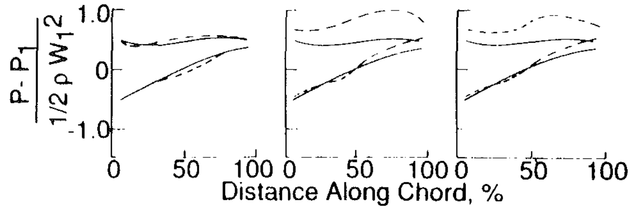

(b) 3% Span from Tip

Fig. 15 Casing treatment influence on blade surface pressure distributions at baseline stall throttle setting

4 Greater suction-surface adverse pressure gradients near the trailing edge can be sustained when a treatment is present; see Fig. 15.

5 Velocity components in axial skewed and blade-angle slots are highly random, and do not seem to correlate with periodic effects such as blade passing.

6 Velocity components in circumferential grooves are primarily circumferential, at a level close to the mean circumferential velocity in the free stream. Amplitude fluctuations at blade-passing frequency are evident. Velocity components into and out of the grooves are relatively small.

More details and much more data are given in [55]. A condensed version of this work is given in [56].

General Electric has not employed casing treatment in its commercial engines but has used it in some military engines.

4.4 Hub Treatment Unsuccessful Attempt. Based on the demonstrated success of casing treatment as a means for increasing compressor stall margin for tip-critical single stages, an experimental program was undertaken to investigate the potential benefits of applying similar treatments to those stages where stall originates in the stator hub region. A 0.5 radius-ratio two-stage Low Speed Research Compressor configuration, which had been used previously and which showed evidence of stall inception in the hub region, was chosen as the test vehicle. This fan configuration was modified by removing the stator hub shrouds and replacing them with rotating hub spools, which incorporated stator hub treatment. A smooth-spool (baseline) configuration, a circumferential groove treatment configuration, and a baffled wide-blade-angle slot treatment configuration were tested.

Although extensive tuft probing showed that the test vehicle was indeed hub critical, the performance data, obtained for the baseline and the two treatment configurations, showed that stator hub treatment did not modify performance in any discernible fashion. It was suspected that stall might be originating in the rotors rather than the stators. The near-hub rotor 1 *D*-factor near stall was 0.65 compared to 0.71 for stator 1; both values in stage 2 were somewhat lower. Therefore, the blades and vanes of the test vehicle were restaggered in order to load the stators relative to the rotors. Tuft probing showed that the flow in the stator hub region was then worse than before; however, performance was not affected by the treatment. The blades and vanes were then returned to their original staggers and one-half of the vanes in each stator were removed, raising the stator diffusion factors substantially. For this case the flow in the stator hub region was in even worse shape, aerodynamically speaking, with large regions of separation and backflow appearing on the stator suction surfaces. However, just as for the other configurations tested, stator hub treatment did not modify the onset, extent, or severity of flow unsteadiness. It did not delay the point of onset of rotating stall, nor did it modify the performance of the compressor in any discernible fashion.

In retrospect, it seems likely that rotating stall was being initiated in the inner one-third span of rotor 1, which was designed to be rather heavily loaded. The energizing of the hub flow in the following stators by the hub treatment must have been too localized to affect this. This work is reported in [57].

5 Concluding Remarks

Some conclusions reached from the research described in this paper are:

1 Transonic rotor airfoil shapes can significantly affect the trend of efficiency with speed (Fig. 6).

2 Increases in blade camber cause peak efficiencies to occur closer to the stall line but may not raise the stall line and may cause a peak efficiency level reduction (Figs. 4 and 5).

3 Addition of a stator downstream of a rotor can affect the performance of the rotor (Sect. 2.2).

4 Variable inlet guide vanes can significantly affect the flow pumping rate of a stage but the effect on the stage's stall line is minor (Fig. 8).

5 If designed with excessive internal contraction, rotors with tip Mach numbers around 1.5 may exhibit discontinuous operation transitioning from an unstarted to a started mode of operation. A part-span shroud may cause excessive internal contraction if the airfoil shape adjacent to it is not properly designed (Sec. 2.4-C).

6 Variable-pitch fans with variable fan nozzles can produce worthwhile reverse thrust levels, but the scope of the program did not permit a complete feasibility demonstraction (Sect. 2.5-UTW).

7 High efficiencies and excellent operability features with growth potential can be obtained from a fan with part-span shrouds and a quarter stage, (Sect. 2.6).

8 Unconventional compressor airfoil shapes in the end-wall regions can provide performance improvements (Sect. 3.2.).

9 A compact single-spool multistage compressor with a pressure ratio of 23 and a polytropic efficiency greater than 90 percent has been developed (Figs. 12 and 13).

10 Casing treatments can provide significant stall line enhancements with modest efficiency losses (Tables 7 and 8).

Acknowledgments

As a member of industry, the author would like to thank NASA for sponsoring the valuable work that has been reported herein. Many NASA personnel, too numerous to mention and thank individually, worked with us during the course of this work, but Bill Benser and Mel Hartmann are especially deserving of thanks.

The author would also like to thank all of the many General Electric contributors, particularly those whose names appear as authors in the list of references. Also, he would like to thank General Electric management for giving him the responsibility for directing the preliminary and detailed aerodynamic designs of all of the fans and compressors described.

References

NOTE: NASA Contractor Reports may be obtained from: Center for Aerospace Information, P. O. Box 8757, Baltimore, MD 21240-0757.

1 Seyler, D. R., and Smith, L. H., Jr., "Single Stage Experimental Evaluation of High Mach Number Compressor Rotor Blading, Part 1-Design of Rotor Blading," NASA CR-54581, Apr. 1967.

2 Seyler, D. R., and Gostelow, J. P., "Single Stage Experimental Evaluation of High Mach Number Compressor Rotor Blading, Part 2—Performance of Rotor 1B," NASA CR-54582, Sept. 1967.

3 Gostelow, J. P., and Krabacher, K. W., "Single Stage Experimental Evaluation of High Mach Number Compressor Rotor Blading, Part 3—Performance of Rotor 2E," NASA CR-54583, Sept. 1967.

4 Krabacher, K. W., and Gostelow, J. P., "Single Stage Experimental Evaluation of High Mach Number Compressor Rotor Blading, Part 4—Performance of Rotor 2D," NASA CR-54584, Oct. 1967.

5 Gostelow, J. P., and Krabacher, K. W., "Single Stage Experimental Evaluation of High Mach Number Compressor Rotor Blading, Part 5—Performance of Rotor 2B," NASA CR-54585, Oct. 1967.

6 Gostelow, J. P., Krabacher, K. W., and Smith, L. H., Jr., "Performance Comparison of High Mach Number Compressor Rotor Blading," NASA CR-1256, Dec. 1968.

7 Koch, C. C., Bilwakesh, K. R., and Doyle, V. L., "Task I Stage Final Report, Evaluation of Range and Distortion Tolerance for High Mach Number Transonic Fan Stages," Vol. 1, NASA CR-72806, Aug. 1971.

8 Doyle, V. L., and Koch, C. C., "Design Report, Evaluation of Range and Distortion Tolerance for High Mach Number Transonic Stages," NASA CR-72720, July 1970.

9 Bilwakesh, K. R., "Task II Stage Data and Performance Report for Undistorted Inlet Flow Testing, Evaluation of Range and Distortion Tolerance for High Mach Number Transonic Fan Stages," Vol. 1, NASA CR-72787, Jan. 1971.

10 Bilwakesh, K. R., Koch, C. C., and Prince, D. C., "Final Report on Task II: Performance of a 1500-Foot-Per-Second Tip Speed Transonic Fan Stage with Variable Geometry Inlet Guide Vanes and Stator, Evaluation of Range and Distortion Tolerance for High Mach Number Transonic Fan Stages," NASA CR-72880, Jun. 1972.

11 Tesch, W. A., "Task IV: Stage Data and Performance Report for Casing Treatment Investigations, Evaluation of Range and Distortion Tolerances for High Mach Number Transonic Fan Stages," Vol. 1, NASA CR-72862, May 1971.

12 Tesch, W. A., and Doyle, V. L., "Task II Stage Data and Performance Report for Inlet Flow Distortion Testing, Evaluation of Range of Distortion Tolerance for High Mach Number Transonic Fan Stages," Vol. 1, NASA CR-72786, Jan. 1971.

13 The General Electric Co., "Experimental Quiet Engine Program, Phase I—Engine Design Report, Vol. I. Sect. 4.0—Fan Aerodynamic Design," NASA CR-72967, Mar. 15, 1970.

14 Giffin, R. G., Parker, D. E., and Dunbar, L. W., "Experimental Quiet Engine Program, Aerodynamic Performance of Fan A," NASA CR-120858, May 1971.

15 Giffin, R. G., Parker, D. E., and Dunbar, L. W., "Experimental Quiet Engine Program, Aerodynamic Performance of Fan B," NASA CR-72993, Aug. 1972.

16 Giffin, R. G., Parker, D. E., and Dunbar, L. W., "Experimental Quiet Engine Program, Aerodynamic Performance of Fan C," NASA CR-120981, Aug. 1972.

17 Jutras, R. R., Fost, R. B., Chi, R. M., and Beacher, B. F., "Subsonic/Transonic Stall Flutter Investigation of a Rotating Rig," NASA CR-174625, Feb. 1981.

18 Smith, L. H., "Some Aerodynamic Design Considerations for High Bypass Ratio Fans," presented at the Second International Symposium on Air Breathing Engines, Sheffield, United Kingdom, Mar. 24-29, 1974.

19 The General Electric Company, "The Aerodynamic and Mechanical Design of the QCSEE Under-the-Wing Fan," NASA CR-135009, Mar. 1977.

20 Giffin, R. G., McFalls, R. A., and Beacher, B. F., "Aerodynamic and Aeromechanical Performance of a 50.8-cm (20-in) Dia. 1.34 PR Variable Pitch Fan With Core Flow," NASA CR-135017, Aug. 1977.

21 The General Electric Company, "Under-the-Wing (UTW) Engine Boilerplate Nacelle Test Report, Vol. II, Aerodynamics and Performance," NASA CR-135250, Dec. 1977.

22 Samanich, D. C., Reemsnyder, X. X., and Bloomer, H. E., "Reverse Thrust Performance of the QCSEE Variable Pitch Turbofan Engine," NASA TM 81558; also SAE Paper No. 801196, Oct. 1980

23 The General Electric Company, "Over-the-Wing (OTW) Propulsion System Test Report, Vol. II-Aerodynamics and Performance," NASA CR-135324, July 1978.

24 The General Electric Company, "Over-the-Wing (OTW) Propulsion System Test Report, Vol. II—Aerodynamics and Performance," NASA CR-135324, July 1978.

25 Sullivan, T. J., Leubering, G. W., and Gravitt, R. D., "Energy Efficient Engine, Fan Test Hardware Detailed Design Report," NASA CR-165148, Oct. 1980.

26 Cline, S. J., Halter, P. H., Kutney, J. T., Jr., and Sullivan, T. J., "Energy Efficient Engine, Fan and Quarter-Stage Component Performance Report," NASA CR-168070, Jan. 1983.

27 Sullivan, T. J., and Hager, R. D., "The Aerodynamic Design and Performance of the General Electric/NASA E^3 Fan," Paper No. AIAA-83-1160, Jun. 1983.

28 Jennions, I. K., and Turner, M. G., "Three-Dimensional Navier-Stokes Computations of Transonic Fan Flow Using an Explicit Flow Solver and an Implicit k-ϵ Solver," ASME JOURNAL OF TURBOMACHINERY, Vol. 115, 1993, pp. 261-272.

29 Neitzel, R. E., Hirschkron, R., and Johnston, R. P., "Study of Turbofan Engines Designed for Low Energy Consumption," NASA CR-135053, 1976.

30 Koch, C. C., "Stalling Pressure Rise Capability of Axial Flow Compressor Stages," ASME *Journal of Engineering for Power*, Vol. 103, Oct. 1981, p. 645.

31 Koch, C. C., and Smith, L. H., Jr., "Loss Sources and Magnitudes in Axial-Flow Compressors," ASME *Journal of Engineering for Power*, Vol. 98, No. 3, 1976, p. 411.

32 Wisler, D. C., Koch, C. C., and Smith, L. H., Jr., "Preliminary Design Study of Advanced Multistage Axial Flow Core Compressors," NASA CR-135133, Feb. 1977.

33 Wisler, D. C., "Loss Reduction in Axial-Flow Compressors Through Low-Speed Model Testing," ASME *Journal of Engineering for Gas Turbines and Power*, Vol. 107, 1985, p. 354.

34 Fessler, T. E., and Hartmann, M. J., "Preliminary Survey of Compressor Rotor-Blade Wakes and Other Flow Pheonomena With a Hot-Wire Anemometer," NACA RM E56A13, June 1956.

35 Brent, J. A., and Clemmons, D. R., "Single-Stage Experimental Evaluation of Tandem-Airfoil Rotor and Stator Blading for Compressors," NASA CR-134713, Nov. 1974.

36 Wisler, D. C., "Core Compressor Exit Stage Study, Vol. I—Blading Design," NASA CR-135391, Dec. 1977.

37 Wisler, D. C., "Core Compressor Exit Stage Study, Vol. II—Data and Performance Report for the Baseline Configurations," NASA CR-159498, Nov. 1980.

38 Wisler, D. C., "Core Compressor Exit Stage Study, Vol. III—Data and Performance Report for Screening Test Configurations," NASA CR-159499, Nov. 1980.

39 Wisler, D. C., "Core Compressor Exit Stage Study, Vol. IV—Data and Performance Report for the Best Stage Configuration," NASA CR-165357, Apr. 1981.

40 Wisler, D. C., "Core Compressor Exit Stage Study, Vol. V—Design and Performance Report for the Rotor C/Stator B Configurations," NASA CR-165358, May 1981.

41 Wisler, D. C., "Core Compressor Exit Stage Study, Vol. VI—Final Report," NASA CR-165554, Dec. 1981.

42 Holloway, P. R., Knight, G. L., Koch, C. C., and Shaffer, S. J., "Energy Efficient Engine, High Pressure Compressor Detail Design Report," NASA CR-165558, May 1982.

43 Stearns, E. M., and the GE E^3 Staff, "Energy Efficient Engine, Core Design and Performance Report," NASA CR-168069, Dec. 1982.

44 Stearns, E. M., and the GE E^3 Staff, "Energy Efficient Engine, Integrated Core/Low Spool Design and Performance Report," NASA CR-168211, Feb. 1985.

45 Hosny, W. M., Lenhardt, C. H., Liu, H. T., Lovell, R. C., and Steenken W. G., "Energy Efficient Engine, High Pressure Compressor Component Performance Report," NASA CR-174955, Aug. 1985.

46 Dvorak, S. D., Hosny, W. M., and Steenken, W. G., "E^3 10C Compressor Test, Analysis of High-Speed Post-stall Data," NASA CR-179521, Oct. 1986.

47 Giffin, R. G., and Smith, L. H., Jr., "Experimental Evaluation of Outer Case Blowing or Bleeding of Single Stage Axial Flow Compressor, Part I—Design of Rotor and Bleeding and Blowing Configurations," NASA CR-54587, Apr. 1966.

48 Koch, C. C., and Smith, L. H., Jr., "Experimental Evaluation of Outer Case Blowing or Bleeding of Single Stage Axial Flow Compressor, Part II—Performance of Plain Casing Insert Configuration With Undistorted Inlet Flow and Boundary Layer Trip," NASA CR-54588, Aug. 1968.

49 Koch, C. C., and Smith, L. H., Jr., "Experimental Evaluation of Outer Case Blowing or Bleeding of Single Stage Axial Flow Compressor, Part III—Performance of Blowing Insert Configuration No. 1," NASA CR-54589, Nov. 1968.

50 Koch, C. C., and Smith, L. H., Jr., "Experimental Evaluation of Outer Case Blowing or Bleeding of Single Stage Axial Flow Compressor, Part IV—

Performance of Bleed Insert Configuration No. 3," NASA CR-54590, Aug. 1968.

51 Koch, C. C., "Experimental Evaluation of Outer Case Blowing or Bleeding of Single Stage Axial Flow Compressor, Part V—Performance of Plain Casing Insert Configuration With Distorted Inlet Flow," NASA CR-54591, May 1969.

52 Koch, C. C., "Experimental Evaluation of Outer Case Blowing or Bleeding of Single Stage Axial Flow Compressor, Part VI, Final Report," NASA CR-54592, Jan. 1970.

53 Bailey, E., and Voit, C. H., "Some Observations of Effects of Porous Casings on Operating Range of a Single Axial-Flow Compressor Rotor," NASA TM X-2120, Oct. 1970.

54 Smith, L. H., Jr., "Casing Boundary Layers in Multistage Axial-Flow Compressors," *Flow Research on Blading*, L. S. Dzung, ed., Elsevier Publishing, Amsterdam, Netherlands, 1970.

55 Prince, D. C., Jr., Wisler, D. C., and Hilvers, D. E., "Study of Casing Treatment Stall Margin Improvement Phenomena," NASA CR-134552, Mar. 1974.

56 Prince, D. C., Jr., Wisler, D. C., and Hilvers, D. E., "A Study of Casing Treatment Stall Margin Improvement Phenomena," ASME Paper No. 75-GT-60, Mar. 1975.

57 Wisler, D. C., and Hilvers, D. E., "Stator Hub Treatment Study," NASA CR-134729, Dec. 1974.

A Review of Research on Turbomachinery at MIT Traceable to Support From Mel Hartmann

J. L. Kerrebrock
Department of Aeronautics and Astronautics,
Massachusetts Institute of Technology,
Cambridge, MA 02139

Research conducted at MIT since 1968 stemming from early initiatives on the Blowdown Compressor Experiment and on transonic three-dimensional CFD is reviewed from the viewpoint of the consequences of enlightened support of research by exceptionally capable leaders of government research. Among the consequences in this case are development of detailed understanding of the unsteady flows in transonic compressors and their contribution to losses, and the ability to compute the three-dimensional transonic flow in such machines. Analogous results for turbines include the ability to measure and compute the unsteady heat flux distribution on turbine blades and vanes as well as the flow field. In addition to these research results, the programs traceable to Mel Hartmann's early support have produced more than seven faculty members who continue to teach and conduct research in aircraft propulsion and closely related fields, and a corresponding number of students.

Introduction

This paper is intended as an historical review of research conducted at MIT in the Department of Aeronautics and Astronautics, which is traceable to either technical or financial support from Mel Hartmann. It is not a scholarly work in the usual sense, since most of the work that will be mentioned has been published in some scholarly journal, and since the logic of the contributions will not be found in complete form in this paper. But it is the hope of the author, who has been involved with much of the work in one way or another, that a connected account, that is a kind of research genealogy, will help to show the effect that dedicated and exceptionally capable leaders of government research can have on research efforts. There is need for such examples at a time when criticism of our federal research institutions and their staff is much more common than praise.

As is often the case, no one person is responsible for the work to be described, and indeed I am sure that Mel would not want it said, incorrectly, that he was. It was Dr. John C. Evvard, one-time head of supersonic research and later Chief Scientist of NASA Lewis Research Center, who initiated the programs I will describe. He did this by placing at MIT a stepfunded research grant to support research in propulsion and power generation, in the amount of $100,000 per year. This was in 1968 when that was a good bit of money. The grant was written so that I, as Principle Investigator, could apportion the money amongst various research efforts more or less as I judged appropriate. John retained a veto but seldom exercised it. After about three years, the responsibility for this grant was transferred to Mel Hartmann, because it had developed in the direction of turbomachinery fluid mechanics, as will become clear as I describe its evolution. For the remainder of the period of the grant, Mel was a champion of our work and of this flexible form of research funding. Furthermore, his own keen technical insight had a strong positive influence on the research.

Although a number of other research threads were explored, the grant initially supported two main efforts, which were almost entirely novel at the time. These were first the study of unsteady flow in transonic compressors, enabled by the development of the Blowdown Compressor Experiment (BDC), and second the application of the then newly emerging techniques of computational fluid mechanics (CFD) to the three-dimensional flow in transonic compressors. I was the originator, with my students, of the work on the BDC, while the CFD work was initiated by Prof. David A. Oliver and his doctoral student Panos Sparis. My intention is first to describe these two original efforts and their interrelationship, then briefly outline some of the many research activities they have spawned. As a help to understanding of the work and the interrelationships, I offer the schematic diagram of Fig. 1, to which I will refer as I discuss the various research activities. The names associated with each of the efforts on the figure are those of the students whose theses represented the bulk of the research effort. In most cases, one or more faculty members, and in some cases a research staff member, shared the work, the responsibility, and the credit, as can be seen from the list of references.

The Blowdown Compressor Experiment

This approach to compressor research was founded in the desire to examine the unsteady flow in transonic compressors in detail, resolving phenomena that occur at the blade-passing and even shorter time scales. Since this was the focus of the work rather than steady-state performance or durability, it was

---

Contributed by the International Gas Turbine Institute and presented at the 38th International Gas Turbine and Aeroengine Congress and Exposition, Cincinnati, Ohio, May 24-27, 1993. Manuscript received at ASME Headquarters March 17, 1993. Paper No. 93-GT-328. Associate Technical Editor: H. Lukas.

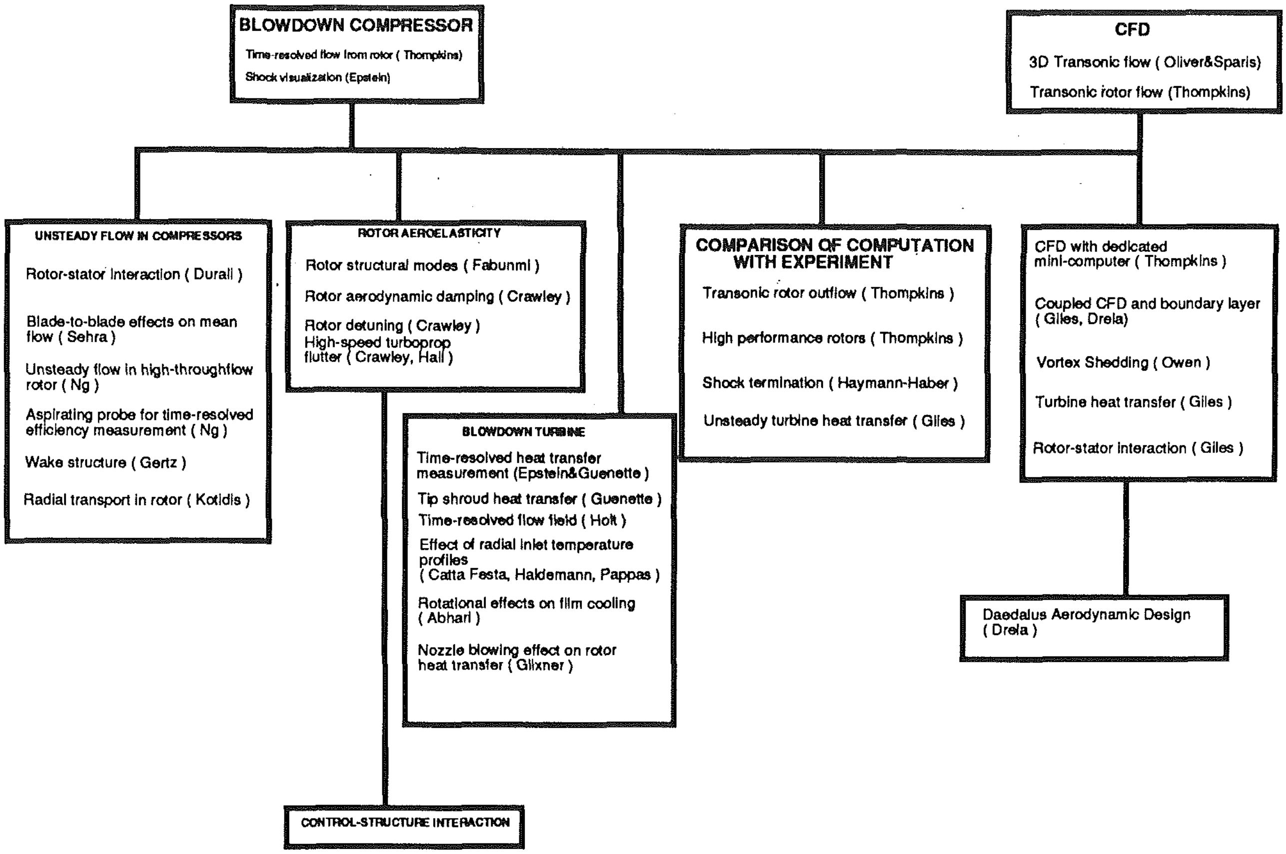

Fig. 1 Schematic of research at MIT, which stemmed from two original research initiatives, the blowdown compressor experiment and three-dimensional transonic CFD, supported by NASA-Lewis

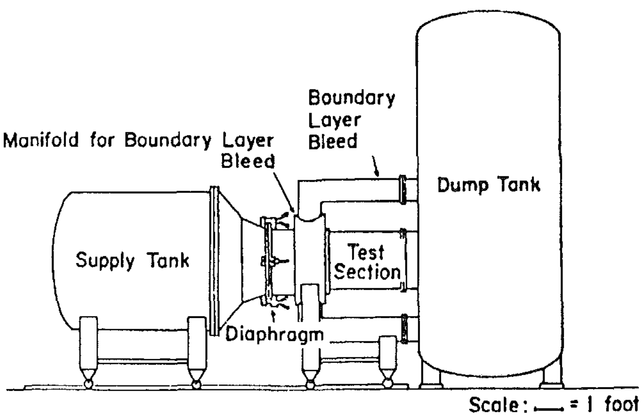

Threshold 9. Brightness 9, Halftone pattern spiral, Normal Detail 2/3/93 7:06 PM

Fig. 2 Schematic diagram of the blowdown compressor experiment

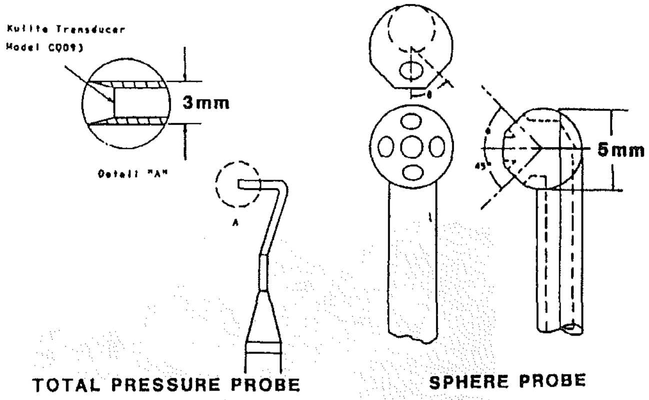

Threshold 4. Contrast 3, Brightness 9, Halftone Pattern Spiral, Normal Detail 2/3/93 7:22 PM

Fig. 3 Five-diaphragm sphere and total pressure probes using miniature silicon diaphragm pressure transducers

postulated that there was no need for continuous operation, rather a short flow period of several rotor rotations should be adequate. This gave rise to the blowdown concept shown in Fig. 2, where gas passes through the rotor from the supply tank to the dump tank after a separating diaphragm has been cut [1]. The rotor was spun up in vacuum prior to the diaphragm cutting, and was driven by its own inertia during the test time of about 40 ms. It turned out that by choosing the rotor's inertia and the initial gas pressure appropriately, the rotor could be made to operate at very nearly constant Mach number during the test time. By using as the test gas a mixture of argon and freon 12 with a ratio of specific heats of 1.4 but a higher molecular weight than air, the tip speed was cut by about a factor of 1.4, hence the stress level by a factor of 2, enabling the use of aluminum for the rotor and simplifying the mechanical design. This concept enabled the study of large high mass flow transonic rotors in an academic laboratory.

It would have been relatively useless, however, without the simultaneous development of miniature silicon diaphragm pressure transducers by the Kulite Co. Initially these were available either as complete transducers or as silicon diaphragms 0.058 in. in diameter, with integral strain gage bridges. Using these diaphragms, I fabricated multi-diaphragm probes of the sort shown in Fig. 3 [2]. From time-resolved measurements of pressure over the surface of the approximately spherical probe head (about 0.25 in. in diameter) it was possible to deduce the stagnation pressure, the static pressure, and the flow angles in the radial and tangential directions, all with sufficient spatial and temporal resolution to describe the unsteady flow downstream of the rotor, which had blade chords of about 3 in. and a 2 ft diameter.

The first measurements in this apparatus led to some surprising results, namely that there were very large fluctuations in the structure of the blade wakes from one blade to the next, with large radial flow angle in the wakes, equally large fluctuations in the tangential flow angles, and large fluctuations in static pressure. We concluded very early that the accepted picture of steady, essentially solenoidal flow in rotor coordinates was invalid, but the correct explanation for the unsteadiness came much later, from the work of Ng and Gertz.

The first major results from the BDC were obtained by two of my PhD students, Alan H. Epstein and William T. ("Tilt") Thompkins. Thompkins obtained the first complete set of measurements of the outflow from the transonic rotor, and presented them in the form of flow angles, Mach numbers, entropy, and efficiency as functions of radius and tangential distance [3]. A typical plot of entropy is shown in Fig. 4. (We knew at the time that such a plot, which assumed blade-to-blade periodicity, was at best a qualitative summary of the real behavior, but were unable at the time to see how to present the results so the intrinsic unsteadiness could be understood. The efficiency (and entropy) were derived from the measured stagnation pressure, and a stagnation temperature computed from the measured tangential velocity via the Euler equations. In this same time period Epstein developed a technique for quantitative visualization of the density field in the rotor by fluorescence of a trace gas, biacetyl, in the beam of a dye laser. He thus obtained some of the first quantitative measurements of the shock structure in a transonic rotor. One of his photographs is shown in Fig. 5 [4].

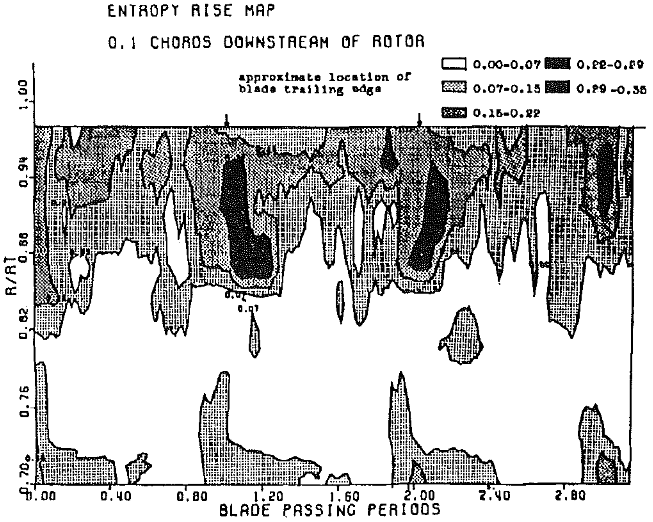

Threshold 3. Contrast 3, Brightness 9, Halftone Pattern Spiral, Normal Detail 2/3/93 7:27 PM

Fig. 4 Map of entropy, relative to the upstream flow, computed by Thompkins from measured stagnation pressures and Mach numbers. The abscissa is time (or circumferential distance), the ordinate is the radial position.

Three-Dimensional Transonic CFD

Also in the same time period with the above happenings, David Oliver and his student Panos Sparis were applying the newly developed techniques of transonic CFD to the three-dimensional flow in transonic compressors. In these early days most other CFD practitioners limited their work to two dimensions. But the flow in the transonic compressor is intrinsically three dimensional by virtue of the variation of the relative Mach number from values above unity near the tip, to values below unity near the hub. Oliver was interested in this as a fundamental problem. I was interested in a calculation that could be compared to the detailed measurements from the BDC. Sparis began by computing a sheared flow passing over a half-airfoil, in a rectangular geometry, the approach Mach number being above unity at one wall and below unity at the other. This is shown in Fig. 6 [5].

As part of his doctoral thesis, W. T. Thompkins applied the approach of Oliver and Sparis to the geometry of the BDC rotor, to obtain the first comparison of a computed transonic compressor flow field with measurements, at a sufficient level

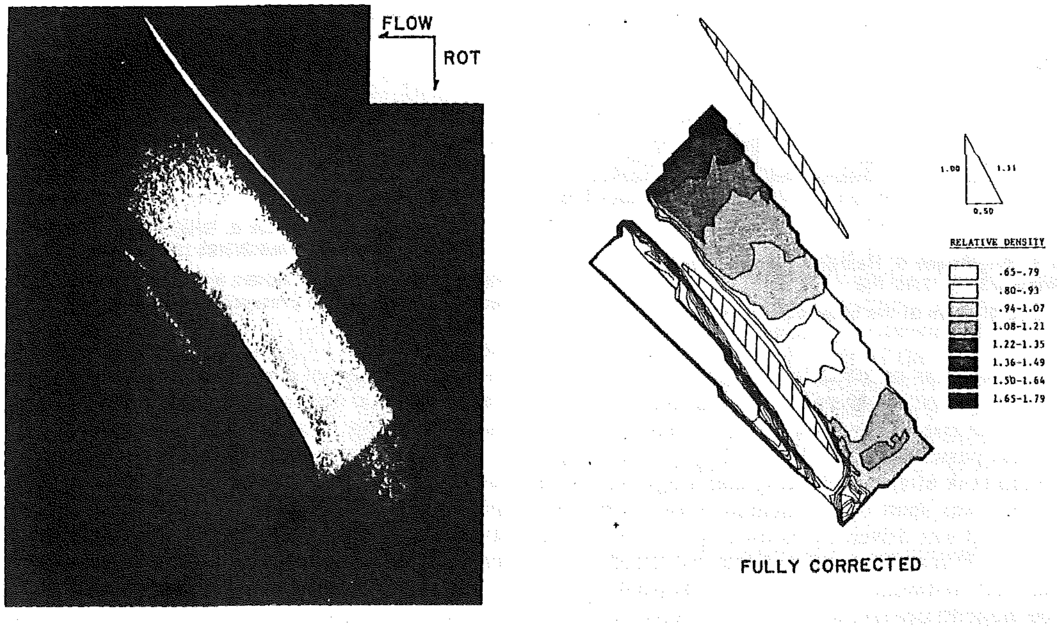

FULLY CORRECTED

UNPROCESSED

Fig. 5 Density map in the rotor of the blowdown compressor, obtained by gas flourescence by Epstein, showing passage shocks. Original photograph is at left, corrected map at right.

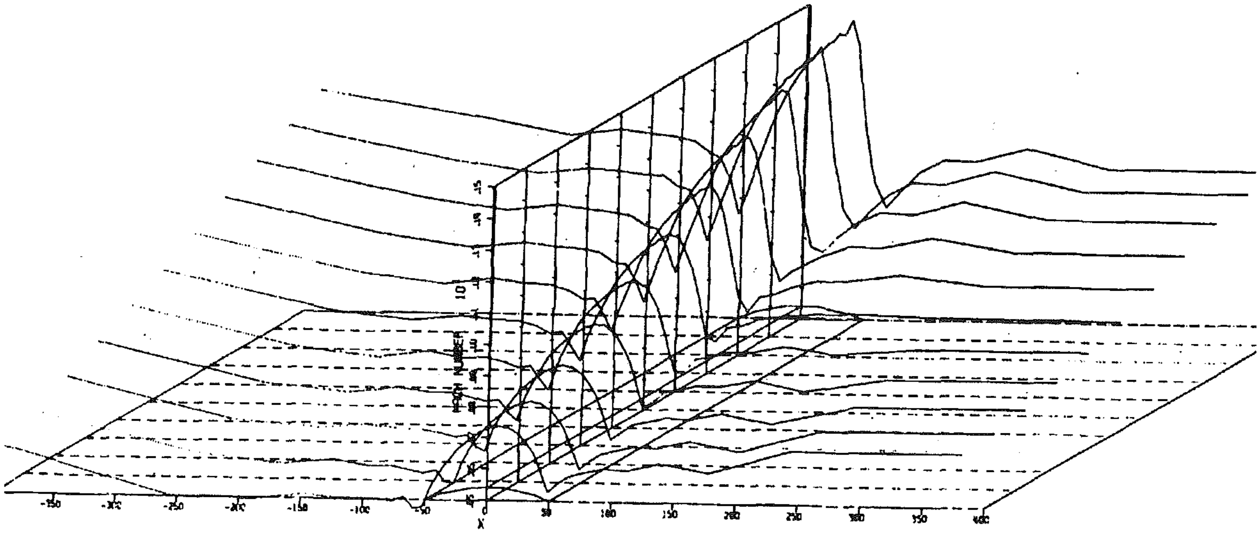

Threshold 2, Contrast 3, Brightness 9, Halftone Pattern Spiral, Normal Detail 2/3/93 7:44 PM

Fig. 6 Mach number at surface of a rectangular airfoil in a transonic shear flow, by Oliver and Sparis

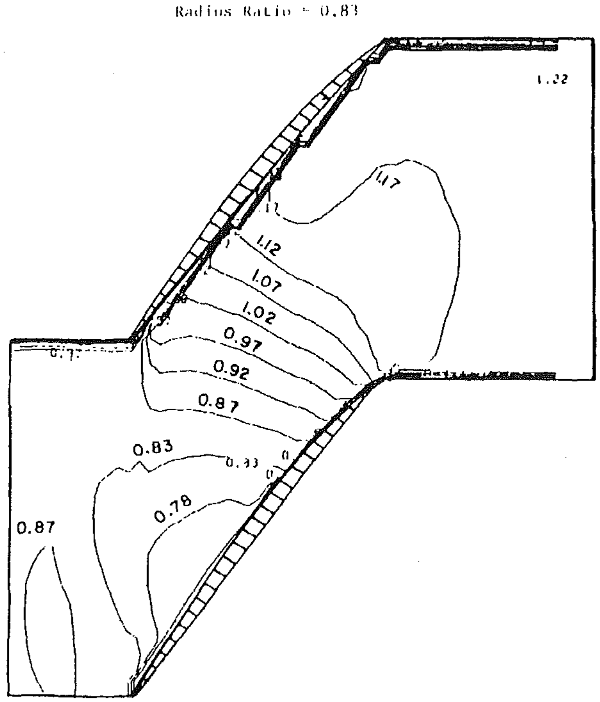

Threshold 9, Contrast 3, Brightness 9, Halftone pattern spiral, Normal Detail 2/3/93 7:49 PM

Fig. 7 Density map in the rotor of the blowdown compressor, computed by Thompkins for comparison to the data of Fig. 5. Density ratio of 1.0 is sonic line.

of detail to illuminate the differences [3]. Of course the differences were large, because the CFD calculation was inviscid while the rotor flow exhibited strong viscous effects. Nevertheless, with the encouragement of Mel Hartmann and his staff we pursued this comparison approach with other rotors, as will become clear below. Thompkins' calculation of the density field in the rotor is shown as Fig. 7, for comparison to Fig. 5.

High-Performance Rotor Studies. While the techniques developed on the BDC were judged interesting and useful, it was felt by many interested parties that the results might be somewhat pathological because the performance of the MIT transonic rotor was substandard. It had been designed by relatively simple techniques and had not been refined beyond the first design. Although it produced the design pressure ratio of about 1.6 at the design tip Mach number of 1.2, it had rather high losses. So with the help and support of Mel Hartmann and Calvin Ball of NASA Lewis, two state-of-the-art transonic rotors were made available for testing in the BDC, and three-dimensional computations were carried out for both of them. The two rotors were NASA Rotor 67, a high-throughflow design with very good performance, and the high-throughflow rotor designed and tested at the Air Force Aeropropulsion Laboratory by Wennerstrom [6].

The results for the NASA Rotor 67 confirmed the findings from the MIT rotor tests, that the rotor wakes were highly unsteady in rotor coordinates and exhibited large radial and tangential velocity fluctuations that were not explainable in terms of contemporary models for the wake behavior [7].

Equally important was the finding that the time-averaged performance of the rotors as measured in the BDC was essentially identical to that obtained in steady-state compressor test rigs. This validated the BDC as a compressor research tool, enabling us to proceed with confidence to study the unsteady flow knowing that the phenomena under study were ones that could exist in actual compressors.

The detailed measurements in these high-performance rotors (and later stages) preceded and may have helped stimulate similar studies at Lewis Research Center, using LDV techniques, which have established an important experimental benchmark for CFD computations in transonic rotors.

Comparison of Measurements and CFD Results—Shock Termination. Arguably the most sophisticated comparison of transonic inviscid CFD results to experimental results in the early time period was by Haymann-Haber, a student of Thompkins, who was by this time a faculty member at MIT. We had noticed from study of Epstein's shock visualizations that the passage shock in the rotor showed a sudden variation in strength near the sonic radius, just before it disappeared (shock structure). Some qualitative modeling of this phenomenon showed that there was an inconsistency in the usual radial equilibrium or strip theory model for the shock, in that the radial acceleration of the flow was discontinuous at the sonic radius [8]. Although the initial computations of Thompkins

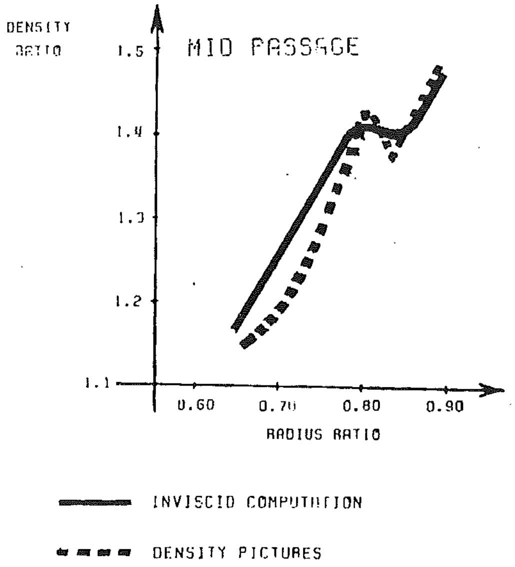

Threshold 9, Contrast 3, Brightness 9, Halftone pattern spiral, Normal Detail 2/3/93 7:54 PM

Fig. 8 Density ratio (to upstream flow) in midpassage as a function of radius, computed by Haymann-Haber and measured by Epstein, showing the shock termination phenomenon at a radius ratio of approximately 0.8.

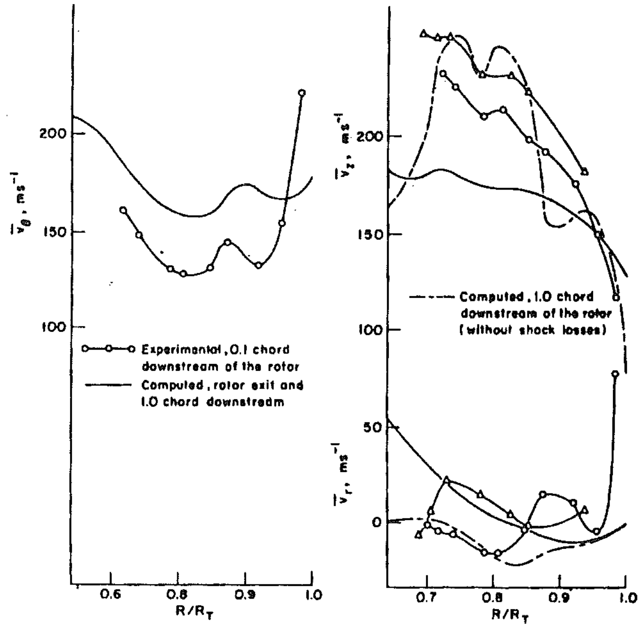

Threshold 3, Contrast 3, Brightness 9, Halftone pattern spiral, Normal Detail 2/3/93 8:00 PM

Fig. 9 Comparison of the tangential, axial, and radial velocities computed by Sehra with inclusion of blade-to-blade effects, to measurements of Thompkins. The experimental data marked by circular symbols were measured 0.1 chords downstream of the rotor, those with triangular symbols 1.0 chords downstream of the rotor.

showed some unusual behavior at the sonic radius they had insufficient grid resolution to sort out this phenomenon. Haymann-Haber set out to compute this shock termination phenomenon more accurately using the inviscid CFD approach of Thompkins, run on a minicomputer. He found the results shown in Fig. 8, which seemed to be little noted at the time [9]. They showed what seemed to me a remarkable agreement between the computed variation near the sonic radius of the density ratio across the shock and the measurements of Epstein by gas fluorescence.

Further Developments

From this point the work traceable to these beginnings branched into several distinguishable paths, which may be understood by reference to Fig. 1. They were:

1 Continued studies of unsteady flow in the BDC.
2 Studies of aeroelastic behavior of rotors, in the BDC.
3 CFD, initially focused on compressors and using dedicated minicomputers, that later evolved into more generic CFD research.
4 The Blowdown Turbine Experiment (BDT).

There was a continuous thread of comparison of the experimental results to those from the CFD calculations, so this is shown as another research line.

Some highlights of each of these threads will be discussed. Obviously this discussion cannot be comprehensive; in fact it will also be strongly influenced by my own perceptions and limited understanding of much of the work.

Unsteady Flow in Compressors

The line of investigation begun by Thompkins was subsequently expanded by a succession of doctoral students, each addressing a physically different aspect of the unsteady flow.

Blade-to-Blade Effects on Mean Flow. The data set obtained by Thompkins represented an unique opportunity to examine the effect of blade-to-blade flow variations on the mean flow. For his doctoral research Arun Sehra undertook to include the effects of these flows in the streamline-curvature calculation of the axisymmetric flow, using the acutal measured flows on the blade-passing length scale to estimate the Reynolds stresses and the "Apparent Entropy," a term we coined in the course of the work to express the effect on the flow of velocity fluctuations whose energy was not recoverable by the blading. Some results are shown in Fig. 9 [10]. With the corrections for the blade-to-blade flows, he found excellent agreement between the computed axisymmetric flow and that measured. Even a peak in the tangential velocity at about the sonic radius was reproduced, as shown in the left plot of Fig. 9.

This work was the precursor to that pursued recently by Adamczyk at NASA Lewis, in which the blade-to-blade flows predicted by CFD calculations and inferred from measurements are incorporated in three-dimensional calculations for multistage compressors.

Rotor-Stator Interaction. The next in this succession was Mohammed Durali, who undertook to extend the study of the MIT transonic rotor to a complete stage. To this end he constructed the apparatus shown in Fig. 10. A stator was added to complete the stage. The stator blades were mounted on a set of bearings so that, initially stationary, they would rotate slowly during the blowdown test so that a probe traversing radially downstream of them would survey the stator gap circumferentially as well as radially. In addition one of the stator vanes could be substituted by a special vane instrumented at one point on its length by an array of high-frequency response flush transducers, which gave the pressure distribution on the pressure and suction surfaces of the stator vane. This vane could be translated radially during the test, so a map of the unsteady pressure distribution was obtained as a function of radius as well as time. Together with surveys of the flow angles and Mach numbers upstream and downstream of the stator, this gave a very complete set of data on the flow in a transonic stage, probably the most complete ever obtained, even to this day. It was reported as a Gas Turbine Laboratory Report [11], but never published or pursued further.

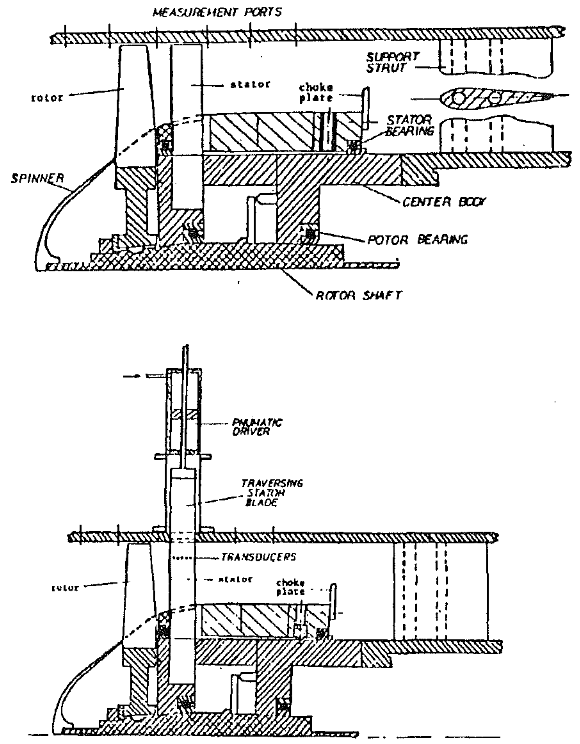

Threshold 6, Contrast 3, Brightness 9, Halftone
Pattern Spiral, Normal Detail 2/3/93 8:08 PM

Fig. 10 Apparatus of Durali for stage measurements: with rotating stator at top and with translating stator blade at bottom

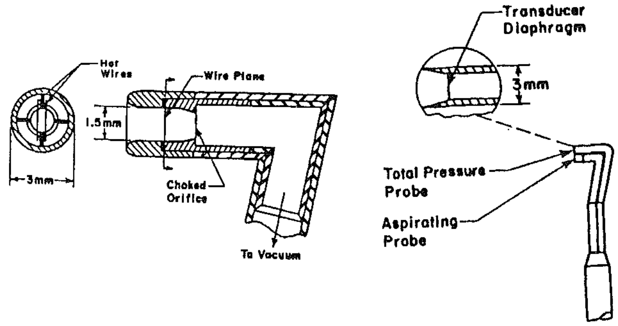

Threshold 6, Contrast 3, Brightness 9, Halftone
Pattern Spiral, Normal Detail 2/3/93 8:12 PM

Fig. 11 Aspirating probe at left, and its association with stagnation probe at right

Unsteady Flow in a High-Throughflow Stage. The high-throughflow stage developed by Wennerstrom was studied in detail by Ng [12]. In the course of this work, a new instrument called the aspirating probe was developed for time resolved measurement of the stagnation temperature [13]. Shown schematically in Fig. 11, it used two hot wires upstream of a choked orifice into which the flow was pulled, hence the title. The Mach number in the passage being fixed, the mass flow density and temperature in the passage depend only on the upstream stagnation pressure and temperature. By operating the two wires at different overheats, both stagnation pressure and stagnation temperature can be deduced. From these two values, the local entropy of the flow can be found, or equivalently, the efficiency. In practice it was better to associate the aspirating probe with a high-frequency response stagnation pressure probe using a Kulite transducer, as shown in Fig. 11, because the latter gave a more accurate indication of the stagnation pressure and added redundancy to the measurements.

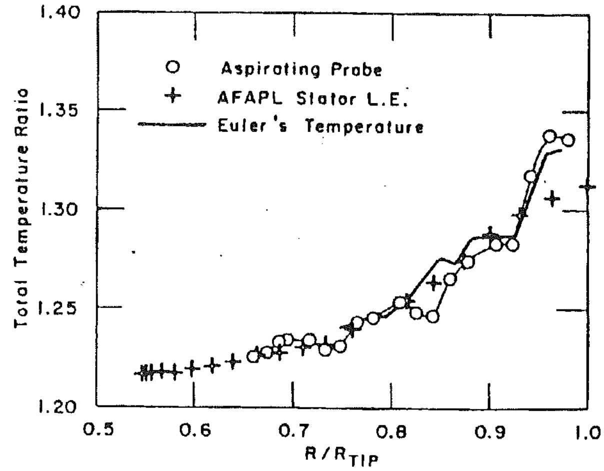

Threshold 6, Contrast 3, Brightness 9, Halftone
Pattern Spiral, Normal Detail 2/3/93 8:17 PM

Fig. 12 Comparison of total temperature, as a function of radius, as measured by the aspirating probe, and by stator leading edge thermocouples, with that calculated by the Euler equation

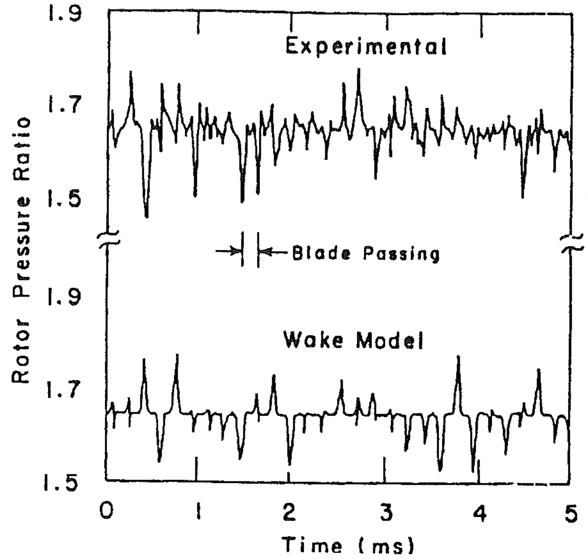

Threshold 6, Contrast 3, Brightness 9, Halftone
Pattern Spiral, Normal Detail 2/3/93 8:20 PM

Fig. 13 Comparison of rotor-exit pressure ratios versus time as measured in the blowdown compressor, and calculated from the vortex street model

For the first time this enabled time-resolved measurements of the efficiency. They indicated at least two interesting and/or important things:

(*a*) There seemed to be locations in the flow where the entropy was below the value upstream of the rotor (but see below under Kotidis).

(*b*) Averaging the time-resolved efficiency gave results very close to those from steady-state tests of the same rotor in other facilities, and just as close to those computed from the Euler equation by the method of Thompkins. This comparison is shown in Fig. 12 [14].

Attempts by Ng to explain the unsteadiness of the rotor flow in terms of shock-boundary layer interactions on the blades were not convincing, however.

Wake Structure. The correct explanation for the unsteadiness (at least in rotor 67 and in the Air Force High-Through-

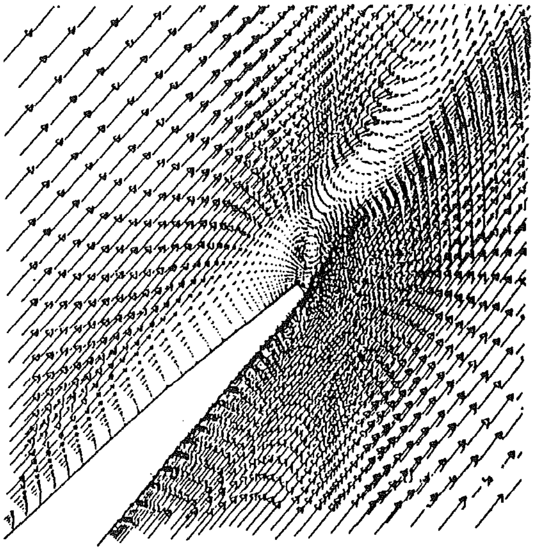

Threshold 6, Contrast 3, Brightness 9, Halftone Pattern Spiral, Normal Detail 2/3/93 8:23 PM

Fig. 14 Computed vortex shedding into wake of highly loaded transonic blade

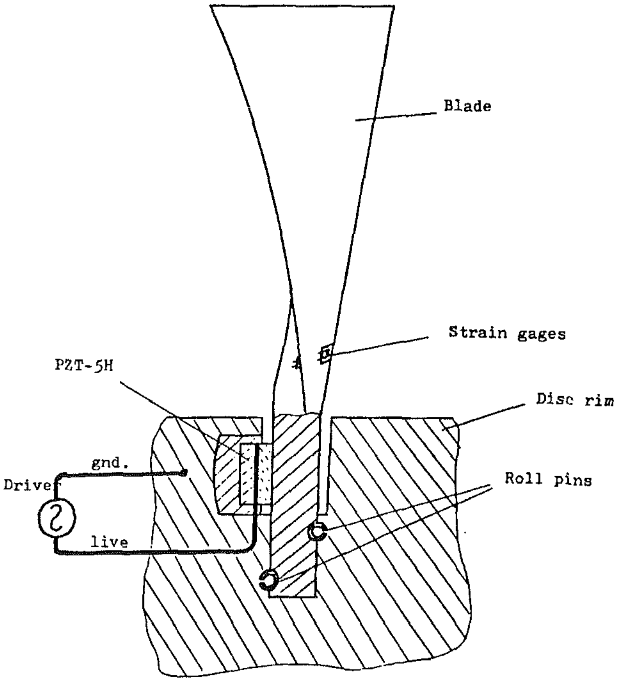

Threshold 6, Contrast 3, Brightness 9, Halftone Pattern Spiral, Normal Detail 2/3/93 8:26 PM

Fig. 15 Apparatus for vibrational excitation of the individual blades of the blowdown compressor

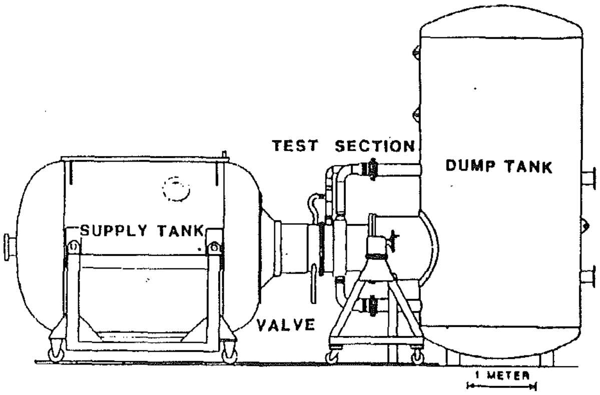

Threshold 6, Contrast 3, Brightness 9, Halftone Pattern Spiral, Normal Detail 2/3/93 8:30 PM

Fig. 16 The blowdown turbine experiment

flow Rotor, whether the result is generic remains controversial) was developed by Gertz et al. [15, 16]. The realized that large-scale vortex shedding into the wakes could lead to a structure very like the Karman street behind a cylinder, and a model based on this idea predicted wake behavior very similar to that observed, the unsteadiness resulting from the probe's more or less random sampling of the vortex street. this comparison is shown in Fig. 13 [15]. This model provided acceptable explanations for the observations of large static pressure and tangential flow angle variations in the wakes. Furthermore a close working relationship with Hathaway and Strazisar of NASA Lewis, who had carried out detailed LDV measurements in a transonic rotor, led to the realization that a bimodal wake behavior he had observed could also be understood in terms of the shed vortices. This technique was then applied to two E^3 fans at Pratt & Whitney. Lastly, by this time the CFD capability had advanced to the level that Owen succeeded in computing the unsteady vortex shedding, as shown in Fig. 14 [16].

Radial Transport in the Rotor. One phenomenon that was still not quantitatively understood was the large radial velocities observed in the wakes. I had hypothesized [17] that there was extensive radial transport in the boundary layers or wakes of the transonic rotor, and that this might explain the very high losses observed near the tips of such rotors, combined with extremely low losses near the hubs. A careful investigation of this possibility was undertaken by Kotidis, using the same high-throughflow rotor studied by Ng. He used a trace gas, injected upstream of the rotor and sampled downstream by the aspirating probe, to track the motion of the boundary layer flow through the rotor and wakes. He found that indeed there is strong transport, some radially inward but mostly outward, of a magnitude sufficient to explain a good part of the efficiency decrement at the tip [18].

In addition, Kotidis found that if he accounted for the time lag in the signal from the aspirating probe due to the flow time from its mouth to the hot wire, the regions of entropy lower than the upstream value disappeared. This was a very satisfying resolution of a nettlesome issue.

Rotor Aeroelasticity

In parallel with the work on unsteady flow, the potential of the BDC for study of compressor rotor flutter was explored. The concept initially was that a structural mode of the rotor would be excited while the rotor turned in vacuum, and its decay or excitation then studied as the flow passed through it. The method of exciting the blades shown in Fig. 15 was developed by James Fabunmi [19]. It provided for independent excitation of the bending modes of each of the blades by a piezoelectric transducer at its base. In the event it transpired that this task was of such magnitude that Fabunmi studied only the structural behavior of the rotor.

The apparatus was then refined and used by Crawley for a measurement of the aerodynamic damping [20]. He was able to obtain a measurement of the damping and show that it was sensitive to the variation of the frequencies of the individual blades, a result expected since the neighboring blades dominate in controlling the damping of any individual blade. This gave rise to some excellent work on the effect of "detuning" on flutter.

Later, this line of effort developed into research on the flutter of thin, highly swept blading for advanced turboprops, more specifically the unducted fan (UDF) [21].

It is interesting to noted that Crawley's work in structural dynamics of rotors ultimately led to his development at MIT of an entirely new and separate research program in Control-Structure Interaction, which is now the focus of a NASA Space Engineering Research Center.

Blowdown Turbine

The Blowdown Turbine Experiment (BDT) was conceived by Epstein et al. as a direct analog of the BDC [22]. In addition to the advantages of the BDC it offered the opportunity to measure the heat transfer by transient techniques. The basic idea was to scale down all temperatures of an actual engine so that the blade temperature is equal to ambient, the supply tank temperature is at the corresponding equivalent of the turbine inlet temperature, and cooling flow if desired, is cooled below room temperature. By choice of the size, pressure, and test gas, the Mach number and Reynolds number are matched to those of the actual engine. The apparatus is shown in Fig. 16.

This experiment called for the development of a new technology of heat transfer measurement, using thin film sensors separated by insulating plastic, as shown at the right in Fig. 17 [23]. The idea is that the film on the top of the insulator responds rapidly to fluctuations in heat flux, resolving the high frequencies due to blade passing events or turbulence, while the temperature difference between the top and bottom films responds more slowly, giving the variation on the time scale of the blowdown transient. Measurements taken in this way on a full-scale Rolls-Royce research rotor are shown in Fig. 18 [24].

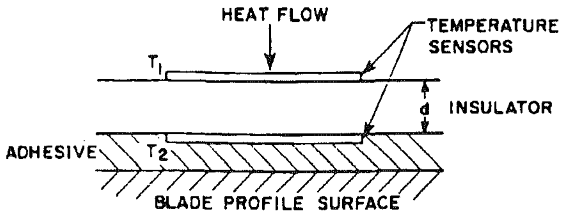

Threshold 6, Contrast 3, Brightness 9, Halftone Pattern Spiral, Normal Detail 2/3/93 8:33 PM

Fig. 17 Multilayer heat transfer gauge for use in the blowdown turbine experiment

The BDT has produced much quantitative data not formerly available about real turbine flow fields. Some of it is described in [25–27]. Another measure of its success is that it is being replicated by the Air Force Aeropropulsion Laboratory, and perhaps elsewhere, a form of praise the BDC has yet to receive.

CFD Developments

The development of computational techniques applicable to transonic flows in compressors continued in parallel with the experimental programs outlined above. At intervals, comparisons between the computed and experimental results enriched both efforts, as indicated at several points in the above discussion. But there were also aspects unique to the MIT CFD development that I think deserve mention. Some of these follow.

CFD With Dedicated Minicomputers. In the early time period, it was normal to carry out extensive CFD work on mainframe computers or the supercomputers of the day. Thompkins conceived the idea of doing the work instead on the small but quite capable minicomputer available full time in the Gas Turbine Laboratory, initially a Digital PDP 11-70, which was allowed to run for times of days or even weeks to generate a single solution. This turned out to be a highly cost-effective approach at the time, although it required a high level of sophistication in the programming, particularly for data management. It is still used by some of the most successful practitioners of CFD for turbomachinery, although in general it has been overtaken by "computational plenty."

Coupled CFD and Boundary Layer Computation. Two students of Thompkins, Mark Drela and Michael Giles, undertook for their doctoral research to develop efficient means for computation of internal flows including viscous effects. It was clear that this was necessary if CFD was to be quantitatively useful for turbomachinery, since viscous processes are limiting

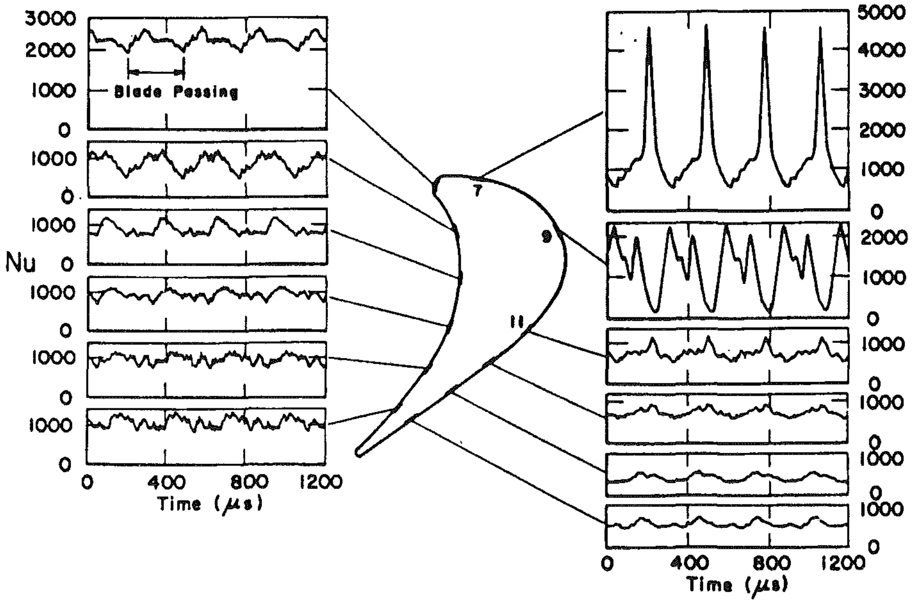

Threshold 4, Contrast 3, Brightness 9, Halftone Pattern Spiral, Normal Detail 2/3/93 8:37 PM

Fig. 18 Time-resolved heat fluxes at various points on a turbine airfoil

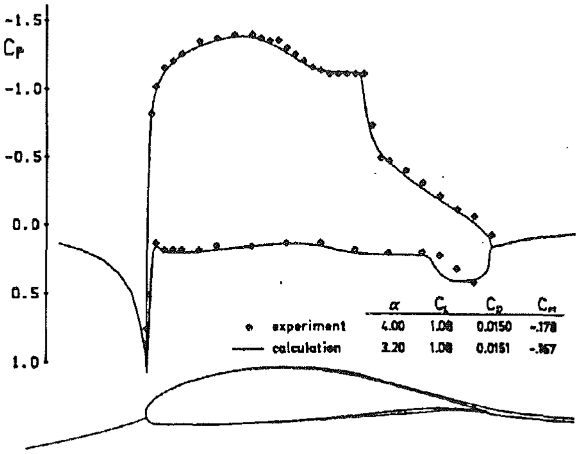

Threshold 4, Contrast 3, Brightness 9, Halftone
Pattern Spiral, Normal Detail 2/3/93 8:41 PM

Fig. 19 Comparison of calculated pressure distribution on an LA203A airfoil at M = 0.100 and Re = 250,000, to measured distribution

in all turbomachines in some way. This was a pioneering venture in another way, since they wished to collaborate in the work. They were able to convince their faculty committee of the viability of the idea, and proceeded together to produce an excellent computational scheme.

The idea was to adapt the streamline curvature approach used so successfully in computing the axisymmetric flow in turbomachinery, to produce a streamline-based adaptive computational grid. The boundary layer was included through a displacement thickness at the wall, and computed by an integral method [28, 29]. This led to an inverse design code, which enables the designer to specify the Mach number or pressure distribution on the airfoil, and generate the corresponding shape. Figure 19 shows the kind of agreement they obtained with experiment. Their method has since been used extensively by industry.

Rotor–Stator Interaction. Michael Giles undertook to develop computational methods capable of dealing efficiently with the unsteady flows due to stator–rotor interaction. He introduced the concept of "time-inclined" computational planes to enable his code UNSFLO [30] to handle arbitrary stator/rotor pitch ratios [31]. This is one of those ideas that is obvious once one sees it, but that eluded many previous workers in the field. His plot of the behavior of the nozzle wakes in passage through a turbine rotor, shown in Fig. 20, is especially appealing to me because it shows in detail a phenomenon I had modeled crudely much earlier [32], namely the transport across the rotor gaps of the fluid in the stator wakes.

Turbine Heat Transfer. As a final example of comparison of CFD results with experiment, in this case from the BDT, I will cite the work of Abhari et al. [33], who compared detailed heat transfer calculations by Giles to equally detailed time resolved heat transfer measurements made in the BDT. One of their figures is reproduced as Fig. 21. It seems that very little more could be asked of the modeling.

People

It has often been said that the most important products of academic research are the highly trained people who emerge from the educational process. Without agreeing that the research results are any less important, and without attempting a complete listing of those many who have gone on to successful careers in industry after participating in the above programs, I can list a number of contributions to the ranks of academe, each of whom has in the past or is now educating more students and producing more research results:

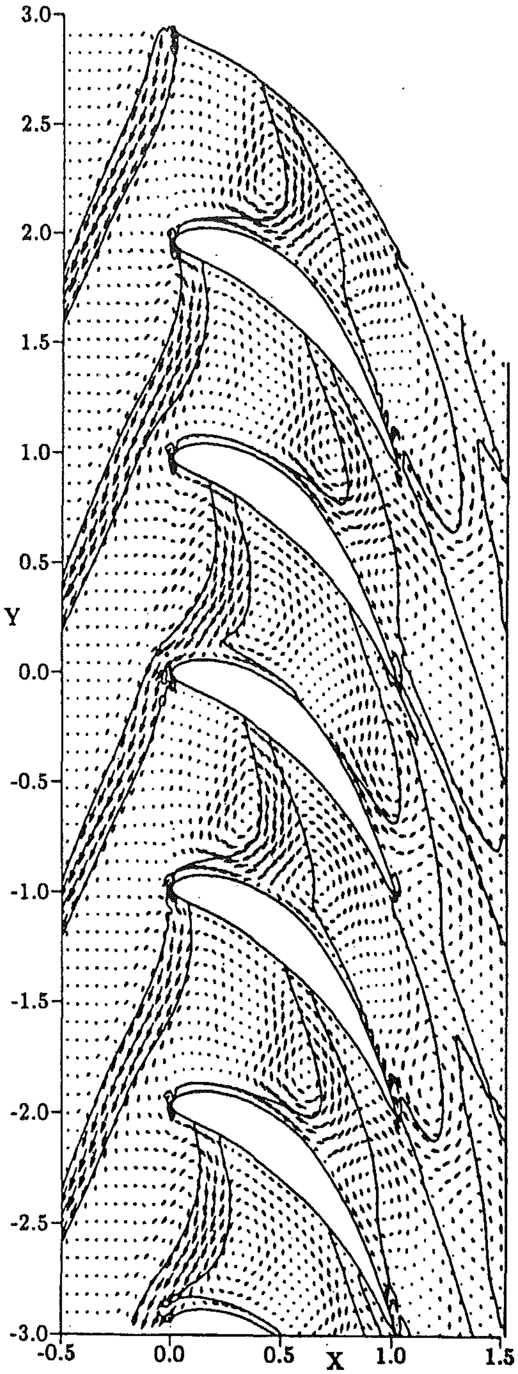

Threshold 4, Contrast 3, Brightness 9, Halftone
Pattern Spiral, Normal Detail 2/3/93 8:44 PM

Fig. 20 Computed entropy and unsteady velocity for a low-speed turbine

Present or Past Faculty at MIT
Crawley, Drela, Epstein, Giles, Thompkins.

Faculty at Other Universities
Fabunmi, University of Maryland
Farokhi, University of Kansas
Hall, Duke University
Lewis, University of Maryland
Ng, VPI&SU
Sparis, University of Athens

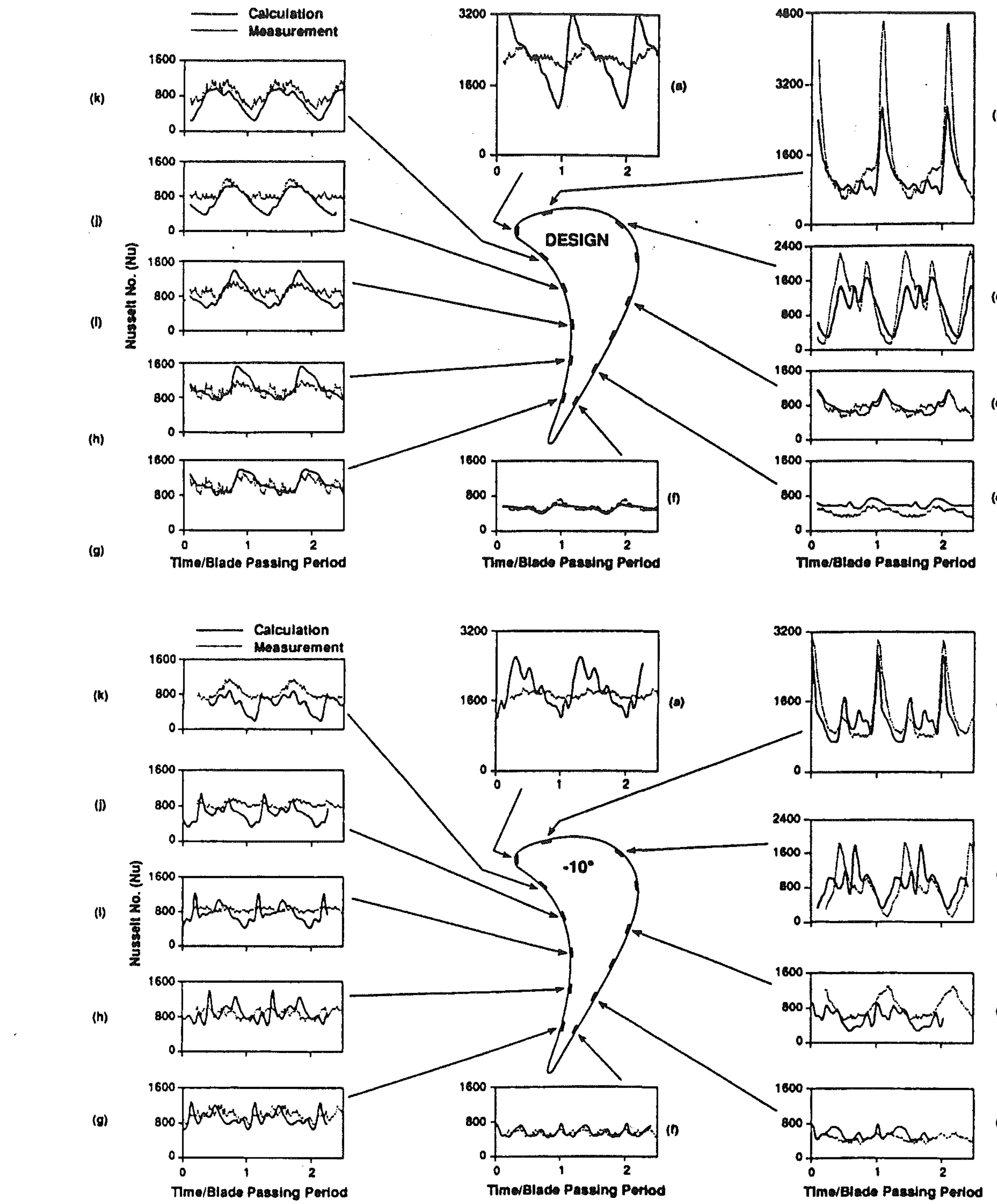

Threshold 4, Contrast 3, Brightness 9, Halftone Pattern Spiral, Normal Detail 2/3/93 8:48 PM

Fig. 21 Time-resolved heat flux measurements on a turbine airfoil at midspan, compared to calculations

I am quite sure Mel would approve of these results. Very few if any of them would have arisen without his early and steadfast support of research in the MIT Gas Turbine Laboratory.

References

1 Kerrebrock, J. L., Epstein, A. H., Haines, D. M., and Thompkins, W. T., "The MIT Blowdown Compressor Facility," ASME *Journal of Engineering for Power*, Vol. 96, No. 4, 1974.

2 Kerrebrock, J. L., Thompkins, W. T., and Epstein, A. H., "A Miniature High Frequency Sphere Probe," in: *Measurement Methods in Rotating Components of Turbomachinery*, Lakshminarayana and Runstadtler, eds., ASME, 1980.

3 Thompkins, W. T., "An Experimental and Computational Study of the Flow in a Transonic Compressor Rotor," PhD Thesis, MIT, Cambridge, MA, June 1976; see also MIT GTL Report 129, May 1976.

4 Epstein, A. H., "Quantitative Density Visualization in a Transonic Compressor Rotor," ASME *Journal of Engineering for Power*, Vol. 99, 1977, pp. 460–475.

5 Oliver, D. A., and Sparis, S., "Computational Studies of Three Dimensional Transonic Shear Flow: Work in Progress," MIT GTL Report No. 101, Sept. 1970.

6 Wennerstrom, A. J., "Experimental Study of a High-Throughflow Transonic Axial Compressor Stage," ASME *Journal of Engineering for Gas Turbines and Power*, Vol. 106, 1984, pp. 552–560.

7 Thompkins, W. T., and Epstein, A. H., "A Comparison of the Computed and Experimental Three-Dimensional Flow in a Transonic Compressor Rotor," AIAA Paper No. 76-368, July 1976.

8 Epstein, A. H., Kerrebrock, J. L., and Thompkins, W. T., "Shock Structure in Transonic Compressor Rotors," *AIAA Journal*, Apr. 1979.

9 Haymann-Haber, G., "A Computational Study of the Flow in a Transonic Axial Compressor Using an Inviscid, Three-Dimensional Finite Difference," MIT GT&PDL Report No. 145, May 1979.

10 Sehra, A. K., and Kerrebrock, J. L., "Blade-to-Blade Effects on Mean Flow in Transonic Compressors," *AIAA Journal*, Vol. 19, No. 4, Apr. 1981, p. 476.

11 Durali, M., "Rotor Wake Behavior in a Transonic Compressor Stage and Its Effect on the Loading and Performance of the Stator," MIT GT&PDL Report No. 149, Apr. 1980.

12 Ng, W. F., and Epstein, A. H., "Unsteady Losses in Transonic Compressors," ASME *Journal of Engineering for Gas Turbines and Power*, Vol. 107, No. 2, Apr. 1985.

13 Ng, W. F., and Epstein, A. H., "High Frequency Temperature and Pressure Probe for Unsteady Compressible Flows," *Rev. Sci. Inst.*, Vol. 54, No. 12, Dec. 1983.

14 Epstein, A. H., "Short Duration Testing for Turbomachinery Research and Development," presented at the Second International Symposium on Transport Phenomena, Dynamics, and Design of Rotating Machinery, Honolulu, HI, Apr. 4-6, 1988.

15 Hathaway, M., Gertz, J., Epstein, A. H., and Strazisar, A., "Rotor Wake Characteristics of a Transonic Flow Fan," *AIAA Journal*, Vol. 24, No. 11, Nov. 1986.

16 Epstein, A. H., Gertz, J., Owen, P. R., and Giles, M. B., "Vortex Shedding in Compressor Blade Wakes," *AIAA Journal of Propulsion and Power*, Vol. 4, No. 3, May-June 1988, pp. 236-244.

17 Kerrebrock, J. L., "Flow in Transonic Compressors," *AIAA Journal*, Vol. 19, No. 1, Jan. 1981, p. 4.

18 Kotidis, P. A., and Epstein, A. H., "Unsteady Radial Flows in a Transonic Compressor," ASME JOURNAL OF TURBOMACHINERY, Vol. 113, pp. 207-218.

19 Fabunmi, J. A., "Forced Vibrations of a Single Stage Axial Compressor Rotor," PhD thesis, MIT, Feb. 1978.

20 Crawley, E. F., "Measurements of Aerodynamic Damping in the MIT Transonic Rotor," GTL Report No. 157, Feb. 1981.

21 Ducharme, E. H., and Crawley, E. F., "Velocity Scaled Aeroelastic Testing of an Unducted Fan," MIT GTL Report No. 191, Sept. 1987.

22 Epstein, A. H., Guenette, G. R., and Norton, R. J. G., "The MIT Blowdown Turbine Facility," ASME Paper No. 84-GT-116, June 1984.

23 Epstein, A. H., Guenette, G. R., Norton, R. J. G., and Yuzhang, C., "High Frequency Response Heat Flux Gauge," *Rev. Sci. Inst.*, Vol. 57, No. 4, Apr. 1986.

24 Guenette, G. R., Epstein, A. H., Haimes, R., and Giles, M. B., "Fully Scaled Transonic Turbine Rotor Heat Transfer Measurements," ASME JOURNAL OF TURBOMACHINERY, Vol. 111, Jan. 1989, pp. 1-7.

25 Guenette, G. R., Pappas, G., and Epstein, A. H., "The Influence of Nonuniform Spanwise Inlet Temperature on Turbine Rotor Heat Transfer," 80th PEP/AGARD Symposium, Antalya, Turkey, Oct. 1992.

26 Abhari, R. S., and Epstein, A. H., "An Experimental Study of Film Cooling in a Rotating Transonic Turbine," ASME JOURNAL OF TURBOMACHINERY, Vol. 116, 1994, pp. 63-70.

27 Cattafesta, L., and Epstein, A. H., "Gas Temperature Measurement in Short Duration Turbomachinery Test Facilities," AIAA Paper No. 88-3039, July 1988.

28 Giles, M. B., and Drela, M., "Two-Dimensional Transonic Aerodynamic Design Method," *AIAA Journal*, Sept. 1987.

29 Drela, M., and Giles, M. B., "Viscous-Inviscid Analysis of Transonic and Low Reynolds Number Airfoils," *AIAA Journal*, Oct. 1987.

30 Giles, M. B., "UNSFLO: A Numerical Method for the Calculation of Unsteady Flow in Turbomachinery," GTL Report No. 205, May 1991.

31 Giles, M. B., "Calculation of Unsteady Wake/Rotor Interaction," *AIAA Journal of Propulsion and Power*, Vol. 4, No. 4, July-Aug., 1988, pp. 356-362.

32 Kerrebrock, J. L., and Mikolajczak, A. A., "Intra-stator Transport of Rotor Wakes and Its Effect on Compressor Performance," ASME *Journal of Engineering for Power*, Oct. 1970, p. 359.

33 Abhari, R. S., Guenette, G. R., Epstein, A. H., and Giles, M. B., "Comparison of Time-Resolved Turbine Rotor Blade Heat Transfer Measurements and Numerical Calculations," ASME JOURNAL OF TURBOMACHINERY, Vol. 114, 1992, pp. 818-827.

G. K. Serovy

T. H. Okiishi

Department of Mechanical Engineering,
Iowa State University of Science
and Technology,
Ames, IA 50011

Some Results of NASA-Iowa State University Research on Axial-Flow Pumps

This paper is a commentary on a small chapter in the recent history of turbomachinery research. It was written to describe the positive influence of an individual, Melvin J. Hartmann, working in a federal research center, on a particular university research program. However, in its final form, it cannot help but shed some light on the long-term effects of small-scale, mission-oriented, federal agency funding of engineering research in universities. Secondarily, it will recall a series of experimental investigations of axial-flow pump configurations, which produced data of possible relevance to current compressor and pump problems.

Legacy of the NACA Compressor Research Program

After the end of World War II, the National Advisory Committee for Aeronautics (NACA) initiated extensive research programs on compressor and turbine aerodynamics in its Cleveland and Langley Field laboratories. Numerous test rigs were built between 1947 and 1953, and in the axial-flow compressor program, there was a strong emphasis on the accumulation of systematic experimental data supporting and extending the range of applicability of the "blade-element" design system. The blade-element design method, utilizing the radial equilibrium concept, might be considered a product of the NACA Compressor and Turbine (C&T) Research Division in Cleveland. While the radial equilibrium concept did not originate in the C&T Division, there is little question in our minds that the blade-element method was first developed there as a routine design tool and that its success was based on the accumulation of experimental linear cascade data in the Langley Laboratory and on the wide spectrum of data coming from rotor, stage, and multistage test rigs in Cleveland. There is no doubt that the calendar years 1947 through 1955 could be called a "Golden Age" of axial-flow compressor aerodynamics in the NACA. Among its best-known products were the empirically based blade-element compressor design system, the transonic compressor stage, and recognition of the principal features and problems of compressor off-design performance. The work of this period has been well documented, both during and subsequent to the time in question. Example materials include Savage et al. (1961), Lieblein and Johnsen (1961), Wilcox et al. (1959), Klapproth (1961), Serovy (1966), and Johnsen and Bullock (1965).[1]

By the end of 1955, it was becoming apparent that, for the time being, the zone of diminishing returns in axial-flow compressor work had been reached. In the following years, until 1958, fewer new stages were designed, fewer results were evaluated and correlated, and many of the C&T staff were dispersed to other research assignments and work inside and outside the NACA.

Initiation of NASA Axial-Flow Pump Research

The National Aeronautics and Space Administration (NASA) came into existence on 1 October 1958. NASA incorporated all of the laboratories and facilities of the NACA and in its own words, NASA (1959) was soon "rapidly shifting from research primarily on air-breathing power plants, to rockets—chemical, liquid propellant, nuclear, and electrical." Nearly all of those still engaged in turbomachinery programs at the new NASA Lewis Research Center became members of the Fluid Systems Components Division, and "rapidly shifted" their attention to learning about "new" turbomachines such as centrifugal and axial-flow pumps. For axial-flow pump research, a water test loop was designed and built (Fig. 1), an inducer test installation was developed and larger-scale hydrogen test facilities were constructed near Sandusky, Ohio (Plum Brook).

Contributed by the International Gas Turbine Institute and presented at the 38th International Gas Turbine and Aeroengine Congress and Exposition, Cincinnati, Ohio, May 24–27, 1993. Manuscript received at ASME Headquarters March 17, 1993. Paper No. 93-GT-330. Associate Technical Editor: H. Lukas.

---

[1] Documentation of some of the personalities involved in the work is less complete. Mel Hartmann is remembered as a large, bearlike figure with a friendly and constant smile, in continuous lumbering motion between his desk and his test rig. Mel believed in rig data and its analysis. He was exhilarated by the building and operation of test rigs, new and old. He never met a data point that he did not like and use to best advantage.

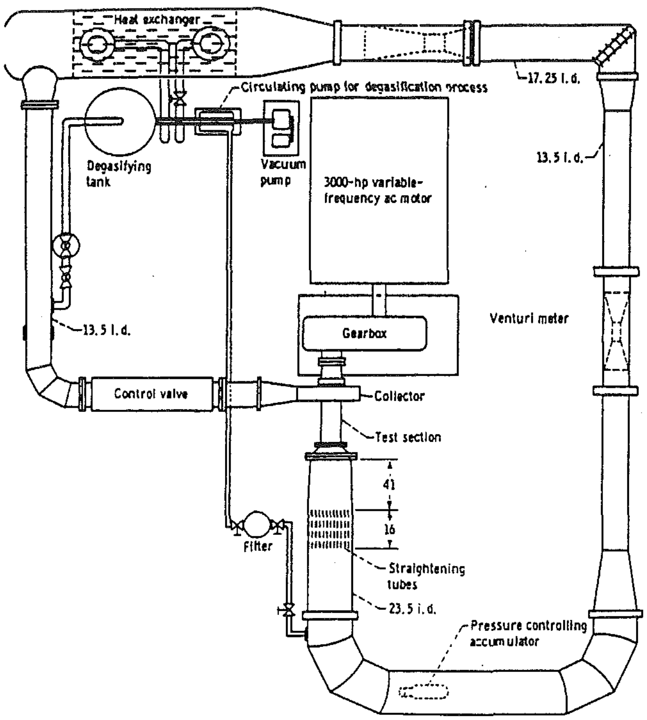

Fig. 1 Schematic diagram of NASA-Lewis water tunnel (dimensions are in in.)

The design method developed at Lewis for experimental axial-flow pump rotors and stages was an incompressible flow version of the blade-element, quasi-three-dimensional compressor system. Early reports of the NASA work include Crouse et al. (1961a, b). In fact, for most of the test configurations, design point blade selection was primarily based on the cascade correlations, which had come from the NACA compressor program. This resulted in the continued use of double-circular-arc and 65-series blade section profiles and the possibility of comparison between cascade plane performance in water and air.

Status of University Turbomachinery Research—1958

Looking back toward the 1945–1958 time period, it is apparent that the European countries, particularly Germany and Switzerland, were moving rapidly in rebuilding and developing University teaching and research on turbomachinery fluid dynamics. In the United States, experimental research on axial-flow compressor aerodynamics reported then at MIT, Caltech, and Johns Hopkins remains of interest today. Pump research related to naval applications was initiated at Penn State by George F. Wislicenus (1960).

In 1956 the textbook *Principles of Turbomachinery* by Professor D. G. Shepherd of Cornell University was published. This book had an influence that reached into universities, industry, and research laboratories because it was well organized and easily understood, and because it was an "American style" text with examples and problems. In addition, the book dealt with turbomachinery as a broad class of fluid machinery including fans, pumps, compressors, and turbines.

George Serovy returned to Iowa State from NACA in 1953. He received a research grant from NACA in 1956 to study prediction of the performance of axial-flow compressors by blade-element methods. This was a one-man effort, directed toward goals including a doctoral dissertation and a NACA technical report. One of the elements of the project was the utilization of an IBM Model 650 digital computer, newly installed in the Iowa State Statistics Laboratory (Serovy and Anderson, 1959). In a report based on April 1956 discussions in Cleveland concerning the proposed grant, one of the participants was M. J. Hartmann, Head, Supersonic and Transonic Compressor Research Section of NACA-Lewis. During that same year Serovy taught a new course in the "principles of turbomachinery" at Iowa State. Shepherd's book was the first text used. The course has been offered each year from 1956 to the present and has involved numerous prominent guest lecturers. Students continue to be eager to learn about the application of fluid mechanics and thermodynamics to turbomachine design and analysis.

Contributions to the NASA Pump Program

Early in 1959 it was evident that the new NASA was, at least for the time being, not interested in sponsoring additional compressor performance prediction work at Iowa State. However, similar research directed at pumps and coordinated with the emergent Fluid Systems Components Division of NASA-Lewis was suggested and after a new proposal was submitted, NASA Headquarters awarded Grant NsG-62-60 to Iowa State in the amount of $11,430 for research beginning in February 1960 on "Application of Blade-Element Techniques to the Design and Performance Prediction Problems for Axial-Flow Pumps." This initiated a series of grants and extensions covering projects up to the last part of 1972. The work involved real cooperation and mechanisms for sharing the time of individuals at NASA-Lewis and Iowa State. Some abbreviated comments in the following subsections indicate what was done. Reference to a few retrievable reports, such as Kavanagh and Miller (1970), Kavanagh et al. (1970), Serovy et al. (1973), and Miller et al. (1973) should lead readers to more detailed technical documentation of the major elements of the 13-year effort.

Data Plotting and Analysis

One of the activities supported at Iowa State by the NASA pump research group was plotting and preliminary analysis of passage survey data for a number of axial-flow rotors. Several undergraduate and graduate students were employed on a part-time basis, to hand plot the many sets of data associated with each rotor. While this was tedious and sometimes boring work, the plotting process did focus attention on trends and patterns in a way that is not likely to occur with current plotting and data presentation systems. Our best students were involved. They took their work seriously, studied the data in a critical sense, and genuinely liked the idea that they were working on "real" research projects.

Developing a Design System Data Base

There was a strong sense within NASA that for noncavitating performance situations, the design of high hub-to-tip diameter

Nomenclature

D = diffusion parameter defined by Miller et al. (1973)

DEQ_r = equivalent diffusion factor defined by Serovy et al. (1973)

$(\theta/C)_A$ = blade wake momentum thickness to chord ratio defined by Serovy et al. (1973)

r_h/r_t = ratio of rotor inlet hub radius to tip radius (radius measured from pump rotational axis) ratio axial-flow pump stages by the blade-element method would be successful. It was believed by all concerned that for constant-density fluids, steady flow on axisymmetric stream surface approximations could be assumed. This meant that a radial-equilibrium condition could be used at axial stations upstream and downstream of each blade row.

Blade-element (cascade plane) profile, solidity, and setting angle selection for design was based on correlation of experimental data from rotors, stators, and linear cascades. There was some confidence that existing aerodynamic loading limits such as the Lieblein diffusion parameters (Johnsen and Bullock, 1965, and Lieblein, 1959), would be as effective in pumps as they had been in axial-flow compressors.

The radial-equilibrium condition used required experimental input in terms of correlations of deviation angle and loss parameter. These correlations generated radial distributions of blade-row exit angle and loss, which in turn permitted the computation of static head and velocities.

Considerable effort was devoted at both NASA-Lewis and Iowa State to comparing the emerging pump blade-element data with the best existing loss and deviation (turning angle) correlations from linear cascade and compressor experiments in air. Modifications were made independently at NASA-Lewis and at Iowa State. A computer code was written and tested by Kavanagh and Miller (1970) and Kavanagh et al. (1970) for axial-flow pump stage design.

Performance Prediction Using Blade-Element Methods

At Iowa State, a major objective throughout the 1959–1973 period was to formulate and develop computer codes and supporting data correlations for noncavitating axial-flow pump performance prediction. As the NASA-Lewis data appeared, it became obvious that while the NACA aerodynamic loading parameters (compressors) could be utilized as hydrodynamic loading parameters (pumps), the numerical limiting values could not be confidently transferred from compressor experience to pumps.

Furthermore, the NACA compressor-based loss correlations, which generally gave a loss parameter as functions of a loading parameter and radial location in the hub-to-tip plane, simply did not work. This influenced both design and performance estimation results. A similar conclusion was reached in the case of deviation angle, where the influences of axial velocity ratio across a blade row and incidence angle were difficult to accommodate. Consequently, a large fraction of the Iowa State work on performance prediction was devoted to studying the correlation problem and to use of the NASA rotor experiments as the base for comparison of potential improvements. An example of the type of loss correlation generated is shown in Fig. 2.

At the conclusion of the Iowa State work, an axial-flow pump performance prediction program was reported by Serovy et al. (1973). This report included the correlation studies, the code structure, and comparative results.

Axial-Flow Pump Results—A First Look

The conclusions reached in 1972 by the Iowa State group were positive. It was believed that we had, considering the limitations of the blade-element method and of the computing facilities available (IBM 360/65 System) then, done about as much as the existing data base would allow.

We certainly recognized that the correlation approach required more data, preferably from both linear cascade tests and a broader range of rotors and stages. The linear cascade experiments of Taylor et al. (1969a, b) were too new to be utilized, and the NASA test rigs were being phased out.

To end the Iowa State pump effort, we did believe that all of the NASA rotor data should be preserved in an archival document. Fortunately, we found that our NASA colleagues, D. M. Sandercock, W. R. Britsch, J. E. Crouse, and most importantly M. J. Hartmann, agreed. The summary report (Miller et al., 1973) was the result. Table 1 shows for the record

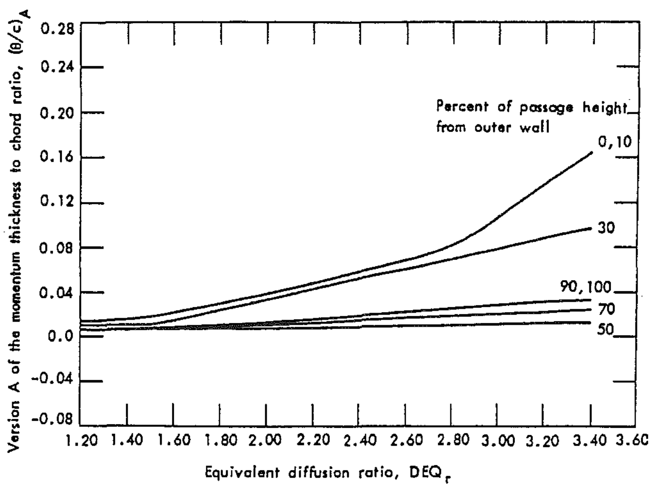

Fig. 2 Loss correlation curves derived from experimental data for NASA pump rotors identified in Table 1, taken from Serovy et al. (1973)

Table 1 NASA axial-flow pump rotor design data taken from Serovy et al. (1973)[a]

NASA configuration number	Tip diameter, in.	r_h/r_t	Number of blades	Blade section profile[b]	Blade chord length,[c] in.	Radial tip clearance,[d] in.	Design tip section D-factor	Design point flow coefficient	Minimum blade chord Reynolds number
02[e]	9.0	0.4	16	DCA	1.5	0.013-0.020	0.23	0.293	1.0×10^6
07[e]	9.0	0.7	19	DCA	1.5	0.005-0.012	0.43	0.294	1.5×10^6
09	9.0	0.7	8	DCA	3.04	0.013-0.020	0.46	0.294	3.0×10^6
5[e]	9.0	0.8	19	DCA	1.5	0.015-0.017	0.66	0.466	1.5×10^6
6	9.0	0.8	19	DCA	1.5	0.025-0.027	0.66	0.466	1.5×10^6
8	5.0	0.8	19	DCA	0.834	0.007-0.009	0.66	0.466	8.0×10^6
9	5.0	0.8	19	DCA	0.834	0.015-0.017	0.66	0.466	8.0×10^6
10	5.0	0.8	19	DCA	0.834	0.022-0.024	0.66	0.466	8.0×10^6
13A[e]	9.0	0.85	33	DCA	1.172	0.009-0.011	0.72	0.5	1.0×10^6
14A[e]	9.0	0.9	19	DCA	1.5	0.009-0.011	0.63	0.7	1.5×10^6
15	9.0	0.8	19	DCA	1.5	0.009-0.010	0.55	0.466	1.5×10^6
16	9.0	0.85	33	Cubic	1.172	0.009-0.011	0.72	0.5	1.0×10^6

[a] All rotors were tested without inlet guide vanes and downstream stator blades. Data are taken from Miller et al. (1973).
[b] DCA indicates a Double Circular Arc blade section profile.
[c] All blade chord lengths were uniform along the blade span.
[d] The range of circumferential variation of radial tip clearance is indicated.
[e] Rotors used for obtaining loss and deviation angle correlations.

some design information about the NASA pump rotors. We remain very proud of this document because it represents cooperation in the ultimate research product, a carefully planned and written report of good test rig work.

Re-emergence of the Axial-Flow Compressor as a Research Focus

Although a small axial-flow compressor research effort existed within NASA-Lewis between 1958 and 1964, it was confined to specific applications. However, during 1964 there was a realization that serious and challenging problems remained in development of turbomachinery for aeronautical air-breathing propulsion systems, and that these problems were endangering the position of leadership held by the United States in the production of both military and commercial aircraft turbine engines. Several sets of proposals were solicited by NASA-Lewis for external research on axial-flow compressors, including development of design and analysis computer codes, and design and testing of families of transonic stages and special blade profile geometries. This was a radical change from the 1947-1958 program because now much of the work was to be done by industrial contractors.

Axial-Flow Pump Results—A Second Look

From a 1993 viewing point, the first thing evident is how much our understanding of turbomachine flows has improved. A second conclusion might be that, considering progress in computation hardware and in measurement systems, we should understand more and in greater depth.

The pump configurations tested after 1958 probably do not have much application outside the liquid-propellant rocket field. That they have application there is evident by such papers as Huppert and Rothe (1970) and a look at a cross section of typical high-thrust, hydrogen turbopumps.

The differences between blade-element operation in pumps and compressors were understood to be due to the dominant end-wall and other secondary flows in the high hub-to-tip ratio, low aspect ratio pump stages. Reynolds number levels in the pump tests were known to be greatly different from those in much of the compressor-related data. It would be interesting to see how well current CFD codes predict the flows measured 25-30 years ago.

Other Results

The NASA-Iowa State pump work motivated considerable local interest in fluid dynamics problems related to propulsion that extended far beyond the primary sponsored projects already mentioned. Thesis and dissertation research at both the M.S. and Ph.D. levels completed during the "pump years" include[2]:

J. L. Hall —Combustion-related shock tube studies
F. B. Hamm —Computation of duct flow using streamline-curvature method
B. L. Johnson—Analysis of fluid transfer line dynamics
P. Kavanagh —Computation of linear cascade flows
J. C. Lysen —Computation and measurement of compressor inlet flows
M. J. Miller —Deviation angle prediction
T. H. Okiishi —Velocity profile development in annular passages
C. R. Pullen —Failure of radial-equilibrium solutions
M. D. Smith —Measurement of flow in curved diffusing passage

Subsequent to the NASA pump research years at Iowa State, other organizations funded work on turbomachine fluid dynamics there. Sponsors include the U.S. Air Force Office of Scientific Research, the U.S. Air Force Aeropropulsion Laboratory, GE Aircraft Engines, the Allison Gas Turbine Division of General Motors, and Textron Lycoming. Over the years, NASA support of a variety of turbomachine-related fluid dynamics studies also continued. Some examples of the archival journal articles that resulted from this subsequent effort are listed in the references under the following authors:

Copenhaver and Okiishi (1993)
Delaney and Kavanagh (1976)
Hansen and Okiishi (1989)
Hansen, Serovy, and Sockol (1980)
Miller and Serovy (1975)
Schmidt and Okiishi (1977)
Serovy and Okiishi (1988)
Tweedt, Okiishi, and Hathaway (1986)
Wagner, Okiishi, and Holbrook (1979)
Wisler, Bauer, and Okiishi (1987)
Zierke and Okiishi (1982)

An outstanding outcome of the research work described in this paper is the significant number of former students who are now prominent in the turbomachinery business. Mel Hartmann's positive influence on the Iowa State University turbomachine fluid dynamics program during its inception and formative years led to the placement of important contributors to the continuing advancement of turbomachine technology.

References

Copenhaver, W. W., and Okiishi, T. H., 1993, "Rotating Stall Performance and Recoverability of a High-Speed 10-Stage Axial-Flow Compressor," *AIAA Journal of Propulsion and Power*, Vol. 9, pp. 281-292.

Crouse, J. E., Montgomery, J. C., and Soltis, R. F., 1961a, "Investigation of the Performance of an Axial Flow-Pump Stage Designed by the Blade-Element Theory," NASA TN D-591.

Crouse, J. E., Soltis, R. F., and Montgomery, J. C., 1961b, "Investigtion of the Performance of an Axial-Flow-Pump Stage Designed by the Blade-Element Theory—Blade-Element Data," NASA TN D-1109.

Delaney, R. A., and Kavanagh, P., 1976, "Transonic Flow Analysis in Axial-Flow Turbomachinery Cascades by a Time-Dependent Method of Characteristics," ASME *Journal of Engineering for Power*, Vol. 98A, pp. 356-364.

Hansen, E. C., Serovy, G. K., and Sockol, P. M., 1980, "Axial-Flow Compressor Turning Angle and Loss by Inviscid-Viscous Interaction Blade-to-Blade Computation," ASME *Journal of Engineering for Power*, Vol. 102, pp. 28-34.

Hansen, J. L., and Okiishi, T. H., 1989, "Rotor Wake Segment Influence on Stator Surface Boundary Layer Development in an Axial-Flow Compressor Stage," *AIAA Journal of Propulsion and Power*, Vol. 5, pp. 89-94.

Huppert, M. C., and Rothe, K., 1970, "Axial Pumps for Propulsion Systems," U.S. NASA SP-304, Part II, pp. 629-654.

Johnsen, I. A., and Bullock, R. O., eds., 1965, "Aerodynamic Design of Axial-Flow Compressors," NASA SP-36.

Kavanagh, P., and Miller, M. J., 1970, "Axial-Flow Pump Design Digital Computer Program," Iowa State University Technical Report ISU-ERI-Ames-66300.

Kavanagh, P., Miller, M. J., and Serovy, G. K., 1970, "Application of Blade Element Design Methods to the Design of Highly Loaded Axial-Flow Pump Stages," *International Association for Hydraulic Research*, Symposium Stockholm 1970, Part I, Paper A-3.

Klapproth, J. F., 1961, "A Review of Supersonic Compressor Development," ASME *Journal of Engineering for Power*, Vol. 83A, pp. 248-268.

Lieblein, S., 1959, "Loss and Stall Analysis of Compressor Cascades," ASME *Journal of Basic Engineering*, Vol. 81D, pp. 387-400.

Lieblein, S., and Johnsen, I. A., 1961, "Resumé of Transonic-Compressor Research at NACA Lewis Laboratory," ASME *Journal of Engineering for Power*, Vol. 83A, pp. 219-234.

Miller, M. J., Okiishi, T. H., Serovy, G. K., Sandercock, D. M., and Britsch, W. R., 1973, "Summary of Design and Blade-Element Performance Data for 12 Axial-Flow Pump Rotor Configurations," NASA TN D-7074.

---

[2] Mel Hartmann supported some of this work with NASA funding. Some he tolerated as a source of data of possible future use. Some developed because he mentioned other possible contacts in NASA-Lewis. When we visited Cleveland, he usually asked us to visit his office at the end of the day. For those who knew of his Nebraska background, it will not be surprising to learn that his first words were seasonally, "How's the corn?" or "How is the snow cover?" He always kept a drawing board in his office, and often could be found checking a rig drawing. His comments were, without exception, constructive and encouraging. We hope that we made a useful contribution to the NASA pump program, in keeping with the influence that he had on our lives and professional development.

Miller, M. J., and Serovy, G. K., 1975, "Deviation Angle Estimation Axial-Flow Compressors Using Inviscid Flow Solutions," ASME *Journal of Engineering for Power*, Vol. 97, pp. 163–168.

NASA, 1959, "The National Aeronautics and Space Administration, First Semiannual Report to the Congress, October 1, 1958–March 31, 1959," NASA, Washington, DC.

Savage, M., Boxer, E., and Erwin, J. R., 1961, "Resumé of Compressor Research at the NACA Langley Laboratory," ASME *Journal of Engineering for Power*, Vol. 83A, pp. 269–285.

Schmidt, D. P., and Okiishi, T. H., 1977, "Multistage Axial-Flow Turbomachine Wake Production, Transport and Interaction," *AIAA Journal*, Vol. 15, pp. 1138–1145.

Serovy, G. K., and Anderson, E. W., 1959, "Method for Predicting Off-Design Performance of Axial-Flow Compressor Blade Rows," NASA TN D-110.

Serovy, G. K., 1966, "Recent Progress in Aerodynamic Design of Axial-Flow Compressors in the United States," ASME *Journal of Engineering for Power*, Vol. 88A, pp. 251–261.

Serovy, G. K., Kavanagh, P., Okiishi, T. H., and Miller, M. J., 1973, "Prediction of Overall and Blade-Element Performance for Axial-Flow Pump Configurations," NASA CR-2301.

Serovy, G. K., and Okiishi, T. H., 1988, "Performance of a Compressor Cascade Configuration With Supersonic Entrance Flow—A Review and Comparison of Experiments in Three Installations," ASME JOURNAL OF TURBOMACHINERY, Vol. 110, pp. 441–449.

Shepherd, D. G., 1956, *Principles of Turbomachinery*, The Macmillan Company, New York.

Taylor, W. E., Murrin, T. A., and Colombo, R. M., 1969a, "Systematic Two-Dimensional Cascade Tests, Vol. 1: Double Circular-Arc Hydrofoils," NASA CR-72498.

Taylor, W. E., Murrin, T. A., and Colombo, R. M., 1969b, "Systematic Two-Dimensional Cascade Tests, Vol. 2: Multiple Arc Hydrofoils," NASA CR-72499.

Tweedt, D. L., Okiishi, T. H., and Hathaway, M. D., 1986, "Stator Endwall Leading-Edge Sweep and Hub Shroud Influence on Compressor Performance," ASME JOURNAL OF TURBOMACHINERY, Vol. 108, pp. 224–232.

Wagner, J. H., Okiishi, T. H., and Holbrook, G. J., 1979, "Periodically Unsteady Flow in an Imbedded Stage of a Multistage, Axial-Flow Turbomachine," ASME *Journal of Engineering for Power*, Vol. 101, pp. 42–51.

Wilcox, W. W., Tysl, E. R., and Hartmann, M. J., 1959, "Resume of the Supersonic-Compressor Research at NACA Lewis Laboratory," ASME *Journal of Basic Engineering*, Vol. 81D, pp. 559–568.

Wisler, D. C., Bauer, R. C., and Okiishi, T. H., 1987, "Secondary Flow, Turbulent Diffusion and Mixing in Axial-Flow Compressors," ASME JOURNAL OF TURBOMACHINERY, Vol. 109, pp. 445–482.

Wislicenus, G. F., 1960, "Hydrodynamics and Propulsion of Submerged Bodies," *Journal of the American Rocket Society*, Vol. 30, pp. 1140–1148.

Zierke, W. C., and Okiishi, T. H., 1982, "Measurement and Analysis of Total Pressure Unsteadiness Data From an Axial-flow Compressor Stage," ASME *Journal of Engineering for Power*, Vol. 104, pp. 479–488.

Turbulence Characteristics in a Supersonic Cascade Wake Flow

P. L. Andrew

Wing-fai Ng

Virginia Polytechnic Institute and State
University,
Blacksburg, VA 24061

The turbulent character of the supersonic wake of a linear cascade of fan airfoils has been studied using a two-component laser-doppler anemometer. The cascade was tested in the Virginia Polytechnic Institute and State University intermittent wind tunnel facility, where the Mach and Reynolds numbers were 2.36 and 4.8 × 10^6, respectively. In addition to mean flow measurements, Reynolds normal and shear stresses were measured as functions of cascade incidence angle and streamwise locations spanning the near-wake and the far-wake. The extremities of profiles of both the mean and turbulent wake properties were found to be strongly influenced by upstream shock-boundary -layer interactions, the strength of which varied with cascade incidence. In contrast, the peak levels of turbulence properties within the shear layer were found to be largely independent of incidence, and could be characterized in terms of the streamwise position only. The velocity defect turbulence level was found to be 23 percent, and the generally accepted value of the turbulence structural coefficient of 0.30 was found to be valid for this flow. The degree of similarity of the mean flow wake profiles was established, and those profiles demonstrating the most similarity were found to approach a state of equilibrium between the mean and turbulent properties. In general, this wake flow may be described as a classical free shear flow, upon which the influence of upstream shock-boundary-layer interactions has been superimposed.

Introduction

Study of the flow in the wake of an airfoil is justified from both engineering and scientific perspectives. To the turbomachinery engineer, wake flows are of interest in the contexts of viscous blockage, rotor/stator-interaction-noise generation, mechanical vibration [1], and the loss generation associated with the mixing and dissipation of the wake with the freestream flow. Wake turbulence measurements also support efforts to improve turbulence models within the framework of the Reynolds-averaged Navier-Stokes equations. Typically, measurements such as these are fundamental to new modeling concepts and/or empirical relationships, which eventually yield more accurate numerical prediction of mean flow quantities.

Airfoil wake flows are of scientific interest as they constitute the merging of two turbulent shear layers whose wall shear stress has been discontinuously removed. The compressible wake of this paper has the additional complexity of the influence of upstream shock-boundary-layer interaction and attendant separation.

Investigation of the turbulent character of wake flows has been heretofore confined to the subsonic and transonic flow regimes. Chevray and Kovasznay [2] measured the turbulent normal and shear stresses in the wake formed by low-speed flow over a thin flat plate. Using hot-wire anemometry (HWA) these authors reported that the location of maximum turbulence intensity migrates from the wake centerline with increasing streamwise distance, and that this maximum is coincident with the location of maximum shear stress. Narasimha and Prabhu [3] focused on the relaxation to equilibrium of a similar low-speed turbulent wake. Low-speed rotor wake flows have been investigated by Reynolds et al. [4], and by Lakshminarayana and Davino [5]. One of their principal observations was the existence of significant spanwise flow velocities that alter the turbulence properties relative to two-dimensional cascade wakes.

The incompressible wake of an isolated symmetric airfoil was surveyed by Yu [6], where the maxima in profiles of turbulence intensity and shear stress were found to migrate transverse to the wake centerline as in [2]. Orloff and Olson's [7] study of the low-speed flow about a flapped airfoil focused mainly on the experimental technique. Viswanath et al. [8] investigated the compressible wake of an isolated airfoil using laser-doppler anemometry (LDA). A salient finding therein was that the shear stress profiles were "frozen" or constant with streamwise location in the near wake.

Petrie and Emmer [9], Johnson and Bachalo [10], and Johnson and Spaid [11] all used dual-component LDA systems to document the turbulent characteristics of the transonic wakes of isolated airfoils. These studies collectively indicate a first-order influence of incidence angle (and therefore the severity of shock-boundary-layer interaction) on the magnitude and development of turbulence properties in the wake. Typically in these studies the boundary layer does not re-attach after separation, which, significantly, is in contrast to the nature of separations encountered in the present cascade flow.

Raj and Lakshminarayana [12] provided an early and one

Contributed by the International Gas Turbine Institute and presented at the 38th International Gas Turbine and Aeroengine Congress and Exposition, Cincinnati, Ohio, May 24-27, 1993. Manuscript received at ASME Headquarters March 17, 1993. Paper No. 93-GT-348. Associate Technical Editor: H. Lukas.

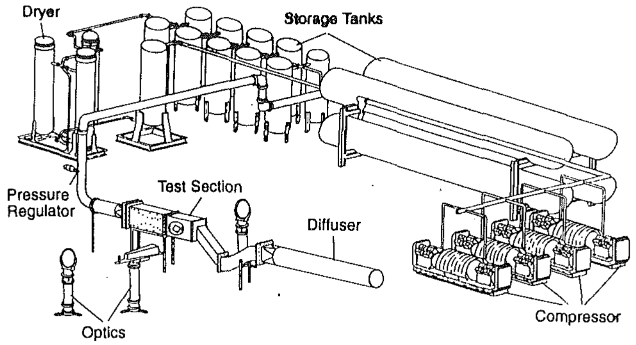

Fig. 1 VPI&SU intermittent cascade wind tunnel facility

of the few investigations of the wakes of airfoils mounted in cascade. More recently, Baydar [13] and Elazar [14] applied HWA and LDA respectively in their studies of a cascade of controlled diffusion airfoils. Although no shear stress results were reported, their measurements of turbulence intensity using the two experimental techniques compared generally well.

The most important distinction of this contribution relative to the efforts cited above is the characterization of the wake turbulence in the *supersonic* flow regime. It is a fundamental investigation of the streamwise development of wake turbulence properties at design and off-design incidence conditions. The fact that the airfoils were mounted in cascade is also significant, in that the favorable pressure gradient associated with supersonic axial flow always caused the shock-induced separations to re-attach. The use of a two-component, coincident LDA enabled the nonintrusive measurement of not only the mean flow and turbulence intensities but also the less-frequently reported Reynolds shear stress. The supersonic wake turbulence characteristics obtained here will be compared and contrasted to the low-speed and transonic results cited above as appropriate, in the section entitled Results. Discussion of the direct application of these measurements, in the form of the calibration of a turbulence model used in simulating the cascade flow field, is deferred to a subsequent publication.

Experimental Apparatus

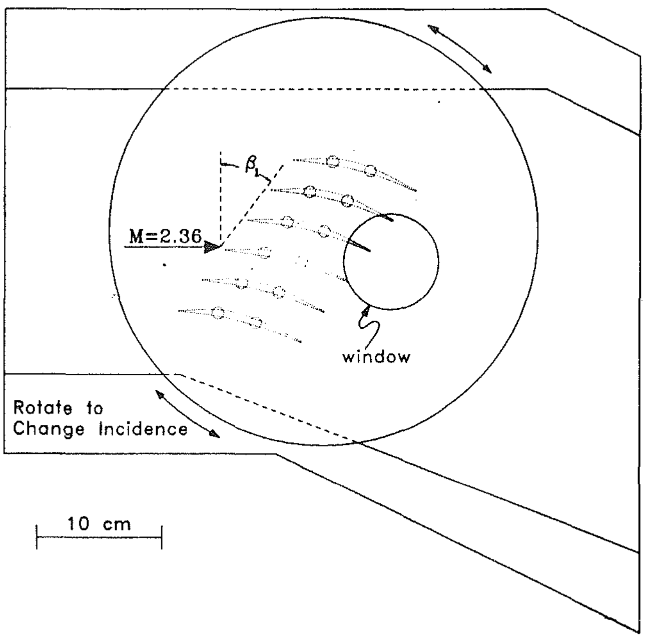

Fig. 2 VPI&SU cascade test section

Facility. The experiments described herein were conducted in the Virginia Polytechnic Institute and State University (VPI&SU) intermittent cascade wind tunnel facility shown in Fig. 1. The facility stagnation pressure and temperature were 4.5 atm and 285 K, respectively, yielding a free-stream unit Reynolds number of approximately 48 million per meter. The nominal Mach number at the test section inlet was 2.36. The facility air was dried using a cycling desiccant system, which, in combination with the high stagnation pressure employed here, minimized the influence of condensation shocks. A flow straightening section and screens were used to reduce the free-stream turbulence level to approximately 1 percent as measured by Bowersox et al. [15]. The cascade test section depicted in Fig. 2 measures 22.86 cm in height and 15.25 cm in span. The cascade consists of six full-scale rotor blades of 10.03 cm chord, spaced 3.02 cm apart. The resulting solidity was 3.32 and the maximum blade thickness-to-chord ratio was 5.78 percent. The inlet flow angle is 37 deg, and 26 deg of turning occurs through the passage. Incidence was varied experimentally by mounting the blades in a circular sidewall section that could be rotated relative to the incoming flow as indicated in Fig. 2. Incidences ranging from -10 deg to +5 deg were herein investigated, accurate to ±0.5 deg.

Laser-Doppler Anemometer System. The laser-Doppler anemometer was applied as the principle diagnostic tool in this research, primarily due to its ability to produce spatially resolved measurements of the cross correlation $-\overline{u'v'}$. The two-color, two-component system was arranged in a dual-beam configuration. A temperature-controlled etalon was used to ensure single longitudinal mode operation of the laser in both the green and the blue colors. One beam of each color was shifted in frequency by 40 MHz by means of a Bragg cell. The two pairs of beams were rotated to measure components of velocity at 45 deg to the mean flow direction as depicted in Fig. 3. The measurement volume is estimated to be 0.3 mm in cross-sectional (streamwise) extent and 3 mm in spanwise extent. Optical access ranging from 0.95 chord to 1.4 chord was achieved through the schlieren glass window shown in Fig. 2. The collection optics were arranged to collect forward-scattered radiation on axis, and were mounted on a truss, which extended from the main optical table on one side of the test section, under the wind tunnel, to the opposite side of the test section. The main optical table was mounted on a three-di-

Nomenclature

a_1 = structural coefficient of turbulence
C = chord
i = incidence
M = Mach number
Re_c = Reynolds number based on chord
S = blade spacing or pitch
$-\overline{u'v'}$ = kinematic Reynolds shear stress
u = streamwise velocity fluctuations
v = transverse velocity fluctuation
X = streamwise direction
Y = transverse or pitchwise direction
σ = standard deviation

Superscripts

$\overline{}$ = time-average
= fluctuation

Subscripts

c = centerline
e = edge
m = maximum
t = turbulent
∞ = upstream reference condition

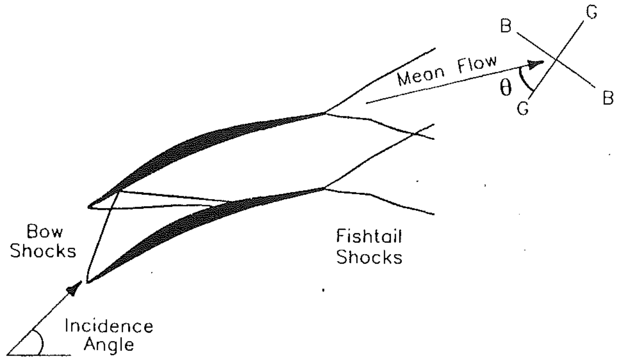

Fig. 3 Supersonic cascade flow schematic

mensional traverse system. In this manner, the transmitting and receiving optics were traversed in unison relative to the wind tunnel.

Burst counters of 1 ns resolution were employed to measure the doppler frequency. A coincidence window of between 2 and 10 μsec was imposed between the two counter channels, and samples ranging in size between 1024 and 2048 instantaneous realizations were obtained.

Seeding. The cascade flow was seeded globally using 0.6 μm polystyrene-latex (PSL) spheres. Ethyl alcohol was used as a carrier solution, in the proportion 40 parts alcohol to 1 part PSL by volume. The mixture was injected at a point 3 m upstream of the test section to ensure complete evaporation of the carrier fluid. Samples of the seed particles collected in situ from the test section and examined using an electron microscope were free of agglomeration and uniform in size. The seeder was a simple atomizing type. Since the injection took place upstream of the straightening section, the atomizer had no detrimental influence on flow uniformity. Data rates using the seeding system described above were experimentally verified to increase by a factor of thirty, relative to those resulting from only ambient particles.

A primary advantage of PSL for use as a seed particle is the ability to manufacture spheres of a desired size with a uniform size distribution. The intrinsic conflict between particle lag and signal quality that complicates the selection of the proper seed size is only exacerbated in supersonic flow. In order to optimize the seed particle size, and to gage the influence of particle lag in this experiment, a separate study [16] was undertaken. To describe this study in brief, PSL spheres of three different diameters (0.24 μm, 0.6 μm, 1.5 μm) were used to measure the velocity variation through a 10-deg oblique shock. The wind tunnel facility and LDA system was as described above. By comparing the measurement of fluid velocity for this contrived flow to predictions using one-dimensional gas dynamics, an assessment of particle lag could be made.

The salient results of this study were as follows. The 0.24 μm spheres, in conjunction with the burst counters employed herein, proved to be too small to generate a viable signal. Both of the larger PSL sphere sizes produced an acceptable signal level, although the particle lag associated with the 1.5 μm spheres was significantly greater than that observed using the 0.6 μm seed. Therefore, the 0.6 μm sphere was selected as the best compromise between particle lag and the signal-to-noise ratio for this flow condition. In this vein it may be additionally noted that the use of a forward-scatter optical system, with its two-order-of-magnitude increase in signal intensity relative to back-scatter systems, is indispensable under these high-speed flow conditions.

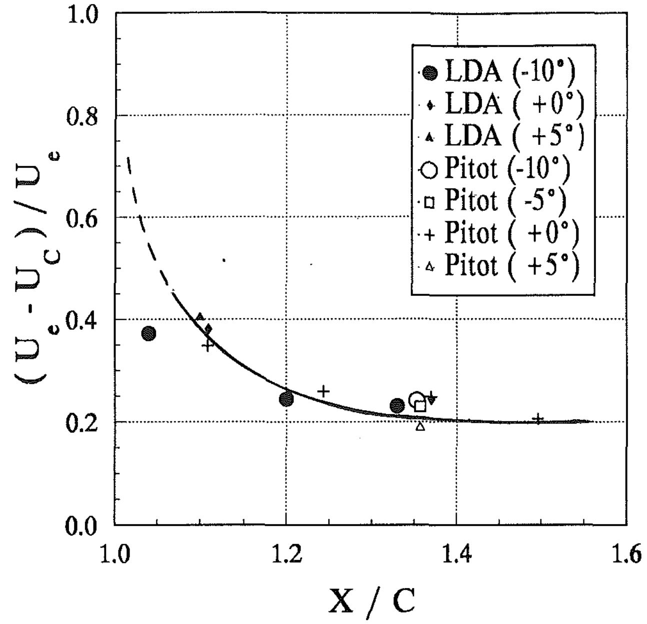

Fig. 4 Streamwise variation of velocity defect

Flow Field

The blade cascade and wake flow field are represented schematically in Fig. 3. The cascade is operated at a supersonic axial Mach number, such that the bow shocks emanating from the leading edge are contained within the blade passage. The severity of the interaction of these shocks with the blade boundary layer varies parametrically with cascade incidence angle. The blade profile was designed to avoid separation due to shock-boundary-layer interaction at design incidence [17]. At +5 deg incidence, separation was verified (via surface oil flow visualization) to occur on the suction surface from 42 percent to 54 percent chord. At-10 deg incidence, the pressure surface was separated from 10 to 24 percent chord, with the separated region extending much further into the blade passage.

Data Reduction

Data reduction was accomplished in a standard fashion as in [10]. Due to the low turbulence intensities encountered herein, the potential for velocity bias was considered negligible, and therefore no corrections for velocity bias have been applied to the data [18]. The mean statistics were calculated in the orthogonal blue-green frame of reference defined by the measurement system, and later rotated to a shear-layer-aligned coordinate system. The mean velocities were rotated from the blue/green coordinate system to the shear-layer-aligned system simply by:

$$\overline{u} = \overline{b} \cos \theta + \overline{g} \sin \theta.$$

$$\overline{v} = \overline{g} \cos \theta - \overline{b} \sin \theta.$$

As stated previously, the coordinate system defined by the blue/green measurement system was rotated 45 deg relative to the mean flow vector, such that θ was in this case 45 deg. To obtain the turbulence intensity in the shear-layer-aligned system, the variances in each of the two channels is necessary, in addition to the cross-correction between the two channels:

$$\sigma_u^2 = \sigma_b^2 \cos^2\theta + 2\overline{-b'g'} \sin\theta \cos\theta + \sigma_g^2 \sin^2\theta, \quad u'_{\rm rms} = \frac{\sigma_u}{U_\infty}$$

$$\sigma_v^2 = \sigma_g^2 \cos^2\theta - 2\overline{-b'g'} \sin\theta \cos\theta + \sigma_b^2 \sin^2\theta, \quad v'_{\rm rms} = \frac{\sigma_v}{U_\infty}.$$

The kinematic shear stress in the shear-aligned system is obtained from:

$$\overline{-u'v'} = \frac{(\sigma_b^2 - \sigma_g^2)}{2} \sin 2\theta + \overline{-b'g'} \cos 2\theta$$

where it may be noted that for $\theta = 45$ deg, only the difference

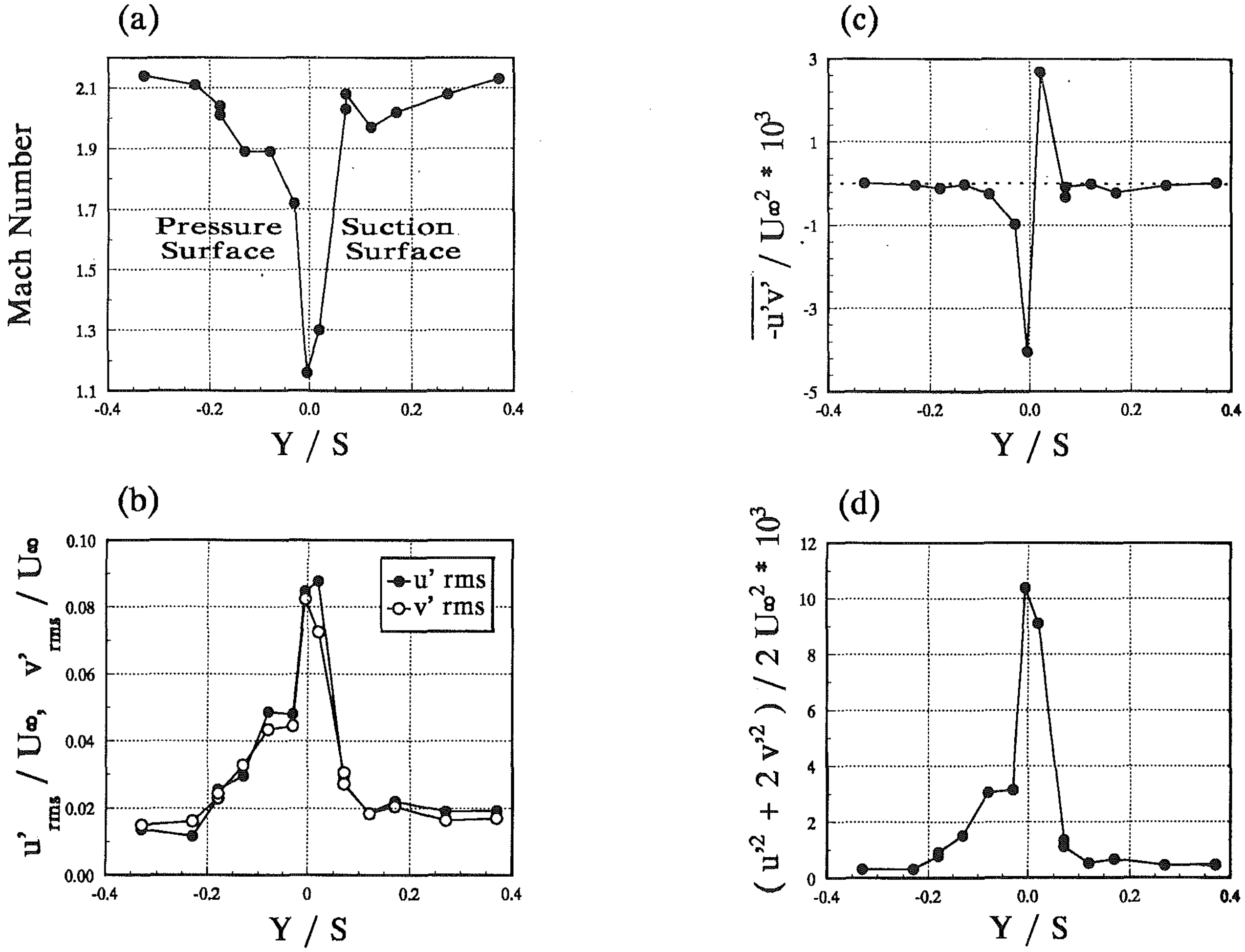

Fig. 5 Turbulence profiles—i: −10 deg; X/C; 1.04

in the variances comes into play in determining $-\overline{u'v'}$. The experimental uncertainty in the experimental results to be presented may be found in the appendix of this paper.

Results

Some insight as to the near-wake, far-wake behavior of this cascade may be obtained from Fig. 4, wherein the velocity defect is plotted as a function of streamwise distance X normalized by chord. Included in this figure is the velocity defect derived from pitot-static probe data obtained by Chesnakas [19]. A wide variety of loading (incidence) conditions are represented in this figure, which accounts for some of the observed scatter. A second source of the scatter is the uncertainty in defining the wake edge, and therefore U_e, in the presence of the trailing edge shocks and the upstream shock-boundary-layer interactions. Figure 4 serves to characterize the mean flow data of the LDA surveys herein as belonging in the near-wake category for $X/C < 1.2$, with the balance falling in the early far-wake region. In the discussion of the equilibrium state of the wake to follow, a somewhat different interpretation of the near-wake, far-wake status based on the turbulence properties will be made evident.

Selected wake turbulence profile results obtained herein are presented in Figs. 5–8. Each wake survey consists of a pitchwise traverse from the free-stream region below the pressure surface, through the blade wake, to the free-stream region above the suction surface. The pitchwise, or transverse direction Y is defined as parallel to the locus of points connecting the blade trailing edges and is normalized by the interblade spacing S. Negative values of Y/S are associated with the pressure surface, while positive values are associated with the suction surface. All of the profiles have been shifted, such that the wake centerline corresponds to $Y/S = 0$. In each figure, the Reynolds normal and shear stresses are plotted, along with the turbulent kinetic energy. The Mach number profile is included to facilitate the interpretation of the turbulence results. After the mean and turbulence results for selected tests conditions are discussed, the streamwise evolution of the peak levels of properties within the profiles will be presented.

−10 deg Incidence Cases $X/C = 1.04, 1.20, 1.33$

$X/C = 1.04$. Figure 5 contains the results of the wake survey at the streamwise location of 1.04 chord and at a cascade incidence angle of −10 deg. It is the first of a sequence of three wake surveys obtained at this incidence for streamwise stations spanning the near-wake and early far-wake. This incidence condition is an off-design flow case characterized by a massive shock-separated region on the blade pressure surface near the leading edge. The asymmetry in the Mach number profile of Fig. 5(a) near the wake centerline is due to loading. A further source of the asymmetry in the outer fraction of the pressure surface side of the wake is interpreted as the loss in momentum incurred during the upstream shock-boundary-layer interaction.

Figure 5(b) depicts the streamwise (u') and transverse (v') normal Reynolds stresses, nondimensionalized by the free-stream velocity U_∞. The level of maximum turbulence intensity of 9 percent is commensurate with the levels measured by, for example, Johnson and Rose [20], Johnson [21], Kistler [22], and Elena et a. [23] in wall-bounded supersonic flows. This

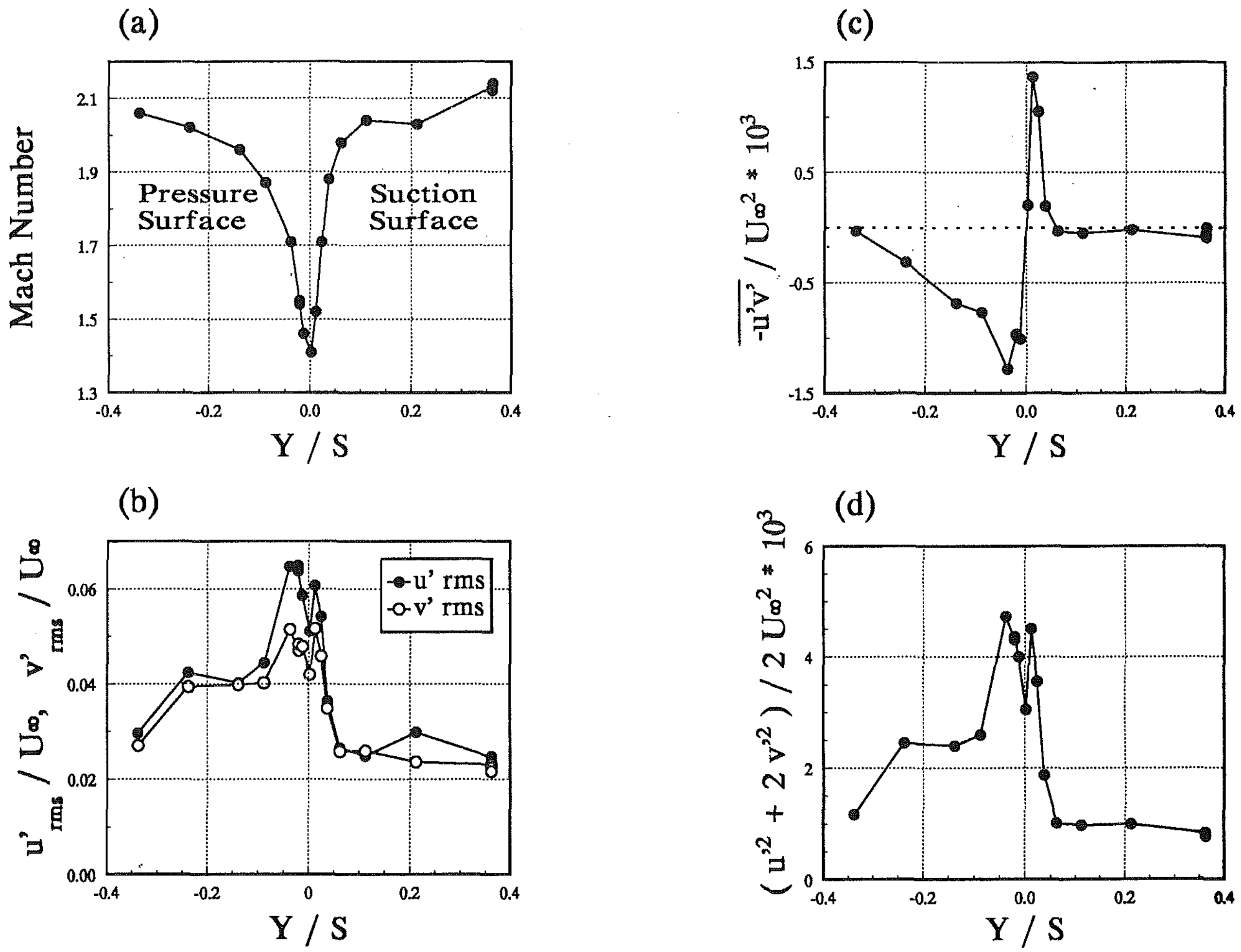

Fig. 6 Turbulence profiles—*i*: − 10 deg; *X/C*: 1.20

level is also in accord with the peak turbulence intensity of 10 percent measured herein in a boundary-layer profile obtained at 95 percent chord. In the free stream, a high degree of isotropy is apparent, and the measured free-stream turbulence intensity is 2 percent.[1] The elevated levels of turbulence intensity (≈ 4 percent) below the pressure surface are interpreted as a further manifestation of the upstream shock boundary-layer interaction and separation. Thus, the residual influence of this interaction is apparent not only in the mean flow property of Mach number but also in the turbulence properties. One may make a similar observation from the transonic airfoil wake measurements of Johnson and Bachalo [10].

The variation of Reynolds shear stress through the wake is presented in Fig. 5(*c*). This quantity may be interpreted physically as the net transport of axial momentum in the transverse direction by transverse velocity fluctuations. The measured stress is nondimensionalized by the square of the free-stream velocity and scaled by 10^3. The profile has a classical shape common to free turbulent shear flows, e.g., wakes [2, 7, 8, 10, 11, 12] and jets [25].

The reader may have observed that the shear stress distribution in the inner part of the shear layer is not very well spatially resolved, which is due in part to the narrow wake thickness at this streamwise station, in combination with the extreme gradients that are characteristic of this region. It may be noted that the two peaks of greatest absolute value in Fig. 5(*c*) correspond to the two values of minimum Mach number in Fig. 5(*a*), and are separated by only 2 percent of blade spacing. Wake surveys obtained further downstream are of improved spatial resolution because the wakes are broader in the transverse direction.

Returning to Fig. 5(*c*), some limited influence of the shock-boundary-layer interaction on the shear stress in the vicinity of the pressure surface is apparent (see $-0.10 < Y/S < 0.$). The effect of the interaction on the shear stress profile is not as pronounced as it is on the turbulence intensities, which has relevance in regard to the interpretation of shear stress profiles obtained farther downstream.

Figure 5(*d*) depicts the distribution of turbulent kinetic energy within the shear layer, which is a general measure of the turbulence level within the flow. In the definition of turbulent kinetic energy used here, the unmeasured spanwise component of velocity fluctuation, w', has been set equal to v', as in [10, 26], for example. As expected from the profiles of turbulence intensity, higher levels of turbulent kinetic energy are observed corresponding to the location of the shock-boundary-layer interaction.

− 10 deg Incidence Case $X/C = 1.20$. The next wake profile case to be considered was obtained at the same cascade incidence of − 10 deg, but at a further downstream location of 1.20 chord. The greater transverse extent of this wake allowed for the turbulence properties to be spatially resolved in greater detail.

Figure 6(*a*) shows the Mach number profile for this case. Relative to the previous survey at 1.04 chord, the wake defect has decreased significantly, and, to a lesser extent, the profile

---

[1] It is noted that the actual free-stream turbulence level in this flow is approximately 1 percent, as reported by Bowersox et al. [15]. This level of intensity is below the resolution limit of the employed LDA system for this supersonic flow due to the use of burst counters of 1 nsec resolution. A similar problem was encountered by Kuntz et al. [24], and is discussed in more detail by Johnson [18].

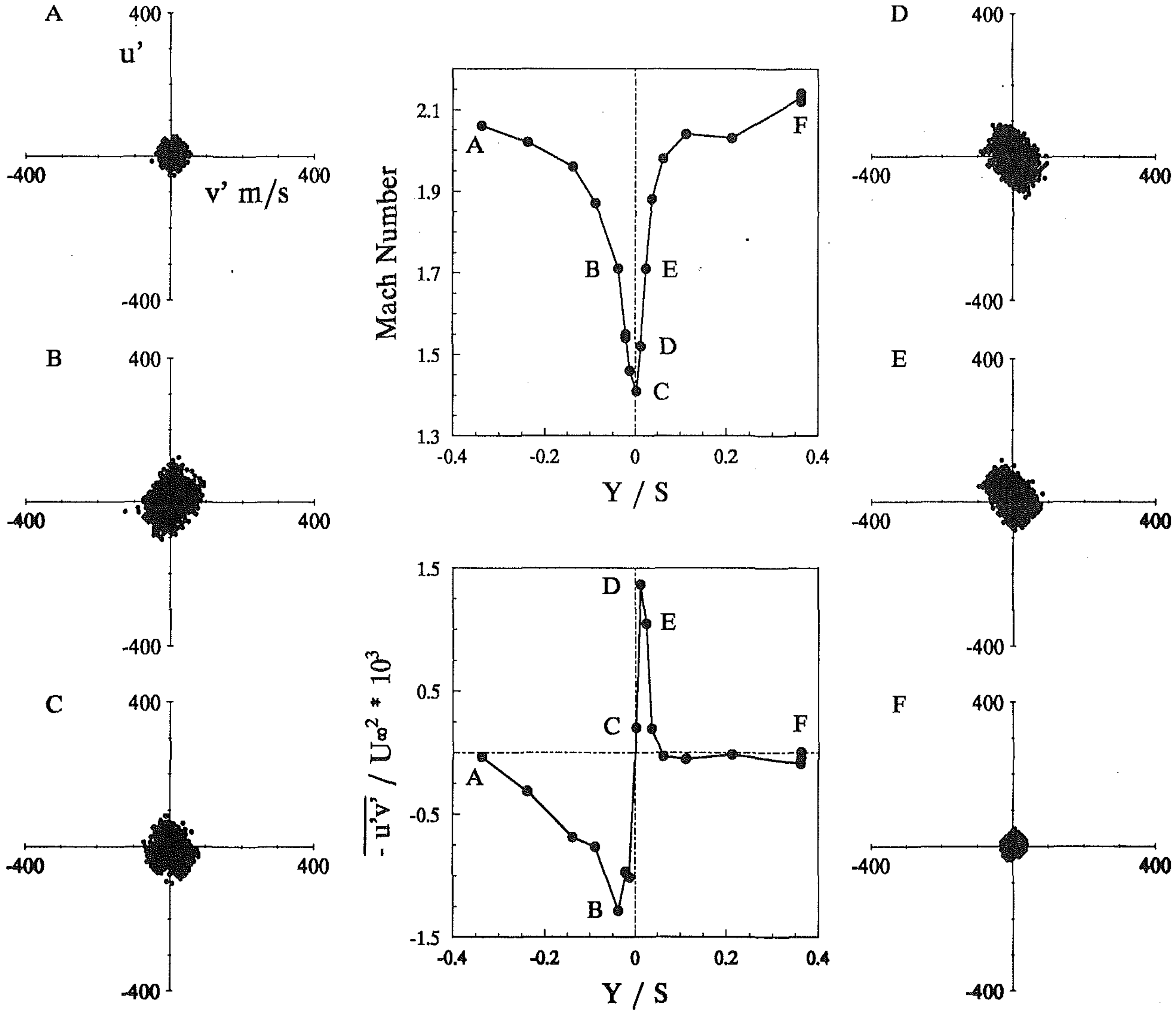

Fig. 7 Turbulence intensity scatter plot—i: −10 deg; X/C: 1.20

has broadened. Asymmetry due to the combined effects of loading and the upstream separation remains apparent.

A comparison of the turbulence intensities shown in Fig. 6(*b*), to those of the previous survey indicated that the maximum levels have attenuated from ≈9 to ≈6 percent. The elevated levels of turbulence intensity on the pressure side of the wake due to the upstream interaction remain extant, while in the free stream the turbulence intensity remains biased high at 2 percent.

A salient feature of this profile is the two local maxima in turbulence intensity that are displaced outward from both sides of the wake centerline. This is a common characteristic in wake flows as may be observed from the work of, for example, Chevray and Kovasznay [2], Baydar [13], and Johnson and Bachalo [10], which spans flow regimes from very low speed to transonic. The displacement of the maxima in turbulence intensity away from the wall in *wall-bounded* turbulent flows is also well documented (see, e.g., [10]) and was observed herein in a boundary-layer survey in this cascade obtained at 0.95 chord. For these wall-bounded flows, one may be tempted to ascribe the phenomena to the attenuation of turbulent eddies as they interact with the wall. However, this would obviously not apply to flow in the far-wake, and a more tenable explanation arises from the consideration of the production of turbulent kinetic energy.

For two-dimensional mean motion, the two turbulent energy production terms of the turbulence energy equation may be written as functions of the Reynolds shear and normal stresses [27]:

$$-\overline{u'v'}\,\frac{\partial \bar{u}}{\partial y}, \qquad (\overline{u'^2}-\overline{v'^2})\,\frac{\partial \bar{u}}{\partial x}.$$

In words, the first term represents turbulent energy production by shear stress working against the transverse gradient in mean axial velocity. It is normally considered to be the primary mechanism for the extraction of turbulent kinetic energy from the mean kinetic energy of the flow. Physically, this transfer of energy may be interpreted as taking place through a stretching process of the turbulent vortices by the mean motion [28]. The second source term is obviously a function of the degree of isotropy and has been shown to be important in separating flows by Simpson [27]. Except near the trailing edge, the slow rate of change of the streamwise velocity with distance X would seem to justify the neglect of this second production source, leaving the term involving the Reynolds shear stress as the primary turbulent kinetic energy production mechanism in this flow. Since the shear term $-\overline{u'v'}$ peaks at a location displaced from the wake centerline (see, e.g., Fig. 6*c*) and this location coincides with a region of high-velocity gradient, it is not surprising that the turbulence intensity displays a proximate maxima.

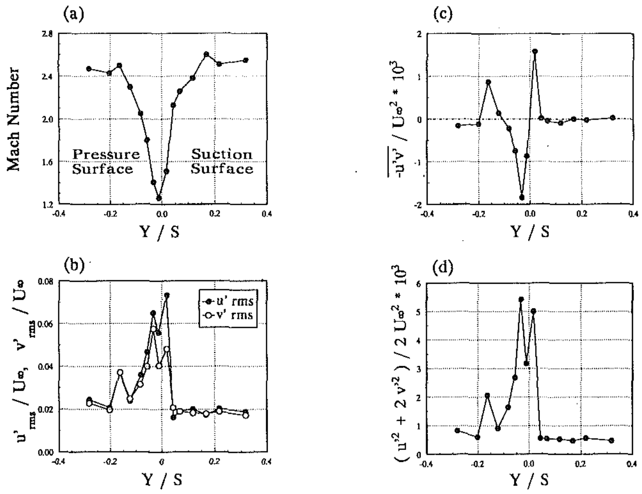

Fig. 8 Turbulence profiles—*i*:0 deg; *X/C*: 1.11

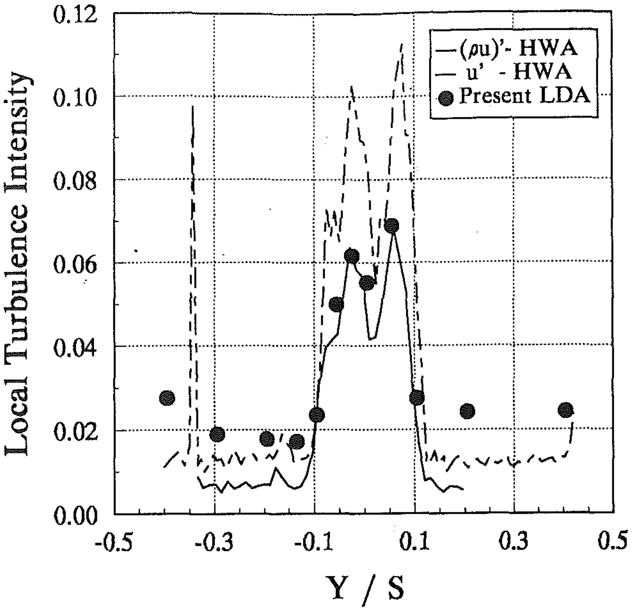

Fig. 9 HWA and LDA turbulence intensity comparison—*i*:0 deg; *X/C*: 1.11

The Reynolds shear stress profile for this case is presented in Fig. 6(*c*). A number of similarities and distinctions may be pointed out between this profile and the profile obtained at 1.04 chord. One similarity is the expected zero shear stress in the free-stream. Second, extremely high transverse gradients in shear are observed in both directions from the wake centerline. The shear is observed to vary linearly in this narrow region as has been commonly noted in the previously cited literature pertaining to a wide range in flow regimes.[2] This shear stress profile differs from that of the previous station in that the levels of peak shear on both the suction and pressure surface sides have been attenuated by approximately half. Further, significant levels of shear are now evident below the wake centerline, where formerly there was none. Two candidate mechanisms may be proffered to explain this elevated level of shear. One explanation is that the peak levels of shear stress near the wake centerline have diffused outward. Alternatively, the elevated shear could be an artifact of the upstream shock-boundary-layer interaction. The first explanation is precluded, since there is not a concomitant diffusion of shear stress along the suction surface side of the wake. It is well known that the shear stress does not respond instantaneously to distortions in the mean flow field, and therefore it is conjectured that these elevated levels of shear were spawned in the upstream shock-boundary-layer interaction near the leading edge.

The turbulent kinetic energy profile for this case is given in Fig. 6(*d*). As expected, this parameter mirrors the trends observed in the turbulence intensity profiles. Namely, there exist two local maxima displaced from the wake centerline, and there are elevated levels of turbulence intensity on the pressure surface side of the wake due to the upstream separation.

−10 deg Incidence Case X/C = 1.33. Although not shown here, profiles obtained at this same incidence but farther downstream at 1.33 chord were markedly similar to those just discussed at 1.20 chord. This suggests that the wake had attained a self-preserving state [3], analogous to the "frozen" shear stress profiles in the wake of a transonic airfoil reported by Viswanath et al. [8].

Figure 7 contains scatter plots of the turbulent fluctuation velocity u' in m/s plotted versus the abscissa v' for six locations designated in the Mach number and shear stress profiles of Figs. 6(*a*) and 6(*c*). The scatter plots obtained at other streamwise locations were qualitatively similar to those presented in Fig. 7. The relatively large, circular cluster at point *A* indicates an elevated level of turbulence intensity, but nearly free-stream levels of shear. The elliptical scatter plot at point *B* corresponds to the maximum levels of measured shear along the pressure surface. The shear stress changes sign at the wake centerline near point *C*, resulting in a large, nearly circular plot, indicative of high turbulence and low shear. The change in sign of $-u'v'$ between the pressure surface and the suction surface is reflected in the change in orientation of the major axis of the ellipses at points *D* and *B*. Low levels of shear and turbulence intensity are indicated at the free-stream point *F*.

The scatter plots of Fig. 7, in addition to lending physical insight, serve also to justify the assumption of Gaussian velocity distributions in calculating the mean turbulence properties presented here. Had this wake flow been dominated by a Karman vortex street as is sometimes the case in airfoil wake flows, such an assumption would not have been warranted. The collective experimental insight obtained through HWA and LDA surveys, in addition to nano-shadowgraphs, offers no conclusive evidence of periodic vortex shedding into the wake. This may be attributable to the relative "thinness" of the trailing edge of 0.5 mm.

Design Incidence Case X/C = 1.11. The next wake survey to be considered was obtained at design incidence at the streamwise station X/C = 1.11 and is presented in Fig. 8. There are no significant shock-boundary-layer interactions associated with this incidence condition, and therefore the asymmetry observable in the Mach number profile of Fig. 8(*a*) is attributable to loading. The anomaly in turbulence intensity, shear stress, and turbulent kinetic energy at $Y/S = -0.16$ is attributed to the influence of the lower of the two trailing edge "fishtail" shocks. Many of the same observations made regarding the profiles at −10 deg incidence apply to this incidence case as well, including the two local maxima in turbulent kinetic energy, the linear variation of the shear stress through the wake centerline, and the level of free-stream turbulence of 2 percent.

A direct comparison between these results and those obtained using HWA in the same facility is presented in Fig. 9, adapted from Bowersox et al. [15]. The hot-wire results are presented both in terms of the mass-flux intensity $(\rho u)'$ and in terms of the velocity fluctuation u', which agrees closely with the LDA measurements obtained near the wake centerline. Due to the high velocities encountered in the free-stream region exterior to the wake, the LDA exaggerates the turbulence intensity due to the finite resolution of the burst counters.

---

[2] Townsend [29] has derived a qualitative explanation for this linear variation in shear stress for the far-wake region.

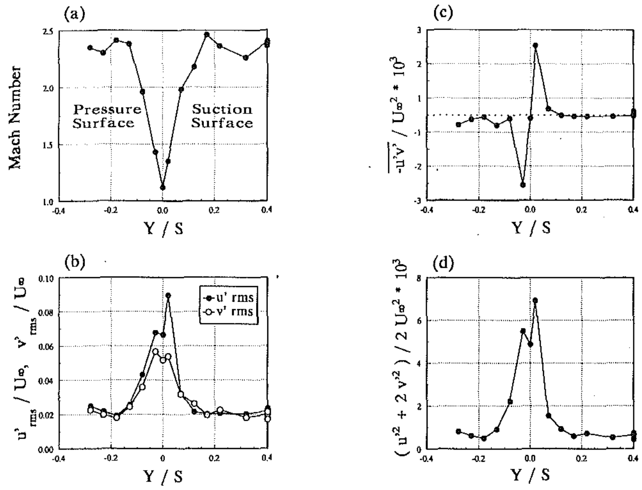

Fig. 10 Turbulence profiles—*i*: +5 deg *X/C*: 1.10

+5 deg Incidence Case $X/C = 1.10$. Profiles obtained at +5 deg and 1.10 chord are presented in Fig. 10. This case is an off-design case characterized by a large, shock-separated region at approximately half chord on the suction surface. It is perhaps most reasonable to compare this profile to the profile obtained at design incidence and 1.11 chord. In doing so, it is apparent that the upstream separation has caused the suction surface side of the wake to broaden, such that the wake, taken as whole, is nearly symmetric. The reader will recall that the design incidence wake at nearly this same station was asymmetric. In addition, the shear and the turbulent kinetic energy are elevated on the suction surface side of the wake due to the interaction, again relative to the design incidence case.

Selected wake profiles from three incidence cases have been discussed individually in detail. Although not shown explicitly, the differences in these profiles due to differences in incidence are largely confined to the extremity of the wake shear layers, such that the peak values of the turbulence properties within the shear layer are largely independent of incidence. This permits the combination of the wake turbulence data at all incidences, to reveal the streamwise development of the wake turbulence properties.

Streamwise Wake Development. The peak correlation coefficient for each of the suction and pressure surface shear layers is presented versus streamwise distance in Fig. 11. All of the incidence conditions surveyed in this experiment are included in this figure. The range in correlation coefficient of between 0.3 and 0.6 is in general agreement with free shear layer data presented by Johnson and Bachalo [10], Yu [6], and Liepmann and Laufer [30], for example.

Figure 12 summarizes the streamwise development of the mean peak turbulence quantities through the near wake and early portion of the far-wake.[3] Included in this figure are the Reynolds shear stress, the turbulent kinetic energy, and the production rate of turbulent kinetic energy. The former two parameters are defined as previously, with the production rate of turbulent kinetic energy taken as:

$$\frac{-\overline{u'v'}}{U_\infty^2}\,\frac{\partial(u/U_\infty)}{\partial(y/S)}\times 10^2$$

Included in this figure are data from all three of the incidence conditions surveyed. Significantly, it should be noted that the streamwise distance parameter is much more important in characterizing the wake development than is the incidence parameter. Near the trailing edge, the wake parameters decay exponentially, as in the experiment of Narasimha and Prabhu [3]. The observed rapid decay of the production rate of turbulent kinetic energy is in accord with the behavior of the turbulent kinetic energy itself. Perhaps most importantly, the shear stress and the turbulent kinetic energy may be observed to be in constant proportion throughout the wake; this fact will be addressed in more detail in the next section.

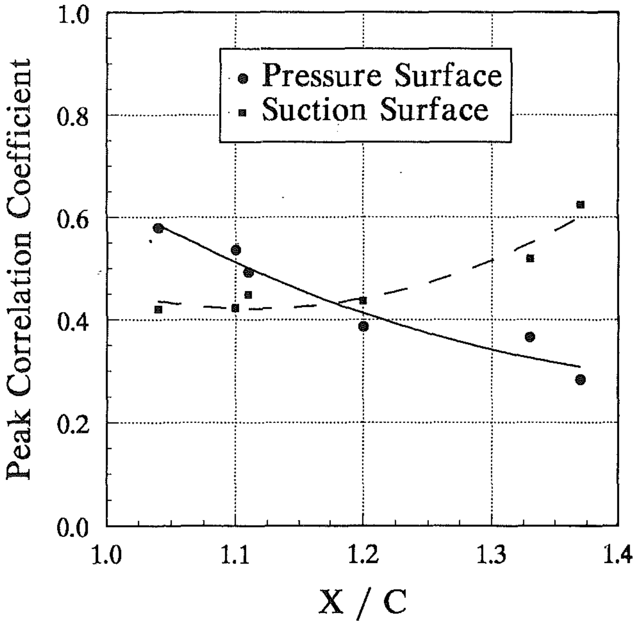

Fig. 11 Correlation coefficient at peak shear: $-\overline{u'v'}/\sigma_u\sigma_v$

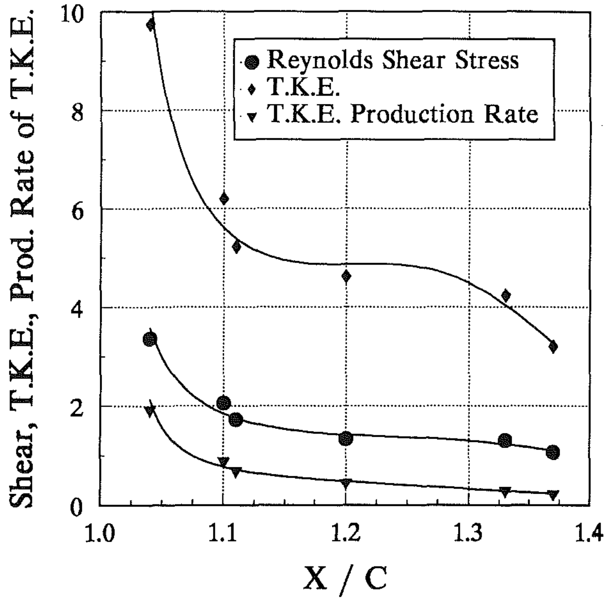

Fig. 12 Streamwise turbulence decay

Structural Coefficient of Turbulence. In a survey of numerous wake and jet shear flow experiments, Harsha and Lee [26] demonstrated a simple relationship between the Reynolds shear stress and the turbulent kinetic energy. The result of their survey of four low-speed wake experiments is reproduced in Fig. 13, which has been modified to include data from the present experiment. It may be noted that the levels of $-\overline{u'v'}$ and turbulent kinetic energy encountered here are comparable

---

[3] Due to the extreme gradients within the portion of the shear layer where these maxima are located, and due to the finite spatial resolution of the wake survey, the mean suction surface and the pressure surface values were used in this figure.

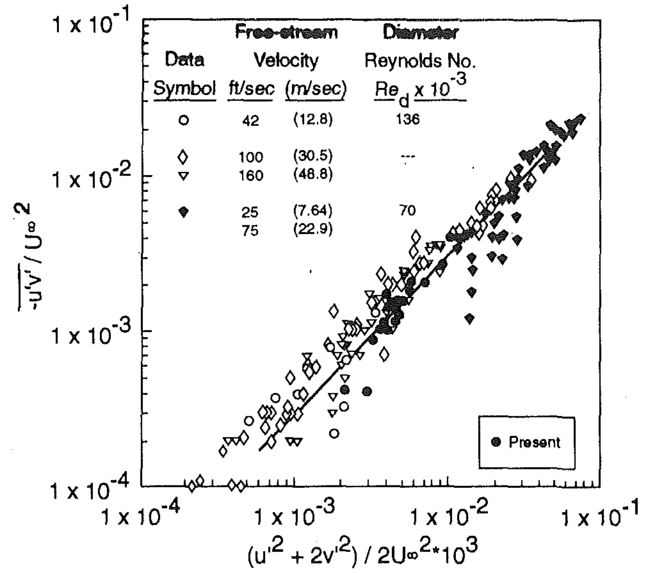

Fig. 13 Relation between Reynolds shear stress and T.K.E. for wakes

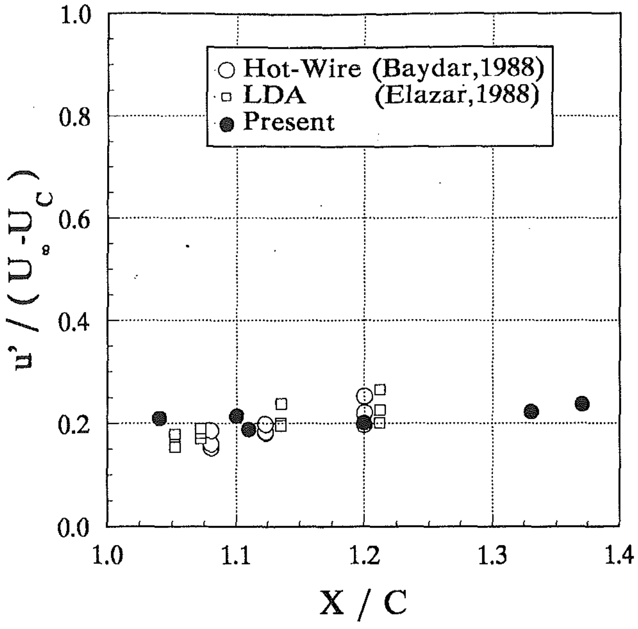

Fig. 14 Streamwise variation of velocity defect turbulence level

to those observed at low speed. Moreover, the linear relationship between these two turbulence properties demonstrated by Harsha and Lee for low-speed wakes is preserved at high speed. The line through the data of Fig. 13 is an attempt by these authors to fit the data to an expression of the form:

$$-\overline{u'v'} = a_1 \frac{1}{2} [\overline{u'^2 + v'^2 + w'^2}]$$

where a_1 is a constant equal to 0.3 and w'^2 is set equal to v'^2. This functional form, while appealing for other reasons, is physically incorrect along lines of symmetry, e.g., where zero shear is associated with finite turbulent kinetic energy, as along the wake centerline of this experiment. The constant a_1 is generally known as the structural coefficient of turbulence, and is not only of academic interest but has been practically applied in the formulation of turbulence models by Bradshaw et al. [31], Bradshaw [32], and by Johnson and King [33], for example. Specifically, these authors used the concept of the structural coefficient as the mechanism by which the turbulent kinetic energy budget is transformed into a rate equation for the streamwise development of the Reynolds shear stress. Although the concept of the structural coefficient strictly applies only to the outer region of the shear layer, this constant is typically treated as a universal constant, applicable to the entire flow field. The structural coefficient was assigned a value of 0.3 and 0.25 in the closure models of Bradshaw et al. [31] and Johnson and King [33], respectively.

The peak measured turbulence intensity from each wake survey, nondimensionalized by the local velocity defect ($U_\infty - U_c$) is presented in Fig. 14. The present results are in good agreement with those inferred from turbulence intensity and velocity defect results from the cascade test reported by Baydar [13] and Elazar [14]. With the employed nondimensionalization, the turbulence intensity does not decay monotonically, but rather approaches asymptotically a value of about 0.23 in the far wake.

Similarity and Equilibrium. An attempt has been made to establish the state of the wake development, within the observational interval of this experiment, in terms of similarity and equilibrium.[4] Toward this end, the following operational definition is adopted, after Narasimha and Prabhu [3]: "A turbulent shear flow is in equilibrium in a region if, at every streamwise station in the region, the distributions of mean velocity and turbulent stresses exhibit similarity, with essentially the same scales." To illustrate this definition, consider a mean flow property, the velocity defect: $w(x,y)$; consider also a turbulence quantity, the Reynolds shear stress: $\tau(x, y) = -\overline{u'v'}$. Each of these parameters demonstrates similarity (but not necessarily equilibrium), if one may write:

$$w(x, y) = w_0(x) f\left[\frac{y}{\delta(x)}\right] \quad \tau(x, y) = \tau_0(x) g\left[\frac{y}{\delta_\tau(x)}\right]$$

where w_o, τ_o, δ, and δ_τ are local scale factors. At equilibrium, these mean and turbulence scale factors are interrelated, such that the ratios:

$$\frac{w_0(x)}{\tau_0^{1/2}(x)}, \quad \frac{\delta(x)}{\delta_\tau(x)} \tag{1}$$

are independent of streamwise location. It is emphasized that similarity is a necessary, but not a sufficient, condition for equilibrium.

These concepts will now be explored relative to the present cascade wake flow. The test cases under which similar conditions occurred will first be identified, prior to a check for equilibrium.

In order to investigate the existence of similarity in the mean flow properties, it was attempted to reduce the Mach number profiles to a single curve through the selection of appropriate normalizing length and velocity scales. Following Raj and Lakshminarayana [12], the employed velocity scale was the aforementioned wake defect ($M_e - M_c$), where the edge value is denoted by "e" and the centerline Mach number by "c." As to the length scale, some of the uncertainty associated with ascertaining the edge of the wake is obviated by defining pressure surface and suction surface semi-wake widths. These are the distances on the suction and pressure surface sides of the wake centerline from the point of minimum velocity to a point where the velocity is 1/2 ($M_e - M_c$).

The results of the similarity analysis are shown in Fig. 15. Figure 15(*a*) contains all six nondimensionalized profiles while Fig. 15(*b*) contains the two profiles at design incidence. Only these latter profiles demonstrate a significant degree of similarity, although all of the profiles have become more sym-

---

[4] This section follows closely arguments found in [3].

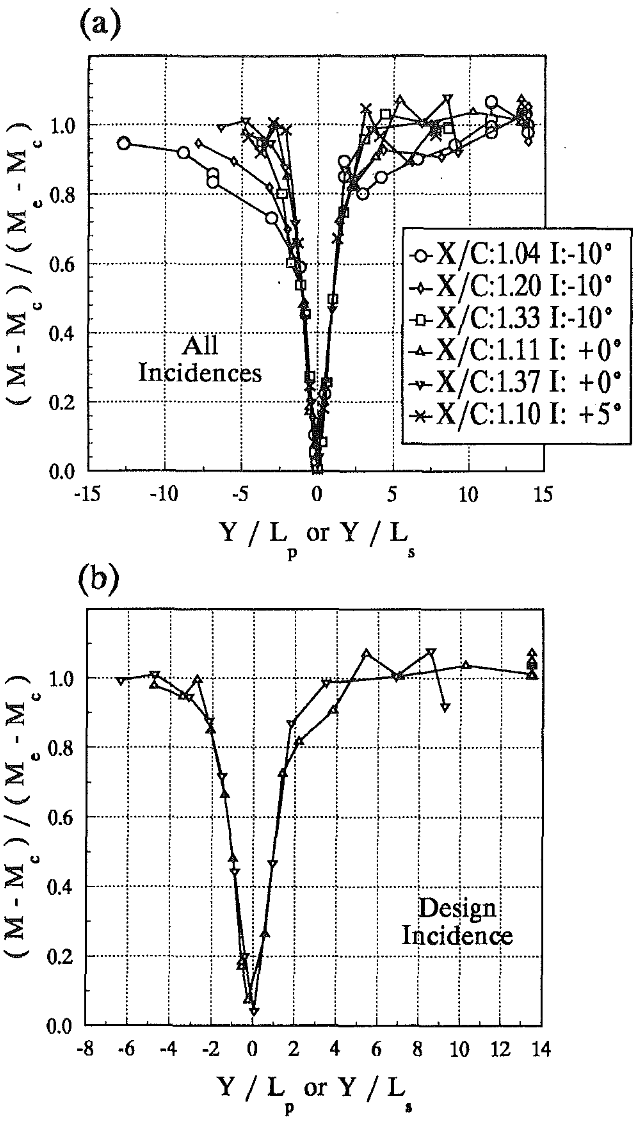

Fig. 15 Mach number profile similarity

metric, as in Raj and Lakshminarayana [12]. The greatest similarity occurs for the design incidence profiles because the lack of any significant shock-boundary-layer interaction in this incidence case permits the most accurate determination of the appropriate semiwake widths. This brings to light a distinguishing feature of this free shear flow, in that it is not merely a wake flow as in previous fundamental studies, but rather, it is a wake flow upon which the residual influence of a severely shock-separated boundary layer has been superimposed.

With the necessary condition of similarity established, at least for the design incidence case, it is worthwhile to look for the additionally restrictive condition of equilibrium. Figure 16 presents an equilibrium parameter,

$$\frac{\tau_0(x)}{w_0^{1/2}} = \frac{-\overline{u'v'}_m}{w_0^{1/2}}$$

analogous to that defined in Eq. (1), versus streamwise distance. The means of the peak values across the shear layer were used in its definition. This parameter relates mean and turbulent scales and should be invariant with X under the condition of equilibrium. The two profiles showing the greatest similarity, those of design incidence, may be observed also to demonstrate the closest approach to equilibrium, and are approaching the same value of the equilibrium parameter (0.045) as in the relaxing wake experiment of Narasimha and Prabhu [3] indicated by the dashed line in Fig. 16. The most severe off-design cases demonstrate the longest relaxation distance, as one might expect, and as observed in [3].

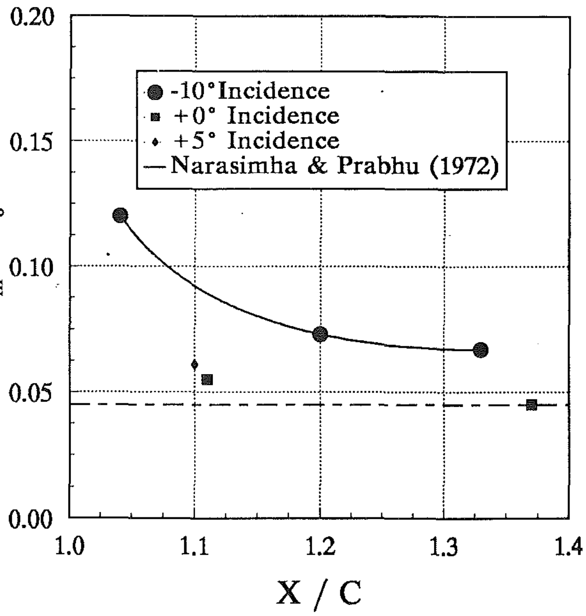

Fig. 16 Wake relaxation to equilibrium

In summary, Fig. 16 indicates that the flow has reached a far-wake state, in terms of the turbulence properties, at the end of the observational interval of this experiment. A similar conclusion regarding the mean flow parameter of wake defect was reached from Fig. 4, although the far-wake state was indicated to be attained further upstream.

Conclusions

The turbulence structure in the supersonic wake of an airfoil tested in cascade has been investigated using a nonintrusive technique. The character of the turbulence properties has been studied as a function of both cascade incidence angle and streamwise location. The observational interval of this experiment was determined to encompass both the near-wake and the far-wake for both the mean and turbulent flow properties.

The *extremities* of profiles of the mean and turbulent wake properties were found to be strongly influenced by shock-boundary-layer interactions in the upstream blade passage, the strength of which varied parametrically with cascade incidence. The *peak* levels of turbulence properties within the shear layer were found to be largely independent of cascade incidence, and could be characterized in terms of the streamwise position only. This fact permitted the determination of the decay of the peak Reynolds shear stress, the production rate of turbulent kinetic energy, and the turbulent kinetic energy itself with streamwise location in the wake.

Profiles of Reynolds shear stress were found to vary linearly through the center of the shear layer, and to pass through local maxima at points displaced slightly from the wake centerline. These local extrema in $-u'v'$ were found to be proximate with peaks in the production rate of turbulent kinetic energy and with the turbulent kinetic energy itself. The defect velocity turbulence level was found to be approximately 23 percent.

The concept of a proportional relationship between the Reynolds shear stress and the turbulent kinetic energy in the outer fraction of the shear layer was found to be valid for this flow. The value of this constant of proportionally, known as the structural coefficient of turbulence, a_1, was found to agree with lower-speed free shear flow data. The individual levels of Reynolds shear stress and turbulent kinetic energy, not only their ratio, were also found to be in accord with lower-speed tests.

The degree of similarity of the wake profiles was established, and those profiles demonstrating the most similarity were found to approach a state of equilibrium between the mean flow and turbulent properties in the far-wake. Those profiles perturbed most severely by shock-boundary-layer interactions were found to relax more slowly to equilibrium.

For the reasons described above, the wake turbulence behavior observed here is akin to that observed in previous studies of classical free shear flows. Consequently, this wake under consideration may be viewed as a classical wake, upon which the influence of an upstream shock-boundary-layer interaction has been superimposed.

Acknowledgments

The continued support of the Turbomachinery Technology Branch of the NASA Lewis Research Center, L. J. Bober, Branch Chief, is gratefully acknowledged. The authors would also like to acknowledge the assistance of C. J. Chesnakas in obtaining the LDA measurements.

References

1 Majjigi, R. K., and Gliebe, P. R., "Development of a Rotor Wake/Vortex Model," NASA-CR-174849, Vol. 1, June 1984.

2 Chevray, R., and Kovasznay, L. S. G., "Turbulence Measurements in the Wake of a Thin Flat Plate," *AIAA Journal*, Vol. 7, No. 8, 1969, pp. 1641–1643.

3 Narasimha, R., and Prabhu, A., "Equilibrium and Relaxation in Turbulent Wakes," *Journal of Fluid Mechanics*, Vol. 54, Part 1, 1972, pp. 1–17.

4 Reynolds, B., Lakshminarayana, B., and Ravindranath, A., "Characteristics of the Near Wake of a Compressor of a Fan Rotor Blade," *AIAA Journal*, Vol. 17, No. 9, 1979, pp. 959–967.

5 Lakshminarayana, B., and Davino, R., "Mean Velocity and Decay Characteristics of the Guidevane and Stator Blade Wake of an Axial Flow Compressor," ASME Paper No. 79-GT-9, 1979.

6 Yu, J. C., "Mean-Flow and Turbulence Measurements in the Vicinity of the Trailing Edge of an NACA 63_1-012 Airfoil," NASA-TP-1845, May 1981.

7 Orloff, K. L., and Olson, L. E., "High-Resolution LDA Measurements of Reynolds Stress in Boundary Layers and Wakes," AIAA Paper No. 80-0436.

8 Viswanath, P. R., Cleary, J. W., Seegmiller, H. L., and Horstman, C. C., "Trailing-Edge Flows at High Reynolds Number," *AIAA Journal*, Vol. 18, No. 9, 1980, pp. 1059–1065.

9 Petrie, S. L., and Emmer, D. S., "Investigations of Transonic Trailing Edge Flows," *Proceedings of the Conference on Aerospace Simulation II*, held at San Diego, CA, 1986, in Simulation Series, M. Ung, ed., Vol. 16, No. 2, Jan. 1986, see also NASA-CR-176904.

10 Johnson, D. A., and Bachalo, W. D., "Transonic Flow Past a Symmetrical Airfoil-Inviscid and Turbulent Flow Properties," *AIAA Journal*, Vol. 18, No. 1, 1980, pp. 16–24.

11 Johnson, D. A., and Spaid, F. W., "Measurements of the Boundary Layer and Near Wake of a Supercritical Airfoil at Cruise Conditions," AIAA Paper No. 81-1242, 1981.

12 Raj, R., and Lakshminarayana, B., "Characteristics of the Wake Behind a Cascade of Airfoils," *Journal of Fluid Mechanics*, Vol. 61, Part 4, 1973, pp. 707–730.

13 Baydar, A., "Hot-Wire Measurements of Compressor Blade Wakes in a Cascade Wind Tunnel," Master of Science Thesis, Naval Postgraduate School, Monterey, CA, Mar. 1988.

14 Elazar, Y., "A Mapping of the Viscous Flow Behavior in a Controlled Diffusion Compressor Cascade Using Laser Doppler Velocimetry and Preliminary Evaluation of Codes for the Prediction of Stall," Doctoral Dissertation, Naval Postgraduate School, Monterey, CA, Mar. 1988.

15 Bowersox, R. D. W., Ng, W. F., and Schetz, J. A., "Hot-Wire Techniques Evaluated in the Wake of a 2-D Supersonic Compressor Cascade," *Proceedings From the Yokohama International Gas Turbine Conference*, Yokohama, Japan, 1991.

16 Chesnakas, C. J., Andrew, P. L., and Ng, W. F., "An LDV Evaluation of Particle Lag Prediction Techniques in Supersonic Flows," *Proceedings From the Yokohama International Gas Turbine Conference*, Yokohama, Japan, 1991.

17 Schmidt, J. F., Moore, R. D., Wood, J. R., and Steinke, R. J., "Supersonic Through-Flow Fan Design," AIAA Paper 87-1746, 1987.

18 Johnson, D. A., "Laser Doppler Anemometry," AGARD-AG-315, May 1989.

19 Chesnakas, C. J., personal communication.

20 Johnson, D. A., and Rose, W. C., "Laser Velocimeter and Hot-Wire Anemometer Comparison in a Supersonic Boundary Layer," *AIAA Journal*, Vol. 13, No. 4, 1975, pp. 512–515.

21 Johnson, D. A., "Turbulence Measurements in a Mach 2.9 Boundary Layer Using Laser Velocimetry," *AIAA Journal*, Vol. 12, No. 5, 1974, pp. 711–714.

22 Kistler, A., "Fluctuation Measurements in a Supersonic Turbulent Boundary Layer," *The Physics of Fluids*, Vol. 2, No. 3, May-June 1959, pp. 290–296.

23 Elena, M., Lacharme, J. P., and Gaviglio, J., "Comparison of Hot-Wire and Laser Doppler Anemometry Methods in Supersonic Turbulent Boundary Layers," in: *Proceedings of the International Symposium on Laser Anemometry*, ASME, A. Dybb, and P. A. Pfund, eds., Nov. 17–22, 1985.

24 Kuntz, D. W., Amatucci, V. A., and Addy, A. L., "Turbulent Boundary-Layer Properties Downstream of the Shock-Wave/Boundary Layer Interaction," *AIAA Journal*, Vol. 25, No. 5, May 1987, pp. 668–675.

25 Schetz, J. A., *Foundations of Boundary Layer Theory for Momemtum Heat, and Mass Transfer*, Prentice-Hall, Inc., Englewood Cliffs, N.J., 1984, pp. 225.

26 Harsha, P. T., and Lee, S. C., "Correlation Between Turbulent Shear Stress and Turbulent Kinetic Energy," *AIAA Journal*, Vol. 8, No. 8, 1970, pp. 1508–1510.

27 Simpson, R. L., "Two-Dimensional Turbulent Separated Flow," A. D. Young, ed., AGARD-AG-287, Vol. 1.

28 Morrison, G. L., and Swan, D. H., "Vorticity, Turbulence Production, and Turbulence Induced Accelerations in a Rectangular Jet as Measured Using Three-Dimensional LDA," AIAA Paper No. 90-0363.

29 Townsend, A. A., *The Structure of Turbulent Shear Flow*, 2nd ed., Cambridge University Press, Cambridge, United Kingdom, 1976, pp. 224.

30 Liepmann, H. W., and Laufer, J., "Investigations of Free Turbulent Mixing," NACA-TN-1257, 1947.

31 Bradshaw, P., Ferriss, D. H., and Atwell, N. P., "Calculation of Boundary-Layer Development Using the Turbulent Energy Equation," *Journal of Fluid Mechanics*, Vol. 28, Part 3, 1967, pp. 593–616.

32 Bradshaw, P., "The Turbulence Structure of Equilibrium Boundary Layers," *Journal of Fluid Mechanics*, Vol. 29, Part 4, 1967, pp. 625–645.

33 Johnson, D. A., and King, L. S., "A Mathematically Simple Turbulence Closure Model for Attached and Separated Turbulent Boundary Layers," *AIAA Journal*, Vol. 23, No. 11, 1985, pp. 1684–1692.

34 Kline, S. J., and McClintock, F. A., "Describing Uncertainties in Single-Sample Experiments," *Mechanical Engineering*, Jan. 1953, pp. 3–8.

35 Dancey, C. L., "Measurement of Second Order Turbulent Statistics in an Axial-Flow Compressor Via Three-Component LDA," AIAA Paper No. 90-2017, 1990.

36 Cline, V. A., and Lo, C. F., "Application of the Dual Scatter Laser Velocimeter in Transonic Flow Research," AGARD-CP-193.

APPENDIX

Experimental Uncertainty

The experimental uncertainties associated with this experiment have been evaluated according to the recommendations of Kline and McClintock [34]. The uncertainty in the mean velocity of 2 percent is due to the uncertainty in the beam crossing angle and due to flow turbulence. The uncertainty in the mean flow velocity, in combination with the uncertainty in stagnation temperature, results in an uncertainty in Mach number of 2.6 percent in the free-stream and 4.2 percent in the wake. The uncertainties in the turbulence intensity and Reynolds shear stress were estimated to be 10 and 20 percent, respectively, assuming normal distributions [35].

Although difficult to quantify, error introduced in positioning the probe volume is thought to be a contributing factor to the overall error in this experiment. This is because there was no unambiguous datum point in the flow geometry from which to reference displacements of the probe volume. The best reference point available was the blade trailing edge at midspan, although the curvature and bluntness of the trailing edge made this reference point ambiguous. This problem is exacerbated by the extreme gradients encountered near the wake centerline. A related concern is the thermal contraction of the wind tunnel after several tunnel runs. This problem was also noted by Cline and Lo [36], where as much as 5 mm of movement was observed. In this experiment, frequent zeroing of the traverse system was carried out to maintain accurate positioning.

Development of a New Front Stage for an Industrial Axial Flow Compressor

B. Eisenberg
Dipl.-Ing.,
Development Engineer,
MAN Gutehoffnungshuette AG,
Bahnhofstr. 66,
4200 Oberhausen,
Federal Republic of Germany

Industrial axial flow compressors are specially designed to achieve a wide operating range. The analysis of an existing six-stage axial flow research compressor indicated that the front stage could be improved significantly using modern design technique. To demonstrate the advantages of such a technique a redesign of the current front stage was conducted. By controlling the diffusion inside the blade sections with an inverse design method, loading was enlarged. Higher loading normally results in a reduction of profile incidence range. For compensation a wide chord application was chosen. Compared to the original compressor version, experiments resulted in steeper characteristic curves together with larger usable operating range. Keeping the same outer and inner diameter, mass flow was increased by 6 percent. Measurements of performance curves with variable speed and for guide vane control are presented. Theoretical calculations achieve a high degree of agreement with measured performance.

1 Introduction

Industrial axial flow compressors are used in a variety of different applications. Apart from traditional use as blast furnace blowers and in air separation plants, they are found in FCC (Fluid Catalytic Cracking) plants and other chemical and petrochemical processes. The common feature for all these applications is that they need large amounts of compressed air. Due to the complexity of the process a reliable machine is required that is well suited to the downstream process conditions. For economic reasons the power consumption has to be kept as low as possible. In many applications the production output of the process and the gas supply are coupled so that the axial flow compressor often has to permit variations between 65 and 110 percent of the design mass flow at constant design pressure ratio.

The typical difference between the performance map of an industrial and a gas turbine application is demonstrated by Fig. 1. As an example the front part of an industrial axial compressor [1] is compared to the transonic front part of a gas turbine compressor [2]. The industrial test compressor has six stages with a pressure ratio of about 2.1 whereas the gas turbine compressor studied has only three stages with a higher pressure ratio of 2.9. The increased pressure rise is the consequence of a transonic design as well as a higher circumferential speed. The much smaller operating range of the gas turbine compressor is due to different operating requirements. Gas turbine compressors are optimized for higher pressure rise and efficiency. They operate only in a small range (which follows a throttle curve) whereas the industrial compressor has to allow larger flow variations.

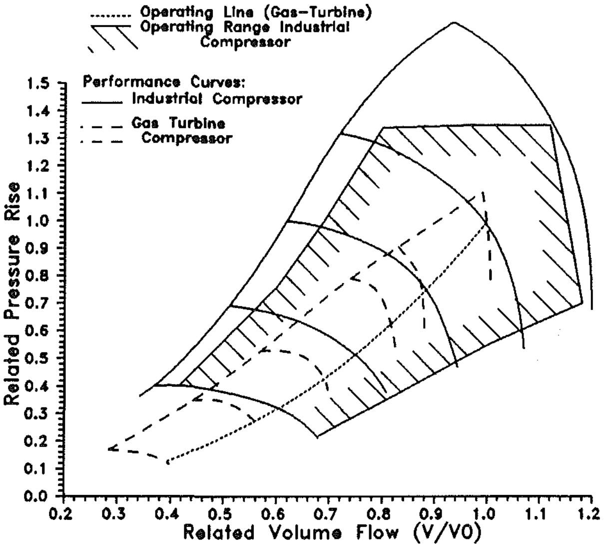

Fig. 1 Difference in performance range for axial flow compressor front part between a gas turbine and an industrial application

In order to meet these variations in mass flow, industrial compressors are specially designed according to customers' specifications. Such a compressor is built out of a modular system of standard blade rows and casing sizes. The varying process conditions are covered by selecting stage number and speed. These compressors allow operation on their total characteristic curve between choke and stall. A wide operating range can be reached by keeping the circumferential speed and thus the inlet Mach number in a region where the characteristic curves of the blade sections have no restriction in their exten-

---

Contributed by the International Gas Turbine Institute and presented at the 38th International Gas Turbine and Aeroengine Congress and Exposition, Cincinnati, Ohio, May 24–27, 1993. Manuscript received at ASME Headquarters March 17, 1993. Paper No. 93-GT-327. Associate Technical Editor: H. Lukas.

sion. This results in a subsonic design with relatively low stage pressure ratio (in the range of 1.1–1.15).

However, for reduction of machine size, the Mach number must be kept as high as possible to reduce the number of stages needed to achieve the specified pressure ratio. Thus, a compromise has to be found between operating range and number of stages. At present, development work centers on the following main aspects:

- higher stage pressure rise
- better efficiency
- more mass flow with same casing size
- wider operating range from surge to choke

Starting the axial compressor business with a repeating stage blading of 100 percent reaction in the early 1950s, the previous development steps at MAN GHH have concentrated on reducing hub–tip ratio of the front stage, increasing the circumferential speed and reducing the degree of reaction in the front part. This was achieved by a restaggering of existing blade rows, twisting of the guide vanes, and continuous manufacturing improvement of the existing blade sections [1, 3]. These modifications had the advantage that the same proven blading could be used for the rotor, which was helpful for design accuracy and manufacturing processes, as well as for reference reasons. Moreover, they enabled a precise prediction of stress and vibration behavior of the rotor blades. Starting from the original version, these modifications helped to increase the mass flow by about 200 percent within the same casing size.

However, the restaggering of blading has limitations because it is only meaningful within a small incidence range. With the help of modern engineering tools the latest version of a research compressor had been investigated using blade-to-blade (*S*1) as well as flowpath (*S*2) codes. *S*2 calculation for this compressor showed that the front stage was limiting the usable operating range in the part-load region. Here, diffusion factors as well as blade loading parameters indicated high values. In order to check the advantages of modern, controlled diffusion design technique on compressor performance it was decided to design a new front stage.

2 Design Requirements

Before starting with redesign, a study concerning work input Γ and flow coefficient Φ of modern axial flow compressors was undertaken. As far as the work input is concerned the previous design was below the level of the current state of the art. The Γ distribution along the stages of the current compressor could be improved. The investigations on Φ values within the speed-controlled performance range of the current compressor showed that contrary to the rear stages, which reached the full range from surge to choke, the front stage was only operating in a range near the design point up to surge (Fig. 2).

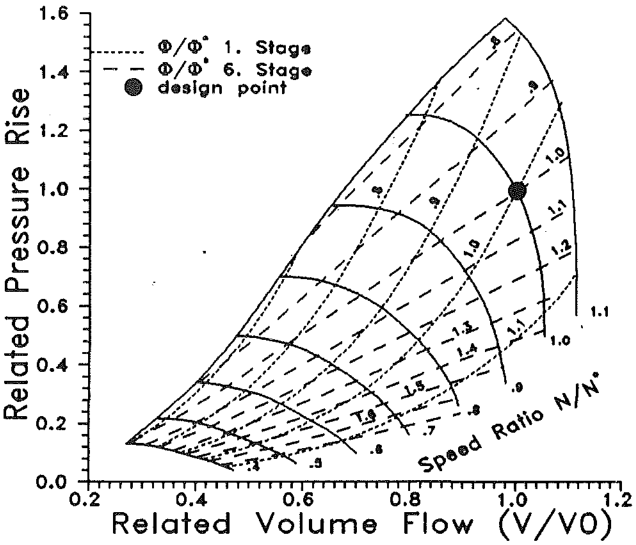

Fig. 2 Flow coefficient distribution of front and rear stage for an industrial axial flow compressor

As Φ only represents blade midspan values, the study was extended to check the needed incidence angles along the blade height. Within the complete compressor performance map the front stage needed an incidence range that was nearly constant along the blade height. This is quite different from the rear stages (Fig. 3). These stages require at the hub region a high incidence from positive to negative. However, in the tip region incidence variations compared to the front stage are relatively low. To verify the difference in incidence, *S*1 calculations of the midsection for first and sixth stages were performed for two points in the performance map, one near choke, the other near stall (Fig. 4). For both stages the same incidence range had been calculated. However, the front stage section operates at higher positive incidence whereas for the sixth stage this has been shifted into the negative direction. Mach number near choke of the last stage is much higher compared to the first. It demonstrates that this is the stage to choke the compressor at design speed. This means that compared to the rear stages a different design criterion for front stage velocity distributions has to be considered.

It was planned to verify whether with modern controlled diffusion design technique an increase of the current stage loading level is possible without penalty in performance. In general, higher stage loading means lower operating range. The desired increase in loading should be achieved by optimizing the profile pressure distributions in the range between choke and stall.

Nomenclature

C = chord length
C_{ax} = rotor outlet axial velocity
C_u = tangential component of absolute velocity
Δh_i = enthalpy rise from Euler equation
L = blade length
N = speed
N^* = design speed
P_a = total suction pressure
P_a^* = total suction pressure at design point
P_e = total discharge pressure
P_e^* = total discharge pressure at design point
$P1 \ldots 6$ = wall pressure after rotor 1 . . . 6
R = radius
U = rotor outlet midspan circumferential speed
V = volume flow
V_0 = design volume flow
W = absolute velocity for stators and relative velocity for rotors
X = coordinate in direction of blade height or chord
related pressure rise = $(P_e/P_a - 1)/(P_e^*/P_a^* - 1)$
Γ = work input $= \Delta h_i/U^2$
σ = solidity
Φ = flow coefficient $= C_{ax}/U$
Φ^* = flow coefficient at design point
1, 2 = indices before and after blade row

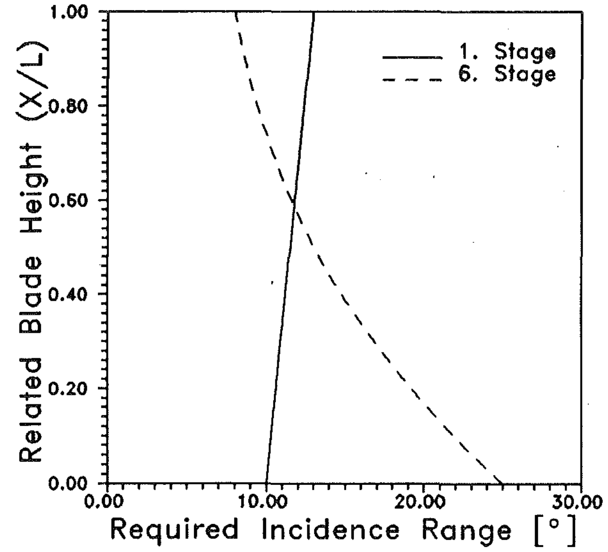

Fig. 3 Variation of incidence range within the performance curves

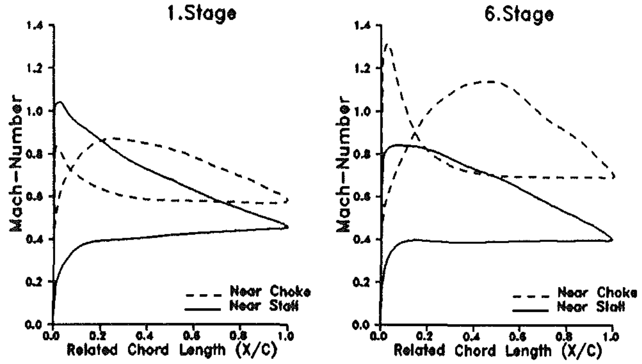

Fig. 4 Variation of Mach number distribution for front and rear stage of the original compressor between choke and stall

With higher compressor speed, the Mach number reaches, at optimum incidence, a value that causes a rise in profile losses by shocks inside the blade rows. In choosing a velocity distribution with controlled diffusion, inside the blade passage, the point of increased losses can be transferred to higher Mach numbers. This has been proved by various cascade investigations [4, 5], which compared controlled diffusion airfoils to NACA as well as DCA profiles. As Mach number reaches its highest value in the front stage, the design of a modified blade could also give information for a future potential to increase design speed of the compressor.

Both goals, a higher inlet Mach number as well as a higher profile deflection, should be achieved by using the advantages of modern controlled diffusion airfoils.

3 Compressor Design Concept

The modified front stage was conceived as a substitute for the existing first of a six-stage axial flow research compressor. It was designed to fit into the geometry of the existing test rig. The objective to design a front stage with higher pressure ratio causes the rear stages to be supplied with a volume flow smaller in comparison with their original design intent. To avoid this effect, axial velocity of the front stage was increased in a way that the higher pressure rise of the front stage was compensated for. By this a 6 percent increase of compressor mass flow as well as inlet Mach number was achieved, which fits the abovementioned development goals.

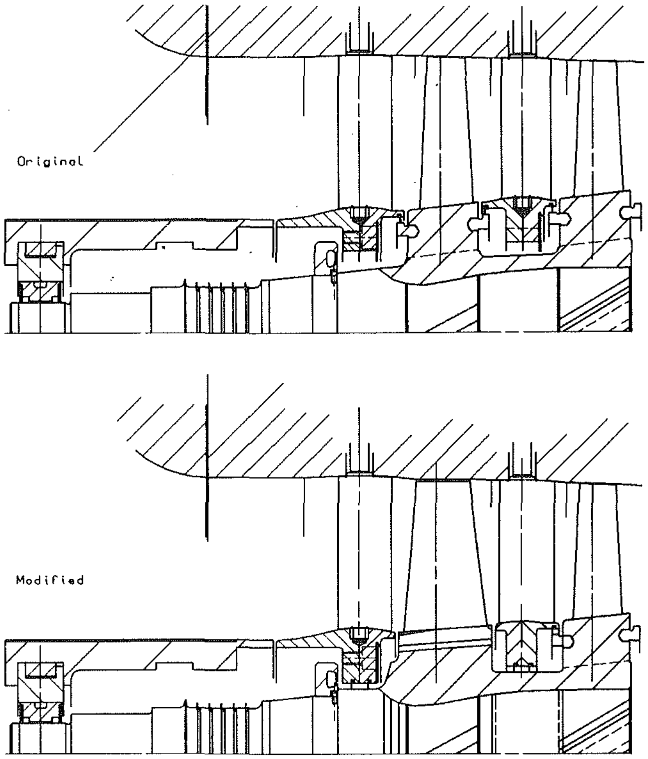

Fig. 5 Comparison of the original and modified front stages

During the development steps of the recent years, the mass flow of MAN GHH compressors has been continuously enlarged, keeping the same casing size. This was partly achieved by an elongation of blade length. These elongations have been made with the same number of blades because of mechanical limitations at the blade root. This resulted in a permanent rise of aspect ratio as well as a decrease in solidity in the outer blade region. Compared to modern axial gas turbine compressors, this is inverse with the trend of solidity as well as aspect ratio [6, 7].

A lower aspect ratio results in a higher mechanical resistance of the blading. Higher solidity, especially in the outer blade region, improves the off-design deflection of the blading. Moreover, the effects of higher loading on compressor performance can be compensated for by higher solidity. Therefore, it was decided to follow the current trend for both values. Lower aspect ratio as well as higher solidity can be achieved by increasing the chord of the blade and keeping the number of blades. To obtain a significant difference the chord length of the modified first rotor blade was increased by approximately 50 percent (Fig. 5). Blade number was reduced from 17 to 15.

4 Design Procedure

(*a*) **Aerodynamic Design.** Besides the design of the modified rotor blade for the front stage and its IGV to supply it with an adequate swirl distribution, a modified guide vane was planned. This was necessary to improve the adaptation of the front stage to the rear section. The spanwise work distribution for the modified blade rows was defined using an axisymmetric flow path code [8]. It has a built-in loss model, which has a basis similar to the one described by Koch and Smith [9]. However, profile incidence losses are calculated using correlations based on measurements by Bahr [10]. The whole loss model as well as the influences of incidence on profile deflection had been calibrated using measurements of existing compressors.

To take the influences on the rear stages into account the six-stage compressor was modeled as a whole and effects of different work distributions on total compressor performance were calculated. Stall for the different compressor models was predicted using correlations based on maximum diffusion factor, as well as maximum stalling pressure rise [11]. Spanwise work distribution turned out to be better if more work was put into the hub region. With the help of these calculations, the operating range of the compressor characteristic from stall to choke for the different profile sections could be defined as well as the particular Mach numbers and contraction ratios of the streamsurfaces. The larger chord length was chosen to improve the solidity of the blade row. With the same pressure rise as before the diffusion factor would have been reduced. However, the blade deflection was so drastically increased that the wide chord was not able to compensate for the rise in diffusion factor (Fig. 6).

The blade sections were designed using a fully inverse method as well as a direct blade-to-blade calculation. Both methods solve the potential flow field inside the blading. Viscous influences are included by coupling a McNally integral boundary layer code. Both codes were adapted to industrial use for the design of controlled diffusion airfoils with high subsonic Mach number. The design code allows calculations on cylindrical planes as well as on those that follow the streamline pattern [12–14].

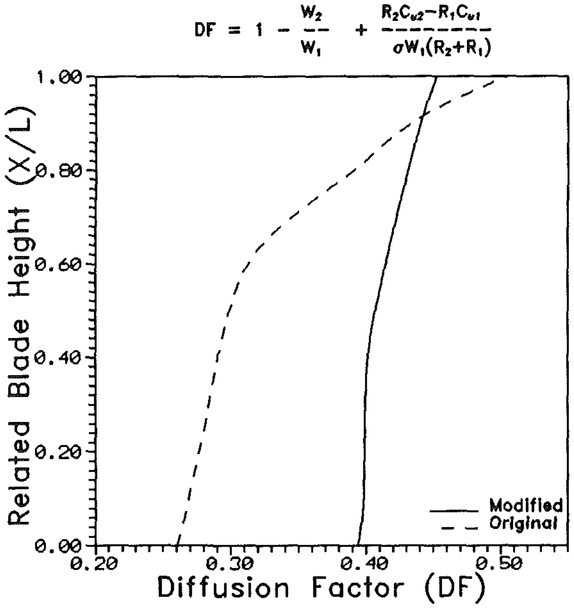
$$DF = 1 - \frac{W_2}{W_1} + \frac{R_2C_{u2}-R_1C_{u1}}{\sigma W_1(R_2+R_1)}$$

Fig. 6 Spanwise distribution of diffusion factor for original and modified front stages

In the beginning of the design phase a separation free Mach number distribution was chosen. Its shape was derived from a study with the target to define an optimum design pressure distribution. On the suction side the boundary layer was kept laminar as long as possible. After the transition point, Mach number is decelerated with a decreasing turbulent diffusion in the rear part. Starting with the inverse design method, the boundary behavior of the profile was checked before the respective flow field and the resulting profile geometry were calculated. Afterward the direct method was used to check the off-design performance of the profile pressure distribution from choke to stall as well as the losses at design point. A more detailed description of the design process and cascade measurements for the hub section of the rotor blade is given in [15]. In the first approach, the inverse design was done on three sections. The other sections were defined by spline interpolation and analyzed using the direct calculation method.

The resulting Mach number distribution for hub, mid, and tip section are shown in Fig. 7. Contrary to the original blade, which indicated high incidence for the outer section, the modified blade row shows the same tendency for velocity distribution in all sections. At the point near choke of the compressor, characteristic calculations indicate a separation free boundary layer for suction side. However, with higher incidence the shape factor increases so that near stall point a separation is predicted for all sections at 70 percent of chord length.

(*b*) **Mechanical Design.** For stress and vibration analysis, the blade was defined by stacking the different sections at their center of gravity (Fig. 8). Calculations showed that stress levels were moderate. Even though the loading of the modified rotor was higher compared to the original blade, stress analysis results show a lower influence of gas bending. This is due to the wider chord, which has a higher section modulus. Vibration analysis showed only a small influence of speed on natural frequencies. These were tuned during the design process to avoid excitations of resonance points with the lower harmonics and number of IGV.

5 Test Instrumentation

The test rig consists of a six-stage axial flow compressor, which has a continuous increase of reaction from 70 percent in the front to 95 percent in the last stage (Fig. 9). It is equipped with an IGV, to minimize a possible inlet distortion and to supply the front stage with the desired swirl distribution. In many applications the axial flow compressor has an electric driver so that pressure and mass flow is controlled by adjustable guide vanes. To test the influence of different schedules for guide vane adjustment, all stators can be moved individually. An axial inlet configuration makes it possible to check the inlet

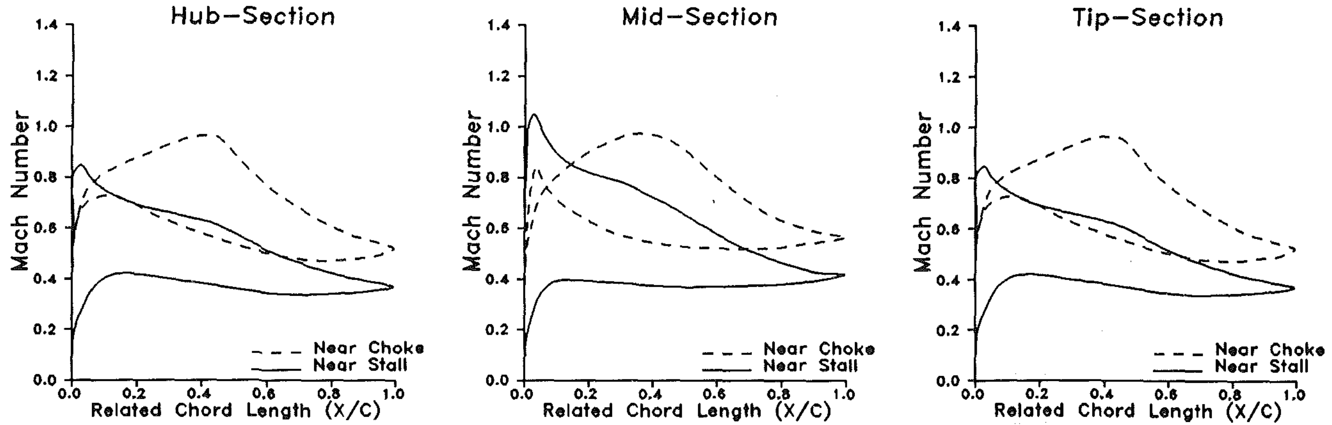

Fig. 7 Variation of Mach number distribution for modified rotor between choke and stall

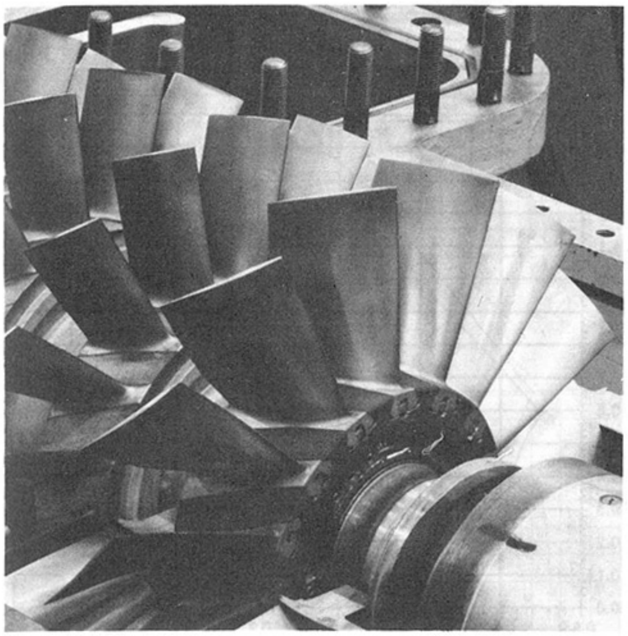

Fig. 8 Picture of the modified front stage blading

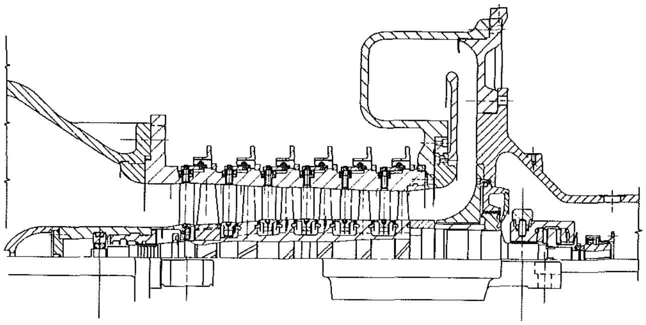

Fig. 9 Section drawing of used test compressor

flow field to ensure it is free from distortion. Kinetic energy at the end of the compressor is recovered by a radial diffuser.

The compressor is instrumented with temperature and pressure probes at inlet and outlet planes. An additional instrumentation area was put immediately at the end of the blading to make measurements from the blading itself. Efficiency of the compressor can be measured in two ways: thermodynamically via temperature rise of the compressed air, and mechanically via reaction moment of the electric driver. In order to get a precise comparison with the previous compressor version, the same instrumentation was used as in a former research program. Traverse measurements inside the blading were performed using a five-hole thermocouple probe (United Senor DAT 187), which was traversed along the blade height.

6 Measurement Results

(*a*) Variable Speed. An overall compressor map for speed variation is presented in Fig. 10. Compared to the previous rotor version the curves have a steeper characteristic from choke to stall. This is an advantage for the control of the compressor because changes in volume flow cause similar changes in pressure rise. Because of the steeper characteristic the stall points of the modified version lie nearly at the same volume flow value as the old one, but at a much higher pressure ratio. The total mass flow at design pressure has risen 6 percent. The usable operating range of the compressor was enlarged by 3 percent of the design mass flow.

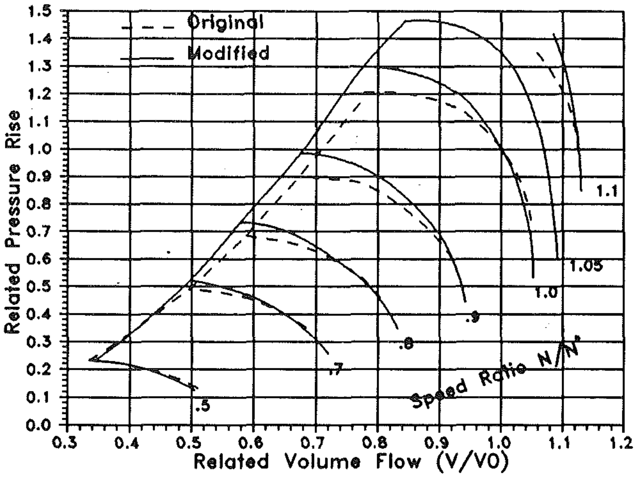

Fig. 10 Measured performance maps for original and modified compressors

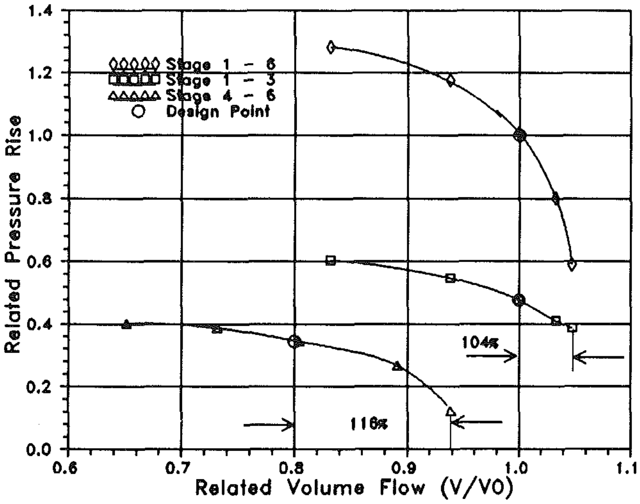

Fig. 11 Performance derived from traverse measurement for first and second stage group: first stage group: stages 1-3; second stage group: stages 4-6

Stall line was defined by measuring mass flow of stable operating points immediately before the stall line. In using this method a good reproduction of stall data was possible to exclude influences of measurement tolerances.

Though the front stage has a much higher loading, as well as a higher inlet Mach number, efficiency at optimum points of the compressor performance has been kept at the same level as in the previous version.

Traverse measurements after the third stage allow a splitting of the compressor into two stage groups. As the original compressor was designed with the same pressure ratio in all stages, the influence of the higher loading in the front stage could be checked by comparing both parts (Fig. 11). By integrating the pressure along the blade span the characteristic curves for both groups can be determined. At design point the pressure rise of the first group reaches a level above the maximum pressure rise of the second.

Both groups give the typical behavior within such a compressor configuration. From design point to stall both groups have a relatively flat characteristic with nearly the same changes in relative volume flow. However, below design pressure ratio, the second stage group has to allow large variations in volume flow (104 percent of first stage group compared to 116 percent in the second). This proves the above-cited theoretical investigation on different operating conditions and design criteria for first and last stage within the compressor performance map.

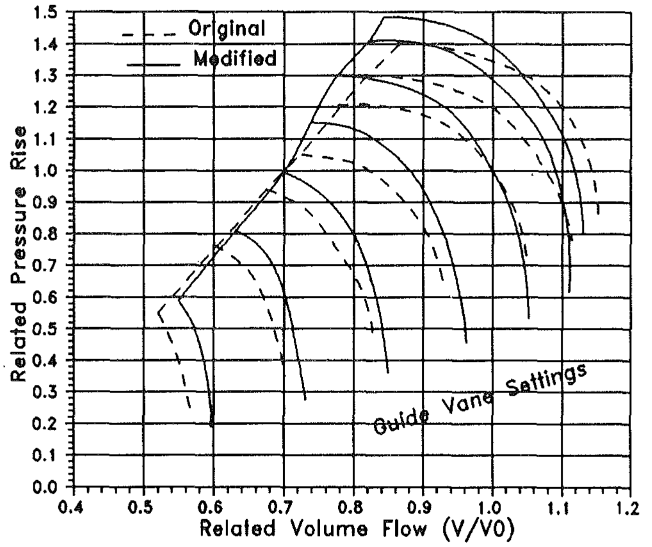

Fig. 12 Comparison of performance for five adjustable guide vanes of *original and modified compressors*

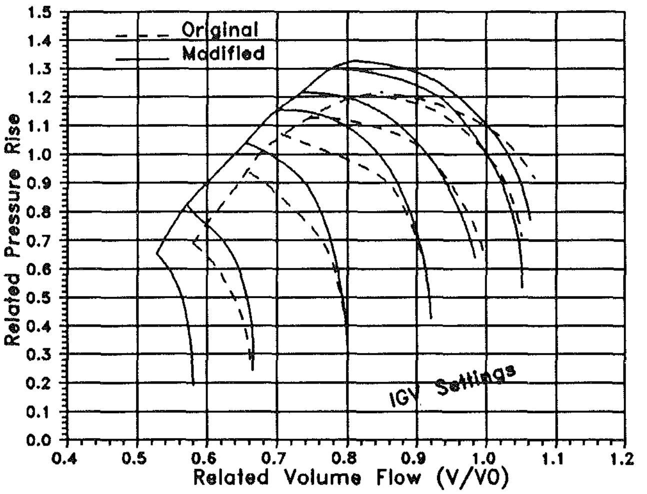

Fig. 13 Comparison of performance with IGV control for original and modified compressors

(*b*) **Guide Vane Control.** Up to now MAN GHH has built more than 250 compressors for various industrial applications. About 50 percent of these compressors are equipped with adjustable guide vanes to control the required mass flow. To reduce investment cost and to keep the number of movable parts as low as possible only the front part of the complete compressor has guide vane control. The reduction of mass flow is achieved by using the front part as a control instrument for the rear stages. Thus the pressure rise of the rear part is kept for different guide vane positions.

To investigate the influences of a different number of adjustable guide vanes, three maps with increased number of controlled stages have been measured. Compared to the previous version the performance maps for five adjustable guide vanes have the same relative stall margin at design pressure ratio (Fig. 12). The flow at maximum guide vane position has been lowered. However, maximum mass flow for the same casing size has been increased by 6 percent. Stall margin at pressure ratios above design has improved. At part load, pressure ratio has been kept. Because of the lower mass flow of the first stages, stall margin is determined by the last stage in this region.

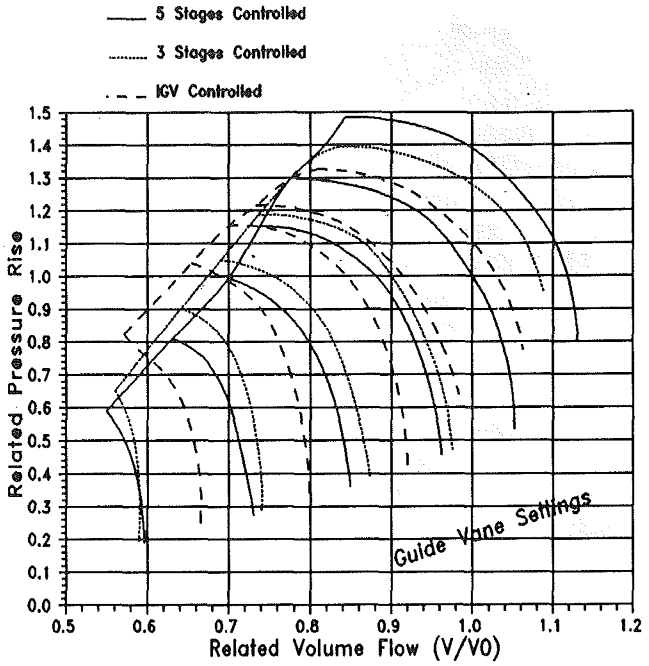

Fig. 14 Change in performance depending on the stage number with adjustable guide vanes

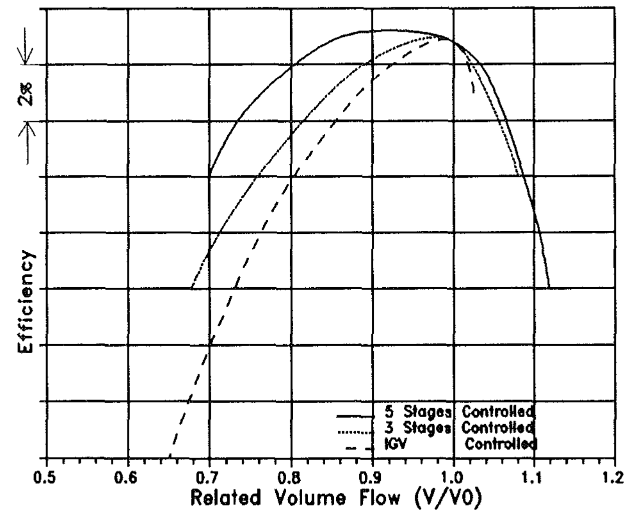

Fig. 15 Gain in measured efficiency with enlarged stage number with adjustable guide vanes at constant pressure ratio

A comparison for IGV control is presented in Fig. 13. Stall margin has been improved throughout the whole performance map by more than 5 percent. Even at minimum guide vane position performance curves have a steeper characteristic than before. This might be a result of using a wide chord blading for the front stage.

By changing the number of adjustable guide vanes, the operating range as well as the accompanying efficiency distribution are influenced. Test results have shown that with an increase of the rows of adjustable guide vanes the mass flow was enlarged at maximum guide vane position (Fig. 14). However, the stall margin has decreased so that the usable operating range from stall to maximum position nearly remains constant. Figure 15 gives the measured efficiency distribution varying the mass flow at constant design pressure ratio as dependent on the stage number with controlled guide vanes. Efficiency rises in the region of lower mass flow depending on the number of controlled stages. In order to optimize compressor per-

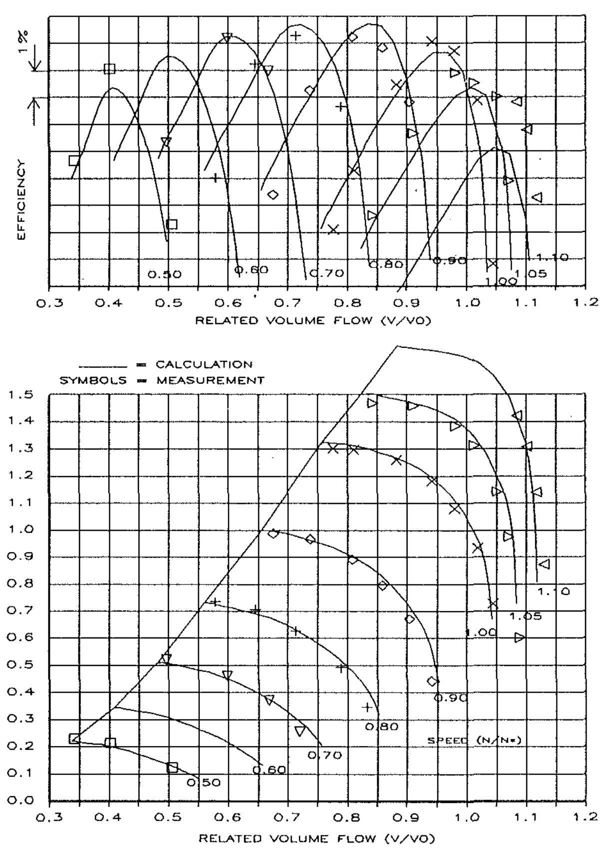

Fig. 16 Measured and calculated performance and efficiency distribution for speed controlled six-stage test compressor

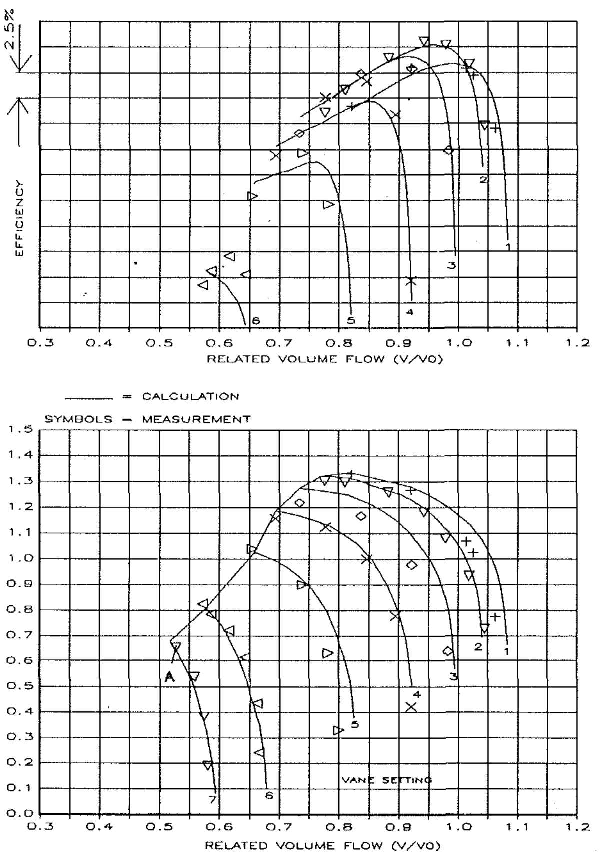

Fig. 18 Measured and calculated performance and efficiency distribution for six-stage test compressor with IGV control

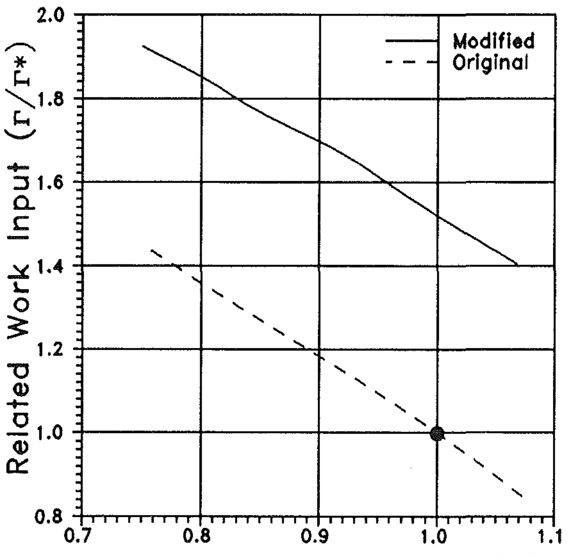

Fig. 17 Comparison of calculated Φ-Γ of first stage for original and modified compressors

formance, a good compromise between the number of rows of adjustable guide vanes and the resulting improvement of the efficiency has to be chosen.

7 Theoretical Investigations Based on Measurements

For practical application, measurement results have to be transferred from research compressors to serial machines. These machines are generally scaled in size by a factor up to 20 in mass flow and are equipped with additional rear stages. For this procedure, well-proven design codes have to be generated. To investigate the influences of the modified front stage in bigger compressors a well-adapted loss model, as well as functions for blade deflection, had to be established.

With the help of cascade measurements [11, 15] as well as blade-to-blade calculations performance models for the different blade sections were derived. In the second step the spanwise flow distribution was calculated. These results were compared to wall and traverse measurements. If deviations occurred the performance model for the blade sections was changed based on the information of blade-to-blade calculations for the appropriate point in the performance map. During this iterative adaptation process between blade-to-blade and spanwise direction, most of the corrections for the original model were necessary in the region of high profile incidence. For variable speed the modifications resulted in a good reproduction of the measured performance (Fig. 16). Peak efficiencies for the different speed curves as well as the overall shape of efficiency show a high degree of agreement.

In order to prove the higher stage loading of the front stage, Φ–Γ curves for original and modified test compressor were calculated. A comparison of the results for the front stage behavior is given in Fig. 17. Although the modified front stage has a higher loading, the original and the modified performance curves have nearly the same steepness. Compared to the rear stages, which had the same Γ level for both compressors, loading has also been increased.

Calculation for IGV control turned out to be more problematic. Due to the high variation of IGV-stagger (up to 70 deg) a model for the different IGV sections had to be generated taking into account flow separation for large control angles. As the blade-to-blade calculations were not able to predict losses for heavily separated flows a new model had to be

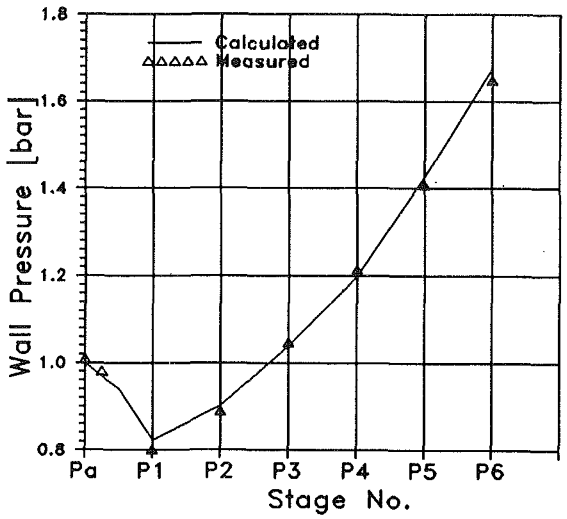

Fig. 19 Measured and calculated pressure rise at minimum guide vane position for six-stage test compressor (point A in Fig. 18)

established for the larger stagger variations. This was achieved by regarding the loss function of the IGV as a throttle for the rest of the compressor blading. Having passed the region free of separation where losses were modeled according to the blade-to-blade calculations, losses in the high stagger region were increased rapidly as a function of IGV-stagger. The increase of losses was defined arbitrarily based on the results of the measured performance map. A comparison between measured and calculated performance for the six-stage research compressor confirms the validity of this assumption (Fig. 18). Even at minimum volume flow, pressure rise and efficiency have a relatively good agreement with measured values.

To demonstrate the effectiveness of these loss assumptions for the IGV a comparison between measured and calculated wall pressure rise was made. As an example of an extreme condition, point A (Fig. 18) at minimum IGV position was chosen. Although at this position a sharp throttling effect of the IGV occurs a close agreement between measured and calculated data was achieved Fig. 19.

8 Conclusion

For an industrial axial flow compressor a modified front stage has been designed successfully. Along with a higher loading and a higher Mach number, the profile sections have been optimized using controlled diffusion technology in combination with a wide chord length.

The modified front stage replaced an existing one in a six-stage compressor test rig. Measurements for variable speeds resulted in an improvement of the relative performance map by 3 percent and a higher mass flow by 6 percent. Maximum efficiency was kept as before.

With adjustable guide vanes, different performance maps have been presented, varying the number of controlled stages. Besides the influence on maximum achievable mass flow, efficiency distribution at part load is changed. The operating range for IGV control was improved by 5 percent, which is regarded as a result of the wide chord application.

Acknowledgments

The author wishes to thank MAN GHH for their permission to publish this paper. Particular thanks are due to Dr. Turanskyj and Dipl.-Ing. Voss for their guidance during design and testing of the modified compressor and finally for their encouragement to write this paper.

References

1 Turanskyj, L., "Ueber die Entwicklung und Erprobung von Axialverdichtern grosser Leistungsaufnahme," *Atomkernenergie* (*ATKE*), Vol. 32, 1978.

2 Volkmann, H., Fottner, L., and Scholz, N., "Aerodynamische Entwicklung eines dreistufigen Transonik-Frontgeblases," *A. Flugwiss.*, Vol. 22, No. 4, 1974.

3 Turanskyj, L., and Voss, H., "Recent Developments to Increase Operating Efficiencies and Performance of Industrial Axial-Flow Compressors," IMechE Paper No. C280/87, 1987.

4 Rechter, H., Steinert, W., and Lehmann, K., "Comparison of Controlled Diffusion Airfoils With Conventional NACA 65 Airfoils Developed for Stator Blade Application in a Multistage Axial Compressor," ASME *Journal of Engineering for Gas Turbines and Power*, Vol. 107, 1985, pp. 494-498.

5 Hobbs, D. E., and Weingold, H. D., "Development of Controlled Diffusion Airfoils for Multistage Compressor Application," ASME *Journal of Engineering for Gas Turbines and Power*, Vol. 106, Apr. 1984.

6 Wisler, D. C., "Tip Clearance Effects in Axial Turbomachines," von Karman Institute Lecture Series 1985-05.

7 Wennerstrom, A. J., "Highly Loaded Axial Flow Compressors: History and Current Developments," ASME Journal of Turbomachinery, Vol. 112, Oct. 1990.

8 Bammert, K., and Fiedler, K., "ZurAuslegung von axialen Turbomaschinen," *VDI-Z.*, Vol. 104, No. 36, Dec. 21, 1962.

9 Koch, C. C., and Smith, L. H., Jr., "Loss Sources and Magnitudes in Axial-Flow Compressors," ASME *Journal of Engineering for Gas Turbines and Power*, Vol. 98, July 1976.

10 Bahr, J., "Untersuchungen uber den Einfluss der Profildicke auf die kompressible ebene Stromung durch Verdichtergitter," *Forsch. Ing.-Wes.*, Vol. 30, No. 1, 1964.

11 Koch, C. C., "Stalling Pressure Rise Capability of Axial Flow Compressor Stages," ASME *Journal of Engineering for Power*, Vol. 103, Oct. 1981.

12 Schmidt, E., and Grein, H. D., "Verdichterbeschaufelungsentwurf," *FVV-Forschungsberichte*, Vol. 433, 1989.

13 Grein, H. D., and Schmidt, E., "Ein Berechnungsverfahren fuer die Auslegung von Verdichterbeschaufelungen," *MTZ Motortechnische Zeitschrift*, No. 51, June 1990, pp. 248-255.

14 Schmidt, E., and Grein, H. D., "Supercritical Blade Design on Stream Surfaces of Revolution With an Inverse Method," *Proceedings of the ICIDES III Conference*, Washington, DC, Oct. 23-25, 1991, pp. 293-305.

15 Steinert, W., Eisenberg, B., and Starken, H., "Design and Testing of Controlled Diffusion Airfoil Cascade for Industrial Axial Flow Compressor Application," ASME Journal of Turbomachinery, Vol. 113, Oct. 1991.

Y. Katoh
Mechanical Engineering Research
Laboratory,
Hitachi, Ltd.,
Hitachi, Ibaraki, Japan

Y. Kashiwabara
Department of Mechanical
Systems Engineering,
Kanagawa Institute of Technology,
Atsugi, Kanagawa, Japan

H. Ishii

Y. Tsuda

M. Yanagida

Mechanical Engineering Research
Laboratory,
Hitachi, Ltd.,
Hitachi, Ibaraki, Japan

Development of a Transonic Front Stage of an Axial Flow Compressor for Industrial Gas Turbines

This paper describes the aerodynamic blade design of a highly loaded three-stage compressor, which is a model compressor for the front stage of an industrial gas turbine. Test results are presented that confirm design performance. Some surge and rotating stall measurement results are also discussed. The first stator blade in this test compressor operates in the high subsonic range at the inlet. To reduce the pressure loss due to blade surface shock waves, a shock-free airfoil is designed to replace the first stator blade in an NACA-65 airfoil in a three-stage compressor. Comparison of the performance of both blades shows that the shock-free airfoil blade reduces pressure loss. This paper also presents some experimental results for MCA (multicircular arc) airfoils, which are used for first rotor blades.

Introduction

For industrial gas turbines, higher thermal efficiency has become increasingly important, resulting in a trend toward steadily increasing turbine inlet temperatures and cycle pressure ratios. Along with the development of high-temperature turbines and combustors, the development of high pressure ratio compressors with high efficiency has also become important. The overall cost of compressors can be reduced by decreasing the number of stages, but current compressor efficiency must be maintained. Compressors with both high aerodynamic load and high efficiency are therefore needed.

In order to test highly loaded aerodynamic blade designs, we have developed a highly loaded three-stage compressor. This compressor is a model compressor for the front stages of industrial gas turbines. The tip relative Mach number of the first stage rotor is 1.1. The DCA (double circular arc) airfoils are used for the first and second stage rotor blades, which operate in the transonic range at the inlet. For the rest of the blading, NACA-65 profiles are used.

The first stage stator blade operates in the high subsonic range at the inlet, especially at the hub of the blades. Shock wave occurrence on the NACA-65 blade suction surface is presumed in such a high subsonic flow. In order to reduce the pressure loss due to blade surface shock waves, a shock-free airfoil was designed to replace the first stator blades of the NACA-65 airfoil in a three-stage compressor. It was designed using the inverse design method, which is based on the compressible potential flow calculation coupled with a boundary layer calculation. Comparison testing of the aerodynamic performance of the NACA-65 and shock-free airfoil blades was done using a single-stage compressor.

The first stage rotor, which operates in the transonic range at the inlet, was redesigned utilizing an MCA (multicircular arc) airfoil in order to reduce the pressure loss due to shock waves. Using the single-stage compressor, the performance of the DCA and MCA airfoils was compared.

This paper describes the development of these test compressors and blades. Their aerodynamic designs are described and the test results are presented. The test facilities, instrumentation, and data acquisition system are also described.

Aerodynamic Design

Three-Stage Compressor. A highly loaded three-stage compressor has been designed and tested. It is a model compressor for the front stages of industrial gas turbines. The main compressor specifications are shown in Table 1. The design pressure ratio is 2.2 for the three stages using an inlet guide vane (IGV) and an exit guide vane (EGV). Design polytropic efficiency is 90 percent. The average pressure ratio for each stage is 1.3.

To achieve this relatively high pressure ration, the rotor must operate in the transonic range at the inlet, which means that the NACA-65 profiles used in subsonic blades are not appropriate for the rotor blading. To avoid large shock losses caused by higher Mach numbers, DCA profiles were used for the first

---

Contributed by the International Gas Turbine Institute and presented at the 38th International Gas Turbine and Aeroengine Congress and Exposition, Cincinnati, Ohio, May 24–27, 1993. Manuscript received at ASME Headquarters March 12, 1993. Paper No. 93-GT-304. Associate Technical Editor: H. Lukas.

Table 1 Main compressor specifications

NUMBER of STAGE	3
PRESSURE RATIO	2.2
MASS FLOW (kg/s)	16.1
ROTATIONAL SPEED (rpm)	17,000
HUB/TIP RATIO (1st Stage)	0.621

Table 2 Main first stage parameters

		1st ROTOR	1st STATOR
AIRFOIL of BLADES		DCA	NACA 65
HUB/TIP RATIO		0.621	0.658
ASPECT RATIO		1.65	3.09
SOLIDITY	TIP	0.88	0.93
	HUB	1.41	0.93
BLADE HEIGHT (mm)		77.2	69.6

and second stage rotor blades of the compressor. For the rest of the blading, NACA-65 profiles with a modified trailing edge thickness were used. The tip relative Mach number of the first stage rotor is 1.1. The outer casing of the flow path has a constant diameter and the hub/tip ratio of the first stage inlet is 0.621. The test compressor size was determined by taking into account both the nominal output of the electrical driver and the Reynolds number based on the blade chord length. After several vortex designs were examined, stator blades with constant efflux angles were selected, because of their small twist.

The aerodynamic design of blading was done by the streamline analysis method of repeating the streamline approximation based on the radial equilibrium equation for the compressible axisymmetric flow through blade rows (Novak, 1967). The velocity triangles were determined for each blade row by taking into account the shape of the meridional streamline through the flow path and the end wall boundary layer development. Secondary flow losses are also introduced in the calculation. The blade parameters for the first stage rotor and stator are shown in Table 2. The low aspect ratio for the rotor blades is used to achieve a wide stable operating range.

The predicted characteristics of the three-stage compressor were compared with the measured results, as shown later in Fig. 12. The results confirm the validity of the design method for highly-loaded design stages. The surge occurrence point at each rotational speed was predicted using Ohyama's theory (1978); agreement with the measured surge point was good (see Fig. 12).

Based on these test results for the three-stage compressor, we redesigned the aerodynamics of the first stage blades in order to achieve the higher efficiency of the compressor over the original compressor using the above-described blading.

Shock-Free Airfoil. Since the hub inlet of the front stage stators operates at such a high subsonic Mach number, the NACA-65 profiles used in subsonic blades are not appropriate because of the resulting large pressure losses due to shock occurrence on the blade surfaces. To avoid such losses at high subsonic flows, and possible flow separation due to shock-boundary layer interaction along the blade surfaces, shock-free airfoils are needed to reduce pressure losses, which will improve compressor efficiency. We have therefore applied a shock-free airfoil to the first-stage stator of the original three-stage compressor and investigated the effect of the redesigned stator blades on the aerodynmaic performance of the compressor. This shock-free airfoil has come to be known as the supercritical airfoil (Stephens, 1978) and also the controlled diffusion airfoil (Hobbs and Weingold, 1984; Steinert et al., 1991).

To determine the effect of the blade profile modification, the shock-free airfoil was designed using the same flow path configurations as found in the first stage of the original three-stage compressor and also under the same inlet and outlet velocity triangles as those of the original stator. The same number of blades was used for both stators. The hub inlet Mach number of the first stage stator is 0.82. The shock-free airfoil shape was designed by calculating the blade profile using Schmidt's inverse method (1980) for a two-dimensional, isentropic, compressible flow on cylindrical stream surfaces, which satisfies the prescribed velocity distribution along the blade surfaces.

Using Schmidt's inverse method, the velocity distributions along the blade surfaces, the required pitch/chord ratio, and the turning flow angle permit the associated flow channel within each blade to be defined. The final design contour of the blade is determined by subtracting the displacement thickness obtained by the boundary layer calculation from the channel contour determined by the potential flow calculation. The thickness change of stream surfaces through blade rows is considered in the calculation. For the two-dimensional blade profile calculation, radius of the stream surface is assumed unchanged in the blade rows.

If the conventional direct approach to designing the blade geometry is used, iteration between the blade-to-blade flow calculation and the boundary layer calculation is needed until the desired blade geometry is determined. If Schmidt's inverse design method is used, however, the boundary layer can be directly calculated by using the Mach number distribution prescribed on the blade surfaces, which is described on the physical plane. Accordingly, the Mach number distribution that prevents boundary layer separation can be determined prior to blade calculation (Schmidt, 1980). After the blade profiles were determined, the off-design performance of these blades was checked using the direct method.

In the design process, blade aerodynamic loading is optimized by limiting the peak Mach number on the suction surface and the diffusion at the rear part of the suction surface. The boundary layer separation is checked using the shape factor H_{12} (displacement thickness/momentum thickness), which is determined by the boundary layer calculation. Considering these factors, we determined the Mach number distribution on the blade surfaces for the first stator of our model compressor.

Figure 1 shows the prescribed Mach number distributions at blade heights of 50 and 100 percent (measured from the outer casing). These distributions are characterized as follows:

1 The peak Mach number on the suction surface is less than 1.1 at a position set at 35 to 40 percent from the leading edge in order to minimize shock waves.
2 The shape of the Mach number distribution from the peak to the trailing edge on the suction surface is used in order to provide smooth deceleration, to prevent boundary layer separation, and to reduce the displacement thickness.
3 The Mach number distribution on the pressure surface is selected to provide nearly constant pressure, to maintain circulation around the blade, and to secure the blade thickness, which is needed for blade strength and reliability.

The shock-free airfoils thus obtained are the middle-loading type shown in Fig. 1. Using the inverse design method, the Axial Velocity Density Ratio (AVDR) is assumed to vary linearly from the leading edge to the trailing edge of the blade. The AVDR is determined using the results of the streamline analysis calculation described previously. A shock-free airfoil shape at the 100 percent height of the blade is shown in the Fig. 2. It satisfies the prescribed Mach number distribution shown in Fig. 1. This airfoil has a smaller camber height in

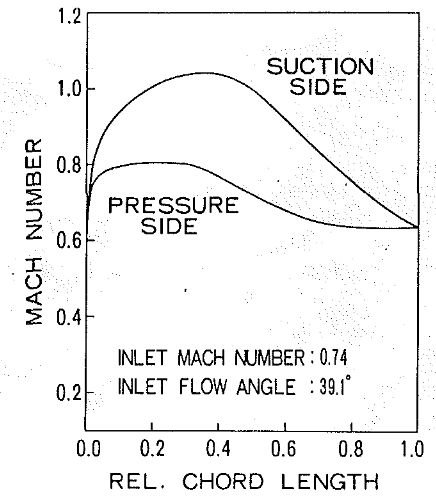

(a) H = 50%

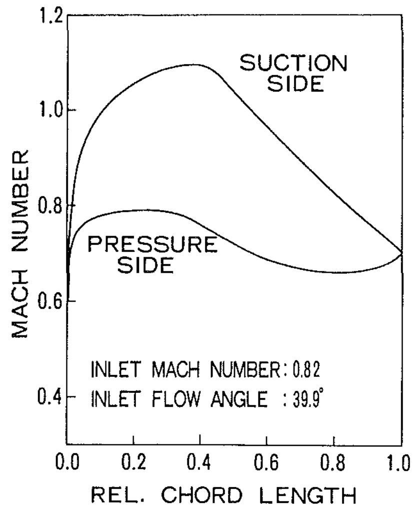

(b) H = 100%

Fig. 1 Designed Mach number distribution at the 50 and 100 percent blade heights

Fig. 2 Blade contour of a shock-free airfoil (100 percent blade height)

its middle portion than that of NACA-65 profile with the same maximum thickness.

Figure 3 shows the calculated iso-Mach lines for the flow at the 100 percent height section of the blade. It shows the smooth deceleration from supersonic to subsonic range without any shock wave. The incompressible shape factor H_{12} variation from the transition point to the trailing edge is shown in Fig. 4. The turbulent flow separation is defined as the first point at which the value of H_{12} exceeds 2.5 in the boundary layer calculation. The designed shock-free airfoils therefore have adequate margins for turbulent flow separation, as seen in Fig. 4.

For the designed airfoils, the smooth deceleration along the suction surface without shock waves was verified by the direct method calculation using the time-marching two-dimensional Euler code, as shown in Fig. 5. In this calculation, the same AVDR was used. Comparison between design and calculation shows good agreement, except for the trailing edge region. The differences in Mach number near the trailing edge are caused by the differences in treatment of the trailing edge configuration in the computational mesh systems of both calculations. The off-design flow conditions of the designed blade were also checked using the direct method calculation.

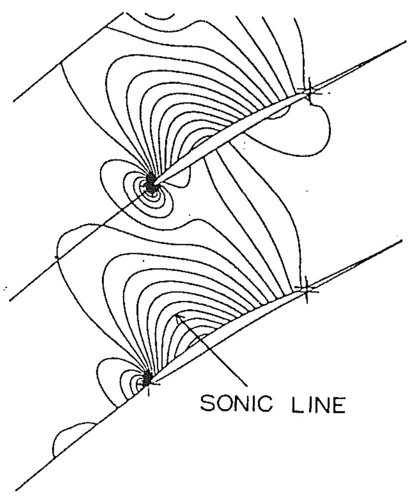

Fig. 3 Calculated iso-Mach lines (100 percent blade height)

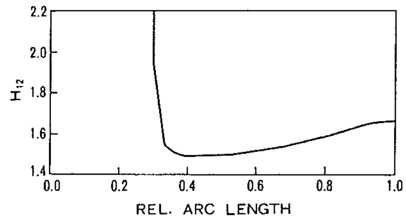

Fig. 4 Variation of the incompressible shape factor H_{12} (suction surface)

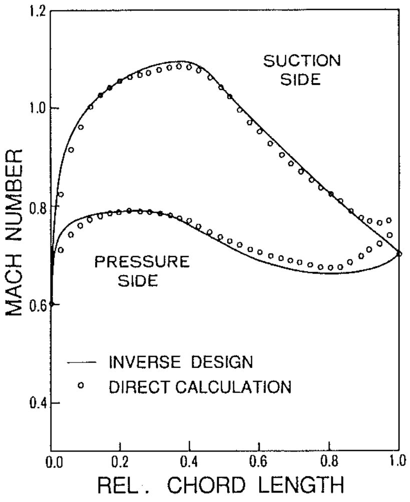

Fig. 5 Comparison of design and calculated Mach number distribution

Multicircular Arc Airfoil. While the test results for using the DCA profiles for the first rotor blade in the three-stage compressor confirm that the desired performance was achieved, the possibility of further reduction in pressure loss was indicated by the test results, mainly for the upper part of the first rotor. We therefore designed an MCA profile for the upper half of the first rotor, while the DCA profile was used for the lower part because of the lower inlet Mach number compared with the upper half region. This newly designed transonic rotor

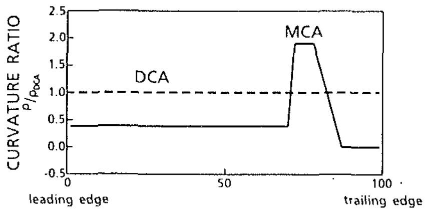

Fig. 6 Curvature of the suction surface (tip)

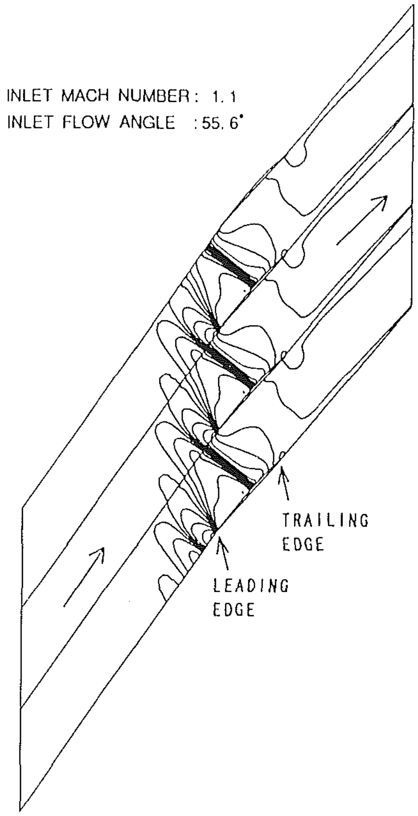

Fig. 7 Calculated iso-Mach lines with an MCA airfoil (tip)

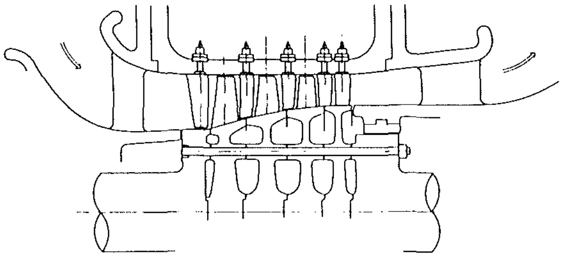

Fig. 8 Cross section of the three-stage compressor

blade then replaced the original first rotor blade of the DCA airfoil in the three-stage compressor.

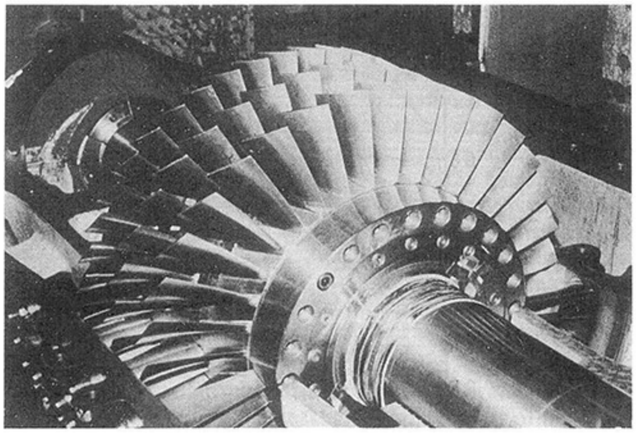

Fig. 9 Three-stage compressor with upper casing removed

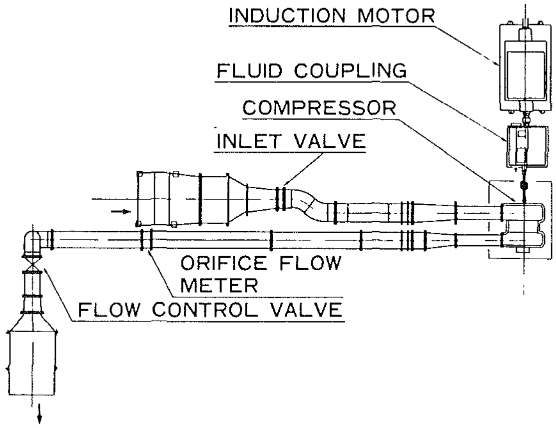

Fig. 10 Test facility arrangement

Since the MCA profile is composed of several circular arcs, it is desirable to reduce the acceleration near the leading edge by using a small curvature on the suction surface. The MCA profile can then reduce the shock losses for a blade operating in type of MCA airfoil using the same flow path configurations and inlet and outlet velocity triangles as those of the first rotor of the original three-stage compressor. The number of rotor blades is also the same. The chord length of the MCA airfoil at the tip section is longer by 10 percent than the DCA airfoil, in order to maintain moderate diffusion on the suction side. For the remainder, the chord length was shortened linearly from the tip to the hub, while keeping the same length at the hub as the original one.

Figure 6 shows the curvature variations along the suction surface at the tip section for MCA and DCA airfoils. The curvature of the MCA airfoil is composed of three circular arcs in order to reduce the maximum Mach number on the suction surface. Figure 7 shows the calculated iso-Mach lines at the tip section for the MCA airfoil. The calculated maximum Mach number on the suction surface is 1.25, which is less than the design target.

Test Facility

The facility for testing our three-stage compressor was designed to provide the needed aerodynamic and mechanical detailed measurements under the various operating conditions. Based on the aerodynamic design mentioned previously, the three-stage compressor has been manufactured first. Figure 8 shows a cross section of the three-stage compressor. Figure 9 shows the three-stage compressor with the upper half of the outer casing open. The arrangement of the test facility is shown in Fig. 10. The air flow comes from the side perpendicular to the centerline of the compressor axis in order to simulate the inlet flow conditions of a real machine. The compressor is driven by an electrical motor with a nominal output of 1500 kW. The rotational speed of the output shaft of the motor is constant at 3600 rpm. A hydrodynamic power transmission (with a variable speed fluid coupling and a step-up gear) is located between the driver and the test compressor, however,

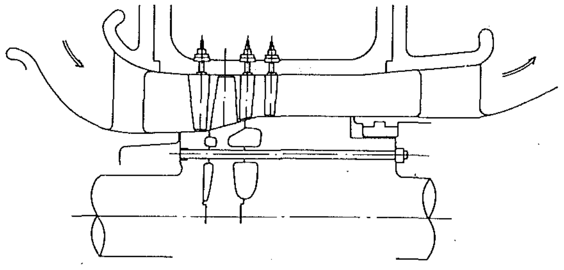

Fig. 11 Cross section of the single-stage compressor

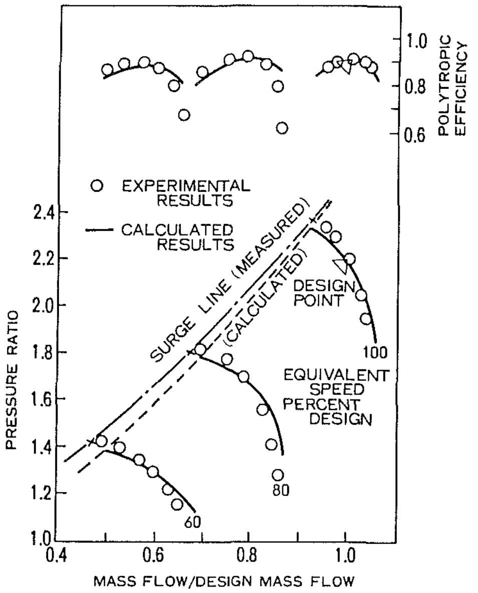

Fig. 12 Three-stage compressor characteristics

to allow the rotational speed of the compressor to be changed without discontinuity from the design speed to the part speed simply by moving the scoop-tube of the fluid coupling.

The outlet pressure of the compressor is controlled by a throttle valve in the discharge ducting. A small blow-off valve prevents pressure overflows by opening quickly at surge onset using the compressed air from the surge. The discharge mass flow is measured using an orifice plate in the discharge ducting. All of the facilities described above are operated through the control panel in the control room.

After testing the three-stage compressor, we tested the single-stage compressor. A cross section of it is shown in Fig. 11. Its flow path configuration is the same as that for the first stage of the three-stage compressor. While the single-stage compressor uses the same IGV as the three-stage compressor, the EGV was newly designed.

Instrumentation

The test compressors were extensively tested under various operating conditions. The total pressure distribution in the radial direction at the inlet plane immediately before the IGV and at the outlet plane immediately after the EGV was measured using the kiel-type total pressure rakes located at four different positions on the circumference of the outer casing of the compressor. The wall static pressure was measured at a position between each stage on the outer casing by means of the static pressure orifices, so that the circumferential distribution could be examined. The pressure measurement data were connected to the pressure transducer via a scanivalve. The total temperature distribution was measured using total temperature rakes at the inlet and outlet planes.

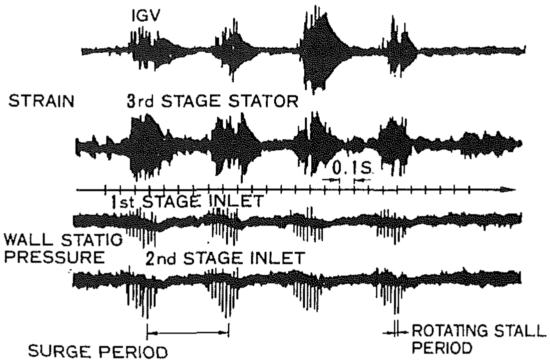

Fig. 13 Blade vibration and wall static pressure variation during rotating stall in three-stage compressor

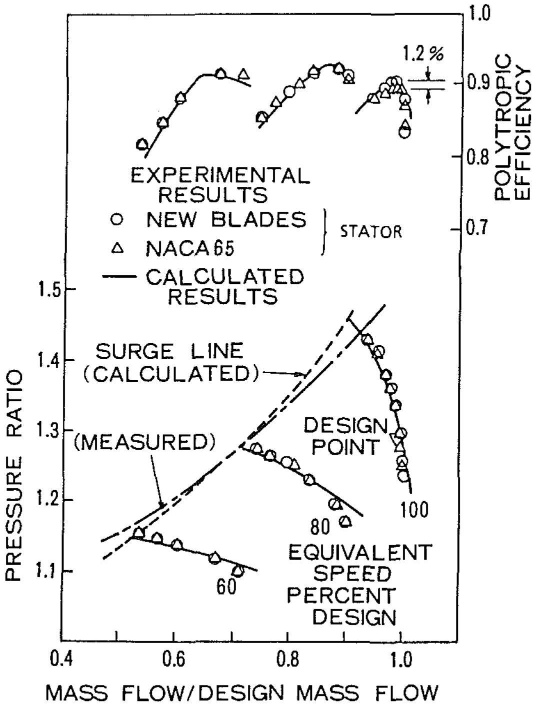

Fig. 14 Single-stage compressor characteristics with a shock-free airfoil

In order to measure the internal flow, an attempt was made to traverse a three-hole probe in the radial direction. The traversing apparatus was attached to the outer casing and the probe was driven into the gap between the blade rows by stepping motors. Circumferential grooves are located at the outlet of stator rows and rings holding the traversing apparatus were placed into these grooves so that the wake from the stator blades could be examined.

The unsteady phenomenon of rotating stall and surge has been studied extensively, but so far no theory can predict it accurately. We therefore measured the dynamic wall static pressure by means of a miniature strain gage pressure transducer attached to the pressure orifices in the outer casing. While the aerodynamic measurements were being taken, the vibratory stress on the blades was measured by means of strain gages located at the base of the blades.

The usual monitoring of shaft vibration, bearing temperature, etc., was done to protect the compressor mechanically.

All the data obtained on the compressor were transmitted

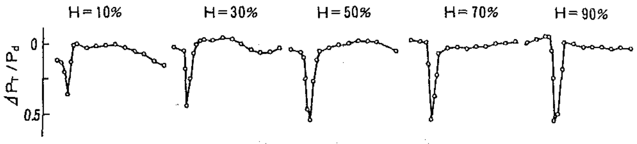

Fig. 15 Total pressure loss coefficient variation with shock-free airfoil

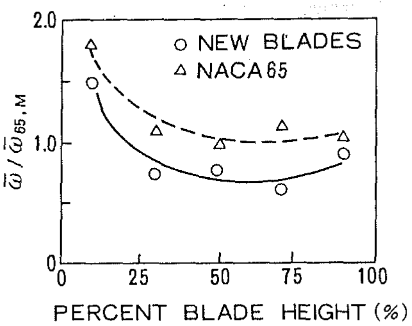

Fig. 16 Comparison of total pressure loss coefficient between shock-free airfoil and NACA-65 airfoil

to the control room. A minicomputer was used to sample and analyze the data. Peripherals such as a line printer, a graphic plotter, and a visual display unit (VDU) with keyboard were also used. Characteristics of the compressor and the results of the traverse measurements could be quickly displayed on these peripherals.

Test Results

The Three-Stage Compressor. The three-stage compressor was tested first. The measured overall characteristics are shown in Fig. 12. The design performance was achieved in terms of mass flow, pressure ratio, and target efficiency. The comparison between measured and predicted characteristic calculated by the streamline analysis method stated previously shows good agreement. The surge line was predicted by the Ohyama's theory (1978). As mentioned already, the accuracy of this method seems to be acceptable. Figure 12 also shows that the compressor has an adequate surge margin at each operating point.

Surge testing was also performed. Figure 13 shows one of the surge test results, which was obtained at the operating point beyond the limit of surge occurrence at the design speed. It indicates that rotating stall and surge occur simultaneously in this case. Such a concurrent phenomenon of rotating stall and surge has been theoretically investigated and its occurrence has been demonstrated by numerical simulation for the three-stage compressor (Ishii and Kashiwabara, 1989).

When a stall cell passes a blade, it causes the blade to vibrate with an impulsive force. An analysis of blade vibration during rotating stall in the three-stage compressor has been performed (Hagiwara et al., 1987).

The Single-Stage Compressor. As described previously, the shock-free airfoil was designed to replace the first stator blade of the NACA-65 airfoil. Its aerodynamic performance was investigated during the single-stage compressor described above. In this test the DCA airfoil was used for the first rotor blade. The original NACA-65 airfoil was first tested to provide a basis for comparison. The rotor blade was the same for both tests. Compressor performance was tested from choke to surge for speeds at 60, 80, and 100 percent of design speed.

A comparison of the measured overall characteristics is shown in Fig. 14. It shows that the design mass flow and pressure ratio at the design speed are achieved for both blades.

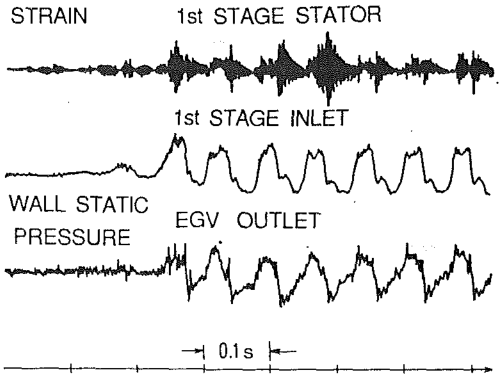

Fig. 17 Blade vibration and wall static pressure variation during rotating stall in single-stage compressor using shock-free airfoil

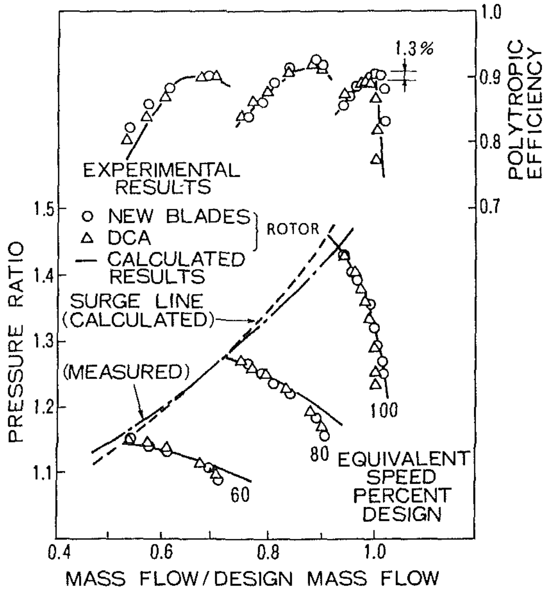

Fig. 18 Single-stage compressor characteristics with a MCA airfoil

On the other hand, the efficiency curve at the design speeds shows an improvement of 1.2 percent for the single-stage compressor with the shock-free airfoil. The surge test results show that there is little difference between the limits of surge occurrence in both compressors.

To determine the reasons for efficiency improvement with the shock-free airfoil, the internal flow at the inlet and the outlet of the stator blade was measured at the design point. A cobra-type pneumatic three-hole probe with a 5-mm diameter was used. Figure 15 shows the circumferential distribution of the total pressure loss coefficient of the shock-free airfoil at various radial positions. At each radial position, the measured results for one pitch from the suction to the pressure side are shown.

Figure 16 shows a comparison of the average total pressure loss coefficient at each blade height for the shock-free and the NACA-65 airfoils. The average total pressure loss coefficient is normalized using the NACA-65 loss coefficient at the 50 percent height. A 30 percent reduction in loss can be achieved with a shock-free airfoil located at around the middle of the flow path. This reduction of losses seems reasonably to correspond to the efficiency improvement shown in Fig. 14. Since the flow measurement between blades has not been done, the reasons for this loss reduction cannot be determined. It may be due to the effects of the weakened or eliminated shock waves on the blade surface, based upon the blade-to-blade

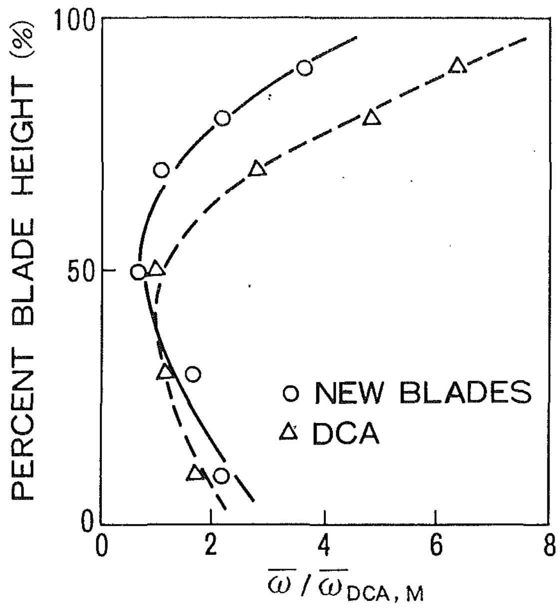

Fig. 19 Comparison of total pressure loss coefficient between MCA airfoil and DCA airfoil

calculation shown previously. As to the flow through the blade passage, we plan to perform detailed measurements in the near future.

The surge test results for a compressor with a shock-free airfoil are shown in Fig. 17. As there is little difference in the unsteady pressure behavior between both blades and since the limit line of surge occurrence is nearly the same for both compressors, as shown in Fig. 14, the stable operating range of both stators is considered to be the same.

In Fig. 16, an increase in loss near the casing can be seen. The reason for this is believed to be the increase in loss at the rotor tip section from the measured total pressure distribution at the outlet plane of the rotor. We therefore designed the MCA airfoil, as already stated, for the rotor blading and used it in the DCA airfoil for the single-stage compressor. For the stator blade, the same shock-free airfoil was used in both tests.

The measured characteristics for the single-stage compressor using the MCA airfoil are shown in Fig. 18 in comparison to the measured results for the compressor with a DCA airfoil rotor. It shows that for the MCA airfoil rotor, the design performance in terms of the mass flow and the pressure ratio was achieved. It also shows that the efficiency curve at the design speed indicates the improvement in the polytropic efficiency of the compressor with a MCA rotor was 1.3 percent in comparison to the DCA rotor.

Figure 19 shows a comparison of the average total pressure loss coefficient for the MCA airfoil and the DCA airfoil at each blade height. The average total pressure loss is normalized using the DCA loss at the 50 percent height. These results show a considerable improvement in compressor performance with the MCA rotor in our single-stage compressor, especially at the upper half of the rotor blade.

Conclusion

A three-stage axial flow compressor with a pressure ratio of 2.2 and a polytropic efficiency of 90 percent was presented. The main features of the aerodynamic design, the test facility, and the instrumentation were described. The test results verify the achievement of design performance.

The aerodynamic design of a shock-free airfoil for high subsonic inlet flow and of an MCA airfoil for relative transonic flow were also presented.

The test results for the single-stage compressor using the first stage of the three-stage compressor show that lower losses are achieved by using the shock-free airfoil stator and the MCA airfoil rotor compared with using the NACA-65 stator and the DCA rotor. Based upon our tests on model compressors, we can expect improvement in the performance of transonic front stages in industrial multistage compressors.

Acknowledgments

We would like to acknowledge the contributions of all personnel at the Mechanical Engineering Research Laboratory and Hitachi Works, Hitachi, Ltd., who were involved in the development of the compressor, construction of the test facility, and test of the compressor.

References

Hagiwara, N., Yoneyama, M., Ishii, H., Matsuura, Y., and Kashiwabara, Y., 1987, "Blade Vibration During Rotating Stall in Axial Flow Compressor," *Proc. 1987 Tokyo International Gas Turbine Congress*, 87-TOKYO-IGTC-92, Vol. III, pp. 349-355.

Hobbs, D. E., and Weingold, H. D., 1984, "Development of Controlled Diffusion Airfoils for Multistage Compressor Application," ASME *Journal of Engineering for Gas Turbines and Power*, Vol. 106, pp. 271-278.

Ishii, H., and Kashiwabara, Y., 1989, "Surge and Rotating Stall in Axial Compressors," AIAA Paper No. AIAA-89-2683.

Novak, R. A., 1967, "Streamline Curvature Computing Procedures for Fluid Flow Problems," ASME *Journal of Engineering for Power*, Vol. 89, pp. 478-490.

Ohyama, K., 1978, "Investigation on Compressor Surge," *Transactions Japan Society of Mechanical Engineers*, Vol. 44, No. 387B, pp. 3810.

Schmidt, E., 1980, "Computation of Supercritical Compressor and Turbine Cascades With a Design Method for Transonic Flows," ASME *Journal of Engineering for Power*, Vol. 102, pp. 68-74.

Steinert, W., Eisenberg, B., and Starken, H., 1991, "Design and Testing of a Controlled Diffusion Airfoil Cascade for Industrial Axial Flow Compressor Application," ASME JOURNAL OF TURBOMACHINERY, Vol. 113, pp. 583-590.

Stephens, H. E., 1978, "Application of Supercritical Airfoil Technology to Compressor Cascades: Comparison of Theoretical and Experimental Results," AIAA Paper No. 78-1138.

A. M. Wo
Institute of Applied Mechanics,
National Taiwan University,
Taipei 106, Taiwan

J. P. Bons
Captain, USAF,
Wright Laboratory,
Wright Patterson AFB, OH 45433

Flow Physics Leading to System Instability in a Centrifugal Pump[1]

The off-design performance in a centrifugal pump is investigated experimentally. The objective is to identify flow features that lead to the onset of surge as the fundamental pumping system instability. Results show that there are primarily two reasons for the onset of surge as the flow is reduced in the pump studied: (a) adverse flow in the tongue region, and (b) destabilizing effect of the pipe diffuser. The former is due to premature diffusion of the flow entering the tongue region, which is manifested by increased flow recirculation through the tongue/impeller gap and flow separation on the volute outer side-wall opposite the tongue. These effects in the tongue region flow coupled with the destabilizing behavior of the pipe diffuser lead to the eventual unstable pump operation.

Introduction

Most axial and centrifugal compression systems exhibit unstable operation at flow rates well below the designed flow. There are inherently two modes of instabilities involved: rotating stall and surge (Emmons et al., 1955; Greitzer, 1976a, 1976b). Rotating stall is a region (or regions) of separated flow rotating at a fraction of the shaft speed; thus circumferentially nonuniform unsteady flow is developed. Surge is a global unsteadiness of flow over the entire flow annulus; thus essentially axisymmetric unsteady flow is dominant. In a typical axial compressor, the frequency scale is about an order of magnitude larger for rotating stall than for surge. Sustained operation in either mode for any compression system is avoided due to loss in performance and potentially catastrophic effects for the blades and its subsystems. As an example, flow fluctuation amplitude during surge can grow to exceed 50 percent of the time mean pressure rise and twice the time mean flow rate for the low specific speed (high power density) pump considered in this work.

The slope of the pressure rise characteristic for the entire compression system has a large influence on the onset of flow instability. Unlike the necessary criterion for static instability, which states that the local pressure rise characteristic must be steeper than the throttle characteristic for a flow perturbation to depart from its equilibrium, dynamic instability can occur in any region of positively sloped pressure rise characteristic region. A perturbation in mass flow on the negatively sloped portion of the pressure rise characteristic results in a net energy dissipation in the flow. On the positively sloped region, however, the phase relationship between the mass flow and pressure perturbations can correspond in such a way so that net energy is added to the flow. If this energy input matches the energy dissipation in the entire flow, which is usually dominated by the throttle, the system can sustain a periodic oscillation.

The precise nature of these unstable oscillations was first characterized by Emmons et al. (1955). In this landmark study, the global oscillations in compressor throughflow (surge) were first formally differentiated from local flow fluctuations (rotating stall). Subsequent efforts to understand and model the global instability phenomenon using lumped parameter representations by Taylor (1964), Stenning (1980), Greitzer (1976a, 1981), and others resulted in considerable success. The mechanism of instability was further determined and a suitable nondimensional parameter representing the potential for instability in a given pumping system was developed (Greitzer, 1976a). The Greitzer B parameter weighs the relative magnitudes of compliant (energy storing) forces and inertial forces in the pumping environment. Comparison of experimental results to lumped parameter based predictions of instability by Greitzer (1976b), Hansen et al. (1981), Fink et al. (1991), and others have validated the usefulness of this type of approach.

While many have successfully captured the global unsteady behavior of compression systems using the lumped parameter and other models, there has been much less work on the detailed internal flow investigation near the instability inception point. In the former case, stability analysis is studied while treating the compressor essentially as a black box with a known steady state, or quasi-steady, performance characteristic. Few attempts have been made at explaining why the performance characteristic has the shape that it does, which requires a detailed investigation of flow structures. Among others, Dean and Young (1977), Toyama et al. (1977), and Fink et al. (1991) undertook rigorous component-by-component investigations of compressor surge. By tracing the individual performance of each component, they were able to identify probable "triggers" for the global unsteadiness. The overall pump response is much more complex, however, since surge is generally due to the interaction of the stalled and unstalled components. It does seem clear, though, that further advances in the understanding and control of compressor stability will come through this type of detailed investigation.

---

[1] This work was performed while the authors were at the M.I.T. Gas Turbine Lab.

Contributed by the International Gas Turbine Institute and presented at the 38th International Gas Turbine and Aeroengine Congress and Exposition, Cincinnati, Ohio, May 24-27, 1993. Manuscript received at ASME Headquarters March 10, 1993. Paper No. 93-GT-283. Associate Technical Editor: H. Lukas.

Table 1 Performance parameter near maximum efficiency for the actual and the experimental pumps at two rotational speeds

	Sundstrand Pump	Experimental Pump	
		50% speed	23% speed
Φ	0.108	0.1023	0.1021
Ψ	0.489	0.574	0.561
Re	4.73×10^4	1.03×10^5	4.73×10^4
N_s	870	813	804
Q(GPM)	-	303.5	140.6
RPM	10^5	204.3	94.8

Objective

The intent of this work is to seek physical reasons for the positively sloped portion of the characteristic in a volute type centrifugal pump, *not* find the most stable design for a pump. Of course the magnitude of the unstable flow phenomenon would change if we vary the geometry of the tongue gap, the volute, or the diffuser. But this would also change the pump performance, which was specified by its manufacturer. Besides, design modifications will still not explain "why" the characteristic has a positive slope at low flows for this class of pumps. Certainly, minor modifications can be made to "alleviate" the instability, but it would always be present (though to a lesser degree).

Specifically, the following questions are addressed:

- What is the performance of each pump component at off-design conditions?
- Which component contributes the most to the positive slope in the overall pump characteristic?
- How rapid is the deterioration in component performance as the flow rate is reduced?
- What flow features are evident prior to surge?

Answers to these and other related questions will enhance the design of efficient pumping system components, thereby increasing the useful range of pump operation.

Experimental Aspects

Pump and Piping Design. The experimental pump used in this study was modeled after a developmental low specific speed fuel pump designed by the Sundstrand Corporation. Table 1 lists design data for the original and the experimental pumps. Figure 1 sketches the top view, along with the pressure tap locations (also refer to Table 2). The impeller is of shrouded single suction variety. The blade design consists of eight backward leaning blades, four full length and four splitters, with an exit angle of 34.0 deg. The volute is a scroll type with a rectangular cross section designed for constant meridional velocity. The pipe diffuser has a rectangular inlet section (62.7 mm height and 91.44 mm width) mating with the volute exit and a circular exit (112 mm diameter). This transition section *is located between pressure Taps T12 and D16. The exit to* inlet area ratio is 1.72. Thus the transitional section is considered as a part of the pipe diffuser throughout this work.

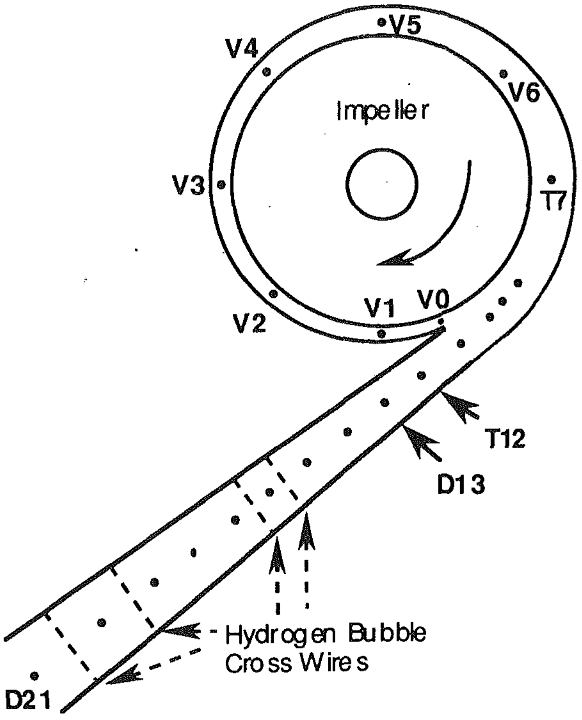

Experimental Pump Dimensions

Impeller diameter	**0.61 m**
Blade exit angle	**34.0 degrees**
Tongue/impeller gap to tongue/volute width	**0.28**
Pipe Diffuser length	**0.8 m**

Fig. 1 Top view of the experimental pump, pressure tap locations, and major pump dimensions (also refer to Table 2)

The designs of the experimental pump and piping components are primarily based on the following considerations. First, the experimental pump is designed as large as practically feasible to enlarge possible small-scale flow events. Thus, the geometry of the pump is scaled up nearly twenty times the size of the Sundstrand pump to allow ease of accessibility for flow visualization and improved spatial resolution in measured flow parameters. Second, piping and plenum dimensions are scaled based on system dynamic considerations; that is, diameters

Nomenclature

b = blade height at the impeller exit = 0.015 m
Cp = diffuser static pressure rise coefficient, see Eqs. (2) and (3)
D = impeller diameter = 0.6096 m
$D\#$ = pressure tap No. in the pipe diffuser; see Table 2 and Fig. 1
H = pressure head
L = distance from the impeller/tongue gap to diffuser exit along the meridional centerline = 3.135 m
m = mass flow, kg/m^3
Ns = specific speed = $\sqrt{Q}/H^{0.75}$, rpm
p = local static pressure
Q = volume flow rate, gpm
Re = Reynolds number = Ub/ν
$T\#$ = pressure tap No. in the tongue region; see Table 2 and Fig. 1
U = wheel speed at the impeller exit
$\bar{V}$ = area-averaged flow velocity
$V\#$ = pressure tap No. in the volute; see Table 2 and Fig. 1
x = coordinate along the meridional centerline
ν = kinematic viscosity
Φ = mass flow coefficient = $m/(\pi DbU)$
Ψ = static pressure rise coefficient = $(p-p_i)/(\rho U^2)$

Subscripts

d = diffuser
di = diffuser inlet
i = pump inlet station
e = pump exit station

Table 2 Designations and locations of static pressure taps; refer also to Fig. 1 (the length L is the distance from the tongue/impeller gap to the diffuser exit along the meridional centerline)

Tap No.	X/L	θ in volute (Degrees)	Comments
i			Pump Inlet Tap
V0	0.0	0	Tongue/ Impeller Gap
V1	0.027	15.4	
V2	0.106	60.4	
V3	0.185	105.4	
V4	0.267	150.4	Volute
V5	0.350	195.4	
V6	0.434	240.4	
T7	0.520	285.4	
T8	0.608	330.4	
T9	0.633		Tongue Region
T10	0.647		
T11	0.662		
T12	0.700		
D13	0.732		
D14	0.757		
D15	0.789		
D16	0.829		Pipe Diffuser
D17	0.861		
D18	0.892		
D19	0.924		
D20	0.955		
D21	0.987		
e	1.42		Pump Exit Tap

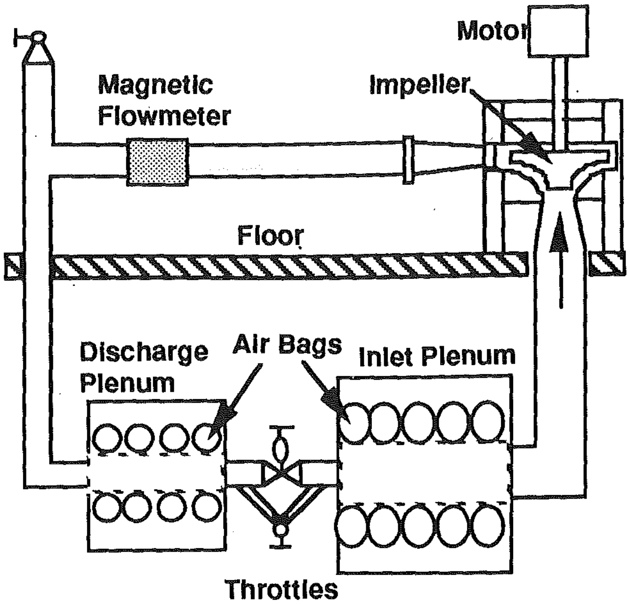

Fig. 2 Sketch of the experimental facility (Bons, 1990)

and lengths of system piping (inertial components) and air content in the plenums (energy storing components) are selected to allow the maximum range of surge frequencies, which cover the range of reduced surge frequencies ($\omega_{\text{reduced}} = \omega_{\text{surge}}/\omega_{\text{shaft}}$) in the Sundstrand pump. Third, water is used as the working fluid to match the range of Reynolds number for the actual pump. Cavitation is absent over the entire range of normal pump operation.

A sketch of the apparatus is shown in Fig. 2. Water is circulated in a closed loop by the pump under investigation powered by a 15 hp, 4 pole A/C drive with an adjustable frequency drive controller. The maximum pump rotation (100 percent speed) is near 450 rpm. To simulate compliance in the flow, since the experimental working fluid (water) is essentially incompressible, discrete pockets of compressibility are placed in the exit plenum (inner tubes with a maximum air volume of 415 liters). The air in the inlet plenum (maximum air volume of 1000 liters) as well as its exaggerated size serve to decouple the throttle exit flow from the pump inlet flow. There are approximately 7.7 m of 0.203 m I.D. PVC piping between the pump diffuser exit and the exit plenum, 3.3 m of 0.203 m I.D. PVC between the plenums (through the throttle), and 3.0 m of 0.305 m I.D. PVC between the inlet plenum and pump inlet. Two throttles are used to allow coarse and fine adjustment of the flow rate. The main throttle is a 0.203 m diameter butterfly valve and the bypass throttle is a 0.0254 m ball valve.

The pump design allows for leakage flow from the back of the impeller to the pump inlet pipe. Three 1/2 in. I.D. tubings, just upstream of the lip seal in the bearing housing, connect this leakage flow to a manifold prior to re-entering the inlet section (6.6 inlet pipe diameters upstream). This leakage flow is approximately 1.5 percent of the total flow at the design flow coefficient, 4.0 percent at surge onset, and 10 percent near shutoff. The front leakage flow, between the impeller shroud and the pipe wall, is inhibited by a circumferential labyrinth seal. This leakage is considered negligible compared to the back leakage flow.

Instrumentation. Combinations of static and dynamic instrumentation are used to characterize the overall and component performance. Dynamic pressure data are measured using high response Kulite (XTM-190) transducers in the pump inlet (7.5 impeller inlet diameters, *Di*, upstream of the impeller shroud inlet) and exit (7.5*Di* downstream of diffuser exit). Steady-state pressure rises along specific pump components are acquired using a water manometer to minimize measurement uncertainty. To match Reynolds number ($\text{Re} = 47300$) with available data taken on the Sundstrand pump, a rotation speed of 94.8 rpm, or 23 percent speed, is used (see Table 1). This relatively low speed is necessary due to near twenty times geometric enlargement of the experimental pump. At the 23 percent speed, a pressure rise of approximately 0.8 psi is observed at the pump exit. Flow rate data are acquired using a magnetic flow meter located at 8*Di* downstream of the diffuser exit. The frequency response of the flow meter (about 75 Hz) is more than sufficient to capture the flow oscillation during surge (0.25 Hz). The leakage flow is measured using a 3.18 cm I.D. Omega FP5300 turbine flowmeter. The impeller shaft rotational frequency is measured by a Lebow 1604 Rotary Transformer. The signal is processed by the Lebow 7540 strain gage indicator and fed into the data acquisition system. The rpm is calibrated using a stroboscope. The shaft torque is measured by a Lebow 1604 torque sensor. The torque sensor is calibrated using a weight and pulley system. Torque tares are determined by running the pump without water.

Pressure taps are distributed from the tongue/impeller gap to the pipe diffuser exit along the meridional centerline to resolve the expected pressure gradients. Table 2 and Fig. 1 show the corresponding tap locations. They are drilled through the lower surface of the pump (as viewed in Fig. 2) along the volute, the tongue region, and the rear portion of the pipe diffuser (Taps D16 through D21). Taps along the forward portion of the diffuser (Taps T12 through D15) are drilled from the upper surface due to obstruction from the supporting structure in the lower surface. Off-centerline pressure taps are located near the tongue region to check the extent of pressure nonuniformity.

To visualize the flow through the pipe diffuser, platinum wires (0.102 mm dia) are located in four stations, as shown in

Table 3 Summary of measurement uncertainties for mass flow and pressure rise coefficients

		W_Φ/Φ	W_Ψ/Ψ
23% Speed	Φ_{Design} (=0.102)	2.1%	3.3%
	Φ_{Surge} (=0.035)	4.1%	3.3%
50% Speed	Φ_{Design} (=0.102)	1.0%	1.5%
	Φ_{Surge} (=0.035)	1.9%	1.5%

Fig. 1, to generate hydrogen bubbles. A cross is formed in each station with portions of both legs insulated so that time-streak flow markers can be produced.

The analogue-to-digital signal processing was done using the Data Translation DT2801 board with PCLAB as software. When using the Kulite transducers, typical sampling rate for each steady-state data point was 50 Hz for 2 seconds of duration. The transient measurement were acquired between 10 Hz and 50 Hz depending on the anticipated system frequency.

Measurement Uncertainties. The experimental uncertainties are calculated based on a knowledge of the instrumentation used and a simple root-mean-squared error analysis (Kline and McClintock, 1953). This method assumes contributions to uncertainties arise mainly from unbiased and random sources. Repeatability in the results and experience to date with the instrumentation employed justify this approximation.

The total uncertainty for the quantity F with variables x_1, x_2, . . . , x_n can be written as

$$W_F=\left[\sum_{i=1}^{n}\left(\frac{\partial F}{\partial X_i}W_{x_i}\right)^2\right]^{1/2} \tag{1}$$

where the total number of variables n contains all steps involved to calculate F. Application of this approach to calculate uncertainties in mass flow and pressure rise, W_Φ and W_Ψ, follow.

The uncertainty in mass flow coefficient arises mostly from measurement of the volume flow downstream of the pump (using a Yokogawa Model AM200A magnetic flowmeter) and measurement of the shaft rotation (using a Lebow 1604 rotary transformer). The contribution from the flowmeter dominates the overall uncertainty near the surge mass flow. At the volume flow of interest, the flowmeter has an uncertainty of 0.5 percent of preset flow span, which corresponds to 1.83 gpm. Hence, the uncertainty in measured volume flow near surge is 3.75 percent at 23 percent speed and 1.72 percent at 50 percent speed. The uncertainty in rpm measurement is estimated to be 1.5 rpm or 1.6 percent at 23 percent speed and 0.74 percent at 50 percent speed. The overall uncertainties in the mass flow coefficient, as well as other quantities, are tabulated in Table 3.

Uncertainties in the calculated time mean pressure coefficient are primarily attributable to error in reading the height of the water manometer when the pressure is not fluctuating and error in visually averaging the height of the water column during pressure fluctuations. Typically, the former contributes ±0.05 in. of water, while the latter ±0.1 in. (For comparison, the term ρU^2 corresponds to 37.10 in. of water at Re = 47,300 or 23 percent speed, where most of the data are presented.) For conservative estimates, the higher of the two is used in calculating actual uncertainties. The summary of uncertainties is listed in Table 3.

Results and Discussions

Results will be presented and discussed focusing on the pressure rise performance and flow features in various pump components. First, the overall pump dynamics near surge will be studied (with air in plenums), mainly to define the surge onset flow coefficient. Then, off-design performance of pump components will be examined using steady state (without air in plenums) pressure distributions and flow visualization. Our interest here lies primarily in revealing flow events in various components which contribute to the positive slope in the overall pressure rise characteristic prior to surge, and not so much in what happens after surge initiation.

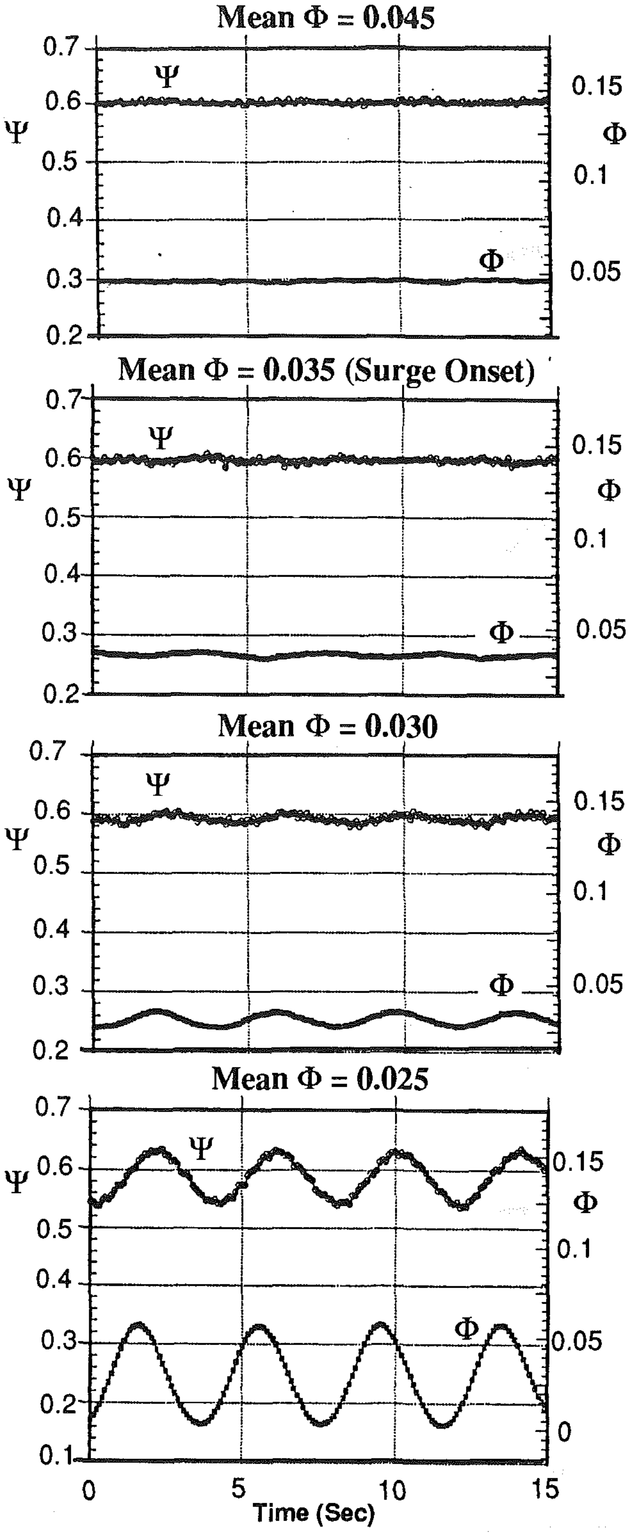

Fig. 3 Excursion of compressor pressure rise and mass flow rate as the throttle is reduced; from this figure, surge onset is defined as Φ = 0.035

Onset of Surge. Dynamic pressure rise and mass flow data are acquired to identify the onset of surge instability in the

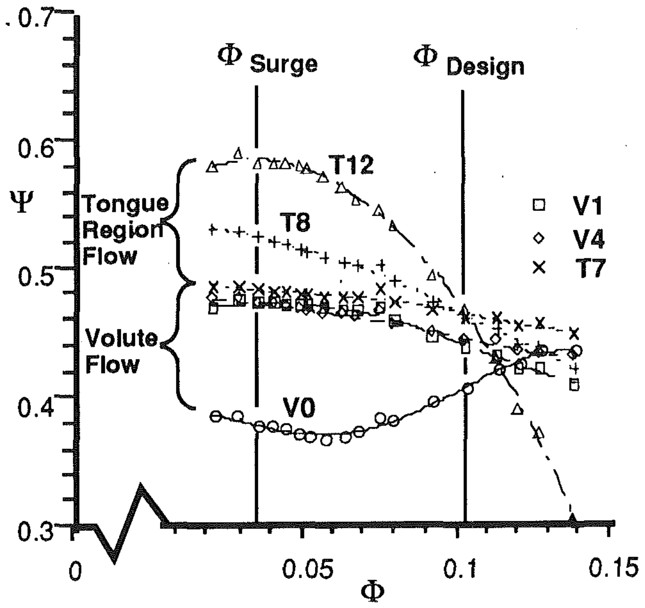

Fig. 4 Static pressure rise characteristic in the volute at Re = 4.73 × 10^4, or 23 percent speed (refer to Table 2 and Fig. 1 for pressure tap locations)

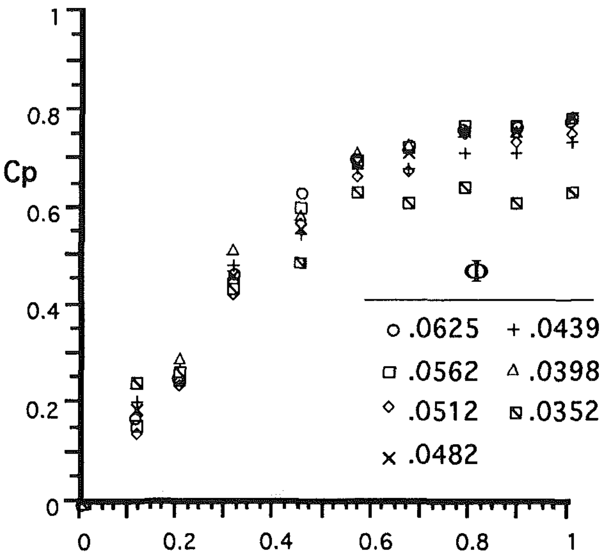

Fig. 5 Diffuser performance prior to surge onset (Re = 4.73 × 10^4)

pumping system. To introduce compliance in the flow, 300 liters of air (maximum amount) are fed into both plenums while holding the pump loop pressure the same as prior to air injection. The excursions of pressure rise and mass flow coefficients for 50 percent speed (Re = 1.03 × 10^5) are presented in Fig. 3 near the surge onset. Data are acquired after transient effects have decayed, since we are interested in whether the system will eventually become unstable at a particular flow coefficient. At time mean $\Phi = 0.045$, the system exhibits no oscillation in either pressure or mass flow. At $\Phi = 0.035$, a definite amplitude is noticeable (compared to the $\Phi = 0.045$ case). As the flow coefficient decreases further to $\Phi = 0.030$ and 0.025, the flow oscillation is clear, with a surge period of 4.0 seconds. Thus, the onset of surge is defined to occur at $\Phi = 0.035$ for this case. At other wheel speeds, variation in the surge onset Φ is small. That is, the flow mechanism that causes the positively sloped portion of the characteristic is only weakly dependent on the wheel speed (see Fig. 12 in Fink et al., 1991). The virtually identical overall pump characteristics for two speeds tested, as shown in Fig. 10, also support this view.

Pump Component Performance. Performance characteristics and flow features will be presented for various components; the volute, tongue region, and pipe diffuser. The spatial extents of these components are defined by Table 2; also refer to Fig. 1.

Volute and Tongue Region Flow. Pressure rise characteristics in the volute and the tongue region are presented in Fig. 4 (refer to Table 2 and Fig. 1 for pressure tap locations). Data show significant differences in the shape of the characteristic at various pump locations. The pressure trace in the gap between the tongue and the impeller, Tap V_o, first shows a gradual decrease in Ψ as Φ is reduced below the design flow ($\Phi = 0.10$) then an increase in Ψ near the surge onset Φ. This is due to local influence of the tongue, which is manifested by increased recirculation flow around the volute at lower flow coefficients. The similarity in the pressure signature between Taps $V1$ ($\theta = 15.4$ deg) and $T7$ ($\theta = 285.4$ deg) implies that the flow in this section of the volute (*i*) decouples from that in the beginning and the end sections, represented by Taps $V0$ and $T8$, respectively, and (*ii*) behaves essentially as a flow collector. The first fact is evident from the significant difference in the pressure rise characteristic, both in the magnitude and in the shape, between this section of the volute and other regions. Note that this region exhibits a negative pressure characteristic slope, which implies that the flow is stable under small perturbations (Greitzer, 1981). Thus, we expect that flow features prior to surge onset will be decoupled spatially as well. The second fact is suggested by the small variation in pressure rise measured at each location within this section of the volute (about 6 percent of the overall pressure rise) over the entire range of flow coefficient tested. These facts, however, do not hold true for the flow near the tongue.

An increasing effect of the tongue on the local pressure rise is evident as the flow traverses through the tongue region, as shown by the pressure traces of Taps $T7$ and $T8$. (Unfortunately, no pressure tap exists between Taps $T7$ and $T8$ to quantify the upstream influence of the tongue more definitively.) Downstream of the tongue, Tap $T12$, the pressure rise is substantially different from the "collecting" portion of the volute. It is significant that the pressure trace at $T12$ exhibits a zero slope at the surge onset $\Phi = 0.035$, as defined by the dynamic data (Fig. 3), and a positive slope at lower flow rates. Thus, this spatial variation of the slope of the local pressure rise characteristic and the fact that a positive slope is first observed near the tongue region suggest that the flow near the tongue plays a vital role to determine the onset of the system instability.

Diffuser Flow. Diffuser flow data are presented and discussed next. The definition of diffuser static pressure rise coefficient, C_p, used here is conventional and is based on the diffuser mean inlet states. Explicitly,

$$C_p = \frac{p - p_{di}}{\frac{1}{2}\rho \bar{V}_{di}^2} \tag{2}$$

$$= 2\left(\frac{U}{\bar{V}_{di}}\right)^2 (\Psi - \Psi_{di}) \tag{3}$$

The diffuser pressure rise data, Fig. 5, below the design flow rate suggest that most of the available kinetic energy is being recovered as pressure, even though the diffuser inlet flow is severely distorted, as will be shown by flow visualization. At the diffuser exit, the diffuser pressure coefficient Cp ranges from 0.6 ($\Phi = 0.035$) to 0.75 ($\Phi = 0.063$). In fact, the majority of pressure rise is attained when the flow reaches the diffuser midlength. Hence, little is gained from the latter half of the

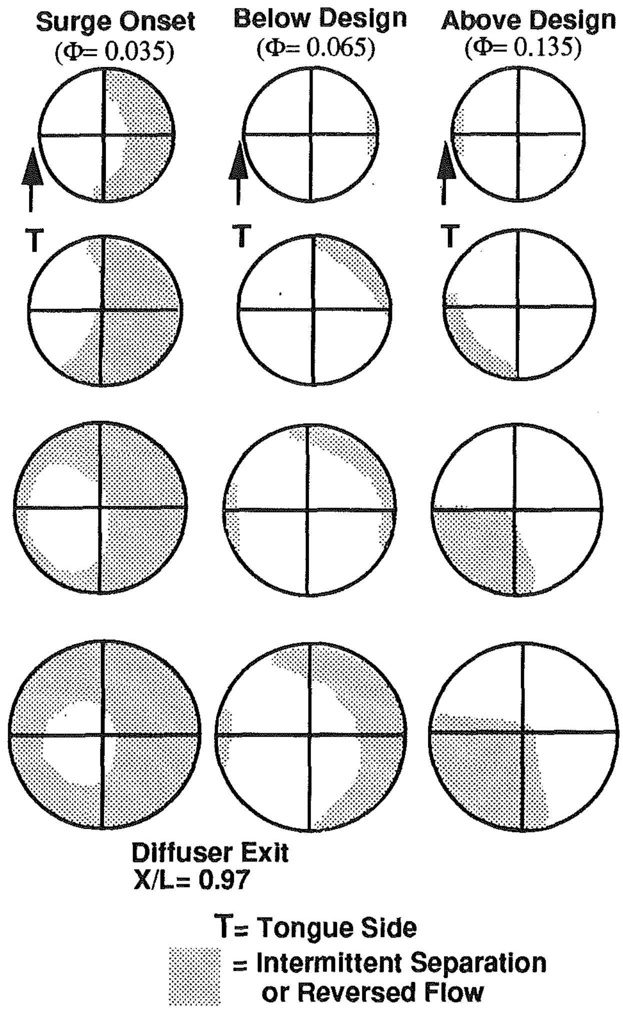

Fig. 6 Hydrogen bubble flow visualization results of diffuser flow at off-design conditions (refer to Fig. 1 for hydrogen bubble wire locations)

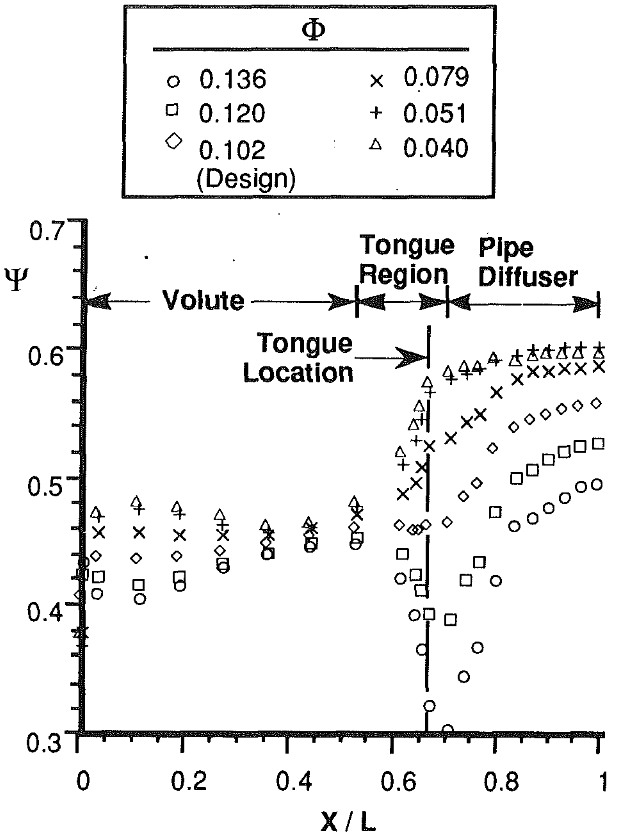

Fig. 7 Meridional variation of static pressure rise (Re = 4.73 × 10^4)

pipe diffuser. On the whole, however, the performance of the diffuser alone is considered acceptable, though severely mismatched with the tongue region flow at off-design conditions. (This will be more evident when the pressure rise along the meridional direction, Fig. 7, is discussed.) This severeness in flow mismatch at off-design conditions has also been articulated by Cumpsty (1989).

To gain better insight to the diffuser internal flow, hydrogen bubble wires forming a cross are located at four streamwise locations in the diffuser, as shown in Fig. 1. The objective here is to obtain a qualitative representation of the flow behavior in the diffuser by identifying distinct flow regions, especially zones of separation. The results are presented in Fig. 6 (Bons, 1990). At high flow coefficient ($\Phi = 0.135$), results show regions of intermittently or totally reversed flow. (Here, intermittently reversed is defined as the hydrogen bubble flowing upstream at least 50 percent of the time observed after leaving the wire.) Note that a region of separated flow is detected on the tongue side of the diffuser wall. This region originates from the tongue as a result of excessive angle of attack from the impeller flow above the design flow rate. This fact is confirmed by injecting air bubbles, as flow markers, through pressure taps on the tongue side wall, where the separated flow occurs. Results verify the presence of reversed flow. This separated region does not reattach but grows downstream and eventually occupies over a quarter of the diffuser exit cross-sectional area. At design flow ($\Phi = 0.10$), flow visualization reveals no intermittently reversed flow region; the bubble trajectories are essentially in the downstream direction.

At lower flow coefficient ($\Phi = 0.065$) prior to surge, the hydrogen bubble results show the location for the reversed flow has moved to the volute wall facing the tongue. (Again, this fact was confirmed by injecting air bubbles, in this case, through the volute side wall.) This implies a substantial change in the streamline trajectories approaching the tongue region as the pump flow coefficient is reduced.

At the surge onset flow coefficient ($\Phi = 0.035$), a significant increase in the amount of reversed flow throughout the diffuser is evident. This suggests the diffuser inlet flow is highly distorted.

Meridional Pressure Rise. The meridional variation of static pressure rise from near surge onset mass flow to highest flow tested is presented in Fig. 7. Distinct regions can be identified by the pressure signature. The flow in the volute shows a 1/rev type variation, with the amplitude of variation largest at the two extremes of off-design conditions. This is indeed typical of this type of volute configuration (Lorett and Gopalakrishnan, 1986), which act essentially as a flow collector (with little diffusion effect).

The flow in the neighborhood of the tongue plays a major role in determining the pressure rise and stability of the entire pump. At the design flow ($\Phi = 0.102$), the tongue region[2] acts as a gradual transition, with small pressure variation, for flow leaving the volute and entering the diffuser. At off-design conditions, the volute flow far upstream of the tongue and the diffuser flow are in essence decoupled, connected only by the volatile region of interaction near the tongue. This region ex-

---

[2] The tongue region extends from $x/L = 0.52$ (Tap $T7$) to $x/L = 0.70$ (Tap $T12$). The tongue region inlet is defined where the upstream influence of the tongue is negligible. The $x/L = 0.52$ position from available data is chosen based on this criterion, which is justified by Figs. 4 and 8.

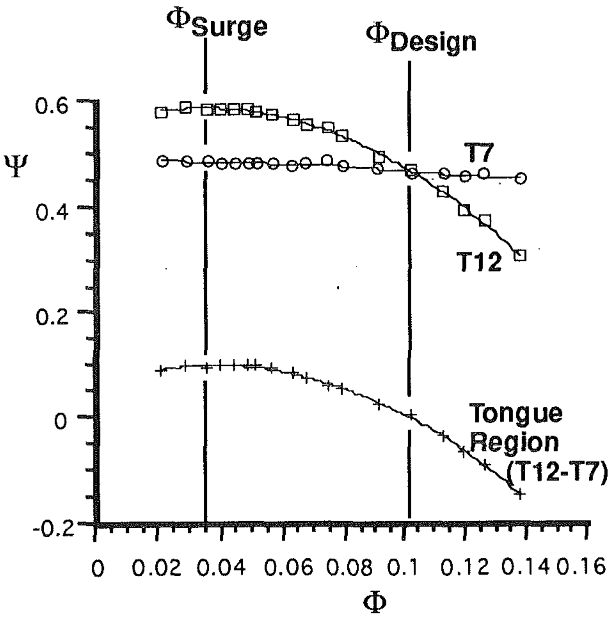

Fig. 8 Static pressure rise in the tongue region. The characteristic of tongue region inlet (Tap *T7*) is decoupled from the tongue region exit flow (Tap *T12*).

hibits a substantial pressure drop at high flow coefficients and a modest pressure rise near surge onset.

At low flows, a premature diffusion effect is responsible for the substantial volute flow being recirculated around the volute through the impeller/tongue gap. This is implied by the favorable pressure gradient between the flow upstream of the tongue (θ approaches 360 deg) and the volute inlet flow (θ approaches 0 deg). At $\Phi = 0.040$, a fluid particle leaving the volute passing through $x/L = 0.647$ with $\Psi = 0.558$ will prefer the recirculated path with $\Psi = 0.474$ at $x/L = 0.03$ over that of the diffuser with $\Psi = 0.584$ at $x/L = 0.70$. This recirculation is also confirmed by trajectories of air bubbles, as flow markers. A summary of the flow structure in the tongue region is presented in Fig. 9, as constructed from measured data and flow visualization results (see Goulet, 1989).

Premature diffusion in the tongue region at low flow gives rise to the first sign of positive slope in the pump characteristic (except that of Tap *V0* which is also influenced by the tongue region flow). Figure 8 articulates this point by plotting the characteristics for the tongue region inlet (Tap *T7*) and exit (Tap *T12*). Fink et al. (1991) also points to the importance of the upstream influence of the tongue in triggering the onset of stall at the inducer tips.

The tongue region acts like a nozzle at flow above design. At $\Phi = 0.138$, Fig. 7 shows a substantial pressure decrease as the flow is accelerated passing the tongue. This acceleration is caused by streamline contraction due to flow separated from the tongue side wall, as discussed earlier. This separation of flow is triggered by excessive angle of attack on the tongue.

Component Stability Characteristics. Figure 10 plots contributions of pressure rise due to various pump components, for two shaft rotational speeds. For all flow coefficients, the impeller provides the largest overall pressure rise; which is mostly due to centrifugal effect. At high flow coefficients, $\Phi = 0.137$, the pressure rise in the diffuser ($\Psi = 0.2$) and the tongue region ($\Psi = 0.15$) have the same order of absolute magnitude. This fact, along with flow phenomenon in the two regions discussed previously, suggests that the majority of the overall pressure drop is due to flow accelerating through the tongue region (between pressure Taps *T7* and *T12*) and being recovered by the diffuser (also refer to Fig. 7). However, a penalty in pressure rise is still incurred as a result of flow separation on the tongue.

Near design, $\Phi = 0.10$, the flow in the volute and the tongue region is matched, as expected, with a small pressure rise ($\Psi = 0.002$) for both components. This indicates that the volute

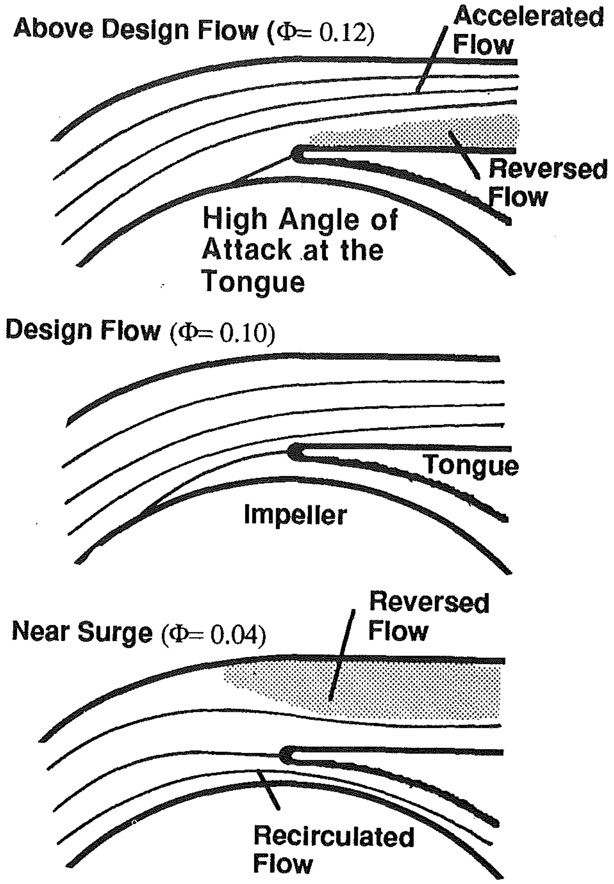

Fig. 9 Flow pattern near the tongue region at three flow coefficients. A fundamental change in the flow feature exists over the range of pump operations (also refer to Goulet, 1989).

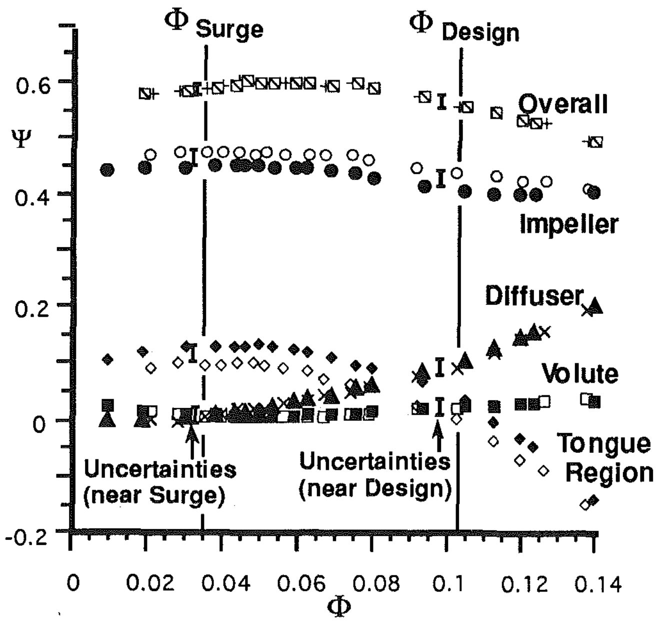

Fig. 10 Static pressure rise characteristic for each pump component (open symbols: $Re = 4.73 \times 10^4$, and solid symbols: $Re = 1.03 \times 10^5$)

and the tongue region are designed essentially to collect and redirect the flow, and not to act as a diffuser.

At surge onset, $\Phi = 0.035$, the volute and the diffuser provide no net overall pressure rise contribution. This is due to passive flow collection in the volute, as occurs over all flow coefficients (the volute pressure rise is essentially flat), and near total flow diffusion in the tongue region, replacing the function of the diffuser. This role switching between the tongue region and the diffuser for the flow diffusion process is indicative of the mismatchedness of components at off-design conditions.

The slope of the pressure rise characteristic of an individual component is perhaps the most important parameter indicating its contribution to the overall system instability. Figure 11[3] presents this information. It is apparent that the slope of all components except the diffuser changes sign, or stability characteristic, near the surge onset ($\Phi = 0.035$). The impeller is a stabilizing component at the design flow coefficient and is essentially neutral near the onset of surge. The volute exhibits a slight destabilizing effect at design and becomes stable near surge onset.

The changes in slope for the tongue region and the diffuser are the most severe as flow is reduced; thus they play a dominant role in determining the overall system instability. The onset of surge is primarily due to the rapid decrease in the flow stabilizing effect of the tongue region, thus allowing the unstable behavior of the diffuser to eventually destabilize the entire pump. Indeed at surge onset, the slope of the overall pump is virtually equal to that of the diffuser. At design flow, the stabilizing effect of the tongue region ($dy/d\Phi = -3.2$) is nearly 1.5 times the destabilizing effect of the diffuser ($dy/d\Phi = 2.0$). This effectively keeps the instability prone diffuser in check at design flow. Near the surge onset, the tongue region stabilizing effect completely vanished, leaving the destabilizing effect of the diffuser dominating the onset of overall system instability.

Further Discussion

The spirit of this paper is similar to one aspect of Fink et al. (1991): seeking the fluid dynamic reason that triggers instability in the machine of interest. Their investigation of surge dynamics in a free-spool centrifugal turbocharger reveal inducer tip stall being the initiating mechanism for surge. The most severe region of inducer stall is found locked onto the tongue circumferential position. Although the impeller in the present study does not have an inducer, the overwhelming effect of the tongue on the overall flow is also evident. At off-design conditions flow tends toward separation on the volute walls near the tongue meridional position, see Fig. 10, indicating a substantial effect of flow mismatch between components (Cumpsty, 1989). This is perhaps the fundamental reason for pressure drop at both extremes of off-design conditions. At design condition, the volute exit flow passes through the tongue with negligible pressure gradient, see Fig. 8.

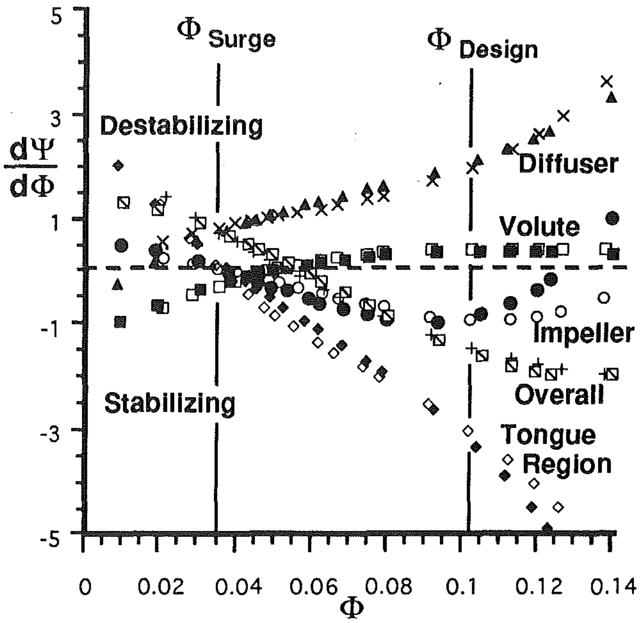

Fig. 11 Slope of the pressure rise characteristic for each pump component, obtained from a fourth order curve fit of data in Fig. 10 (open symbol: $Re = 4.73 \times 10^4$, and solid symbols: $Re = 4.73 \times 10^5$)

The present work agrees qualitatively with the stability study of Dean and Young (1974). In their study, the channel diffuser is the element that has the largest destabilizing effect. With a simple pipe diffuser in the present study, this trend is clearly qualitatively duplicated. Moreover, the comparison between the two studies indicates that as far as the contribution to flow stability due to the diffuser is concerned the channel diffuser and the pipe diffuser behave very similarly. This suggests that the functional characteristic of individual component is more important that its detail design, at least for component stability considerations. Another case for comparison, and support for this view, is between the stability characteristic of Dean's diffuser inlet and the tongue region (which is upstream of the pipe diffuser) in the present study. In both cases, the stability criteria degrade with decreasing flow. There is one difference, however. Both Dean's channel diffuser and diffuser inlet appear to approach a plateau in his stability parameter without crossing the stability/instability boundary but the present study indicates the stability criteria for pipe diffuser and the tongue region actually cross the boundary as the flow is decreased. The reason for the discrepancy is not all apparent. This seems to suggest that the stability behavior for Dean's channel diffuser and diffuser inlet is not sensitive to the decrease in flow, near the lowest flow rate tested, whereas for the present work, this is not the case.

The following hypothesis is proposed to improve the off-design adverse flow conditions in the tongue region for this particular pump. If the volute effective cross-sectional area were to somehow decrease gradually as the mass flow decreases below the design point, with corresponding decrease in the tongue region inlet and exit area as well as diffuser inlet area while keeping the diffuser exit area fixed, then the abrupt pressure rise in the tongue region at low flow (see Fig. 7) would be alleviated. This is simply because the volute pressure decreases with the effective volute area at a constant mass flow. This results in decreased favorable pressure gradient between $\theta = 359$ deg and $\theta = 0$ deg, thus a decrease in the recirculation flow through the gap. With recirculation flow decreased so is the amount of premature diffusion in the tongue region inlet. Thus, the flow separation pattern (refer to Fig. 9) would also be alleviated, resulting in delay of surge onset. At mass flow above design, the converse in the geometry modification would also be effective in preventing flow separation at the tongue. However, with this design modification the diffuser angle must increase for low flow and decrease for high flow, keeping the overall length fixed. This probably would not cause a substantial penalty on the diffuser performance, since the diffuser is effective in recovering its inlet kinetic energy into pressure even with large amount of inlet distorted flow, as shown in Figs. 5 and 6.

Conclusions

Off-design flow in a volute type centrifugal pump has been studied experimentally with the primary objective of identifying flow behavior leading to the onset of surge as the fun-

---

[3] Figure 11 is calculated from fourth-order fit of data in Fig. 10.

damental system instability. Major results are summarized as follows:

1 Surge initiation in the pump studied is due to (*a*) rapid increase in the slope of the pressure rise characteristic due to adverse flow condition in the tongue region, and (*b*) destabilizing effect of the pipe diffuser. The former is due to premature diffusion of the flow entering the tongue region, which is manifested by increased flow recirculation through the tongue/impeller gap and flow separation on the volute outer side-wall opposite the tongue.

2 These effects in the tongue region coupled with the destabilizing behavior of the diffuser, which contributes a positive slope toward the overall pump characteristic for all flow coefficients investigated, produces the observed unstable pump behavior.

3 The impeller is shown to be a stabilizing component at high flow coefficients and essentially neutral near surge. The volute exhibits a small destabilizing effect at high flows and becomes stable near the onset of surge.

4 At flow coefficients above design, separation on the tongue causes the flow to accelerate as it leaves the volute, traverses the tongue region. This effect contributes significantly to the observed reduction in pump pressure rise at high flow rates.

Acknowledgments

This work is jointly supported by the Sundstrand Corporation and the National Science Foundation. Helpful discussions with Mr. Paul Hermann, Mr. Paul Westhoff, and Mr. Tom Tyler of Sundstrand Corporation are much appreciated. The authors are grateful to Prof. E. M. Greitzer for many enlightening discussions during this project. Encouragement from Prof. J. L. Kerrebrock to publish this work is also acknowledged. The help of Mr. Scott Sandler and Mr. Furio Chaccio in taking some of the pressure data is also appreciated. Dr. Belgacem Jaroux oversaw this phase of the project. The preliminary design work for the experiment was performed by Mr. Nicolas Goulet. The excellent support of the technical staff at the M.I.T. Gas Turbine Laboratory also deserve special credit. We want to especially acknowledge the help of God throughout this work, particularly in thinking through the flow physics.

References

Bons, J. P., 1990, "Instabilities and Unsteady Flows in Centrifugal Pumps," M.I.T. Master Thesis, Dept. of Aeronautics and Astronautics, Cambridge, MA.

Cumpsty, N. A., 1989, *Compressor Aerodynamics*, Longman Scientific & Technical, United Kingdom.

Dean, R. C., and Young, L. R., 1977, "The Time Domain of Centrifugal Compressor and Pump Stability and Surge," *J. Fluids Eng.*, Vol. 99, pp. 53-63.

Elder, R. L., and Gill, M. E., 1985, "A Discussion of the Factors Affecting Surge in Centrifugal Compressors," ASME *Journal of Engineering for Gas Turbines and Power*, Vol. 107, pp. 499-506.

Emmons, H. W., Pearson, C. E., and Grant, H. P., 1955, "Compressor Surge and Stall Propagation," *Trans. ASME*, Vol. 77, pp. 455-469.

Fink, D. A., Cumpsty, N. A., and Greitzer, E. M., 1991, "Surge Dynamics in a Free-Spool Centrifugal Compressor System," ASME JOURNAL OF TURBOMACHINERY, Vol. 114, pp. 321-332.

Goulet, N. R., 1989, "An Experimental Facility for the Study of Unsteady Flow in Turbopumps," M.I.T. Master Thesis, Dept. of Aeronautics and Astronautics, Cambridge, MA.

Greitzer, E. M., 1976a, "Surge and Rotating Stall in Axial Flow Compressors. Part I: Theoretical Compression System Model," ASME *Journal of Engineering for Power*, Vol. 98, pp. 190-198.

Greitzer, E. M., 1976b, "Surge and Rotating Stall in Axial Flow Compressors. Part II: Experimental Results and Comparison With Theory," ASME *Journal of Engineering for Power*, Vol. 98, pp. 199-217.

Greitzer, E. M., 1981, "The Stability of Pumping Systems—The 1980 Freeman Scholar Lecture," ASME *Journal of Fluids Engineering*, Vol. 103, pp. 193-242.

Hansen, K. E., Jorgenson, P., and Larsen, P. S., 1981, "Experimental and Theoretical Study of Surge in a Small Centrifugal Compressor," ASME *Journal of Fluids Engineering*, Vol. 103, pp. 391-395.

Howell, W. T., 1964, "Stability of Multi-stage Axial Flow Compressors," *The Aeronautical Quarterly*, Vol. 15, pp. 328-356.

Kline, S. J., and McClintock, F. A., 1953, "Describing Uncertainties in Single-Sample Experiments," *Mech. Engineering*, Jan., pp. 3-8.

Lorett, J. A., and Gopalakrishnan, S., 1986, "Interaction Between Impeller and Volute of Pumps at Off-Design Conditions," ASME *Journal of Fluids Engineering*, Vol. 108, pp. 12-18.

Stenning, A. H., 1980, "Rotating Stall and Surge," ASME *Journal of Fluids Engineering*, Vol. 102, pp. 14-21.

Taylor, E. S., 1964, *The Centrifugal Compressor*, Par J in *Aerodynamics of Compressors and Turbines*, W. R. Hawthorne, ed., Princeton University Press, Princeton, NJ.

Toyama, K., Runstadler, P. W., and Dean, R. C., 1977, "An Experimental Study of Surge in Centrifugal Compressors," ASME *Journal of Fluids Engineering*, Vol. 99, pp. 115-131.

Suppression of Mixed-Flow Pump Instability and Surge by the Active Alteration of Impeller Secondary Flows

A. Goto
Ebara Research Company, Ltd.,
Fujisawa-shi, Japan

An active method for enhancing pump stability, featuring water jet injection at impeller inlet, was applied to a mixed-flow pump. The stall margin, between the design point and the positive slope region of the head-flow characteristic, was most effectively enlarged by injecting the jet in the counterrotating direction of the impeller. The counterrotating streamwise vorticity along the casing, generated by the velocity discontinuity due to the jet injection, altered the secondary flow pattern in the impeller by opposing the passage vortex and assisting the tip leakage vortex motion. The location of the wake flow was displaced away from the casing-suction surface corner of the impeller, thus avoiding the onset of the extensive corner separation, the cause of positive slope region of the head-flow characteristic. This method was also confirmed to be effective for stabilizing a pump system already in a state of surge.

Introduction

The onset of an abrupt decrease in pressure head and positively sloped head-flow characteristic at part-load operating conditions often prevents stable operation of a pumping system. In the present paper, this condition under which the slope becomes positive is referred to as the "stall onset." A variety of flow phenomena can be responsible for the stall onset, depending on the configuration and arrangements of pump components, and very little had been known about flow phenomena that lead to stall onset of mixed-flow pumps. Recently, Goto (1992b) studied the effect of the tip leakage flow on stall onset of a mixed-flow pump impeller, based on experimental observations and computations by a Navier–Stokes code, and the important role of impeller secondary flows was clarified. The present paper proposes an active way of controlling stall phenomena in mixed-flow pumps, based on previous research of impeller secondary flows.

Research on active control techniques has been recently done quite intensely, both at MIT (Pinsley et al., 1990; Paduano et al., 1993) and at the University of Cambridge (Ffowcs Williams, 1990; Day, 1993), with the objective of dynamically stabilizing stall and surge phenomena in centrifugal and axial-flow compressors. In these techniques, initial flow disturbances, which grow into stall and surge, are sensed by an array of sensors. The sensed data are then processed by a variety of feedback control systems, and additional disturbances with proper phase and amplitude are generated by various types of actuators to dump the fluid oscillation. Active control differs from conventional methods for enhancing stability, such as casing treatment and the bypass method, since it induces almost no efficiency penalties.

The motivation for conducting the present study was provided by Dr. I. Day, the Whittle Laboratory, the University of Cambridge, through his research on active control of rotating stall and surge in axial compressors. Day (1993) had used an air injection system, in which fast-acting valves were used as actuators, to generate disturbances into the flow fields. There were two approaches in using the air injection system. In the first approach, air injection was used to generate perturbation so that the prestall modal wave, which promotes the formation of stall cells, would be dumped. In the second approach, stall cells were energized in their initial stages and eliminated by air injection, resulting in the stall margin being improved by 6 percent. In addition, the air injection system was confirmed to be effective to stabilize the compressor already in a state of surge. The latter approach can be regarded as more general as it is applicable to cases where there is no evidence of prestall model waves. According to the studies by Goto (1992b), the onset of the stall in the present mixed-flow pump was caused by the onset of extensive flow separation at the shroud-suction surface corner in the impeller, and there was no evidence of prestall modal waves. The mechanism of stall onset in the mixed-flow pump is different from that in the multistage compressor tested by Day. However, if the second approach by Day succeeded in stall suppression by energizing localized stall cells, as was explained in his paper, it might be effective to suppress the onset of the localized corner separation and the onset of the stall. Based on these considerations, the author applied the second approach to the mixed-

---

Contributed by the International Gas Turbine Institute and presented at the 38th International Gas Turbine and Aeroengine Congress and Exposition, Cincinnati, OH, May 24–27, 1993. Manuscript received at ASME Headquarters March 10, 1993. Paper No. 93-GT-298. Associate Technical Editor: H. Lukas.

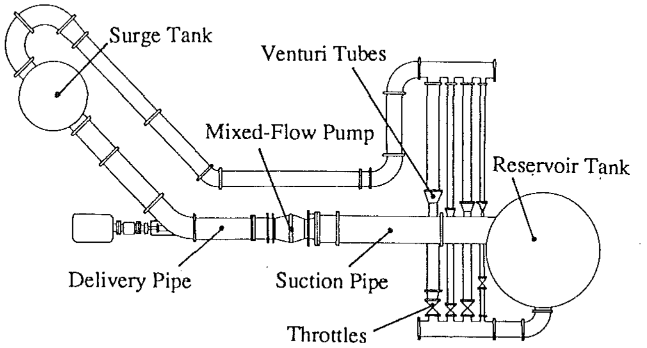

Fig. 1 Schematic picture of closed flow loop for mixed-flow pump experiments

Table 1 Design of impeller

Case	IMP25	IMP30
β_{1b} (deg)	27.8 / 18.3 / 14.8	29.4 / 19.2 / 15.8
β_{2b} (deg)	31.8 / 25.3 / 20.7	41.5 / 30.9 / 24.0
Q (m^3 / min)	8.7	10.0
H (m)	7.0	7.1
Ns	1.34	1.42
Number of blades = 5	r_1 (mm) = 58.0 / 102.3 / 132.5	
Rotational speed = 800 rev / min	r_2 (mm) = 142.5 / 157.8 / 171.7	

(hub / midspan / shroud)

flow pump using a water jet injection system at the inlet of the impeller. Then it was found that this method was not only effective for suppressing stall onset, but also stabilizing the pump system already in a state of surge. The effect of water jet injection was similar to that found by Day (1993). However, the actual flow mechanism of stall suppression was confirmed to be very different from that explained by Day, and it was profoundly connected with the secondary flow behavior within the impeller. The direction of jet injection was also found to be the determinating factor for the present method, and the maximum suppression effect was obtained when the jet was injected in the counterrotating direction.

In the present paper, the effects of jet injection on stall suppression are investigated experimentally at various jet flow parameters, such as the width of jet, number of injection nozzles, jet flow speed, and the direction of jet injection. The mechanism of stall suppression is discussed, based on the results of internal flow measurements and numerical computations, including an explanation on the importance of the direction of jet injection. The results of surge suppression are also introduced and the possibility of stabilizing a mixed-flow pump throughout the whole flow rate range is discussed.

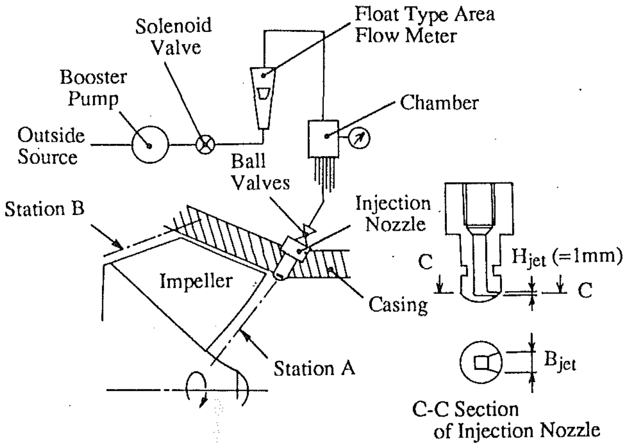

Fig. 2 Schematic diagram of water jet injection system

Experimental Apparatus and Method

Experimental Apparatus. Figure 1 schematically shows the closed-flow loop used for performance tests, flow field measurements, and experiments on surge. The test loop consisted of a reservoir tank (10.3 m^3, open to the atmosphere), a 440-mm-dia suction pipe, a mixed-flow pump (250 mm impeller eye diameter), a 350-mm-dia delivery pipe, a surge tank (2.2 m^3), and a return line with venturi tubes and throttles. Water was used as the test fluid and experiments were carried out on two impellers with different blade angles. The meridional geometry of the impellers was identical. The design conditions of the impellers are shown in Table 1.

As the flow phenomena toward stall onset in IMP25 were already well understood, through previous studies by Goto (1992a, b), experiments on the suppression of stall and investigation on its flow mechanism were carried out using IMP25. The experiments on the suppression of surge were done using IMP30, which had a wider positive slope region of the head-flow characteristic. The air-filled region in the surge tank during experiments on surge was 1.4 m^3 for all tests.

Jet Injection System. Figure 2 shows a schematic diagram of the jet injection system and the cross section of a typical nozzle. Seven types of water jet injection nozzles were manufactured and tested to achieve most effective stall suppression with minimum flow loss. The outlet of the nozzle was rectangular, having a width B_{jet} = 3, 5, 7, and 10 mm, while its height was 1 mm in all types. The head of the nozzle was rounded off so as not to disturb the inlet flow near the casing.

Twelve nozzles were placed circumferentially around the casing at the impeller inlet at pitch intervals of 30 deg. The

Nomenclature

B_{jet} = width of nozzle outlet
H = head, m
H^* = head ratio $= H/(H$ at best efficiency point)
H_{jet} = height of nozzle outlet
L = shaft power
L^* = shaft power ratio $= L/(L$ at best efficiency point)
l = meridional blade chord length
LE = impeller leading edge
N_{jet} = number of nozzles
Ns = nondimensional specific speed $= \omega \cdot \sqrt{Q}/(gH)^{3/4}$
PS = pressure surface
Q = flow rate, m^3/s
Q^* = flow rate ratio $= Q/(Q$ at best efficiency point)
R_o = Rossby number $= W_{ref}/(\omega R_n)$
R_n = radius of streamline curvature
SS = suction surface
TE = impeller trailing edge
U = peripheral blade speed
V = absolute velocity
V_{jet} = nominal speed of jet flow
V_{eff} = velocity of annular flow layer
W = relative velocity
α_{jet} = injection angle of jet measured from axial direction
β_b = blade angle measured from circumferential direction
ω = angular rotation frequency, rad/s

Subscripts

1 = inlet
2 = exit
m = midspan
t = blade tip

gap between the nozzle and the blade leading edge was about 3 mm. Each nozzle outlet was set very close to the casing inner wall to form an annular thin layer flowing along the casing wall. The nozzle could be rotated about its axis to enable changes in the jet injection angle. Flexible tubes, connected to the nozzles, were manifolded into a single chamber pressurized by a booster pump, and injected water was supplied from an outside source. Each nozzle had a ball valve at the inlet and the number of jets was changeable arbitrarily. The on-off of the jet injection was manually controlled by a solenoid valve. The flow rate of the injected water was measured by a float type area flowmeter placed at the discharge of the booster pump.

Performance Tests. Performance tests under steady state were conducted according to ISO standards. The transient performance of the pump during the surge was measured by conventional instrumentation for steady flow measurements. The instantaneous flow rate in the suction pipe was estimated from transducer measurements on pressure sensed by an ordinary three-hole cobra probe placed at the center of the pipe. This flow rate measurement system was calibrated with the flow rate measured by venturi tubes under steady state. The instantaneous pseudo-head was directly measured by transducer measurements of the pressure difference between two total pressure probes placed in the suction and delivery pipes. Although the accuracy of the measured transient performance was unclear, it was considered to be satisfactory for the purpose of the present study, as the frequency of the flow oscillation during the surge was as low as 0.15 Hz, a condition under which the flow may be considered as being quasi-steady.

Flow Field Measurements. Besides the performance tests, inlet and exit flow measurements of the impeller were carried out using two types of pressure probe. The steady exit flow was measured by a two-hole pitot probe with high-frequency response at Station B (Fig. 2), 8 mm downstream of the trailing edge. Two diffusion type semiconductor pressure transducers were placed in the stem tube. The resonance frequency of the pressure sensing system was about 5.6 kHz and was high enough compared with the blade passing frequency of 67 Hz at 800 rpm. Three-dimensional relative flow fields at the impeller exit were measured by the phase-locked multisampling and averaging technique. (For details on the measuring system, the data reduction method, and the accuracy of measurements, see previous paper by Goto, 1988.)

As for measurement of inlet flow fields under a state of surge, an ordinary three-hole cobra probe was used at Station A, 10 mm upstream of the leading edge at midspan. The probe head was truncated at an angle of 45 deg and the transient pressure difference between the two side pressure holes was measured during a surge cycle using a differential pressure transducer. The probe head was located near the casing, having one of the two side holes facing the inflow and the other facing the rotating direction of the impeller. The pressure difference gave the pseudo-velocity of the inflow or the circumferential pseudo-velocity component of the inlet recirculation, according as the absence or the existence of the inlet recirculation. This system was used to monitor qualitatively the global change of the flow pattern within the impeller, including developing or diminishing inlet recirculation occurring during surge cycles.

Suppression of Stall Onset

Pump Characteristics. Figure 3 shows measured pump characteristics of IMP25, with and without jet injection through 12 nozzles. These characteristics were measured when the throttle was being closed. The width of the nozzle outlet was 5 mm and the jet was injected in the counterrotating direction of the impeller at the speed of $V_{jet}/U_{1t} = 1.32$. Here, the nominal speed of jet V_{jet} was obtained by dividing the flow rate per nozzle by the outlet area of the nozzle. When there was no jet injection, the pump head showed abrupt decrease (stall onset) at $Q^* = 0.57$ and then it started recovering gradually. According to the previous study on IMP25 by Goto (1992b), the onset of the corner separation at the casing-suction surface corner in the impeller was the cause of the positive region of head-flow characteristic, and it triggered the onset of the inlet recirculation. Because of this inlet recirculation, the head and the power started increasing gradually after the stall onset. When the jet injection system was activated, the stall onset was avoided and the positive slope region of the head-flow characteristic was successfully eliminated. The flow rate injected through 12 nozzles was about 1 percent of the pump flow rate around the instability region. The power-flow characteristic curve shows abrupt increase at $Q^* = 0.5$ and suggests a drastic change of the flow pattern within the impeller, i.e., the onset of inlet recirculation. Figure 5 (points A and B) schematically shows the flow pattern around this critical point. The same head rise was achieved by the pump having a totally different flow pattern within the impeller.

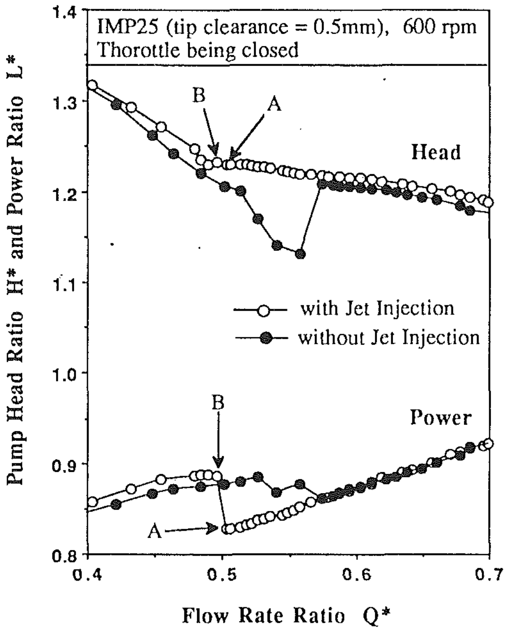

Fig. 3 Pump characteristics with and without jet injection measured as throttle was being closed (jet flow parameters: $V_{jet}/U_{1t} = 1.32$, $\alpha_{jet} = 90$ deg, $N_{jet} = 12$, $B_{jet} = 5$ mm)

When the characteristics were measured when the throttle was being opened (Fig. 4), the presence of hysteresis in the effect of jet injection was observed. The head-flow characteristic did not show any improvement by the jet injection. When the flow rate was increased from the shut-off condition and the operating point moved to point *C* (see Fig. 5), there was already a fully developed inlet recirculation and it was impossible to eliminate the recirculating flow by the injection of a small amount of jet flow. This situation will continue until the ordinary recovery point *E* is reached. It seems as if the hysteresis described here will reduce the value of the present suppression method of stall, since the pump system may be under surge when the pump is operated at the positive slope region when the throttle is being opened. However, according to the experimental investigations described below, the surge will never be sustained under the presence of the jet injection.

Effects of Jet Flow Parameters. The effectiveness of jet flow injection was investigated for various jet flow parameters such as the width of the jet, number of nozzles, jet flow speed, and the injection angle. It was acknowledged that the onset

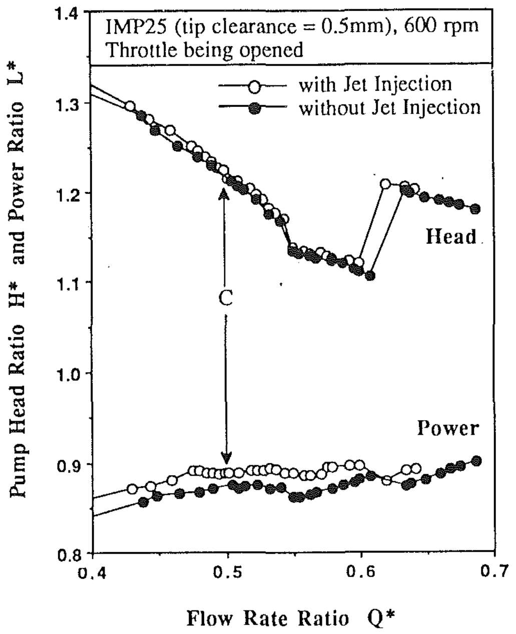

Fig. 4 Pump characteristics with and without jet injection measured as throttle was being opened (jet flow parameters: $V_{jet}/U_{1t} = 1.32$, $\alpha_{jet} = 90$ deg, $N_{jet} = 12$, $B_{jet} = 5$ mm)

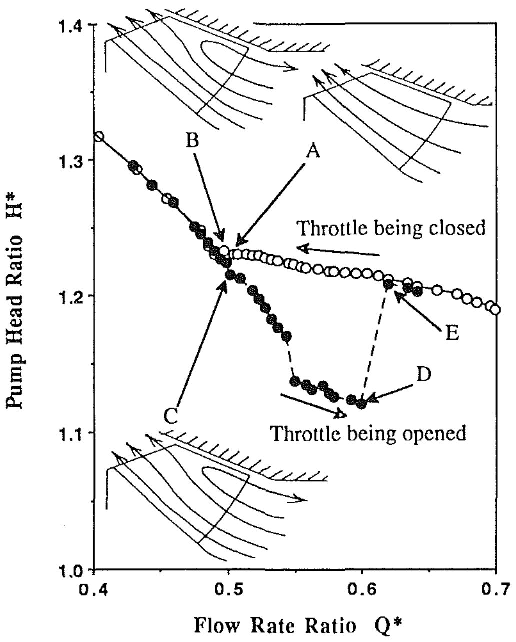

Fig. 5 Hysteresis in pump characteristics with jet flow injection

of stall was suppressed more effectively under a wider jet flow, faster jet flow speed, and more nozzles.

The most interesting parameter was the angle of jet flow injection. In Fig. 6, the effects of the injection angle are shown as changes in critical flow rate ratio of stall onset at two different jet flow speeds. The data were measured when the throttle was being closed. The critical flow rate ratio of stall onset without jet injection is shown by a broken line for reference. The jet injection had positive effects and the stall onset was delayed when the injection angle was set between 0 deg and 180 deg, i.e., when the jet flow had a counterrotating velocity component. Maximum suppression effects were achieved when the jet flow was injected circumferentially in the counterrotating direction of the impeller ($\alpha_{jet} = 90$ deg).

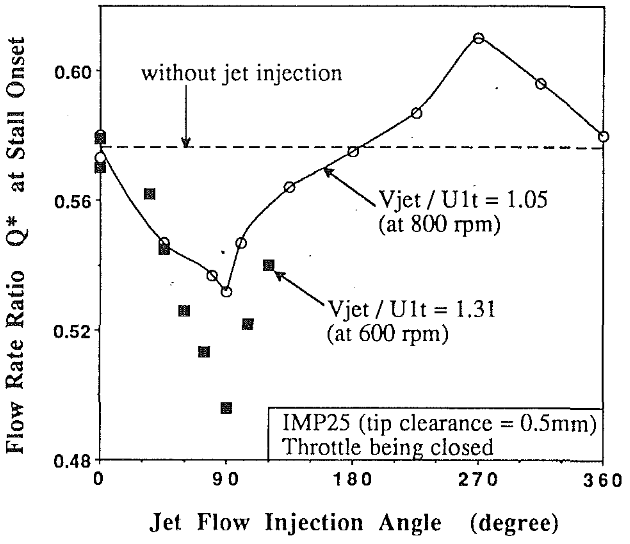

Fig. 6 Critical flow rate ratio of stall onset at different injection angles and jet flow speeds (jet flow parameters: $N_{jet} = 12$, $B_{jet} = 5$ mm)

The no-stall condition was achieved at this injection angle when the jet flow speed was $V_{jet}/U_{1t} = 1.31$. When the jet flow was injected in the direction of impeller rotation, the positively sloped head-flow characteristic appeared at much higher flow rate ratio. The worst effect was obtained when the jet flow was injected circumferentially in the direction of impeller rotation ($\alpha_{jet} = 270$ deg). Note here that the degree of deterioration in the latter case is nearly identical to the degree of maximum improvement.

If the stall of the present impeller is caused by the so-called blade stall, one might expect that the jet injection in the direction of impeller rotation would delay the stall onset, as the flow incidence angle against the blade is reduced by the induced prerotation near the blade tip. Contrary to such expectation, the best effect was obtained when the jet was injected in the counterrotating direction. The explanation that this is due to the energy supply to the low-momentum fluid, within the inlet casing boundary layer, also does not hold, since there was no improvement at all when the jet was injected in the axial direction. The actual flow phenomena toward stall onset in the present impeller were dominated by the interaction between secondary flows within the casing viscous region (Goto, 1992b). Therefore, the dependence of the suppression effects on the jet injection angle must be related to the internal flow behavior toward stall onset. This will be discussed in the next section in detail.

Mechanism of Stall Suppression

Flow Phenomena Toward Stall. Goto (1992a, b) studied the flow phenomena toward stall onset in the IMP25 impeller with different tip clearances, including that in the shrouded case, and found that the impeller is more likely to stall at higher flow rates as the wake flow tends to accumulate closer to the casing-suction surface corner.

Johnson and Moore (1983) had studied the influence of flow rate on the jet-wake flow pattern in a shrouded centrifugal impeller. They presented the Rossby number R_0, which gives the relative magnitude of the centrifugal and Coriolis forces, as a useful indication of where the wake is likely to be formed in the flow passage. The location of the wake flow moves toward the shroud-suction surface corner when the flow rate is decreased, since the effects of Coriolis force increase due to the reduced relative velocity in the flow passage. However, actual flow phenomena are much more complicated because of the strong three-dimensional viscous effects near endwall regions, including the effects of tip leakage flow when there is no shroud. In such cases, the application of reliable three-dimensional Navier–Stokes solvers is the only practical way to study the detailed flow phenomena.

The complex three-dimensional flow fields in the IMP25 impeller have been investigated numerically by Goto (1992a) who applied the incompressible version of Dawes' three-dimensional Navier–Stokes code (Dawes, 1988). The interaction mechanisms between secondary flows and tip leakage flows were well interpreted, using velocity and vorticity contours on quasi-orthogonal planes. The tip leakage vortex interacted with the passage vortex around the midpitch location and low-momentum fluids accumulated in this interaction region. The formation of the wake region, when the tip clearance was enlarged, was investigated by Goto (1992b) based on this research. In a similar way, the mechanism of the wake formation at partial flow rate can be explained as follows. The reduction in flow rate creates high blade loading near the tip, and the tip leakage flow becomes stronger as the flow rate is reduced. Since the inlet blade angle is rather small and the tip leakage flow tends to be perpendicular to the blade camber line, the tip leakage flow has a relatively large velocity component in the upstream direction. These phenomena were confirmed by the flow visualization on the casing (the results are not presented in this paper). The separation line, formed in the interaction region between the tip leakage reverse flow and the incoming flow, moved to a location farther upstream from the blade leading edge, as the flow rate was being reduced. This reverse flow caused a rapid increase in the inlet casing boundary layer thickness. The increased low-momentum region near the casing is unbalanced due to pressure fields established by the centrifugal and Coriolis forces acting on the main flow, and the passage vortex (secondary flows from the pressure side to the suction side) intensifies and develops quickly. In this case, the wake region is located closer to the casing-suction surface corner region, because of the strong passage vortex going against the tip leakage flow, and the impeller finally stalls due to the onset of extensive corner separation.

To summarize this, the wake region in IMP25 is formed in the interaction region between the tip leakage vortex and the passage vortex. As the flow rate becomes reduced, the passage vortex develops more quickly and the wake region tends to form closer to the casing-suction surface corner region. When the flow rate is reduced below a critical value, an extensive corner flow separation occurs and the positively sloped head-flow characteristic appears.

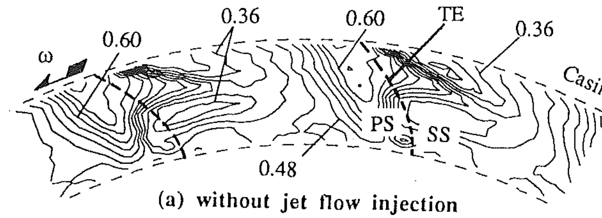

(a) without jet flow injection

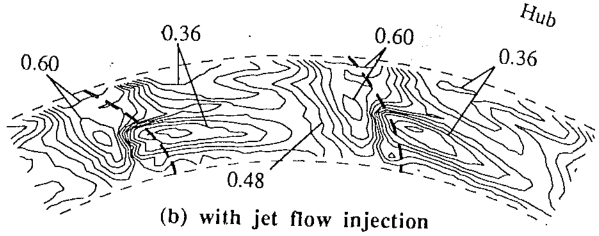

(b) with jet flow injection

Fig. 7 Measured relative velocity contour behind IMP30 impeller with and without jet flow injection ($Q^* = 0.79$, tip clearance = 1.4 mm, at 600 rpm, jet flow parameters: $V_{jet}/U_{1t} = 1.50$, $\alpha_{jet} = 90$ deg, $N_{jet} = 12$, $B_{jet} = 5$ mm, contour interval = 0.03)

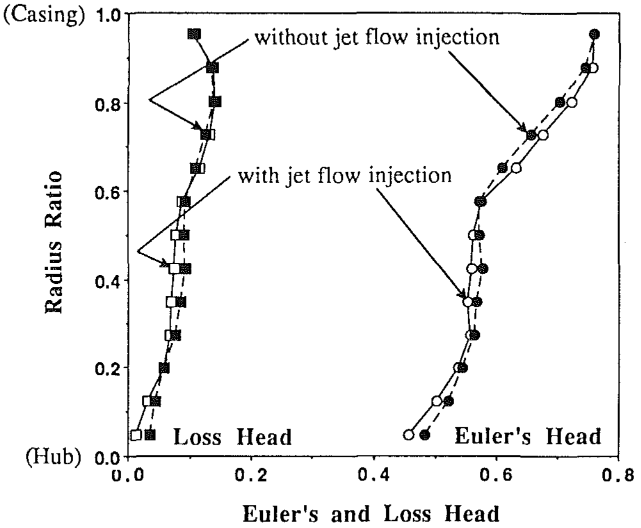

Fig. 8 Spanwise distribution of measured loss and Euler's head distribution (IMP30, $Q^* = 0.79$, tip clearance = 1.4 mm, at 600 rpm, jet flow parameters; $V_{jet}/U_{1t} = 1.50$, $\alpha_{jet} = 90$ deg, $N_{jet} = 12$, $B_{jet} = 5$ mm)

Active Alteration of Secondary Flows. The exit flow fields of IMP30, with and without jet injection, were measured by the two-hole pitot probe at the critical flow rate, just before the stall onset of the impeller without jet injection. Figure 7 shows a comparison in the contour map of the relative velocity W/U_{2m} behind the impeller. When there was no jet flow injection at the inlet, the wake region was formed close to the corner region (the contour lines are apparently dense around the casing-suction surface corner) and more likely to cause an early onset of extensive corner separation. However, when the jet flow was injected through the 12 nozzles at the inlet, the contour lines became rather coarse in this region and the jet-wake flow pattern was more similar to those at higher flow rates. From this, it is suggested that the jet flow injection altered the secondary flows within the impeller and prevented the formation of the wake region in the casing-suction surface corner. Figure 8 shows spanwise distribution of circumferentially averaged loss and Euler's head, normalized by U_{2m}^2/g, with and without jet flow injection. Both distributions were basically unchanged even in the region very close to the casing, irrespective of the existence of the jet flow. Accordingly, the stall suppression in the present method was achieved by altering the secondary flow pattern and not by changing either loss level or work input of the impeller.

In order to confirm the alteration of the secondary flow pattern, the jet flow injection was simulated using Dawes' three-dimensional Navier–Stokes code. Computations were carried out for IMP25 at the flow rate of $Q^* = 0.81$, because of the numerical instabilities experienced at lower flow rates. Figure 9 shows a computational grid on meridional plane and the contour of the tangential velocity V_θ/U_{2m} at the inlet. The flow passage was contracted toward the exit boundary to avoid exit reverse flows and resulting numerical instabilities. At the grid points, located within the nozzle outlet on the meridional plane, the circumferential velocity component was fixed to $V_{eff}/U_{1t} = 0.97$ to simulate the annular flow layer generated by the jet flow injection at $\alpha_{jet} = 90$ deg. Figure 10 compares the streamwise vorticity distribution on quasi-orthogonal planes at around 83 percent of meridional blade chord (see Fig. 9). The tip leakage vortex having negative clockwise vorticity is represented by contours in dot-dash lines, and the passage vortex with positive counterclockwise vorticity by contours in solid lines. The shaded area shows the region where the streamwise vorticity was greater than 4ω. It is confirmed that the

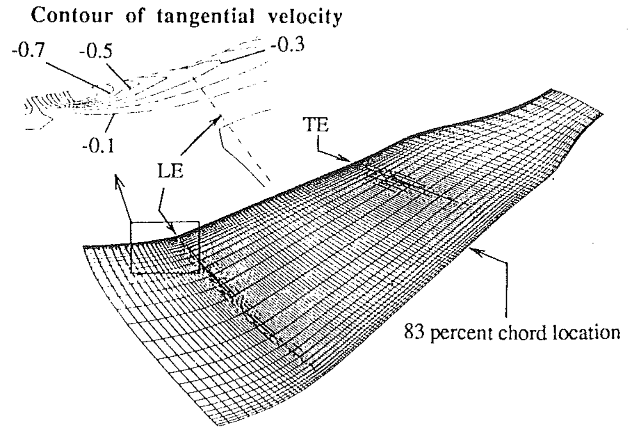

Fig. 9 Computational grids on meridional plane and simulated jet flow injection (IMP25, $Q^* = 0.82$, tip clearance = 0.5 mm, at 800 rpm, simulated jet flow; $V_{eff}/U_{1t} = 0.97$, $\alpha_{jet} = 90$ deg, $B_{jet} = 5$ mm)

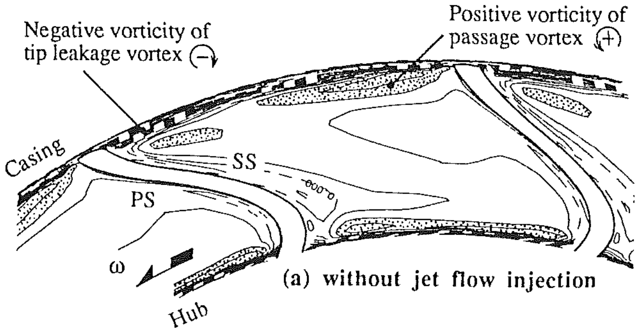

(a) without jet flow injection

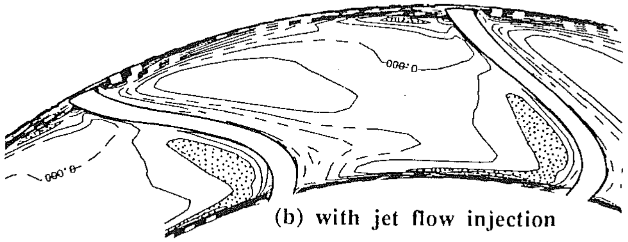

(b) with jet flow injection

Fig. 10 Computed streamwise vorticity distribution on quasi-orthogonal planes with and without jet injection (IMP25, $Q^* = 0.82$, tip clearance = 0.5 mm, at 800 rpm, simulated jet flow; $V_{eff}/U_{1t} = 0.97$, $\alpha_{jet} = 90$ deg, $B_{jet} = 5$ mm, 83 percent chord location in Fig. 9, ▨: streamwise vorticity > 4 ω)

development of the passage vortex was well suppressed by the introduction of the jet flow at the impeller inlet.

Figure 11 shows schematically the flow fields along the casing viewed from the impeller inlet. Here, the axial inflow was assumed. The jet was injected in the counterrotating direction of the impeller. The jet flows injected through the nozzles decay by mixing with the surrounding fluids until they reach the neighboring nozzles. The rotating impeller will see time-averaged jet flows, equivalent to the annular flow layer with constant flow velocity of V_{eff}. As shown in Fig. 11, a vortex sheet was introduced along the boundary of velocity discontinuity, between the annular flow layer and the incoming flow, and the vortex sheet had very strong negative vorticity in the counterrotating direction. This vorticity is conveyed into the flow passage by the main flow, and interacts with the vorticity near the casing already existing within the impeller. Since the introduced vortex has negative vorticity, it promotes the development of the tip leakage vortex and suppresses the development of the passage vortex motion near the casing. As a result of this alteration of the secondary flow pattern, the movement of the wake flow toward the suction side will become well suppressed and the onset of corner separation will be avoided. When the jet flow was injected in the opposite direction, a vortex sheet having positive vorticity was generated and the stall margin was reduced as it promoted the development of the passage vortex.

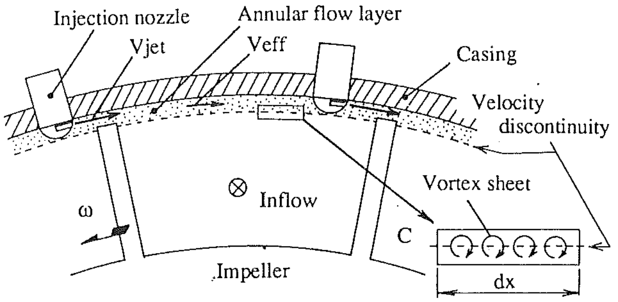

Fig. 11 Schematic picture of annular flow layer formed by jet flow injection ($\alpha_{jet} = 90$ deg) at impeller inlet (axial inflow was assumed here)

The strength of the streamwise vorticity became maximized when the jet flow was injected perpendicular to the inlet flow. The reason why the injection angle of $\alpha_{jet} = 90$ deg had maximum suppression effects (see Fig. 6) can be understood from this. In cases where prerotation exist at the inlet, possibly due to a suction scroll or inlet guide vanes, caution should be taken so that the annular flow layer becomes formed by injecting jet flows nearly perpendicular to the inflow direction.

Circulation Parameter. If we assume a two-dimensional vortex sheet along the velocity discontinuity, the circulation γ per unit length can be evaluated as follows by calculating circulation within the domain C (see Fig. 11). The streamwise vorticity is generated by the velocity component of the annular flow perpendicular to the inflow, and so the effect of jet flow injection angle is included.

$$d\Gamma = dx V_{eff} \sin \alpha_{jet}, \quad \gamma = d\Gamma/dx = V_{eff} \sin \alpha_{jet}$$

where V_{eff} represents the effective average flow speed of the annular flow layer.

The jet flow velocity at each location between adjacent nozzles was calculated using the experimental correlation (Yevdjevich, 1966) of jet decay for slender jets. Then the velocity was averaged over one pitch and the effective flow velocity V_{eff} was obtained. The effects of nozzle number and the aspect ratio of the nozzle outlet were included in the calculation of jet decay. If we include the effect of width of the jet flow, the following parameter is expected to be a useful indication of the effects of jet flow injection. The reference length l_t is the meridional blade chord length at the tip.

$$\Gamma_{jet} = \frac{B_{jet}}{l_t} \frac{V_{eff} \sin \alpha_{jet}}{2\omega H_{jet}} = \frac{B_{jet}}{l_t} \frac{V_{eff} \sin \alpha_{jet}}{U_{1t}(2H_{jet}/r_{1t})}$$

The degree of dissipation of the induced vorticity will depend on the thickness of the jet, kinetic viscosity, and the traveling time through the impeller. In the present experiments, the location of the nozzle and the nozzle height remained unchanged. Accordingly, further investigation will be required to improve the generality of this parameter. However, this representation is sufficient for summarizing the effects of jet injection obtained in the present study.

Figure 12 shows the correlation between the critical flow rate ratio and the circulation parameter Γ_{jet}. The data include a variety of different jet flow parameters, such as the width of the nozzle outlet, number of nozzles, injection angles, and jet flow speed. Experiments were carried out under two impeller revolutions, 800 rpm and 600 rpm, and so the data also include the effects of rotational speed.

A set of data, measured under different nozzle numbers, are shifted downward and run nearly parallel to the other large

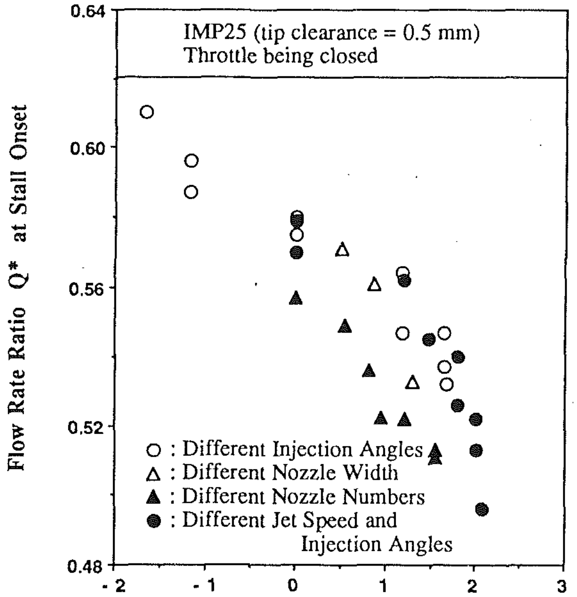

Fig. 12 Correlation between circulation parameter Γ_{jet} and critical flow rate ratio of stall onset

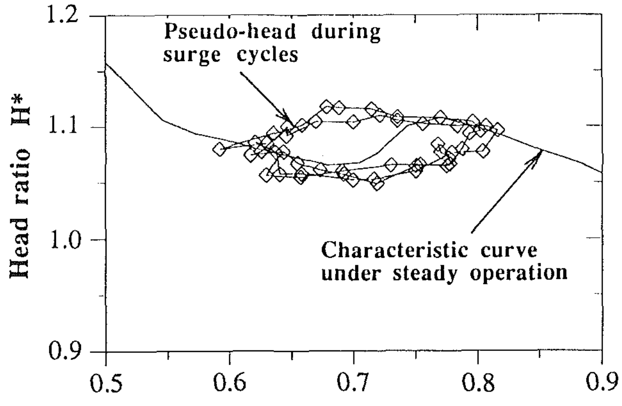

Fig. 13 History of measured head in a state of surge (IMP30, tip clearance = 1.4 mm, at 800 rpm)

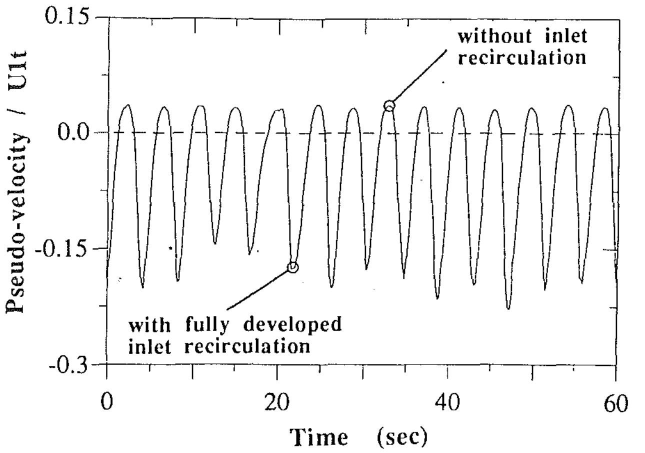

Fig. 14 Pseudo-velocity oscillations in surge cycles showing periodical change of flow pattern at impeller inlet (IMP30, tip clearance = 1.4 mm, at 800 rpm)

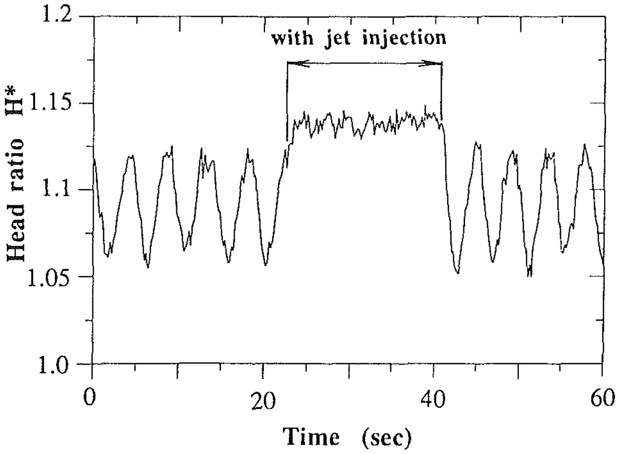

Fig. 15 Recovery from surge by jet injection at inlet (IMP30, tip clearance = 1.4 mm, at 800 rpm)

set of data. However, since the critical flow rate without jet injection ($\Gamma_{jet} = 0.0$) also shifted downward, the offset is considered to be caused by another effect, most probably by the slight difference in the tip clearance. So, as a whole, the correlation is very satisfactory and gives another evidence to support the proposed mechanism of stall suppression. Other correlations, based on either injected energy (proportional to V_{jet}^3) or momentum (proportional to V_{jet}^2), do not hold at all (the results are not presented in this paper).

Suppression of Surge

Flow Behavior Under Surge. Figure 13 shows a typical history of pseudo-head of IMP30 in a state of surge. The head-flow characteristic under steady state is also shown for reference. Although the air-filled region of the surge tank was not large enough to cause a deep surge, the flow rate was oscillating under an amplitude of about 17 percent of the flow rate under a steady state. The frequency of the cycle was about 0.15 Hz. Figure 14 shows the oscillations of pseudo-velocity measured by a cobra probe placed at section A of Fig. 2. The positive peak value corresponds to the pseudo-velocity of the inflow, while the negative bottom value corresponds to the circumferential pseudo-velocity component of the inlet recirculation. When the pump is operating in a state of surge, the internal flow fields are expected to be changing periodically between two very different flow patterns, i.e., one with extensive inlet recirculation and the other without recirculation. As discussed in the previous section, there was hysteresis in the present suppression method. Namely, the small amount of the jet was not capable of eliminating the flow pattern with developed inlet recirculation, and the positive slope region of the head-flow characteristic appeared when the throttle was being opened. Because of this, there was a possibility of surge under this situation. However, once the pump undergoes a surge cycle, the entire flow field oscillates under relatively low frequency between the two flow patterns (see Fig. 14), and the pump does operate with a flow pattern without inlet recirculation over part of the surge cycle. If the jet flow injection system is activated during the period, it will be possible to recover the pump out of the surge cycle within the first cycle owing to the mechanism described in the previous section.

Recovery From Surge. The concept mentioned above was tested using IMP30 with a tip clearance of 1.4 mm. Figure 15 shows the oscillations of pseudo-head during surge cycles. The pump was successfully recovered out of the surge during the period of jet flow injection.

Figure 16 shows the change in instantaneous flow rate at the inlet when the throttle was being closed. The broken lines represent activated jet injection. The surge started when the operating point moved to region A, but the pump successfully

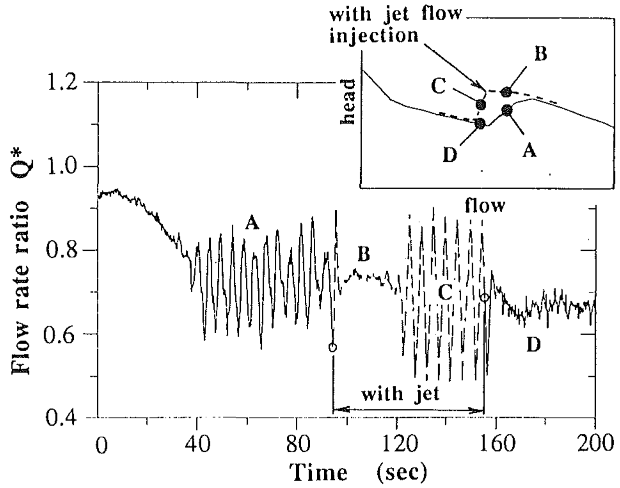

Fig. 16 History of instantaneous inlet flow rate ratio as throttle was being closed (IMP30, tip clearance = 1.4 mm, at 800 rpm)

recovered from this first surge by jet injection (point B). However, the pump system again went into surge cycles at a lower flow rate (region C), despite the activated jet flow injection system. In the present case, the tip clearance was set to 1.4 mm to enable a relatively wide instability region. The jet, in this case, was not strong enough to eliminate the whole instability region, and the positive region of the head-flow characteristic appeared again at a lower flow rate (region C). Because of this, the surge started at the instability region C, on the altered characteristic curve with jet injection, when the flow rate was further reduced. Under this situation, however, the pump will be recovered out of the surge cycles again (point D) if we turn off the jet injection. When the jet injection is turned off at region C, the operating point will move to the characteristic curve without jet injection (for example, point D), which is originally stable, and the surge is not allowed to last. This fact shows that it is sufficient to alter only the characteristic curve in the positive region of the original head-flow characteristic curve. The pump thus stabilized by the present method will be stable throughout the whole operating range.

Conclusions

A new active method to suppress the onset of stall, positive slope region of head-flow characteristic, was proposed for a mixed-flow pump. The main conclusions are as follows:

1 The onset of stall, positively sloped head-flow characteristic of the mixed-flow pump, was successfully eliminated or suppressed by applying water jet injection along the casing at the inlet of the impeller.

2 The most effective injection angle was found to be perpendicular to the incoming flow and in the counterrotating direction of impeller.

3 The streamwise vorticity in the counterrotating direction of the impeller was generated by the velocity discontinuity between the incoming flow and the annular flow layer formed by the jet injection. This vorticity suppressed the development of the passage vortex and promoted the tip leakage flow. Because of this alteration of secondary flows within the impeller, the high loss fluids were moved away from the corner, thus avoiding the onset of the extensive corner separation (the cause of the onset of the positive slope region of head-flow characteristic).

4 The present control method was also effective for stabilizing the pump system already in a state of surge. The surge was eliminated within one cycle after activating the jet injection system.

5 There was a hysteresis in the head-flow characteristic with jet injection, and the positively sloped region appeared when the throttle was opened from the shut-off condition. However, once the surge starts in this instability region, the pump will recover out of the surge within the first cycle.

According to the recent study on a mixed-flow fan impeller by Inoue (1992), the secondary flow movements, similar to the present impeller, were observed. In particular, it was observed that high loss fluids moved toward the casing-suction surface corner along with a decrease in the flow rate. Since the mechanism of the stall suppression method presented in this paper is the active alteration of the secondary flows within the impeller, it is expected to be applicable to mixed-flow turbomachines, which reveal similar flow phenomena that lead to stall onset.

Acknowledgments

The author is extremely grateful to Dr. I. Day of the Whittle Laboratory, the University of Cambridge, who motivated the author to start the work described here, and from whom the author had received useful comments. The author would like to express his deepest appreciation to Mr. T. Katsumata for his assistance in setting up the experimental apparatus and conducting the measurements. The author would also like to thank Mr. T. Takemura who developed the data acquisition system for transient flow measurements, Mr. S. Nishiwaki for useful discussions, and Ebara Research Co., Ltd., for permission to publish this paper.

References

Day, I. J., 1993, "Active Suppression of Rotating Stall and Surge in Axial Compressors," ASME Journal of Turbomachinery, Vol. 115, pp. 40–47.

Dawes, W. N., 1988, "Development of a 3D Navier-Stokes Solver for Application to All Types of Turbomachinery," ASME Paper No. 88-GT-70.

Ffowcs Williams, J. E., 1990, "An Engine Demonstration of Active Surge Control," ASME Paper No. 90-GT-224.

Goto, A., 1988, "Phase-Locked Measurements of Three-Dimensional Periodic Flow From an Impeller Using a Two-Hole Pitot Probe," *Proceedings of the 2nd International Symposium on Fluid Control and Measurements* (*FLUCOME '88*), Sheffield, United Kingdom, Sept. 5–9, 1988.

Goto, A., 1992a, "Study of Internal Flows in Mixed-Flow Pump Impellers With Various Tip Clearances Using Three-Dimensional Viscous Flow Computations," ASME Journal of Turbomachinery, Vol. 114, pp. 373–382.

Goto, A., 1992b, "The Effect of Tip Leakage Flow on Part-Load Performance of a Mixed-Flow Pump Impeller," ASME Journal of Turbomachinery, Vol. 114, pp. 383–391.

Inoue, M., 1992, Kyushu University, private communication.

Johnson, M. W., and Moore, J., 1983, "The Influence of Flow Rate on the Wake in a Centrifugal Impeller," ASME *Journal of Engineering for Power*, Vol. 105, pp. 33–39.

Paduano, J. D., Epstein, A. H., Valavani, L., Longley, J. P., Greitzer, E. M., and Guenette, G. R., 1993, "Active Control of Rotating Stall in a Low-Speed Axial Compressor," ASME Journal of Turbomachinery, Vol. 115, pp. 48–56.

Pinsley, J. E., Guenette, G. R., Epstein, A. H., and Greitzer, E. M., 1990, "Active Stabilization of Centrifugal Compressor Surge," ASME Journal of Turbomachinery, Vol. 113, pp. 723–732.

Yevdjevich, V. M., 1966, "Diffusion of Slot Jets With Finite Orifice Length-Width Ratios," *Hydraul. Pap.*, Vol. 2, Colorado State University, Fort Collins, CO.

Thermal Tip Clearance Control for Centrifugal Compressor of an APU Engine

G. Eisenlohr

H. Chladek

BMW Rolls-Royce GmbH,
Oberursel, Federal Republic of Germany

To master today's demand for efficiency and compactness of centrifugal compressor components for small gas turbine engines the main attention must not only be given to the aerodynamic design of the impeller and diffuser components, but also to the installation situation of the surrounding parts. A vital aspect is the tip clearance control between impeller and shroud casing over the total operating range. Using the radial compressor for a small gas turbine engine, developed at BMW Rolls-Royce, the importance of tip clearance control is demonstrated. The possibilities for influencing and optimizing passive tip clearance control by design features are described; transient expansion processes must be considered when using a thermal tip clearance control. The results of the design calculations are compared with the results on the test stand and the engine itself. An effort is made to find a qualitative influence of tip clearance to the engine power output at operating conditions. This qualitative description is substantiated by test results with different tip clearances at the compressor teststand.

Introduction

This work is based on the BMW Rolls-Royce APU T312 (formerly KHD T312), which is in service as Auxiliary Power Unit for the MRCA Panavia Tornado. A cross section of the T312 is shown in the upper part of Fig. 1. The single shaft gas turbine comprises a two-stage axial/radial compressor and a two-stage axial turbine. Some data of the engine are listed in Table 1. A characteristic feature of the gas turbine is the demand for almost constant speed between idle and maximum power $P_{\text{peak}} = 108.5$ percent rated power.

Within the scope of a power enhancement of the APU (P_{Peak} up to 130 percent rated power), the two-stage compressor component was to be replaced by a single-stage radial compressor. Certain constraints were given, such as same outer dimensions, same weight, and same mounting pads. Changes at the engine were limited to the compressor section alone. No changes of the bearing retainer or adaption of the turbine to the new compressor design were permitted. The new compressor had to meet the calculated design parameters precisely in order to match the existing turbine. The lower part of Fig. 1 shows the design of the power-enhanced APU. This design is used as the basis for the following description.

Base Line Design

Figure 2 shows the compressor design in more detail. It consists of a titanium impeller, item 1, which has a very high aerodynamic and stress load. The vaned diffuser is a combination of a radial diffuser, item 2, and an axial diffuser, item 3; the split of the diffusing system was necessary to meet the constraints in the outer dimensions. The compressor housing, item 4, is used as the shroud contour to the impeller; at the same time, together with the collecting housing, item 5, it has to establish the contours needed for the bleed systems. The shroud contour of the axial diffuser is a thin cover band, item 6. A conical disk, the diffuser carrier, item 7, connects the vaned diffuser to the compressor housing. Relative movements among items 4, 5, and 6 are controlled by sliding fits, items 8.1 through 8.3. O-rings and piston rings provide the necessary seals. All parts are manufactured of aluminum except the radial impeller, item 1, which is made of titanium, and the collecting housing, item 5, which is made of magnesium.

Design Aspects at Steady-State Conditions and Analysis Results

As the speed is almost constant over the whole operating range, typical for an APU, a relative tip clearance, $s/(s + b) = 0.06$, item 9 in Fig. 2, was to be designed for steady-state conditions at rated power output. Using an axisymmetric FE method, a steady-state growth analysis was used to determine the value of the corresponding cold clearance. Boundary conditions were rotational speed, pressure force, and temperature distributions at design point.

At one of the first tests of the engine, however, during start up of the APU, the impeller rubbed heavily on the compressor housing. The transient minimum clearance obviously was less than the desired steady-state clearance. Investigations at the engine showed the need for more than $s/(s + b) = 0.155$ of cold relative clearance to start up safely without rubbing. Under these conditions, minimum relative clearance at steady state

---

Contributed by the International Gas Turbine Institute and presented at the 38th International Gas Turbine and Aeroengine Congress and Exposition, Cincinnati, Ohio, May 24–27, 1993. Manuscript received at ASME Headquarters March 1, 1993. Paper No. 93-GT-137. Associate Technical Editor: H. Lukas.

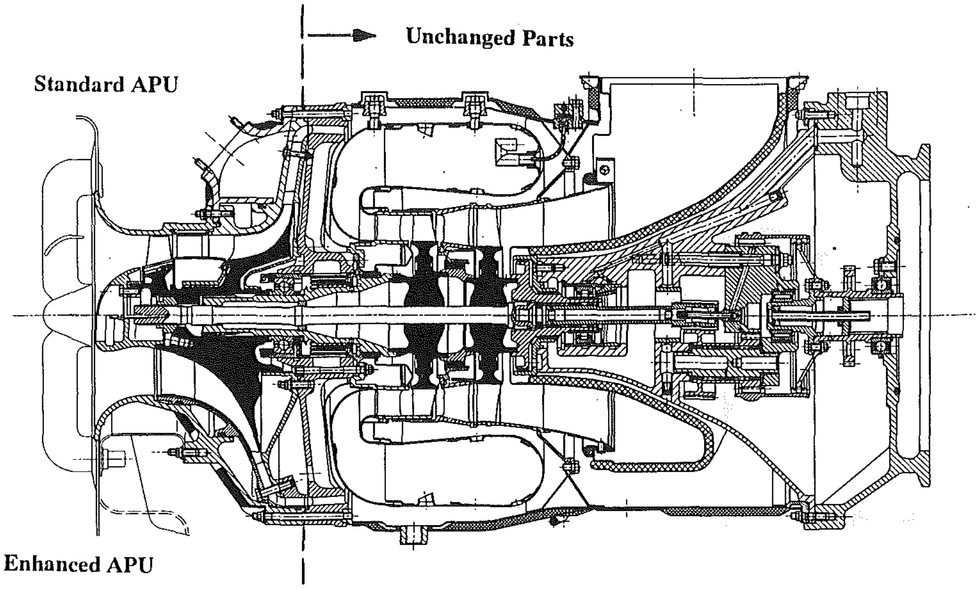

Fig. 1 Sketch of the standard and the enhanced APU T312

was about $s/(s + b) = 0.113$. This type of design, therefore, did not lead to the required power enhancement. An intensive study of the transient behavior of the compressor parts proved necessary to optimize clearances at all running conditions.

Design Aspects at Transient Conditions and Analysis Results

Again an axisymmetric FE method was used to evaluate the temperature rise during start-up. Results of fluid dynamic calculations throughout the complete flow path at different speeds were used as inputs. The resulting temperature distributions at engine start-up are shown in Fig. 3 for the compressor casing at positions 10.1 through 10.3 from Fig. 2. At these positions, the temperature development was traced during start-up of the engine. The temperature developments at position 11.1 through 11.4 from Fig. 2 on the guide vane carrier, calculated and measured, are shown in Fig. 4. For both parts the measurements and the calculations show very good agreement. The short heating phase and the strong temperature gradient along the radius can clearly be seen. Steady-state temperature conditions are achieved after about 50 seconds. Nominal speed of the APU is reached almost one order of magnitude faster.

The following thermal growth analysis revealed the condi-

Table 1 Performance data for the APU T312

APU	P_{Mean} [%]	P_{Peak} [%]	η_C [-]
Standard T312	100	108.5	0.76
Base Line Design	-	107.5	-
Modified Design	110.5	121	0.745
Optimized Design	124	133	0.795
Enhanced APU	121	130	0.80

Nomenclature

A = area, m^2
APU = Auxiliary Power Unit
b = impeller exit width
FE = Finite Element
K = factor = $\left(\frac{\gamma + 1}{2}\right)^{1/\gamma - 1} \times \sqrt{\frac{\gamma + 1}{\gamma} \frac{R_{Gas}}{2}}$
$\dot{m}$ = mass flow, kg/s
n = rotational speed
P_{Mean} = continuous rated power output
P_{Peak} = maximum power output
Pos. = position
p = pressure, Pa
R_{Gas} = gas constant, J/kgK
r_2 = impeller exit radius, mm
s = clearance between impeller exit and casing
s/b = nondimensional tip clearance
$s/(s + b)$ = relative tip clearance
T = temperature, K
r/r_2 = nondimensional radius
α = absolute flow angle, deg
β = relative flow angle, deg
γ = ratio of specific heats = c_p/c_v
η_{is} = isentropic efficiency
Θ^* = mass flow parameter = $\frac{\dot{m} * \sqrt{T_t}}{p_t} * \frac{K}{A}$
Θ_A^* = mass flow parameter at design point

Subscripts

0 = ambient
1 = compressor inlet
2 = impeller exit
3 = vaneless space
7 = compressor exit
A = design point
C = compressor
t = total

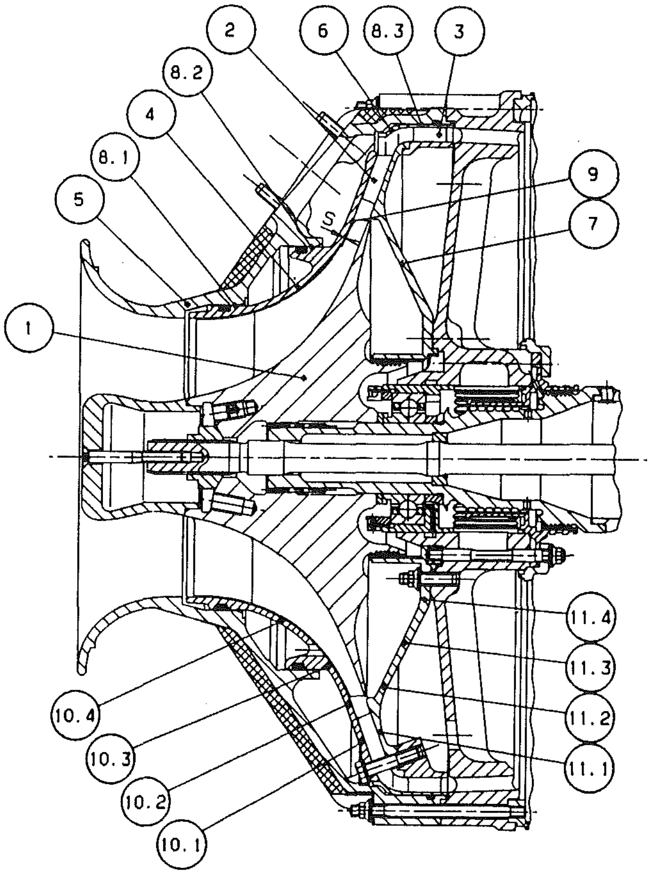

Fig. 2 Baseline design of the compressor section of the enhanced APU T312

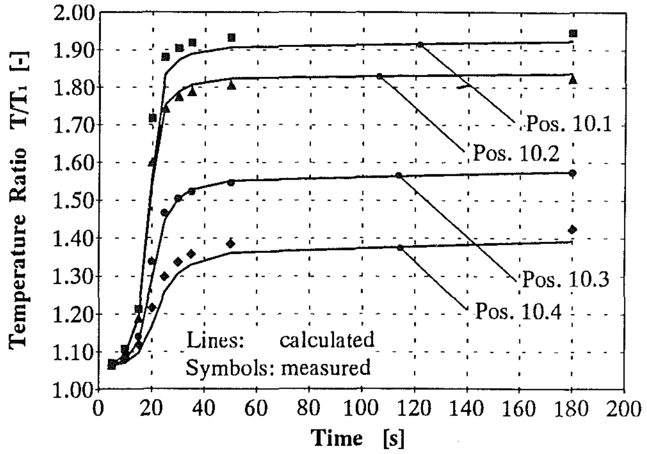

Fig. 3 Transient temperatures of the compressor casing for the Pos. 10.1 to 10.4 in Fig. 2 of the enhanced APU T312

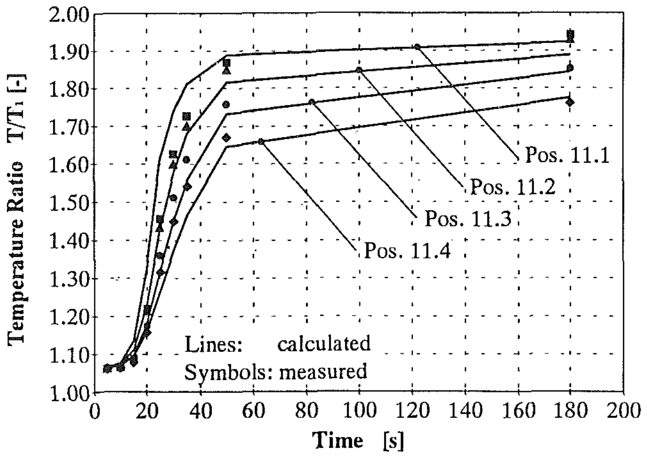

Fig. 4 Transient temperatures of the guide vane carrier for the Pos. 11.1 to11.4 in Fig. 2 of the enhanced APU T312

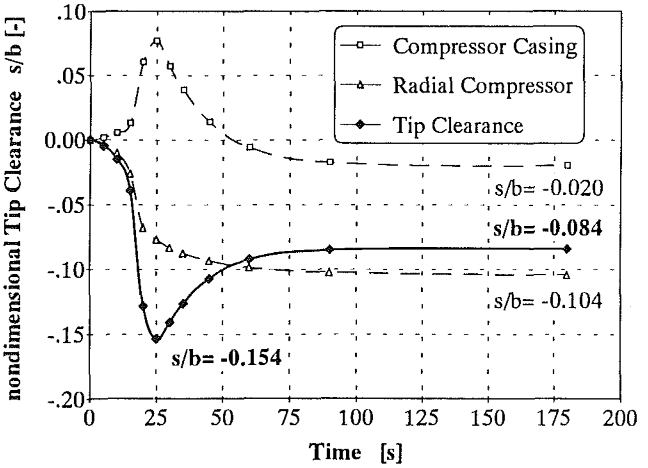

Fig. 5 Transient tip clearance for the baseline design of the enhanced APU T312

tions that appeared in the engine with respect to clearance. Figure 5 shows the resulting nondimensional clearance s/b between impeller and casing near impeller exit (see item 9, Fig. 2). Thus, starting with a nondimensional cold clearance $s/b = 0.0$, impeller and casing overlap by almost $s/b = 0.16$ before achieving a steady-state overlap of $s/b = 0.084$. For a safe start-up, a cold nondimensional clearance of $s/b = 0.215$ would have to be provided. This would lead to an operating nondimensional clearance of $s/b = 0.135$, which is disastrous for efficiency and flow in a radial compressor of this size.

The reason for the thermal growth behavior, shown in Fig. 5, is the difference in heating times of the vaned diffusers including the guide vane carrier and the compressor casing. Due to the tilt of the vane carrier with increasing temperatures from the inner to the outer region (Figs. 3 and 4), the radial elongation is linked to an axial shortening. Therefore a sliding of the impeller into the casing is unavoidable.

Modified Design

The task of a redesign of the compressor was to define the connection of vaned diffuser and compressor housing in such a way that the transient clearance would be greater or at least equal to the steady-state clearance. To achieve this the connection of the parts had to be changed so that the radial elongation due to temperature would also result in an axial elongation. This was obtained by reversing the tilt of the carrier, as can be seen in Fig. 6. Now, with higher temperatures at the outer region, the carrier moves axially forward, and the clearance between casing and impeller increases. The value of the axial movement can be influenced by the geometry, i.e., tilt and thickness distribution of the cone.

The nondimensional clearance with respect to time for the modified design is shown in Fig. 7. With the impeller exit growth as before, the reference point on the casing moves in the opposite direction compared to the previous design. In other words compressor casing and impeller move in the same direction. The clearance thus remains small and converges toward an overlap of $s/b = 0.053$ at steady-state conditions. Therefore it will be possible to meet the required steady-state relative tip clearance of $s/(s + b) = 0.06$ with a cold relative tip clearance of $s/(s + b) = 0.106$. Tests with the modified gas turbine verified the results of the calculations for the clearance behavior with respect to time. The power outputs of the

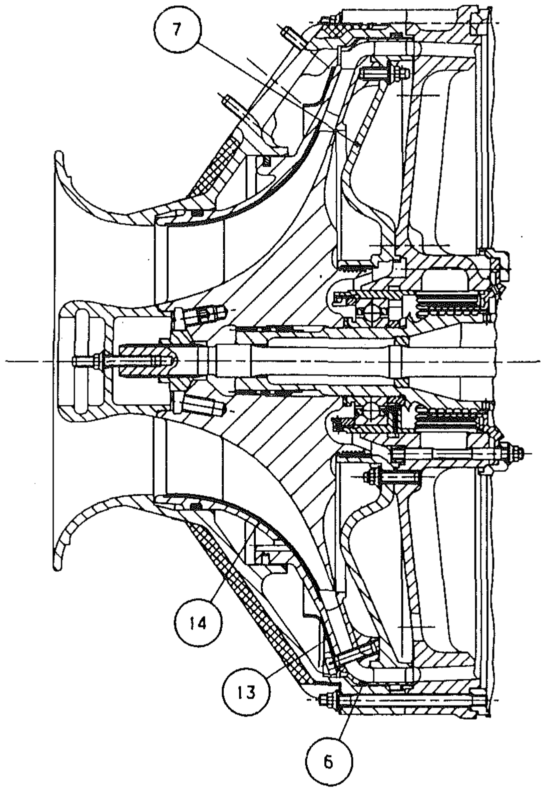

Fig. 6 Modified design of the compressor section of the enhanced APU T312

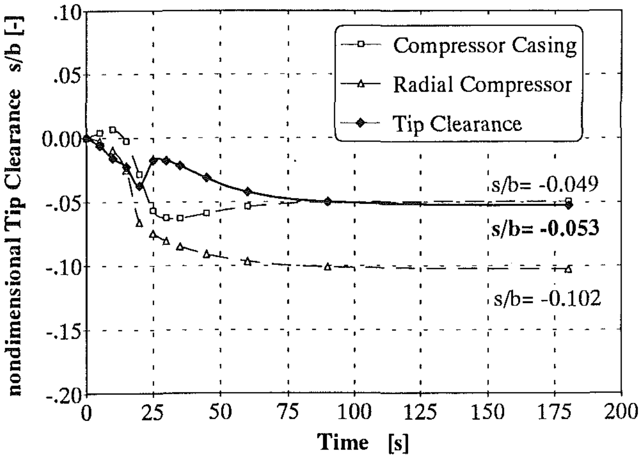

Fig. 7 Transient tip clearance for the modified design of the enhanced APU T312

modified gas turbine are shown in Table 1. The target values necessary for the power enhancement of the APU, however, required a further optimization.

Optimization

There were two possible areas for further optimization:

- Improving the clearance between impeller and casing along the complete outer contour,
- Preventing the casing from lifting off the radial and axial diffuser vanes.

If the casing separates from the diffuser vanes, due to the elongation caused by the temperature distribution, the resulting gap disturbs the flow in the throat and thus the matching of the compressor.

The dislocation of points on the impeller blading at the shroud and the corresponding points at the casing were evaluated, to optimize the clearance along the shroud. The casing contour was then changed to get a constant clearance along the whole contour at steady state running conditions. The variation of the clearance along the shroud contour for steady-state conditions prior to the optimization is shown in Fig. 8. A sickle-shaped gap of the two contours of an additional nondimensional tip clearance of $s/b = 0.036$ can be observed at midspan (position 14, Fig. 6), because the rear part of the impeller tilts up. This kind of clearance optimization was possible, since the running speed of the APU is constant, the centrifugal forces for the impeller and the temperature distributions for impeller and casing, causing this gap, were known and/or could be calibrated with test measurements.

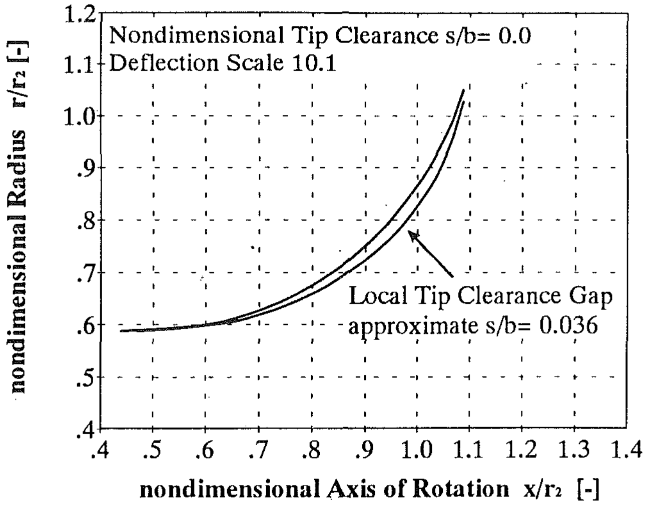

Fig. 8 Deformed contour lines between blades of radial compressor wheel and casing for the steady-state point of the modified enhanced APU T312

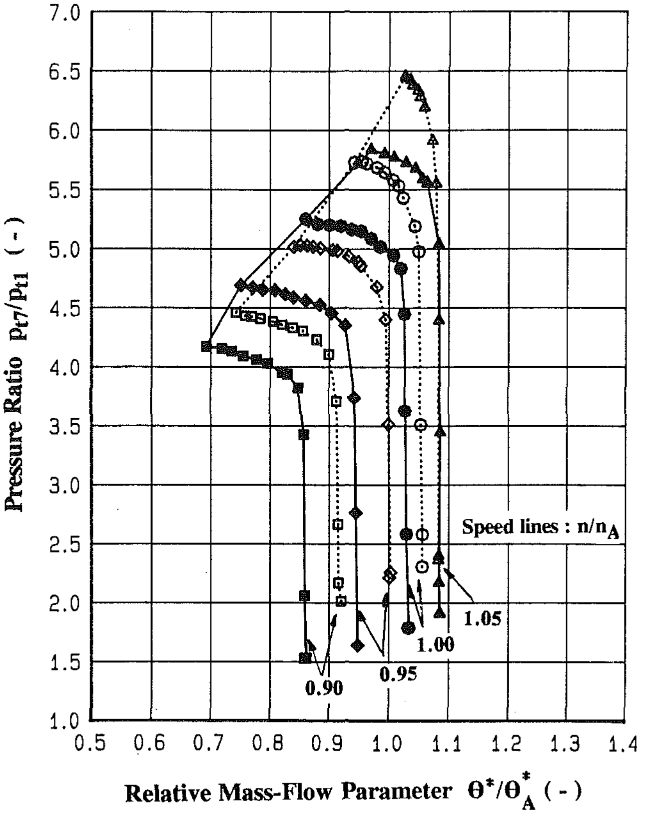

Fig. 9 Performance maps of compressor: filled symbols: relative tip clearance 0.127; open symbols: relative tip clearance 0.007

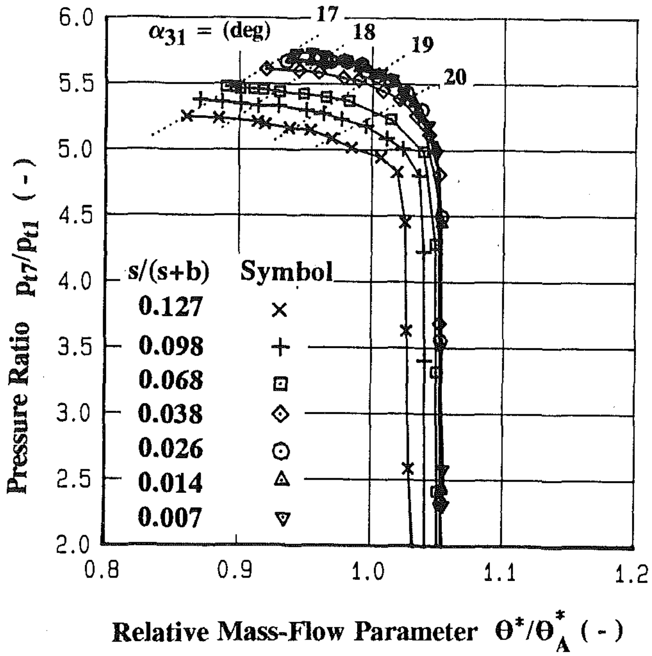

Fig. 10 100 percent speed line for all tip clearances investigated

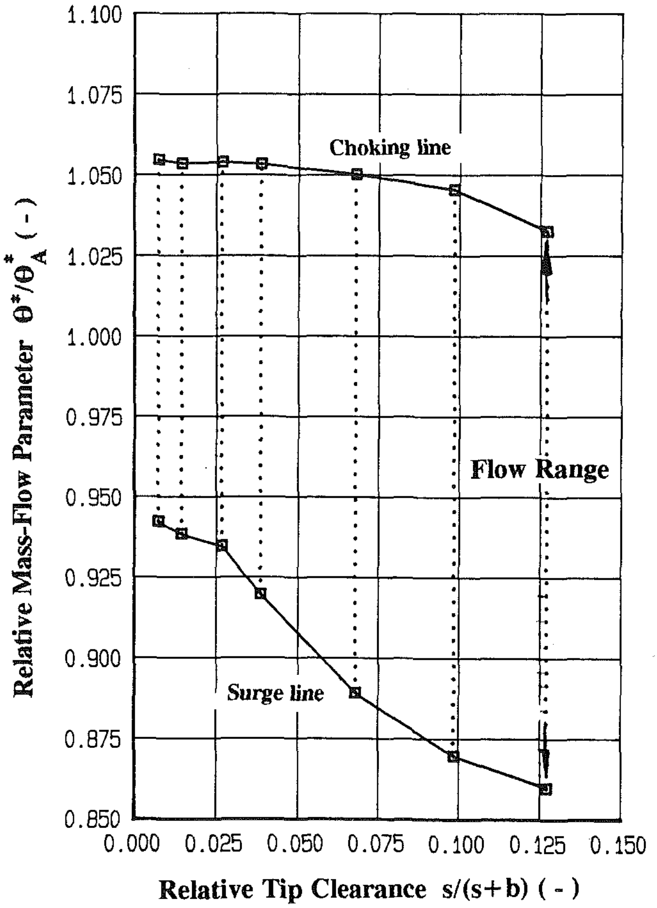

Fig. 11 Change of flow range on speed line with relative tip clearance

To avoid the gap between the radial vanes and the casing a spring element is used (item 13, Fig. 6). By this means the casing is pressed onto the vanes and the gap is avoided at running conditions. This also meets the demand for exchangeability of the various parts.

At the axial vanes a thin cover band (item 6, Fig. 6) with a press fit is used to have a closed cross section.

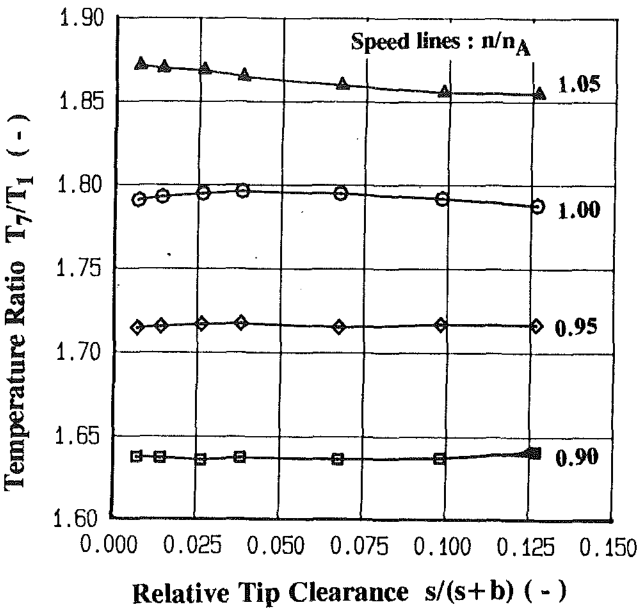

Fig. 12 Change of temperature ratio at surge with relative tip clearance

The importance of these optimizations can be seen in Table 1. After incorporating all these means into the gas turbine, the measured performance data corresponded to the target values of the enhancement.

Influence of Tip Clearance Changes on the Compressor Performance

To substantiate quantitatively the need for a close clearance, investigations on the compressor teststand with a very similar setup were carried out. To examine the effect of tip clearance on this compressor, the cold clearance between impeller and casing was altered systematically. By merely altering the thickness of the adjustment disk, the clearance at impeller exit could be changed. These alterations were achieved without dismounting the compressor test stand. Therefore the influences on the performance map could be attributed to these changes of the cold clearances and, presuming no changes in thermal response of the test stand, to the changes of running clearances. Seven steps for varying the relative clearance were investigated starting from $s/(s + b) = 0.127$ down to 0.0072.

Figure 9 shows the resulting characteristics for minimum and maximum clearance. It shows the pressure ratio p_{t7}/p_{t1} versus relative mass flow parameter Θ^*/Θ^*_A for four speed lines. The influence of the different clearances can be seen clearly. Figure 10 shows the speed line $n/n_A = 100$ percent for the seven clearances investigated. At large clearance the speed line is relatively broad with a moderate pressure ratio. As the clearance becomes smaller the characteristic becomes steeper with a narrower range between choke and surge. To clarify this Fig. 11 shows the flow range of this characteristic versus relative clearance $s/(s + b)$. Whereas the choking conditions show only minor variations, the influence at surge is very obvious. This is due to the impeller exit flow angle and/or the vaned diffuser inlet flow angle. The improved pressure build-up in the impeller at low clearances causes the mean inlet flow angle to the vaned radial diffuser to change if the mass flow remains constant. As the incidence behavior of the vanes cannot be changed the mass flow at surge has to adapt.

By means of pressure measurements via static pressure taps in the vaneless space we were able to evaluate the flow angles upstream of the diffuser vanes. These angles have been added to the plot of Fig. 10. This verifies that the surge line moves as claimed.

The strong effect of clearances on the behavior of the whole

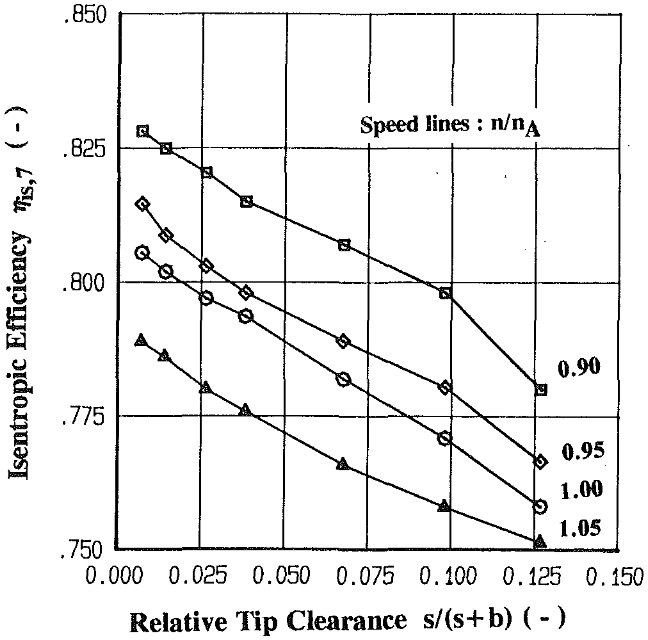

Fig. 13 Change of isentropic efficiency at surge with relative tip clearance

compressor is shown in the following figures, all referring to the respective point on the surge line. This time the points of all four speed lines are plotted. The work input of the compressor to the fluid is reflected in the temperature ratio T_7/T_1, Fig. 12. While at lower speeds the work input is almost independent of the relative tip clearance, at higher speeds the work input shows some relation to the relative clearance. This could be explained with an exchange of fluid between pressure and suction side of the blades. Lower clearances and therefore less leakage between pressure and suction side lead to more stable exit flow conditions. Finally, Fig. 13 shows the isentropic efficiency in relation to relative clearance. It shows that a one point change of relative clearance $s/(s + b)$ causes change in isentropic efficiency $\eta_{is,C}$ of about 0.35 to 0.45 points. This agrees with values found in the literature.

Conclusions

An actual gas turbine engine project was used to show the effect and the importance of thermal clearance control for radial compressors of small gas turbines. Results of calculation and measurements were presented and the subject of transient clearance behavior was discussed in detail. Starting from a baseline design of the compressor component and using calculations for transient conditions, the influence of clearance control by design measures was described. It was possible to optimize the design details such that the aerodynamic requirements for compressor behavior were met.

The qualitative effect of relative clearances on the performance were substantiated quantitatively with measurements on an impeller at the compressor teststand. It shows that a one point change of the relative clearance $s/(s + b)$ causes a change in the isentropic efficiency $\eta_{is,C}$ of about 0.35 to 0.45 points. This strong effect on the efficiency of the compressor component and thus on the power output of the whole engine shows the need for thermal clearance control and the importance of careful design in the development of such components.

Acknowledgments

The authors wish to thank PANAVIA AIRCRAFT GmbH, Munich for the permission to prepare and publish this paper.

References

Block, J. A., and Runstadler, P. W., Jr., 1975, "Effect of Specific Heat Ratio, Impeller Tip Running Clearance, and Compressor Insulation on High-Pressure-Ratio Centrifugal Compressor Modeling," ASME Paper No. 75-FE-9.

Farge, T. Z., Johnson, M. W., and Maksoud, T. M. A., 1989, "Tip Leakage in a Centrifugal Impeller," ASME JOURNAL OF TURBOMACHINERY, Vol. 111, pp. 244-249.

Fowler, H. S., 1966, "An Investigation of the Flow Processes in a Centrifugal Compressor Impeller," National Research Laboratories, Canada Report No. ME-220, July.

Senoo, Y., and Ishida, M., 1986, "Pressure Loss Due to the Tip Clearance of Impeller Blades in Centrifugal and Axial Blowers," ASME *Journal of Engineering for Gas Turbines and Power*, Vol. 108, pp. 32-37.

Senoo, Y., and Ishida, M., 1987, "Deterioration of Compressor Performance Due to Tip Clearance of Centrifugal Impellers," ASME JOURNAL OF TURBOMACHINERY, Vol. 109, pp. 55-61.

Weimer, M., 1992, "Design and Test of an Active Tip Clearance System for Centrifugal Compressors," AIAA Paper No. 92-3189.

M. A. Howard
Rolls-Royce plc,
Derby, United Kingdom

P. C. Ivey
School of Mechanical Engineering,
Cranfield Institute of Technology,
Bedford, United Kingdom

J. P. Barton

K. F. Young

Rolls-Royce plc,
Derby, United Kingdom

Endwall Effects at Two Tip Clearances in a Multistage Axial Flow Compressor With Controlled Diffusion Blading

Effects of tip clearance, secondary flow, skew, and corner stall on the performance of a multistage compressor with controlled diffusion blading have been studied experimentally. Measurements between 1 and 99 percent annulus height were carried out in both the first and the third stages of a four-stage low-speed compressor with repeating-stage blading. Measurements were obtained at a datum rotor tip clearance and at a more aerodynamically desirable lower clearance. The consequences of the modified rotor tip clearance on both rotor and stator performance are examined in terms of loss coefficient and gas exit angle. Stator losses close to the casing are found to increase significantly when the clearance of an upstream rotor is increased. These increased stator losses cause 30 percent of the stage efficiency reduction that arises with increased rotor tip clearance. The deviation angles due to tip clearance from the multistage measurements are found to be similar to data from single-stage machines with conventional blading, which suggests that the unsteady flow phenomena associated with the multistage environment do not dominate the physics of the flow.

Introduction

The vital role of endwall effects on compressor efficiency and stall margin has been recognized for many years, as has the need for study of the associated endwall flow structures. One common approach to the study of endwall effects is to measure the flow details at different tip clearances. Much work of this type has been carried out on single-stage machines with conventional circular arc camberline blading (Hunter and Cumpsty, 1982; Lakshminarayana et al., 1982; Inoue et al., 1986; Goto, 1992). There is, however, less work on multistage compressors (Dring and Joslyn, 1986) at alternative tip clearances. No published work on multistage compressors with modern controlled diffusion blading over a range of rotor tip clearance is known to the authors. One objective of the work described in this paper is to examine a multistage machine with contemporary controlled diffusion blading in order to improve the understanding of the endwall flows associated with tip clearance in both blade ends, with and without clearance.

A further objective is to measure flow details that support the improvement of theoretical models. For example, the viscous throughflow method of Howard and Gallimore (1993) requires specification of the actual radial variation of loss and deviation across the span including endwall details. These authors acknowledged a need to improve their correlations for the radial distributions of loss and deviation due to tip clearance. The viscous throughflow method, in common with three-dimensional Navier-Stokes methods (Moore, 1985; Dawes, 1992; Denton, 1992; Adamczyk et al., 1990) solves the flowfield with a no-slip condition on the annulus walls. Consequently there is also a requirement for measurements close to the annulus walls of a multistage axial flow compressor in order to calibrate models for turbulence and spanwise mixing in this region.

Of the three-dimensional methods referenced, only that of Adamczyk et al. (1990) attempts a rigorous modeling of the unsteady flow resulting from circumferential variations in a stationary frame when viewed in a rotating reference frame, and vice versa. A physical example of this is the interaction of a rotor tip leakage vortex with a downstream stator. The importance of this unsteadiness relative to reasonably well-understood endwall flow phenomena, such as secondary flow, is unclear. Comparison of single-stage and multistage measurements is therefore relevant to identify any major differences in endwall flow phenomena that may arise due to these effects.

This paper documents an experimental study in a four-stage low-speed axial compressor of large scale aimed at addressing these issues.

Compressor Design

The large-scale low-speed compressor with repeating-stage blading has been designed to be representative of a subsonic

---

Contributed by the International Gas Turbine Institute and presented at the 38th International Gas Turbine and Aeroengine Congress and Exposition, Cincinnati, Ohio, May 24–27, 1993. Manuscript received at ASME Headquarters March 10, 1993. Paper No. 93-GT-299. Associate Technical Editor: H. Lukas.

Table 1 Midspan stage and aerofoil loading parameters

	Rotor	Stator
$\Delta H/U^2$	0.428	
V_a/U	0.715	
α_1	23.5°	45.8°
r_{hub}/r_{casing}	0.85	0.85
$\Delta P/D_1$	0.376	0.369
DF	0.395	0.410
Re_1	2.2×10^5	2.2×10^5

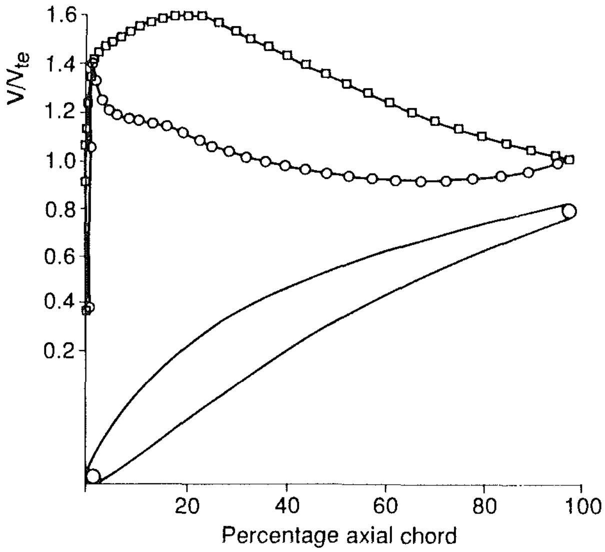

Fig. 1 Rotor midspan aerofoil and predicted velocity distribution

middle stage of a highly loaded multistage compressor. The stage and aerofoil loading parameters are given in Table 1.

These parameters are taken from the third stage of the design throughflow calculation. Low-speed blading is designed to match these conditions and this geometry is used to produce the four identical stages in the parallel annulus of 0.85 hub/casing ratio.

Low-speed controlled diffusion aerofoils are "tailored" via camberline shape and thickness to give a velocity distribution typical of a high-speed, but subsonic, compressor. The low-speed aerofoils are thicker than their high-speed counterparts in order to compensate for the lack of density reduction in the low-speed flow but the velocity distribution is representative of thin high-speed controlled diffusion profiles. The rotor and stator aerofoil shapes and predicted velocity distributions are shown in Figs. 1 and 2, respectively.

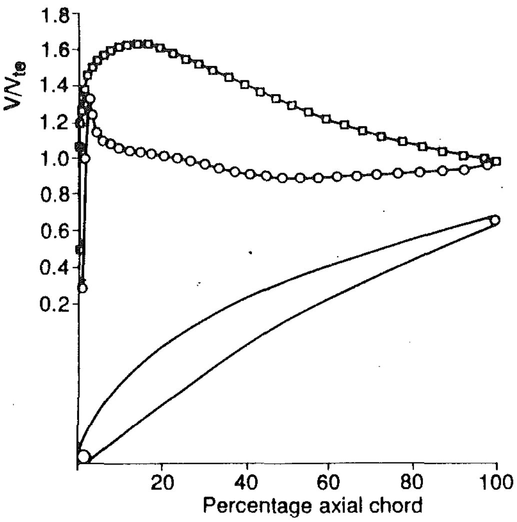

Fig. 2 Stator midspan aerofoil and predicted velocity distribution

Table 2 Aerofoil geometry

	Rotor	Stator
No. of blades	79	72
Aspect ratio	1.54	1.59
Chord (mm)	59.2	57.7
Space/Chord ratio	0.758	0.854
Thickness/Chord ratio	0.110	0.097
Inlet metal angle (deg.)	52.7	57.8
Stagger (deg.)	28.2	30.2
Camber (deg.)	36.9	38.3
Axial gap/chord (Trailing edge (TE) to downstream LE)	0.44	0.45
Clearance/tip chord (t/C_{tip})%	1.2 or 3.0	2.4

Geometric details of the blading are given in Table 2. The geometric details are smooth across the span with no attempt made to tailor the profiles to improve endwall flow (i.e., the blading is "conventional").

An existing inlet guide vane was restaggered to give the

Nomenclature

C = aerofoil chord
D = dynamic head = $P_0 - P$
DF = diffusion factor
P = static pressure
P_0 = total pressure
P_{0in} = total pressure at entry to first rotor
r = radius
Re = Reynolds number, based on inlet velocity and chord
t = tip clearance
U = blade speed
V = velocity
V_{te} = velocity relative to aerofoil at trailing edge
x = axial coordinate
α = absolute whirl angle (from axial) = $\tan^{-1}(V_\theta/V_a)$
Δx = distance from aerofoil trailing edge to traverse plane
δ = deviation (aerofoil exit gas angle − exit metal angle)
θ = circumferential coordinate
ρ = density
ω = pressure loss coefficient = $(P'_{02is} - P'_{02})/(P'_{01} - P_1)$

Subscripts

1 = inlet to blade row
2 = exit to blade row
a = axial
casing = outer annulus line of compressor
hub = inner annulus line of compressor
is = isentropic process
mid = midspan
r = rotor
s = stator
tip = tip of aerofoil, i.e., rotor near casing, stator near hub
2D = value for "two-dimensional" flow (actually quasi-3D from blade to blade flow solution)

Superscripts

$'$ = relative to blade row
$\_$ = circumferential average
$=$ = circumferential and radial average
$\wedge$ = peak value

Table 3 Location of traverse planes

Plane	$\frac{\Delta x_{mid}}{C_{mid}}$
Inlet Guide Vane exit	0.83
Rotor 1 exit	0.25
Stator 1 exit	0.25
Stator 2 exit	0.25
Rotor 3 exit	0.25
Stator 3 exit	0.25

desired inlet swirl angle of 23.5 deg (the swirl angle is constant in the spanwise direction away from the endwall effects). The inlet guide vane design details are given by Robinson (1991).

Experimental Facility and Instrumentation

The measurements were carried out on a four-stage low-speed compressor facility previously described by Robinson (1985, 1991). The large physical size of this facility (casing diameter = 1.22 meters) eases the instrumentation task and enables three-dimensional endwall phenomena to be measured and identified. The mechanical arrangement of the facility allows rotation of the casing over the rotor relative to the stators, which allows circumferential traversing to be carried out. This minimizes any flowpath disturbance close to the casing.

Combined circumferential and radial traversing was carried out on planes upstream and downstream of the first and third stage rotors and stators, Table 3. Two types of miniature pneumatic traverse probes were used, often termed "cobra" and "wedge" probes, Fig. 3.

Circumferential traversing is carried out by holding the probe in the casing at a fixed radius and orientation ("yaw") to the machine axis and rotating the casing relative to the stator.

In addition to detailed traverse data, the performance of the compressor is measured by conventional means, torquemeter, calibrated inlet, etc. Details are given by Robinson (1985, 1991).

A formal uncertainty analysis of the performance and traverse data is reported by Robinson (1991) and yields confidence limits of ±0.5 deg for deduced whirl angle and ±0.02 kPa (0.003 lbf/in^2) for deduced total pressure. These uncertainties are those associated with random error in resolution of pressure levels and calibration coefficients. There are, however, other significant flow measurement uncertainties in the turbomachinery environment as discussed in the following section.

Analysis Techniques and Results

This section describes analysis techniques specific to this measurement program and also presents and discusses some salient results from the traversing.

The distribution of total pressure at the exit of the first stator from a conventional analysis of the calibrated cobra probe is shown in Figure 4. This distribution is for a rotor tip clearance of 1.2 percent chord with the compressor operating at peak efficiency. Collections of low-energy fluid in the suction side corner with the casing are due to combined effect of casing secondary flow, inlet skew and corner stall. The low-energy fluid between the wakes at the hub is the result of the clearance flow around the ends of the cantilevered stators.

In order to calculate stator loss and deviation from the radial/circumferential traverse data (e.g., Fig. 4) "mass and momentum" circumferential averaging was carried out. This technique was recommended by Dring and Joslyn (1989). Its advantage is that the results of the procedure are theoretically independent of the axial location of the traverse plane since it yields "fully mixed" conditions. This averaging method gives radial distributions of absolute total pressure and absolute whirl angle, which may be used to compute stator loss coefficient and deviation directly.

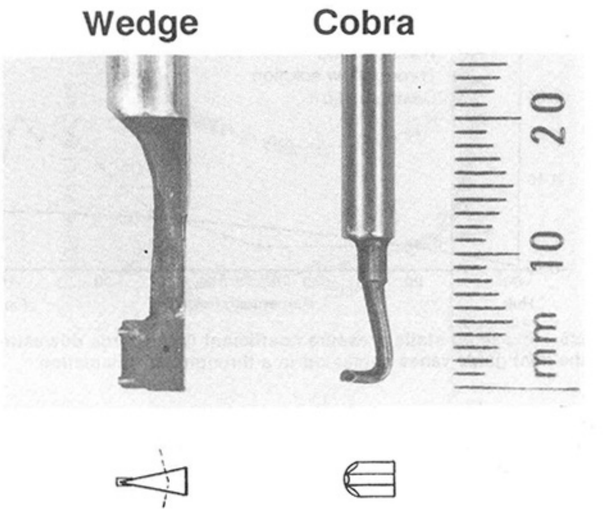

Fig. 3 Pneumatic probes

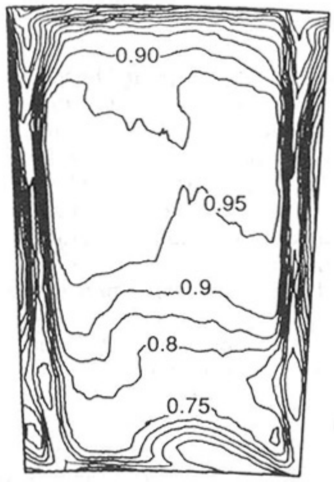

Fig. 4 Distribution of total pressure rise coefficient, $(P_0 - \bar{\bar{P}}_{0in})/{}^1\!/_2 \rho U^2_{mid}$, downstream of the first stator at peak efficiency; t_r/C = 1.2 percent

The calculation of rotor loss coefficient and deviation requires total pressure and whirl angle relative to the rotor. To calculate these directly from the traverse data would involve using the radial distribution of static pressure from the calibrated traverse probes. This was felt to be unwise since it was observed that the measured static pressure from the calibrated traverse probes did not match the casing static pressure measurement. For example Fig. 5 shows the static pressure profiles derived from the wedge probe at the exit of the inlet guide vane compared with a throughflow calculation and casing static pressure tapping measurements. Close to the hub the wedge probe measurements are well aligned with the throughflow calculation. The casing static pressure is recorded at various circumferential locations as the casing rotates relative to the IGV. An average value over one passage is plotted. This direct measure of static pressure is much more reliable than deductions from calibrated probes. Since the throughflow calculation gives the same static pressure as this casing static pressure tapping, it seems likely that the probe is giving misleading results from 70 percent height to the casing. Robinson (1991) observed similar problems in static pressure measurement using a wedge probe due to interaction with the endwall. These problems were reduced, but not eliminated, by using a wedge probe with a lower including wedge angle. Further work on

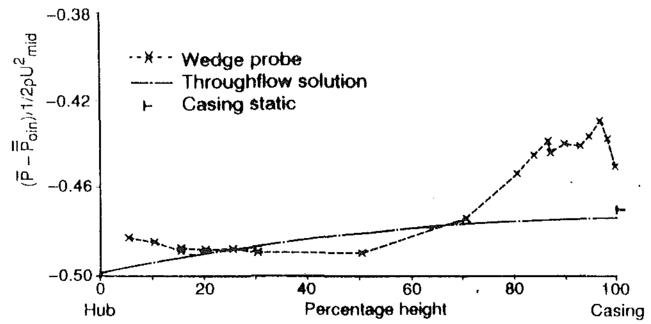

Fig. 5 Measured static pressure coefficient 0.83 chords downstream of the inlet guide vanes compared to a throughflow calculation

Table 4 Midspan rotor and stator losses from the initial analysis of the cobra probe measurements in the first stage; rotor tip clearance = 1.2 percent of chord

	ω
Rotor	0.016
Stator	0.044

probe/endwall interaction is reported by Smout (1990). A similar problem was observed with the Cobra probe.

Since an absolute velocity is required to deduce velocities relative to the rotor, and hence rotor performance, an alternative to using static pressure deduced from the probes is required. A throughflow solution would appear to be a more reliable source of circumferentially averaged static pressure, since it gives both agreement with the wedge probe away from the endwalls and with casing static pressure tappings, Fig. 5. Consequently the combination of measured absolute total pressure and absolute whirl angle from the probe combined with throughflow analysis has been chosen as a means of computing rotor loss coefficient and deviation. The throughflow method achieves specified absolute stagnation pressure and absolute whirl angle on traverse planes between the blades by conservation of entropy and the product of radius and whirl velocity on streamlines between trailing edges and traverse planes. Since the measured distributions of absolute total pressure and absolute swirl angle are achieved by the throughflow solution, its results are equivalent to a conventional traverse analysis using static pressure from the throughflow analysis instead of measured static pressure. The throughflow analysis procedure adopted does, however, imply some additional benefits, such as calculation of aerofoil losses along stream surfaces, and checks for consistency between measured mass flow, traverse flow angles, and torque (Appendix B).

This throughflow analysis procedure was used and in common with some earlier results (Robinson, 1991), gave unexpectedly low loss in the rotor and high loss in the stator, Table 4.

To investigate this, the circumferential distribution of total pressure at stator inlet and exit were compared in regions uninfluenced by endwall effects. An example is shown in Fig. 6 which compares wedge probe data at midheight. The measurements appear to indicate that a loss in total pressure occurs in the free-stream flow through the stator. This will contribute to the falsely high stator loss. Cyrus (1985, 1986) has examined the influence of rotor wakes on stationary probes at rotor exit and shown that stationary probes record a total pressure that is too high. It therefore seems likely that the measurements at stator inlet in Fig. 6 are in error because of the high levels of periodic flow unsteadiness associated with rotor wakes. At stator exit there is less unsteadiness and the measurements there are considered to be more reliable for use in the throughflow analysis. A constant adjustment to the total pressure at rotor exit was applied at all radii such that similar midheight loss coefficients in both rotor and stator resulted. The assumed similarity of rotor and stator losses at midspan is based on the reaction being close to 50 percent. Consequently a similar midspan flow in rotor and stator, including any unsteady mixing of upstream wakes, is expected. For the analysis of the cobra probe measurements the adjustment required was approximately half of the free-stream pressure difference, which was derived from diagrams such as Fig. 6. The rotor exit measured whirl angle was also adjusted in the throughflow analysis such that the deduced stage efficiency is equal to the measured efficiency (Appendix B). In view of the difficulty in measurement of total pressure at rotor exit it seems reasonable to expect higher errors in whirl angle at this plane than at stator exit.

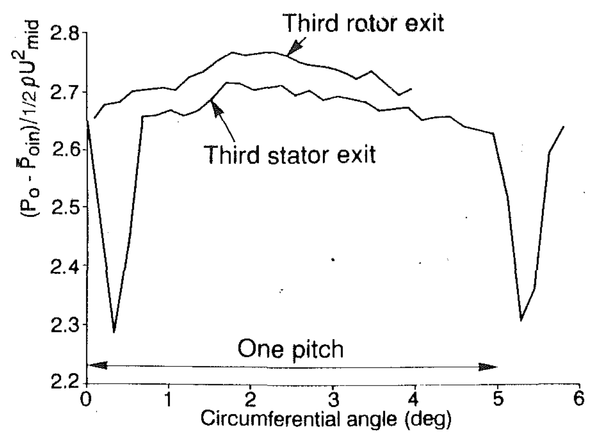

Fig. 6 Circumferential distribution of midspan total pressure rise coefficient at peak efficiency

This type of data adjustment for the throughflow analysis, while common, is worthy of further consideration. It suggests that experimental errors that cannot be readily included in formal uncertainty analyses are present. The use of different types of pneumatic probe (cobra and wedge, see Fig. 3) is a pragmatic attempt to assess the reliability of the measurement/analysis combination by providing redundant data. Loss coefficients and whirl angles for the third stage from the cobra and wedge probes are compared in Fig. 7. Uncertainties of around ±1.5 deg and ±0.02 are suggested for angle and loss coefficient, respectively. The data shown in Fig. 7 are for a rotor tip clearance of 3 percent of chord with the compressor operating at peak efficiency. Other comparisons between the two probes suggest similar uncertainties.

Also shown in Fig. 7 are the design intent whirl angles and predicted profile losses. The design intent curves show the distribution of whirl angle that would exist if the flow were two-dimensional because the design was carried out using a two-dimensional blade-to-blade method. This allows regions of the blade height influenced by three-dimensional endwall effects to be identified in Fig. 7 and shows that the trends of loss and deviation due to these three-dimensional flow effects are the same based on both types of probe. The three-dimensional effects extend well away from the endwalls leaving only some 25 percent of the annulus height with substantially two-dimensional flow (between ~40 and ~65 percent of annulus height). In the region of two-dimensional flow the measured aerofoil loss and deviation are close to the blade to blade predictions. Closer to the endwalls, however, losses are an order of magnitude higher than the profile loss. Throughflow calculations, outlined in Appendix A, indicated that these large endwall losses, in both rotor and stator, cause half of the stage losses, the remainder being due to profile losses (the stage efficiency of ~90 percent would increase to ~95 percent with only profile losses).

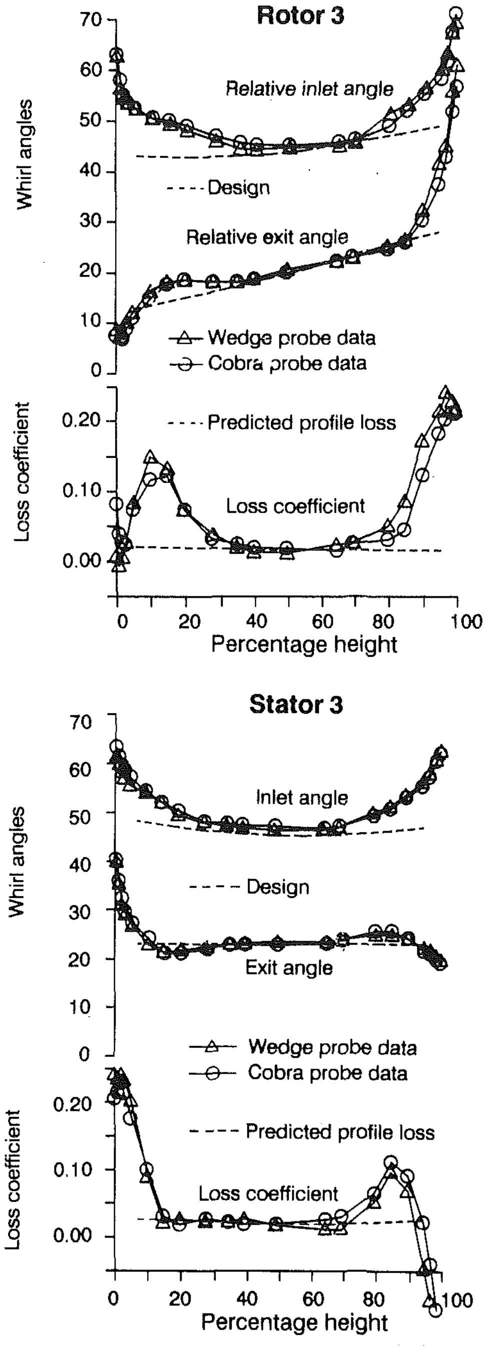

Fig. 7 Comparison of the blading performance deduced from cobra and wedge probes with a rotor tip clearance of 3 percent chord at peak efficiency

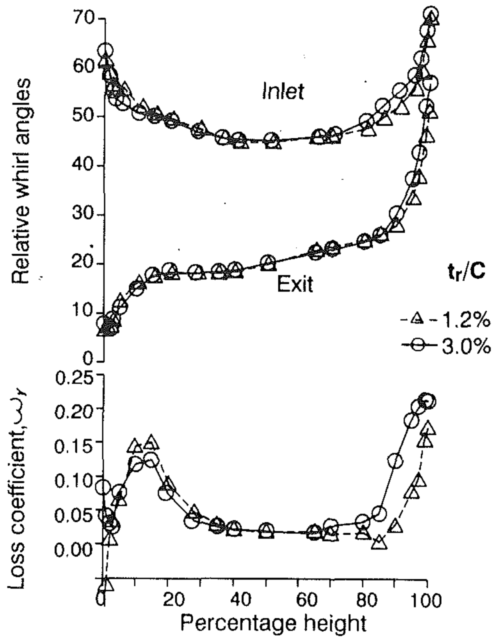

Fig. 8 Comparison of the third rotor's performance at 1.2 and 3 percent chord rotor clearance deduced from cobra probe measurements at peak efficiency

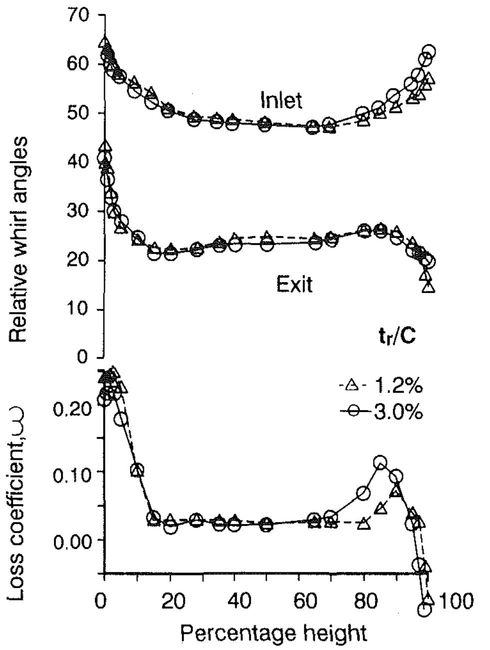

Fig. 9 Comparison of the third stator's performance at 1.2 and 3 percent chord rotor tip clearance deduced from cobra probe measurements at peak efficiency

Effect of Increased Rotor Tip Clearance

The relative whirl angles and loss coefficients derived from the cobra probe for the third rotor are shown in Fig. 8 for rotor tip clearances of 1.2 and 3.0 percent of chord, with the compressor operating at peak efficiency. The expected increases of rotor loss and deviation resulting from larger tip clearance are observed with substantial increases in loss in the 90 to 95 percent annulus height region (i.e., near the casing). The stator hub clearance is unaltered between the two tests so similar loss and deviation values from the hub to 70 percent height would be expected. The small differences in this region seen in Fig. 8 are within the range of uncertainty quoted in the previous section.

The whirl angles and loss coefficient for the third stator are presented in Fig. 9, again for both levels of rotor tip clearance and at peak efficiency. Significant differences in trend are perceived in the stator casing region. Increasing rotor tip clearance results in increased stator losses, between 70 and 90 percent annulus height, with reduced losses closer to the casing. A local reduction of stator loss adjacent to casing with increased rotor tip clearance was previously observed by Dring and Joslyn (1986). They attributed this to the redistribution of the stator inlet flow by secondary flow with fluid of higher total pressure moving toward the casing on the pressure side of the passage. The contour plots of total pressure at the exit of the third stator for the two clearance levels, shown in Fig. 10, support this mechanism. In the casing region there is a

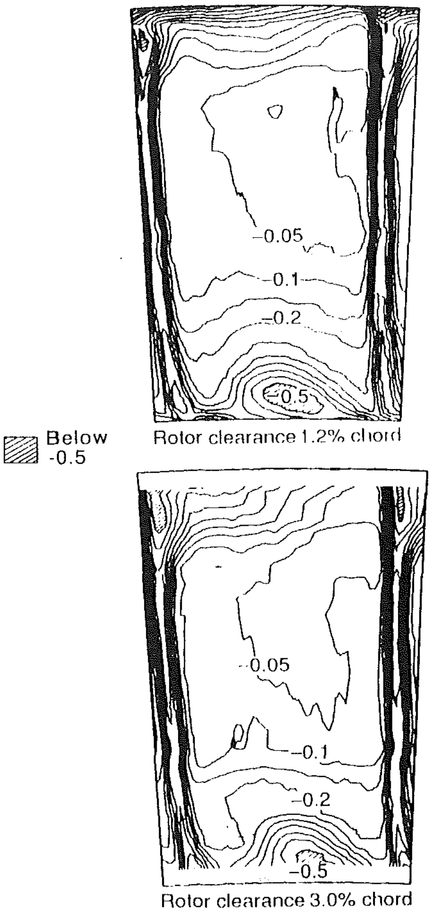

Fig. 10 Distribution of total pressure defect, $(P_0 - \hat{P}_0)/\frac{1}{2}\rho U_{\mathrm{mid}}^2$, at the exit of the third stator

larger twist of the isobars between the wakes for the larger clearance.

This redistribution mechanism is overshadowed by substantially higher stator losses between 70 and 90 percent span at the larger rotor tip clearance to the extent that the average stator losses are significantly increased. This additional stator loss causes 30 percent of the drop in stage efficiency that arises with increased rotor clearance, the other 70 percent being due to the increase in rotor loss shown in Fig. 8. The method used to split the drop of stage efficiency between the rotor and the stator is outlined in Appendix A.

The higher stator loss with increased rotor tip clearance can also be observed in the total pressure contour plots, Fig. 10. At the larger rotor tip clearance there is a thicker wake in the region of the casing which has a greater total pressure defect. This effect is quantified in Fig. 11, which shows the total pressure rise coefficient at 87 percent of annulus height plotted against circumferential angle for both higher and lower rotor tip clearances.

The higher stator losses associated with larger clearance (shown in Figs. 9, 10, and 11) can be attributed to greater "spoiling" of the stator inlet flow by the rotor flow at higher tip clearance. In an axisymmetric flow the "net secondary loss" is expected to increase with a thicker inlet boundary layer. The radial profiles of circumferentially averaged total pressure measurements show a thicker casing boundary layer at rotor exit with a higher rotor tip clearance. It would therefore appear that the multistage flow is similar to an axisymmetric flow in regard of higher "net secondary loss" with a thicker inlet boundary layer. This offers a simple way of explaining the increased stator losses in the region of the casing that occur at higher rotor tip clearance.

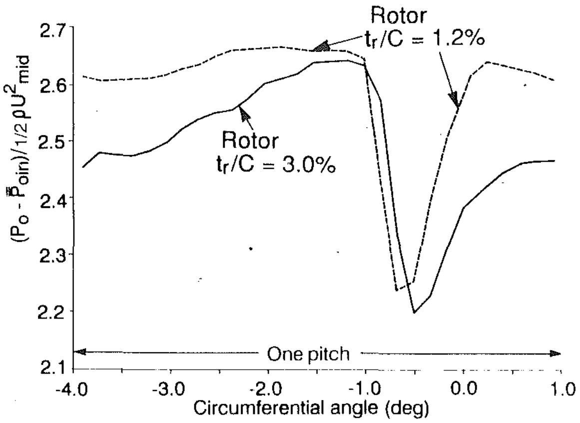

Fig. 11 Circumferential distribution of total pressure rise coefficient at 87 percent annulus height at the exit of the third stator

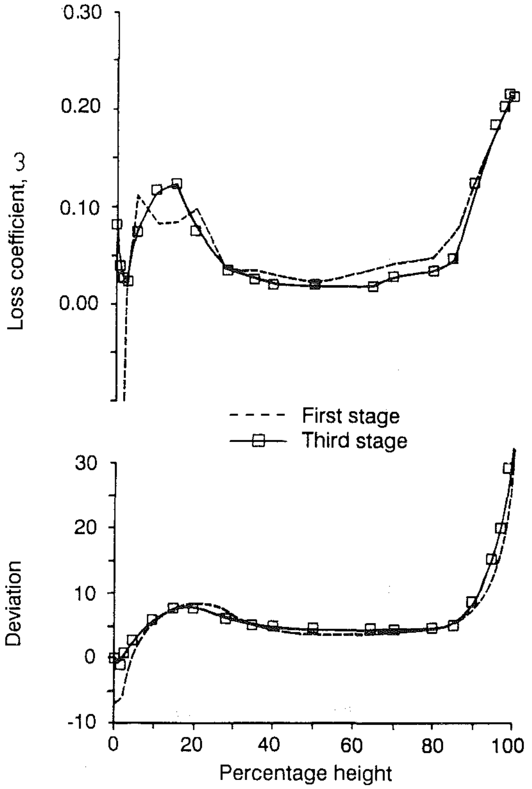

Fig. 12 Comparison of the first and third rotor's performance from the cobra probe with a rotor tip clearance of 3 percent chord at peak efficiency

Comparison of First and Third Stages

The rotor loss and deviation deduced from the cobra probe for the first and third stages are compared in Fig. 12 for a rotor tip clearance of 3 percent chord at peak efficiency.

The exit conditions from the IGV are substantially different from those from the second stator, and consequently the first and third rotors have very different inlet conditions, Fig. 13. The rotor hub gives an excellent illustration of the effect of inlet skew on secondary flow. The repeating stage velocity profile results in large skew into the third rotor hub, Fig. 13. This results in a less severe secondary flow for the third rotor, as shown in the deviation data presented in Fig. 12. In the third rotor the overturning adjacent to the hub is 5 deg lower than the overturning in the first rotor. The loss coefficients in the rotor hub also demonstrate sensitivity to inlet conditions. For the first stage the peak of the loss coefficient in the hub

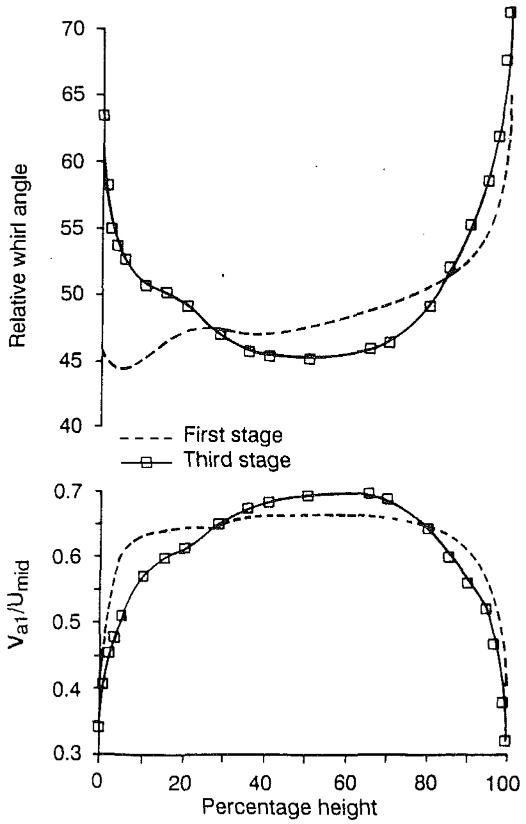

Fig. 13 Comparison of first and third rotor's inlet conditions from the cobra probe with a rotor tip clearance of 3 percent chord at peak efficiency

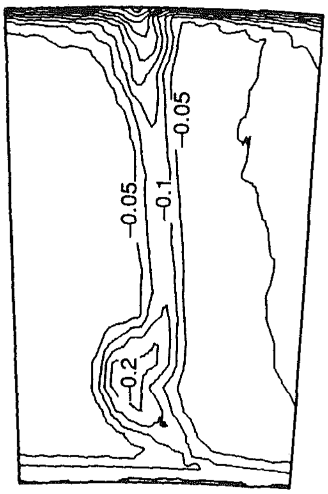

Fig. 14 Distribution of total pressure defect, $(P_0 - \bar{P}_0)/\frac{1}{2}\rho U^2_{\mathrm{mid}}$, downstream of the IGV with a rotor tip clearance of 1.2 percent chord at peak efficiency

region is close to the inner wall, at 5 percent height, and there is an extended region of high loss outboard of this with a local maximum at 20 percent height. The third stage, however, shows a peak of loss coefficient in the hub region further from the wall, at 15 percent height, in the region where the deviation is also high. For both the first and third rotor the hub is rotating for a large distance upstream, i.e., the inlet guide vane and stators have hub clearance with a rotating surface underneath. The extended region of high loss in the hub region of the first rotor may be associated with an inlet guide vane loss core at around 20 percent annulus height, Fig. 14.

By contrast the tip clearance flow at the casing shows little sensitivity to inlet conditions, Figs. 12 and 13. The deviation due to tip clearance flow is similar for both first and third rotors, but slight differences appear in the loss coefficients. Hunter and Cumpsty (1982) also observed little sensitivity of tip clearance flow to inlet conditions and discussed a "natural" outlet condition in this context.

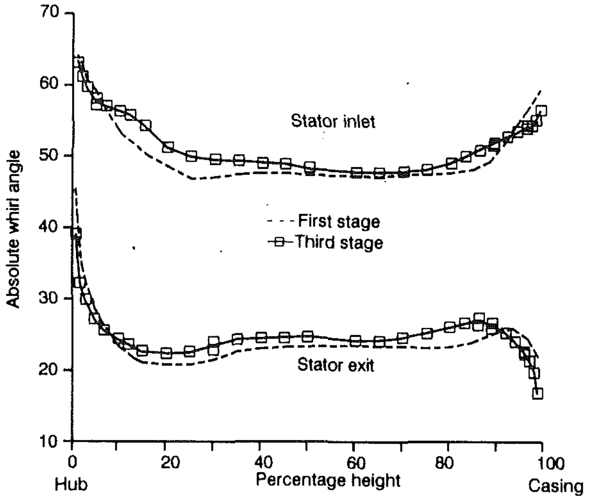

Fig. 15 Comparison of absolute whirl angles in the first and third stages with a rotor tip clearance of 1.2 percent chord at peak efficiency

Figure 15 compares the inlet and exit gas angles for the first and the third stators. The behavior of the hub clearance flow is similar to the rotor tip clearance flow. The deviation due to hub clearance measured by the cobra probe is fairly insensitive to differing inlet conditions. At the casing, however, the secondary flow and corner stall phenomena are sensitive to the inlet conditions with different radial variations of deviation above 70 percent height in the first and third stages. In a steady rectilinear cascade the spanwise extent of secondary flow has been previously observed to scale on the thickness of the inlet boundary layer. The stator flow behavior at the casing is consistent with this because the annulus wall boundary layer is thicker in the third stage and consequently the region of flow underturning and overturning would be expected to occupy a larger proportion of span as is the case. The difference in the inflow to the first and third stators is visible in the inlet whirl angles, Fig. 15. In the third stage regions of lower axial velocity spread farther from the wall, resulting in increased whirl angles over a larger proportion of the span.

Comparison With Single-Stage Data

In order to examine the importance of the unsteadiness associated with a multistage environment comparison with data from a single-stage compressor, with axisymmetric inflow, is relevant.

Hot-wire measurements downstream of a C4 rotor with axial inflow (no inlet guide vane) and a large axial gap prior to the subsequent stator, are presented by Goto (1992). These measurements are compared with deviation data for the third rotor by plotting the additional deviation due to the three-dimensional endwall flow against distance from the casing normalized by rotor tip chord, Fig. 16. Measurements at two levels of rotor tip clearance for both the single and multistage compressors are plotted with both compressors running close to peak efficiency. At the lower tip clearance the two sets of data are similar especially close to the casing. At the higher level of clearance the single-stage data are comparable to the multistage data given the significant experimental difficulties in angle measurement (as evidenced in the difference between the cobra and wedge probes). These comparisons indicate that neither multistage effects, nor aerofoil type have a first-order

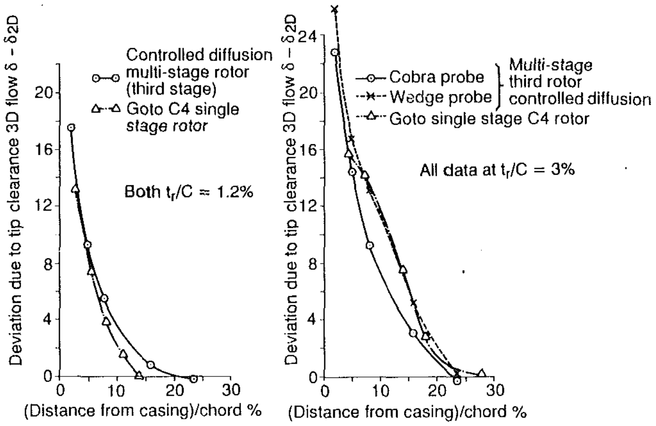

Fig. 16 Comparison of deviation due to three-dimensional tip clearance flow between single stage and multistage compressor rotors

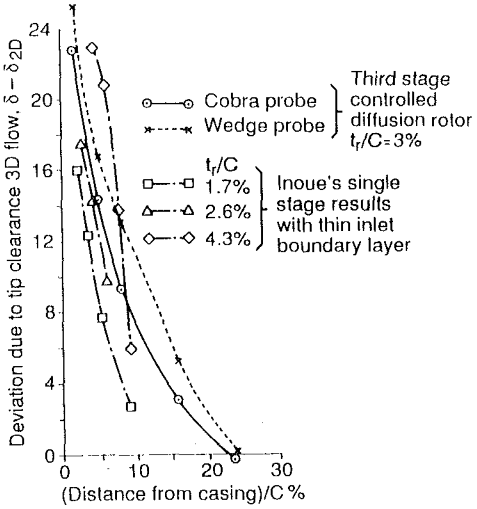

Fig. 17 Comparison of deviation due to tip clearance between a single-stage rotor with a thin inlet boundary layer and a multistage rotor

impact on tip clearance flow. Evidence of the insensitivity of tip clearance flow to aerofoil type has also been presented by Storer (1991). For both Goto's single-stage test and the present work there is a thick annulus wall boundary layer on the casing at rotor entry.

In contrast measurements made behind an isolated rotor with a thin inlet casing boundary layer are presented by Inoue et al. (1986). These are compared with the deviation angles for the third rotor from both cobra and wedge probes in Fig. 17. The three-dimensional flow effects are more localized to the casing, at a given clearance level, for the case with a thin inlet boundary layer. However, close to the casing the deviation due to three-dimensional flow is similar, at a given clearance, for both Inoue's NACA 65 aerofoils and the multistage controlled diffusion blading. This suggests that while inlet conditions do not have a first-order effect on tip clearance flow (the "natural" exit condition, Hunter and Cumpsty (1982)) there is some influence.

Effect of Aerofoil Type

Controlled diffusion aerofoils are designed using two-dimensional blade-to-blade computational methods with a view to reducing profile losses. Their effect on endwall loss is also of interest. Results for conventional blading from the four-stage facility used for the present tests have been published by Robinson (1991). These results have been compared with the present test on controlled diffusion aerofoils and the distributions of loss due to rotor tip clearance are shown in Fig. 18. The aerodynamic duties of the aerofoils are different but to a first order there is no difference in the distribution of the tip clearance losses.

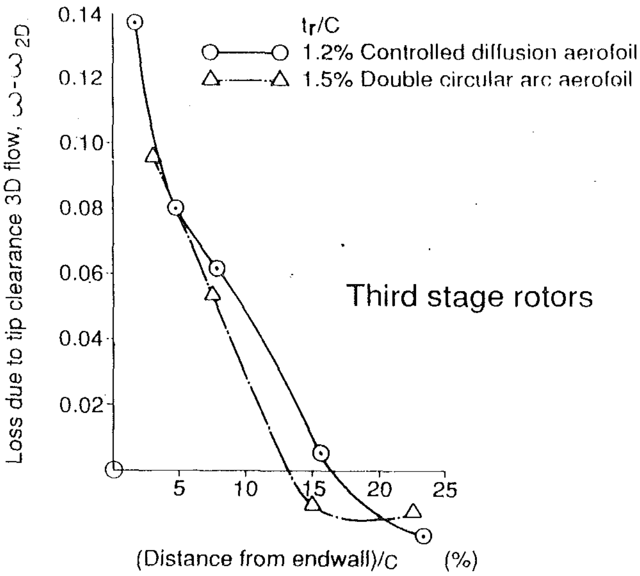

Fig. 18 Radial distributions of loss due to tip clearance for both controlled diffusion and double circular arc aerofoils

The qualitative behavior at the stator casing is also similar for a conventional stator (Robinson, 1991) and the controlled diffusion stator of the present work.

Near-Wall Velocity Defects

Many of the new design methods emerging for compressor design are viscous methods. Both two-dimensional (Howard and Gallimore, 1993; Miller and Reddy, 1991) and three-dimensional (Dawes, 1992; Adamczyk et al., 1990) methods are being pursued. Measured details of the variation of velocity close to the annulus walls in multistage compressors are useful in guiding the development of models for turbulence and spanwise mixing in these methods.

The measured total pressure, static pressure, and deduced axial velocity at stator 1 exit, from the cobra probe and both heads of the four-hole wedge probe, and presented in Fig. 19. The total pressures from the cobra probe and both heads of the wedge probe are consistent with each other. The scatter in the axial velocity is caused by scatter in the static pressure measurement. The accurate radial positioning of the probe is confirmed by a total pressure measurement adjacent to the casing being close to the static pressure. The plot presented is a circumferential average of a very nonuniform flow such as those shown in Figs. 4 and 10. Despite this nonuniformity the radial variation has some similarities with an axisymmetric turbulent boundary layer. For instance within 1 percent of height of the annulus walls rather high velocities are retained, much like a turbulent boundary layer. This has important implications for the modeling of turbulence and spanwise mixing for multistage viscous calculation methods. This justifies the assumptions made in the near-wall turbulence model of Howard and Gallimore (1993) in a viscous throughflow method. In this method the turbulent viscosity is continuously reduced close to the endwalls relative to the free-stream value used to model spanwise mixing. This results in a predicted velocity profile close to the endwall similar to the measured profile presented in Fig. 19.

Farther from the wall, not unexpectedly, the three-dimensional effects result in unconventional profiles of axial velocity,

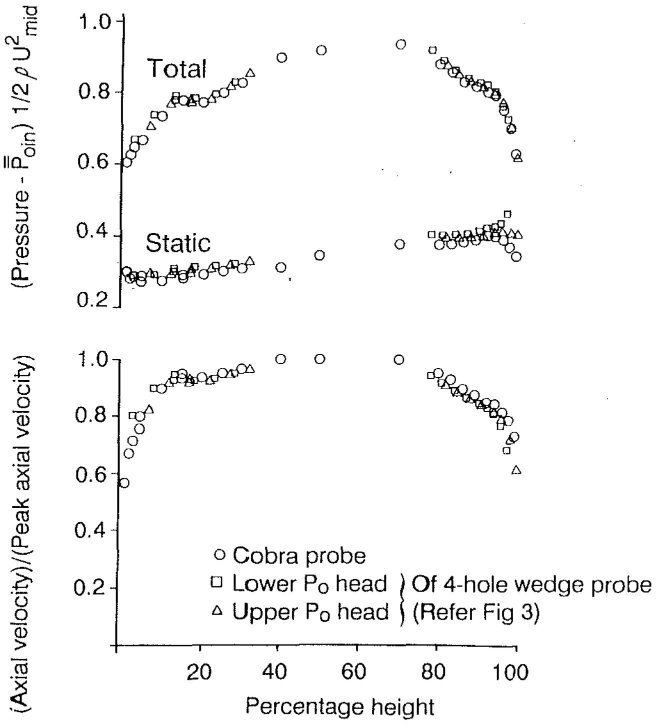

Fig. 19 Measured pressures and deduced axial velocity at the exit of the first stator with a rotor tip clearance of 3 percent chord

which could not be represented by power law forms. Inflections in the radial variation of axial velocity are observed at 15 percent height and 92 percent height due to these three-dimensional flow phenomena.

Discussion

The rotor tip clearance has been shown to exert a large influence upon the flow in the downstream stator. As rotor tip clearance is modified, the radial distribution of inlet conditions to the stator changes. Higher rotor tip clearance results in greater incidence and skew in the region of the casing at stator inlet. Improved compressor performance could be achieved if the detail of the radial distributions of flow parameters such as whirl angle and axial velocity could be taken into account during the design. A viscous throughflow calculation aimed at achieving this is described by Howard and Gallimore (1993). The accuracy of this method is improved if accurate variations of the loss and deviation due to three-dimensional effects can be specified for the calculation.

The measurements described in this paper improve the ability to do this in two ways. First, the data obtained may be used to improve correlations for the radial distributions of the loss and deviation due to three-dimensional flow. Second, the finding that tip clearance data from single-stage rotors, with representative inlet boundary layers, is very similar to the present multistage data increases the amount of data that may be used to derive correlations.

A feature of multistage compressors that has been confirmed by the present work is that a large proportion of the total losses can be attributed to endwall effects. Indeed the proportion of annulus height where the flow can be considered two-dimensional is small, Fig. 7. This is the motivation for geometric changes to the blading in the endwall region with the aim of increased stall margin and efficiency. Modified and conventional blades were studied experimentally and theoretically by Robinson et al. (1989). The ability reliably to specify this type of geometric adjustment to the blading in the endwall region would be much improved by more accurate theoretical methods for both predicting the inlet and exit conditions for the blading in a multistage machine and the details within each blade row. The viscous throughflow method (Howard and Gallimore, 1993) and steady three-dimensional viscous flow methods (e.g., Moore, 1985) offer a means of achieving this. The observation that the unsteady and nonaxisymmetric flow effects in a multistage machine are not dominating the endwall flow phenomena justifies the use of steady flow three-dimensional methods as an interim means of examining alternative blade designs. Clearly in the longer term the more rigorous method of Adamczyk et al. (1990) and a new approach by Giles (1992) should be pursued.

The conclusion that unsteady and nonaxisymmetric effects are not dominating the endwall flow phenomena could be influenced by relative circumferential positioning of stators because wakes from upstream stators may at some settings flow directly onto a downstream stator. The traverse measurements were carried out at peak efficiency and near stall and no major difference in the character of the endwall flow was observed between these two operating points. Since the deviation and transport of wakes across the rotor will change with throttle setting, this suggests that the endwall flow is not extremely sensitive to the relative circumferential positioning of stators. Clearly more study is needed in this area since in practical machines, with unequal numbers of stators in each row, sensitivity to the location of upstream wakes will be a source of aperiodicity.

The measurements presented provide useful data for the evaluation of three-dimensional calculation methods, but are rather incomplete since only inlet and exit conditions are available. To assist in the development of theoretical methods, it would be beneficial to obtain measurements inside the blading. Some two-spot laser measurements were carried out in the present test series and improved measurements are planned for the future.

Previous single-stage measurements at a range of rotor tip clearances (Hunter and Cumpsty, 1982; Lakshminarayana et al., 1982; Inoue et al., 1986; Goto, 1992) have suggested that the sensitivity of the flow to tip clearance is nonlinear. For small values of clearance a given change in clearance increases the thickness of the casing boundary layer by a greater amount than would occur if the initial tip clearance were large. Also the distribution of the additional deviation that arises due to tip clearance is sensitive to the ratio of tip clearance to chord, Fig. 16. A more complete understanding would be obtained by repeating the measurements at an even higher level of rotor tip clearance.

Conclusions

Increased rotor tip clearance results in significant changes in the performance of a downstream stator in the region of the casing. The loss of the stator is both redistributed and increased with a higher rotor tip clearance. The increase in the stator losses accounted for 30 percent of the drop in stage efficiency caused by increased rotor tip clearance (the remaining 70 percent is due to the increase in rotor loss coefficient). The geometry of compressor stators could be improved in the region of the casing by accounting for the influence of rotor tip clearance on the radial distributions of whirl angle and total pressure into the downstream stator in the design calculations. Valuable data have been collected to aid the development of design methods capable of predicting these details.

To examine the influence of the unsteady and nonaxisymmetric multistage flow environment results from the third-stage rotor have been compared with data from single-stage rotors that have axisymmetric inflow. The deviation angles due to tip clearance have been compared with measurements by Inoue et al. (1986) and Goto (1992). For a given level of rotor tip clearance the radial distributions of deviation angle, in the region of the rotor tip, showed similarity between the steady flow in the single-stage rotors and the unsteady flow in the third-stage rotor. This suggests that the blade row interaction effects associated with the multistage environment do not exert a first-order influence on tip clearance flow.

A related finding is that the endwall phenomena observed at the ends where the blades are attached (rotor hub, stator casing) can be explained by a conventional understanding of secondary flow and corner stall. Since this understanding was largely derived from cascades and single-stage machines it can be inferred that effects related to the unsteady flow in multistage machines are at least not dominating the flow physics. Because of this it seems likely that improvements can be made to multistage compressors by utilizing existing steady-flow three-dimensional Navier–Stokes computational methods, combined with the viscous throughflow method, to enhance the blading design close to the endwalls.

The measurement and analysis procedures used have been successful in isolating sources of loss. In the repeating stages, at the higher tip clearance, the losses due to three-dimensional endwall flow are found to have the same importance as profile losses in producing stage losses. With profile losses alone the stage efficiency would be 95 percent compared to the measured efficiency of approximately 90 percent. This emphasizes the need to improve blade design in the region of the endwalls.

Acknowledgments

The authors would like to thank Rolls-Royce plc for permission to publish this work. The project was funded by the European Community as BRITE/EURAM Program AERO-0021-C, which was monitored by Dr. R. Dunker.

References

Adamczyk, J. J., Celestina, M. L., Beach, T. A., and Barnett, M., 1990, "Simulation of Three-Dimensional Viscous Flow Within a Multistage Turbine," ASME Journal of Turbomachinery, Vol. 112, pp. 370–376.

Cyrus, V., 1985, "Experimental Investigation of Losses and Secondary Flow in an Axial Compressor Stage," *Forschung im Ingenieur Wesen*, Vol. 51, No. 2.

Cyrus, V., 1986, "Experimental Study of the Three-Dimensional Flow in an Axial Compressor Stage," ASME Paper No. 86-GT-118.

Dawes, W. N., 1992, "Toward Improved Throughflow Capability: The Use of Three-Dimensional Viscous Flow Solvers in a Multistage Environment," ASME Journal of Turbomachinery, Vol. 114, pp. 8–17.

Denton, J. D., 1992, "The Calculation of Three Dimensional Viscous Flow Through Multistage Turbomachines," ASME Journal of Turbomachinery, Vol. 114, pp. 18–26.

Dring, R. P., and Joslyn, H. D., 1986, "Through-Flow Analysis of a Multistage Compressor: Part I—Aerodynamic Input; Part II—Analytical-Experimental Comparisons," ASME Journal of Turbomachinery, Vol. 108, pp. 17–31.

Dring, R. P., and Joslyn, H. D., 1989, "The Effects of Compressor Endwall Flow on Airfoil Incidence and Deviation," AGARD CP 469, Paper No. 2.

Giles, M., 1992, "An Approach for Multi-stage Calculations Incorporating Unsteadiness," ASME Paper No. 92-GT-282.

Goto, A., 1992, "Three-Dimensional Flow and Mixing in Axial Flow Compressor With Different Rotor Tip Clearances," ASME Journal of Turbomachinery, Vol. 114, pp. 675–685.

Howard, M. A., and Gallimore, S. J., 1993, "Viscous Throughflow Modeling for Multistage Compressor Design," ASME Journal of Turbomachinery, Vol. 115, pp. 296–304.

Hunter, I. H., and Cumpsty, N. A., 1982, "Casing Wall Boundary-Layer Development Through an Isolated Compressor Rotor," ASME *Journal of Engineering for Power*, Vol. 104, pp. 805–818.

Inoue, M., Kuroumaru, M., and Fukuhara, M., 1986, "Behavior of Tip Leakage Flow Behind an Axial Compressor Rotor," ASME *Journal of Engineering for Gas Turbines and Power*, Vol. 108, pp. 7–14.

Lakshminarayana, B., Pouagare, M., and Davino, R., 1982, "Three-Dimensional Flow Field in the Tip Region of a Compressor Rotor Passage: Part I—Mean Velocity Profiles and Annulus Wall Boundary Layer; Part II: Turbulence Properties," ASME *Journal of Engineering for Power*, Vol. 104, pp. 760–781.

Miller, D., and Reddy, D., 1991, "The Design/Analysis of Flows Through Turbomachinery. A Viscous/Inviscid Approach," Paper No. AIAA-91-2010-CP.

Moore, J. G., 1985, "An Elliptic Calculation Procedure for 3-D Viscous Flow," *3-D Computational Techniques Applied to Internal Flows in Propulsion Systems*, AGARD LS-140, ISBN 92-835-1503-X.

Robinson, C. J., 1985, "Measurement of the Vortex Flows in a Low-Speed Axial Flow Compressor," Paper No. AIAA-85-1360.

Robinson, C. J., Northall, J. D., and McFarlane, C. W. R., 1989, "Measurement and Calculation of the Three-Dimensional Flow in Axial Compressor Stators, With and Without End Bends," ASME Paper No. 89-GT-6.

Robinson, C. J., 1991, "Endwall Flows and Blading Design for Axial Flow Compressors," PhD Thesis, Cranfield Institute of Technology, United Kingdom.

Smout, P. D., 1990, "The Problem of Static Pressure Measurement in Turbomachinery Annuli Using Traversable Instrumentation," presented at the 10th Symposium on Aerodynamic Measurement, Von Karman Institute.

Storer, 1991, "Tip Clearance Flow in Axial Compressors," PhD Thesis, University of Cambridge, United Kingdom.

APPENDIX A

Throughflow Calculations to Split Losses Between the Rotor and the Stator and Between Two-Dimensional and Three-Dimensional Sources

To ensure that the blade performance remains identical in the inner portion of the annulus (between the hub and 65 percent height) when rotor tip clearance was varied, the input data for these additional throughflow calculations were specified by radial variations of loss coefficient and relative exit angle for the third stage. Other consequences of this type of throughflow calculation are that the stage efficiency emerges as part of the solution and that the loss and deviation can be smoothed and forced to be consistent with two-dimensional blade-to-blade calculation in the relevant central portion of the annulus. This latter point is the key to splitting the stage losses into two and three-dimensional sources.

The values of loss coefficient and exit angle for the calculation at the higher clearance were obtained as a judged "average" of data from both cobra and wedge probe analyses (as presented in Fig. 7) over the whole span. Data from the lower clearance build was used in the creation of this "average" for the inner portion of the annulus. A smooth variation was chosen in the endwall region and in the midspan region the loss and deviation were from two-dimensional blade-to-blade predictions. The validity of the specified "average" radial variations of loss coefficient and deviation was verified by comparison of the calculated total pressure and absolute angle data with measurements. After minor adjustments, the calculated profiles were within experimental error of the measured profiles.

To determine the proportion of the stage efficiency rise, due to reduced rotor tip clearance, occurring in the rotor and stator, respectively, two further throughflow calculations were carried out. For the first only the rotor loss and deviation were changed local to the casing (between 80 percent height and the casing). This gives the stage efficiency rise due to the rotor. In the second calculation both rotor and stator loss and deviation were altered in the region adjacent to the casing. This yields the stage efficiency rise due to both rotor and stator. The changes in loss and deviation for the calculation were taken from the difference between cobra probe results at the two levels of clearance (presented in Figs. 8 and 9). Differences were forced to be zero at the judged edge of the casing three dimensional flow effect (80 percent height for rotor and 65 percent height for the stator) by application of radially constant deltas, in loss coefficient and exit angle, as necessary.

Based on mass average total pressures, these calculations revealed that of the total drop of stage efficiency caused by increased rotor tip clearance only 70 percent was due to changes in rotor performance with the remaining 30 percent being caused by changes in the stator performance.

APPENDIX B

Data Checking Resulting From Throughflow Analysis

One of the advantages of arranging for the throughflow analysis calculation to achieve traverse results between the blades is that the consistency between measured absolute whirl angles, mass flow, and torque is checked.

Table B1 Adjustments to cobra probe rotor exit angle measurements for the throughflow analysis at peak efficiency; rotor tip clearance = 3 percent chord

Stage	Stator, $\alpha_{1\,\text{mid}}$ measured	adjusted	$\Delta\alpha_{1\,\text{mid}}$	stage efficiency "deduced"	adjusted
1	47.4	47.8	0.4	92.0	90.0
3	46.4	47.6	1.2	96.9	90.0

For the rotors the radial distribution of absolute whirl angle and total pressure are specified at inlet and exit from the traverse data. The measured mass flow is also specified for the throughflow calculation. From these two boundary conditions the throughflow calculation will give radial distributions of both axial and tangential velocity at rotor inlet and exit. The deduced torque may then be computed from:

$$2\pi \int_{r_{\text{hub}}}^{r_{\text{casing}}} r(V_{\theta 2} - V_{\theta 1})\rho V_a r dr$$

Since the total pressure rise for the stage is also specified from the traverse data, a deduced stage efficiency can be calculated. This calculation is available for the first and third stages and can be compared with efficiency for all four stages measured using the torquemeter.

It is found that the deduced torque and stage efficiency are very sensitive to the values of absolute swirl angle at rotor exit. For instance Table B1 shows deduced stage efficiency from the cobra probe and measured and adjusted angles for the first and third stages.

Table B1 Adjustments to cobra probe rotor exit angle measurements for the throughflow analysis at peak efficiency; rotor tip clearance = 3 percent chord

Stage	Stator, α_{1mid} measured	adjusted	$\Delta\alpha_{1mid}$	stage efficiency "deduced"	adjusted
1	47.4	47.8	0.4	92.0	90.0
3	46.4	47.6	1.2	96.9	90.0

For the rotors the radial distribution of absolute whirl angle and total pressure are specified at inlet and exit from the traverse data. The measured mass flow is also specified for the throughflow calculation. From these two boundary conditions the throughflow calculation will give radial distributions of both axial and tangential velocity at rotor inlet and exit. The deduced torque may then be computed from:

$$2\pi \int_{r_{\text{hub}}}^{r_{\text{casing}}} r(V_{\theta 2}-V_{\theta 1})\rho V_a r dr$$

Since the total pressure rise for the stage is also specified from the traverse data, a deduced stage efficiency can be calculated. This calculation is available for the first and third stages and can be compared with efficiency for all four stages measured using the torquemeter.

It is found that the deduced torque and stage efficiency are very sensitive to the values of absolute swirl angle at rotor exit. For instance Table B1 shows deduced stage efficiency from the cobra probe and measured and adjusted angles for the first and third stages.

DISCUSSION

N. A. Cumpsty[1]

This is an interesting and substantial paper and the results will be of use to anyone concerned with the aerodynamics of multistage compressors. I would like to raise two points.

The first point can be expressed quite briefly. The first conclusion of the paper is that the rotor tip clearance has an effect on the downstream stator, so increased rotor clearance increases the loss in the downstream stator. This is something I do not think had been widely appreciated before. It relates very conveniently to another paper presented at the same conference, by Storer and Cumpsty (1994), which was directed specifically at the estimation of loss associated with clearance. Storer and Cumpsty considered *only* the loss in the blade row having the clearance (i.e., rotor at the casing or stator at the hub). The loss due to clearance, which they measured, predicted with a Navier-Stokes solver, and predicted with a simple model was found to be similar in magnitude for rotor and stator geometries and almost proportional to clearance; for conventional loading and flow coefficients the loss coefficient was equal to about 1/2 percent for a clearance of 1 percent of blade span. This is significantly less than that conventionally assumed to be caused by clearance from estimates of loss magnitude that have been found necessary to match the performance in compressor stages. It seems very probable that the effect Howard et al. have shown explains the low levels of clearance loss found in Storer and Cumpsty's work.

The second point takes longer to explain and relates to Fig. 6 in the paper. This figure shows substantially higher stagnation pressure at rotor 3 exit than stator 3 exit even at stator midpitch, well away from the wakes of stator 3. The mechanism to be described is so well known in other contexts that I have been inclined to feel that I may be presenting something so obvious that it is unnecessary to put it on paper; the reception I received from a number of people, however, has made me think that it may serve some purpose to explain it as part of a discussion.

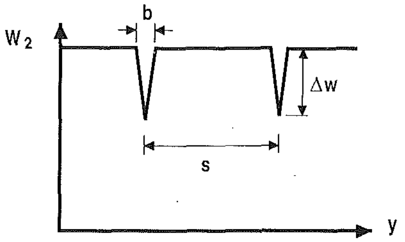

Fig. A Model of wakes in otherwise uniform flow downstream of a rotor

Discrepancies in the measurement of stagnation pressure in multistage compressors are common, and the normal explanation is probe error associated with the unsteadiness of the flow. The problem is made acute in the multistage compressor because of the need to put the probes very close to the upstream blade rows. Although not denying the existence of probe errors, it is important to realize that this is not the only cause of discrepancy. A simple analysis, given in outline below, shows that the change in the frame of reference between moving and stationary blade rows also introduces an error, causing loss in rotors to be normally underestimated and loss in stators correspondingly overestimated.

Imagine a rotor that produces as series of **V**-notch wakes (of isosceles triangle form) like those sketched in Fig. A. This is not a bad model of what real wakes look like well away from the endwall regions for compressor blades that are not near major boundary layer separation. Measurements have shown that even about 15 percent of chord downstream of the blades the decrement in resultant relative velocity Δw is only about 30 percent of the midpitch value leaving the rotor, W_2. The width of the wake b is normally much less than the pitch s. If we carry out an *area* average of the stagnation pressure from the rotor row at a particular spanwise location we get, neglecting compressibility effects,

$$p_{02\text{rel}}=\frac{1}{s}\int_0^s\left(p_2+\frac{\rho}{2}w_2^2\right)dy$$

where w_2 is the velocity leaving the row in the relative frame of reference. The area average in the moving frame may not be the best choice (there continues to be discussion of what average to use) but is likely to be the only practical one. In particular when one considers measurement made by probes in the stationary frame of reference, the time average in the stationary frame is likely to correspond at best to an area average in the moving frame.

The relative stagnation pressure can be rewritten

$$p_{02\text{rel}}=\frac{1}{s}\int_0^s\left(p_2+\frac{\rho}{2}W_2^2\right)dy-\frac{\rho}{2s}\int_0^b(W_2^2-w_2^2)dy$$

where W_2 is the resultant velocity outside the wake. The first of these integrals is the free-stream stagnation pressure and the second is the loss, to be denoted by $(\Delta p_0)_{\text{rel}}$. Note that the limits in the integral defining the loss are only for the range 0 to b, since the nonuniformity in the wake is restricted to this region. With uniform static pressure the average stagnation pressure is therefore given by

$$p_{02\text{rel}}=p_2+W_2^2-(\Delta p_0)_{\text{rel}}.$$

For the simple model of a **V**-notch wake the integral for the loss can be evaluated as

$$(\Delta p_0)_{\text{rel}}=\frac{\rho}{2s}\int_0^b(W_2^2-w_2^2)dy=\frac{\rho}{2}\frac{b}{s}\left\{W_2\Delta w-\frac{\Delta w^2}{3}\right\} \qquad (1)$$

---

[1] Whittle Laboratory, Cambridge University Engineering Department, Madingley Road, Cambridge CB2 2BN United Kingdom.

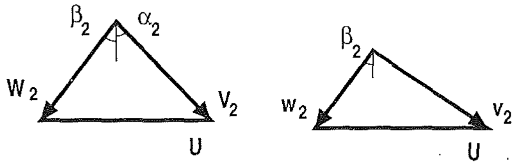

In free stream In wake

Fig. B Velocity triangles downstream of rotor; flow direction uniform in rotating frame of reference

Suppose that downstream of the rotor we have an ideal probe, which will produce a true time average of the stagnation pressure. This might well be a Kiel probe (which is insensitive to flow direction over a wide range of inlet angle) with a pressure transducer close behind the measuring port. The pressure transducer can be assumed to be stiff so that there is a negligible flow of air into and out of the probe as the pressure it is exposed to fluctuates. This probe will indicate as an estimate of stagnation pressure in the *stationary* frame of reference

$$p_{02\mathrm{abs}} = \frac{1}{s}\int_0^s \left(p_2 + \frac{\rho}{2}\,v_2^2\right)dy$$

where the absolute velocity is v_2. This may be rewritten as

$$p_{02\mathrm{abs}} = \frac{1}{s}\int_0^s \left(p_2 + \frac{\rho}{2}\,V_2^2\right)dy - \frac{\rho}{2s}\int_0^b (V_2^2 - v_2^2)dy$$

where V_2 is the velocity outside the rotor wake. Again the integral across the wake is only between the limits 0 and b. As before the first integral is the free-stream stagnation pressure, while the second integral gives the contribution of the flow deficit in the wake. For convenience we will denote the integral associated with wake deficit in the absolute frame by $(\Delta p_0)_{\mathrm{abs}}$ and refer to it as the loss in the absolute frame. The term loss is appopriate since it is the difference between the actual stagnation pressure recorded and that with a uniform velocity at the free-stream value; as will be shown it does not give a satisfactory or meaningful estimate of the rotor loss.

Both V_2 and v_2 can be found from the velocity triangle, sketched in Fig. B. It is assumed here that the relative flow direction, β_2, measured from the axial, is the same in the main flow and the wake. It is then easy to show that

$$V_2^2 = (W_2\cos\beta_2)^2 + (W_2\sin\beta_2 - U)^2$$

$$= W_2^2 - 2W_2U\sin\beta_2 + U^2$$

and $$v_2^2 = w_2^2 - 2w_2U\sin\beta_2 + U^2.$$

Then carrying out the integral for the V-notch wake gives

$$(\Delta p_0)_{\mathrm{abs}} = \frac{\rho}{2}\frac{b}{s}\left\{\Delta w(W_2 - U\sin\beta_2) - \frac{\Delta w^2}{3}\right\} \qquad (2)$$

The second-order terms in Eqs. (1) and (2) can be estimated by assuming the wake depth Δw to be equal to $0.30W_2$, which leads to

$$\frac{\Delta w^2}{3} \approx 0.1\Delta w W_2.$$

In other words, the contribution from the squared term is small though not negligible. It is, however, identical in both the rotating and stationary frames.

Comparing Eqs. (1) and (2) shows that the stagnation pressure deficit measured by the ideal probe in the stationary frame therefore underestimates that obtained in the steady rotating frame by an amount

$$\frac{\rho}{2}\frac{b}{s}\Delta w U\sin\beta_2.$$

Alternatively one can say that the first-order term for the stagnation pressure deficit is attenuated in the ratio

$$R = 1 - \frac{U\sin\beta_2}{W_2}$$

when measured in the stationary frame. This can be written more conveniently in terms of the flow coefficient $\phi = \overline{V}_x/U$. $\overline{V}_x$ is the mean axial velocity and is well approximated by $\overline{V}_x = W_2\cos\beta_2$, so

$$R = 1 - \frac{\sin 2\beta_2}{2\phi}.$$

The crucial term ($\sin 2\beta_2/2\phi$) shows that the error in the perceived rotor loss will increase as the flow coefficient falls. It is in the nature of blade design constraints that as the design flow coefficient is reduced the relative flow direction out of the blades tends to increase; as a result ($\sin 2\beta_2)/2\phi$ rises rapidly as ϕ falls. For $\sin 2\beta_2 = 2\phi$ no loss would be detected in the absolute frame from the first-order term. If $\sin 2\beta_2 > 2\phi$ the rotor wakes are perceived as a raised stagnation pressure (and also stagnation temperature) and the term loss for tangential 2 becomes a misnomer. Indeed it has been recognized that misleading estimates of loss are produced in this way and various ways of transferring estimates of the absolute velocity vector to the relative frame in order to estimate the relative loss more meaningfully have been used.

The case $U\sin\beta_2 = W_2$ corresponds to the relative and absolute velocity vectors for the freestream being at right angles, $\alpha_2 + \beta_2 = 90$ deg. At this condition Fig. B shows that a small reduction in the length of vector W_2 leads to a rotation of the vector V_2 but no alteration in its length. This may remind readers of the recovery ratio described by Smith (1958), which relates the manner in which decrements in velocity are treated by one row following another moving relative to it. The effects are indeed the same, but as far as I am aware the reasoning had not been applied to the case of measurement errors before.

For the tests of Howard et al. $\phi = 0.715$ and (from Fig. 7) $\beta_2 \approx 2\ 0$ deg. As a result the ratio R is approximately 0.44, representing a very serious underestimate of the rotor loss and overestimate of the stagnation pressure. Taking the second-order part $\Delta w^2/3$ into account, and assuming that this is around 10 percent of the first-order loss in the relative frame of reference, suggests that the loss perceived in the stationary frame would be about half that actually occurring. I would suggest that this is an important contributor to the high levels of stagnation pressure measured at stator 3 inlet. As the rotor wakes mix out, and the flow approaches uniform, the discrepancy between stagnation quantities in the moving and stationary frames of reference disappears, and the stationary instruments give a more accurate estimate of stagnation pressure at the exit of stator 3.

The type of error that the change in reference frame gives rise to is systematic, and is therefore difficult to detect from the usual statistical approaches. It may be argued that the attempt to give an assessment of error based on evidence of the nonsystematic type of error (as in the requirements for the ASME *Journal of Fluids Engineering*) may in circumstances like this give rise to greater risk than making no claim for accuracy at all. Although it is possible to use the analysis such as the one in this discussion to estimate errors at spanwise positions well outside the endwall regions and when the blades are well away from major separation, this would not be possible under more general conditions.

References

Smith, L. H., 1958, "Recovery Ratio—a Measure of Loss Recover Potential of Compressor Stages," *Trans. ASME*, Vol. 80, No. 3.

Storer, J. A., and Cumpsty, N. A., 1994, "An Approximate Analysis and Prediction Method for Tip Clearance Loss in Axial Compressors," ASME JOURNAL OF TURBOMACHINERY, Vol. 116, this issue, pp. 648–656.

Authors' Closure

The authors would like to thank Professor Cumpsty for his interest in, and thought provoking comments on, our paper.

We agree with the first point made by Professor Cumpsty regarding the need to include the additional losses in blade rows downstream of the one that has the tip clearance (e.g., in the stator for the usual case of a rotor tip clearance) when estimating the loss of stage efficiency from rotor loss coefficients determined from a fundamental rather than empirical viewpoint. A distinction of the origin of the loss coefficient is necessary because the empirical approach is self-correcting in that loss coefficient changes consistent with many observed stage efficiency changes are correlated. By contrast the work of Storer and Cumpsty seeks to compute tip clearance losses from consideration of the fundamental fluid mechanics of tip clearance flow with no reference to measured stage efficiency changes. In this case additional losses arising downstream will need to be included. It would be most interesting to evaluate a three-dimensional Navier–Stokes calculation in this way, initially as a rotor-alone case and then as a stage calculation.

Professor Cumpsty's second point addresses the issue of deduction of rotor losses from stationary frame traverses with pneumatic probes. We remain to be convinced that there is a fundamental error due to use of a probe in the stationary frame on the basis that the main issue requiring ingenuity is the appropriate way of analyzing the measurements. Given an ideal probe that resolves absolute stagnation pressure and angle through time our approach would be to transform the absolute frame data to the relative frame through the rotor exit velocity triangle and then to average.

Because no such ideal probe exists we have adopted a more pragmatic approach, which, due to space limitations, is only outlined in the paper. In Appendix B of the paper the importance of the rotor exit absolute swirl angle measurement is highlighted. Given the severe temporal fluctuation in absolute swirl angle the pneumatic results are remarkably good. Used with no adjustment these absolute swirl angles can be used to compute the work input distribution across the span. When combined with stator exit pressure measurements a central region of constant stage efficiency is often revealed. From the stator exit traverses similar wakes are usually observed at the different radial heights within this region, suggesting constant stator losses in this central region of the annulus (between 40 and 65 percent of height based on Fig. 7). Clearly within this region constant rotor loss with span should also result from the analysis. Our approach does give this (Fig. 7) but since adjustments were found necessary the data presented in the paper are more reliable for obtaining radial distributions than absolute levels of loss. Our view is that the agreement in deduced radial distributions of blade performance from alternative types of pneumatic probe (wedge versus cobra) shown in Fig. 7 is significant and offers considerable justification of our approach.

The theme of our paper is a study of endwall effects where reliable radial distributions allow many valuable conclusions to be drawn. If it was important to determine both rotor and stator midspan losses accurately the best approach would be to arrange for traversing in the rotating reference frame, which is considered practical for low-speed rigs only. Such a capability has now been designed and manufactured for the Cranfield four-stage rig and will be tested before the summer of 1995.

Faced with the difficulty of stationary frame traversing, as is the case for high-speed research, there are two alternatives:

1 a high-response instrument (work on this has commenced, Cook, 1989)
2 phase-locked laser anemometry

Professor Cumpsty is correct to point out the importance of the shape of the velocity triangle on the signal to be expected from such a probe, but it is not clear to us why it should be valid to compare his Eqs. (1) and (2), which are for relative and absolute pressure differences, respectively. Our view is that losses to be deduced from the measurements must be in the relative frame for the rotor.

References

Cook, S. C., 1989, "Development and Use of a High Response Aerodynamic Wedge Probe and Its Use on a High Speed Research Compressor," *Proc. of the Ninth International Symposium on Air Breathing Engines*, Athens, Vol. 1, pp. 1113–1125.

An Approximate Analysis and Prediction Method for Tip Clearance Loss in Axial Compressors

J. A. Storer[1]

N. A. Cumpsty

Department of Engineering,
Whittle Laboratory,
Cambridge University,
Cambridge, United Kingdom

A simple model for loss created by the tip clearance flow in axial compressors is presented, based on an experimental program performed in conjunction with the Dawes three-dimensional Navier–Stokes calculation method. The principal mechanism of loss (entropy creation) caused by tip leakage flow has been established to be the mixing of flows of similar speeds but different direction. Calculations show that relative motion of the endwall relative to the tip has a small effect on clearance flow. The simple model correctly predicts the magnitude of tip clearance loss and the trend with changes of tip clearance for the cascade tested. For a given geometry the loss is almost exactly proportional to the ratio of tip clearance to blade span; the loss directly associated with the clearance is smaller than often assumed. The simple model for tip clearance loss has been expressed in terms of conventional nondimensional design variables (for example: solidity, aspect ratio, flow coefficient, loading coefficient) and from these the contribution to the overall loss of efficiency caused by tip leakage flow is conveniently represented. The trends are illustrated for a number of possible compressor design choices. Blade row loss increases more slowly than blade loading (for example, diffusion factor). As a result the decrement in stage efficiency associated with clearance flow decreases as the stage loading is raised in the practical range of flow and loading coefficients.

Introduction

As much as 30 percent of the total loss in compressors is sometimes attributed to the flow through the tip clearance. The work described in this paper suggests 10 percent is a more realistic proportion attributable to the clearance flow itself and for well-designed compressors this corresponds to only about 1 percent decrement in overall efficiency. The lower level of loss found here may be because the present study is restricted to blading of good aerodynamic design at realistic loading. It is also probable that in the past some of the loss in the endwall region has been wrongly attributed to clearance flow.

Despite its importance and the large amount of effort expended over the years in studying it, the nature of the flow caused by the clearance has not been well understood. The sensitivity of axial compressors to tip clearance varies significantly (Moyle, 1988), but there are often no very good explanations for this. In the last few years three-dimensional calculation methods have been able to solve the Reynolds-averaged Navier–Stokes equations for blades with tip clearance and the agreement between calculated and measured features of the flow is frequently very good. These methods do not by themselves yield an appreciation of the dependence of clearance flow on parameters defining the whole flow, nor do they make it convenient to carry out optimization studies, since the time to carry out such a calculation is still long. The most common methods for estimating clearance loss currently in use in the industry rely almost entirely on empirical information; see Chap. 8 of Cumpsty (1989). There are, in addition, several methods in the literature that calculate the loss after making assumptions about the blade forces in the clearance region, but these are not solidly grounded on combined measurements of both flow and loss in a blade row.

The present paper describes an approximate method for estimating tip loss based on what is believed to be the correct physical model derived from measurements. The loss is created by mixing the clearance jet with the main flow, and the model is simple enough that the dependence of loss on clearance magnitude, blade geometry, and loading is easily revealed. The approximations introduced in creating the simple expressions have been checked against measured loss versus clearance data. As a result of its solid base it should provide reasonably accurate estimates for loss and should be capable of improvement in the light of experience with relatively small amounts of empirical input. Given that the magnitude of the loss in efficiency associated with the clearance is only about 1 percent,

---

[1] Present address: Howmedica International, Staines, United Kingdom.

Contributed by the International Gas Turbine Institute and presented at the 38th International Gas Turbine and Aeroengine Congress and Exposition, Cincinnati, Ohio, May 24–27, 1993. Manuscript received at ASME Headquarters March 1, 1993. Paper No. 93-GT-140. Associate Technical Editor: H. Lukas.

an error of 10 percent or even 20 percent in the absolute level of loss is less important than predicting the correct trend. Such levels of uncertainty are anyway comparable with the precision of efficiency measurement.

This paper describes a method of loss prediction, which, together with the measurements on which it is based, forms the doctoral dissertation of Storer (1991). Measurements were made in a large linear cascade of blades with endwall clearance and aspects of the tip leakage flow were reported by Storer and Cumpsty (1991). A number of observations from these measurements, some of which had been anticipated by Rains (1952), made modeling of the flow and loss production very much easier. For the sake of brevity, details of the flow described by Storer and Cumpsty (1991) will not be repeated, but certain salient observations are necessary as a basis for the present paper and these are outlined below. Because of its greater accessibility the reference by Storer and Cumpsty (1991) (abbreviated to S&C) will be referenced throughout this paper, rather than the original dissertation.

Background. Extensive measurements in a linear cascade of blades, similar in geometry and loading to the hub of a stator, are described by S&C. This section first highlights the aspects needed here for the prediction of loss that were previously published.

(*i*) It was found that the clearance flow experiences virtually no loss in stagnation pressure in passing through the clearance gap; as a result the stagnation pressure of most of the clearance flow emerging on the suction side of the blade has the stagnation pressure of the free-stream flow. This is true so long as the flow does not reattach on the tip of the blade and this appears to be the case provided the clearance was more than about 0.4 times the local blade thickness.

(*ii*) The static pressure across the clearance flow emerging from the gap has the same static pressure as the blade suction surface near the tip. This pressure varies along the chord and is a function of the magnitude of the ratio of tip clearance to the blade chord. On the pressure side the static pressure remains uniform in the spanwise direction until very close to the tip (within one or two clearance heights) at which point it drops rapidly.

(*iii*) The static pressure distribution on the suction side of the blade near the tip is very different from the distribution well away from the endwall and is affected by the clearance flow and the clearance vortex. Minimum pressure occurs at about 40 percent chord with a clearance equal to 4 percent of chord and at about 20 percent chord for 2 percent clearance. (With a skewed inlet flow, such as occurs into a rotor, it appears that the minimum pressure is nearer the leading edge.) The *average* static pressure near the tip of the suction surface is, however, nearly independent of the clearance, which is equivalent to saying the blade force varies little toward the tip.

(*iv*) If the clearance flow has the same stagnation pressure and static pressure as the main flow near the tip of the blade it follows from Bernoulli's equation that the speed of the clearance jet must be the same as the local free-stream speed on the suction side of the blade. What differs is the direction. The flow carried into the clearance gap has the same velocity parallel to the camber line direction as the free-stream flow on the pressure surface at that chordwise position, V_s. (This involves treating the blades as thin and assuming that the suction and pressure surfaces are locally parallel to the camber line.) The flow emerging from the clearance has a streamwise component of velocity V_s and a normal leakage component V_L. The resultant speed of the clearance flow is $\sqrt{V_s^2 + V_L^2}$, which is the same as the speed of the free-stream flow on the suction side. The angle between the leakage flow and the local free-stream flow (assumed parallel to the camber line) is given by $\tan \zeta = V_L/V_s$.

(*v*) The leakage velocity is given by $V_L/V_1 = \sqrt{C_{pp} - C_{ps}}$, where V_1 is the inlet velocity to the blade row. C_{pp} and C_{ps} are the local pressure coefficients on the pressure and suction surfaces, respectively, well away from the tip on the pressure surface and near the tip on the suction surface. The average clearance velocity over the height of the clearance gap can be approximated by $V_L = C_D V_L$; a discharge coefficient C_D equal to 0.8 was found to give best agreement. Based on the measured pressure coefficients the calculated leakage flow rate and direction agree well.

(*vi*) It was found that the Dawes (1987) method of solving the Navier–Stokes equations gave good estimates for many aspects of the flow, even with a relatively crude modeling of the tip geometry, and this allowed aspects to be investigated that would have been difficult or impossible to measure. Figure 1 shows measured and calculated values of mass-averaged loss downstream of the cascade. Most of the loss measured downstream was already present in the endwall boundary layer upstream of the cascade. At zero clearance the Navier–Stokes method seriously underestimates the loss, because a corner separation develops that the calculation does not replicate. At the 2 percent and 4 percent clearance levels the calculated and measured loss agree reasonably well, but, more significantly, the trend with clearance is accurately reproduced. The basis for the present work on loss is measurements in a cascade with collateral inlet flow, whereas the application is rotors or stators with highly skewed inlet flow. The Dawes calculation had shown that although there are differences, the overall clearance flow is not radically altered and, in particular, motion of the end wall relative to the blade tip plays a small part in determining the flow.

Nomenclature

a = area
c = chord
h = blade height
k = thermal conductivity
l = distance along blade chord
C_D = discharge coefficient (actual flow ÷ ideal flow rate)
C_P = static pressure coefficient = $(p - p_1)/ 1/2\, \rho V_1^2$
F = blade force per unit span
p = static pressure
P_0 = stagnation pressure
s = specific entropy; blade row pitch
T = temperature
U = blade speed
V = velocity
α = flow direction relative to axial
β = blade direction relative to axial
γ = blade row stagger
Δh_0 = stage stagnation enthalpy rise
ζ = angle of leakage jet with respect to mainstream
θ = blade camber
ρ = density
σ = solidity, c/s
τ = tip gap height
ϕ = flow coefficient = V_x/U
Φ = viscous dissipation function
χ = area of gap divided by mainstream flow area
ψ = stage loading = $\Delta h_0/U^2$
ω = total pressure loss coefficient = $(P_{01} - P_0)/ 1/2\, \rho V_1^2$

Subscripts

0 = stagnation
1 = at inlet to blade row
2 = at outlet from blade row
E = at outlet from control volume
L = in leakage direction
R = of rotor
S = of stator; in streamwise direction
x = in axial direction
θ = in tangential

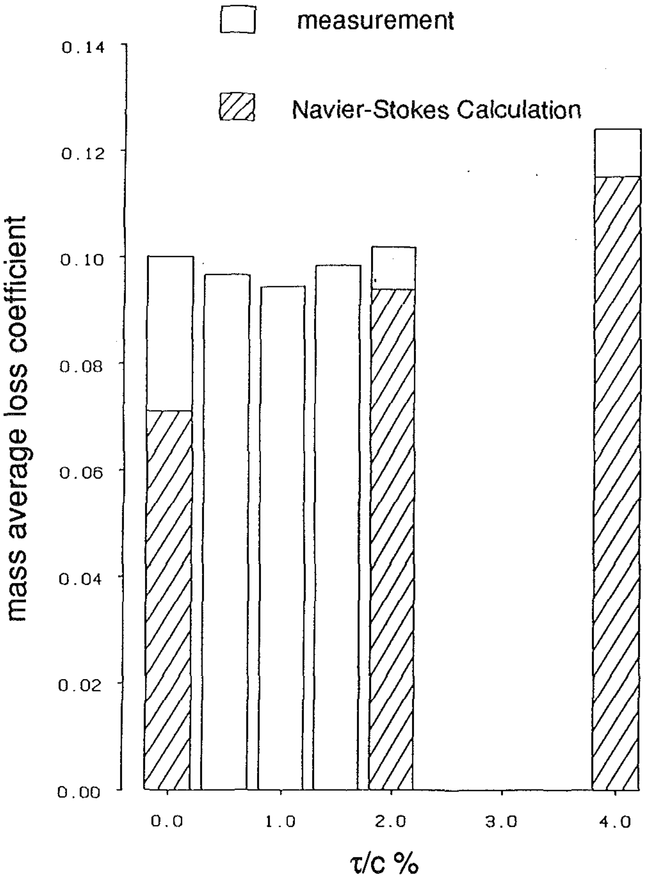

Fig. 1 Mass average loss in the endwall region measured and predicted by N-S calculation. Plane approximately 50 percent chord downstream of trailing edge. Natural inlet boundary layer on endwall.

The Approach to Modeling the Flow. The results and observations summarized above provide the basis for the modeling of loss associated with the clearance flow. The approach adopted is explained in the later sections of the paper but the steps in the argument and the important approximations are summarized here.

(*a*) The clearance loss is caused by the mixing of the clearance flow with the free stream on the suction side of the clearance, which is a result of the difference in direction between the two flows, each having the same speed. At each chordwise position the loss generation depends on the local flow direction of the clearance flow and a simple control volume analysis allows this to be calculated.

(*b*) A mass-averaged leakage flow direction along the blade chord is defined and this direction is used in the mixing analysis to predict loss. (A comparison of loss calculated using this mass-averaged direction was made with measured losses in the S&C cascade.)

(*c*) It is further assumed that the tangent of the mean leakage direction may be reasonably approximated by the average leakage velocity divided by streamwise velocity.

(*d*) The average pressure on the suction surface of the blade at the tip is assumed to be adequately approximated by the average well away from the tip.

(*e*) The average leakage velocity is assumed to be proportional to the square root of the average pressure difference across the blade, which is determined by the flow turning well away from the tip.

(*f*) The average leakage flow direction derived from the free-stream turning can then be used to estimate loss using the control volume analysis.

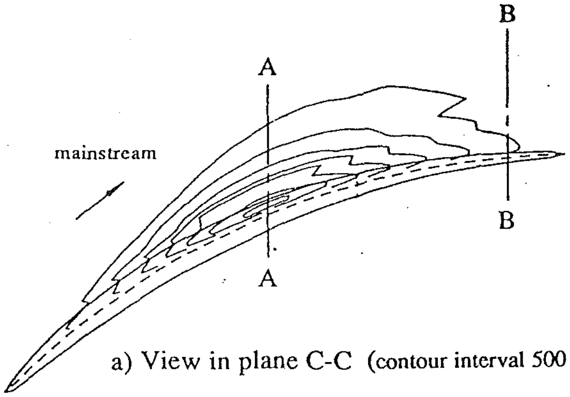

a) View in plane C-C (contour interval 500 Wm^{-3})

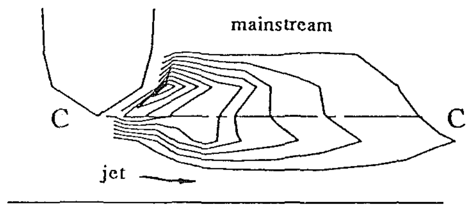

(contour interval 500 Wm^{-3})

b) View in plane A-A at 50% axial chord

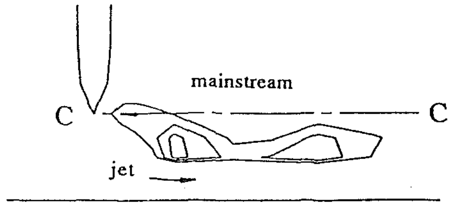

(contour interval 200 Wm^{-3})

c) View in plane B-B at 92% axial chord

Fig. 2 Contours of Φ near blade tip predicted by N-S calculation for clearance equal to 4 percent of chord

Generation of Loss

The flow through the clearance gap experiences almost no loss and the clearance loss must therefore be created after the flow leaves the gap. The entropy creation rate in the flow direction is given by

$$\rho U \cdot \nabla s = \frac{\Phi}{T} + \frac{k}{T} \nabla^2 T.$$

For low Mach number flow without heat transfer the only source of entropy is Φ, the viscous dissipation function, given by

$$\Phi = -\left(u \frac{\partial P_0}{\partial x} + v \frac{\partial P_0}{\partial y}\right).$$

Contours of Φ computed by the Dawes (1987) Navier-Stokes solver are shown in Fig. 2 for the S&C cascade with a tip clearance of 4 percent. Very clearly the loss production is primarily taking place in the shear layer between the clearance flow and the mainstream, with the shear resulting from the different flow direction. The calculation shows the loss creation to be highest at around 40 percent chord and measurements for the 4 percent clearance gap had also shown that the loss coefficient in the shear layer at the edge of the blade was a maximum at this position.

The flow in the tip region where the loss is being created is

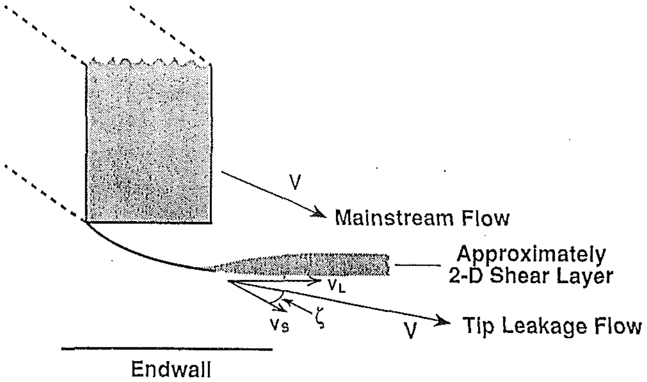

Fig. 3 Simple model of a shear layer forming outside tip gap

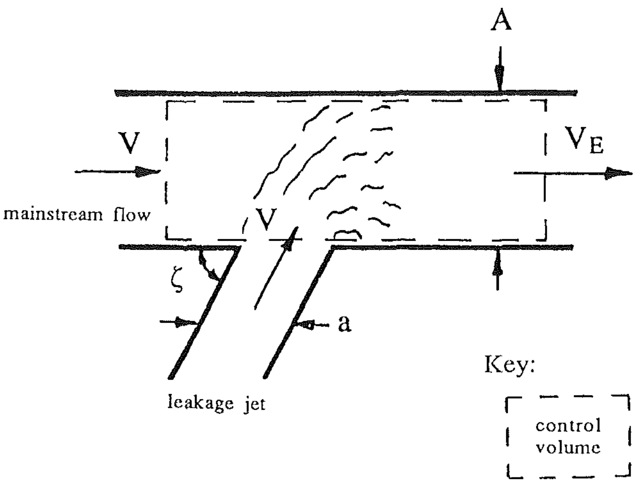

Fig. 4 Simple model for mixing of leakage jet with mainstream flow

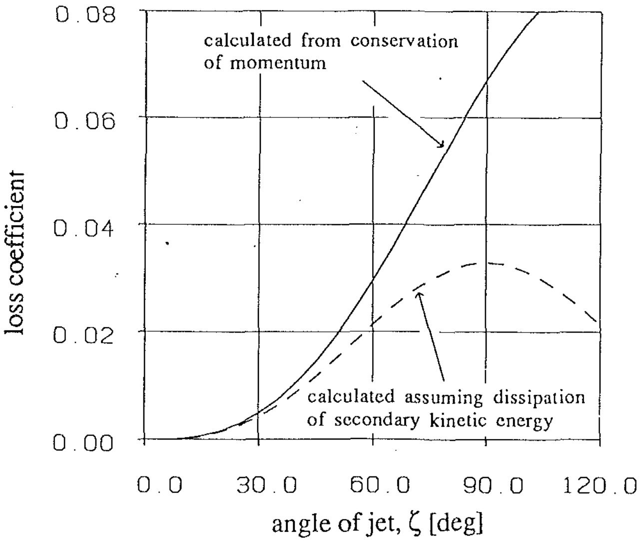

Fig. 5 Loss predicted by simple model as function of angle of leakage jet with respect to mainstream flow

shown schematically in Fig. 3. The total production in entropy, equivalent to the loss in stagnation pressure, is determined by overall conservation constraints as the flow mixes out to uniform and the details of the flow processes do not influence the overall result. The process may therefore be shown even more schematically as in Fig. 4 where two incompressible flows are mixed to form a uniform flow downstream with speed V_E. Each stream enters with a uniform and equal speed V, the main flow with area A, and the leakage flow with area a. The ratio of the flow areas is denoted by $\chi = a/A$ and it is assumed that $\chi \leq 1$. The angle between the two streams is ζ. Applying conservation of mass flow and conservation of momentum in the direction of the main flow between inlet and outlet, with the skin friction neglected, defines the stagnation pressure loss averaged over the whole flow, which is given by

$$\frac{\Delta P_0}{\frac{1}{2}\rho V_E^2}=\chi \sin\zeta\left\{\frac{2+\chi\sin\zeta-2\cos\zeta}{(1+\chi\sin\zeta)^2}\right\} \qquad (1)$$

This approach is an extension of one proposed by Denton and Cumpsty (1987) who assumed the leakage flow to be perpendicular to the main flow, corresponding to $\zeta = 90$ deg, and the two approaches agree at this angle. The variation in loss with inclination of the jet is shown in Fig. 5 for a fixed value of χ corresponding to a tip clearance of 2 percent of chord with the geometry used for the experiments. Also shown in this figure is the result of calculating the kinetic energy of the secondary flow, that is, the leakage velocity, and assuming that all this kinetic energy will be lost (see Vavra, 1960, and Yaras and Sjolander, 1992). The kinetic energy based approach shows a peak at 90 deg, whereas the conservation-based method adopted here shows no turning point, and the kinetic energy method underestimates the loss by substantial amounts when $\zeta > 30$ deg. Kinetic energy is a scalar and it is not clear that resolving the scalar like this has any validity.

Measurements of flow downstream of rotors, for example Hunter and Cumpsty (1982), shows that there is flow nonuniformity associated with the clearance flow remaining at exit. Loss would be created as this flow mixed out to the uniform condition far downstream, but Navier–Stokes calculations have shown that the magnitude of loss created in this way is so much less than that created in the flow near the clearance gap itself that it may be neglected.

Application to a Compressor Cascade

The expression given in Eq. (1) for the loss is essentially exact, except for the assumption of negligible friction at the wall. In Eq. (1) the loss is nondimensionalized by the dynamic pressure based on the mixed-out exit velocity, V_E, which will be the outlet velocity from the row. In compressor practice, however, it is normal to use the inlet dynamic pressure. By assuming that the inlet and outlet axial velocities are equal, $V_1 \cos\alpha_1 = V_E \cos\alpha_2$, the conventional form of loss coefficient in terms of inlet dynamic pressure can be written

$$\frac{\Delta P_0}{\frac{1}{2}\rho V_1^2}=\chi \sin\zeta\left\{\frac{2+\chi\sin\zeta-2\cos\zeta}{(1+\chi\sin\zeta)^2}\right\}\frac{\cos^2\alpha_1}{\cos^2\alpha_2} \qquad (2)$$

where the loss is averaged over the entire passage flow.

The clearance area parameter χ must be expressed in terms of the cascade geometry. The total area of the clearance gap for a blade is the product of the chord and the clearance height, $a = \tau \times c$. The primary flow area is the height of the blade multiplied by the staggered gap. As an approximation the staggered gap is equal to the blade pitch multiplied by the cosine of the blade stagger and the pitch is equal to the blade chord divided by the solidity. (The use of stagger in characterizing the effective width between two blades is reasonable for compressors because the camber is normally small. For blades that vary substantially along their span a value of stagger should be used appropriate for the end under consideration.) The ratio χ can therefore be written

$$\chi=\frac{\tau c}{(c/\sigma)h\cos\gamma}=\frac{\sigma(\tau/c)}{(h/c)\cos\gamma} \qquad (3)$$

It was found by S&C that Eq. (3) overestimated the clearance

Table 1 Mass average of measured inclination of leakage jet to the mainstream direction, $\bar{\zeta}$

	Boundary layer on end wall	
τ/c, percent	Natural	Thickened
1	49.4 deg	-
2	50.4 deg	51.6 deg
4	50.0 deg	49.8 deg

flow rate and a more accurate estimate was obtained if a discharge coefficient were used

$$\chi = C_D \frac{\sigma(\tau/c)}{(h/c)\cos\gamma}; \qquad (4)$$

$C_D = 0.8$ was found to be appropriate and Eq. (4) is therefore used here with this value.

In Eq. (2) a single angle ζ is specified, but the clearance flow angle varies along the chord and across the gap. S&C showed that the variation across the gap is actually quite small and can reasonably be neglected. The variation along the chord is not negligible and a strict application of Eq. (2) should require it to be evaluated at a number of positions along the chord and averaged with each value weighted by the local clearance flow rate. Such an integration does not lend itself to making a simple method. Instead Eq. (2) is evaluated using a mass-averaged mean angle defined by

$$\bar{\zeta} = \frac{\int^{c} \zeta V_L dl}{\int^{c} V_L dl}. \qquad (5)$$

Here V_L and ζ are the local values of leakage velocity and angle and l is the distance along the blade camber line. (Density is omitted from the mass average because it is essentially uniform for the current work.) For the cascade described by S&C the value of $\bar{\zeta}$ derived from measurements using Eq. (5) remained very nearly constant at 50 deg regardless of the magnitude of the tip clearance, Table 1.

Using Eq. (2) and taking $\bar{\zeta}$ = 50 deg the clearance loss was calculated for the cascade tested by S&C for a range of tip clearances from τ/c = 0.5 percent up to 4 percent. Measurements were made with the natural and thickened endwall boundary layers for which overall thickness δ and momentum thickness θ, nondimensionalized by the blade chord, were as follows:

Natural $\delta \approx 0.06c$, $\theta = 0.0067c$;
Thickened $\delta \approx 0.32c$, $\theta = 0.027c$.

Measurements of loss for each boundary layer are shown by the symbols in Fig. 6 together with the clearance loss estimated by Eq. (2) shown as solid lines. Both the calculations and the measurements assess the loss over a spanwise distance equal to 75 percent of chord; the measurements were made 50 percent of chord downstream of the trailing edge. Because the clearance loss is only a part of the total the lines in Fig. 6 need to spring from a datum at zero clearance. For the thickened boundary layer this is easily drawn, but with the natural boundary layer the loss increases for clearances below about 1 percent of chord. This upturn is caused by a region of separation in the suction surface corner, an effect that is not modeled by this simple method for clearance loss. With the natural endwall boundary layer a least-squares fit has been used to draw a straight line through the points with clearance of 1 percent and more, and the extrapolation of this to zero clearance is used as the datum for the simple method. The prediction of the trend for loss with clearance is very good, supporting the use of the average angle $\bar{\zeta}$ in the computation using Eq. (2). The comparison in Fig. 6 shows not only the appropriate dependence on χ but, since the slope is correct, the correct dependence on $\bar{\zeta}$. It may be noted that the Denton and Cumpsty model, which is equivalent to taking $\bar{\zeta}$ = 90 deg, would have predicted a rate of increase in loss with clearance about three times as great.

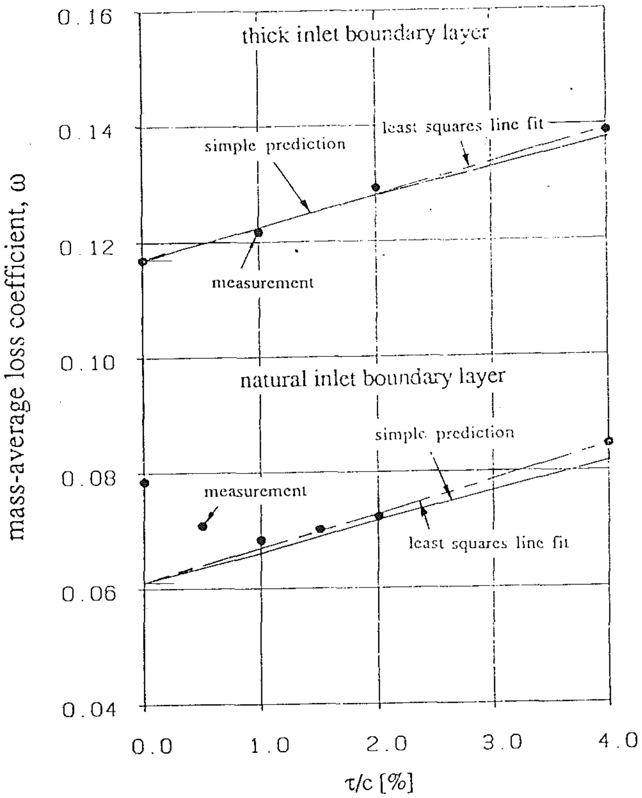

Fig. 6 Tip clearance loss calculated by simple method compared with mass-averaged loss measured 50 percent chord downstream of cascade

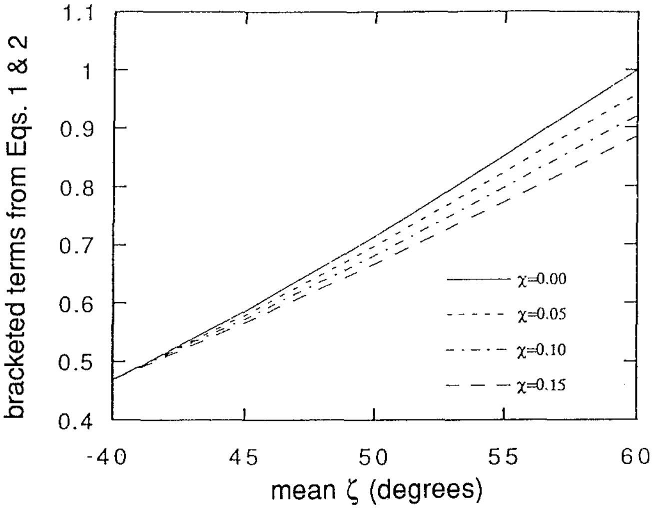

Fig. 7 Influence of leakage flow angle ζ on bracketed terms in Eqs. (1) and (2)

It will be observed in Fig. 6 that the results of the simple model lie very nearly on a straight line, that is, the clearance loss is very nearly proportional to the clearance area parameter χ. This can be explained in terms of Eq. (2) by evaluating the terms in the bracket for a range of values of χ and $\bar{\zeta}$. To allow this the upper value likely for χ must be estimated: A high value of clearance would be 4 percent of chord, a high solidity would be 2.0, and a high stagger 60 deg; together these give something like an upper limit on χ of 0.16. The bracketed term of Eq. (2) is plotted in Fig.7 from which it can be seen that the value is almost proportional to $\bar{\zeta}$ with the gradient determined by χ, though the range of gradients is very small. In the range of interest for $\bar{\zeta}$, which will be shown below to be between about 42 and 52 deg, Eq. (2) may therefore be approximated, within about ±5 percent, by

$$\frac{\Delta P_0}{\frac{1}{2}\rho V_1^2} = \chi \sin \bar{\zeta}\{0.46 + 0.023(\bar{\zeta} - 40)\} \frac{\cos^2 \alpha_1}{\cos^2 \alpha_2} \qquad (6)$$

where $\bar{\zeta}$ is expressed in deg.

The present simple model for clearance loss is based on the assumption that the flow through the clearance gap does not reattach to the tip, but emerges as a jet with the free-stream stagnation pressure. The results of S&C showed that this assumption is reasonable provided that the clearance gap is at least 0.4 times the local blade thickness. The blade on which the measurements shown in Fig. 6 were obtained had a maximum thickness of 5 percent of chord, so a clearance of 1 percent of chord corresponds to a ratio of clearance to maximum thickness of 0.2. There is reason to think that the discrepancy between measurement and the model shown in Fig. 6 for the natural endwall boundary layer at 1 percent clearance is due to the corner separation, not to reattachment at the tip. This view is reinforced by the good agreement for the thicker endwall boundary layer. The model therefore seems to give adequate estimates of clearance loss when the ratio of clearance to maximum thickness is as low as 0.2; it is probably qualitatively reliable down to smaller values still.

In Fig. 6 the loss can be seen to increase by about 0.5 percent for every 1 percent increase in clearance-to-chord ratio for this geometry with fairly typical aspect ratio and solidity. This is around one half of the gradient normally assumed and it must be assumed that other loss mechanisms are frequently being wrongly attributed to the clearance flow process.

Loss Model Applied to Compressor Blade Rows

During the design phase some of the quantities in Eq. (2), such as the clearance term χ and the flow angles α_1 and α_2, are known or may be estimated. The leakage angle ζ is, however, not generally known in advance. To make Eq. (2) useful it is necessary to have a method for estimating $\bar{\zeta}$ from the more well-known variables. At this point another approximation is adopted, which is to assume that

$$\tan \bar{\zeta} = \frac{\int^c V_L dl}{\int^c V_s dl}; \qquad (7)$$

in words, to assume that the tangent of the mean angle is equal to the average leakage velocity divided by the average streamwise velocity of the flow on the pressure side of the blade. (In Eq. (7) V_L and not the average value $\bar{V}_L$ including a discharge coefficient is used as more appropriate.) As a further approximation, the velocity V_s on the pressure side is taken to be equal to the outlet velocity from the blade row, $V_s = V_2$, an approximation which is frequently reasonable, particularly for low camber tip sections.

Finding the average leakage velocity is more involved. First it should be recalled (Storer and Cumpsty, 1991), that the leakage velocity at any chordwise position is determined by the difference in pressure between the pressure side of the blade well away from the tip and the suction side of the blade very near the tip according to

$$V_L/V_1 = \sqrt{C_{pp} - C_{ps}}. \qquad (8)$$

The pressure distribution near the tip on the suction side differs from that some distance away in the spanwise direction, say a quarter of a chord. Nevertheless the *average* pressure on the suction surface near the tip is very similar to the average suction side pressure well away from the endwall, and in calculating the average leakage velocity it is possible to use the same pressure difference at the tip as at, say, midspan. If $\overline{\Delta p}$ denotes the chordwise average pressure difference at midspan, the average leakage velocity is given by

$$\frac{\int^c V_L dl}{V_1} = \left(\frac{\overline{\Delta p}}{\frac{1}{2}\rho V_1^2}\right)^{1/2}. \qquad (9)$$

The average pressure difference can be obtained from the flow directions by considering the blade force. It is assumed here that the axial velocity into and out of the row may be taken as equal. The tangential blade force per unit span is therefore given by

$$F_\theta = \rho s V_x (V_{\theta 2} - V_{\theta 1}) = \rho s V_x^2 (\tan \alpha_2 - \tan \alpha_2),$$

and for blades of small camber with low profile loss the resultant force will be equal to

$$F = F_\theta / \cos \gamma,$$

where γ is the stagger angle. The resultant force is also equal to the average pressure difference multiplied by the chord, so

$$\overline{\Delta p} = \rho V_x^2 \frac{\tan \alpha_1 - \tan \alpha_2}{\sigma \cos \gamma}.$$

This expression for the mean pressure difference, together with Eqs. (8) and (9), gives the mean leakage velocity and using Eq. (7) with the approximation that $V_s = V_2$ gives

$$\tan \bar{\zeta} = \cos \alpha_2 \sqrt{2 \frac{\tan \alpha_2 - \tan \alpha_2}{\sigma \cos \gamma}} \qquad (10)$$

Applying Eq. (10) to the cascade tested by S&C gave a mean clearance flow direction $\bar{\zeta}$ of 47 deg, in reasonable agreement with the mass-averaged measured angles of about 50 deg given in Table 1. Inserting the value of 47 deg into Eq. (2) gives a loss 15 percent lower than if the more accurate value of 50 deg is used. Such a discrepancy would be regarded as serious in the calculation of many quantities, but in estimating the absolute level of a component of loss it is not too serious because the total magnitude of the clearance loss for a blade row is likely to be on the order of only 1 percent of inlet dynamic pressure.

Because Eq. (10) relies only on the pressure distribution or flow turning well away from the endwall, $\bar{\zeta}$ does not change when the clearance is altered, but depends on the blade row performance or specification well away from the endwall. Equations (2) and (10) provide a convenient method for estimating the clearance loss within an accuracy of about 15 percent.

Parameter Studies of Clearance Loss in Cascades

The simple Eqs. (2) and (10) make it possible to assess the loss in efficiency due to clearance loss associated with changes in compressor design. The basic premise is that the clearance flow and loss are governed primarily by the flow conditions well away from the clearance itself. It is also assumed that the leakage flow is relatively insensitive to the blade profile shape: It is the pressure distribution that matters and above all the average pressure difference associated with the blade loading. The results presented by S&C suggest that these are reasonable assumptions. (For blades with low hub/casing ratio, for which the flow varies substantially along the span, it is clearly essential to choose an appropriate part of the span to define the mean conditions.) The approach is more applicable for blades near their design condition and it cannot be expected to be reliable when there are substantial regions of separated flow.

In carrying out a study of the effect of blade geometry and loading it is convenient to use as a so-called design condition

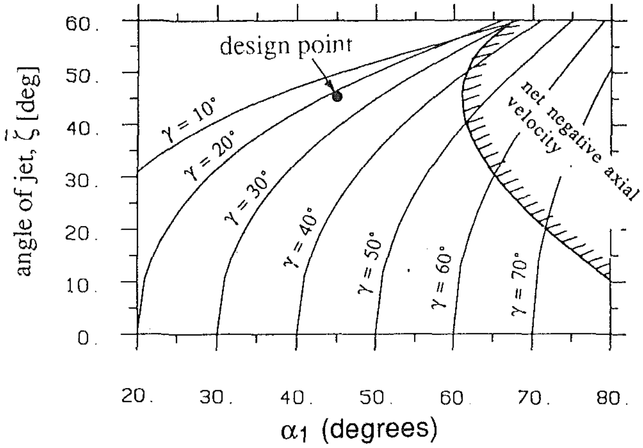

Fig. 8 Approximate dependence of leakage flow angle $\bar{\zeta}$ on cascade stagger and inlet flow direction (zero incidence assumed)

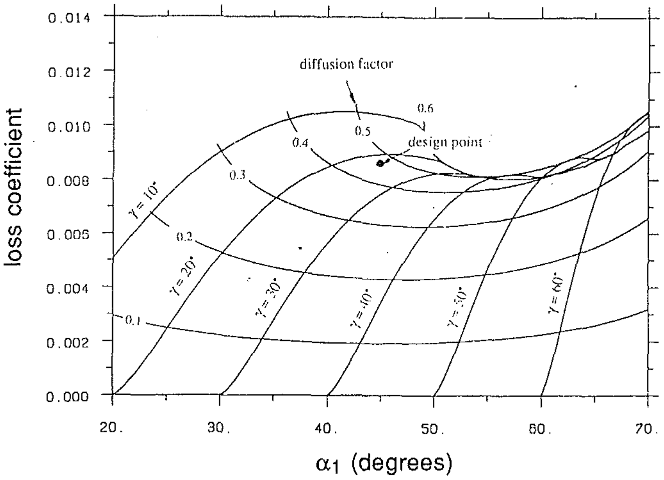

Fig. 9 Effect of cascade design on tip clearance loss: $\tau/c = 0.02$, $h/c = 0.75$, $\sigma = 1.67$

one in which the incidence is zero, so $\alpha_1 = \beta_1$. For a circular arc camber line the blade outlet angle is then given by

$$\beta_2 = 2\gamma - \alpha_1.$$

In the present calculations the outlet flow angle α_2 was obtained using Carter's rule, see Cumpsty (1989), for the deviation.

The variation in the mean leakage direction, $\bar{\zeta}$, calculated from Eq. (10) is shown in Fig. 8, with inlet flow angle as abscissa and curves of constant stagger. (With the assumption that there is zero incidence, the difference between α_1 and the stagger is half the camber.) This diagram was created using the solidity of the cascade tested by S&C and the point corresponding to the angles of this are marked as the design point. Similar plots created for other blade row geometries are presented by Storer (1991) but, since they were found to be very similar in form, they are not shown here. It is shown below that in practice most blade rows will have values of $\bar{\zeta}$ in the range 42 to 52 deg. The hatched region to the right indicates where the jet has an axial component in the upstream direction, which will occur for blade rows with a stagger higher than about 45 deg.

The estimates of clearance flow angle shown in Fig. 8 were used to produce Fig. 9, a plot of loss created by the clearance flow for the same cascade solidity. This has been produced for a clearance equal to 2 percent of chord but, as discussed above, the term in brackets in Eq. (2) changes so slowly with χ that loss averaged over the passage may reasonably be taken as proportional to clearance. (In preparing Fig. 9 the span was taken to be 0.75c. Since span appears in the denominator of χ, and because loss is proportional to χ, loss is inversely proportional to span.) The design point of the cascade used by Storer and Cumpsty is shown, and the loss for this is 0.0086. This estimate, obtained using the overall turning of the free-stream flow to obtain the mean pressure difference across the tip and thence the angle $\bar{\zeta}$, is in reasonable agreement with the loss of 0.0107 obtained for the same clearance using the value of $\bar{\zeta}$ derived from measured flow directions, see Fig. 6. It is also in reasonable agreement with the measured increment of loss attributable to clearance.

Figure 9 also shows lines of constant diffusion factor evaluated assuming that the axial velocity is equal upstream and downstream. Diffusion factor is normally taken as a reasonable measure of the loading of blades well away from the endwall region. A diffusion factor of 0.45 is a typical design point and 0.6 is regarded as fairly extreme, though it can easily occur towards the hub in machines with low hub-casing ratio. Figure 9 shows that the clearance loss does not rise uniformly with diffusion factor, but instead the increments in loss become smaller as diffusion factor approaches its practical upper limit.

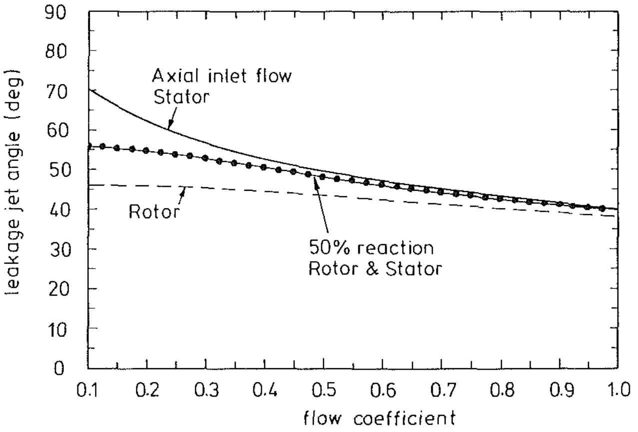

Fig. 10 Predicted change in leakage flow angle $\bar{\zeta}$ with design flow coefficient for two types of repeating stage: stage loading $\psi = 0.35$

Near the upper limit of diffusion factor it can be seen that the loss is least in the region around $\gamma = 40$ deg and $\alpha_1 = 55$ deg (corresponding to a circular arc camber of 30 deg).

Parameter Studies of Clearance Loss in Stages

In considering a compressor stage, the loss from both the rotor and stator must be considered separately. In the present comparison it will be assumed that there is clearance at the stator hub as well as the rotor tip. Only the loss contribution from the clearance flow will be considered here. The first step requires $\bar{\zeta}$ to be obtained. If each blade row is considered part of a repeating stage Eq. (10) may be rewritten, for both the rotor at the casing and stator at the hub, as

$$\tan \bar{\zeta} = \cos \alpha_2 \sqrt{\frac{2\psi/\phi}{\sigma \cos \gamma}} \tag{10a}$$

where subscript 2 refers to relative outlet conditions for each row; $\phi = V_x/U$ is the local flow coefficient, and $\psi = \Delta h_0/U^2$ is the local stage loading. Plots of $\bar{\zeta}$ are shown in Fig. 10 for two possible designs of repeating stage, each with $\psi = 0.35$. One is 50 percent reaction, the other with axial inlet flow into the rotor. In each case the abscissa is the flow coefficient. For most stages $\bar{\zeta}$ will be in the range 42 to 52 deg.

For simplicity in the examples taken here the stage is assumed to be a repeating stage with equal axial velocity and flow direction at inlet and outlet. It is also assumed that the hub-casing ratio is sufficiently high that ϕ and ψ are equal at hub

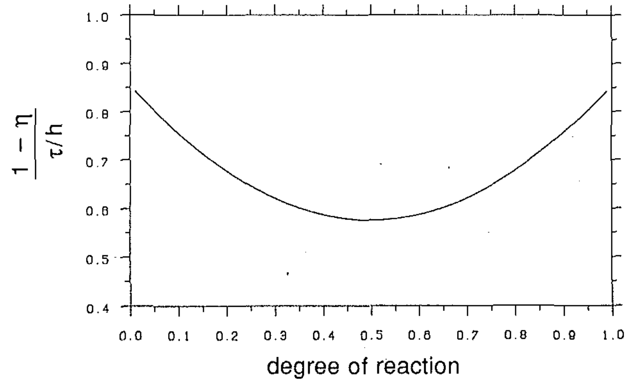

Fig. 11 Predicted influence of stage reaction on loss caused by tip clearance for repeating stage

and casing. With this restriction the loss in efficiency can be written (see Cumpsty, 1989) as

$$1-\eta=\frac{\phi}{2(\tan\alpha_1-\tan\alpha_2)}\left[\frac{\omega_R}{\cos^2\alpha_R}+\frac{\omega_S}{\cos^2\alpha_S}\right] \qquad (11)$$

or

$$1-\eta=\frac{\phi^2}{2\psi}\left[\frac{\omega_R}{\cos^2\alpha_R}+\frac{\omega_S}{\cos^2\alpha_S}\right]$$

where η is the stage efficiency, ω_R and ω_S are the rotor and stator loss coefficients, and α_R and α_S are the inlet flow directions relative to the rotor and stator. For the present example ω_R and ω_S are the losses from tip clearance alone calculated using Eq. (2) with $\bar{\zeta}$ derived from Eq. (10a). In displaying the trends it is assumed here that there are equal clearances and aspect ratios for the rotor and stator and that the loss is almost linearly proportional to the parameter χ, as shown earlier, so that it is then possible to normalize the efficiency decrement as $(1-\eta)h/\tau$. It is also assumed for convenience in presenting the results that velocity triangles are the same for the rotor and stator, equivalently that the ratio of hub and casing radius is nearly unity. For any investigation of a specific geometry it would be easy to put in appropriate velocity triangles for the free ends of the rotor and stator, as well as the appropriate clearance and aspect ratio for each row.

Figure 11 shows the variation in the normalized efficiency decrement with degree of reaction for a stage having a flow coefficient $\phi = 0.6$ and loading parameter $\psi = 0.35$. The solidity and aspect ratio are each unity. Since the reaction is assumed to be uniform along the blades the loss is a minimum at 50 percent reaction and symmetric about this condition, since the rotor and stator will contribute equal amounts of loss by the mechanism described here. Moving to a reaction of about 0.8, which corresponds approximately to a stage with axial inlet flow to the rotor, the clearance loss is predicted to be about 18 percent greater.

Figures 12 and 13 show contours of normalized efficiency loss on plots with flow coefficient and loading coefficient as abscissa and ordinate, respectively. Figure 12 is for a 50 percent reaction stage and Fig. 13 for a stage with axial flow into each rotor. The solid lines denote normalized efficiency loss while the broken lines show the diffusion factor for the rotor. Both figures show that for values of ϕ and ψ of normal practical application the clearance loss decreases with increase in loading. An explanation seems to be as follows. The pressure difference across the blades is proportional to the blade force, which rises in proportion to the loading. The clearance loss is proportional to $\sin\bar{\zeta}$, but since $\tan\bar{\zeta} = V_L/V_s$ the clearance loss is therefore very approximately proportional to V_L in the range of values of $\bar{\zeta}$ expected. V_L is proportional to the square root of blade loading. The work input, which is proportional to blade loading, therefore increases more rapidly than the rise in loss.

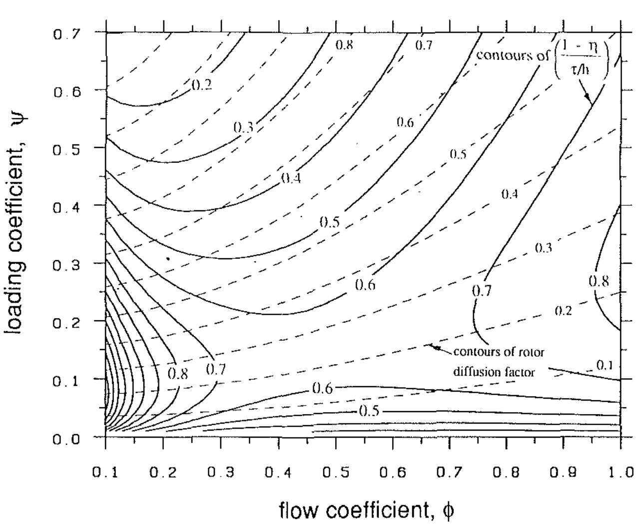

Fig. 12 Loss in efficiency $(1-\eta)$ caused by tip clearance flow predicted for 50 percent reaction repeating stage as function of loading and flow coefficients (efficiency loss normalized by τ/h)

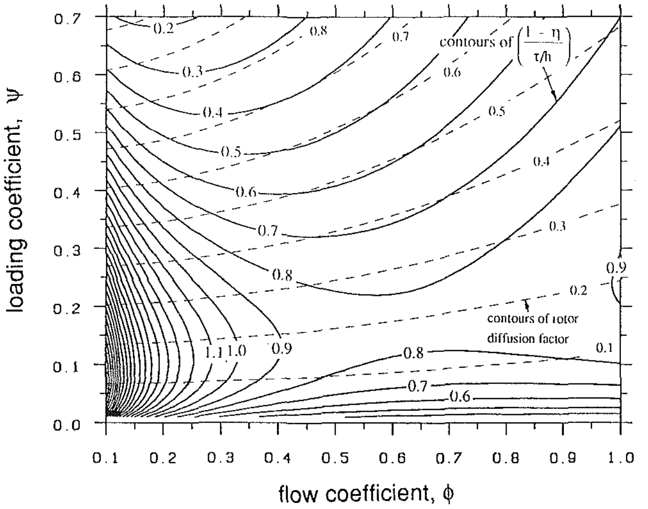

Fig. 13 Loss in efficiency $(1-\eta)$ caused by tip clearance flow predicted for reaction repeating stage with axial flow into the rotor as function of loading and flow coefficients (efficiency loss normalized by τ/h)

Figure 13 shows that a stage with axial inlet to the rotor leads to a loss in efficiency, which is greater by between 20 and 30 percent than the 50 percent reaction machine. Because the contribution from the tip clearance is smaller than sometimes imagined, this difference in loss may be insignificant compared with differences associated with other flow changes between the two types of stage.

Conclusions

1 From Navier-Stokes calculations it is believed that the loss mechanism associated with the flow through blade tip clearance can be well modeled experimentally and theoretically by the flow around the clearance gap of a linear cascade of blades. The experimental evidence and the model of the clearance loss derived from it suggest that for a typical tip clearance, say 2 percent of chord, and an aspect ratio and solidity near unity, the loss in stagnation pressure averaged over the passage associated with the clearance flow itself is only about one percent of inlet dynamic pressure in a blade row of good design and currently acceptable loading. It is believed that loss in the

endwall region associated with other mechanisms, not at present understood or quantified, has sometimes been erroneously attributed to the tip clearance flow.

2 Navier-Stokes calculations, in agreement with measurements of leakage flow in a compressor cascade, revealed very high rates of dissipation close to the blade tip in the shear layer formed between the leakage jet and the mainstream flow. The calculations predicted that the power dissipated per unit volume in the shear layer was greater than anywhere else in the flow field, and arose because of the difference in direction of the clearance jet and the main passage flow. The nonuniformity associated with the clearance flow remaining downstream of the blade row contributes a negligible additional amount to the loss as it mixes out.

3 A simple model for loss, based on the mixing of a jet into a main flow of the same speed, established the importance of the angle between the mainstream flow and the leakage jet where it emerges from the tip gap. The model demonstrated that the magnitude of the loss does not depend on the mechanism of dissipation, the magnitude of loss being dictated by conservation constraints. For this reason the quantitative estimates of tip clearance loss by the Navier-Stokes method are only weakly affected by the details of turbulence modeling (or details of the computational mesh). The same calculations show that the motion of the endwall relative to the blade tips does not significantly alter the flow in the clearance gap or the mixing outside it.

4 Prediction methods for loss based on dissipation of "secondary" kinetic energy will tend to underpredict loss because some "primary" kinetic energy may be dissipated during the mixing of the tip leakage flow. This problem highlights the difficulty of treating energy, a scalar quantity, in terms of components depending on flow direction.

5 The simple model for loss based on the mixing of a jet in a crossflow may be used to predict the loss caused by tip leakage flow in a compressor blade row when blade loading or mainstream flow angles are given. The calculation requires the angle of the leakage jet to the mainstream flow to be given and an approximate method for estimating this is presented; the estimates indicate that this angle varies comparatively little for different blade row designs. In other words the level of loss caused by tip leakage flow is fundamentally similar in high stagger rotor tips and low stagger stator hubs.

6 In a practical range of design and operating parameters the clearance loss averaged over the passage is almost exactly proportional to the ratio of clearance flow to main flow, denoted in the paper by χ. For blades of any fixed shape and solidity this loss is therefore proportional to the ratio of tip clearance to blade height. This ratio has frequently been used in the past to correlate measurements for prediction purposes, and it may also be used to normalize the loss from the simple model in plots intended to show trends. Although loss depends on the ratio of clearance to blade height, the aerodynamic behavior near the blade tip depends primarily on the ratio of tip clearance to blade chord or staggered gap.

7 The loss prediction method revealed how the loss caused by tip clearance in a compressor blade row can be influenced by the aerodynamic design. Loss from this source increases more slowly than blade loading (for example, the diffusion factor) for a wide range of blade parameters in the range of practical interest. For a given blade loading and clearance height there would seem little scope for altering the clearance loss by adjustment of pressure distribution about the blades or alteration in blade shape.

8 The degree of reaction was predicted to have some influence on the overall tip clearance loss of a compressor stage, with minimum loss being predicted for a 50 percent reaction design (all blade rows being cantilevered so there was clearance for the rotor at the casing and the stator at the hub). Loss caused by tip clearance for the axial inlet stage was between 20 and 30 percent greater than that for the 50 percent reaction stage. The maximum decrement in efficiency occurred in each case at a loading coefficient and diffusion factor below those normally employed in practice and in the normal operating range the decrement decreases continually with increase in stage loading at design point.

Acknowledgments

The authors would like to thank Dr. W. N. Dawes for his assistance and for the use of his code. The authors are grateful for the assistance of the technical staff of the Whittle Laboratory, particularly Mr. P. Hunt for making the probes. The work was supported by Rolls-Royce plc. and the permission to publish the results is greatly appreciated.

References

Cumpsty, N. A., 1989, *Compressor Aerodynamics*, Longman Scientific and Technical Publications, United Kingdom.

Dawes, W. N., 1987, "A Numerical Analysis of the Three-Dimensional Viscous Flow in a Transonic Compressor Rotor and Comparison With Experiment," ASME JOURNAL OF TURBOMACHINERY, Vol. 109, pp. 83-90.

Denton, J. D., and Cumpsty, N. A., 1987, "Loss Mechanisms in Turbomachines," *Proc. IMechE Int. Conf. Turbomachinery—Efficiency Prediction and Improvement*, Paper No. C260/87.

Freeman, C., 1985, "Effect of Tip Clearance on Compressor Stability and Engine Performance," von Karman lecture series *Tip Clearance Effects in Axial Turbomachines*, von Karman Institute.

Hunter, I., and Cumpsty, N. A., 1982, "Casing Wall Boundary Layer Development Through an Isolated Compressor Rotor," ASME *Journal of Engineering for Gas Turbines and Power*, Vol. 104, pp. 872-879.

Moyle, I. N., 1988, "Analysis of Efficiency Sensitivity Associated With Tip Clearance in Axial Flow Compressors," ASME Paper No. 88-GT-216; published in a revised version as "A Note on Efficiency Sensitivity to Tip Clearance Changes in Axial Flow Compressors," ASME JOURNAL OF TURBOMACHINERY, Vol. 112, pp. 795-796.

Raines, D. A., 1954, "Tip Clearance Flows in Axial Flow Compressors and Pumps," California Institute of Technology Hydrodynamics Laboratory Report 5.

Smith, L. H., 1970, "Casing Boundary Layers in Multi-stage Axial Flow Compressors," *Brown Boveri: Flow Research in Blading*, L. S. Dzung, ed., Elsevier, Amsterdam.

Storer, J. A., 1991, Ph.D. Thesis, University of Cambridge.

Storer, J. A., and Cumpsty, N. A., 1991, "Tip Leakage Flow in Axial Compressors," ASME JOURNAL OF TURBOMACHINERY, Vol. 113, pp. 252-259.

Vavra, M. H., 1960, *Aerothermodynamics and Flow in Turbomachines*, Wiley, New York.

Yaras, M. I., and Sjolander, S. A., 1992, "Prediction of Tip-Leakage Losses in Axial Turbines," ASME JOURNAL OF TURBOMACHINERY, Vol. 114, pp. 204-210.

S. Kang[1]

C. Hirsch
Professor.
Mem. ASME

Department of Fluid Mechanics,
Vrije Universiteit Brussel,
Brussel, Belgium

Tip Leakage Flow in Linear Compressor Cascade

Tip leakage flow in a linear compressor cascade of NACA 65-1810 profiles is investigated, for tip clearance levels of 1.0, 2.0, and 3.25 percent of chord at design and off-design flow conditions. Velocity and pressure data are collected from three transverse sections inside tip clearance and sixteen sections within flow passage. Tip separation vortex influence is identified from the data. Leakage flow mixing is clearly present inside the clearance and has a significant influence on the internal loss.

Introduction

It has been recognized that the flow in a blade passage of an axial compressor rotor is influenced by various aerodynamic phenomena. One significant phenomenon is the leakage flow passing through the clearance between rotor blade tip and casing shroud. The losses produced due to the existence of the clearance have been known to occupy an important portion of the rotor overall losses. Many loss correlations and models have been proposed (Rains, 1954; Vavra, 1960; Lakshminarayana, 1970). But there is less detailed information on the fundamental flow nature existing inside the clearance over the whole chord, which limits the complete understanding of the actual loss mechanisms.

Recently, detailed investigations on the tip leakage flow mechanisms in turbine cascades have been published by Moore and Tilton (1988), Sjolander and Amrud (1987), and Bindon (1989). Despite the fact that the experimental models are limited to linear cascades, their results have revealed useful information on the clearance flow and losses. It was found that the losses produced inside the gap are related to the formation of a vena contracta in the gap entrance region and the mixing following the separation. In a compressor cascade, normally with lower ratio of blade thickness to tip clearance height, the flow leaving the tip gap may not be fully mixed out, as in the case of Storer and Cumpsty (1991). These authors studied the tip leakage flow in an axial compressor cascade with circular-arc camber blading in which the ratio of the thickness to the gap height is 2.5, corresponding to 2 percent chord clearance. For other typical compressor bladings, such as the NACA 65 series used by Inoue and Kuroumaru (1989) in their series of studies on a compressor rotor, the ratio of thickness to tip height may be larger, so that the mixing may not be negligible.

In this paper, attention is given to the tip leakage flow in a linear compressor cascade with stationary walls at different tip clearances and two flow conditions. The leakage flow is explored with the help of wall static pressure tappings, which are distributed over a large portion of the pitch at several chord sections, and a small size pitot tube used to measure the gap velocity profiles. In addition, the whole flow field inside and behind the passage is also measured with a five-hole probe. From the collected data, a number of flow features occurring in the tip gap can be clearly identified.

Experimental Facility and Instrumentation

The present investigations were carried out in the low-speed compressor cascade wind tunnel of the Department of Fluid Mechanics, Vrije Universiteit Brussel (VUB), described by Kang and Hirsch (1991). The cascade consists of seven NACA 65-1810 blades with flat tips. The aspect ratio is 1.0 with blade chord of 200 mm. The pitch is 180 mm. The tip clearance heights are 1.0, 2.0, and 3.25 percent of chord with an uncertainty of ±0.1 mm for the seven tip gaps. The system and methods for data acquisition are the same as that described by the authors in the previous paper (Kang and Hirsch, 1993a).

Traverse measurements with a five-hole probe were conducted at 16 planes from 7.5%c upstream of the leading edge to 50%c downstream of the trailing edge. In each plane, 24 stations from the suction side to the pressure side and 33 stations behind the cascade were arranged; fifteen points from near wall to midspan were recorded.

The tip leakage flow studied are those at three tangential sections No. 4 (22%c), 6 (44%c), and 8 (66%c), indicated in Fig. 1. The ratios of the local blade thickness to the tip gap heights are presented in Table 1. These sections are of course not coincident with the tip leakage flow traces. But, from the results of Moore and Tilton (1988), who measured the wall static pressures beneath a turbine blade tip, the profile of static pressure is not sensitively affected by whether the tappings are aligned in the flow direction or not. The wall pressure distributions along these three sections were measured using static pressure tappings (with diameter of 0.6 mm) under the middle blade of the cascade, covering about half of the pitch.

Leakage flow velocity was measured at the tip gap exit with a pitot tube, for the inlet flow angle of 36.5 deg (off-design)

---

[1] Permanent address: Power Engineering Dept., Harbin Institute of Technology, Harbin 150006, People's Republic of China.

Contributed by the International Gas Turbine Institute and presented at the 38th International Gas Turbine and Aeroengine Congress and Exposition, Cincinnati, Ohio, May 24–27, 1993. Manuscript received at ASME Headquarters March 12, 1993. Paper No. 93-GT-303. Associate Technical Editor: H. Lukas.

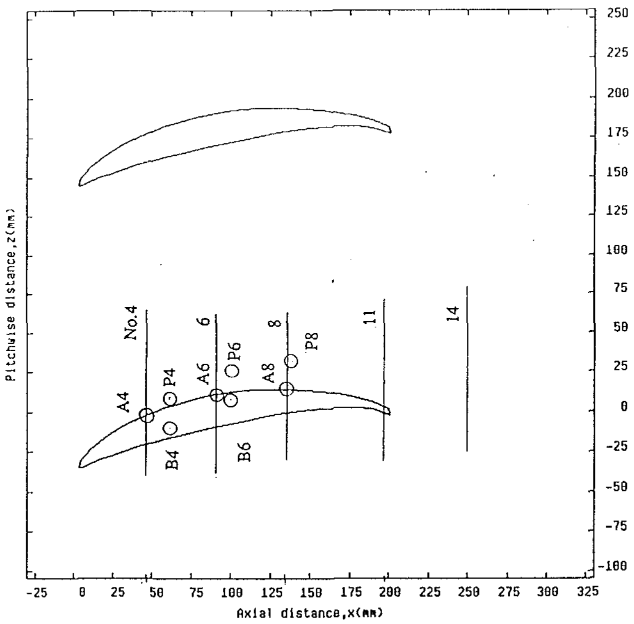

Fig. 1 Cascade geometry and measurement locations

Table 1 Ratios of local blade thickness t_b to tip gap height τ

	τ/c=1.0%	τ/c=2.0%	τ/c=3.25%
No.4	8.65	4.33	2.66
No.6	9.96	4.98	3.06
No.8	7.95	3.98	2.45

at 2.0 and 3.25 percent clearances. By using the wall static pressure at the exit, the velocity could be approximately calculated. The probe with a flatten tip with thickness of 0.5 mm has an uncertainty of 5 percent on the flow direction. The measurement locations at each of the tangential sections are indicated by A4, A6, and A8 in Fig. 1. The probe was located respectively at P4, P6, and P8 and aligned in the wall flow direction, as read from the visualization pictures. It was found that for increasing clearances from 2.0 to 3.25 percent, the flow direction at the three measured location changes less than 10 deg. Hence, the probe was always inserted into the flow field from these points, for both clearances. With the help of a special device, the probe can be moved down and up over the gap height with a readable displacement of 0.01 mm. Over most of the gap height, the measurement accuracy is acceptable with the largest difference of the flow direction between the wall and the blade tip being 15 ~ 25 deg, read from the visualization pictures, at the three measured locations.

In addition, the flows at locations B4 ($z = 5$ mm from the pressure side edge; $x = 60$ mm from the leading edge) and B6 (95 mm from the leading edge and 15 mm from the pressure side edge), inside the tip gap, were also measured. At these two locations, the probe was still placed at P4 and P6 but aligned in the local flow direction at midgap, along which the probe took its highest readings. Although it is argued that the probe would not be aligned exactly in the flow direction over the whole gap, this does not adversely affect accuracy in the measurement of total pressure and speed, due to the above-mentioned direction insensitivity of the probe.

Test Conditions

The inlet boundary layer was incompressible and turbulent as indicated by Kang and Hirsch (1991). The integral parameters of the inlet endwall boundary layer, at 40 percent chord upstream of the leading edge, are $\delta^*/c = 0.144$, $\theta/c = 0.118$, and $H = 1.22$. The test Reynolds number, based on blade chord, was about 3.0×10^5; free-stream turbulence intensity was 3.4 percent. Two flow conditions, with different inlet flow angles, were studied. The mass-average inlet flow angles, measured 40 percent chord upstream, were 29.3 and 36.5 deg (design and off-design), the corresponding outlet flow angles, measured 25 percent chord downstream, were -2.5 and -1.4, deg respectively.

Static Pressure Distribution on Blade Surfaces

The static pressures of blade surfaces were recorded by static pressure tappings on the middle blade of the cascade at three spanwise positions, 1.5, 15, and 50 percent (midspan) from the tip. Figure 2 shows the pressure distributions near the tip (1.5 percent span) at various clearance cases, including zero clearance, at both inlet flow conditions.

Without clearance, the pressure distribution near the tip is similar to those at other span heights, except for a slight unloading or blade force defect, caused from the endwall secondary flow. With increasing tip clearance, the unloading increases near the leading edge, and the minimum pressure on the suction surface decreases at both flow conditions. The strong reloading, from 15 percent chord downstream of the leading edge, results from the low pressure core of the tip leakage vortex. It is seen that the reloading decreases with increasing flow angle from 29.3 deg (Fig. 2*a*) to 36.5 deg (Fig. 2*b*), which may be related to the difference in the locations of the tip leakage vortex core. It is found that the vortex core center shifts away from the suction surface with increasing flow angle, as shown in Fig. 3. Figure 3 presents the pitchwise coordinate L_z of the vortex core center, with the method described by Kang and Hirsch (1993b). The minimum pressure (or maximum loading) point shifts downstream, at the off-design condition, from $x/c = 0.2$ at $\tau/c = 1.0$ to $x/c = 0.27$ and 0.33 at $\tau/c = 2.0$ and 3.25 percent, respectively. But, it remains almost at the same location ($x/c = 0.41$) at the design conditions, with increasing clearance from 1.0 to 2.0 percent. As we will see later, up- or downstream of the minimum pressure point, the leakage flow exhibits different features.

The locations of the tip leakage flow measurements are also indicated in Fig. 2. It is seen that at the design condition, plane No. 4 is immediately downstream of the point where the suction surface pressure at midspan reaches its minimum value, at

Nomenclature

$Av.$ = averaged
BT = blade tip
c = blade chord
C_p = static pressure coefficient
C_{tp} = total pressure coefficient
C_{tpa} = averaged tip exit total pressure coefficient
H = shape factor
LE = leading edge
P_{01} = total pressure at gap entrance
P_{exit} = static pressure at gap exit
Re_τ = tip leakage flow Reynolds number
s = pitch
SS = suction side
t_b = local blade thickness
TE = trailing edge
U_a = mass-averaged tip exit velocity
V_1 = inlet resultant velocity
x, y, z = axial, spanwise, and pitchwise distance
β_1 = inlet flow angle
δ^* = displacement thickness
θ = momentum thickness
τ = tip clearance

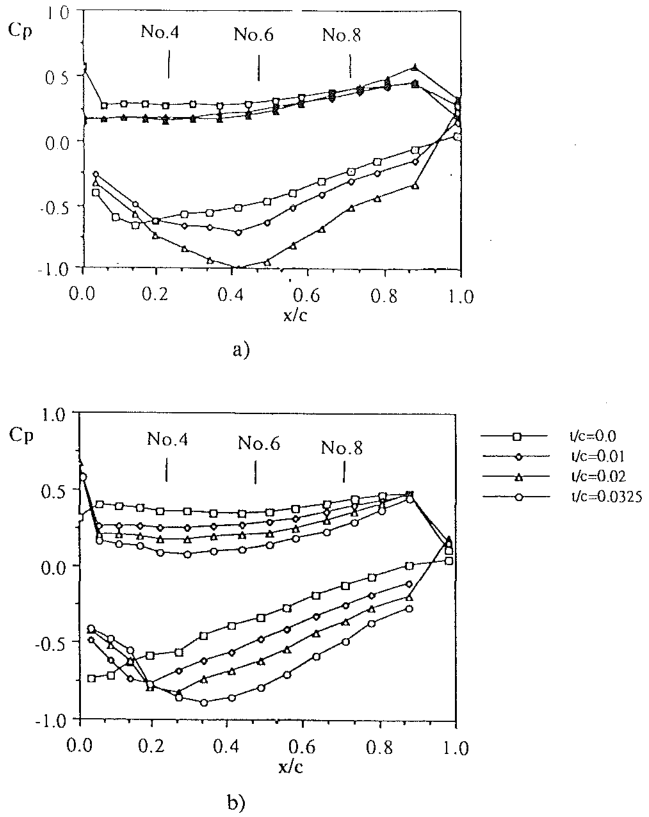

Fig. 2 Static pressure distribution on blade surface near the tip, 1.5 percent span away from the tip, at (*a*) design and (*b*) off-design conditions

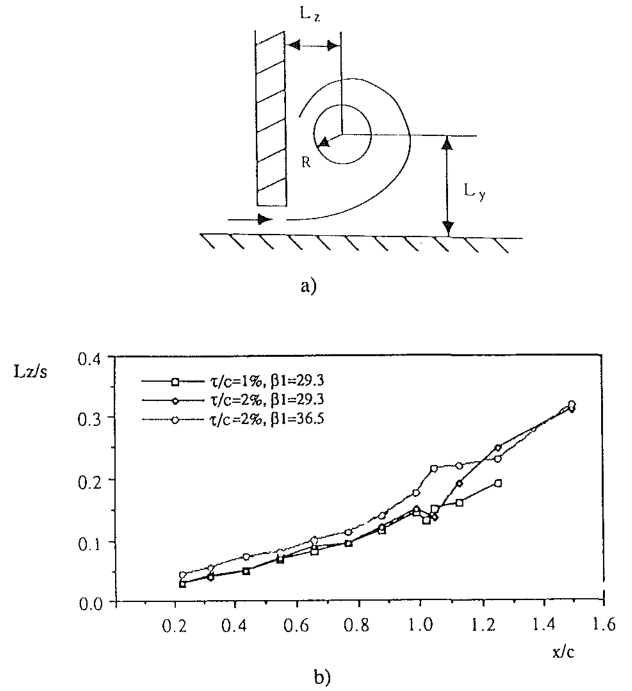

Fig. 3 (*a*) Definition of tip vortex geometry, and (*b*) evolution of tip vortex core location L_z in the main stream direction, obtained with the method of Kang and Hirsch (1993b)

about 15%c, but is upstream of the minimum pressure point near the tip; plane No. 6 is immediately behind the point of the highest blade thickness where the pressure near the tip at 1.5 percent span reaches a minimum value; while plane No. 8 is located at the region with a large adverse gradient.

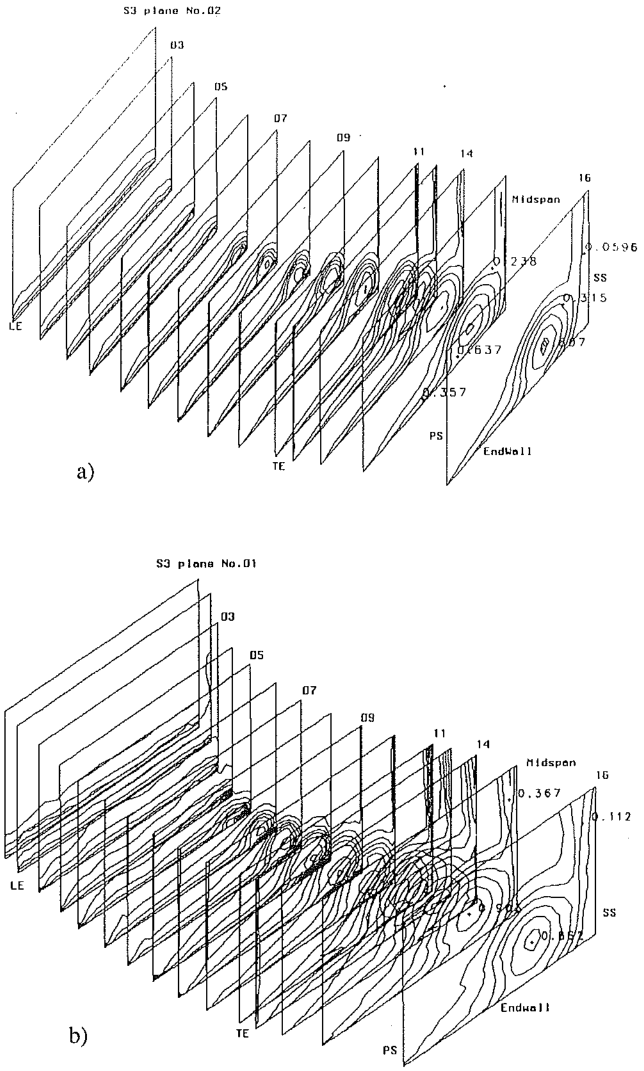

Fig. 4 Contours of total pressure loss on traverse planes at 2.0 percent clearance at (*a*) design and (*b*) off-design conditions, interval = 0.14

Total Pressure Loss in the Passage

Figure 4 shows the contours of total pressure loss on all the traverse planes (S_3 planes) measured from 7.5%c (S_3 plane No. 01) upstream of the leading edge to 50%c (S_3 plane No. 16) downstream of the exit at 2.0 percent clearance for both flow conditions. The leading edge is at plane No. 02 and the trailing edge is located 2 mm downstream of plane No. 11. Close to the leading edge, the total pressure contours are basically uniform over the whole pitch for both cases. Starting from plane No. 03, however, the loss is reaching lower values in the pressure side corner and higher values in the suction side corner. The high total pressure loss region with quasi-circular isolines in the corner represents the development of the tip leakage vortex. As seen from plane No. 16 in Fig. 4, the core loss is increased about 7 percent from the design to off-design conditions.

Leakage Flow Behavior

(*a*) **Distributions of Wall Static Pressures.** Figure 5 and 6 show the wall static pressure coefficient for different clearances along the traverse planes No. 4, 6, and 8 at design and off-design conditions, respectively. The pressure coefficient is nondimensionalized with the cascade inlet static pressure and dynamic pressure. The tangential coordinate z is nondimen-

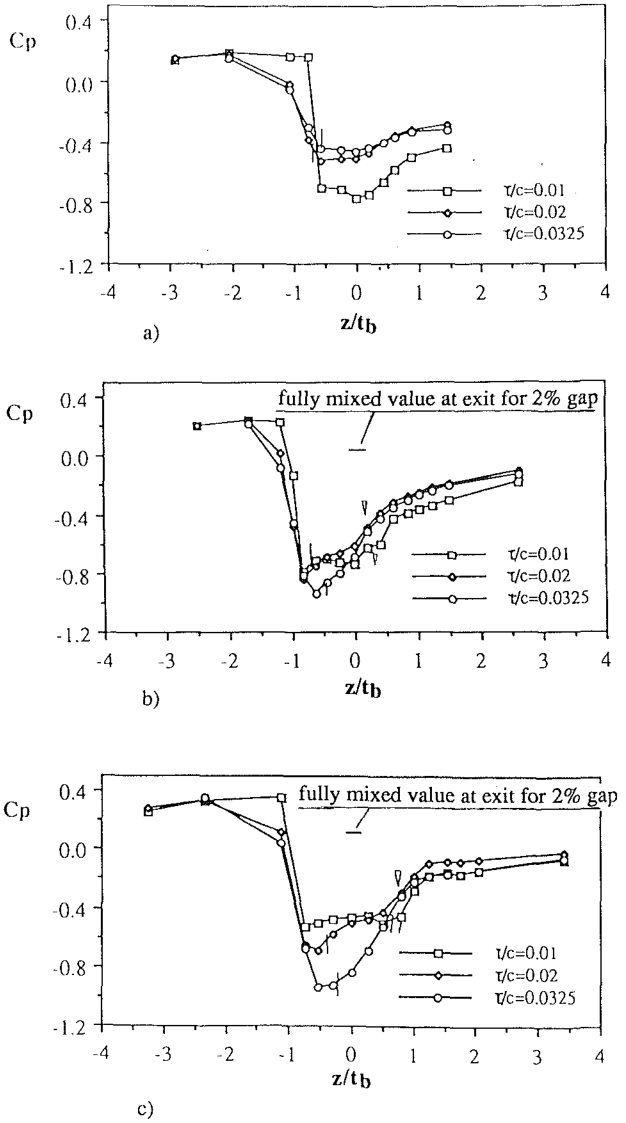

Fig. 5 Wall static pressure distribution across the blade profile for various clearances at the design condition at the sections: (*a*) No. 4, (*b*) No. 6; and (*c*) No. 8; ▽ position of separation line L_L (Fig. 7); and | position of divergence line in tip surface (Fig. 8)

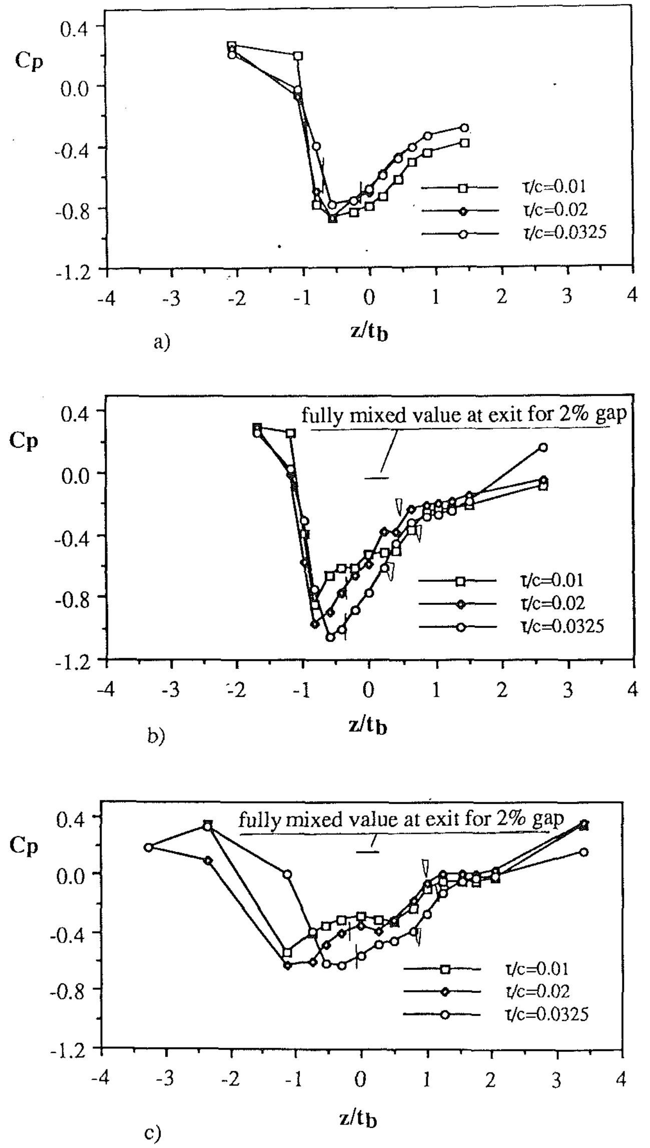

Fig. 6 Wall static pressure distribution across the blade profile for various clearances at the off-design condition at the sections: (*a*) No. 4, (*b*) No. 6; and (*c*) No. 8; ▽ position of separation line L_L (Fig. 7); and | position of divergence line on the tip surface (Fig. 8)

sionalized with the local blade thickness t_b. Hence, $z/t_b=0$ refers always to the suction side and $z/t_b=-1.0$ to the pressure side. Figure 7 represents the visualization observations of the endwall flow pattern, by Kang and Hirsch (1993a). The locations of the tip leakage vortex separation line L_L (Fig. 7) are indicated in Figs. 5 and 6 with a downward pointing triangle. Figure 8 presents the flow pattern on the tip surface, based on the visualizations of Kang and Hirsch (1993a). It was observed that limiting streamlines on the tip surface diverged from about the middle of the blade profile (the dashed line in Fig. 8) and converged toward the tip edges over about 70 percent chord length from the leading edge. The limiting streamlines, converging toward the pressure side edge, are related to the rotation of the tip separation vortex. This vortex is similar to the so-called separation bubble or vena contracta, as referred to by Rains (1954) and Moore and Tilton (1988). It increases in size and strength along the chordwise distance. The locations of the divergence line on the tip surface at each of the sections are also indicated in Fig. 5 and 6 with short vertical lines for 2.0 and 3.25 percent clearances.

Figures 5 and 6 show that in the pressure side corner, $z/t_b<-1.0$, the pressure reaches almost the same maximum value for different tip clearances. The location of the points with maximum pressure value coincides with the reattachment line L_L in Fig. 7. Close to the tip gap entrance, $z/t_b=-1.0$, the flow experiences an abrupt contraction of the flow cross-sectional area. Hence, the static pressure falls down rapidly. With increasing tip clearance, or decreasing contraction ratio, the pressure tends to fall down slowly. This phenomenon is similar to orifice flow.

Inside the tip gap, the pressure distribution at the smallest clearance 1.0 percent is basically different from those at the larger clearances. At low clearance level, the dominating term of the momentum balance of the leakage flow is the shear forces. But at the high level clearance, convection will become dominant with relatively small viscous effects. At the higher clearance, 2.0 and 3.25 percent, the pressure reaches its minimum value just in the entrance. This is related to tip separation vortex in Fig. 8 or the vena contracta mentioned by Rains (1954). With increasing tip clearance, the minimum pressure tends to decrease, as shown in Table 2, except for section No. 4. After the tip separation vortex, the wall pressure starts recovering from its minimum value. With the recovery process, the tip flow would be mixing, as mentioned by Moore and Tilton (1988). But, due to the relatively thin blade thickness

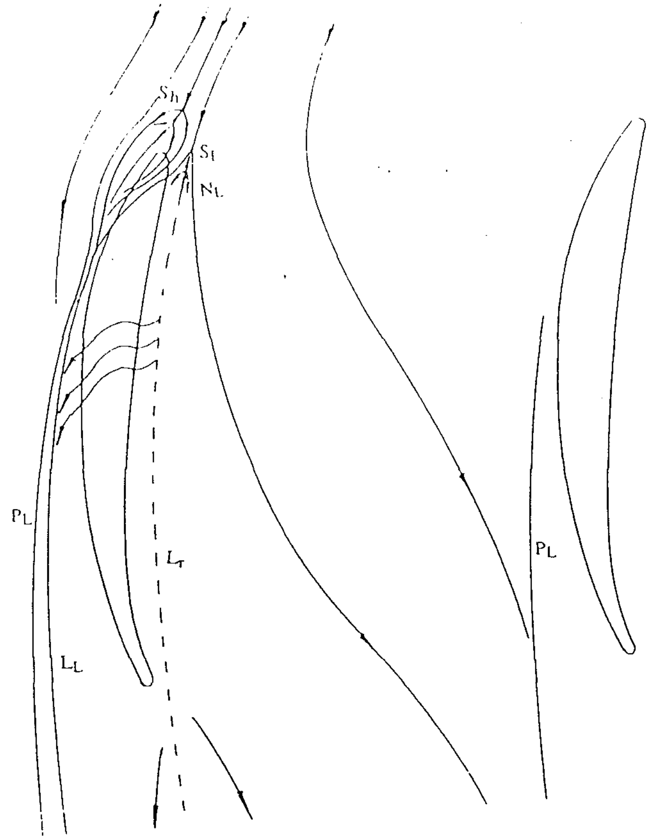

Fig. 7 Schematic of the endwall flow pattern at $\tau/c = 0.02$ at the design condition, from Kang and Hirsch (1993a); P_L—separation line of passage vortex; L_L—separation line of tip leakage vortex; L_r—reattachment line of passage vortex; S_h and S_L—saddle points; and N_L—node point

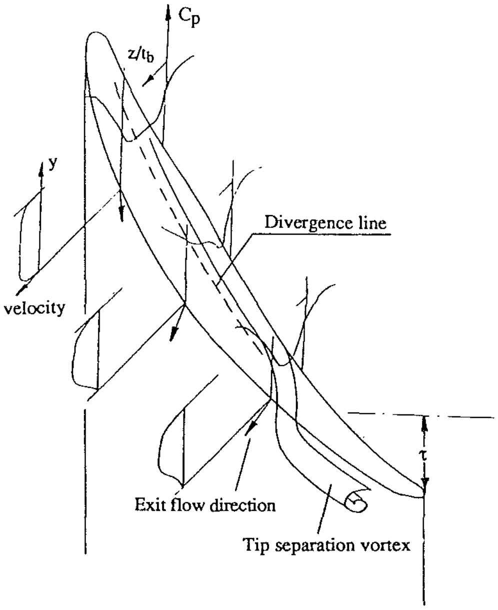

Fig. 8 Schematic of tip leakage flow pattern, with the pitchwise profiles of wall static pressures and the exit velocities in clearance

Table 2 Minimum pressures on the endwall under the blade

$\beta_1 = 29.3$ deg

	τ/c=1.0%	τ/c=2.0%	τ/c=3.25%
No.4	-0.777	-0.520	-0.462
No.6	-0.780	-0.838	-0.939
No.8	-0.525	-0.697	-0.937

$\beta_1 = 36.5°$

	τ/c=1.0%	τ/c=2.0%	τ/c=3.25%
No.4	-0.881	-0.879	-0.787
No.6	-0.844	-0.967	-1.052
No.8	-0.531	-0.626	-0.626

in the present case, the mixing process is not completed at the gap exit. Figure 5 and 6 also show the fully mixed pressure value at the exit for 2.0 percent clearance at sections No. 6 and 8. This value is predicted by means of the method of Moore and Tilton (1988), assuming the leakage flow is fully mixed out at the gap exit. The difference between the measured value and the predicted one may indicate the incomplete mixing of the present leakage flow. The recovery process tends to continue in the flow passage.

With increasing tip clearance, the static pressures in sections No. 6 and 8 decrease, while the reverse tendency occurs at section No. 4, especially when the tip gap is increased from 1.0 to 2.0 percent at the design condition, Fig. 5(*a*). The visualization (Kang and Hirsch, 1993a) shows that at larger clearance, the wall flow traces under the tip, from the leading edge to about 30%c, are less inclined to the tangential direction than at smaller clearances, and also that the flow near the leading edge is less inclined to the tangential direction than around midchord. This implies that the leakage flow is dominated by streamwise pressure gradient near the leading edge and by transverse pressure gradient over the other portion of the chord. With increasing tip clearance, streamwise pressure gradient tends to dominate the leakage flow.

(*b*) **Pressure Drop Over Clearance Gap.** The pressure differences over the clearance gap at the three sections are presented in Table 3, which includes the data from both the endwall and the blade tip at the two flow conditions. The pressure difference of the blade at 1.5 percent span, taken from Fig. 2, is approximately considered as the tip pressure difference, denoted by "*BT*" in Table 3. The endwall data ("Wall"), taken from Figs. 5 and 6, are the pressure difference between the largest value at the pressure side corner and the pressure at the gap exit. The averaged data of the tip and wall are also given in Table 3 with "*Av.*" From this table, the following observations can be made.

Near the blade tip the pressure differences increase with tip clearance at all the sections, except at section No. 4 at the off-design condition. This indicates that the reloading around the blade tip due to the existence of tip leakage vortex is stronger at higher tip gap scale.

On the wall, the pressure difference at section No. 4 decreases with tip clearance at all the conditions, but at section No. 8 the difference increases with tip clearance. At section No. 6, the data seem scattered. However, realizing that the maximum loading (close to section No. 6) near the tip is shifted forward with inlet flow angle (see Fig. 2), it can be concluded that with increasing tip clearance the wall pressure drop decreases before the maximum loading point but increases after that point.

The average, between tip and wall, of the clearance gap pressure drop, which would be the driving force of the leakage flow, decreases with clearance at section No. 4, and increases at the other sections.

(*c*) **Profiles of Exit Velocity and Loss.** The tip gap exit velocity and total pressure loss, measured at the three locations A4, A6, and A8 (Fig. 1), are shown in Figs. 9 and 10 for 2.0 and 3.25 percent clearances at off-design condition. The velocity and total pressure are both nondimensionalized with cascade inlet data. The value $y/\tau = 0$ corresponds to the endwall

Table 3 Pressure differences between tip gap inlet and exit

β_1=29.3°

	τ/c=1.0%			τ/c=2.0%			τ/c=3.25%		
NO.	BT	Wall	Av.	BT	Wall	Av.	BT	Wall	Av.
4	0.820	0.966	0.893	0.950	0.791	0.871		0.615	
6	0.896	0.986	0.941	1.170	0.850	1.010		0.907	
8	0.692	0.819	0.756	0.944	0.837	0.891		1.182	

β_1=36.5°

	τ/c=1.0%			τ/c=2.0%			τ/c=3.25%		
NO.	BT	Wall	Av.	BT	Wall	Av.	BT	Wall	Av.
4	0.984	1.078	1.031	0.987	0.956	0.972	0.908	0.887	0.898
6	0.793	0.823	0.808	0.861	0.886	0.874	0.958	1.020	0.988
8	0.643	0.630	0.637	0.700	0.542	0.621	0.793	0.886	0.840

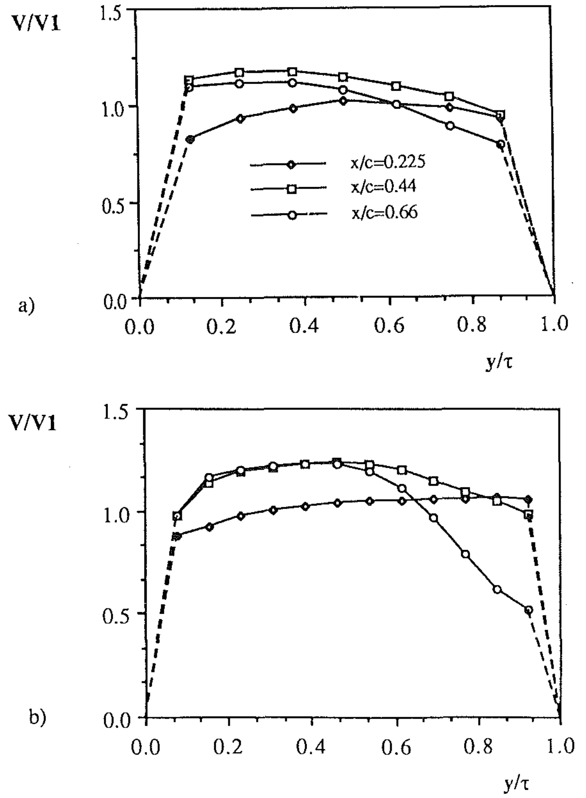

Fig. 9 Tip gap exit velocity distribution at different sections for clearance of (*a*) 2.0 percent and (*b*) 3.25 percent at off-design condition

and $y/\tau = 1.0$ is at the blade tip surface. The flow directions at the three locations, averaged from the limiting streamline directions on the wall and tip surface, are shown in Fig. 8. It is seen that the tip leakage flow exhibits different behavior upstream and downstream of the minimum suction surface pressure near the blade tip. Downstream of the minimum pressure point, No. 6 and No. 8, the profiles show a distinct wake character. The wake profiles, caused from the development of the tip separation vortex or vena contracta, indicate the incomplete mixing of the leakage flow. Due to the increasing vortex size, the wake profiles become much more apparent with distance, especially at 66 percent chord location (No. 8) at 3.25 percent clearance. In section No. 4, however, the velocity at both clearances show clearly symmetric profiles.

From the exit loss distributions in Fig. 10, it is seen that at section No. 4, upstream of the maximum loading point at the tip, the loss near the endwall is higher than at the other sections. As indicated in Fig. 7, the clearance flow near the leading edge comes directly from the inlet boundary layer, but over the rear 75%c, the clearance flow comes from the reattachment line L_r in the pressure side corner, with thin boundary layer and high energy as seen from Fig. 4.

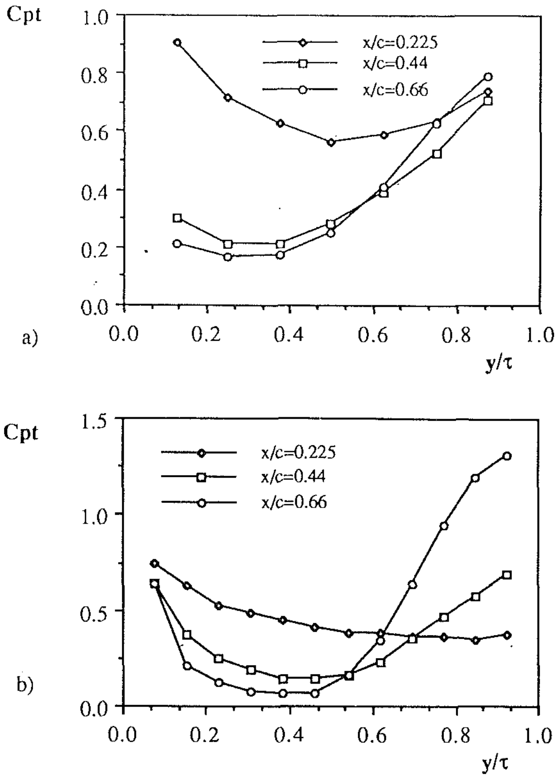

Fig. 10 Tip gap exit total pressure loss distribution at different sections for clearance of (*a*) 2.0 percent and (*b*) 3.25 percent at off-design condition

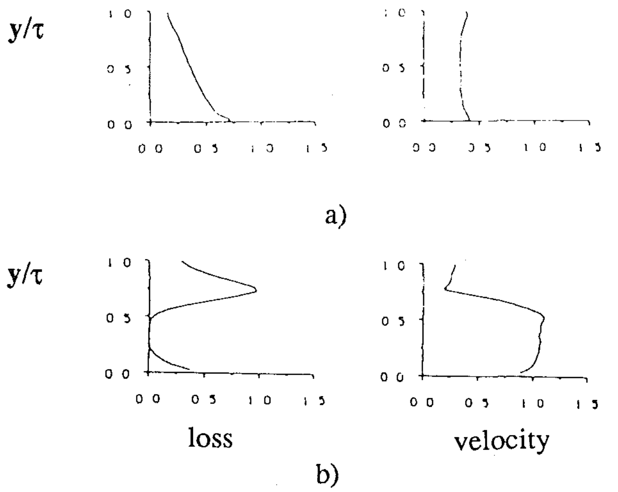

Fig. 11 Profiles of total pressure loss and velocity at gap exit at 4 percent clearance, measured by Storer and Cumpsty (1991), at (*a*) 14%c and (*b*) 63%c

Figure 11 shows the profiles of total pressure loss and velocity at gap exit, measured by Storer and Cumpsty (1991) at 4 percent clearance in (*a*) 14%c and (*b*) 63%c. Comparing to Figs. 9 and 10, it is seen that the profiles over the whole chord in the two measurements are quite similar. Since the ratio of blade thickness to gap height in the present case is almost twice

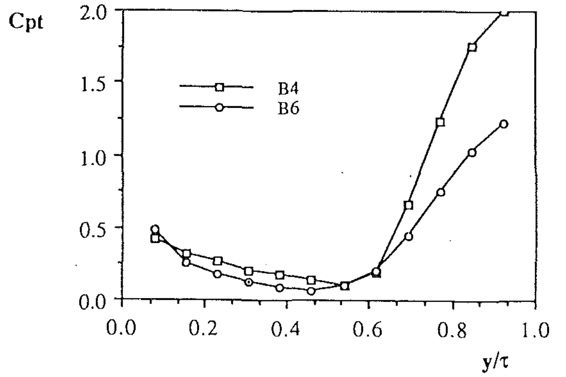

Fig. 12 Total pressure loss distribution inside the tip gap at locations B4 and B6, indicated in Fig. 1, at 3.25 percent clearance at off-design condition

the value in Storer and Cumpsty (1991), the wake profile is not so clear in Figs. 9 and 10 as in Fig. 11.

Figure 12 shows the distributions of the total pressures at the locations B4 and B6 inside the tip gap, as indicated in Fig. 1. From visualization observations (Kang and Hirsch, 1993a), it is known that B6 is located at the suction side of the divergence line on the tip surface (Fig. 8), but B4 is near the divergence line at its pressure side. It is seen that at both locations the total pressure losses close to the tip are much larger than those at the gap exit, A4 and A6, since the traverse measurement may go into or close to the vena contracta.

Averaged Quantities

The overall nature of the tip leakage flow is analyzed by means of the area-averaged exit velocity, leakage flow Reynolds number, discharged coefficient, and total pressure loss, shown in Tables 4 and 5 with their definitions, for both tip clearance cases at the three axial locations.

(*a*) Averaged Velocity and Total Pressure Loss. Table 4 shows the averaged exit velocities, tip leakage flow Reynolds numbers, and discharge coefficients. It is seen that with increase tip clearance, the exit velocity at each section increases. At sections No. 6 and 8, the increment is correlated with the increase of the pressure drop in Table 3. At the near-leading edge section, No. 4, the increment may be due to both the local static pressure and dynamic pressure of the cascade inlet flow. At each clearance, the largest exit velocity takes place at 44 percent chord, No. 6, which is just downstream of the largest tip pressure difference point (Fig. 2). The variation of exit flow Reynolds number, shown in Table 4, exhibits a tendency similar to the velocities with locations and tip gap size.

But the variation of the exit total pressure loss in Table 5 is unclear. As seen from Fig. 10, the averaged losses at section No. 4 are higher. Total pressure loss measured at the gap exit should include the gap inlet loss and the gap internal loss. The internal loss is due to the generation of the separation followed by mixing and the development of the endwall boundary layer passing through the gap region. The gap inlet loss, however, is due to the endwall shear layer flow being entrained into the gap. Considering the short distance from inlet to exit and that the development of the clearance loss is mainly limited to the tip side, the core values (the minimum) in the exit loss distributions (Fig. 10) may be approximately taken as the inlet loss value. The internal loss, the difference between the exit and the inlet losses, is also shown in Table 5. It is seen that the internal loss is low at section No. 4 and increases along chord with the growth of the tip separation vortex, corresponding to the development of the tip separation vortex. The internal loss, mainly caused from mixing, takes about 35 to 80 percent of the exit loss, except near the leading edge, even though the mixing process is not complete at the exit.

Table 4 Area-averaged velocity U_a/V_1, tip leakage flow Reynolds $Re_\tau = U_a\tau/\nu$ and discharge coefficient $D_c = U_a/(1 - C_{pexit})^{1/2}$; $\beta_2 = 36.5$ deg

	τ/c=2.0%			τ/c=3.25%		
	U_a/V_1	$Re_\tau x10^{-4}$	D_c	U_a/V_1	$Re_\tau x10^{-4}$	D_c
No.4	0.835	0.49	0.638	0.939	0.90	0.723
No.6	0.963	0.56	0.763	1.055	1.01	0.793
No.8	0.885	0.52	0.760	0.949	0.90	0.760

Table 5 Area-averaged C_{pta}, $\beta_1 = 36.5$ deg

	τ/c=2.0%		τ/c=3.25%	
	exit	internal	exit	internal
No.4	0.597	0.036	0.421	0.074
No.6	0.329	0.116	0.324	0.184
No.8	0.329	0.159	0.427	0.356

(*b*) Discharge Coefficient. The discharge coefficient of the leakage flow passing through the tip gap is evaluated by using the averaged exit velocities and the pressure difference $P_{01} - P_{\text{exit}}$. In the present study, the wall static pressure at the exit is taken as P_{exit} with the approximate consideration that the exit flow is uniform. With the thin endwall boundary layer in the pressure side corner (Fig. 4), the total pressure at the corner is approximately equal to the cascade inlet one. It is seen from Table 4 that with increasing clearance, the discharge coefficients at sections No. 6 and 8 remain almost constant with a variation of ±0.015. But the discharge coefficient at section No. 4, close to the leading edge, is significantly smaller, about 10 to 20 percent, than at the other sections. This might justify the observations of Storer and Cumpsty (1991), who took a constant discharge coefficient to calculate the leakage flow with Rains' model, obtained a good agreement between the predicted and experimental data over the rear 70%c, but overpredicted the leakage flow near the leading edge. The discharge coefficient taken to fit their experimental results is 0.8, which is close to the present data 0.77, averaged over the two cases at sections No. 6 and No. 8. Comparing to the data obtained in turbine cascades, such as 0.843 by Moore and Tilton (1988) at Reynolds number of 1.0×10^4 and 0.851 by Wadia and Booth (1982) at Reynolds number of 0.65×10^4, the discharge coefficients at all the sections in the present compressor cascade are smaller, which may be due to the fact that the present leakage flow is not fully mixed at the gap exit due to the relatively thin blade profile. In addition, the tip leakage flow would be increased with the relative motion between the blade tip and the wall in a compressor rotor. Hence the discharge coefficients in a real machine may be larger than those obtained here from a stationary cascade.

Conclusions

Detailed mechanisms of the tip leakage flow in a linear compressor cascade have been investigated, by means of the endwall static pressures and tip gap exit velocities at different chordwise sections. As summarized in Fig. 8, the flow close to the tip surface diverges from about the middle of the blade profile and produces a tip separation vortex at the gap entrance. This vortex increases in size and strength along the chord. Due to the contracted area of the tip gap, the fluid moving toward the gap is accelerated. This acceleration continues a short distance inside the gap, affected by the vortex motion. After the vortex, the wall pressure tends to recover with the leakage flow mixing. In the present cases, the mixing process is not fully completed at the gap exit, especially at section No. 8, as the gap exit velocity shows a wakelike profile close to the tip. With increasing tip clearance, or decreasing ratio of blade thickness to tip clearance, the mixing process tends to disappear. Near the blade leading edge or upstream of the maximum blade loading point, the wall static pressure inside the gap is normally uniform due to the fact that the leakage flow here is dominated by the streamwise pressure gradient, and the gap exit flow is fully developed. No apparent difference is found between the leakage flows at the design and off-design conditions.

References

Bindon, J. P., 1989, "The Measurement and Formation of Tip Clearance Loss," ASME JOURNAL OF TURBOMACHINERY, Vol. 111, pp. 257-263.

Inoue, M., and Kuroumaru, M., 1989, "Structure of Tip Clearance Flow in an Isolated Axial Compressor Rotor," ASME JOURNAL OF TURBOMACHINERY, Vol. 111, pp. 250-256.

Kang, S., and Hirsch, Ch., 1991, "Three Dimensional Flows in a Linear Compressor Cascade at Design Conditions," ASME Paper No. 91-GT-114.

Kang, S., and Hirsch, Ch., 1993a, "Experimental Study on the Three-Dimensional Flow Within a Compressor Cascade With Tip Clearance: Part I—Velocity and Pressure Fields," ASME JOURNAL OF TURBOMACHINERY, Vol. 115, pp. 434-443.

Kang, S., and Hirsch, Ch., 1993b, "Experimental Study on the Three-Dimensional Flow Within a Compressor Cascade With Tip Clearance: Part II—The Tip Leakage Vortex," ASME JOURNAL OF TURBOMACHINERY, Vol. 115, pp. 444-452.

Lakshminarayana, B., 1970, "Method of Predicting the Tip Clearance Effects in Axial Flow Turbomachinery," ASME *Journal of Basic Engineering*, Vol. 92, pp. 467-480.

Moore, J., and Tilton, J. S., 1988,"Tip Leakage Flow in a Linear Turbine Cascade," ASME JOURNAL OF TURBOMACHINERY, Vol. 110, pp. 18-26.

Rains, D. A., 1954, "Tip Clearance Flow in Axial Compressors and Pumps," California Institute of Technology, Mech. Eng. Laboratory, Report 5.

Sjolander, A., and Amrud, K. K., 1987, "Effects of Tip Clearance on Blade Loading in a Planar Cascade of Turbine Blades," ASME JOURNAL OF TURBOMACHINERY, Vol. 109, pp. 237-244.

Storer, J. A., and Cumpsty, N. A., 1991, "Tip Leakage Flow in Axial Compressors," ASME JOURNAL OF TURBOMACHINERY, Vol. 113, pp. 252-259.

Vavra, M. H., 1960, *Aero-thermodynamics and Flows in Turbomachines*, Wiley, New York.

Wadia, A. R., and Booth, T. C., 1982, "Rotor-Tip Leakage: Part II—Design Optimization Through Viscous Analysis and Experiment," ASME *Journal of Engineering for Power*, Vol. 104, pp. 162-169.

Numerical Simulations of Unsteady Cascade Flows

D. J. Dorney
Computational & Design Methods.

J. M. Verdon
Theoretical & Computational Fluid Dynamics.

United Technologies Research Center,
East Hartford, CT 06108

A time-accurate Navier–Stokes analysis is needed for understanding the relative importance of nonlinear and viscous effects on the unsteady flows associated with turbomachinery blade vibration and blade-row noise generation. For this purpose an existing multi-blade-row Navier–Stokes analysis has been modified and applied to predict unsteady flows excited by entropic, vortical, and acoustic disturbances through isolated, two-dimensional blade rows. In particular, time-accurate, nonreflecting inflow and outflow conditions have been implemented to allow specification of vortical, entropic, and acoustic excitations at the inlet, and acoustic excitations at the exit, of a cascade. To evaluate the nonlinear analysis, inviscid and viscous numerical simulations were performed for benchmark unsteady flows and the predicted results were compared with analytical and numerical results based on linearized inviscid flow theory. For small-amplitude unsteady excitations, the unsteady pressure responses predicted with the nonlinear analysis show very good agreement, both in the field and along the blade surfaces, with linearized inviscid solutions. Based on a limited range of parametric studies, it was also found that the unsteady responses to inlet vortical and acoustic excitations are linear over a surprisingly wide range of excitation amplitudes, but acoustic excitations from downstream produce responses with significant nonlinear content.

Introduction

The need for improved structural durability and reduced noise levels has motivated engineers to understand and predict the effects of flow unsteadiness on the aeroelastic and aeroacoustic performance of axial-flow turbomachinery blade rows. Until recently, the unsteady aerodynamic analyses that have been used in turbomachinery aeroelastic and aeroacoustic design studies were based on classical linearized theory (Whitehead, 1987), which essentially applies to cascades of unloaded flat-plate blades that operate in entirely subsonic or entirely supersonic flow environments. During the past decade, more general unsteady aerodynamic linearizations have been developed (e.g., Verdon, 1990; Whitehead, 1990; Hall and Clark, 1993), which account for the effects of important design features, such as real blade geometry, finite steady blade loading, and operation at transonic Mach numbers, on the unsteady aerodynamic response. This type of model has received considerable attention in recent years and numerical methods and computer codes for solving the resulting linearized equation sets are beginning to be applied in aeroelastic design prediction systems (Smith, 1990).

Although linearized inviscid analyses meet the needs of aeroelastic designers for computationally efficient unsteady aerodynamic predictions, of necessity, they ignore potentially important physical and geometric properties of the flow, including the effects of viscous layer displacement and separation, and the effects of nonlinear unsteady excitation. Since the early 1980s, a number of time-accurate Euler and Navier–Stokes procedures have been developed to predict blade-row unsteady flows (see Verdon, 1993, for a review). These have been applied to predict flows through single blade rows in which the unsteadiness is caused by blade vibrations (Huff and Reddy, 1989; He, 1990; Siden, 1991) or by aerodynamic disturbances at the inflow or outflow boundaries (Giles, 1988), and flows through aerodynamically coupled arrays in which the unsteadiness is caused by the relative motions between the blade rows (Rai, 1987, 1989).

These recent and important advances in the numerical simulation of unsteady turbomachinery flows suggest that it is now appropriate to validate carefully and, if necessary, extend a time-accurate, unsteady, Navier–Stokes procedure for the prediction of turbomachinery aeroelastic and aeroacoustic response phenomena. Usually, numerical procedures are verified via comparisons with experimental data (e.g., Manwaring and Wisler, 1993), but because of the numerous controlling parameters involved it is often difficult to ascertain precise causes for the differences between the numerical and experimental results. In the present effort, we have taken a different approach, one in which solutions based upon very different analytical procedures are compared both to validate the procedures and to understand relevant unsteady flow phenomena better.

A validated Navier–Stokes analysis for high-frequency unsteady flows will represent a major advance in turbomachinery unsteady aerodynamic theory. This numerical simulator (or "wind tunnel") can provide engineers with new insights on the nonlinear and viscous effects associated with blade vibration and discrete-tone noise generation. It can also provide a test bed for assessing and improving the analytical (i.e., lin-

---

Contributed by the International Gas Turbine Institute and presented at the 38th International Gas Turbine and Aeroengine Congress and Exposition, Cincinnati, Ohio, May 24–27, 1993. Manuscript received at ASME Headquarters February 19, 1993. Paper No. 93-GT-87. Associate Technical Editor: H. Lukas.

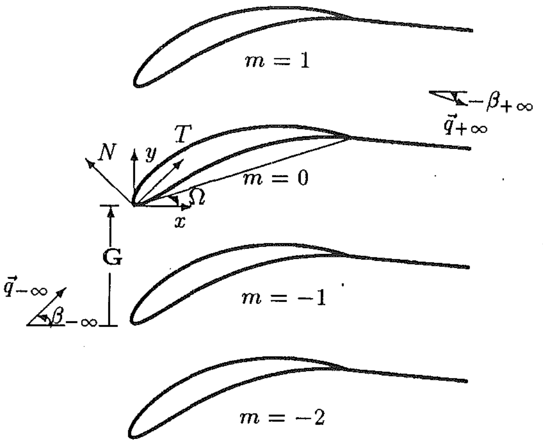

Fig. 1 Two-dimensional compressor cascade

earized inviscid and high Reynolds number inviscid/viscid interaction) models that are currently being developed for use in turbomachinery aeroelastic and aeroacoustic design prediction systems.

Thus, the primary goal of the present investigation has been to extend and validate a comprehensive Navier–Stokes analysis for the prediction of unsteady flows through the blade rows of axial-flow turbomachines. For this purpose, we have focused on a simple geometric configuration (i.e., a two-dimensional, isolated blade row), and on unsteady flows excited by time-dependent flow distortions at the inflow and outflow boundaries. The analysis and code developed during this investigation, called NGUST, is a modified version of the two-dimensional ROTOR2 analysis, developed by Rai (1987, 1989). ROTOR2 was chosen as the basis for the current analysis because of its high-order accurate integration scheme and flexible O-H grid topology. The main contributions of the present study are the formulation and implementation of the computational boundary conditions needed to simulate external unsteady aerodynamic excitations, the validation of the numerical analysis through comparisons with analytical and linearized unsteady aerodynamic solutions, and the understanding gained concerning the nonlinear behavior of unsteady flows.

Physical Problem and Mathematical Description

We consider time-dependent subsonic flow, with negligible body forces, of a calorically perfect gas through a two-dimensional cascade (see Fig. 1). The unsteadiness in the flow is assumed to be due to one or more of the following excitations: upstream entropic, vortical or acoustic disturbances, or downstream acoustic disturbances, that carry energy toward the blade row. Entropic and vortical disturbances can be used to model the wakes from upstream blade rows and combustor hot streaks entering a turbine. Acoustic disturbances model the potential flow variations associated with adjacent blade rows. The entropic, vortical, and acoustic excitations are prescribed functions of location (**x**) and time (t) that satisfy the equations that govern the fluid motion. The field equations considered in this study are the time-dependent, Reynolds-averaged, thin-layer Navier–Stokes equations and, in the limit $\mathrm{Re}\rightarrow\infty$, the Euler equations, where Re is the flow Reynolds number. These equations can be written in nondimensional form, in terms of body-fitted computational coordinates (ξ, η, τ) as

$$\tilde{Q}_\tau + (\tilde{F}_i)_\xi + (\tilde{G}_i + \mathrm{Re}^{-1}\tilde{G}_v)_\eta = 0 \tag{1}$$

The vector of conserved variables is $\tilde{Q} = J^{-1}Q$, and the inviscid flux vectors are $\tilde{F}_i = J^{-1}(\xi_t Q + \xi_x F_i + \xi_y G_i)$ and $\tilde{G}_i = J^{-1}(\eta_t Q + \eta_x F_i + \eta_y G_i)$. The Jacobian of the transformation (from physical Cartesian (x, y) to computational curvilinear (ξ, η) coordinates) and the other metric quantities are given by

$$J = x_\xi y_\eta - y_\xi x_\eta \tag{2}$$

$$\xi_x = y_\eta/J,\quad \xi_y = -x_\eta/J,\quad \eta_x = -y_\xi/J,\quad \eta_y = x_\xi/J \tag{3}$$

In the Cartesian coordinate frame, the conserved variable and inviscid flux vectors are defined as

$$\begin{aligned} Q &= [\rho, \rho u, \rho v, e_t]^T \\ F_i &= [\rho u, \rho u^2 + P, \rho u v, (e_t + P)u]^T \\ G_i &= [\rho v, \rho u v, \rho v^2 + P, (e_t + P)v]^T \end{aligned} \tag{4}$$

where ρ is the density, u and v are the Cartesian velocity components, P is the thermodynamic pressure, and e_t is the total specific internal energy. The viscous flux vector, $\tilde{G}_v$, in Eq. (1) is given by

$$\tilde{G}_v = -\begin{bmatrix} 0 \\ K_1 u_\eta + K_2 \eta_x \\ K_1 v_\eta + K_2 \eta_y \\ K_1[(a^2)_\eta/\mathrm{Pr}(\gamma-1) + (q^2/2)_\eta] + K_2 K_3 \end{bmatrix} \tag{5}$$

where $K_1 = \mu(\eta_x^2 + \eta_y^2)$, $K_2 = \mu/3(\eta_x u_\eta + \eta_y v_\eta)$, $K_3 = u\eta_x + v\eta_y$, $q = (u^2 + v^2)^{1/2}$ is the flow speed, Pr is the Prandtl number, and a is the speed of sound. In the limit as $\mathrm{Re}\rightarrow\infty$, the viscous terms become negligible and the inviscid (Euler) equations of motion are obtained.

An eddy viscosity formulation is used to model turbulent phenomena. Thus, the effective viscosity and effective thermal conductivity are defined as

$$\mu = \mu_L + \mu_T \qquad \kappa/c_p = \mu_L/\mathrm{Pr}_L + \mu_T/\mathrm{Pr}_T \tag{6}$$

where κ is the thermal conductivity, c_p is the specific heat at constant pressure, and the subscripts L and T refer to the laminar (molecular) and the turbulent (eddy) quantities, respectively. The turbulent viscosity, μ_T, is calculated using the two-layer Baldwin–Lomax algebraic turbulence model (Baldwin and Lomax, 1978) for the boundary layers along the blade surface. In the current implementation, the turbulence model is applied only on the O-type grids, and no wake model is used.

In addition to the foregoing field equations, boundary conditions must be specified at the blade surfaces and at the inflow and outflow boundaries. For viscous flow simulations, a no-slip condition and a prescribed heat flux or wall temperature distribution are enforced along the blade surfaces. For inviscid flow, a flow tangency condition is enforced along the surface of each blade. The flows at periodic boundaries, e.g., those associated with the blades at $m = 0$ and $m = 2\pi/\sigma$ (see Fig. 1), where σ is the interblade phase angle of the excitation, are solved implicitly using the interior solution algorithm. The boundary conditions at the inlet and exit of the cascade are determined using linearized theory. Thus, inflow entropic, vortical, and acoustic excitations and acoustic excitations at the outflow boundary are represented as small amplitude perturbations to a uniform free stream and have the form

$$s'(\mathbf{x},t) = \mathrm{Re}\{s_{-\infty}\exp[i(\boldsymbol{\kappa}_{-\infty}\cdot\mathbf{x} + \omega t)]\} \tag{7}$$

$$\mathbf{v}_R'(\mathbf{x},t) = \mathrm{Re}\{\mathbf{v}_{R,-\infty}\exp[i(\boldsymbol{\kappa}_{-\infty}\cdot\mathbf{x} + \omega t)]\} \tag{8}$$

$$p'(\mathbf{x},t) = \mathrm{Re}\{p_{I,\mp\infty}\exp[i(\boldsymbol{\kappa}_{\mp\infty}\cdot\mathbf{x} + \omega t)]\} \tag{9}$$

Here κ is the wave number vector, ω is the temporal reduced frequency (based on the inlet flow speed and blade chord), Re denotes the real part of a complex quantity, and $s_{-\infty}$, $\mathbf{v}_{R,-\infty}$, and $p_{I,\pm\infty}$ are the complex amplitudes of the entropic, vortical velocity, and acoustic excitations, respectively. In the foregoing relations $\kappa_{y,\pm\infty} = \sigma G^{-1}$, where G is the cascade pitch. The temporal frequency and wave number of an entropic or vortical excitation are related by $\omega = -\boldsymbol{\kappa}_{-\infty}\cdot\mathbf{q}_{-\infty}$, where $\mathbf{q}_{-\infty}$ is the

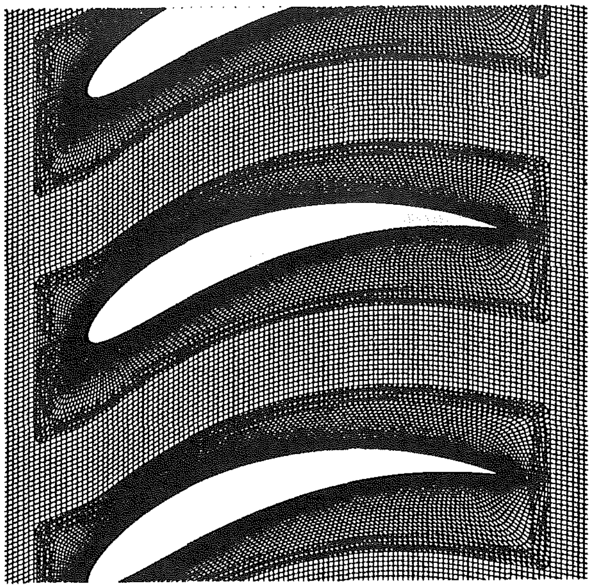

Fig. 2 Computational grids used in the NGUST analysis

uniform relative inlet velocity, but more complicated relationships exist between ω and $\kappa_{\pm\infty}$ for acoustic excitations (see Verdon et al., 1991). Only acoustic excitations of the propagating type are considered in this study.

Numerical Integration Procedure

The current numerical procedure is an extended version of the ROTOR2 analysis (Rai, 1987, 1989), which was developed to predict flows through aerodynamically coupled blade rows. In ROTOR2, a combination of O- and H-type grids is used to discretize the field (see Fig. 2). H-grids are used in the regions upstream of the blade row, downstream of the blade row, and in the interblade region. O-grids, which are body-fitted to the surface of each blade and patched into the H-grids, are used to resolve the viscous flow in each blade passage and to allow for the convenient implementation of the algebraic turbulence model. The equations of motion are integrated in time using a third-order spatially accurate, upwind, finite-difference scheme. The inviscid fluxes are discretized according to the scheme developed by Chakravarthy and Osher (1982), while the viscous fluxes are calculated using standard central differences. In the original ROTOR2 analysis, the inviscid equations are solved on the H-grids; the viscous equations on the O-grids. An alternating direction, approximate factorization technique is used to compute the temporal changes in the dependent flow variables, and inner Newton iterations are applied to enhance stability and reduce linearization errors.

The present version of the ROTOR2 analysis, called NGUST, can be used to analyze flow through a single blade row, as well as that through an arbitrary number of blade rows. In the former case the effects of neighboring blade rows are represented via prescribed unsteady flow variations at the inlet and exit boundaries. Two versions of the NGUST procedure have been developed, one using H-grids only, and the other using the O-H grid topology. The H-grid version of the analysis is used only for flat-plate cascades; the O-H grid version for "real" blade configurations. In addition, the O-H version of NGUST uses overlaid, rather than patched, grids to minimize spurious distortions in the predicted values of the flow variables at the O-H zonal boundaries. The NGUST procedure can be used to solve the inviscid (Euler) or viscous (Navier–Stokes) equations of motion. In the latter case, the viscous terms are retained in both the O- and the H-grid calculations. Implicit inlet, exit, and surface boundary conditions have been implemented. The inlet and exit boundary conditions, which represent an important part of the current effort, are described in some detail below.

Consider the approximate factorization scheme of Beam and Warming (1977), which can be represented in semi-discretized form using only one Newton iteration as

$$[I+\Delta t(\partial_\xi \tilde{A})][I+\Delta t(\partial_\eta \tilde{B})]\Delta\tilde{Q} = -\Delta t(\partial_\xi \tilde{F}+\partial_\eta \tilde{G}) \tag{10}$$

Here $\tilde{A}=\partial\tilde{F}/\partial\tilde{Q}$ and $\tilde{B}=\partial\tilde{G}/\partial\tilde{Q}$ are Jacobian matrices with respect to the dependent variables, I is the identity matrix, and $\Delta\tilde{Q}$ is the change with time of the dependent variables. The approximate factorization scheme is an implicit procedure, which requires the inversion of two block tridiagonal matrices. Equation (10) can be solved for the points within the solution domain in the following manner. First, a residual is defined as

$$\Delta\tilde{Q}^{**} = -\Delta t(\partial_\xi \tilde{F}+\partial_\eta \tilde{G}) \tag{11}$$

Next, a solution sweep in the η-coordinate direction (parallel to the inlet/exit boundaries) is performed to determine an intermediate solution, i.e.,

$$[I+\Delta t(\partial_\eta \tilde{B})]\Delta\tilde{Q}^{*} = \Delta\tilde{Q}^{**} \tag{12}$$

Finally, a solution sweep is made in the ξ-direction to obtain the updated solution

$$[I+\Delta t(\partial_\xi \tilde{A})]\Delta\tilde{Q} = \Delta\tilde{Q}^{*} \tag{13}$$

To determine $\Delta\tilde{Q}$ at the inlet and exit boundaries, the first two steps of the foregoing procedure are retained, but the boundary conditions are incorporated into the third step. The procedure begins with the transformation of the governing equations into characteristic form through premultiplication by the matrix T_ξ^{-1}, which contains the left eigenvectors of the Jacobian matrix, $\tilde{A}$ (Merkle, 1987), i.e.,

$$T_\xi^{-1}[I+\Delta t(\partial_\xi \tilde{A})]\Delta\tilde{Q} = T_\xi^{-1}\Delta\tilde{Q}^{*} \tag{14}$$

In characteristic form each of the equations is associated with an eigenvalue of the Jacobian matrix, and a corresponding characteristic wave (see Eqs. (7)–(9)). Next, the equations of motion are premultiplied by a selection matrix, which accounts only for the characteristic waves that leave the computational domain (Merkle, 1987; Chakravarthy, 1982; Rai and Chaussee, 1984). For subsonic flow at the inlet, for example, one characteristic (pressure) wave leaves the computational domain, so the selection matrix, L_i, becomes

$$L_i = \begin{bmatrix} 0 & 0 & 0 & 0 \\ 0 & 0 & 0 & 0 \\ 0 & 0 & 0 & 0 \\ 0 & 0 & 0 & 1 \end{bmatrix} \tag{15}$$

and

$$[L_i T_\xi^{-1} I + L_i T_\xi^{-1}\Delta t(\partial_\xi \tilde{A})]\Delta\tilde{Q} = L_i T_\xi^{-1}\Delta\tilde{Q}^{**} \tag{16}$$

The technique used to determine the numerical fluxes on the right-hand side of Eq. (16) is different from that used in the interior of the computational domain. The fluxes parallel to the boundary (i.e., in the cascade tangential direction) are calculated using the interior differencing scheme, but the fluxes normal to the boundary (i.e., in the axial direction) are calculated using second-order-accurate one-sided differences.

The boundary conditions corresponding to the positive eigenvalues are then combined with the equations of motion, and solved implicitly with the interior flow field. Thus, the modified third step of the approximate factorization procedures becomes

$$\begin{aligned}&[C+L_i T_\xi^{-1} I + L_i T_\xi^{-1}\Delta t(\partial_\xi \tilde{A})]\Delta\tilde{Q} \\ &\qquad = L_i T_\xi^{-1}\Delta\tilde{Q}^{**} + (W_i^{n+1}-W_i^{n})\end{aligned} \tag{17}$$

where W_i is the vector containing the characteristic variables and $C=\partial W/\partial\tilde{Q}$ is the Jacobian of the characteristic variables with respect to the dependent variables. The forcing function $(W_i^{n+1} - W_i^n)$ will be zero for steady problems (since the characteristic variables will be constant in time), but it will have prescribed values for unsteady flow problems.

The implicit boundary conditions outlined above represent approximate, quasi-two-dimensional, nonreflecting boundary conditions. The term quasi-two-dimensional refers to the assumption that circumferential variations in the pressure waves leaving the computational domain have been regarded as negligible; "nonreflecting," to the condition that pressure waves pass through the inflow and outflow boundaries with little or no artificial reflection. Since the characteristic boundary conditions are based on a linearized analysis, a post-iteration update of the boundary variables can often improve the solution accuracy. In this study, the full two-dimensional boundary conditions of Giles (1990) are used for this purpose. In this method, the characteristic variables, w_i, can be written in perturbation form such that

$$W = \begin{bmatrix} w_1 \\ w_2 \\ w_3 \\ w_4 \end{bmatrix} = \begin{bmatrix} -a^2 & 0 & 0 & 1 \\ 0 & 0 & \rho a & 0 \\ 0 & \rho a & 0 & 1 \\ 0 & -\rho a & 0 & 1 \end{bmatrix}_{\mp\infty} \begin{bmatrix} \delta\rho \\ \delta u \\ \delta v \\ \delta P \end{bmatrix} \qquad (18)$$

and

$$\begin{bmatrix} \delta\rho \\ \delta u \\ \delta v \\ \delta P \end{bmatrix} = \frac{1}{2} \begin{bmatrix} -2\mathrm{M} & 0 & \mathrm{M} & \mathrm{M} \\ 0 & 0 & N & -N \\ 0 & 2N & 0 & 0 \\ 0 & 0 & 1 & 1 \end{bmatrix}_{\mp\infty} \begin{bmatrix} w_1 \\ w_2 \\ w_3 \\ w_4 \end{bmatrix} \qquad (19)$$

where $\mathrm{M} = 1/a^2$, $N = 1/(\rho a)$, $\delta\rho = \rho - \rho_{\text{inlet/exit}}$, $\delta u = u - u_{\text{inlet/exit}}$, $\delta v = v - v_{\text{inlet/exit}}$, and $\delta P = P - P_{\text{inlet/exit}}$. The subscripts $-\infty$ and $+\infty$ refer to the underlying steady flow variables at the inlet and the exit, respectively, and the subscripts "inlet" and "exit" refer to the prescribed unsteady flow variables at the inlet and the exit boundary. The two-dimensional boundary condition update calculates the change in the incoming characteristic waves based on the values of the outgoing characteristic waves. Since the outgoing characteristic waves are determined from the governing field equations during the implicit portion of the numerical procedure, this explicit update is easily incorporated into the framework of the NGUST analysis.

At the inlet, the incoming characteristics are determined by (Giles, 1990)

$$\frac{\partial}{\partial t} \begin{bmatrix} w_1 \\ w_2 \\ w_3 \end{bmatrix} + \begin{bmatrix} v & 0 & 0 & 0 \\ 0 & v & R & Q \\ 0 & Q & v & 0 \end{bmatrix}_{-\infty} \frac{\partial}{\partial y} \begin{bmatrix} w_1 \\ w_2 \\ w_3 \\ w_4 \end{bmatrix} = 0 \qquad (20)$$

where $Q = (a-u)/2$ and $R = (a+u)/2$, and at the exit, the incoming characteristic is determined by

$$\frac{\partial w_4}{\partial t} + [0 \;\; u_{+\infty} \;\; 0 \;\; v_{+\infty}] \frac{\partial}{\partial y} \begin{bmatrix} w_1 \\ w_2 \\ w_3 \\ w_4 \end{bmatrix} = 0 \qquad (21)$$

Equation (20) is solved implicitly by inverting a block tridiagonal matrix. Equation (21) is solved for w_4 along the exit boundary by inverting a scalar tridiagonal matrix. In both cases, implicit second-difference dissipation is added to the equation to prevent odd-even decoupling. For characteristic waves leaving the computational domain at an angle θ relative to the boundary, the two-dimensional boundary condition update will produce artificially reflected waves of amplitude $O(\theta^2)$, compared to waves of amplitude $O(\theta)$ for the quasi-two-dimensional boundary condition update (Giles, 1990).

For inviscid flows, the theory of characteristics also forms the basis of the airfoil surface boundary conditions. More details on the integration procedure and numerical boundary conditions can be found in Rai (1989) and Dorney (1992).

Numerical Results

Extensive numerical results have been determined for unsteady flows through flat plate and compressor exit guide vane (EGV) cascades (see Dorney, 1992). The flat plate test cases served as benchmarks to validate the numerical analysis against semi-analytical solutions. The EGV simulations were intended both to validate the numerical analysis and to demonstrate the use of the NGUST procedure as a "numerical wind tunnel" for investigating the effects of nonlinearity and viscosity on unsteady flow solutions. The results of the numerical simulations have been compared with classical linear solutions and solutions obtained using the linearized inviscid flow analysis, LINFLO, developed by Verdon (1990), Verdon et al. (1991), and Hall and Verdon (1991).

In the following discussion, we will present selected results from this study. Unsteady flow quantities will be described using a complex representation. The complex amplitudes $\mathbf{v}_{R,-\infty}$, and $p_{I,\pm\infty}$ of the unsteady vortical and acoustic excitations are assumed to be real, e.g., an upstream acoustic excitation prescribed to have an amplitude equal to 4 percent of the steady inlet pressure will have a complex amplitude of $p_{I,-\infty} = (0.04\overline{P}_{-\infty}, 0)$. The magnitude and phase of an unsteady response quantity at the location $\mathbf{x}$, say $\tilde{p}(\mathbf{x},t)$, is then given by $|\tilde{p}| = ([\mathrm{Re}(\tilde{p})]^2 + [Im(\tilde{p})]^2)^{1/2}$ and $\phi = \tan^{-1}[Im(\tilde{p})/\mathrm{Re}(\tilde{p})]$, where the phase angle is measured relative to the phase of the excitation.

Comparisons With Analytical Solutions. The H-grid version of the NGUST analysis was used for the flat plate simulations. Here, a mesh with 301 axial and 51 tangential grid lines, with constant spacings between grid lines, was used in each extended blade passage region. The number of passages to be considered depends on the interblade phase angle of the unsteady excitation. For example, if $\sigma = 2\pi$, only one blade passage is analyzed, if $\sigma = \pi$, two passages are analyzed, etc. The flat plate numerical computations were performed on six processors of an Alliant FX-2800 mini-supercomputer. Typical flat plate calculations required 0.000365 seconds of CPU time per grid point per iteration and approximately seven periods, at 500 iterations (with one Newton subiteration) per period, to reach a time-periodic solution. Thus, the flat plate calculations required a total of approximately 325 minutes per extended blade passage to achieve a time-periodic solution.

The first set of simulations was performed to study the capability of the NGUST analysis to predict the convection of a vortical gust by a uniform mean flow. For this purpose we consider the solution domain of a flat plate cascade, but remove the plates (blades) to eliminate spurious numerical vorticity generation due to gust/solid-surface interactions. For these simulations the steady Mach number was set at 0.30, the steady flow angle (cascade stagger angle) at 40 deg, and the "blade" spacing was set at 0.60. A vortical gust with interblade phase angle, σ, of -180 deg and temporal reduced frequency, ω, of 5 was imposed at the inlet boundary. Four different gust amplitudes were investigated; $v_g = |\mathbf{v}_{R,-\infty} \cdot \mathbf{e}_N| = 0.05\overline{q}_{-\infty}$, $0.10\overline{q}_{-\infty}$, $0.25\overline{q}_{-\infty}$, and $0.50\overline{q}_{-\infty}$, where $\mathbf{v}_{R,-\infty}$ is the upstream rotational velocity (i.e., the velocity associated with the vorticity) and $\overline{q}_{-\infty}$ is the steady inlet flow speed. Both inviscid (Euler) and viscous (Navier–Stokes) simulations were performed.

The unsteady axial velocity distributions, $u(x, x \tan\beta)$, where x is the axial distance, as determined by the inviscid and

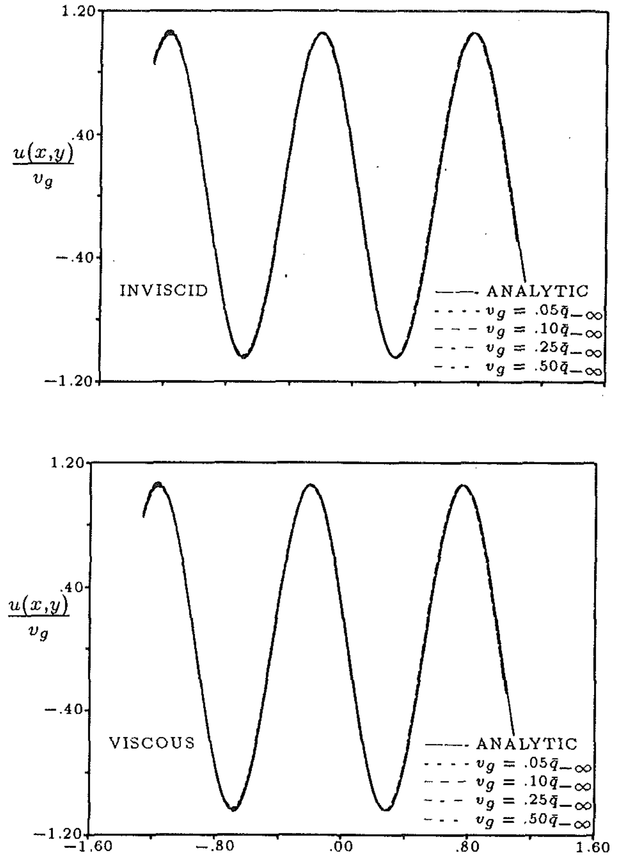

Fig. 3 Unsteady axial velocity due to a vortical gust with $v_g = (0.05 - 0.50)\bar{q}_{-\infty}$, $\sigma = -\pi$, and $\omega = 5$

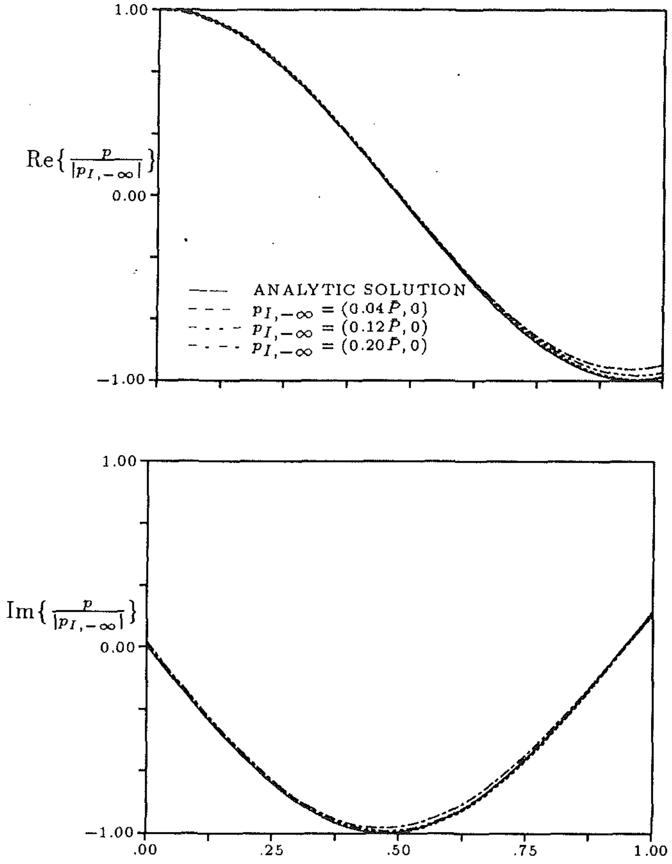

Fig. 4 First harmonic unsteady surface pressure for an unstaggered flat plate cascade subjected to an incident acoustic wave from upstream with $p_{I,-\infty} = [(0.04 - 0.20)\bar{P}_{-\infty}, 0]$, $\sigma = 0$, and $\omega = 10$

viscous numerical simulations, are shown in Fig. 3, along with the linearized inviscid solution given in Eq. (8). The first-harmonic analytical solution and the nonlinear numerical solution, which contains all harmonics, are in excellent agreement, even for a gust amplitude of 50 percent of the inlet free-stream speed. The results in Fig. 3 indicate that the numerical algorithm is properly convecting the unsteady vortical disturbance, and that the nonlinear effects associated with the convection of a vortical wave are negligible. The latter is especially important since the inlet boundary conditions currently used in nonlinear unsteady aerodynamic simulations are, of necessity, based on linearized inviscid solutions. The imposed vortical disturbances did not excite pressure or entropy disturbances, indicating that even for large amplitude gusts the different modes of excitation (i.e., entropy, vorticity, and pressure) are uncoupled. The inclusion of viscous terms in the numerical simulation does not alter these conclusions.

A second set of simulations was performed to examine the capability of the Navier–Stokes analysis to describe the propagation of pressure disturbances relative to a uniform mean flow. In these calculations, acoustic waves were introduced at the inlet and the exit of an unstaggered ($\Omega = 0$ deg) flat plate blade row. The flat plates have a chord, $\bar{c}$, of 1.0 and a pitchwise gap, G, of 0.60. The steady Mach number is 0.50 and the steady flow angle is 0 deg. To determine the ability of the analysis to simulate high-frequency unsteadiness, the temporal reduced frequency, ω, of the incident acoustic waves was set equal to 10. To limit the solution domain to a single blade passage the interblade phase angle, σ, was taken to be 0 deg. Three different wave amplitudes were studied; i.e., $|p_{I,\pm\infty}| = 0.04\bar{P}_{\pm\infty}$, $0.12\bar{P}_{\pm\infty}$, and $0.20\bar{P}_{\pm\infty}$, where $|p_{I,\pm\infty}|$ is the amplitude of the incident unsteady pressure waves from upstream ($-\infty$) or downstream ($+\infty$), and $\bar{P}_{\pm\infty}$ are the corresponding steady free-stream pressures. The analytical solution for the unsteady pressure excitation is given by

$$p(\mathbf{x},t) = \mathrm{Re}\{p_{I,\mp\infty} \exp[i(\kappa_{\mp\infty}\cdot\mathbf{x} + \omega t)]\} \qquad (22)$$

where $\kappa_{x,\mp\infty} = \mp\omega M(1 \pm M)^{-1}$ and $\kappa_y = 0$. Note that for these flows, since the pressure waves travel parallel to the plates, there is no pressure response associated with the interactions of the acoustic excitations with the flat plate blade row.

The real and imaginary components of the first harmonic of the unsteady pressure along the surface of blade, as determined from the NGUST analysis and from Eq. (22), are shown in Fig. 4 for inlet acoustic excitations. Even at this relatively high frequency, the numerical algorithm accurately predicts the propagation of the acoustic wave. At the larger amplitudes, some differences between the in-phase components of the nonlinear first-harmonic and the analytical solutions are noticeable near the trailing edge of the plate. The predicted second and third harmonic components of the unsteady pressure were very small, however, indicating that the unsteady pressure field remains linear for these examples.

The analytical (Eq. (22)) and numerical (NGUST) predictions for the first harmonic of the unsteady surface pressures for acoustic excitations introduced at the cascade outflow boundary are shown in Fig. 5. In this case, the predicted results for the lowest amplitude excitation are in good agreement, but some differences exist. At the higher amplitudes, significant discrepancies develop between the numerical and analytical solutions. Since the computational grid was fine enough (approximately 60 grid points per wavelength) to resolve the acoustic wave, these differences are probably due to nonlinear effects associated with acoustic excitations at high axial wave numbers. An investigation of the higher harmonics of the unsteady

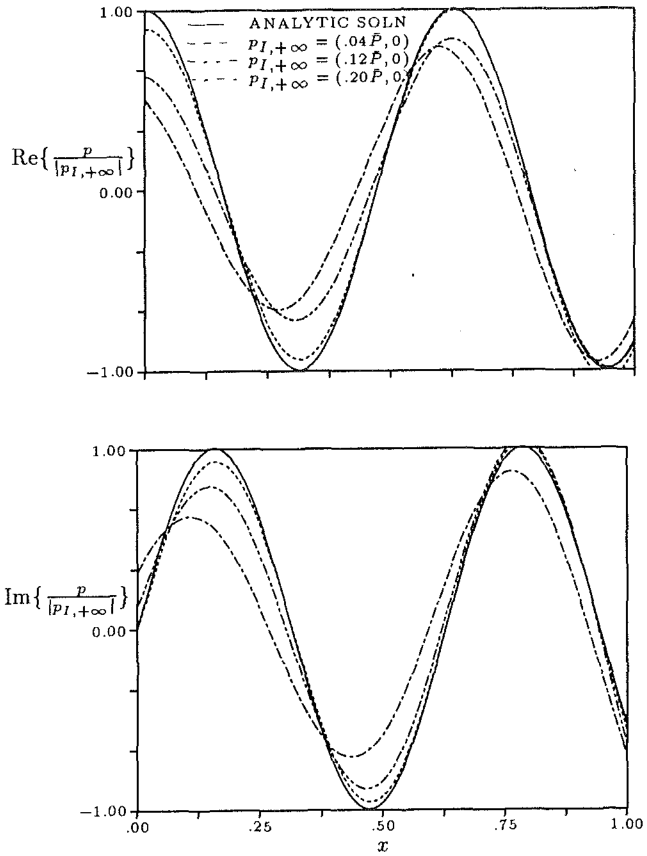

Fig. 5 First harmonic unsteady surface pressure for an unstaggered flat plate cascade subjected to an incident acoustic wave from downstream with $p_{I,-\infty} = [(0.04-0.20)\bar{P}_{-\infty},0]$, $\sigma = 0$, and $\omega = 10$

surface pressure revealed that for the largest amplitude excitation ($p_{+\infty} = 0.20\bar{P}_{+\infty}$), the amplitude of the second harmonic was approximately 55 percent of that of the first harmonic, while the amplitude of the third harmonic was nearly 30 percent of the first harmonic value. The imposed acoustic disturbances did not excite vorticity or entropy disturbances, again indicating that the modes of excitation are uncoupled.

Additional simulations (see Dorney, 1992) were performed for vortical excitations introduced at the inflow boundary of a cascade of staggered flat plate blades. In these simulations, the interblade phase angle was varied from $-\pi$ to -2π, and the temporal frequency was varied from 5 to 10. The predicted unsteady vorticity fields showed good agreement with the linearized inviscid solutions, although the interaction of the disturbances with the blade leading edge generated spurious vorticity, which was convected along the blade wakes. The predicted (nonlinear) unsteady pressure fields were in excellent agreement with the results of the linearized analysis.

In performing the foregoing nonlinear simulations, it was determined that use of the total pressure to represent the characteristic wave associated with the linear entropy at the inlet boundary resulted in an artificial reflection of upstream traveling pressure waves at this boundary. The specification of the entropy, instead of the total pressure (which is not a characteristic variable), allowed the acoustic waves to pass through the upstream boundary with minimal reflection. This observation is very important, since many contemporary Euler and Navier–Stokes analyses use the total pressure as a specified variable at the inlet boundary.

The foregoing flat plate simulations indicate that for inlet acoustic excitations, the unsteady pressure field remains linear. For downstream acoustic excitations, however, even those at low frequency and small amplitude, the unsteady pressure field exhibits a strong nonlinear behavior. This nonlinear reaction of the fluid to acoustic excitations traveling upstream against the mainstream flow may be due to the high wave numbers associated with such waves, which give rise to relatively large pressure gradients.

Compressor Exit Guide Vane (EGV) Simulations. To study the response of realistic blade rows to unsteady vortical and acoustic excitations, inviscid and viscous simulations have been performed for the compressor exit guide vane studied by Hall and Verdon (1991). The EGV blades are constructed by superimposing the thickness distribution of a NACA 0012 airfoil on a circular arc camber line with a height at midchord of 0.13. The cascade has a stagger angle, Ω, of 15 deg, a pitchwise gap, G, of 0.60, and operates at an inlet Mach number and inlet flow angle of $M_{-\infty} = 0.30$ and $\beta_{-\infty} = 40$ deg, respectively. In the viscous simulations, the Reynolds number, based on the inlet free-stream conditions and the blade chord, was set at $\mathrm{Re} = 5.0 \times 10^5$ and a zero heat flux (adiabatic wall) condition was specified at the blade surfaces. Transition was assumed to occur at the leading edge of each blade.

The EGV simulations were performed using an overlaid O–H grid topology (see Fig. 2). The computational grid used in each blade passage for the inviscid simulations consisted of 263×21 grid points for the O-grid and 250×51 grid points for the H-grid. The grid used in each passage for the viscous simulations consisted of 263×41 grid points for the O-grid and 250×51 grid points for the H-grid. For the viscous simulations the average value of the nondimensional distance, y^+, of the first grid line away from a blade was $y^+ \approx 2.0$, indicating that the grid should be fine enough to resolve the turbulent boundary layer. All numerical simulations performed during this study were computed on six processors of an Alliant FX-2800 mini-supercomputer. Typical inviscid calculations required 0.000680 seconds of CPU time per grid point per iteration; typical viscous simulations required 0.000850 seconds per grid point per iteration. For both the inviscid and viscous flow calculations eight periods, at 500 iterations (with three Newton subiterations) per period, were required to achieve a time-periodic solution. A solution was considered to be time-periodic when the maximum difference in unsteady pressure along a blade at the same point in two consecutive periods was less than a specified small value. Thus, the inviscid EGV calculations required a total of approximately 840 CPU minutes per blade passage to achieve a time-periodic solution, while the viscous EGV calculations required approximately 1340 minutes per blade passage to achieve such a solution.

The inviscid and viscous steady flow solutions obtained with the NGUST procedure were compared with the results of the steady full potential analysis, CASPOF, which provides the mean flow solution for LINFLO and is described by Caspar et al. (1980). The surface pressure coefficient distributions, $C_P = 2(P - P_{-\infty})/(\rho_{-\infty}\bar{q}^2_{-\infty})$, determined from NGUST and CASPOF are shown in Fig. 6. The predicted pressure distributions are in very good agreement. In the viscous NGUST simulation, boundary layer blockage reduces the blade pressure loading, especially in the trailing edge region. It should be noted that the viscous NGUST results have been compared recently with the results of an inviscid/viscid interaction (IVI) analysis (Barnett et al., 1993) for both the EGV cascade and a high-speed compressor cascade. The steady pressure, skin friction, and displacement thickness distributions predicted by the Navier–Stokes and IVI analyses showed very good agreement for the two test cases.

In the first set of unsteady flow simulations, a vortical gust at a reduced frequency of 10, an interblade phase angle of -2π, and a gust velocity amplitude, v_g, equal to 5 percent of the steady inlet flow speed was introduced at the inlet boundary of the EGV cascade. The unsteady vorticity contours at times $t = 2n\pi\omega$, $n = 0, \pm 1, \pm 2, \ldots$, as predicted by LINFLO, an

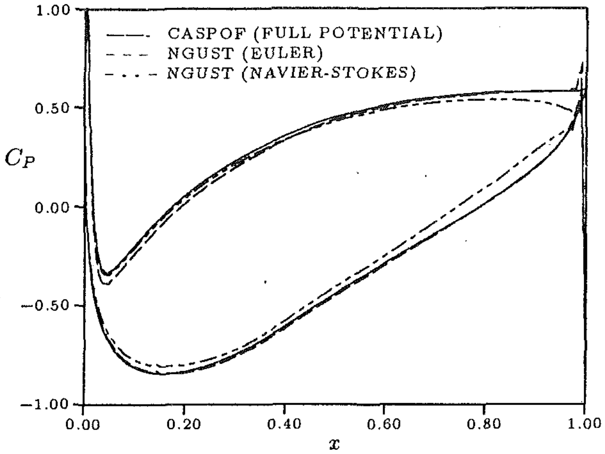

Fig. 6 Predicted surface pressure coefficient distributions for steady flow at $M_{-\infty}=0.3$ and $\beta_{-\infty}=40$ deg through the EGV cascade

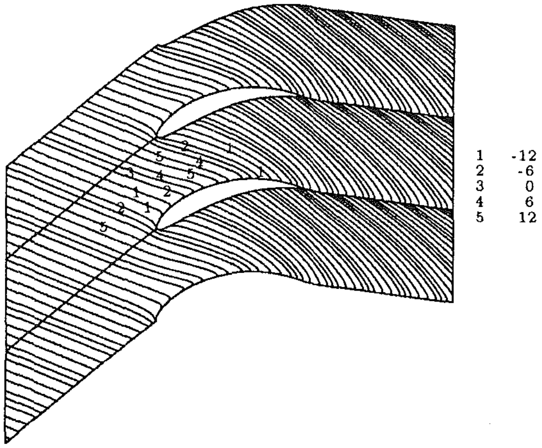

Fig. 7 LINFLO prediction for the in-phase component of the unsteady vorticity for the EGV cascade subjected to an incident vortical gust from upstream with $v_g=0.05\bar{q}$, $\sigma=-2\pi$, and $\omega=10$

inviscid (Euler) and a viscous (Navier-Stokes) numerical simulation are shown in Figs. 7 and 8. The NGUST solutions describe the total unsteady vorticity; the LINFLO solution, the first harmonic component. In the latter case the unsteady vorticity at times $t=2n\pi/\omega$ are determined by the in-phase component (real part) of the predicted complex vorticity field.

The vorticity contours determined from the numerical analyses show very good agreement with the linearized inviscid predictions upstream of the blade row and good agreement within the blade passages. However, both the inviscid and viscous numerical calculations generate large amounts of spurious vorticity at the blade trailing edges. Although the physics of the inviscid problem dictate that a vortex sheet emanates at the trailing edge and extends downstream (as shown in the LINFLO results), most of the vorticity generated in the NGUST simulation is of numerical origin and is associated with discretizing the flow over a sharp trailing edge with an O-type grid. The vorticity associated with the blade surface boundary layer is noticeable in the viscous results. As the boundary layer thickens with increasing distance along the blade surface, the magnitude of the vorticity generated by viscous effects increases. This is especially evident in the results shown in Fig. 8, beginning at about 40 percent axial chord on the blade suction and pressure surfaces. Note that the mean flow separates from the blade suction surface at about 80 percent of the blade chord. Although the spurious vorticity generated at the trailing edge contaminates the contours in the wake, the

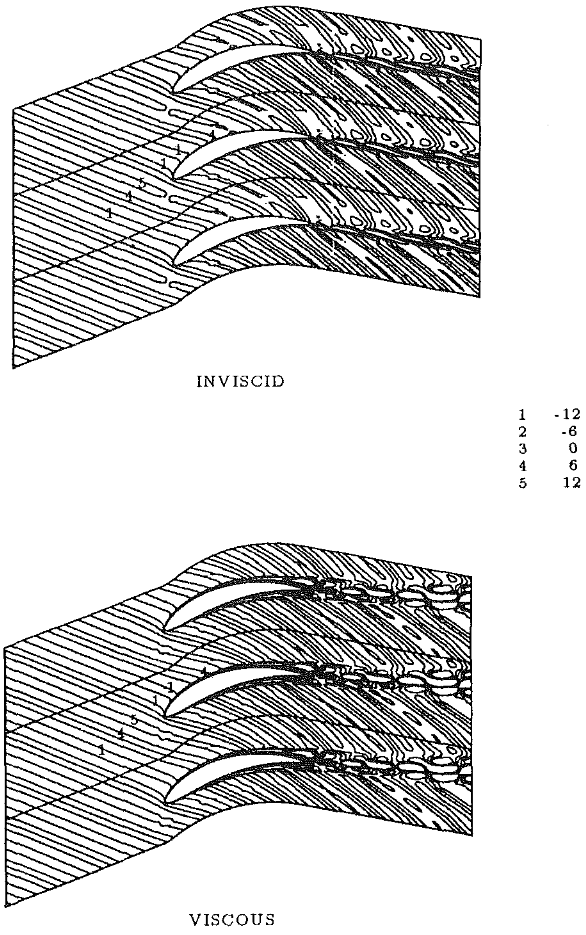

Fig. 8 NGUST predictions for the in-phase component of the unsteady vorticity for the EGV cascade subjected to an incident vortical gust from upstream with $v_g=0.05\bar{q}$, $\sigma=-2\pi$, and $\omega=10$

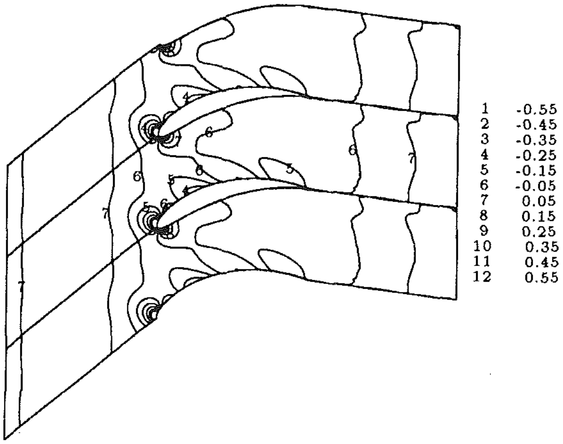

Fig. 9 LINFLO prediction for the in-phase component of the unsteady pressure for the EGV cascade subjected to an incident vortical gust from upstream with $v_g=0.05\bar{q}$, $\sigma=-2\pi$, and $\omega=10$

vorticity contours in the midpassage region show reasonable agreement with those predicted by LINFLO.

Contours of the in-phase component of the first harmonic, unsteady pressure response, resulting from the interaction of the vortical gust with the blade surface, are shown in Figs. 9 and 10. These results were determined by the linearized inviscid analysis, and a Fourier decomposition of the unsteady pres-

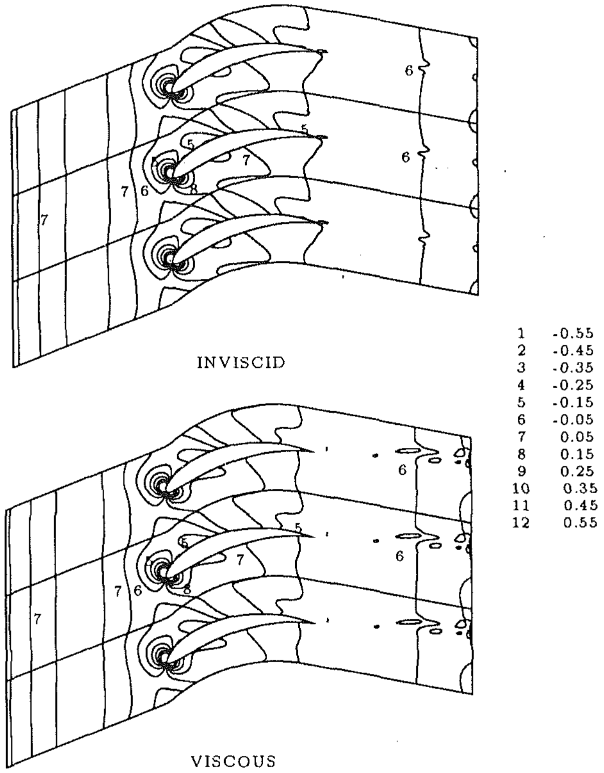

Fig. 10 NGUST predictions for the in-phase component of the unsteady pressure for the EGV cascade subjected to an incident vortical gust from upstream with $v_g = 0.05\bar{q}$, $\sigma = -2\pi$, and $\omega = 10$

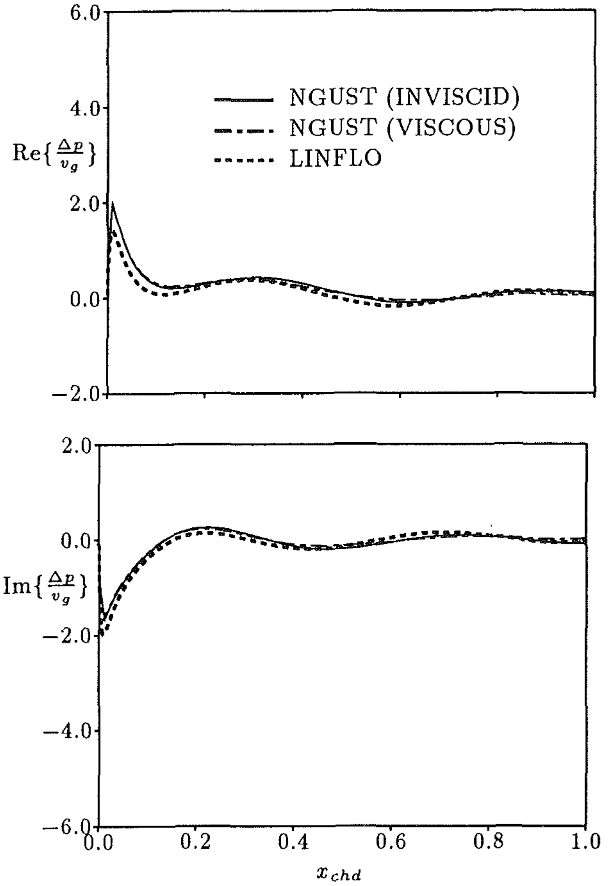

Fig. 11 First harmonic unsteady pressure difference for the EGV cascade subjected to an incident vortical gust from upstream with $v_g = 0.05\bar{q}$, $\sigma = -2\pi$, and $\omega = 10$

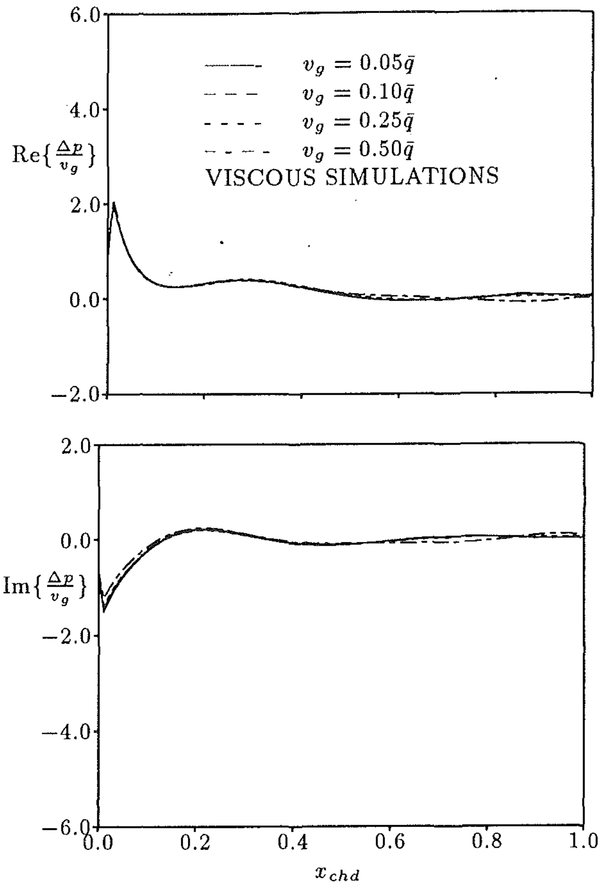

Fig. 12 First harmonic unsteady pressure difference for the EGV cascade subjected to vortical gusts from upstream, viscous, with $v_g = (0.05-0.50)\bar{q}$, $\sigma = -2\pi$, and $\omega = 10$

sures obtained from the nonlinear inviscid and viscous analyses. Conspicuously absent from the nonlinear results is any effect of the spurious unsteady vorticity generated at the blade trailing edge. Even though the vortical gust is the source of the pressure response from the airfoil, the spurious unsteady vorticity generated by the numerical calculations appears to have, at most, a very weak impact on the unsteady pressure response. For an excitation at $\omega = 10$ and $\sigma = -2\pi$, pressure response waves propagate away from the blade row in both the upstream and downstream axial directions. Both LINFLO and the inviscid NGUST solution predict nearly planar pressure response waves upstream and downstream of the blade row. Overall, the agreement between the inviscid NGUST and LINFLO solutions is good. In the viscous simulation, the viscous wake downstream of the blade row is visible in the unsteady pressure contours. There is also a concentration of pressure contours where the viscous wake intersects the outflow boundary of the computational domain. This local variation in the unsteady pressure may be due to the fact that the wake flow is nonlinear, but the computational boundary conditions are based on a linear analysis of the inviscid Euler equations. Away from the wakes, the nonlinear viscous and the linearized and nonlinear inviscid solutions show good agreement.

The foregoing example, since it contains propagating pressure waves, provides an important check on the computational boundary conditions implemented into the NGUST analysis. The use of quasi-two-dimensional boundary conditions for these unsteady flow conditions resulted in large pressure reflections at the downstream boundary. The fully two-dimensional boundary condition update procedure eliminated most of these reflections.

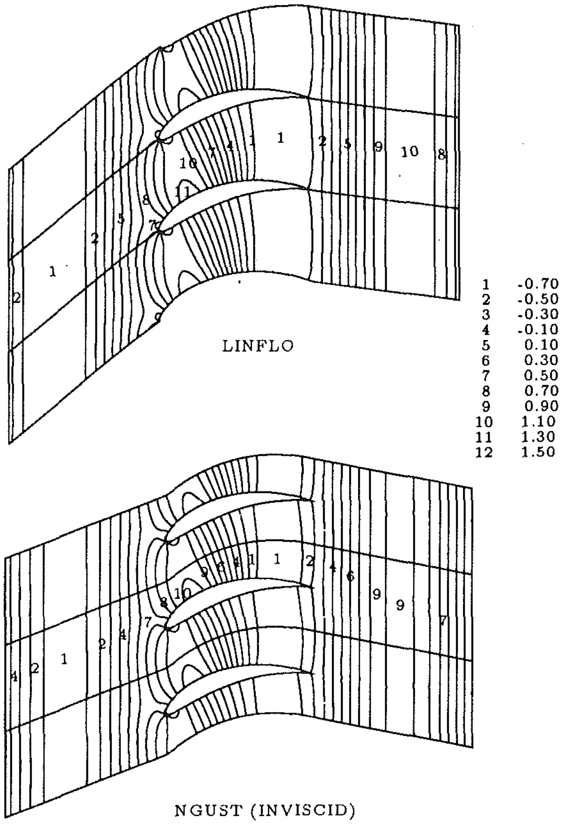

Fig. 13 In-phase component of the unsteady pressure for the EGV cascade subjected to an incident acoustic wave from downstream with $p_{I,+\infty} = [0.04\bar{P}_{+\infty}, 0]$, $\sigma = 0$, and $\omega = 10$

The first harmonic of the predicted unsteady pressure difference, scaled by gust velocity amplitude, is given by

$$\Delta p(x)/v_g = [p^-(x_{chd}, t) - p^+(x_{chd}, t)]/[\bar{\rho}_{-\infty}\bar{q}_{-\infty}v_g] \quad (23)$$

and is shown in Fig. 11, where $\Delta p/v_g$ is dimensionless, x_{chd} is the dimensionless distance along the blade chord, and the superscripts $(-)$ and $(+)$ refer to the lower and upper surfaces of the blade, respectively. The linearized inviscid and the nonlinear solutions for Δp are in excellent agreement. It appears that viscous separation has little or no effect on the unsteady pressure difference response.

To study the effects of vortical gust amplitude on the unsteady pressure response of the exit guide vane, additional inviscid and viscous simulations were performed. For this purpose, we considered vortical gusts at $\omega = 10$ and $\sigma = -2\pi$, and at amplitudes of $v_g = 0.05\bar{q}_{-\infty}$, $0.10\bar{q}_{-\infty}$, $0.25\bar{q}_{-\infty}$, and $0.50\bar{q}_{-\infty}$. The first harmonic unsteady pressure difference responses as determined by the viscous simulations are shown in Fig. 12. The pressure difference responses determined from the inviscid simulations were nearly invariant with increasing gust amplitude, and therefore have been omitted. Increasing the amplitude of the excitation did not significantly affect the acoustic response of the blade row in either set of simulations. At a gust amplitude of $v_g = 0.50\bar{q}$, the unsteady pressure difference predicted in the viscous simulation differs slightly from the results at lower gust amplitudes. This may indicate that the high-amplitude vortical wave is impacting the location of the mean separation point. These results indicate that the normalized, by v_g, unsteady pressure difference response is relatively unaffected by the amplitude of the vortical excitation, and hence, that this response is essentially linear. This is an important result, which if it holds up under more extensive testing, would suggest that linearized analyses are sufficient for predicting the effects of vortical-wake/blade-row interaction, at least for low Mach number flows.

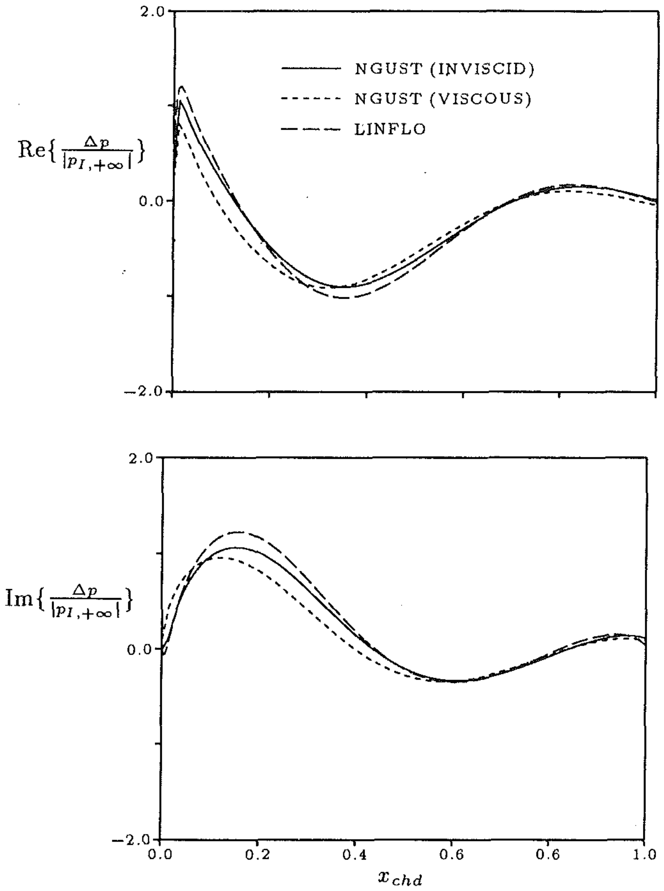

Fig. 14 First harmonic unsteady pressure-difference distributions for the EGV cascade subjected to an incident acoustic wave from downstream with $p_{I,+\infty} = [0.04\bar{P}_{+\infty}, 0]$, $\sigma = 0$, and $\omega = 10$

To determine the viability of the nonlinear analysis to predict cascade response to high-frequency acoustic excitations, numerical experiments were performed in which downstream and upstream traveling acoustic waves were specified at the inlet and exit, respectively, of the EGV cascade. These excitations occurred at a temporal frequency of $\omega = 10$ and an interblade phase angle of $\sigma = 0$. The amplitude of the downstream traveling acoustic excitation was set equal to 4 percent of the steady inlet pressure; that of the upstream traveling acoustic excitation at 4 percent of the steady exit pressure.

The NGUST and LINFLO solutions for acoustic excitations imposed at the inflow and outflow boundaries are in excellent agreement; for brevity, only results for the acoustic excitation from downstream are shown. Contours of the in-phase component of the predicted, first harmonic, unsteady pressure fields as determined by the LINFLO and the inviscid NGUST calculations for the exit acoustic excitation are shown in Fig. 13. Since the interaction of an incident acoustic disturbance with the blade row causes an unsteady pressure response, the pressure contours shown in Fig. 13 represent a combination of excitation and response waves.

The first-harmonic, unsteady, pressure difference distributions acting on a blade due to the exit acoustic excitation are shown in Fig. 14. Included in this figure are the results of a viscous NGUST simulation. The two inviscid predictions (see Fig. 14) are in good agreement, but there are significant differences over the forward half of the blade. These differences may be caused by nonlinear effects. The second harmonic of the unsteady pressure difference predicted by NGUST is nearly 25 percent of the first harmonic value for this excitation. The differences between the inviscid and viscous NGUST solutions may be caused in part by the differences in the underlying

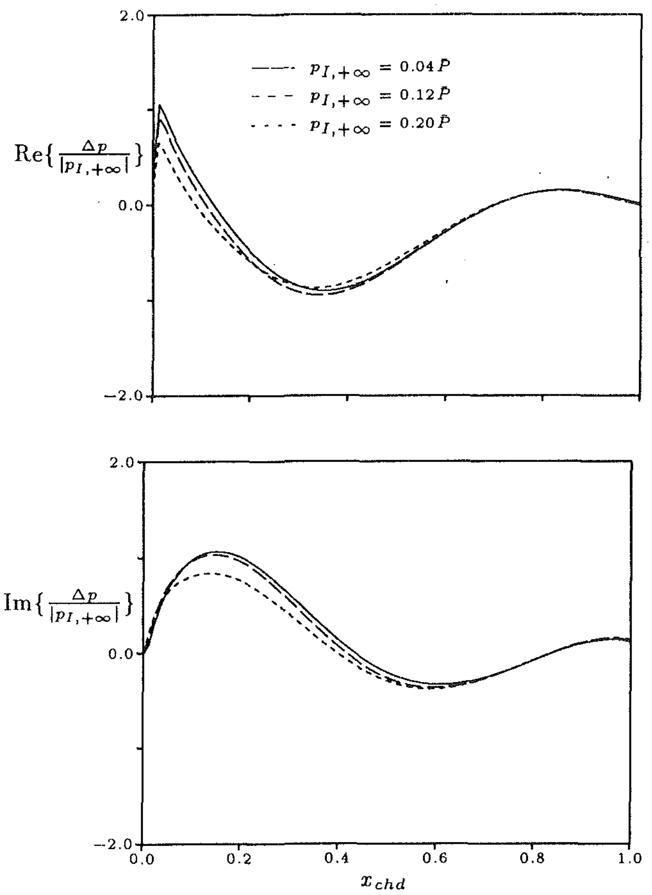

Fig. 15 First harmonic unsteady pressure-difference distributions for the EGV cascade subjected to an incident acoustic wave from downstream with $p_{I,+\infty}=[(0.04-0.20)\bar{P}_{+\infty}, 0]$, $\sigma=0$, and $\omega=10$

steady flow solutions (i.e., the viscous wake) downstream of the blade. It should be noted that for the inlet acoustic excitations, the linear and nonlinear pressure-difference predictions showed excellent agreement.

To quantify the effects of gust amplitude on the acoustic response of the exit guide vane, additional inviscid NGUST simulations were performed. An acoustic excitation from downstream was prescribed with a temporal frequency of $\omega=10$ and gust amplitudes of $p_{I,+\infty}=0.04\bar{P}_{+\infty}$, $0.12\bar{P}_{+\infty}$, and $0.20\bar{P}_{+\infty}$. Figure 15 shows the distributions of the first harmonic of the unsteady surface pressure difference along the blade. The unsteady pressure fields appear to remain linear, except for the case of $p_{I,+\infty}=0.20\bar{P}_{+\infty}$. At this amplitude the imaginary component of the unsteady pressure difference deviates significantly from the lower amplitude results, indicating the presence of nonlinearities.

The predicted numerical results for the acoustic excitations acting on an exit guide vane cascade support the results of the flat plate simulations; i.e., the unsteady pressure fields associated with acoustic excitations from upstream tend to remain linear, while the unsteady pressure fields associated with acoustic excitations from downstream exhibit significant effects of nonlinearity. In addition, the acoustic disturbances did not excite vortical or entropic disturbances.

Conclusions

A nonlinear, viscous analysis, called NGUST, has been extended to predict unsteady flows through isolated, two-dimensional cascades. Solutions for realistic configurations were determined on an overlaid O-H grid topology. Computational boundary conditions were designed to allow the specification of vortical, entropic, and acoustic excitations at the inlet to the blade row, and acoustic excitations at the exit. In addition, the inlet and exit boundary conditions were formulated to be time accurate and nonreflecting. The NGUST analysis has been applied to predict unsteady flows, excited by vortical and acoustic disturbances of varying amplitude, interblade phase angle, and frequency, through flat plate (using an H-mesh alone) and compressor exit guide vane cascades, and the predicted results have been compared with linearized inviscid solutions.

The simulations for unsteady flow excited by vortical disturbances at the inlet produced the following observations:

1 Vortical gusts tend to be convected in a linear manner, even gusts of relatively large amplitude.

2 The unsteady vorticity fields calculated using the nonlinear analysis, NGUST, generally showed good agreement with the results of the linear analysis, LINFLO. However, the nonlinear procedure generates spurious vorticity at blade trailing edges, which is convected downstream along blade wakes. This vorticity has little or no effect on the unsteady pressure response of the blade row. The unsteady pressure differences calculated using NGUST exhibited very good agreement with the linear theory predictions.

3 The linearized far-field boundary conditions implemented into the NGUST analysis appear to be adequate for nonlinear flows, although problems can occur when viscous wakes pass through the exit boundary.

The simulations for unsteady flows excited by inlet or exit acoustic disturbances resulted in the following observations:

1 Use of the total pressure to represent the characteristic wave associated with entropy at the inlet can result in artificial pressure reflections at the upstream boundary. If the total pressure is replaced by the entropy, pressure waves pass through the computational boundary with little or no reflection.

2 Quasi-two-dimensional boundary conditions at the inlet and the exit of the cascade can lead to partial reflections of impinging pressure waves. The use of fully two-dimensional boundary conditions eliminates such reflections.

3 The unsteady pressure fields, which include both incident and response waves, associated with acoustic excitations from upstream, tend to remain linear for excitation amplitudes up to 20 percent of the mean inlet pressure. However, the pressure fields associated with acoustic excitations from downstream exhibit significant nonlinear behaviors.

While Navier–Stokes analyses, such as the one developed in the current study, are necessary for identifying and quantifying nonlinear and viscous effects in unsteady flow fields, a linearized inviscid analysis accurately predicted the unsteady flow phenomena for the configurations studied in this investigation, even over a surprisingly wide range of excitation amplitudes. This is important to blade designers, since linearized, frequency-domain analyses are significantly more efficient than nonlinear, time-marching analyses.

References

Baldwin, B. S., and Lomax, H., 1978, "Thin-Layer Approximation and Algebraic Model for Separated Turbulent Flows," AIAA Paper No. 78-257.

Barnett, M., Verdon, J. M., and Ayer, T. C., 1993, "Analysis of High Reynolds Number Inviscid/Viscid Interactions in Cascades," *AIAA Journal*, Vol. 31, No. 11, pp. 1969–1976.

Beam, R. M., and Warming, R. F., 1977, "An Implicit Factored Scheme for the Compressible Navier-Stokes Equations," *AIAA Journal*, Vol. 16, pp. 393–402.

Caspar, J. R., Hobbs, D. E., and Davis, R. L., 1980, "Calculation of Two-Dimensional Potential Cascade Flow Using Finite Area Methods," *AIAA Journal*, Vol. 18, No. 1, pp. 103–109.

Chakravarthy, S. R., and Osher, S., 1982, "Numerical Experiments With the Osher Upwind Scheme for the Euler Equations," AIAA Paper No. 82-0975.

Chakravarthy, S. R., 1982, "Euler Equations—Implicit Schemes and Implicit Boundary Conditions," AIAA Paper No. 82-0228.

Dorney, D. J., 1992, "Numerical Simulations of Unsteady Flows in Turbomachines," Ph.D. thesis, The Pennsylvania State University, University Park, PA.

Giles, M. B., 1988, "Calculation of Unsteady Wake Rotor Interaction," *AIAA Journal of Propulsion and Power*, Vol. 4, No. 4, pp. 356–362.

Giles, M. B., 1990, "Nonreflecting Boundary Conditions for Euler Equation Calculations," *AIAA Journal*, Vol. 28, No. 12, pp. 2050-2058.

Hall, K. C., and Clark, W. S., 1993, "Linearized Euler Predictions of Unsteady Aerodynamic Loads in Cascades," *AIAA Journal*, Vol. 31, No. 3, pp. 540-550.

Hall, K. C., and Verdon, J. M., 1991, "Gust Response Analysis for Cascades Operating in Nonuniform Mean Flows," *AIAA Journal*, Vol. 29, No. 9, pp. 1463-1471.

He, L., 1990, "An Euler Solution for Unsteady Flows Around Oscillating Blades," ASME JOURNAL OF TURBOMACHINERY, Vol. 112, pp. 714-722.

Huff, D. L., and Reddy, T. S. R., 1989, "Numerical Analysis of Supersonic Flow Through Oscillating Cascade Sections by Using a Deforming Grid," AIAA Paper No. 89-2805.

Manwaring, S. R., and Wisler, D. C., 1993, "Unsteady Aerodynamics and Gust Response in Compressors and Turbines," ASME JOURNAL OF TURBOMACHINERY, Vol. 115, pp. 724-740.

Merkle, C. L., 1987, private communication.

Rai, M. M., and Chaussee, D. S., 1984, "New Implicit Boundary Procedures—Theory and Applications," *AIAA Journal*, Vol. 22, pp. 1094-1100.

Rai, M. M., 1987, "Navier-Stokes Simulations of Rotor-Stator Interaction Using Patched and Overlaid Grids," *AIAA Journal of Propulsion and Power*, Vol. 3, No. 5, pp. 387-396.

Rai, M. M., 1989, "Three-Dimensional Navier-Stokes Simulations of Rotor-Stator Interaction," *AIAA Journal of Propulsion and Power*, Vol. 5, pp. 307-319.

Siden, L. D. G., 1991, "Numerical Simulation of Unsteady Viscous Compressible Flows Applied to Blade Flutter Analysis," ASME Paper No. 91-GT-203.

Smith, T. E., 1990, "Aerodynamic Stability of a High-Energy Turbine Blade," AIAA Paper No. 90-2351.

Verdon, J. M., 1990, "Linearized Unsteady Aerodynamics for Turbomachinery Aeroelastic Applications," AIAA Paper No. 90-2355.

Verdon, J. M., Barnett, M., Hall, K. C., and Ayer, T. C., 1991, "Development of Unsteady Aerodynamic Analyses for Turbomachinery Aeroelastic and Aeroacoustic Applications," NASA CR 4405.

Verdon, J. M., 1993, "Unsteady Aerodynamic Methods for Turbomachinery Aeroelastic and Aeroacoustic Applications," *AIAA Journal*, Vol. 31, No. 2, pp. 235-250.

Whitehead, D. S., 1987, "Classical Two-Dimensional Methods," Chap. III in: *AGARD Manual on Aeroelasticity in Axial-Flow Turbomachines*, Vol. 1, *Unsteady Turbomachinery Aerodynamics*, M. F. Platzer and F. O. Carta, eds., AGARD-AG-298.

Whitehead, D. S., 1990, "A Finite Element Solution of Unsteady Two-Dimensional Flow in Cascades," *International Journal for Numerical Methods in Fluids*, Vol. 10, pp. 13-34.

Unsteady Aerodynamic Forcing Functions: A Comparison Between Linear Theory and Experiment

J. M. Feiereisen

M. D. Montgomery

S. Fleeter

School of Mechanical Engineering,
Purdue University,
West Lafayette, IN 49707

The unsteady flow field generated by rotating rows of perforated plates and airfoil cascades is mathematically split into vortical and potential components using two methods, one relying entirely on velocity data and the other utilizing both velocity and unsteady static pressure data. The propagation and decay of these split flow perturbations are then examined and compared to linear theory predictions. The perforated plate gusts closely resemble linear theory vortical gusts. Both splitting methods indicate that they are dominantly vortical gusts with insignificant unsteady static pressure perturbations. The airfoil gusts resemble linear theory combined vortical and potential gusts. The recombined airfoil gusts using the vortical and potential components calculated by the method using only unsteady velocity data do not necessarily resemble the measured gusts, nor do they behave axially as predicted by linear theory. The recombined airfoil gusts using the linear theory components calculated by the method using both unsteady velocity and unsteady static pressure data do resemble the measured gusts and behave axially as predicted by linear theory, with the vortical component propagating unattenuated and the potential component decaying at the rate predicted by linear theory.

Introduction

In a multistage turbomachine, each blade row generates wakes that enter the inlet flow field of downstream blade rows. In a reference frame fixed to the wake-producing blade row, the flow field is steady but possesses spatial flow nonuniformities. The motion of a downstream blade row relative to the wake-producing blade row produces a temporal flow fluctuation, which is an aerodynamic forcing function, a gust, causing a fluctuating pressure response on the downstream blades. Such unsteady aerodynamic forcing functions can result in blade vibration, causing unacceptable levels of stress and adversely affecting blade fatigue life.

State-of-the-art linearized unsteady aerodynamic models for predicting blade response are essentially limited to two-dimensional, perfect-fluid theory analyses. In flat-plate analyses, the steady flow is uniform relative to the responding blade row, with superimposed small perturbations in the streamwise and transverse directions. Advanced analyses have been developed that model thickness and camber in the responding blade row, thereby distorting the perturbation by linearizing about the nonuniform steady flow around the blade rather than the simpler upstream uniform flow; see for example Goldstein and Atassi (1976), Scott and Atassi (1990), Hall and Verdon (1989), and Fang (1991).

In all of these models, the gust is described in terms of its harmonics, with each harmonic modeled as a gust forcing function boundary condition for the prediction of the corresponding harmonic of the unsteady aerodynamic response. The complete response of a downstream blade row is then the sum of the responses to the individual harmonics. As a consequence of this harmonic analysis, all gusts are modeled in the same manner: a Fourier series of velocity and pressure fluctuations. This assumption that all gusts may be modeled in the same manner was termed the fundamental gust modeling assumption by Henderson and Fleeter (1993a).

Henderson and Fleeter (1993a) investigated the fundamental gust modeling assumption through a series of experiments in which the gust forcing function was measured and analyzed according to linear theory. The unsteady aerodynamic response of downstream blades was measured and compared to linear theory predictions. They proposed two constraints on linear theory gusts. The primary constraint is that the gust component phase angle ϕ_w must be either 0 or 180 deg, that is, the unsteady perturbation velocity vectors are parallel to one another and the gust is divergence free. The secondary constraint is that the gust magnitude direction β_w must be parallel to the rotor downstream mean relative flow $\bar{\beta}_2$.

Their gust analysis and blade response predictions neglected potential effects, with the measured blade response normalized by the normal component of the unsteady velocity measured at the leading edge of the responding blade row. These velocity data were obtained with the responding blade row removed from the facility. The responses to gusts that satisfied the constraints were found to be accurately predicted by linear theory, while gusts that violated the constraints gave much

---

Contributed by the International Gas Turbine Institute and presented at the 38th International Gas Turbine and Aeroengine Congress and Exposition, Cincinnati, Ohio, May 24–27, 1993. Manuscript received at ASME Headquarters March 1, 1993. Paper No. 93-GT-141. Associate Technical Editor: H. Lukas.

poorer agreement between linear theory prediction and experiment. They suggested that their analysis could be improved by modeling the potential component of the gust and incorporating it into the analysis.

For incompressible flow, a method of splitting the measured gust into vortical and potential components proposed by Manwaring and Wisler (1993) utilizes unsteady velocity data only. Their incompressible analysis attributed any violation of the vortical gust constraints to the presence of an unsteady potential perturbation. However, these constraints can be violated by effects not modeled by the theory, such as momentum diffusion in the wake. In addition, any experimental error that affects the acquired unsteady velocity field directly affects the calculated unsteady potential field. Although vortical gusts only involve velocity fluctuations, potential gusts are characterized by static pressure fluctuations as well. Thus, it is important to investigate the effect of this vortical-potential splitting to account directly for the unsteady static pressure field.

In this paper, the splitting method is extended to include unsteady static pressure data. The decay characteristics of the split perturbations calculated by both the velocity-only method and the velocity-pressure method are examined and compared to linear theory predictions.

Facility

The Purdue Annular Cascade Research Facility is an open-loop draw-through type wind tunnel capable of test section velocities of 70 m/s (220 ft/sec). The inlet flow, conditioned first by a honeycomb section and then a settling chamber, accelerates into the annular test section via a bellmouth inlet. The test section exit flow is diffused into a large plenum. The 224 kW (300 hp) centrifugal fan located downstream of the plenum draws the air through the facility, with guide vanes at the fan inlet allowing flow rate adjustment through the facility. The annular test section, Fig. 1, houses a rotor independently driven by a 7.5 kW (10 hp) A-C motor controlled by a variable frequency drive to create the desired unsteady flow field together with the downstream stator row. The separate drive motors on the rotor and system fan uncouple the rotor speed from the throughflow velocity. Thus, independent control over unsteady aerodynamic parameters, for example the reduced frequency, is possible since the system flow rate is independent of rotor speed and the rotor configuration.

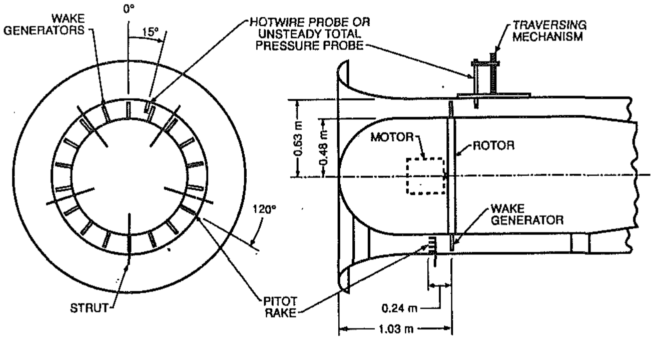

Fig. 1 Annular test section schematic

Basic measurements include the test-section velocity profile upstream of the rotor and the test-section air stagnation temperature and static pressure. The test-section air stagnation temperature is measured using a thermocouple. A pitot tube rake provides the test-section inlet velocity profile. The pitot rake is an assembly of ten total pressure tubes equally spaced across the annular test section and aligned with the annulus axis. Two test-section static taps located on the outer annulus wall are utilized, one near the pitot rake and the other 3.18 cm (1.25 in.) upstream of the leading edge of an optional stator airfoil row. The inlet velocities are calculated from isentropic compressible flow theory using the pitot rake stagnation pressure, the test section air static pressure measurement, and the test section air stagnation temperature measurements as the input parameters.

Gust Generation and Measurement

The unsteady periodic forcing functions are generated with rotating rows of perforated plates and airfoil cascades, Fig. 2. The perforated plates were fabricated from 56 percent porosity aluminum sheet mounted on the rotor such that the plate width was normal to the rotor axis. The airfoils have a 7 deg twist from the hub to the tip to achieve constant spanwise angle-of-attack and are mounted on the rotor at 35 percent chord and set to stagger angles measurable to ±0.5 deg.

Instrumentation. Unsteady data define the forcing function or gust generated by the rotating rows of perforated plates and airfoil cascades. These data are determined by the midspan unsteady velocity and static pressure fluctuations downstream of these rotors. The rotor-exit flow field unsteady total pressure

Nomenclature

A = proportionality constant of harmonic potential disturbance
D = proportionality constant of harmonic vortical disturbance
$\mathbf{k}$ = gust wave number vector
k_η = tangential wave number
k_ξ = axial wave number
M = Mach number
M_η = tangential Mach number
M_ξ = axial Mach number
p = static pressure perturbation
u = axial velocity perturbation
v = tangential velocity perturbation
$\mathbf{U}$ = mean absolute velocity vector
$\overline{U}_1$ = rotor-upstream mean absolute velocity
$\mathbf{w}$ = perturbation velocity vector
$\mathbf{w}_p$ = potential perturbation velocity vector
$\mathbf{w}_v$ = vortical perturbation velocity vector
$\mathbf{W}$ = mean rotor-relative velocity vector
W_p = unsteady pressure data weighting factor
W_v = unsteady velocity data weighting factor
$\overline{W}_2$ = rotor-downstream mean-relative velocity
$\overline{W}_\eta$ = rotor-downstream mean-relative tangential velocity
$\overline{W}_\xi$ = rotor-downstream mean axial velocity
x = rotor-downstream absolute streamwise coordinate
y = rotor-downstream absolute normal coordinate
$\overline{\alpha}$ = mean absolute flow angle
$\overline{\beta}_1$ = rotor-upstream mean-relative flow angle
$\overline{\beta}_2$ = rotor-downstream mean-relative flow angle
β_w = gust magnitude direction
η = tangential coordinate
ξ = axial coordinate
$\overline{\rho}$ = mean density
χ = potential gust component axial decay factor
ϕ_p = unsteady potential
ϕ_w = measured gust component phase angle
Ω = rotor blade speed at test section radius

Superscripts

* = nondimensional

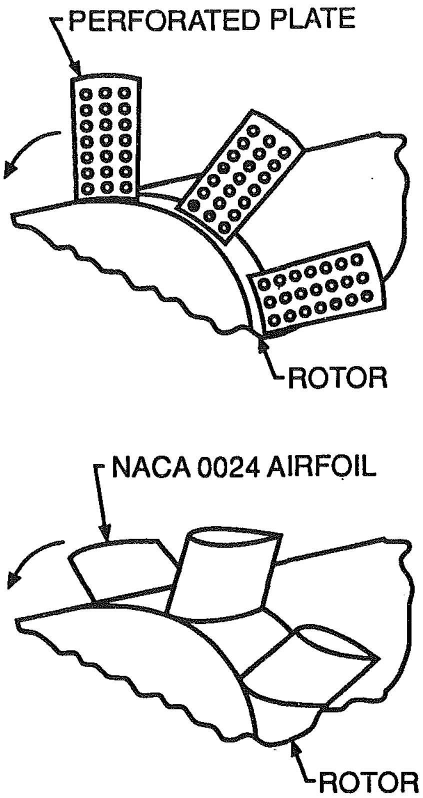

Fig. 2 Test section with wake generators

is measured with a hemispherical-nosed total pressure pitot tube fitted with an unsteady pressure transducer. The amplitude of the incident flow angle is a function of the wake generator, with the angle of the pitot tube set to minimize flow angle variations. The criterion presented by Becker and Brown (1974) shows that the errors produced by the incident flow angle fluctuations should be no more than 6 percent for the perforated plates and less than 1 percent for the airfoils. A cross hot-wire anemometer is used to measure the unsteady velocity field. The absolute velocity magnitude and flow angle errors are estimated at 4 percent and 0.5 deg, respectively. The wake velocity deficits are decomposed into streamwise and transverse velocity components, with the unsteady static pressure calculated as the difference between the unsteady total pressure and the unsteady dynamic pressure.

Data Acquisition and Analysis. The time variant signals are digitized over one rotor revolution using approximately 2000 samples. The number of ensemble averages necessary to obtain clean periodic time traces was investigated. Ensemble averaging the hot-wire and pressure transducer signals 150 and 100 times, respectively, produced very clean periodic time traces with the random fluctuations averaged away. The Fourier components of the ensemble-averaged time traces are numerically determined using Fast Fourier Transform software. The sample frequency is set and the number of samples is adjusted to produce time records of exactly one rotor revolution period to eliminate frequency leakage problems in Fourier Transform analysis. The sample frequency and number of digitizations are set based upon an accurate rotor rotational speed, measured by digitizing the shaft trigger signal at the maximum sample frequency and counting the number of samples between triggers.

Linear Theory Gust Model

To develop the linear theory, flow perturbations are assumed small relative to the uniform, steady flow properties. The linearized equations describing the perturbation pressure p and velocity $\mathbf{w}$ are given in Eqs. (1) and (2):

$$\frac{1}{c_0^2}\frac{\bar{D}p}{Dt}+\bar{\rho}\nabla\cdot\mathbf{w}=0 \tag{1}$$

$$\bar{\rho}\frac{\bar{D}\mathbf{w}}{Dt}+\nabla p=0 \tag{2}$$

where the overbar indicates a mean value, the mean flow material derivative in the rotor frame given by $\bar{D}/Dt=\partial/\partial t+\bar{W}\,\partial/\partial x$ where $\bar{W}$ is the steady mean flow.

Vortical and Potential Splitting. The perturbation velocity field is split into rotational and irrotational components per Goldstein's splitting theorem (Goldstein, 1978), Eq. (3). The rotational velocity is also termed the vortical perturbation velocity or vortical gust, with the irrotational perturbation velocity also referred to as the potential or acoustic perturbation velocity or gust:

$$\mathbf{w}=\mathbf{w}_v+\mathbf{w}_p \tag{3}$$

This splitting assumes that any vortical velocity perturbation satisfies the following constraints:

$$\nabla\cdot\mathbf{w}_v=0 \tag{4}$$

$$\frac{\bar{D}\mathbf{w}_v}{Dt}=0 \tag{5}$$

Thus the linearized equations describing the rotational and irrotational perturbation components are uncoupled, with the coupling occurring in the airfoil surface boundary condition.

The irrotational perturbation velocity $\mathbf{w}_p$ can be derived from a potential function

$$\mathbf{w}_p=\nabla\phi_p \tag{6}$$

and therefore must satisfy

$$\nabla\times\mathbf{w}_p=0 \tag{7}$$

The perturbation potential is related to the pressure perturbation p through the unsteady Bernoulli equation:

$$p=-\bar{\rho}\frac{\bar{D}\phi_p}{Dt} \tag{8}$$

Substituting these relations into Eq. (1) yields the following expression for the perturbation velocity potential:

$$\frac{1}{c_0^2}\frac{\bar{D}}{Dt}\left(\frac{\bar{D}\phi_p}{Dt}\right)-\nabla^2\phi_p=0 \tag{9}$$

where $\mathbf{w}_p=\nabla\phi_p$.

Vortical Gust. In the frame of reference rotating with the wake-producing rotor, the flow is steady, with $\bar{\mathbf{W}}$ denoting the mean velocity, Fig. 3. Periodicity in the axial-tangential (ξ, η) coordinate system shows that the gust propagation vector $\mathbf{k}$ must be perpendicular to the rotor mean flow exit velocity vector $\mathbf{W}_2$, expressed mathematically as

$$\mathbf{k}\cdot\bar{\mathbf{W}}=0 \tag{10}$$

where $\mathbf{k}$ is the gust propagation wave vector $\mathbf{k}=k_\xi\hat{e}_\xi+k_\eta\hat{e}_\xi$, $\hat{e}_\xi$ and $\hat{e}_\eta$ are unit vectors, and k_ξ and k_η are the axial and tangential wave numbers, $\bar{\mathbf{W}}=\bar{\mathbf{W}}_2=\bar{W}_\xi\hat{e}_\xi+\bar{W}_\eta\hat{e}_\eta$ where $\bar{W}_\eta$ and $\bar{W}_\xi$ are the mean rotor-relative velocities in the tangential and axial directions.

The gust propagation vector $\mathbf{k}$ is specified as follows. The flow in the rotor frame is spatially periodic, repeating itself every rotor spacing. The tangential wave number for the nth harmonic is thus

$$k_{\eta n}=\frac{2\pi n}{S_R} \qquad n=1,\,2,\,3,\,\ldots. \tag{11}$$

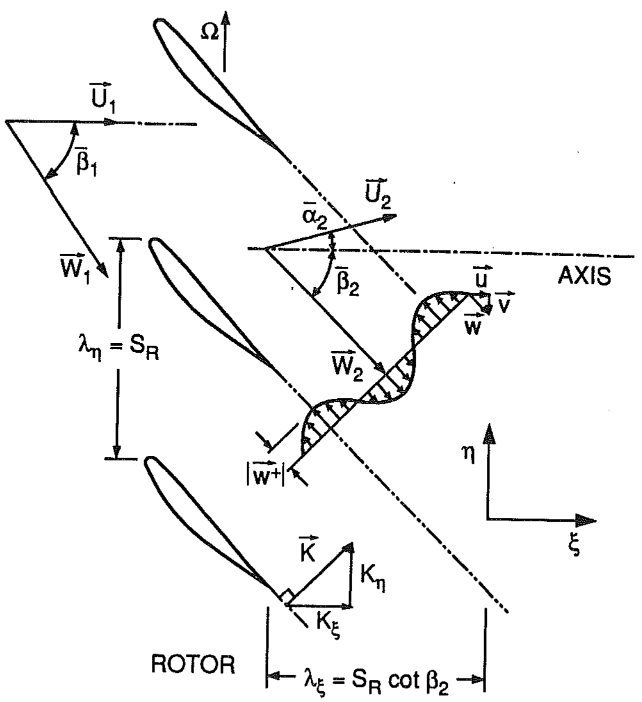

Fig. 3 Vortical gust flow field

where S_R is the rotor blade-to-blade spacing.

The axial wave number for the vortical gust, derived from Eq. (10), is

$$k_{\xi n} = -k_{\eta n} \frac{\overline{W}_\eta}{\overline{W}_\xi} \tag{12}$$

The vortical gust $\mathbf{w}_v$ is specified as follows. The vortical gust convects with the mean flow $\overline{\mathbf{W}}$, Eq. (5). This is expressed as

$$\mathbf{w}_v = \mathbf{w}_v^+ \exp[-i\mathbf{k}\cdot(\mathbf{x}-\overline{\mathbf{W}}t)] \tag{13}$$

where $\mathbf{w}_v^+$ is the vortical gust amplitude vector.

Equations (4) and (13) relate the wave vector and the gust amplitude vector so that the gust propagates in a direction normal to $\mathbf{w}_v$:

$$\mathbf{k}\cdot\mathbf{w}_v^+ = 0 \quad \text{so that} \quad \mathbf{w}_v \perp \mathbf{k} \tag{14}$$

Combining this with the result expressed in Eq. (10) shows that the vortical gust velocity magnitude vector must be parallel to the mean rotor-relative velocity:

$$\mathbf{w}_v^+ \parallel \overline{\mathbf{W}} \tag{15}$$

Manwaring and Wisler (1992) denoted the complex constant of proportionality between these two constant vectors by D. Thus the vortical gust in the rotor frame can be written as

$$\mathbf{w}_v = D\overline{\mathbf{W}} \exp(-i\mathbf{k}\cdot\mathbf{x}) \tag{16}$$

This equation shows that the vortical gust propagates unattenuated in the direction of the gust propagation vector $\mathbf{k}$.

Potential Gust. The potential or acoustic gust $\mathbf{w}_p$ is determined from the steady form of the perturbation velocity potential equation, Eq. (9):

$$(1-\mathrm{M}^2)\frac{\partial^2\phi_p}{\partial x^2} + \frac{\partial^2\phi_p}{\partial y^2} = 0 \tag{17}$$

This has solutions of the form

$$\phi_p = A \exp(-ik_\eta\eta + \chi\xi) \tag{18}$$

where $\chi = (i\mathrm{M}_\xi\mathrm{M}_\eta k_\eta - \sqrt{(1-\mathrm{M}^2)k_\eta^2})/(1-\mathrm{M}_\xi^2)$ is the axial decay factor, A is a complex constant, k_η is the tangential wave number specified in Eq. (11), M is the relative Mach number, M_ξ and M_η are the axial and tangential Mach numbers.

Thus, the potential gust propagates unattenuated in the tangential direction but decays exponentially in the axial direction.

Vortical and Potential Gusts. The vortical and potential gusts $\mathbf{w}_v$ and ϕ_p are thus described in terms of their harmonics:

$$\mathbf{w}_v = \Sigma\, D_n\overline{\mathbf{W}} \exp[-i(k_{\eta n}\eta + k_{\xi n}\xi)] \tag{19}$$

$$\phi_p = \Sigma\, A_n \exp[-ik_{\eta n}\eta + \chi_n\xi] \tag{20}$$

where $\mathbf{w}_p = \nabla\phi_p$.

Thus the linear theory combined potential and vortical gusts are described by the complex constants A_n and D_n. Note that except for A_n and D_n, which must be determined experimentally, these are completely specified.

Relating Measurements to Theory. The complex constants A and D are determined experimentally by measuring the wake, as proposed by Giles and reported by Manwaring and Wisler (1992). The three perturbation quantities measured in the experiments discussed herein are the two components of the unsteady velocity and the unsteady static pressure. Due to measurement uncertainty and limitations of the theory, there are inevitable discrepancies between these three measured quantities and the two complex constants, A and D, available to fit the theory to the data. These discrepancies are minimized by developing a least squares formulation to find a best fit of the two constants A and D to the measurements.

The relationship between the linear theory quantities A and D and the measured perturbation quantities can be put into the following matrix form:

$$\begin{bmatrix} \chi & \overline{W}_\xi \\ -ik_\eta & \overline{W}_\eta \\ \bar{\rho}(-\overline{W}_\xi\chi + \overline{W}_\eta ik_\eta) & 0 \end{bmatrix} \begin{Bmatrix} A \\ D \end{Bmatrix} = \begin{Bmatrix} u \\ v \\ p \end{Bmatrix} \tag{21}$$

where u is the axial component of the measured perturbation velocity, v is the tangential component, and p is the measured unsteady static pressure. Equation (18) shows that there is a different wave number corresponding to each harmonic, thus A and D take on different values for each harmonic analyzed.

In compact notation

$$[T]\{c\} = \{b\} \tag{22}$$

where

$$[T] = \begin{bmatrix} \chi & \overline{W}_\xi \\ -ik_\eta & \overline{W}_\eta \\ \bar{\rho}(-\overline{W}_\xi\chi + \overline{W}_\eta ik_\eta) & 0 \end{bmatrix} \quad \{c\} = \begin{Bmatrix} A \\ D \end{Bmatrix} \quad \{b\} = \begin{Bmatrix} u \\ v \\ p \end{Bmatrix}$$

The least-squares formulation that minimizes the difference between $[T]$ $\{c\}$ and $\{b\}$ is

$$[T]^T[\mathrm{W}][T]\{c\} = [T]^T[W]\{b\} \tag{23}$$

where $[T]^T$ is the transpose of $[T]$ and $[W]$ is a diagonal weighting matrix specifying the relative weighting of the three measured quantities:

$$[W] = \begin{bmatrix} W_{11} & 0 & 0 \\ 0 & W_{22} & 0 \\ 0 & 0 & W_{33} \end{bmatrix} \tag{24}$$

Note that specifying $W_{11} = W_{22} = 1$ and $W_{33} = 0$ removes the measured pressure from the calculation and recovers Manwaring and Wisler's method.

The method developed herein fits two linear theory complex constants, A and D, to three unsteady perturbation measurements, u, v, and p. Only two weighting factors are used herein: $W_v = W_{11} = W_{22}$ for the two unsteady velocity components, and $W_p = W_{33}$ for the unsteady static pressure. The subscript v refers to the unsteady velocity measurements, with the subscript p referring to the unsteady static pressure measurement.

A consequence of this least-squares method is that while the unsteady static pressure measurement can be given a zero weighting, the two unsteady velocity measurements cannot since this would attempt to fit the two linear theory values to one measurement. It should also be noted that if the flow is incompressible, the axial decay factor of the potential field is exactly the negative of the circumferential wave number. This leads to identical rows in the $[T]^T[W][T]$ matrix if and only if all weightings are equal. This is a failure of the normal equation form of least squares for this special case.

With this least-squares method, if the weighting is chosen so as to rely solely on the unsteady velocity measurements, the unsteady velocity field is reconstructed exactly and all the discrepancy between the theoretical gust and the measurement resides in the calculated unsteady static pressure perturbation. If the weighting is chosen to rely mainly on the unsteady static pressure measurement, then the discrepancy resides mainly in the reconstructed unsteady velocity field.

The measured unsteady velocities and static pressure perturbations are nondimensionalized as follows:

$$u^* = \frac{u}{\overline{W}_2} \tag{25}$$

$$v^* = \frac{v}{\overline{W}_2} \tag{26}$$

$$p^* = \frac{p}{\rho \overline{W}_2^2} \tag{27}$$

Using the rotor blade spacing S_R as the characteristic length results in the dimensionless linear theory gust parameters

$$A^* = \frac{2\pi n\, A}{\overline{W}_2\, S_R} \tag{28}$$

$$D^* = D \tag{29}$$

for the potential and vortical gusts, respectively, where n is the number of the particular harmonic being analyzed.

This method of splitting the gust was studied numerically by generating a linear theory gust with $|A^*|$ equal to 0.005 and $|D^*|$ equal to 0.01 and constructing velocity and pressure "time traces" of the "measured" quantities. These time traces were then distorted with Gaussian-distributed random noise to simulate experimental error. This simulated gust was then processed by the same methods to be utilized with the experimentally measured gusts.

Figure 4 shows the computed magnitudes of the dimensionless parameters A^* and D^* as functions of the weighting. In this case $W_v + W_p = 1$, so as W_p approaches one, W_v approaches zero. It can be seen that without any unsteady pressure information, i.e., $W_v = 1$ and $W_p = 0$, there is a small error in both the calculated values of A^* and D^*. As more emphasis is placed on the unsteady static pressure measurement, W_p increasing from zero and W_v decreasing from one, the calculated values of A^* and D^* deviate further from their specified values. This is a consequence of the least-squares method of fitting the calculated values to the data. Beyond the point of equal weighting, $W_p = W_v = 0.5$, as further emphasis is placed on the unsteady total pressure measurement, it can be seen that the calculated value for D^* approaches the specified value and A^* approaches some slightly erroneous value. Note that the total error for the end case, $W_v = 0.01$ and $W_p = 0.99$, is smaller in magnitude than for the case relying on the unsteady velocity measurements alone, $W_v = 1$ and $W_p = 0$. This is presumably due to some of the noise in the unsteady pressure signal canceling some of the noise in the unsteady velocity signal. Also note that the "measured" unsteady static pressure is calculated from unsteady total pressure and unsteady dynamic pressure. Therefore the static pressure "measurement" contains redundant velocity information while carrying along additional pressure information. A similar simulated gust without the artificial noise produced results that accurately split the two components and were unaffected by the weighting.

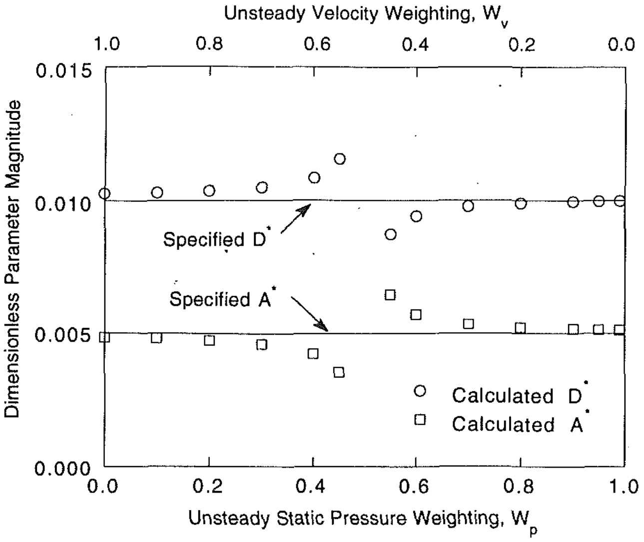

Fig. 4 Predicted values of A^* and D^* versus weighting factors

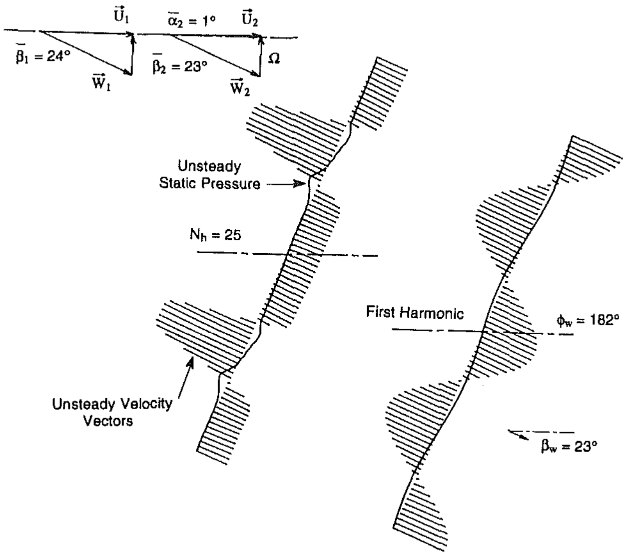

Fig. 5 Typical perforated plate gust

With regard to the experiments, two weighting cases are discussed herein. Method V ($W_v = 1$, $W_p = 0$) places all of the emphasis on the unsteady velocity perturbation, neglecting the unsteady pressure perturbation and thus duplicates the method of Manwaring and Wisler (1993). Any violation of the vortical gust constraints is attributed to the presence of an unsteady potential field. The linear theory gust constructed from the calculated values of A^* and D^* exactly duplicates the measured unsteady velocity field. However, the static pressure perturbation calculated by this method is affected by any effects not modeled by the theory. Method P ($W_v = 0.01$, $W_p = 0.99$) puts

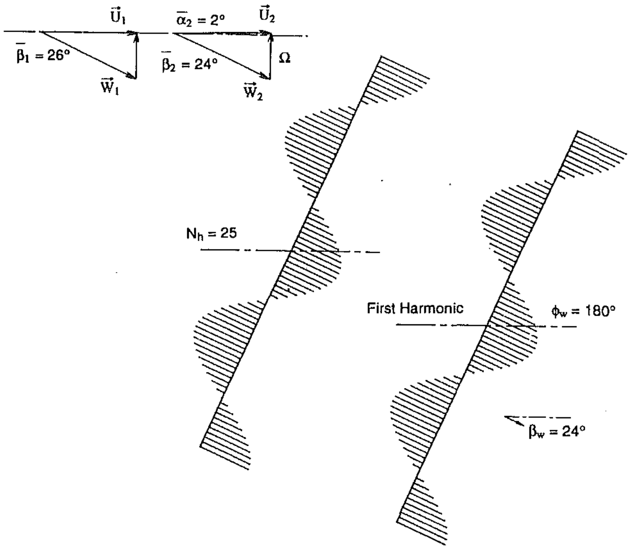

Fig. 6 Idealized gust satisfying both constraints

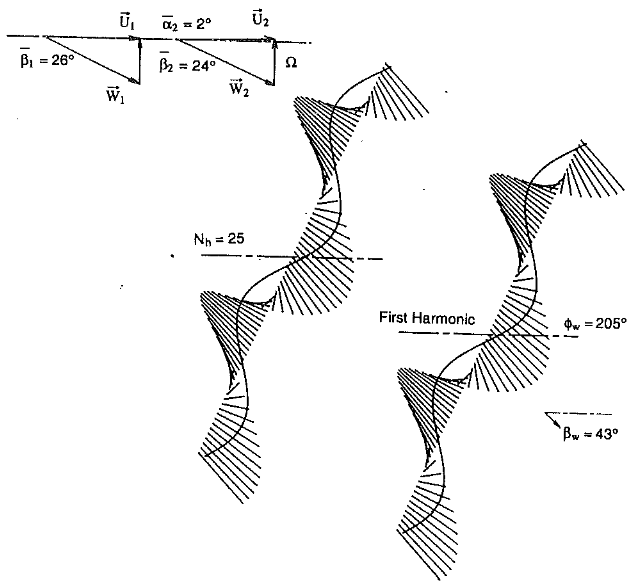

Fig. 7 Idealized gust violating both constraints

most of the emphasis on the measured unsteady static pressure, thus calculating an unsteady potential field, which corresponds closely to the measured static pressure perturbation. As indicated in Fig. 4, the splitting appears most accurate when most of the weighting is placed on the unsteady static pressure. The weighting factors for Method *P* were chosen to give a heavy weighting to the unsteady static pressure while still avoiding the numerical problem encountered when the velocities are given zero weighting. Note that the unsteady static pressure was calculated from an unsteady total pressure and an unsteady dynamic pressure. Thus the unsteady static pressure data contain redundant velocity information so the velocity is actually weighted more heavily than is apparent. The least-squares technique minimizes the overall difference between the calculated theoretical quantities and the measurements.

Gust Presentation. A typical perforated-plate forcing function is presented in Fig. 5 illustrating the forcing function plot construction. The periodic velocity vector profile and static pressure distribution define the forcing function. A complete forcing function plot is shown together with the forcing function fundamental harmonic.

The mean velocity triangles in the upper portion of the figure show the inlet (subscript 1) and downstream (subscript 2) steady flow fields. The mean velocity triangles include the absolute $\bar{\mathbf{U}}$, relative $\bar{\mathbf{W}}$, and rotor velocity Ω vectors together with the absolute and relative flow angles $\bar{\alpha}$ and $\bar{\beta}$, respectively. The inlet flow enters the test section in a purely axial direction. Thus the (rotor speed)-to-(axial velocity) ratio determines the inlet mean relative flow angle, $\tan \bar{\beta}_1 = \Omega / \bar{U}_1$. The inlet mean-relative flow angle increases and decreases with rotor speed and is characteristic of the operating point of the facility.

To construct the forcing function plot, a baseline is defined two fundamental wavelengths long and oriented parallel to the gust propagation direction **k**. Dimensionless unsteady velocity vectors, selected on equal intervals in the periodic cycle, are drawn originating from the baseline. The solid line of Fig. 5 represents the dimensionless periodic unsteady static pressure distribution where the normal distance from the baseline denotes the static pressure fluctuation from the mean. The nondimensionalization discussed in the previous section results in a velocity vector of unit length representing a unit velocity pressure fluctuation. Thus, it is possible to determine the relative magnitudes of the velocity and pressure fluctuations directly.

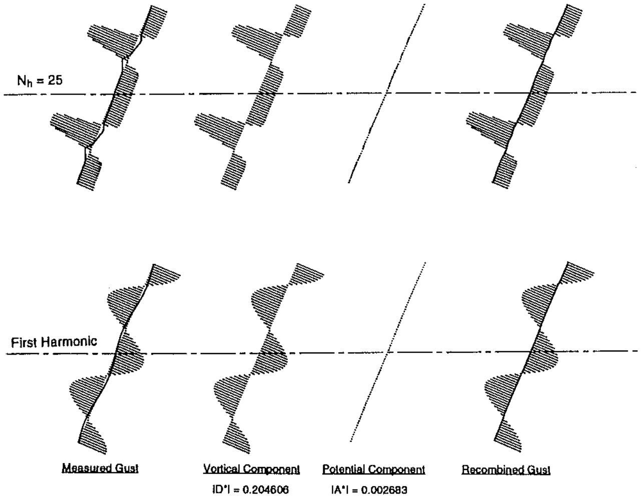

Fig. 8 Method *V* splitting of perforated plate gust

Combined Vortical and Potential Gust. The two linear theory constraints proposed by Henderson and Fleeter (1993a) apply to only the vortical gust component. Any potential gust component must only satisfy continuity and be irrotational. The introduction of such a potential component yields a combined gust, which violates the vortical linear theory constraints yet still conforms to linear theory. This is demonstrated in the following example.

Figure 6 shows an idealized vortical gust with $|A^*| = 0$ and $|D^*| = 0.01$ satisfying both vortical linear theory constraints, i.e., $\phi_w = 180$ deg and $\beta_w = \bar{\beta}_2$. The magnitude of the vortical gust component is one percent of the mean rotor relative flow and there is no potential gust component. Figure 7 shows a combined vortical-potential gust with $|A^*| = 0.005$ and $|D^*| = 0.01$. The vortical gust component is the same as in Fig. 6 and the additional potential gust component is a velocity perturbation of one-half of one percent of the mean rotor-relative flow. The introduction of the potential component results in the combined gust violating both of the vortical linear theory constraints while introducing a static pressure perturbation. Note that A^* and D^* are complex quantities. While their absolute phase angle values are meaningless, the relative

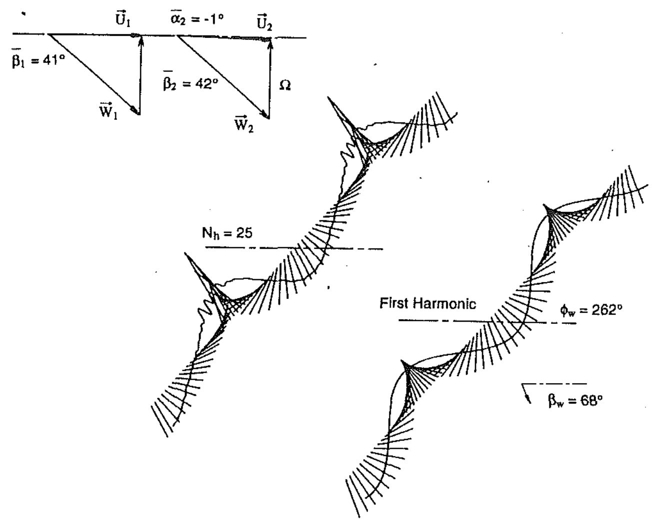

Fig. 9 Typical neutrally loaded airfoil gust

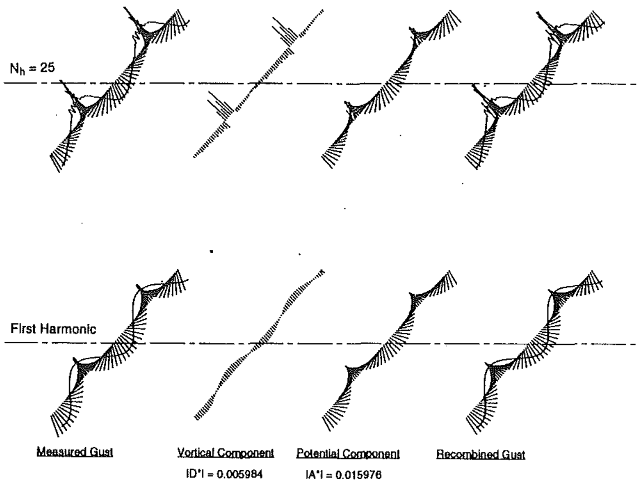

Fig. 11 Method *P* splitting of neutrally loaded airfoil gust

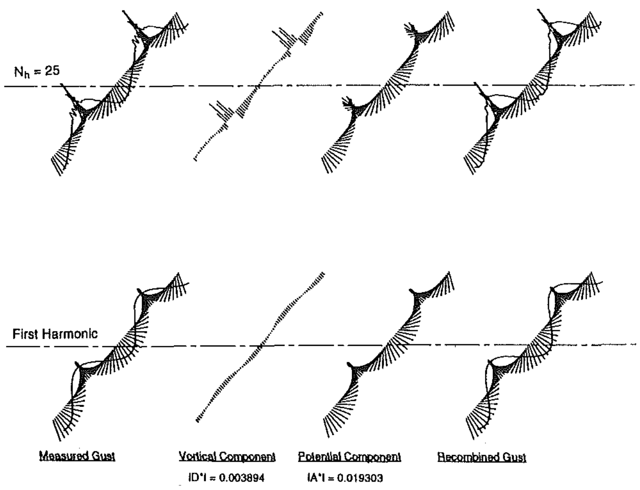

Fig. 10 Method *V* splitting of neutrally loaded airfoil gust

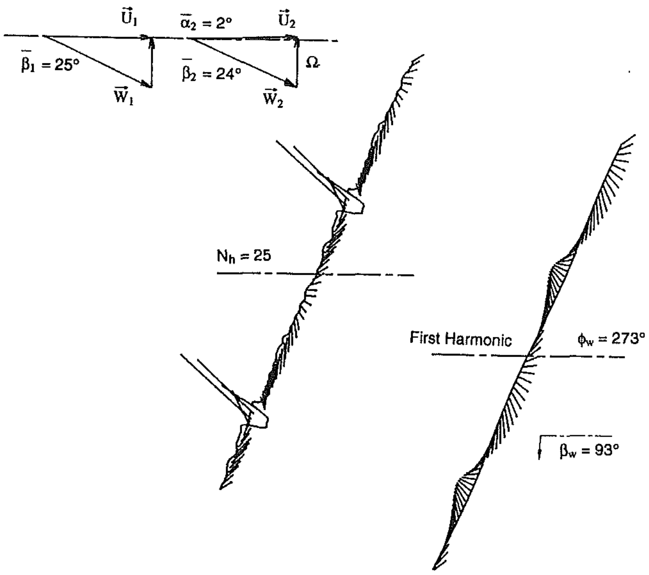

Fig. 12 Compressor-loaded airfoil gust with decayed potential field

phase angle between them as well as their relative magnitudes determine whether they combine to describe a gust violating either of the two vortical linear theory gust constraints individually, or both of them at the same time. Note that $|A^*|$ must be equal to zero for the combined gust to satisfy both constraints. A nonzero value of A^* will always result in a gust that violates either one or both of the vortical linear theory constraints and is always accompanied by an unsteady static pressure perturbation.

Results

To investigate the linear theory splitting of the experimentally measured gust into vortical and potential components, a series of experiments directed at understanding the relevant linear theory gust characteristics were conducted. The periodic flow fields downstream of rotating rows of perforated plates and airfoil cascades were measured and analyzed for consistency with the linear theory predictions. These experiments were conducted with a constant axial velocity corresponding to a Mach number of approximately 0.15. The rotor blade-to-blade spacing was held constant at 0.35 m. The unsteady velocity and pressure fields were measured at several axial locations ranging from 0.13 m to 0.53 m downstream of the rotor center plane. With the wake-generating airfoils installed, the measurement locations ranged over axial distances of 1.1 to 4.7 airfoil chords downstream of the rotor center plane. While instrumented stator vanes may be installed in this facility downstream of the rotor to determine experimentally the unsteady aerodynamic response of such a stator row to the forcing functions, no such stator vane row was installed for the experiments discussed herein.

Perforated Plate Gusts. The perforated plate wake generators generate a negligible potential field as well as viscous diffusion effects on the small length scale associated with the plate holes. Thus the viscous effects within the wake diffuse quite rapidly, leaving a large velocity deficit with a negligible static pressure perturbation.

The perforated plate forcing function presented in Fig. 5 closely resembles a linear theory vortical gust. The periodic velocity vectors are nearly parallel to $\mathbf{W}_2$ and the unsteady static pressure fluctuation is very small. In addition, the fundamental harmonic gust parameters ϕ_w and β_w are very close to their linear theory values with $\phi_w \approx 180$ deg and $\beta_w \approx \bar{\beta}_2$.

Figure 8 shows the gust of Fig. 5 split into vortical and potential components by Method *V*, which uses only the unsteady velocity data. The plots in the upper row represent complete gusts, with N_h harmonics shown. Each plot in the lower row is the fundamental harmonic of the corresponding

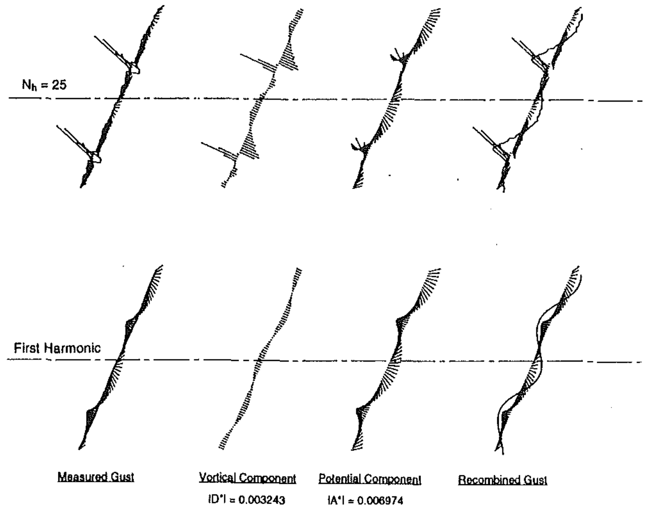

Fig. 13 Method *V* splitting of compressor-loaded airfoil gust with decayed potential field

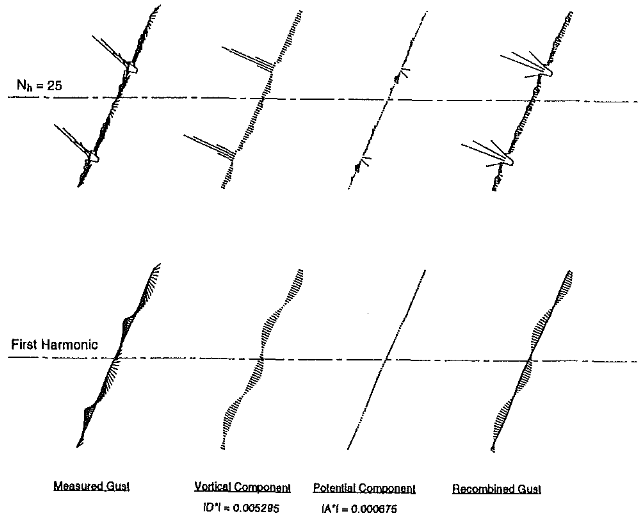

Fig. 14 Method *P* splitting of compressor-loaded airfoil gust with decayed potential field

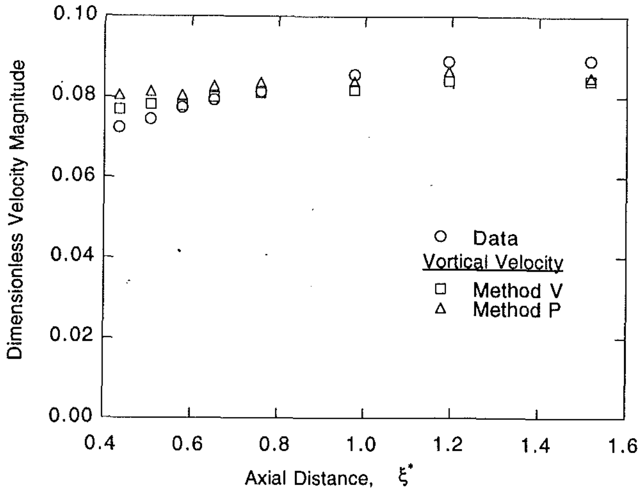

Fig. 15 Axial behavior of perforated plate gust vortical component

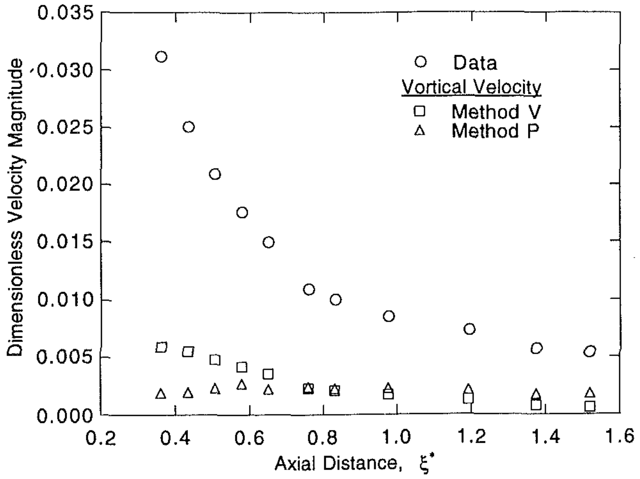

Fig. 16 Axial behavior of compressor-loaded airfoil gust vortical component

gust in the upper row. The leftmost plot in each row is the measured gust. The next two plots are the vortical and potential unsteady velocity fields determined by the analysis, and the rightmost lot is a recombined gust where the split velocity fields are added together and the unsteady static pressure perturbation is calculated via Eq. (21). For this perforated plate gust, the calculated unsteady static pressure perturbation is quite small as is the calculated unsteady potential velocity field. Note that the measured static pressure perturbation is nonzero near the edges of each wake. It is believed that this is a measurement artifact due, in part, to the combination of a rapidly changing instantaneous flow angle at the edge of the perforated plate gust and the angular sensitivity of the total pressure probe.

The excellent reconstruction of this gust from the linear theory components illustrates that it can be well modeled by linear theory. This analysis also shows it is a dominantly vortical gust, indicated by the minimal unsteady static pressure field.

Airfoil Cascade Gusts. The airfoil section used for the wake-generating airfoils is the symmetric NACA 0024 airfoil with a chord of 11.4 cm (4.5 in.). With the airfoil wake generators installed on the rotor, the drive motor may be used to turn the rotor at rotational speeds higher or lower than the freewheel speed. This allows operation of the facility in compressor-loaded, turbine-loaded, and neutrally loaded configurations.

A typical neutrally loaded airfoil gust is shown in Fig. 9. This gust was measured approximately one rotor airfoil chord length downstream of the rotor center plane. Note that the linear theory gust constraints are not satisfied, $\phi_w = 262$ deg and $\beta_w = 68$ deg while $\bar{\beta}_2 = 42$ deg. In addition, there is a significant unsteady static pressure perturbation.

Figure 10 shows splitting Method *V* applied to the gust in Fig. 9. Note that there is a significant potential field, the dimensionless magnitude of which is approximately five times that of the dimensionless vortical field. Neglecting this potential field in the blade response analysis would lead to significant error. While the unsteady velocity field is reconstructed exactly, note that the calculated unsteady static pressure perturbation is slightly different from the measurement. This is a result of all the weighting being giving to the unsteady velocity data with this splitting method. Figure 11 shows Method *P* used to split the same gust into vortical and potential components. Note that this method almost perfectly duplicates the unsteady static pressure measurement while the unsteady velocity field is slightly different from the measurement. This is a result of the majority of the weighting being given to the pressure data with this method.

Both methods of splitting this gust indicate that it is dom-

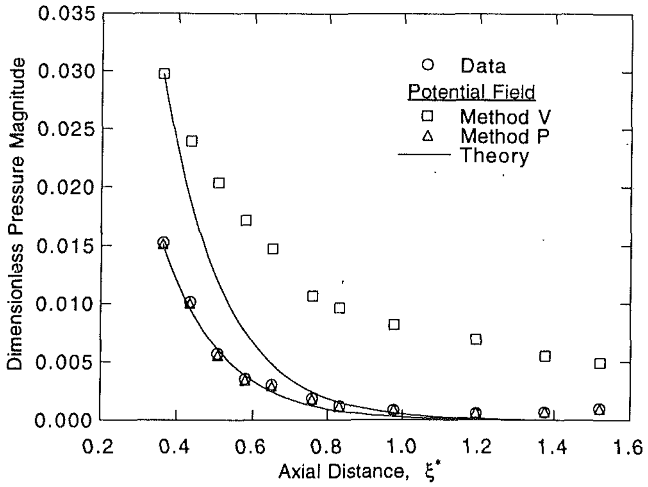

Fig. 17 Axial behavior of compressor-loaded airfoil gust potential component

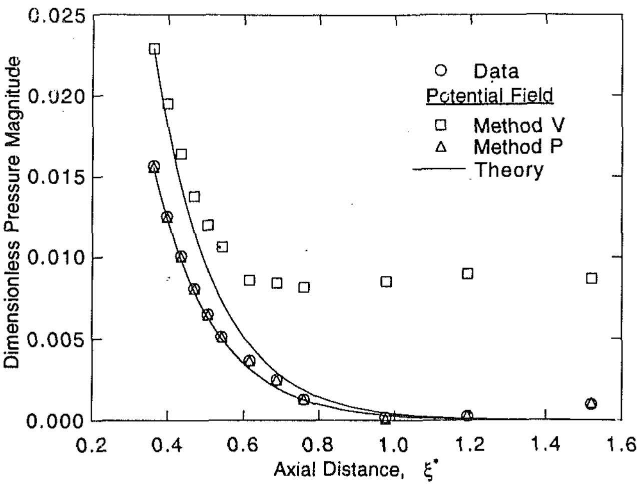

Fig. 19 Axial behavior of turbine-loaded airfoil gust potential component

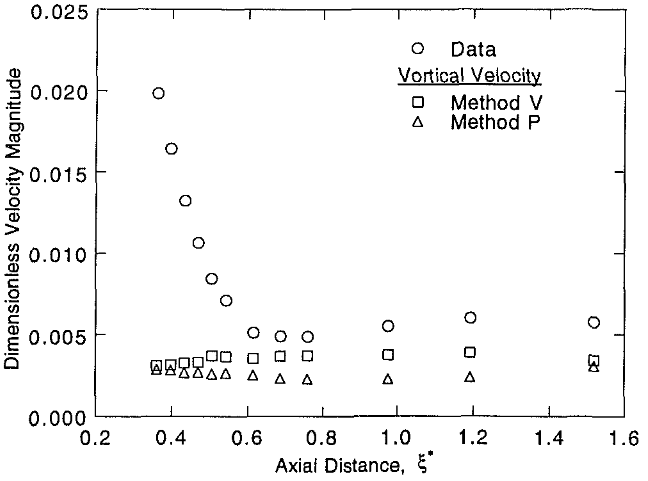

Fig. 18 Axial behavior of turbine-loaded airfoil gust vortical component

inated by potential effects. Due to the additional unsteady static pressure information, the potential field calculated by Method *P* much more closely corresponds to the measurement.

Figure 12 shows a compressor loaded airfoil gust measured approximately 3.7 rotor airfoil chords downstream. Here the potential field has decayed away while there is significant splaying of the velocity field, i.e., $\phi_w = 273$ deg. The absence of a measured unsteady static pressure field would indicate that the splaying of the velocity field in this case is not due to potential effects. In Fig. 13 the gust is split by Method *V*, which attributes any violation of the vortical gust constraints to the presence of an unsteady potential field. The large unsteady potential velocity perturbation calculated by this method is offset by the large unsteady vortical velocity perturbation so the reconstructed unsteady velocity field exactly duplicates the measured unsteady field. The result of this is the prediction of significant vorticity in the free stream between the individual gusts and a significant unsteady static pressure field, which is not reflected in the measurement. Clearly this result is in error. In addition, Method *V* predicts that this gust is dominated by potential effects while the data show that the unsteady static pressure perturbation is insignificant relative to the unsteady velocity perturbation.

Figure 14 shows Method *P* used to split the same gust. The gust reconstructed from the linear theory components calculated by this method resembles the measured gust. This method predicts a potential field, which much more closely corresponds to the measured unsteady static pressure perturbation. The calculated unsteady vortical velocity field shows that there is little vorticity in the free stream between the individual wakes, with the vorticity restricted to the narrow region directly behind the rotor airfoils as expected. Also, Method *P* predicts this gust to be dominated by vortical effects. This would indicate that the splaying of the unsteady velocity field is not due to the presence of an unsteady potential field at the point of measurement, rather the velocity field has been affected by an unsteady potential field upstream, which has decayed away by this point.

Gust Decay Characteristics

Linear theory predicts gust propagation and decay characteristics in the axial and tangential directions. Equation (13) indicates that the vortical gust must propagate unattenuated along the wave propagation vector **k**. Equation (18) states that the potential gust must propagate unattenuated in the tangential direction while decaying in the axial direction.

Perforated Plate Gusts. For the perforated plates, Fig. 15 shows the first harmonic magnitudes of the normal component of the unsteady velocity perturbation **w** measured with the hot wire together with the normal components of the calculated vortical perturbations $\mathbf{w}_v$ from Methods *V* and *P* plotted as functions of the dimensionless axial position ξ^*. Neither the measured velocity perturbation nor either of the calculated vortical perturbations change significantly with axial distance, as expected from linear theory. The potential perturbations are insignificant in all three cases and thus are not presented.

Airfoil Gusts. Figure 16 shows the analogous data for the rotor airfoils in compressor loading. Note that the measured velocity perturbation decays significantly with axial distance. Both Method *V* and Method *P* yield vortical perturbations that remain essentially constant with axial distance, as predicted by linear theory.

Figure 17 presents the first harmonic measured unsteady pressure perturbation, the calculated unsteady perturbations from Methods *V* and *P*, and theory lines based on the upstreammost calculated pressure perturbation for each splitting method decaying exponentially according to the axial decay factor. It can be seen that Method *V* predicts a static pressure perturbation significantly higher than the measurement. While this static pressure perturbation decays with axial distance, it does so at a rate different than that predicted by linear theory. Method *P* produces a static pressure perturbation that agrees with the measurement and decays exponentially in the axial direction as predicted by the linear theory.

The same decay characteristics were examined for the airfoils in turbine loading. Figure 18 shows the measured velocity perturbation decaying rapidly with axial distance, then leveling off at a constant value. Both methods of splitting produce vortical components which do not decay with axial distance. Figure 19 shows that Method V yields a potential component that initially decays with axial distance but then remains constant at some nonzero value. Method P again yields a potential component which decays exponentially in the axial direction as predicted by linear theory.

Both the compressor loaded and turbine-loaded airfoil wakes exhibit a propagating vortical component and a decaying potential component. Close to the rotor the wakes in both cases are dominated by potential effects. However, as the wakes move downstream and the potential effects decay, the wakes become dominantly vortical.

Summary and Conclusions

The fundamental gust modeling assumptions have been investigated through a series of experiments in the Purdue Annular Cascade Research Facility. The unsteady, periodic flow fields downstream of rotating rows of perforated plates and airfoil cascades were measured with a hot-wire anemometer and an unsteady total pressure probe. The unsteady velocity and static pressure fields were then analyzed harmonically and decomposed by two methods into vortical and potential components, which were then compared with linear theory predictions.

The perforated plate gusts closely resemble linear theory vortical gusts. The static pressure fluctuation is small and the periodic velocity vectors are nearly parallel to the rotor downstream mean-relative flow angle over the entire periodic cycle. The correlation of the gust parameters ϕ_w and β_w with their linear theory values is excellent. The vortical component of the gust propagates unattenuated as predicted by linear theory.

The airfoil gusts are well modeled by linear theory, that is, with proper choice of A^* and D^*, the behavior of the gust is accurately predicted as it evolves downstream. The measured velocity perturbations do not satisfy the linear theory vortical gust constraints on the gust parameters ϕ_w and β_w. However, an harmonic decomposition of the unsteady flow field separates the measurements into a propagating vortical component, which satisfies these constraints, and a decaying potential component.

Two methods were used to split the measured gusts into vortical and potential components. Method V, using only velocity data, attributes any violation of the linear theory vortical gust constraints to the presence of an unsteady potential field. These constraints can be violated by effects not modeled by linear theory. Linear theory gusts reconstructed from the components calculated by this method may yield erroneous static pressure perturbations. The least-squares method of splitting the gusts, Method P, uses an unsteady static pressure measurement in addition to the unsteady velocity data. Thus this method incorporates additional information into the analysis, the unsteady static pressure and supposedly redundant information—the velocity information included in the unsteady total pressure data. This results in a more appropriate splitting of the gust into vortical and potential components, with the vortical component remaining constant in magnitude with axial distance and the potential component decaying at the rate predicted by linear theory. This clearly demonstrates that the gust should not be defined utilizing only velocity data.

Acknowledgments

This research was sponsored, in part, by the NASA Lewis Research Center. Both this financial support as well as the technical interchanges with Dr. Daniel Hoyniak are most gratefully acknowledged.

References

Becker, H. A., and Brown, A. P. G., 1974, "Response of Probes in Turbulent Streams," *Journal of Fluid Mechanics*, Vol. 62, Part 1, pp. 85–114.

Fang, J., 1991, "Compressible Flows With Vortical Disturbances Around Cascades of Airfoils," Ph.D. Thesis, University of Notre Dame.

Goldstein, M. E., and Atassi, H., 1976, "A Complete Second-Order Theory for the Unsteady Flow About an Airfoil Due to Periodic Gust," *Journal of Fluid Mechanics*, Vol. 74, Part 4, pp. 741–765.

Goldstein, M. E., 1978, "Unsteady Vortical and Entropic Distortions of Potential Flows Round Arbitrary Obstacles," *Journal of Fluid Mechanics*, Vol. 89, Part 3, pp. 433–468.

Hall, K. C., and Verdon, J. M., 1989, "Gust Response Analysis for Cascades Operating in Nonuniform Mean Flows," presented at the AGARD Conference—Unsteady Aerodynamic Phenomena in Turbomachines, AGARD CPP-468.

Henderson, G. H., and Fleeter, S., 1993a, "Forcing Function Effects on Unsteady Aerodynamic Gust Response: Part 1—Forcing Functions," ASME JOURNAL OF TURBOMACHINERY, Vol. 115, pp. 741–750.

Henderson, G. H., and Fleeter, S., 1993b, "Forcing Function Effects on Unsteady Aerodynamic Gust Response: Part 2—Low Solidity Airflow Row Response," ASME JOURNAL OF TURBOMACHINERY, Vol. 115, pp. 751–761.

Manwaring, S. R., and Wisler, D. C., 1993, "Unsteady Aerodynamics and Gust Response in Compressors and Turbines," ASME JOURNAL OF TURBOMACHINERY, Vol. 115, pp. 724–740.

Scott, J. S., and Atassi, H., 1990, "Numerical Solutions of the Linearized Euler Equations for Unsteady Vortical Flows Around Lifting Airfoils," AIAA Paper No. 90-0694.

Dynamic Forces From Single Gland Labyrinth Seals: Part I—Ideal and Viscous Decomposition

K. T. Millsaps[1]

M. Martinez-Sanchez

Gas Turbine Laboratory,
Massachusetts Institute of Technology,
Cambridge, MA 02139

A theoretical and experimental investigation on the aerodynamic forces generated by a single gland labyrinth seal executing a spinning/whirling motion has been conducted. A lumped parameter model, which includes the kinetic energy carry-over effect, is presented along with a linear perturbation solution technique. The resulting system is nondimensionalized and the physical significance of the reduced parameters is discussed. Closed-form algebraic formulas are given for some simple limiting cases. It is shown that the total cross force predicted by this model can be represented as the sum of an ideal component due to an inviscid flow with entry swirl and a viscous part due to the change in swirl created by friction inside the gland. The frequency-dependent ideal part is solely responsible for the rotordynamic direct damping. The facility designed and built to measure these frequency dependent forces is described. Experimental data confirm the validity and usefulness of this ideal/viscous decomposition. A method for calculating the damping coefficients based on the force decomposition using the static measurements only is presented.

Introduction

Rotordynamic instability is a problem that is frequently experienced in the development programs of high power-density turbomachines. This self-excited vibration of the rotor-bearing system, which typically occurs at the first natural lateral bending frequency, can lead to catastrophic failures. An overview of the problem and a discussion of the various sources of excitation is given by Ehrich and Childs [1]. One element that may contribute strongly to destabilizing a machine is the labyrinth seal. Asymmetric pressure distributions in the seal glands attached to whirling shafts generating forces not in the direction of the instantaneous minimum gap may create or enhance these instabilities.

The possibility of labyrinth seals creating unstable rotor whirl has been known since the 1940s, as reported by Den Hartog (see Ref. [2]). Alford [3] and Thomas [4] were the first to propose analytical models for the prediction of labyrinth seal forces. However, neither of these models is particularly useful, because the influence of the inlet swirl, which is known to dominate in the generation of cross forces, was neglected by both authors. A lumped parameter model that couples the axial flow over the knives to one-dimensional continuity and momentum equations inside the seal gland was developed by Kostyuk [5]. The gland-depth variation with rotor eccentricity was neglected and hence no cross stiffness nor direct damping is predicted directly from this model for a rotor whirling with a parallel precession. Subsequently, Iwatsubo [6] added the necessary term to account for this variation. Many other authors, including Gans [7], Kurahasi and Inoue [8], Kameoka and Abe [9], and Martinez and Lee [10], have used similar lumped parameter models to predict the cross forces for a great variety of geometries and flow conditions. However, very little physical insight has been extracted from the use of these models. Computational Fluid Dynamics (CFD) methods have also been used, most notably by Nordmann and Weiser [11], to predict results similar to those obtained by the lumped parameter models. All analysis so far has assumed uniform upstream boundary conditions. This assumption may not be adequate for the prediction of the forces in short seals. The first experiments to measure the self-exciting forces in isolated labyrinths were those of Benckert and Wachter [12–14], who measured the static pressure distributions around the casing and integrated them to find the direct and cross forces due to a statistically offset rotor. Many different geometries were tested over a wide range of flow conditions. Brown and Leong [15], Thieleke and Stetter [16], Kanki and Morii [17], and Hisa et al. [18] have all made similar measurements yielding a good data base on the displacement dependent rotordynamic coefficients. Experimental investigations on the dynamic characteristics of labyrinths have been conducted by Wright [19], Kanemitsu and Ohsawa [20], Scharrer [21], Scharrer and Childs [22], and Millsaps and Martinez [23].

Kostyuk-type lumped parameter models are capable of predicting the cross-stiffness coefficients for long labyrinth seals (more than six chambers) to within 25 percent. However, the situation with respect to short seals and the dynamic coefficients, especially the direct damping, is far less satisfactory. The measured cross-stiffness coefficients in two and three gland seals, as measured by Benckert [12], are more than 100 percent

---

[1] Present address: Naval Postgraduate School, Monterey, CA 93943.

Contributed by the International Gas Turbine Institute and presented at the 38th International Gas Turbine and Aeroengine Congress and Exposition, Cincinnati, Ohio, May 24–27, 1993. Manuscript received at ASME Headquarters March 12, 1993. Paper No. 93-GT-302. Associate Technical Editor: H. Lukas.

larger than those predicted by theory in many cases. Measured dynamic coefficients for both long and short seals are not well predicted by theory. Discrepancies between the measured and predicted direct damping of nearly 500 percent are shown by Scharrer [21] for some conditions. While the results from many computations have been reported using the various lumped parameter models, little physical understanding on the mechanisms that generate dynamic forces has been obtained from the models. In particular, no analysis has been presented that clearly delineates the importance of the various geometric and flow-related parameters and the origin of the damping. Finally, the general scaling behavior for the static and dynamic force components in a spinning/whirling seal has not been adequately explained.

The purpose of this paper is to explain the general nature of rotordynamic damping in labyrinth seals. To accomplish this, an analytical model is developed for a single gland seal with uniform upstream boundary conditions. In Part II of this paper the importance of nonuniform inlet flow, due to the presence of an upstream preswirl cavity and its impact on force augmentation, is treated. It is believed that this coupling is responsible for the higher than predicted forces described above. However, for the purpose of simplicity all the physical arguments will be developed with uniform inlet conditions to avoid unnecessary algebraic complexity. All of the arguments to be presented can be readily generalized to account for the upstream nonuniformities due to coupling. A technique is presented that yields an approximate solution to the model equations for the case of a small-amplitude whirling motion about a centered location. These equations are nondimensionalized, and formulas for the frequency-dependent direct and cross forces are given. The physical significance of the various parameters is discussed, and the scaling behavior provided. The rotordynamically destabilizing cross force will be shown to be the sum of two distinct components: an "ideal" one due to an inviscid flow, and a "viscous" part due to frictional shear. The direct damping, C_{xx}, will be shown to originate entirely from the ideal component. The experimental apparatus used to measure these forces will be described. Comparisons of the theory to the experimental data will be provided. Finally, methods for extracting dynamic coefficients from purely static data, utilizing the force decomposition, will be described. The validity of these methods was confirmed by the experimental data.

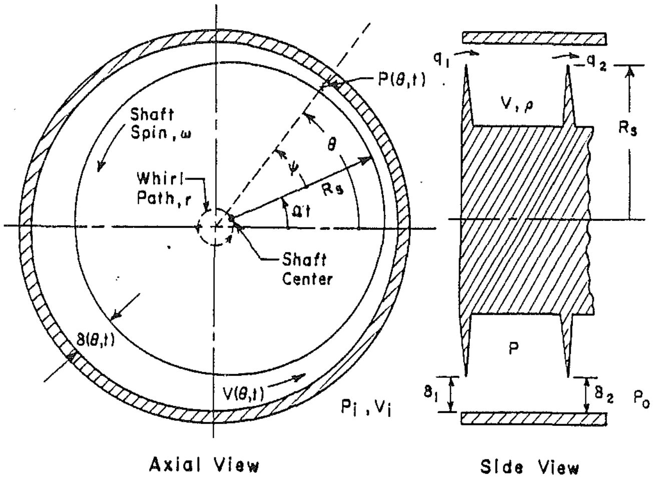

Fig. 1 Geometry and kinematics of a single-gland, spinning/whirling labyrinth seal

Analytical Model

Referring to Fig. 1, the geometry and motion of a single gland spinning/whirling labyrinth seal are defined. The circular seal spins at a rate of ω while simultaneously executing a whirling motion, of amplitude r at an angular frequency of Ω about the center of the casing. All of the state variables inside the gland, such as pressure and velocity, are considered to be a function of the angle, θ, and time, t. The sealing gaps and the gland area also vary with angle and time.

From Fig. 1, a one-dimensional continuity equation for the azimuthal flow in this whirling seal can be written. If the average gland cross-sectional quantities are used, the continuity equation is

$$\frac{\partial[\rho l(h+\delta_1)]}{\partial t}+\frac{1}{R_s}\frac{\partial}{\partial\theta}[\rho l(h+\delta_1)V]+q_2-q_1=0 \qquad (1)$$

The first term is the time rate of change of mass at a given section. The second term is due to convection inside the seal in the θ direction. The last two terms are due to axial mass efflux and influx due to the primary leakage flow.

Similarly the one-dimensional momentum equation that includes the frictional shear stresses from the stator and rotor on the fluid, τ_s and τ_r, is

Nomenclature

C_{xx} = direct damping, Ns/m
C_{xy} = cross damping, Ns/m
$C_{xx}^{**} = \dfrac{C_{xx}\delta_1^*}{lR_s^2\sqrt{P_i-P_o}}$ = nondimensional direct damping [1]
$C_{xy}^{**} = \dfrac{C_{xy}\delta_1^*}{lR_s^2\sqrt{P_i-P_o}}$ = nondimensional cross damping [1]
$D = \delta_1^*/h$ = nondimensional sealing gap [1]
F_N = force on rotor in the direction of instantaneous displacement, N
F_T = force on rotor in the direction tangent to the displacement, N
F_Γ = viscous cross force component, N
F_σ = ideal cross force component, N
$H = h/R_s$ = nondimensional labyrinth depth [1]
h = depth of seal gland, m
h_i = depth of upstream cavity, m
$i = \sqrt{-1}$
$K = \kappa/\mu_2^*$ = normalized carry-over factor [1]
K_{xx} = direct stiffness, N/m
K_{xy} = cross stiffness, N/m
$K_{xx}^{**} = \dfrac{K_{xx}\delta_1^*}{lR_s(P_i-P_o)}$ = nondimensional direct stiffness [1]
$K_{xy}^{**} = \dfrac{K_{xy}\delta_1^*}{lR_s(P_i-P_o)}$ = nondimensional cross stiffness [1]
$L = l/R_s$ = nondimensional sealing pitch [1]
l = sealing pitch, m
l_i = axial gap between the swirl vanes and seal inlet, m
$P = P^*(1+\xi)$ = static pressure inside the gland, Pa
P_i = upstream total pressure, Pa
P_o = downstream static pressure, Pa
q_1 = flow rate through the first knife per unit seal length, kg/ms
q_2 = flow rate through the second knife per unit seal length, kg/ms
R_a = gas constant for air $\doteq$ 287.15 J/kgK

$$\frac{\partial[\rho l(h+\delta_1)V]}{\partial t}+\frac{1}{R_s}\frac{\partial}{\partial\theta}[\rho l(h+\delta_1)V^2]$$
$$+q_2V-q_1V_i+\tau_s l-\tau_r(l+2h)+\frac{lh}{R_s}\frac{\partial P}{\partial\theta}=0 \quad (2)$$

The shear stresses are calculated with pipe flow friction factors from Blasius' turbulent flow formula. The mass influx and efflux, q_1 and q_2, respectively, are related to the conditions in the seal by a quasi-steady Bernoulli equation employing the average jet density between the respective flow origin and destination. This yields

$$q_1=\frac{\mu_1\delta_1}{\sqrt{R_aT}}(P_i^2-P^2)^{1/2}$$
$$q_2=\frac{\mu_2\delta_2}{\sqrt{R_aT}}(P^2-P_o^2)^{1/2} \quad (3)$$

where μ_1 and μ_2 are the flow coefficients for the first and second knives, respectively. The first knife has a constant flow coefficient, $\mu_1=0.65$. However, for the second knife the flow coefficient is a function of the local sealing gap due to kinetic energy carry-over variations. The following empirical formula of Varmes [25] is used:

$$\mu_2=\mu_1\frac{1}{\left(1-\dfrac{8.52}{\dfrac{l_e}{\delta}+7.23}\right)^{1/2}}=\overset{*}{\mu_2}-\kappa r \quad (4)$$

where l_e is the effective seal pitch, $1/\cos(\alpha_i)$, and α_i is the inlet swirl angle. This second flow coefficient varies with the whirling radial displacement. The variation of μ_2 with respect to a radial displacement r will be denoted by κ:

$$\kappa=-\frac{\partial\mu}{\partial r}\Big|_{r=0} \quad (5)$$

Solution Technique

Equations (1) and (2) are first solved for the centered rotor to find the zeroth-order solutions, which will be denoted by P^*, V^*, etc. Then the first harmonic perturbation expressions of the form

$$P=P^*(1+\hat{\xi}e^{i(\theta-\Omega t)}) \qquad V=V^*(1+\hat{\eta}e^{i(\theta-\Omega t)}) \quad (6)$$

are substituted into Eqs. (1) and (2), and the resulting expressions are linearized. A system of two complex algebraic equations in the complex pressure and velocity amplitudes results. The system can be written as

$$\left\{q^*\left[\frac{P^{*2}}{P^{*2}-P_o^2}+\frac{P^{*2}}{P_i^2-P^{*2}}\right]+\frac{\rho^*lh}{\gamma}\left(\frac{V^*}{R_s}-\Omega\right)i\right\}\hat{\xi}$$
$$+\left\{\frac{\rho^*V^*hli}{R_s}\right\}\hat{\eta}=\left\{\frac{q^*\kappa}{\overset{*}{\mu_2}}+q^*\left(\frac{1}{\delta_2^*}-\frac{1}{\delta_1^*}\right)+\rho^*l\left(\frac{V^*}{R_s}-\Omega\right)i\right\}\hat{r} \quad (7)$$

$$\left\{q^*\left[\frac{P^{*2}V^*}{P^{*2}-P_o^2}+\frac{P^{*2}V_i}{P_i^2-P^{*2}}\right]\right.$$
$$+\left(\frac{\rho^*}{8\gamma}\right)(\lambda_s lV^{*2}-\lambda_r(l+2h)(\omega R_s-V^*)^2)$$
$$\left.+\left[\frac{\rho^*V^*lh}{\gamma}\left(\frac{V^*}{R_a}-\Omega\right)+\frac{\rho^*lhR_aT}{R_s}\right]i\right\}\hat{\xi}$$
$$+\left\{q^*V^*+\frac{\rho^*V^*}{4}(\lambda_s lV^*-\lambda_r(l+2h)(V^*-\omega R_s))\right.$$
$$\left.+\rho^*V^*lh\left(\frac{2V^*}{R_s}-\Omega\right)i\right\}\hat{\eta}$$
$$=\left\{\frac{q^*V^*\kappa}{\overset{*}{\mu_2}}+q^*\left(\frac{V^*}{\delta_2^*}-\frac{V_i}{\delta_1^*}\right)+\rho^*V^*l\left(\frac{V^*}{R_s}-\Omega\right)i\right\}\hat{r} \quad (8)$$

The complex amplitudes, $\hat{\xi}$ and $\hat{\eta}$, to be found by inverting this system contain both amplitude and phase information.

Nondimensionalization

An equivalent nondimensional system is obtained by dividing Eqs. (7) and (8) by q^* and q^*V^*, respectively,

$$\left\{\frac{1}{\Delta^2}+\left(\frac{\alpha\mu_2^*}{\Delta\mu_1^*}\right)^2+\left[\frac{\sigma L}{\gamma D}(1-W)\right]i\right\}\hat{\xi}$$
$$+\left\{\frac{\sigma L}{D}i\right\}\hat{\eta}=\left\{\left(\frac{1}{\alpha}-1\right)+K+\sigma L(1-W)i\right\}\hat{\epsilon} \quad (9)$$

Nomenclature (cont.)

r = radial displacement phasor for the whirling shaft, m
$\hat{r}$ = eccentricity magnitude, m
S = $\frac{\omega R_s}{V^*}$ = nondimensional spin rate [1]
T = air temperature, K
t = time, s
V = $V^*(1+\eta)$ = swirl velocity in the seal gland, m/s
W = $\frac{\Omega R_s}{V^*}$ = normalized whirling frequency [1]
α = δ_2^*/δ_1^* = Alford parameter; nondimensional seal divergence [1]
β = μ_2/μ_1 = kinetic energy carry-over coefficient
Γ = $1-\frac{V_i}{V^*}$ = swirl gradient parameter [1]
Δ = $\frac{q^*}{\mu_1^*\delta_1^*\rho^*\sqrt{R_aT}}$ = nondimensional seal flow rate [1]
δ_1, δ_2 = sealing gaps for the knives, m
ξ = $\hat{\xi}e^{i(\theta-\Omega t)}$ = harmonic pressure perturbation [1]
η = $\hat{\eta}e^{i(\theta-\Omega t)}$ = harmonic velocity perturbation [1]
ρ = fluid density, kg/m^3
σ = $\frac{\rho^*\delta_1^*V^*}{q^*}$ = nondimensional swirl parameter [1]
$\bar{\sigma}$ = $\sigma(1-W)$ = swirl parameter as observed in the whirling frame [1]
Ω = whirling frequency of the shaft, 1/s
ω = shaft rotational speed, 1/s
$[\ ]^*$ = steady-state solution for the case of a centered rotor
$[\ ]_1, [\ ]_2$ = quantities at the first or second sealing knife, respectively
ϵ = r/δ_1^* = normalized whirling eccentricity [1]
κ = $-C_c\frac{\partial\beta}{\partial r}\Big|_{r=0}$ = radial carry-over sensitivity, 1/m
λ_r = Darcy function factor for the rotor [1]
λ_s = Darcy function factor for the stator [1]
μ_1, μ_2 = flow coefficients for knives [1]

$$\left\{\frac{\sigma L}{8\gamma DH}\left(\lambda_s-\lambda_r\left(1+\frac{2H}{L}\right)(S-1)^2\right\}\right.$$
$$\left.-\frac{\Gamma}{\Delta^2}+\left[\frac{\sigma LW}{\gamma D}+\frac{L}{\Delta^2\sigma\mu_1^{*2}D}\right]i\right\}\hat{\xi}+\left\{1+\frac{\sigma L}{4DH}\right.$$
$$\left.\left(\lambda_s-\lambda_r\left(1+\frac{2H}{L}\right)(1-S)\right)+\frac{\sigma L}{D}(1-W)i\right\}\hat{\eta}=\Gamma\hat{\epsilon} \quad (10)$$

All of these nondimensional parameters may be categorized as geometric, kinematic, or flow related. The geometric ones are

$$\hat{\epsilon}=\frac{\hat{r}}{\delta_1^*} \quad \alpha=\frac{\delta_2^*}{\delta_1^*} \quad D=\frac{\delta_1^*}{D}$$
$$H=\frac{h}{R_s} \quad K=\frac{\delta_1^*\kappa}{\mu_2^*} \quad L=\frac{1}{R_s} \quad (11)$$

Note that K has been considered along with the geometric parameters because it is analogous to a convergent/divergent gap in the effect that it has on the direct and cross forces. However, from physical arguments, K must be greater than zero and hence, this kinetic energy carry-over effect cannot behave like divergence sealing gaps. The kinematic parameters that specify the motion of the seal are

$$S=\frac{\omega R_s}{V^*} \quad W=\frac{\Omega R_s}{V^*} \quad (12)$$

and the dynamic parameters that indicate the axial flow rate or pressure gradient, the inlet swirl, and the change in swirl, respectively, are

$$\Delta=\frac{q^*}{\mu_1^*\delta_1^*\rho^*\sqrt{R_aT}} \quad \sigma=\frac{\rho^*\delta_1^*V^*}{q^*} \quad \Gamma=1-\frac{V_i}{V^*} \quad (13)$$

There are two combinations of these parameters, $\sigma\Gamma$ and $\sigma(1-W)$, that will be shown to be very important.

Force Scaling

Since changing one primitive variable, such as the inlet swirl velocity, may alter many parameters, like the change in swirl, it is more instructive to employ the nondimensional equations when describing the force scaling behavior. Cramer's rule can be used to write an explicit expression for the nondimensional pressure perturbation, which, upon integration, yields the forces acting on the rotor. The forces are proportional to $P^*\xi$. In general the shear stresses may also contribute to the forces. However, from the equation solutions it has been shown that the shear forces due to velocity perturbations are small when compared to the forces arising from the pressure perturbations as shown by Millsaps [24]. For moderate inlet swirl angles relative to the whirling rotor, which occurs providing the following condition is satisfied:

$$\frac{1+\alpha^2\beta^2}{\Delta^2} >> \frac{\sigma L}{\gamma D}(1-W) \quad (14)$$

the full expression for $\hat{\xi}$ may be simplified to yield the following real and imaginary parts for the pressure perturbation normalized by both the flow and whirling eccentricity:

$$\frac{\hat{\xi}_{\Re}}{\Delta^2\epsilon}=\frac{K-\left(1-\frac{1}{\alpha}\right)-\frac{\sigma^2L^2}{D}(1-W)^2}{1+\alpha^2\beta^2+\frac{L^2}{D^2\mu_1^{*2}}} \quad (15)$$

$$\frac{\hat{\xi}_{\Im}}{\Delta^2\epsilon}=\frac{\frac{\sigma L}{D}\left[\Gamma+(1-W)\left(-D-K+1-\frac{1}{\alpha}\right)\right]i}{1+\alpha^2\beta^2+\frac{L^2}{D^2\mu_1^{*2}}} \quad (15)$$

The first of these is real and therefore is in the direction of the minimum gap and hence is proportional to the direct force, while the second one is imaginary and hence is proportional to the destabilizing cross force. Both forces are proportional to $P^*\Delta^2$. For low inlet-to-exit pressure ratios, this reduces approximately to a simple pressure difference scaling, P_i-P_o, as one would expect for an incompressible flow. For this to hold, all of the other nondimensional parameters must be kept constant. In particular, the inlet swirl flow angle as observed from the whirling rotor must be fixed as the pressure difference is changed. As an example, if the axial pressure difference is increased, the inlet swirl velocity and whirl speed must also be increased to maintain constant σ and W. This is a generalization of the relationship found experimentally by Benckert [12] for statically offset seals.

The direct force is mainly due to the kinetic energy carry-over variations and differences in the nominal sealing clearances, as seen in Eq. (15). These effects generate a direct stiffness, while the smaller terms that are proportional to $\sigma^2(1-W)^2$, generate direct inertia coefficients. It is possible that this direct force may alter the natural frequency of the rotor only slightly. Therefore, no further discussion of the direct force will be given due to the small impact it has on rotordynamic stability.

The cross force can be seen from Eq. (16) to be the summation of two terms, one proportional to $\sigma(1-W)$ and the other proportional to $\sigma\Gamma$. The natures of these two contributions and their crucial differences are very important and will lead directly to the cross-force decomposition given in the next section. The kinetic energy carry-over term, K, and the "Alford" [2] term due to seal convergence/divergence, $(1-1/\alpha)$, do not generate cross force in the absence of swirl. But, they will alter the cross force in the presence of swirl. A convergent seal and/or kinetic energy carry-over will tend to increase the cross-force magnitude. This is destabilizing when $W<1$ or equivalently when the whirl frequency is less than V^*/R_s.

Cross-Force Decomposition

The total cross force, F_T, will now be split into "ideal" and "viscous" contributions. The ideal or inviscid part, F_σ, is the cross force that would be generated in a purely inviscid fluid with inlet swirl. It is proportional to $\sigma(1-W)$. The viscous contribution, F_Γ, which is proportional to $\sigma\Gamma$, is due to the frictional forces changing the swirl velocity inside the seal gland. The two forces tend to be of the same magnitude, but the nature of these two contributions is quite different. The ideal component is *dependent* on the rotor whirl frequency and hence will contribute to both the direct damping and the cross stiffness. The viscous component is *independent* of the whirl speed and hence can *not* contribute to the direct damping. The frequency-dependent behavior of a seal in an inviscid fluid can be readily explained by considering a simple change of reference frame. Let the relative inlet swirl, denoted by $\overline{V}_i=V_i-\Omega R_s$, be the inlet swirl velocity as measured by an observer rotating in the whirling frame. The nondimensional swirl parameter in the whirling frame will be similarly denoted by $\overline{\sigma}$ and is given by

$$\overline{\sigma}=\sigma(1-W)=\frac{\rho^*\overline{V}^*\delta_1^*}{q^*} \quad (17)$$

The cross force generated by an inviscid flow at an inlet swirl of V_i at a frequency of Ω is identically the same as the cross force that would be generated for a static offset with the associated relative inlet swirl of $\overline{V}_i$. This equivalence can be seen by noting that the governing continuity and momentum equations are invariant under Galilean transformation. As a particular case of this argument, consider a rotor whirling so that the minimum gap is traveling at the same speed as the inlet

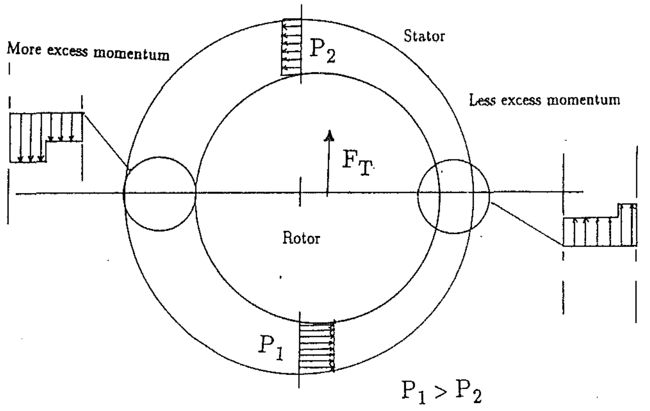

Fig. 2 Physical origin of the viscous force. This force is due to a velocity difference and hence is frequency independent. Therefore, it does not contribute to rotordynamic damping.

swirl. Then there is no swirl relative to the rotating frame observer. Therefore the inviscid cross force must be zero when $\Omega = V_i/R_s$, or equivalently when $W=1$ from symmetry arguments. This behavior is very similar to the quasi-static oscillation of an airfoil. The damping force there is related to the induced angle of attack due to the vertical motion. Here, it is the "induced" inlet swirl angle change, due to the whirling motion, that creates the rotordynamic damping. An interesting consequence of this relationship is that, in the absence of viscosity, the direct damping, C_{xx}, can be calculated from purely static measurements of the cross stiffness, K_{xy}, versus the inlet swirl, V_i, by

$$C_{xx} = R_s \frac{dK_{xy}(V_i)}{d(V_i)} \tag{18}$$

If the stiffness is a linear function of the inlet swirl, then a single measurement of the cross stiffness is needed to find the damping behavior.

$$C_{xx} = R_s \frac{K_{xy}(V_i)}{V_i} \tag{19}$$

A similar argument can be used to extract the direct damping coefficient from the static coefficient measurements in the presence of viscosity. However, a discussion of this will be reserved until later.

The viscous contribution, F_Γ, which is proportional to $\sigma\Gamma$ and hence the swirl velocity difference $V_i - V^*$, contributes to the cross stiffness only. The physical reason that this part of the cross force is independent of the whirling frequency is that it depends on a velocity difference, which is necessarily independent of any change of reference frame due to the whirl. The mechanism that produces this force is shown Fig. 2.

The flow enters the offset seal with a higher swirl velocity than exists inside the seal. Less excess momentum enters through the narrow gap on the right side than the wider gap to the left. As the flow mixes out, it energizes the fluid inside the gland increasing the static pressure like an ejector pump. The place with the highest pressure will be at the bottom yielding a positive cross force as shown. A simple analysis of this is done by using the following simplified momentum equation:

$$\tilde{q}(V - V_i) + \frac{lh}{R_s}\frac{\partial P}{\partial \theta} = 0 \tag{20}$$

This expression can be integrated to yield the viscous cross force

$$F_\Gamma = \frac{i\pi q^* R_s^2 (V_i - V^*)\hat{r}}{h\delta_1^*} \tag{21}$$

From Eq. (16) the relative magnitudes of the ideal and viscous contributions are found. Two limiting cases are possible:

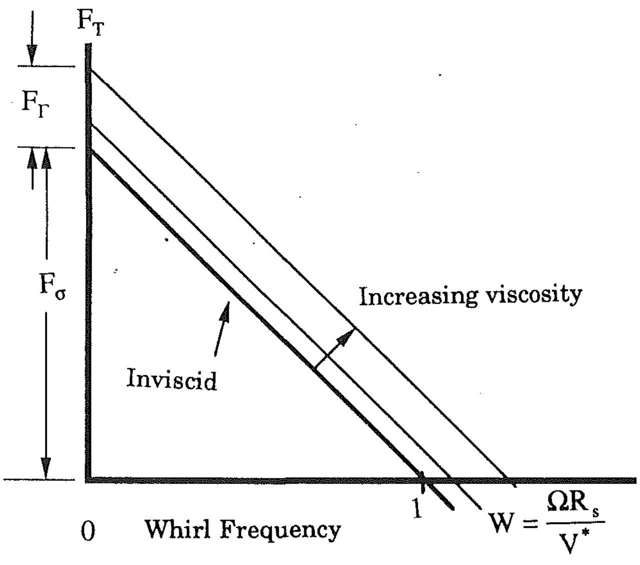

Fig. 3 General frequency-dependent behavior of the cross force showing both the ideal and viscous contributions

$$|\Gamma| = \left|1 - \frac{V_i}{V^*}\right| \ll |D| = \left|\frac{\delta_1^*}{h}\right|, \text{ friction is unimportant} \tag{22}$$

$$|\Gamma| = \left|1 - \frac{V_i}{V^*}\right| \gg |D| = \left|\frac{\delta_1^*}{h}\right|, \text{ friction is dominant} \tag{23}$$

However, in real hardware it is more common to have $|\Gamma| \cong |D| \cong 0.05$ and hence both contributions must be accurately modeled in analysis or properly scaled in experimental investigations.

Figure 3 shows the total cross force versus the nondimensional whirling frequency, W, for an ideal and real (viscous) flow. Increasing the viscosity means that the swirl change is becoming more negative through viscous action. This occurs either through higher friction factors or lower rotational speeds (in the direction of inlet swirl). As stated, the cross force vanishes for an inviscid flow when $W=1$, that is, when the gap travels at the swirl velocity. When the presence of viscosity is considered, the cross force increases the same amount at all whirl frequencies. If the swirl speed decreases through the seal, as is typical, then the frequency at which the force becomes negative shifts to a higher W, as shown. The viscous force will tend to decrease the stability of a rotor if the swirl velocity decreases in the gland.

Experimental Apparatus

The Labyrinth Seal Test Facility (LSTF) was designed and built to measure the dynamic forces in a spinning/whirling labyrinth seal. Figure 4 shows a cross section of the hardware. Air from a compressor, which has been cooled, dried, and metered, enters the first plenum and is turned radially outward through eight 1½ in. holes having honeycomb plugs. Next the air turns axially and accelerates through a set of replaceable swirl vanes into the swirl plenum. The air flows through the test seals and discharges to the atmosphere. The spinning/whirling motion of the seal is produced by the nested bearing arrangement. Different whirl amplitudes are obtained by adjusting and locking the inner spindle bearing seat eccentricity inserts, which support the outer race of the inner bearings. The spin motion (+6700 rpm to −6700 rpm) is driven by an inline flexible coupling driven by an electric motor. The speed of the whirling motion, which can be controlled independently (+3400 rpm to −3400 rpm), is driven by a V-belt on the rotating housing (part 2), which is attached to another motor.

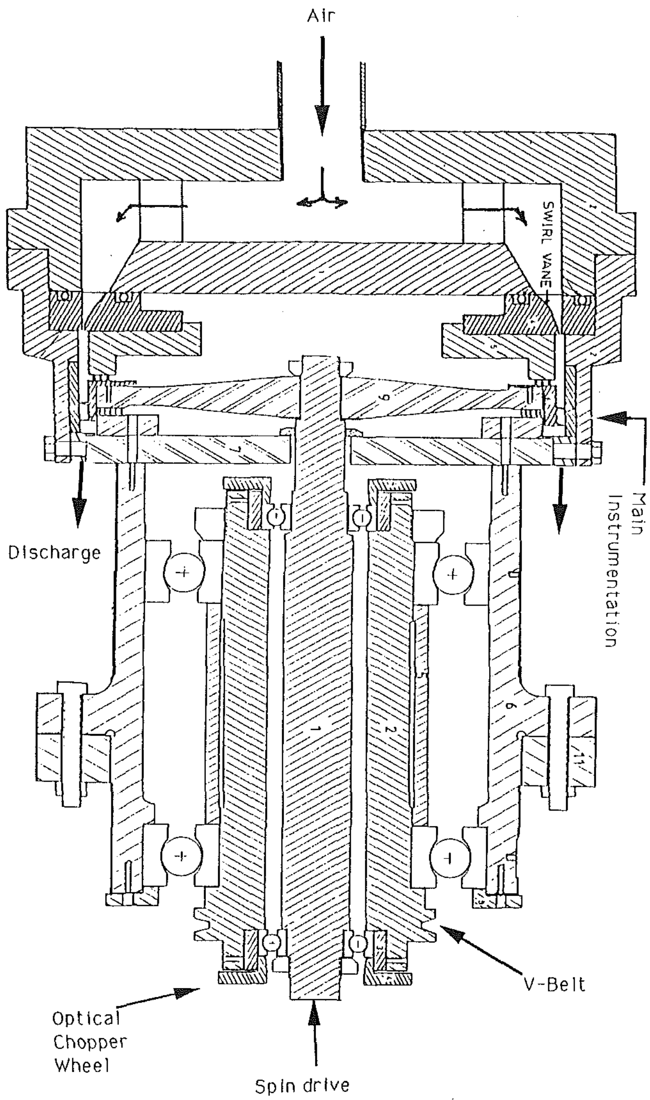

Fig. 4 Cross section of test section and nested spindle spin/whirl producing rotating machinery

Four equally spaced, flush-mounted, high-response, Kulite XCS-190 differential pressure transducers were placed on the seal land to measure the time-resolved gland pressure oscillations created by the seal whirling motion. The back pressure ports were referenced to the gland average pressure to filter the d.c. level. This permitted a higher measurement sensitivity. Proximetors were used to measure the seal whirling motion precisely. Measurements of the swirl angle leaving the second knife were made with a hot-wire anemometer. The data acquisition system was triggered and clocked with a chopper wheel attached to the whirl-producing spindle. Thirty-two phase-locked points were taken for each whirl revolution. Records of 64 revolutions were taken. The pressures were composite phase-locked ensemble averaged to find the forces acting on the rotor for each operating condition. For details see [24]. A total of five different seal geometries, shown in Table 1, were tested under various operating conditions. The inlet pressure, swirl vane angle, spin velocity, whirl eccentricity, and frequency were varied parametrically, yielding an extensive data base. Both smooth and honeycomb landed tooth-on-rotor labyrinth seals were tested.

Comparison of Experiment to Theory

Table 1 Geometry of the sealing knives (rotor) and lands (stator) for the five builds

BUILD	SEAL DIMENSIONS (rotor) cm in.					
	Material	R_s	l	h_1	d	α_s
#1	4140	15.166	1.016	0.508	0	
	steel	5.971	0.400	0.200	0	20°
#2	4140	15.166	1.016	0.508	0	
	steel	5.971	0.400	0.200	0	20°
#3	304 SS	15.177	1.727	0.508	0.043	
		5.975	0.680	0.200	0.017	17°
#4	304 SS	15.177	1.727	0.508	0.043	
		5.975	0.680	0.200	0.017	17°
#5	4140	15.166	1.016	0.508	0	
	steel	5.970	0.400	0.200	0	17°

BUILD	LAND DIMENSIONS (stator) cm in.						
	Material	ϕ_s	h_2	l_s	l_i	h_i	δ_1^*
#1	1117	15.240	0	0	4.064	0.635	0.0737
	steel	6.000	0	0	1.600	0.250	0.029
#2	1117	15.245	0	0	4.064	0.635	0.0787
	steel	6.002	0	0	1.600	0.250	0.031
#3	1117	15.245	0	0	3.683	0.635	0.0686
	steel	6.002	0	0	1.450	0.250	0.027
#4	304 SS	15.245	0.483	1.905	3.683	0.635	0.0686
	Hastolly X	6.002	0.190	0.750	1.450	0.250	0.027
#5	304 SS	15.245	0.483	1.905	4.064	0.635	0.787
	Hastolly X	6.002	0.190	0.750	1.600	0.250	0.031

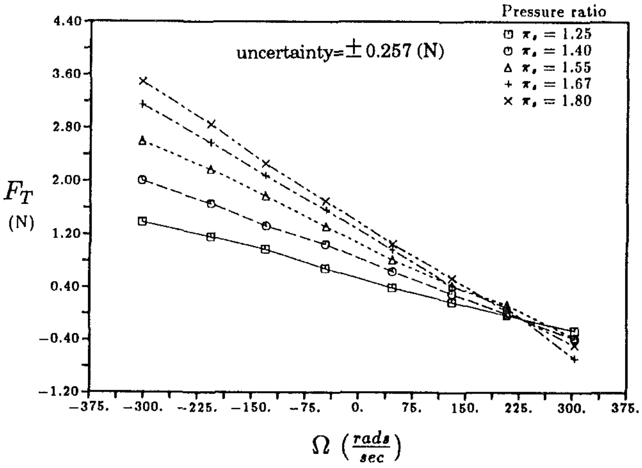

Fig. 5 Experimentally obtained cross force versus whirl frequency for five different pressure ratios. These data are from build #4 with 8.6 deg inlet swirl and no shaft rotation.

The extensive experimental investigation that was conducted with the LSTF provided a large data base that was directly compared with the lumped parameter analysis. A few representative data will be presented here, to show the general similarity between the theory and experimental data with respect to frequency-dependent behavior. These data support the inviscid/viscous cross force decomposition that was presented.

Figure 5 shows a typical plot of the cross force versus whirl frequency for five different pressure ratios from Build #4. There is no shaft rotation and the nominal inlet swirl angle is 8.6 deg. The general frequency-dependent behavior of the experimental data is well predicted with the analytical model. In particular, the cross force is a linear function of the whirl speed and the frequency at which the force changes sign matches the theoretically predicted value within the bounds of experimental uncertainty, which in this case is ±0.257 N. The major problem is that the absolute values of the measured forces tend to be between two and three times that predicted by the model for

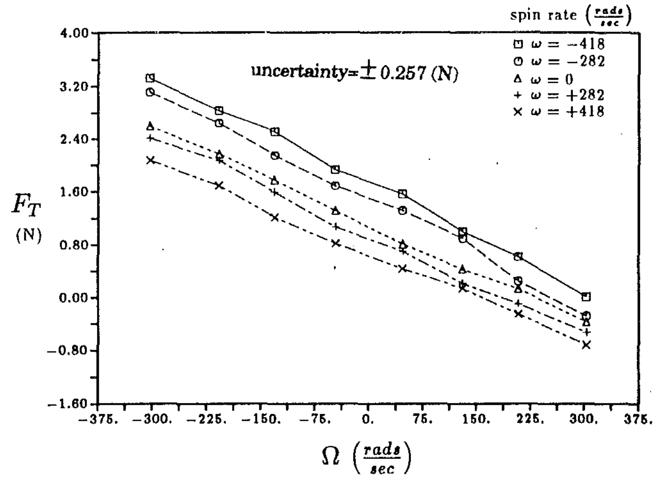

Fig. 6 Experimentally obtained cross force versus whirl frequency for five different spin rates. The pressure ratio is 1.57. These data are for build #4 with 8.6 deg of inlet swirl.

all builds. The reason for this large discrepancy is probably that the nonuniform conditions in the swirl plenum greatly augment the forces. A model that accounts for this upstream coupling has been developed by the authors and is presented in Part II of this paper. This extended model is capable of matching the data from all of the LSTF builds as well as the short seal data of Benckert [12].

Figure 6 shows the cross force versus whirl frequency for five different spin rates for the same build. It can clearly be seen that the data at different spin rates fall on parallel lines. Similar results were found for all builds at all flow conditions. The narrow implication of this is that changes in rotational speed do *not* affect the direct damping. The cross stiffness changes are as expected. The higher the spin speed in the direction of inlet swirl, the lower the cross force. More generally, these data strongly support the general validity of the cross force decomposition into ideal and viscous contributions as presented above.

The method presented previously for predicting the direct damping coefficients from inviscid static values can be readily extended to cases with "viscosity" if the frictional component is properly isolated. There are many ways to separate these two components.

Probably the best method for removing this frictional "contamination" is to handle it directly in the experiment. If the inlet and exit swirl velocities are measured directly, then for every value of the inlet swirl the seal spin speed should be adjusted to maintain a constant swirl difference, $V_i - V^*$. Hence, the additive frictional component is fixed. For $V_i - V^*$ the viscous component is totally eliminated. For typical designs the spin speed needs to be maintained at about 125 percent of the inlet swirl velocity to keep $\Gamma = 0$. If this procedure is not followed, the measurements of a statically offset seal can still be used to obtain damping data. If static data are taken with no rotation, a correlation of the cross-stiffness coefficient, K^{**}_{xy}, versus the swirl parameter, σ, can be obtained. The problem is that as the inlet swirl velocity is increased the total cross force increases due to a higher inlet swirl (inviscid contribution) as well as the frictionally induced change in swirl. The change in the ideal component with inlet swirl, which is equal to the direct damping, must be separated. One procedure is to use the static correlation to calculate a total force, $F_T(\Omega_d R_s)$, at an inlet velocity corresponding to a whirl frequency Ω_d. The viscous force, found from either theory or a correlation, is subtracted from the total force to yield the ideal component. The damping is the rate of change of this ideal force with frequency. This may be written as

Table 2 The first column gives the cross-stiffness correlation coefficient obtained from static measurements. The next two columns give the total, and frictional force, respectively calculated at a whirl speed of *300* (rads/s). *The last two columns give the calculated and measured* direct damping coefficients.

BUILD#	$\frac{\partial K^{**}_{xy}}{\partial\sigma}$	$\frac{F_T(\Omega_d)}{\hat{r}}$	$\frac{F_{T\Gamma}(\Omega_d)}{\hat{r}}$	C^{**}_{xx}	From Static Correlation $C_{xx}\left(\frac{Ns}{m}\right)$	Measured Directly $C_{xx}\left(\frac{Ns}{m}\right)$
2	0.372	7763	953	0.289	22.70	19.95
3	0.416	27821	3162	0.371	82.19	75.80
4	0.283	20001	3162	0.247	56.13	48.54
5	0.338	7053	953	0.231	20.33	15.81

$$C_{xx} = \frac{F_T(\Omega_d R_s) - F_\Gamma(\Omega_d R_s)}{\Omega_d \hat{r}} = \frac{F_\sigma(\Omega_d R_s)}{\Omega_d \hat{r}} \tag{24}$$

Another method that can be used is to recognize that the inviscid contribution varies linearly with the inlet swirl, while the viscous part should vary in approximately a quadratic manner, if Reynolds number variations are ignored. This information can be used to separate the two components if many data are available over a large range of inlet swirl velocities.

Direct damping coefficients, C_{xx}, were calculated from purely static correlations of K^{**}_{xy} versus σ, of the form

$$K^{**}_{xy} = \left(\frac{\partial K^{**}_{xy}}{\partial\sigma}\right)_{\text{data}} \sigma \tag{25}$$

for each build. These were used to find a total cross force at an inlet swirl of $\Omega_d R_s$. Next a frictional force was calculated with the model and subtracted away to leave the "ideal" cross force. This force divided by the whirl frequency and amplitude provides a value of direct damping. These damping coefficients "calculated from static correlation" were compared to those that were directly measured in the LSTF for the same whirling seals. Agreement to within 13, 8, and 15 percent for builds 2, 3, and 4, respectively, was obtained as shown in Table 2. This demonstrates that it is possible to predict the dynamic coefficients with the use of static (nonwhirling) measurements only.

Conclusions

The following conclusions on the nature of rotordynamic damping have been drawn from consideration of the analytical model and the supporting experimental data:

1 The total cross force acting on a labyrinth seal at a given whirl frequency can be decomposed into "ideal" and "viscous" components.

2 The ideal component, which is due to an inviscid swirling flow, is a unique function of the inlet swirl relative to the gap variation phase speed. This force component vanishes when the velocity of the traveling gap is equal to the swirl velocity inside the gland. This component is solely responsible for damping.

3 The viscous component neither creates nor alters the direct damping. It adds to (if the swirl velocity decreases in the gland) or subtracts from (if the swirl increases) the cross stiffness.

4 The direct damping can be calculated from measurements of cross stiffness. The importance of this is that difficult and expensive dynamic measurements are not necessary in order to obtain damping coefficients.

References

1 Ehrich, F. F., and Childs, D. W., "Self-Excited Vibration in High Performance Turbomachinery," *Mechanical Engineering*, May 1984, pp. 66–79.

2 Den Hartog, J. P., *Mechanical Vibrations*, 4th ed., McGraw-Hill, New York, 1956, pp. 319–321.

3 Alford, J. S., "Protecting Turbomachinery From Self-Excited Rotor Whirl," ASME *Journal of Engineering for Power*, Vol. 87, 1965, pp. 333–344.

4 Thomas, H. J., "Instabile Eigenschwing von Turbinelauefern Angefacht durch die Spaltstroemung in Stopfubuchseen und Bechauchflug (Unstable Natural Vibrations of Turbine Rotors Induced by the Clearance Flows in Glands and Blading)," *Bull. de L.A.I.M.*, Vol. 71, No. 11–12, 1958, pp. 1039–1063.

5 Kostyuk, A. G., "A Theoretical Analysis of the Aerodynamic Forces in the Labyrinth Glands of Turbomachines," *Teploenergetica*, Vol. 19, No. 11, 1972, pp. 29–33.

6 Iwatsubo, T., "Evaluation of Instability Forces in Labyrinth Seals in Turbines or Compressors," NASA CP-2133, 1980, pp. 139–169.

7 Gans, B. E., "Prediction of Aeroelastic Forces in a Labyrinth Type Seal and Its Impact on Turbomachinery Stability," Eng. Thesis, Department of Mechanical Engineering, M.I.T., 1983.

8 Kurahashi, Y., and Inoue, T., "Spring and Damping Coefficients of Labyrinth Seals," *Proc. IMechE*, 1980.

9 Kameoka, T., and Abe, T., "A Theoretical Approach to Labyrinth Seal Forces," NASA CP-2338, 1984, pp. 28–30.

10 Martinez-Sanchez, M., Lee, O. W. K., and Czajkowski, E., "Prediction of Force Coefficients in Labyrinth Seals," NASA CP-2338, 1984, pp. 235–256.

11 Nordman, R., and Weiser, P., "Evaluation of Rotordynamic Coefficients of Look-Through Labyrinths by Means of a Three Volume Bulk Flow Model," *Sixth Workshop on Rotordynamic Instability*. Texas A&M Univ., May 21–23, 1990, pp. 141–157.

12 Benckert, H., "Stromungsbedinte Federkennwerte in Labyrinthdithtungen," Doctoral Dissertation, University of Stuttgart, 1980.

13 Benckert, H., and Wachter, J., "Querkrafte aus Spaltdichtungen—Eine Mogliche Ursache fur die Laufunruhe von Turbomachinen," *Atomkernenergie*, Vol. 32, No. 4, 1978, pp. 239–246.

14 Benckert, H., and Wachter, J., "Flow Induced Spring Coefficients of Labyrinth Seals for Applications in Rotordynamics," NASA CP-2133, 1989, pp. 189–212.

15 Brown, R. D., and Leong, Y. M. M. S., "Circumferential Pressure Distributions in a Model Labyrinth Seal," NASA CP-2133, 1982, pp. 222–232.

16 Thielele, G., and Stetter, H., "Experimental Investigation of Exciting Forces in Labyrinth Seals," *Sixth Workshop on Rotordynamic Instability*, Texas A&M University, May 21–23, 1990, pp. 141–157.

17 Kanki, H., and Morii, S., "Destabilizing Forces in Labyrinth Seals," NASA CP-2409, 1985, pp. 205–223.

18 Hisa, S., Sakakida, H., and Asatu, S., "Steam Excited Vibrations in Rotor-Bearing Systems," *Proceedings of the International Conference on Rotordynamics*, Sept. 14–17, 1986, Tokyo, pp. 635–641.

19 Wright, D. V., "Air Model Tests of Labyrinth Seal Forces on a Whirling Rotor," ASME *Journal of Engineering for Power*, Vol. 100, 1978, pp. 533–543.

20 Kanemitsu, Y., and Ohsawa, M., "Experimental Study on Flow Induced Forces of Labyrinth Seals," *Proceedings of the IFTOMM Conference on Flow Induced Force in Rotating Machinery*, Kobe University, Japan, Sept. 18–19, 1986, pp. 106–112.

21 Scharrer, J. K., "A Comparison of Experimental and Theoretical Results for Labyrinth Gas Seals," Ph.D. Dissertation, Mechanical Engineering Department, Texas A&M University, 1987.

22 Scharrer, J. K., and Childs, D. W., "Theory vs. Experiment for the Rotordynamic Coefficients of Labyrinth Gas Seals, Parts 1 & 2," ASME *Journal of Vibration, Acoustics, Stress, and Reliability in Design*, Vol. 110, 1989, pp. 270–287.

23 Millsaps, K. T., and Martinez-Sanchez, M., "Static and Dynamic Pressure Distributions in a Short Labvrinth Seal," NASA CP-2543, 1990, pp. 129–140.

24 Millsaps, K. T., "The Impact of Unsteady Swirling Flow in a Single Gland Labyrinth Seal on Rotordynamic Stability: Theory and Experiment," Ph.D. Dissertation, Department of Aeronautics and Astronautics, M.I.T., 1992.

25 Varmes, G., "A Fluid Mechanics Approach to the Labyrinth Seal Leakage Problem," ASME *Journal of Basic Engineering*, Vol. 82, 1960, pp. 265–275.

Dynamic Forces From Single Gland Labyrinth Seals: Part II—Upstream Coupling

K. T. Millsaps[1]

M. Martinez-Sanchez

Gas Turbine Laboratory,
Massachusetts Institute of Technology,
Cambridge, MA 02139

The standard lumped parameter model for flow in an eccentrically offset labyrinth seal, which assumes constant upstream and downstream boundary conditions, has been extended to include the effects of a nonuniform upstream cavity flow due to coupling. This new model predicts that the upstream perturbations in pressure and azimuthal velocity caused by this coupling can have a very strong impact on the pressure distribution in the seal gland itself. Augmentation by a factor of four, over the uniform inlet model, is predicted under some circumstances. Although no precise comparison to the experimental data with this new model was possible, due to the lack of control over the face seal venting the upstream cavity to the center hub plenum, the calculated effect of this coupling was shown to be approximately what was required to restore quantitative agreement between the data and theory. The new theory can explain the anomalously large pressure nonuniformity previously found by other authors in short seals as well as the first few glands of multicavity seals.

1 Introduction

As discussed in Part I of this paper, the experimental and modeling work proceeded initially on the assumption that the offset seal is fed by fluid from a spatially and temporally uniform upstream reservoir, and discharges to a uniform downstream volume. This has been the common assumption used with the lumped parameter models, in the literature thus far [1-4]. One consequence of this assumption was that measurements of the seal upstream pressure (in cavity *UC* in Fig. 1) were taken at one tangential location only, and no direct data were obtained on the tangential distributions of pressure, velocity or other quantities in this cavity. Similarly, no special care was taken to measure the small axial clearance in the face seal (*FS* in Fig. 1) separating this cavity from the upstream hub plenum (*HP* in Fig. 1). Since the mating ring for this seal was removed and re-installed whenever the swirl vane sets were changed, it is likely that axial gap variations existed from one assembly to the next. The importance of this axial gap will become apparent in the following.

Indications that substantial upstream nonuniformity may exist and be of importance was provided by pressure transducer measurements just upstream of the first seal knife in the Labyrinth Seal Test Facility (LSTF) and from results from the MIT Alford Force Test Facility (AFTF). The AFTF has a one-stage shrouded turbine with the capability to offset the shaft statically by a fraction of the tip clearance [4]. The shroud was fitted with a one-cavity labyrinth seal similar in design to those used in the LSTF. Among the data obtained in the turbine tests were azimuthal wall static pressure distributions at various axial stations, including one between the stator and the shrouded rotor. This is shown in Fig. 2(*a*). For reference, Fig. 2(*b*) shows the pressure variation inside the shroud seal gland itself. The upstream nonuniformity amplitude is seen to be about 1/3 of that in the seal. However, the phase of the upstream minimum pressure is slightly different from that in the labyrinth gland.

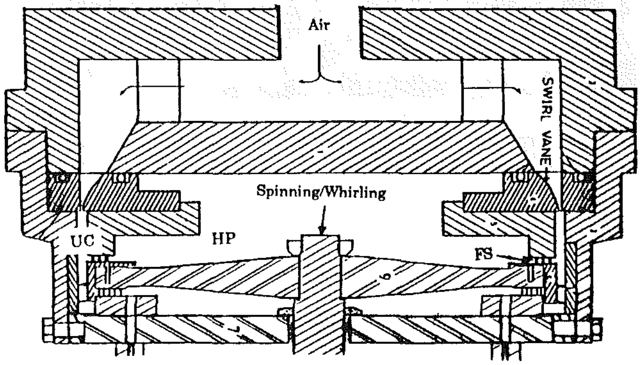

Fig. 1 Cross section of LSTF showing the geometry of the upstream swirl cavity UC and the center hub plenum

Across the labyrinth seal tests were completed and the cross force data were reduced. They were compared to the lumped parameter model having uniform upstream boundary conditions, as described in Part I. From this, it became apparent that the general trends were as predicted. In particular, the frequency-dependent behavior was as predicted; the frequency

---

[1] Present address: Naval Postgraduate School, Monterey, CA 93943.

Contributed by the International Gas Turbine Institute and presented at the 38th International Gas Turbine and Aeroengine Congress and Exposition, Cincinnati, Ohio, May 24–27, 1993. Manuscript received at ASME Headquarters March 17, 1993. Paper No. 93-GT-322. Associate Technical Editor: H. Lukas.

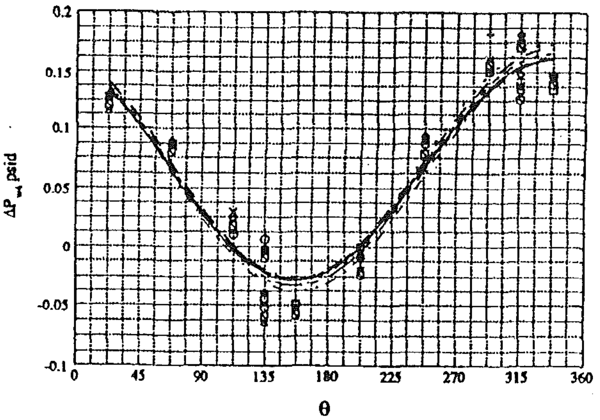

Fig. 2(*a*) Outer casing pressure distribution between the rotor and stator upstream of an eccentric shrouded turbine in the AFTF with a relative eccentricity of 0.46

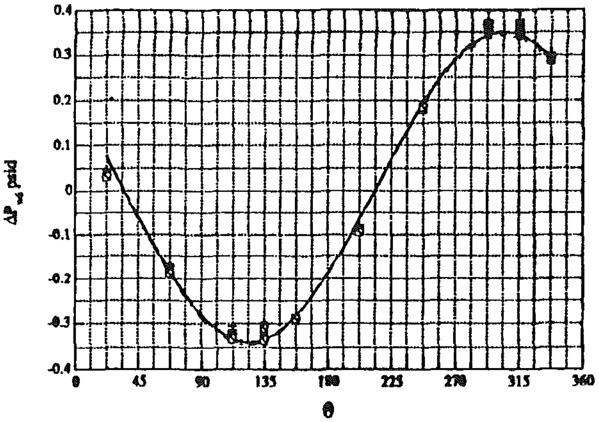

Fig. 2(*b*) Static pressure inside the tip shroud seal gland in the AFTF with the same conditions as above

at which the cross forces became stabilizing was roughly the swirl velocity divided by the seal radius. Also, the separation of the total force into "ideal" and "viscous" contributions was substantiated, along with a method for the extraction of the dynamic coefficients from purely static measurements. However, the measured rotordynamic cross forces were two to four times as large as predicted by this simple uncoupled theory at all whirl frequencies. A reason for this large discrepancy was sought.

A study was made to test the sensitivity of model predictions to uncertainty in factors such as friction coefficients, kinetic energy carry-over factors, geometric imperfections, etc. It was found that, within reasonable ranges of variation, no combination of such factors would suffice to match the experimental data. This was surprising, in that previous experience [3] with application of essentially the same model to the data of Benckert and Wachter [6] has shown agreement to within +20 percent for the cross stiffness. More careful examination of this and other similar comparisons of linearized theory and test data [4, 7, 8] revealed that the theory did perform well in calculating net forces from multicavity seals, but failed, again by factors of the order of 2–4, when it was applied to the calculation of pressure nonuniformity in the first cavity of these seals. The second and third glands from these experiments also show higher than predicted forces. This had been tentatively ascribed to differences in the discharge coefficient of the first gap (no carry-over), but, as noted, our study had already shown such differences to be insufficient to explain these large discrepancies.

As part of the effort to reassess the theory and its assumptions, the model was extended to allow for offset-induced nonuniformity in the upstream cavity. This was straightforward if this cavity feeding the seal was taken to be perfectly isolated from the large hub volume (*HP* in Fig. 1), but complications arose when finite leakage in the face seal was introduced. However, with a modified nonlinear analysis, closed-form analytical solutions were also obtained for these cases. These analytical developments are explained in Section 2 of

Nomenclature

B = beta function
C_{xx} = direct damping, N s/m
C_{xy} = cross damping, N s/m
$C_{xx}^{**} = \dfrac{C_{xx}\delta_1^*}{IR_s^2\sqrt{P_i - P_o}}$ = nondimensional direct damping [1]
$C_{xy}^{**} = \dfrac{C_{xy}\delta_1^*}{IR_s^2\sqrt{P_i - P_o}}$ = nondimensional cross damping [1]
$D = \delta_1^*/h$ = nondimensional sealing gap [1]
F_N = force acting on the rotor in the direction of instantaneous displacement, N
F_T = force on the rotor in the direction tangent to the instantaneous displacement, N
$H = h/R_s$ = nondimensional depth of seal gland [1]
h = depth of seal gland, m
h_i = cavity depth upstream of the seal, m
$i = \sqrt{-1}$
$K = \kappa/\mu_2^*$ = normalized kinetic energy carry-over factor [1]
K_{xx} = direct stiffness, N/m
K_{xy} = cross stiffness, N/m
$K_{xx}^{**} = \dfrac{K_{xx}\delta_1^*}{IR_s(P_i - P_o)}$ = nondimensional direct stiffness [1]
$K_{xy}^{**} = \dfrac{K_{xy}\delta_1^*}{IR_s(P_i - P_o)}$ = nondimensional cross stiffness [1]
$L = l/R_s$ = nondimensional labyrinth sealing pitch [1]
l = sealing pitch, m
l_i = axial gap between the swirl vanes and seal inlet, m
$P = P^*(1+\xi)$ = pressure inside the labyrinth gland, Pa
P_i = total pressure upstream of the first sealing knife, Pa
P_o = static pressure downstream of seal, Pa
q_1 = flow through the first knife, kg/m s
q_2 = flow through the second knife, kg/ms
$q_{c,\text{in}}$ = flow rate into center cavity, kg/m s
$q_{c,\text{out}}$ = flow rate out of center cavity, kg/m s
R_a = gas constant for air = 287.15 J/kg K
r = radial displacement phasor for the whirling shaft, m
$\hat{r}$ = magnitude of radial displacement, m
$S = \dfrac{\omega R_s}{V^*}$ = nondimensional spin rate [1]

this paper. Section 3 discussed the general results of the extended model, and Section 4 shows how these effects can indeed explain the discrepancies. Finally, the implications for future application of seal theory to design and rotordynamic diagnostics are discussed in Section 5.

2 Model Modifications to Account for Upstream Coupling

Before embarking upon algebraic manipulations, it is useful to provide a qualitative description of the coupling mechanism involved. When the shaft is offset and the sealing gap varies around the seal perimeter, a low-pressure area will develop upstream of the seal in the vicinity of the widest gap. This is visible in Fig. 2(a), where the widest gap is at the $\theta = 180$ deg location. Because of this, the velocity magnitude will be higher there, and, in particular, the all-important tangential velocity will have a relative maximum near the widest gap. When the fluid carrying this excess tangential momentum enters the seal cavity and mixes with the swirling seal flow, it will preferentially energize it in this area (similar to the "viscous" mechanism discussed in Part I). The result will be a positive $(\partial P/\partial\theta)$ in this area, and hence a maximum P in the seal about 90 deg ahead of this maximum gap. This will then produce a forward whirling force. One important question about this mechanism is whether it will depend upon whirling seal speed, i.e., whether it will affect damping. To answer this, it is useful to view the situation from the whirling frame, and to focus on the special case where the inlet tangential speed happens to equal the whirling speed ΩR. In this case one would observe purely axial flow being injected into the now stationary seal cavity, and hence, by symmetry, no cross force would be expected. Thus, interestingly, this resembles the effect of the "inviscid" mechanism of Part I, in that it will increase both the cross-stiffness and the direct damping by the same amount, or, putting it differently, it will not affect the whirl speed at which the cross force vanishes.

For a concrete formulation of these effects, consider the geometry of Fig. 3. The swirl vanes, which are located l_i upstream from the first knife, have an effective radial gap of δ_v. There is some blockage due to the vane metal and boundary layer blockage. These deliver air into the first cavity with an effective swirl angle of α_v, which is the metal angle minus some small turning deviation. The cavity is h_i deep and is sealed from a large volume, in the center, by an axial face labyrinth seal with gap δ_c.

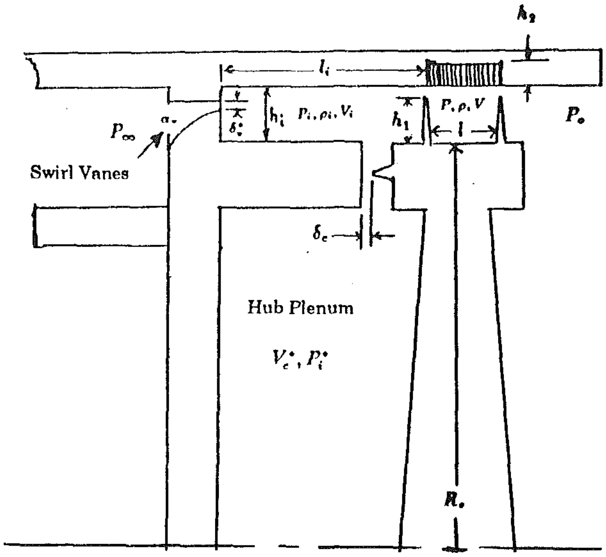

Fig. 3 Schematic of LSTF test section showing upstream swirl cavity flows and the flows into the center hub plenum

Since there is no net flow into this center cavity, the pressure here is uniform and the same as in the swirl cavity, namely P_i^*. The one-dimensional continuity equation for the swirl chamber is

$$\frac{\partial}{\partial t}(\rho_i l_i h_i) + \frac{1}{R_s}\frac{\partial}{\partial\theta}(\rho_i l_i h_i V_i) + q_i + q_v + q_{c,\mathrm{out}} - q_{c,\mathrm{in}} = 0 \quad (1)$$

Nomenclature (cont.)

T = air temperature, K

t = time, s

$V = V^*(1+\eta)$ = swirl velocity inside the seal gland, m/s

V_c = swirl velocity in the center cavity, m/s

V_i = swirl velocity in the swirl cavity, m/s

$W = \dfrac{\Omega R_s}{V^*}$ = nondimensional whirling frequency [1]

$\alpha = \delta_2^*/\delta_1^*$ = Alford parameter; nondimensional seal divergence [1]

$\beta = \mu_2/\mu_1$ = kinetic energy carry-over coefficient [1]

$\Gamma = 1 - \dfrac{V_i}{V^*}$ = swirl gradient parameter [1]

$\Delta = \dfrac{q^*}{\mu_1^*\delta_1^*\rho^*\sqrt{R_a T}}$ = nondimensional seal flow rate [1]

δ_1, δ_2 = seal gaps for the sealing knives, m

δ_c = axial clearance between swirl cavity and center plenum, m

δ_v = effective vane height, m

$\epsilon = r/\delta_1^*$ = nondimensional whirling eccentricity [1]

$\kappa = -C_o \left.\dfrac{\partial\beta}{\partial r}\right|_{r=0}$ = kinetic energy carry-over sensitivity, 1/m

λ_r = Darcy friction factor for the stator, [1]

λ_s = Darcy friction factor for the rotor, [1]

μ_1, μ_2 = flow coefficients for the seal knives, [1]

$\xi = \hat{\xi} e^{i(\theta - \Omega t)}$ = harmonic pressure perturbation [1]

$\eta = \hat{\eta} e^{i(\theta - \Omega t)}$ = harmonic velocity perturbation [1]

ρ = fluid density, ρ/m^3

$\sigma = \dfrac{\rho^*\delta_1^* V^*}{q^*}$ = nondimensional swirl parameter [1]

$\bar{\sigma} = \sigma(1 - W)$ = swirl parameter as observed in whirling frame [1]

Ω = angular frequency of whirl, 1/s

ω = shaft rotational speed, 1/s

$[\,]^*$ = steady-state solution for the case of a centered rotor

$[\,]_1$, $[\,]_2$ = quantities at the first or second knife, respectively

$[\,]_C$ = referring to the flow into or out of the center cavity

$[\,]_V$ = referring to the flow through the swirl vanes where V_i is no longer constant, q_v is the flow rate per unit length issuing from the swirl vanes, and $q_{c,\text{in}}$ and $q_{c,\text{out}}$ are the flows in and out of the center cavity, respectively. Incompressible relations are sufficient for treating these flows since the transfer velocities are very low. These flows can be written as

$$q_c = \mu_c \delta_c \sqrt{2\rho_i^* (P_i - P_i^*)} \tag{2}$$

This relation is fundamentally different from those for q_v, q_1, and q_2 in that there is no flow to or from the center volume when the seal is centered in the casing because $P_i = P_i^*$. This introduces an essential nonlinearity into the analysis and hence must be dealt with in a different manner. Likewise the momentum equation in this cavity is

$$\frac{\partial}{\partial t}(\rho_i l_i h_i V_i) + \frac{1}{R_s}\frac{\partial}{\partial \theta}(\rho_i l_i h_i V_i^2) + q_1 V_1 - q_v V_v$$
$$+ q_{c,\text{out}} V_i - q_{c,\text{in}} V_c + \tau_s(2l_i + h_i) - \tau_r h_i + \frac{l_i h_i}{R_s}\frac{\partial P_i}{\partial \theta} = 0 \tag{3}$$

where V_c is the swirl velocity inside the center volume. In this cavity the cross-sectional area, $l_i h_i$, and the vane gap, δ_v^*, are constant. However, the inlet swirl component of velocity, V_v, is not. The angle of the fluid leaving the vanes, α_v, is constant. Therefore, a drop in the pressure at one location in this cavity will induce a greater mass influx and hence a higher swirl velocity at that location. This is the essence of the mechanism that augments the forces.

The original equations for the seal gland are still valid within the constraints of the model, except that their linearization will yield additional terms from the upstream pressure and velocity nonuniformities.

The same solution procedure used for the single gland seal (Part I of this paper) can be used when there is no flow into the center cavity. However, as previously stated the nature of the oscillating flow between the two upstream volumes requires some modifications and careful treatment. This is because this flow leakage varies as $\sqrt{\tilde{P}_i}$, where $\tilde{P}_i$ is the upstream pressure perturbation, rather than linearly with $\tilde{P}_i$ (first order) or P_i (zeroth order) like the others. Thus, their effect can be disproportionally great at small offset amplitudes. The forces can no longer be linear with relative eccentricity, at least not at small whirl amplitudes. Also, the nonlinearity introduces harmonics other than the first into the analysis. An approximate treatment will be used, based on harmonic balancing, which in essence ignores these higher harmonics. This is done to simplify the analysis and because higher harmonics do not contribute to rotordynamic forces.

The zeroth-order solutions (for the centered rotor) are solved as before (Part I). The velocity, pressure, and density in the swirl cavity will be denoted by V_i^*, P_i^*, and ρ_i^*, respectively. The pressure and velocity in the swirl cavity are expressed as

$$P_i = P_i^*(1 + \hat{\xi}_i e^{i(\theta - \Omega t)}) \quad V_i = V_i^*(1 + \hat{\eta}_i e^{i(\theta - \Omega t)}) \tag{4}$$

where the real parts of all expressions are to be used. The perturbation expressions for $\hat{\xi}_i$, $\hat{\eta}_i$, $\hat{\xi}$, and $\hat{\eta}$ are substituted into the continuity and momentum equations for both the upstream swirl cavity and the seal gland. The nondimensional perturbation leakage flow into the center cavity is

$$\frac{q_c}{q^*} = \frac{\mu_c \delta_c}{\mu_1 \delta_1^*}\sqrt{\frac{2P_i^*}{P_i^* - P^*}} \bullet [\mathrm{Re}\{\hat{\xi}_i e^{i(\theta - \Omega t)}\}]^{1/2} \tag{5}$$

The first harmonic component of this function will be extracted by averaging over one period. The first harmonic of the perturbation reduces, after some manipulation, to

$$[\mathrm{Re}\{\hat{\xi}_i e^{i\Psi}\}]^{1/2} = \frac{4\sqrt{|\hat{\xi}|}}{\pi}\int_0^{\pi/2} \cos^{3/2}\Psi \, d\Psi$$
$$= \frac{4\sqrt{|\hat{\xi}|}}{\pi}\sqrt{2} \bullet B\left(\frac{5}{4}, \frac{5}{4}\right) \tag{6}$$

where B is the beta function. From this the first harmonic of $q_{c,\text{out}} - q_{c,\text{in}}$ is found to be

$$\frac{\tilde{q}_c}{q^*} = 1.57377 \frac{\mu_c^* \delta_c}{\mu_1^* \delta_1^*}\sqrt{\frac{P_i^*}{P_i^* - P^*}} \bullet |\hat{\xi}_i|^{-1/2} \bullet \hat{\xi}_i e^{i(\theta - \Omega t)} \tag{7}$$

Similarly the first harmonic of $q_{c,\text{out}} V_1 - q_{c,\text{in}} V_c$ is

$$1.57377 \frac{\mu_c^* \delta_c}{\mu_1^* \delta_1^*}\sqrt{\frac{2P_i^*}{P_i^* - P^*}} \bullet |\hat{\xi}_i|^{-1/2} \frac{1}{2}(V_c^* + V_i^*)\hat{\xi}_i e^{i(\theta - \Omega t)} \tag{8}$$

The first harmonic of the perturbation continuity equation for the swirl cavity, after dividing by q^*, is

$$\left\{\frac{1.57377\mu_c^* \delta_c}{\mu_1^* \delta_1^* \sqrt{|\hat{\xi}_i|}}\left[\frac{P_i^{*2}}{P_i^{*2} - P^{*2}}\right]^{1/2}\right.$$
$$+ \left[\frac{P_i^{*2}}{P_\infty^{*2} - P_i^{*2}} + \frac{P_i^{*2}}{P_i^{*2} - P^{*2}}\right] + \left.\frac{\rho_i^* l_i h_i}{\gamma q^*}\left(\frac{V_i^*}{R_s} - \Omega\right) i\right\}\hat{\xi}_i$$
$$+ \left\{\frac{\rho_i^* V_i^* l_i h_i}{R_s q^*} i\right\}\hat{\eta} - \left\{\frac{P^{*2}}{P_i^{*2} - P^{*2}}\right\}\hat{\xi}_i = \left\{\frac{1}{\delta_1^*}\right\}\hat{r} \tag{9}$$

and the swirl cavity momentum equation after dividing by $q^* V_i^*$ is

$$\left\{\frac{0.78688\mu_c^* \delta_c\left(1 + \dfrac{V_c^*}{V_i^*}\right)}{\mu_1^* \delta_1^* \sqrt{|\hat{\xi}_i|}}\left[\frac{P^{*2}}{P_i^{*2} - P^{*2}}\right]^{1/2} + \left[\frac{P_i^{*2}}{P_i^{*2} - P^{*2}}\right]\right.$$
$$+ \left(\frac{V_v}{V_i^*}\right)\left(\frac{P_i^{*2} + P_\infty P_i^*}{P_\infty^2 - P_i^{*2}}\right) + \frac{\lambda_{si}\rho_i^* (l_i + h_i) V_i^*}{4\gamma q^*}$$
$$+ \left.\left[\frac{\rho_i^* l_i h_i}{\gamma q^*}\left(\frac{V_i^*}{R_s} - \Omega\right) + \frac{P_i^* l_i h_i}{V_i^* q^* R_s}\right] i \bullet\right\}\hat{\xi}_i$$
$$+ \left\{1 + \frac{\lambda_{si}\rho_i^* (l_i + h_i) V_i^*}{2\gamma} + \left[\rho_i^* l_i h_i\left(\frac{2V_i^*}{R_s} - \Omega\right)\right] i\right\}\hat{\eta}_i$$
$$+ \left\{\frac{P^{*2}}{P_i^{*2} - P^{*2}}\right\}\hat{\xi} = \left\{\frac{1}{\delta_i^*}\right\}\hat{r} \tag{10}$$

The continuity equation for the seal gland, which includes the effect of the upstream cavity coupling, is

$$\left\{\frac{-P_i^{*2}}{P_i^{*2} - P^{*2}}\right\}\hat{\xi}_i + \left\{\left[\frac{P^{*2}}{P^{*2} - P_o^2} + \frac{P^{*2}}{P_i^{*2} - P^{*2}}\right]\right.$$
$$+ \left.\frac{\rho^* lh}{\gamma q^*}\left(\frac{V^*}{R_s} - \Omega\right) i\right\}\hat{\xi} + \left\{\frac{\rho^* V^* lh}{R_s q^*} i\right\}\hat{\eta}$$
$$= \left\{\frac{\kappa}{\mu_2^*} + \left(\frac{1}{\delta_2^*} - \frac{1}{\delta_1^*}\right) + \frac{\rho^* l}{q^*}\left(\frac{V^*}{R_s} - \Omega\right) i\right\}\hat{r} \tag{11}$$

and the coupled momentum equation for the seal gland is

$$\left\{\left(\frac{V_i^*}{V^*}\right)\frac{-P_i^{*2}}{P_i^{*2}-P^{*2}}\right\}\hat{\xi}_i+\left\{\frac{-V_i^*}{V^*}\right\}\hat{\eta}_i$$

$$+\left\{\frac{P^{*2}}{P^{*2}-P_o^2}+\left(\frac{V_i^*}{V^*}\right)\frac{P^{*2}}{P_i^{*2}-P^{*2}}\right.$$

$$+\left(\frac{\rho^*}{8\gamma q^* V^*}\right)(\lambda_s l V^{*2}-\lambda_r(1+2h)(\omega R_s-V^*)^2)$$

$$\left.+\left[\frac{\rho^* lh}{\gamma q^*}\left(\frac{V^*}{R_s}-\Omega\right)+\frac{\rho^* lhR_aT}{R_s}\right]i\right\}\hat{\xi}$$

$$+\left\{1+\frac{\rho^*}{4q^*}(\lambda_s l-\lambda_r(1+2h)(V^*-\omega R_s)^2)+\rho^* lh\left(\frac{2V^*}{R_s}-\Omega\right)i\right\}\hat{\eta}$$

$$=\left\{\frac{\kappa}{\mu_2^*}+\frac{1}{\delta_2^*}-\frac{V_i^*}{V^*\delta_1^*}+\frac{\rho^* l}{q^*}\left(\frac{V^*}{R_s}-\Omega\right)i\right\}\hat{r} \quad (12)$$

This can be written compactly in matrix form as

$$\begin{pmatrix} Z_{1,1} & Z_{1,2} & Z_{1,3} & Z_{1,4} \\ Z_{2,1} & Z_{2,2} & Z_{2,3} & Z_{2,4} \\ Z_{3,1} & Z_{3,2} & Z_{3,3} & Z_{3,4} \\ Z_{4,1} & Z_{4,2} & Z_{4,3} & Z_{4,4} \end{pmatrix}\begin{pmatrix} \hat{\xi}_i \\ \hat{\eta}_i \\ \hat{\xi} \\ \hat{\eta} \end{pmatrix}=\begin{pmatrix} R_1 \\ R_2 \\ R_3 \\ R_4 \end{pmatrix}\hat{r} \quad (13)$$

This is *not* a linear system. The elements $Z_{1,1}$ and $Z_{2,1}$ contain $|\hat{\xi}|^{-1/2}$. Of course if $\hat{\xi}_i=\hat{\eta}_i=0$ the system decouples and the original 2×2 system for the isolated seal with no upstream coupling is recovered. To solve this system a simple iteration scheme was employed. Equation (13) is first solved with $\delta_c=0$; then from this solution, $\hat{\xi}_i^1$ is used on the left-hand side to calculate an updated solution. This iteration procedure continues until a predetermined convergence criterion is satisfied:

$$|\hat{\xi}_i^{n+1}-\hat{\xi}_i^n|<\epsilon \quad (14)$$

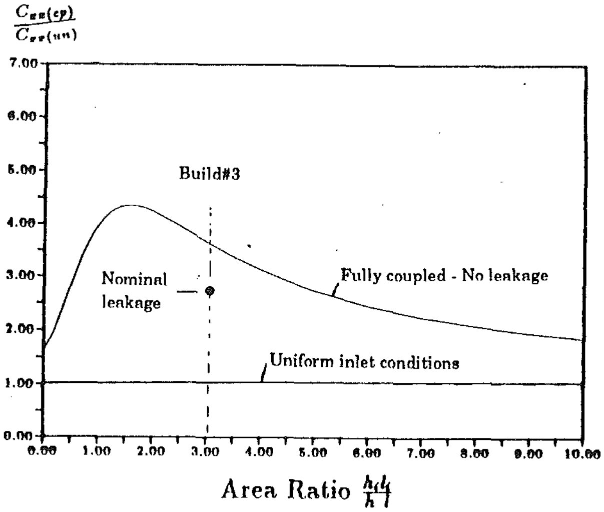

Fig. 4 Ratio of rotordynamic direct damping with upstream coupling to that with no coupling versus swirl cavity to seal gland area ratio

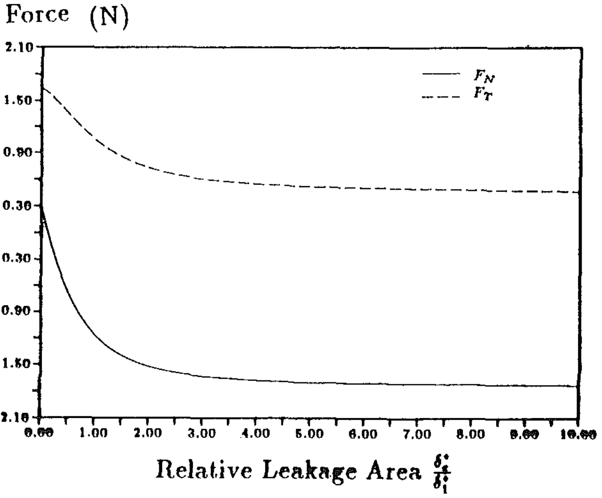

Fig. 5 Predicted direct and cross force at $\Omega=0$ for the coupled model versus the relative axial clearance. The geometry is the same as for build #3. $\pi_s=1.4$, $\alpha_v=15$ deg, $\epsilon_1=0.1407$, and $\omega=0$.

3 Calculated Results

In addition to the parameters that control the generation of rotordynamic forces for an isolated seal, the parameters that characterize the influence of the upstream coupling are:

1 The ratio of the swirl cavity area to the seal gland area, $(l_i h_i)/(lh)$.
2 The relative size of the axial sealing gap to the radial gap(s), δ_c/δ_1^*.
3 The swirl velocity inside the center cavity, V_c. This is strongly influenced by rotation of the seal disk.
4 The relative whirl eccentricity, $\hat{r}/\delta_1^*$. This is a purely nonlinear effect. For the linear system all of the forces are directly proportional to the whirl eccentricity.

Each of these effects will now be considered separately.

According to the model, if there is no leakage into the center cavity, the effect of the upstream coupling always acts to increase the magnitude of both the cross-stiffness and direct damping, and in the same proportions. Figure 4 shows the ratio of the direct damping from the coupled model, with $\delta_c=0$, to that of the uncoupled one for various swirl chamber to seal area ratios. As the swirl cavity area approaches zero the predicted force augmentation does not vanish but, approaches a value of 1.62. This residual effect in the absence of the first cavity is due to the condition imposed at the swirl vanes. In the simple model V_i is constant. If instead the vanes are close coupled a reduction in the gland pressure will still bring in more flow and hence will induce a higher swirl component locally.

The maximum increase in the cross-stiffness and direct damping over the uncoupled model is about 4.42 and occurs at an area ratio, $(l_i h_i)/(lh)$ of 1.35. Even at an area ratio of 10 the forces are increased by a factor of two. The force predicted by the coupled model asymptotically approaches the uncoupled one as $(l_i h_i)/(lh)\rightarrow\infty$. The coupled and uncoupled models match within 1 percent for an area ratio of about 80. Well before this value the assumptions of the model will probably break down. In particular, significant variations in the perturbation quantities are likely to occur in the axial direction within the swirl cavity.

The presence of the axial clearance between the swirl cavity and the large center volume permits for a "venting" that reduces the magnitude of $\hat{\xi}_i$. This effect tends to mitigate the large augmentation of the forces that the upstream cavity may induce. Figure 5 shows the direct and cross force versus the relative leakage area δ_c/δ_1^*. It is assumed that $V_c=V_i^*$ for simplicity. As δ_c goes from 0 to ∞ both force components go from the fully coupled values to those predicted by the uncoupled model. However, this does not occur when $V_c\neq V_i^*$. The forces are very sensitive to small changes in the axial gap when it is less than δ_1^*. However, when $\delta_c/\delta_1^*>1$, there is a greatly reduced sensitivity to small changes in axial gap.

The model predicts that the swirl velocity inside the center volume can have a major impact on the seal pressure perturbations. For cases where there is no seal rotation it is probably safe to say that $V_c=0$. This is because the tangential momentum feed into the seal is of perturbation order and the shear

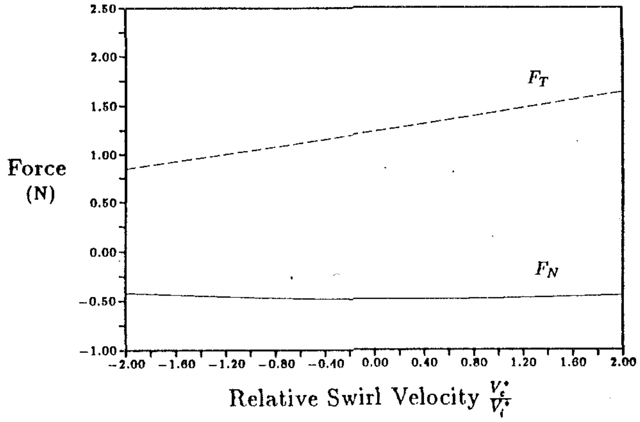

Fig. 6 Direct and cross force predicted by the coupled model versus center cavity swirl velocity. These are for the same conditional as Fig. 5 with $\delta_c/\delta_1^* = 0.37$.

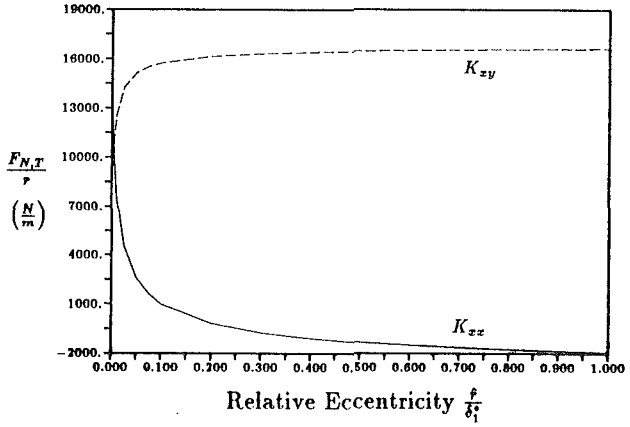

Fig. 7 Effect of relative whirl amplitude on the direct and cross stiffness as predicted by the coupled model with hub plenum leakage. Build #3 geometry and $\delta_c/\delta_1^* = 0.19$.

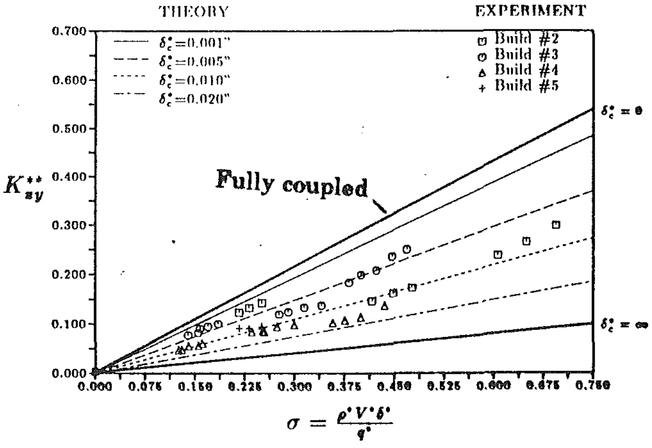

Fig. 8 Nondimensional cross stiffness, K_{xy}, versus swirl parameter, σ, for the experimental data and theory, with the axial gap used as a parameter. All experimental values fall between the theoretical predictions with 0.004 in. (0.0001 m) $< \delta_c <$ 0.017 in. (0.0004 m). The top thick line is the fully coupled case (i.e., no center leakage) and the bottom one is for uniform inlet conditions (i.e., no coupling). Calculations are for build #3 geometry.

stresses acting to retard the flow are of order unity. For cases with seal rotation, it would be very difficult to estimate the swirl velocity inside the center cavity. Figure 6 shows the effect that changes in the center cavity swirl velocity have on the forces.

In the absence of the leakage flow nonlinearity, the theory predicts that the forces should scale with whirl eccentricity and hence the rotordynamic coefficients, and, should be independent of the whirl amplitude. The nonlinearity due to axial leakage is shown in Fig. 7, which shows K_{xx} and K_{xy}, and the relative eccentricity $\hat{r}/\delta_1^*$. The behavior of C_{xx} is the same as for K_{xy}. The direct force is much more sensitive to the whirl amplitude than is the cross force. At large whirl amplitudes, the predicted forces approach those obtained for $\delta_c = 0$ (i.e., the fully coupled case). However, as $r \rightarrow 0$ the center leakage flow is able to "kill" the swirl cavity pressure perturbation completely. This effectively decouples the whirling seal from the upstream cavity.

4 Comparison to Data

As discussed in Section 1, a strict comparison of the preceding theory of the LSFT test results is not possible because of the lack of control over the axial leakage gap, δ_c, the importance of which was shown in Section 3. What can be shown, however, is that for the range of likely values of δ_c, the upstream coupling effects increase the cross forces the required amount to explain the very large deviations between experimental data and the simple, uncoupled theory.

The general character of the comparison can be seen from Fig. 8, which shows the nondimensional cross-stiffness verses the nondimensional inlet swirl. The trends and comparisons for C_{xx} are the same as for K_{xy}, due to the relationships shown in Part I. For Fig. 8, the theoretical lines were calculated using the cavity parameters for Build #3. The volume ratio (upstream to seal cavity) was in that case 3.01, whereas it was 4.64 for Build #2. According to Fig. 4 the amplification factors (for $\delta_c = 10$ mil) are 3.7 for Build #3 and 2.8 for Build #2.

Looking first at the Build #3 data only, we notice a general grouping about the theoretical line for δ_c between 5 and 10 mil. The design value of this gap was 10 mil. We also see that the points appear in groups, each of which is aligned with a somewhat different δ_c line. These groups in fact correspond to the different swirl vane assemblies, and δ_c can be expected to have remained constant within each of them, but perhaps not with exactly the same value from assembly to assembly.

The data for the two outer groups of points for Build #2 are roughly on a line with a slope lower by 1/1.3 than those for Build #3, in accordance with the noted difference between the volume ratios of both cases. The group for the smaller dimensionless inlet swirl is anomalously high, however. In general, for all builds, the data are indeed bracketed between the limits of the uncoupled ($\delta_c \rightarrow \infty$) theory and the fully coupled ($\delta_c = 0$) models.

As a related test of the theory, equations were derived for multicavity seals with upstream coupling [9]. This coupled theory for a two-gland seal, plus the upstream cavity was compared to some two-gland static seal data of Benckert and Wachter [5], whose facility had the same general upstream configuration as the LSTF. These researchers also failed to keep a careful control of their face seal, for which no value is reported. As noted before, no theoretical calculation had been able to match the higher than expected cross forces in these short seals. Using the coupled model, the cross forces obtained in all three two-gland seals that Benckert tested can be matched by the theory with appropriate choices of the axial sealing gap, δ_c (a slightly different one for each build). Not only can the total force be predicted, but the relative contributions from each gland can be matched for the one case for which this was reported. The model predicts that the effects of the upstream coupling die exponentially. After a few glands the upstream influence cannot be seen. The data of Benckert support this conclusion.

Table 1 gives the data of Benckert along with several cases

Table 1 Comparison of the static data of Benckert and Wachter to the coupled model. The first column shows the experimental value. The second column gives the value predicted with full coupling. The third gives predictions for constant upstream conditions (i.e., no coupling). The last column gives the value of the axial sealing gap needed for the model to match the experimentally obtained value.

CONFIG.	$F_T(meas.)$	$F_T(\delta_c^* = 0)$	$F_T(\delta_c^* = \infty)$	Matched δ_c^*
1	10.21(N)	16.28(N)	4.99(N)	0.008"
2	8.28(N)	16.15(N)	4.25(N)	0.011"
3	11.91(N)	15.51(N)	4.09(N)	0.010"

from the model. The cross force as predicted with uniform upstream conditions is given. Finally, the value of the axial gap that matches Benckert's data is given for each case. These values are reasonable and show that the strong upstream coupling is the most likely cause for the high cross forces generated in the first gland of a seal.

5 Discussion

These findings have important implications for design and analysis of short labyrinth seals, and, by extension, probably for other seal types as well. Data on cross forces from such seals should be supplemented by a description of the upstream (and also the downstream) configuration of the test device, unless it can be ascertained by auxiliary tests that no coupling exists. As an example of the latter situation, it was verified that the rotordynamic force data were insensitive to the *downstream* configuration. This was found by blocking parts of the exhaust holes from the downstream chamber. The remaining holes were large enough to equilibrate this chamber with the atmosphere, hence making coupling negligible.

Calculation of seal rotordynamic coefficients, either for design or for rotordynamic diagnostic purposes, should always account for these potential couplings. Ignoring them may make other refinements, such as more precise two or three-dimensional cavity flow modeling or CFD calculations irrelevant by comparison. Including the upstream and downstream coupling is relatively straightforward for single geometries, such as the LSTF rig, but no theory current exists that can be used to predict the nonuniformities ahead of, for example, the seal on a turbine tip shroud, where the tip area interacts strongly with the main turbine through flow. Development of such a theory would seem important. Similar considerations should apply for other seal environments.

References

1 Kostyuk, A. G., "A Theoretical Analysis of the Aerodynamic Forces in the Labyrinth Glands of Turbomachines," *Teploenergetica*, Vol. *19*, No. *11*, 1972, pp. 29–33.

2 Iwatsubo, T., "Evaluation of Instability Forces in Labyrinth Seals in Turbines or Compressors," NASA CP-2133, 1980, pp. 139–169.

3 Martinez-Sanchez, M., Lee, O. W. K., and Czajkowski, E., "Prediction of Force Coefficients in Labyrinth Seals," NASA CP-2338, 1984, pp. 235–256.

4 Scharrer, J. K., "Theory Versus Experiment for the Rotordynamic Coefficients of Labyrinth Gas Seals: Part 1—A Two-Control Volume Model," *11th ASME Conference on Mechanical Vibration and Noise*, Vol. 2, 1987, pp. 411–434.

5 Martinez-Sanchez, M., Jaroux, B., Song, S. T., and Yoo, S., "Measurement of Turbine Blade Tip Rotordynamic Excitation Forces," ASME Paper No. 93-GT-XX, 1993.

6 Benckert, H., and Wachter, J., "Flow-Induced Spring Coefficient of Labyrinth Seals for Application in Rotordynamics," NASA CP-2133, 1980, pp. 189–212.

7 Gans, B. E., "Prediction of the Aeroelastic Forces in a Labyrinth Type Seal and Its Impact on Turbomachinery Stability," Eng. Thesis, Dept. of Mechanical Engineering, MIT, 1983.

8 Kameoka, T., and Abe, T., "A Theoretical Approach to Labyrinth Seal Forces," NASA CP-2338, 1984, pp. 28–30.

9 Millsaps, K. T., "The Impact of Unsteady Swirling Flow in a Single Gland Labyrinth Seal on Rotordynamic Stability: Theory and Experiment," Ph.D. Dissertation, Department of Aeronautics and Astronautics, MIT, 1992.

Application of Computational Fluid Dynamics to Turbine Disk Cavities

G. P. Virr

J. W. Chew

J. Coupland

Rolls-Royce plc,
P.O. Box 31,
Derby, United Kingdom

A CFD code for the prediction of flow and heat transfer in rotating turbine disk cavities is described and its capabilities demonstrated through comparison with available experimental data. Application of the method to configurations typically found in aeroengine gas turbines is illustrated and discussed. The code employs boundary-fitted coordinates and uses the k–ϵ turbulence model with alternative near-wall treatments. The wall function approach and a one-equation near-wall model are compared and it is shown that there are particular limitations in the use of wall functions at low rotational Reynolds number. Validation of the code includes comparison with earlier CFD calculations and measurements of heat transfer, disk moment, and fluid velocities. It is concluded that, for this application CFD is a valuable design tool capable of predicting the flow at engine operating conditions, thereby offering the potential for reduced engine testing through enhanced understanding of the physical processes.

Introduction

The potential benefits of using computational fluid dynamics (CFD) methods to calculate flow and heat transfer in gas turbine engine disk cavities were recognized some years ago. Although early calculations showed some considerable promise (see, for example, Gosman et al., 1976a) progress toward producing validated methods that can be applied with confidence has not been straightforward. Numerical difficulties, lack of suitable experimental measurements, turbulence model limitations, and limited understanding of the flow mechanisms involved have all hampered progress. Nevertheless, it is now considered that certain classes of disk cavity flows can be predicted with some confidence, and in this paper a suitable CFD code is described with discussion and examples of validation and application of the method.

It is appropriate to mention some of the most relevant previous work, with particular reference to turbulence modeling, but for a fuller review the reader is referred to Chew (1990). Studies that employed the well-known high-turbulence Reynolds number k–ϵ model with logarithmic wall functions to model the near-wall region are considered first. Gosman et al. (1976a, 1976b) used this model with two different numerical solution methods and included comparisons with Bayley and Owen's (1970) torque measurements for a shrouded disk system with radial outflow of air. Some agreement with data was found with Gosman et al. (1976b) showing particularly good agreement with measurement. However, at high Reynolds number, Gosman et al. (1976a) had to adjust one of the turbulence model constants in order to match the experimental data. The reason for the difference in the results from these two numerical studies is not clear. Chew (1984) had difficulty in repeating some of the results of Gosman et al. and also found that this turbulence model performed badly when compared to Pincombe's (1983) velocity measurements for radial outflow between corotating disks. Morse (1988) subsequently confirmed the latter result. Comparing calculations with Daily and Nece's (1960) data for an enclosed rotating disk, Williams et al. (1991) found that reasonable agreement could be obtained provided care was taken in specifying the near-wall mesh spacing. These workers recommended that the maximum rotor nondimensional near-wall spacing y^+ should be in the appropriate range for applicability of the logarithmic law. Presumably, y^+ was not in the appropriate range at other points. In a recent paper, Staub (1992) compared CFD predictions with data from a model of a typical disk cavity and has concluded that the k–ϵ model with wall functions "provides correct qualitative with unsatisfactory quantitative predictions."

Many workers have preferred turbulence models that avoid the use of wall functions by including a low Reynolds number model for the near-wall region. Various low Reynolds number versions of the k–ϵ model have been tried with very mixed results (see for example, Chew, 1984; Morse, 1988, 1991a, 1991b; Morse and Ong, 1992; and Roscoe et al., 1988). From Morse's comparisons with Pincombe's (1983) and Northrop and Owen's (1988) data for corotating disks with outflow and Daily and Nece's (1960) and Daily et al.'s (1964) data for the enclosed disk with outflow it is clear that this model can give good results. The sensitivity of the model to slightly different near-wall treatments and different numerical solution methods is less clear.

Mixing length models with van Driest (1956) damping near the wall have been used with some success. For example, Chew (1985a) and Chew and Vaughan (1988) found reasonable agreement of calculations with data for corotating disks with outflow and the enclosed rotating disk with outflow. The mixing length model used was based on one applied to boundary layer

---

Contributed by the International Gas Turbine Institute and presented at the 38th International Gas Turbine and Aeroengine Congress and Exposition, Cincinnati, Ohio, May 24–27, 1993. Manuscript received by the ASME Headquarters February 19, 1993. Paper No. 93-GT-89. Associate Technical Editor: H. Lukas.

flow over rotating disks and cones by Koosinlin et al. (1974). Seeking to combine the best features of the k-ϵ and mixing length models, Iacovides and Theofanopoulos (1991), adopted a zonal approach to turbulence modeling, with a near-wall mixing length treatment and a k-ϵ eddy viscosity or algebraic stress model away from the walls. These authors again compared with data for the rotating cavity and enclosed disk cases. Further extensions of the zonal approach to include a one-equation model in the near-wall region and comparison with heat transfer data are reported by Iacovides and Chew (1993). From comparison with data and potential for further development, the k-ϵ/one-equation model was recommended, though some shortcomings in all the models tested were acknowledged.

In the present study use has been made of the k-ϵ/one-equation model and the k-ϵ model using logarithmic wall functions. Brief descriptions of the models and the numerical methods used are given in the next section. Comparisons with some of the available data, and results of mesh dependency tests, are then given. Limitations of the wall function approach are also clarified in this section. Application of the method to engine configurations is illustrated and discussed, and the main conclusions summarized.

Numerical Method and Turbulence Model

The CFD method used is a finite-volume Navier-Stokes solver using a body-fitted orthogonal curvilinear grid and grid-oriented staggered velocity components. The same solver has been used for a number of other gas turbine internal flows; see Priddin and Coupland (1987) and Coupland et al. (1991).

The solver uses the k-ϵ turbulence model combined with alternative near-wall treatments, hybrid differencing for the convection terms and the SIMPLE or AVPI (time dependent) pressure correction schemes (see Manners, 1988).

The orthogonal grids used by the solver are obtained using a Schwartz-Christoffel transformation based on that of Howell and Trefethen (1990). The procedure allows full control over the positioning of grid nodes on the solution domain boundary.

In general tensor notation, using repeated indices to imply summation and the ",j" notation to denote the spatial covariant derivatives, the Reynolds-averaged mass and momentum conservation equations are

$$(\rho U^i)_{,i}=0 \tag{1}$$

$$(\rho U^i U^j)_{,j}=-g^{ij}\left(p+\frac{2}{3}\rho k\right)_{,j}+\tau_{ij},j \tag{2}$$

where

$$\tau^{ij}=(\mu+\mu_T)(g^{kj}U^i{}_{,k}+g^{ik}U^j{}_{,k}) \tag{3}$$

The energy equation, assumed for a perfect gas and with neglect of some compressible effects in the dissipation term, is

$$(\rho U^i H)_{,i}=\left[\left(\frac{\mu}{\sigma}+\frac{\mu_T}{\sigma_T}\right)c_p g^{ij}T_{,i}\right]_{,j}+(g_{ik}U^k\tau^{ij})_{,j} \tag{4}$$

where the second term on the right-hand side of this equation represents the frictional heating, i.e., the work done by the total (laminar plus turbulent) shear stress.

The turbulent viscosity in the k-ϵ region is obtained using

$$\mu_T=C_\mu\rho\,\frac{k^2}{\epsilon} \tag{5}$$

with k and ϵ being derived from their transport equations

$$(\rho U^i k)_{,i}=\left[\left(\mu+\frac{\mu_T}{\sigma_k}\right)g^{ij}k_{,i}\right]_{,j}+G-\rho\epsilon \tag{6}$$

$$(\rho U^i \epsilon)_{,i}=\left[\left(\mu+\frac{\mu_T}{\sigma_\epsilon}\right)g^{ij}\epsilon_{,i}\right]_{,j}+C_{\epsilon 1}G\,\frac{\epsilon}{k}-C_{\epsilon 2}\rho\,\frac{\epsilon^2}{k} \tag{7}$$

The turbulent energy production rate is given by

$$G=-g_{im}g_{jn}\rho\overline{u^m u^n}\,(g^{kj}U^i_{,k}+g^{ik}U^j_{,k}) \tag{8}$$

and the Reynolds stresses are given by

$$\rho\overline{u^i u^j}=\frac{2}{3}\,\rho k\delta^{ij}-\mu_T(g^{kj}U^i_{,k}+g^{ik}U^j_{,k}) \tag{9}$$

The standard set of constants for the k-ϵ model is used; see Launder and Spalding (1974).

The k-ϵ region is coupled to the near-wall region using either a near-wall low Reynolds number one-equation k-L model or wall functions. In the k-L model, see Iacovides and Chew (1993), the k transport equation is solved normally but with the dissipation rate and turbulent viscosity within the near wall zone set using

Nomenclature

b = outer radius of cavity
Cm = moment coefficient $= 2M/\rho\Omega^2 b^5$
c_p = gas specific heat
Cw = cavity throughflow coefficient $= m/\mu b$
C_μ = k-ϵ turbulence model constant $= 0.09$
$C_{\epsilon 1}$ = k-ϵ turbulence model constant $= 1.44$
$C_{\epsilon 2}$ = k-ϵ turbulence model constant $= 1.92$
E = logarithmic wall function constant $= 8.8$
g^{ij} = grid metric tensor
G = turbulence energy production rate
H = stagnation enthalpy
k = turbulence energy
L = near-wall turbulence model length scale
m = cavity mass flow
M = disk moment
p = static pressure
P_j = Jayatillaka term in stagnation enthalpy wall function
Q = total heat flux
R = recovery factor
r = radius
Re = cavity rotational Reynolds number $= \rho\Omega b^2/\mu$
Re_y = near-wall Reynolds number based on turbulence energy
s = axial gap between disks
T = static temperature
$\overline{u^i u^j}$ = Reynolds stress tensor
U^i = velocity vector
V = radial velocity
W = tangential velocity
y = distance to the wall
y^+ = near-wall Reynolds number based on τ_w $(=(\rho\tau_w)^{1/2}y/\mu)$
δ^{ij} = Kroenecker delta tensor
ϵ = turbulence energy dissipation rate
κ = constant in near wall turbulence model $= 0.43$
μ = viscosity
μ_T = turbulent viscosity
ρ = density
σ = Prandtl number $= 0.7$
σ_k = turbulent Prandtl number for k $(= 1.0)$
σ_T = turbulent Prandtl number for H $(= 0.9)$
σ_ϵ = turbulent Prandtl number for ϵ $(= 1.3)$
τ^{ij} = total shear stress tensor
τ_w = wall shear stress
Ω = angular velocity of disk

Subscripts

ad = adiabatic value
in = inlet value
w = wall value

Table 1 Results for the sealed rotor-stator example

Case	Turb. Model	Mesh Size	Exp. Rat.	Rotor Cm	r/b=0.95		
					y/b	R_y	y^+
1.1	W-F	41x41	1.0	-1.809E-3	1.6E-3	163	173
1.2	W-F	41x41	1.1	-1.885E-3	5.5E-4	59	61
1.3	W-F	41x41	1.2	-1.878E-3	1.7E-4	18	19
1.4	W-F	65x65	1.1	-1.942E-3	1.6E-4	18	18
1.5	2-L	65x65	1.2	-1.946E-3	1.9E-5	0.6	2.1
Daily & Nece Correl.				-1.816E-3			

$$\epsilon = C_\mu^{0.75} k^{1.5} / L [1 - \exp(-0.48 \mathrm{Re}_y)] \tag{10}$$

$$\mu_T = \rho C_\mu^{1/4} k^{1/2} L [1 - \exp(-0.029 \mathrm{Re}_y)] \tag{11}$$

The near-wall turbulent Reynolds number is defined by

$$\mathrm{Re}_y = \rho C_\mu^{1/4} k^{1/2} y / \mu \tag{12}$$

The length scale is defined to be proportional to the distance from the wall using

$$L = \kappa y \tag{13}$$

with $\kappa = 0.43$. The near wall zone is defined using

$$\mathrm{Re}_y < 100 \tag{14}$$

With wall functions, semi-logarithmic profiles are used to describe the velocity and stagnation enthalpy profiles at the grid nodes adjacent to the wall and are of the form

$$\rho (U - U_w) C_\mu^{1/4} k^{1/2} / \tau_w = \frac{1}{\kappa} \ln(E \mathrm{Re}_y) \tag{15}$$

$$\rho (H_w' - H') C_\mu^{1/4} k^{1/2} / (Q_w - U_w \tau_w) = \sigma_T \left[\frac{1}{\kappa} \ln(E \mathrm{Re}_y) + P_j \right] \tag{16}$$

$$H' = H + \frac{(R-1)}{2} U^2 \tag{17}$$

Here H' is the recovery enthalpy, R is a recovery factor, and P_j is the Jayatillaka term (see Launder, 1988). Modifications are also made to the near-wall production term in the turbulence energy equation to characterize the velocity gradient in terms of the semi-logarithmic profile and to fix the near-wall dissipation rate using a length scale equal to κy.

Note that the derivation of the stagnation enthalpy wall function, Eq. (16), follows that of Spalding and Patankar (1967). When frictional effects are small R may be set to unity and the term $U_w \tau_w$ neglected. Equation (16) then reduces to the form used by Gosman et al. (1976a). For the calculations in this paper R has been set to unity or set equal to the turbulent Prandtl number σ_T as described below.

Results

Sealed Rotor-Stator. A suitable test case for comparing turbulence models and examining mesh sensitivity in rotating cavity flows is the sealed rotor-stator studied experimentally by Daily and Nece (1960). Calculations were performed for incompressible flow in a rectangular cross-sectional cavity in which one disk rotates while the other disk and the shroud are stationary. The conditions chosen correspond to an aspect ratio $s/b = 0.0637$ and rotational Reynolds number Re = 4.4E6. Calculations were performed with the wall function (W-F) and two-layer (2-L) models using different numbers of mesh lines, and axial mesh expansion ratios away from the surfaces.

A useful comparison of results is through the predicted values of the moment coefficient, *Cm*, on the rotor; see Table 1. Other quantities listed in this table include the nondimensional axial near-wall mesh spacings y/b, Re_y, and y^+, at the radial position $r/b = 0.95$.

Only in case 1.1 was the predicted moment coefficient less than that obtained from the Daily and Nece correlation. In general, the level of agreement is considered good, all the results being within 8 percent of the correlation.

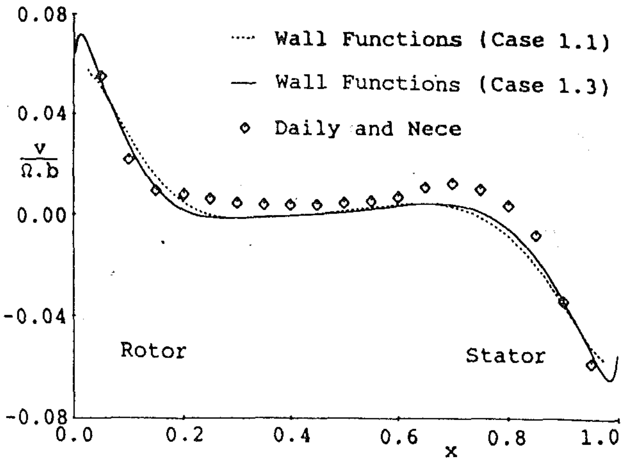

(a) Radial Velocity

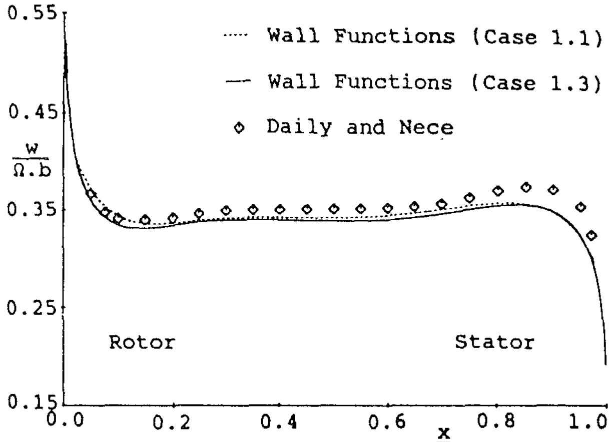

(b) Tangential Velocity

Fig. 1 Sealed rotor-stator (r/b = 0.765, s/b = 0.0637, Re = 4.4E6)

The wall function results of cases 1.1–1.3 clearly indicate a degree of sensitivity to the near-wall mesh spacing. The use of wall functions means that for a constant near-wall mesh spacing, it is not possible to obtain nondimensional distances in the correct range for the application of logarithmic wall functions at each radial position. Since the maximum shear stress occurs toward the outer radius, it is important to obtain an appropriate near-wall mesh spacing in this region. The fact that case 1.1 gives the best agreement with Daily and Nece's correlation may be due to the better near-wall mesh spacing toward the inner part of the cavity. However, with other uncertainties such as measurement and correlation inaccuracies, it would be dangerous to read too much into this result.

Figure 1 shows axial profiles of the tangential and radial velocities at $r/b = 0.765$ for cases 1.1 and 1.3. The resolutions of the boundary layers on the rotor and stator are clearly shown but the peak radial velocity is only adequately resolved for case 1.3. It has been found that for wall functions to give adequate results for rotating cavity flows it is necessary for the near-wall spacing to be sufficiently small to resolve the peak radial velocity as well as being in the preferred range for y^+ of 30–100. An important implication of this is that wall functions are more likely to give valid results at higher rotational Reynolds number for which the peak radial velocity occurs at larger values of y^+. At high Reynolds numbers, placing the near-wall grid line in the log-law range automatically resolves the radial velocity profile. The agreement between calculated and measured velocities in Fig. 1 is comparable to that found in earlier studies.

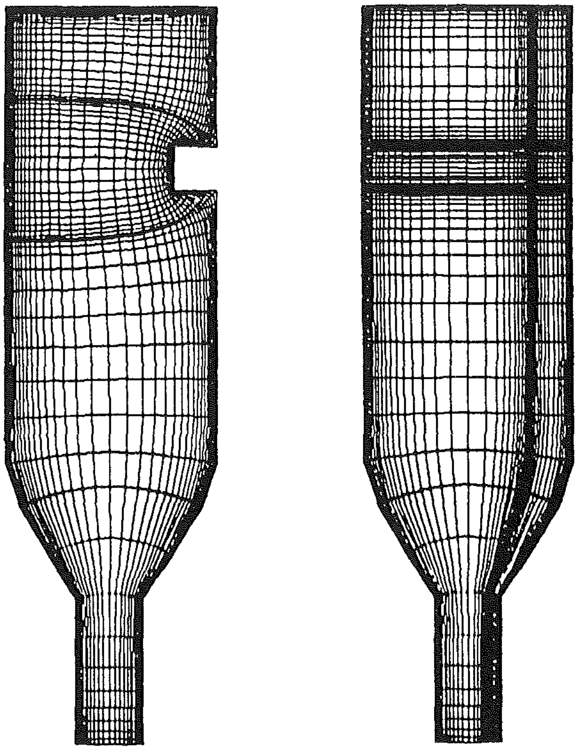

(a) Fitted Mesh (Case 2.1) (b) Blockages (Case 2.5)

Fig. 2 Cobbed disk with bolt cover

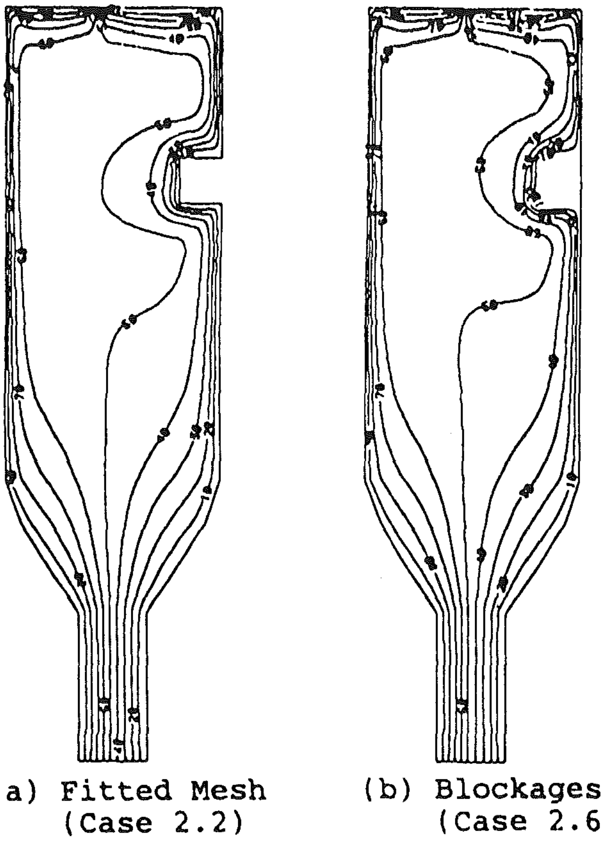

(a) Fitted Mesh (Case 2.2) (b) Blockages (Case 2.6)

Fig. 3 Streamline contours (Cw = 1760, Re = 1.5E5)

Table 2 Results for the cobbed disk example

Case	Meshing Approach	Mesh Size	Exp. Rat.	Cm	
				Left Disc	Right Disc
2.1	Fit.Mesh	41x65	1.2	-5.512E-3	-6.630E-3
2.2	Fit.Mesh	41x65	1.2*	-5.527E-3	-5.960E-3
2.3	Fit.Mesh	41x65	1.3	-5.343E-3	-5.963E-3
2.4	Fit.Mesh	65x65	1.3	-5.311E-3	-5.880E-3
2.5	Blockages	55x65	1.2	-5.524E-3	-6.077E-3
2.6	Blockages	55x65	1.2+	-5.540E-3	-6.017E-3
2.7	No Bolt Cvr	55x65	1.2	-5.593E-3	-5.595E-5

* Mesh as 2.1 but with 6 grid lines moved closer to RH disc.
\+ Mesh as 2.5 but with mesh lines moved closer to blockage.

The zonal modeling approach adopted in the two-layer model overcomes the difficulty noted above for wall functions but at the expense of extra mesh lines and the corresponding increased computational cost. The two-layer model is used here with the maximum near-wall y^+ of order 2 or less. Therefore, provided this is achieved at the outer radius, it will also be achieved at all radial positions. The velocities predicted by the two-layer model (case 1.5) agreed well with the wall function results of case 1.3.

Cobbed Disk With Bolt Cover. In order to demonstrate the geometric capabilities of the code, a cobbed disk with bolt cover was analyzed see Figs. 2 and 3. The flow regime was radial outflow of air between corotating disks and the conditions considered here correspond to a mass flow parameter $Cw = 1760$ and rotational Reynolds number $Re = 1.5E5$. This configuration has been studied experimentally by Farthing and Owen (1988) and Farthing (1988). In the experiments, air left the cavity through a series of discrete holes in the outer circumference, whereas in these two-dimensional calculations, the fluid exits through a narrow slit. A comparison of CFD results with data for this case was reported by Lapworth and Chew (1992) who used a mixing length turbulence model.

Due to the low value of Re it was known that wall functions were not appropriate and so the two-layer model was employed. The presence of the bolt cover on the right-hand disk enabled two different meshing approaches to be adopted and compared. These consisted of either fitting an orthogonal mesh around the bolt cover or meshing through the bolt cover and subsequently blocking it out.

Figure 2 gives examples of the two-dimensional boundary-fitted orthogonal meshes used in the analysis. Note the highly distorted mesh with large variations in near-wall mesh spacing around the bolt cover shown in Fig. 2(*a*). This type of mesh might be expected to give numerical errors due to the distortion and numerical diffusion errors due to the flow deviating markedly from the mesh line directions. The alternative approach shown in Fig. 2(*b*) avoids all problems of mesh distortion and enables a uniform near-wall mesh spacing to be achieved, although numerical diffusion errors may still be present.

The results of a comparison of moment coefficient for different meshing approaches, near-wall mesh spacing, etc., are presented in Table 2. For case 2.1, the fitted mesh resulted in excessive near-wall spacing in the corners where the bolt cover joined the right-hand disk. This was corrected in case 2.2 by moving the first six grid lines closer to the disk. For case 2.3, the greater mesh expansion ratio resulted in sufficiently small near-wall mesh spacing. In case 2.6, the sensitivity of the near-wall spacing on the blockage was examined by moving mesh lines closer to the blockage.

Figure 3 gives contours of stream function for each meshing approach and shows excellent agreement for the overall mass flow distribution. Both plots clearly show the source region at inlet, the formation of the Ekman-type layers on the rotating surfaces, a core region in the center of the cavity and a sink region at outlet. On the right-hand disk, the interesting phenomenon that the Ekman layer does not separate from the corners of the bolt cover was predicted in both cases. This phenomenon was also observed in Farthing's flow visualization for laminar conditions.

The fact that the Ekman layer remains attached to the bolt cover explains why reasonable agreement is obtained for Cm for each meshing approach. Large diffusion errors are not present in the fitted mesh because the actual flow quite closely

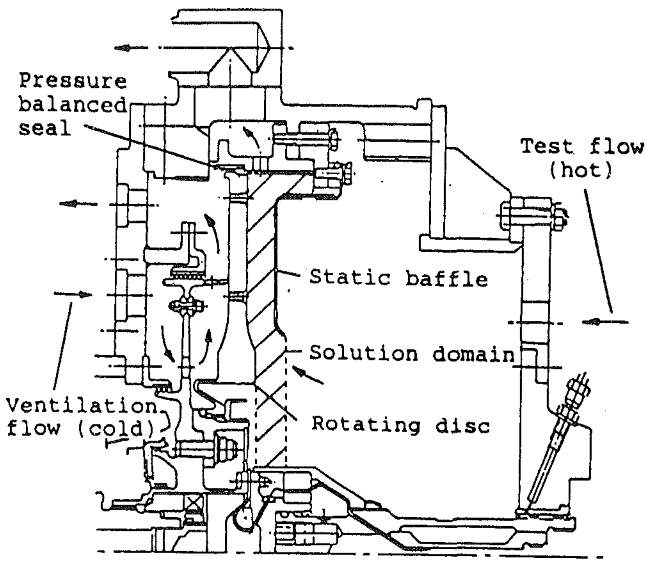

Fig. 4 Diagram of rig

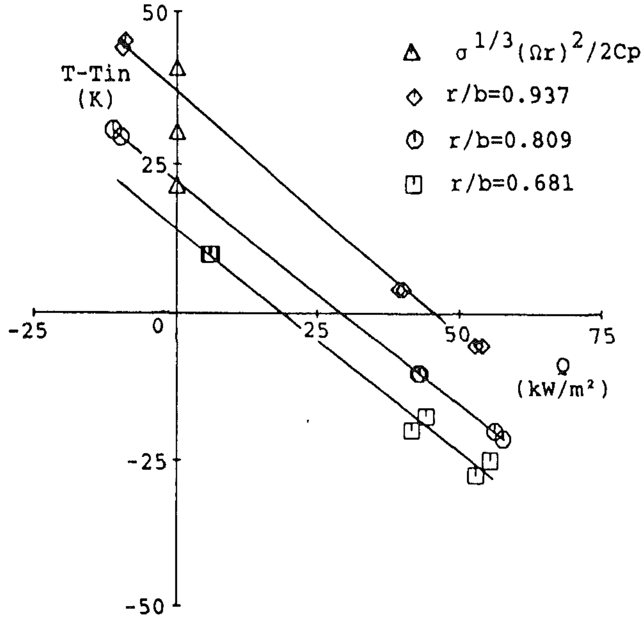

Fig. 5 Measured disk heat flux and temperature (*Cw* = 36,800, Re = 7E6)

follows the mesh. The main problem with this approach is the large variation in near-wall mesh spacing. Comparison of the results of cases 2.1 and 2.2 shows the importance of obtaining a sufficiently small near-wall spacing at all mesh lines, since obtaining the required value in the corners of the bolt cover produced a 10 percent reduction in the predicted moment. The use of blockages to model the bolt cover results in a larger number of mesh lines for the same near-wall spacing since all surfaces of the blockage require the same grid spacing as the disks. This approach also leads to large aspect ratio grid cells in the center of the cavity, which may lead to numerical difficulties.

Comparison of the results of cases 2.2 and 2.3 once again shows how significant the near-wall mesh spacing is in rotating cavity flows. The increased mesh expansion ratio, resulting in reduced near-wall mesh spacing, avoided the need to move mesh lines closer to the right-hand disk, but produced a reduction in moment on the left-hand disk. The results of case 2.4 with extra axial mesh lines confirmed the predicted moment coefficients, thereby showing a degree of mesh independence.

The results of cases 2.5 and 2.6 were in close agreement with those of case 2.2, for which identical near-wall mesh spacings were used on the disks away from the bolt cover. The differences can be attributed entirely to the different meshing approaches for the bolt cover. Case 2.7 used the same mesh as case 2.6 but with no bolt cover. As identical mesh spacing was used on the disk surfaces, the slight difference of moment coefficient on each disk indicates that for this flow any errors associated with large aspect ratio cells in the center of the cavity are small for this particular flow. Comparison of cases 2.6 and 2.7 indicates that the addition of the bolt cover gives a 7.5 percent increase in moment on the disk with the cover, and a slight reduction of about 1 percent on the opposing disk. However, further comparison with case 2.4 shows that the prediction of such small effects may be subject to numerical errors.

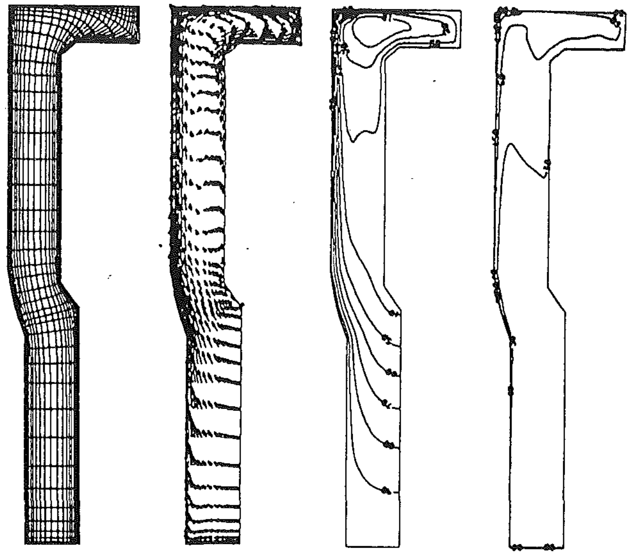

(a) Mesh (b) Streaklines (c) Streamlines (%) (d) Tangential Velocity (m/s)

Fig. 6 Rotor-stator with radial outflow (*Cw* = 36,800, Re = 7E6)

Rotor-Stator Heat Transfer. Validation of the code for the prediction of local heat transfer was undertaken by comparing with the experimental results of Millward and Robinson (1989). These data are at typical engine operating conditions and has not previously been compared with CFD predictions. The case chosen was a rotor-stator with radial outflow. A diagram of the rig is given in Fig. 4, which differs slightly, from that shown by Millward and Robinson, in terms of the pressure balanced seal and geometry of the stator at the outer radius.

The case analyzed was a plane disk rotating at 13,325 rpm with a hot side test airflow of 0.2268 kg/s at nominal temperature 471 K and pressure 345 kPa. The conditions correspond to Re = 7E6 and Cw = 36,800 based on an outer radius b = 0.233 m. In the experiment, the hot side conditions were kept approximately constant. The mass flow rate of the cold side ventilation airflow was varied to alter the heat transfer rate through the rotor. The disk was instrumented with "plug-meters" and thermocouples to measure the heat flux through the disk and the hot side metal temperature at three radial positions.

For a given hot side test condition, experiments were carried out for various cold side mass flows, thus varying the thermal boundary conditions on the disk in the test section. Plots of disk temperature against heat flux were produced, as in Fig. 5. By plotting lines through the data points, estimates of adiabatic disk temperature were obtained from values for the zero heat flux condition.

Table 3 Moment predictions for the rotor-stator with outflow

Case	Turb. Model	Mesh Size	Cm	Total Air Temp. Rise (K)	
				$\Omega M/\dot{m}Cp$	Energy Eqn.
3.1	W-F	41x45	-3.354E-3	33.29	32.97
3.2	2-L	53x57	-3.209E-3	31.84	31.83

Table 4 Results for adiabatic disk temperature

Plugmeter Radius r/b	Experiment $T_{ad}-T_{in}$ (K)	Predicted $T_{ad}-T_{in}$ (K)		$\sigma^{1/3}(\Omega r)^2/2Cp$ (K)
		W-F	2-L	
0.681	14.0	17.4	22.7	21.5
0.809	22.0	27.7	34.2	30.4
0.937	37.0	38.3	46.1	40.7

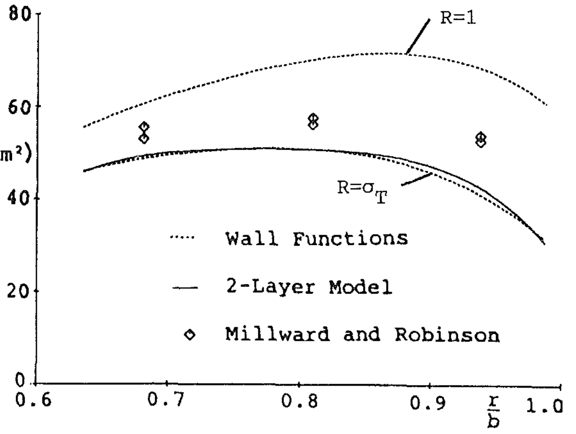

Fig. 7 Comparison of calculated and measured heat flux for the rotor-stator with radial outflow

In order to reduce the sensitivity of the CFD results to the assumed inlet conditions, the solution domain was extended upstream of the region where the measurements were taken, as indicated by the cross-hatched lines in Fig. 4. The geometry of the stator, in the outer part of the cavity, and the inner region of the rotor, was also simplified slightly. Calculations were performed with both wall functions and two-layer model and the results compared with measurements. Figure 6 gives details of the mesh used for the calculations, predicted streaklines, contours of stream function, and tangential velocity for the wall function calculations. The two-layer and wall function model calculations were in reasonable overall agreement as highlighted in Table 3.

The wall function approach predicted a higher moment on the rotor but, due to the limitations described earlier, it was not possible to obtain the correct near-wall spacing at the inner radii. The mesh used for the two-layer model was created from the wall function mesh by placing extra mesh lines in the near-wall regions. In both cases, consistent results for the total air temperature rise were obtained by the separate calculations of work input to the air and solution of the energy equation with frictional heating source terms and adiabatic walls. Although care was taken to ensure appropriate near-wall mesh spacings, guided by experience gained from earlier test cases, exhaustive mesh-dependency tests were not undertaken for this example.

A comparison of the predicted adiabatic wall temperatures with measured values is given in Table 4. The quantity $\sigma^{1/3}(\Omega r)^2/2Cp$, which is the expected frictional temperature rise for a free disk (see, e.g., Chew, 1985b), is also tabulated. The most notable feature of the results is that the measurements are somewhat lower than all the theoretical results, particularly at the lower radii. It should be noted that for the wall function calculations, while Q_W was correctly set to zero in the control volume energy balances, the values of stagnation enthalpy at the wall were approximated by those at the near-wall nodes. This accounts for the disk temperatures for the wall function model being somewhat lower than those for the two-layer model. The techniques used to deduce the experimental adiabatic disk temperature, from measurements in which the disk was not truly adiabatic, might account for some differences with theory. Examination of measurements for other flow conditions showed adiabatic disk temperatures considerably closer to the free disk result, reinforcing confidence in the theory.

Heat transfer calculations were performed with both near-wall treatments using measured disk temperatures from the case with the maximum cold ventilation flow, i.e., maximum disk heat fluxes. Disk temperatures were only measured at three radial positions and so a temperature profile was derived from a spline fit to the measured values. This profile was used in the CFD model with fixed temperature boundary conditions applied on the disk, and with other surfaces specified as adiabatic. The flow field was assumed to remain unchanged and the full energy equation alone solved in order to determine the heat fluxes through the disk surface. It may be noted that for the conditions considered, heat flux from the air to the disk and work done on the air due to frictional drag on the disk are of similar magnitude. Thus, this is quite a sensitive test case.

Considering the above-mentioned difficulties regarding the adiabatic wall temperature, a direct comparison of measured and predicted surface heat fluxes was preferred to use of Nusselt numbers. The results are shown in Fig. 7. The level of agreement between the two-layer model and the measurements is considered very encouraging. At the outer measurement point, the two-layer model predictions are 22 percent below the experimental value, while at the other two points, agreement is within 11 percent. The discrepancy at the outer point may be associated with the extrapolation of temperature measurements in defining boundary conditions for the calculation. Any inaccuracies introduced in this manner may well be most severe toward the outer radius of the disk.

Results from the wall function model also show encouraging agreement with the data. For $R = \sigma_T$ good agreement between the two-layer and wall function models is apparent. The results for $R = 1$ show the importance of frictional effects in this test case. Provided care is taken in applying the wall functions, it is clear that this model can be useful, particularly if the number of mesh points must be restricted.

Applications

An example where the methods described in this paper have been applied to a modern high bypass ratio gas turbine is given in Fig. 8. This composition, from a number of separate calculations, shows streakline plots of the predicted flows in the cavities surrounding the low-pressure turbine disks. The classes of disk flow calculated include corotating disks, rotor-stator systems, and differentially rotating disks. In these calculations, wall functions were used and maximum take-off operating conditions were assumed. These CFD predictions have provided detailed information, which would otherwise have been extremely difficult and costly to obtain by engine testing.

Use of wall functions enabled the overall mesh size to be kept to a minimum, but in these two-dimensional calculations, it would have been equally possible to employ the two-layer model without excessive increase in computing cost. For three-dimensional calculations, the increased mesh size inherent in the two-layer model is more likely to limit use of the code. The greater generality of the two-layer model must be weighed against the more demanding mesh requirements for individual applications.

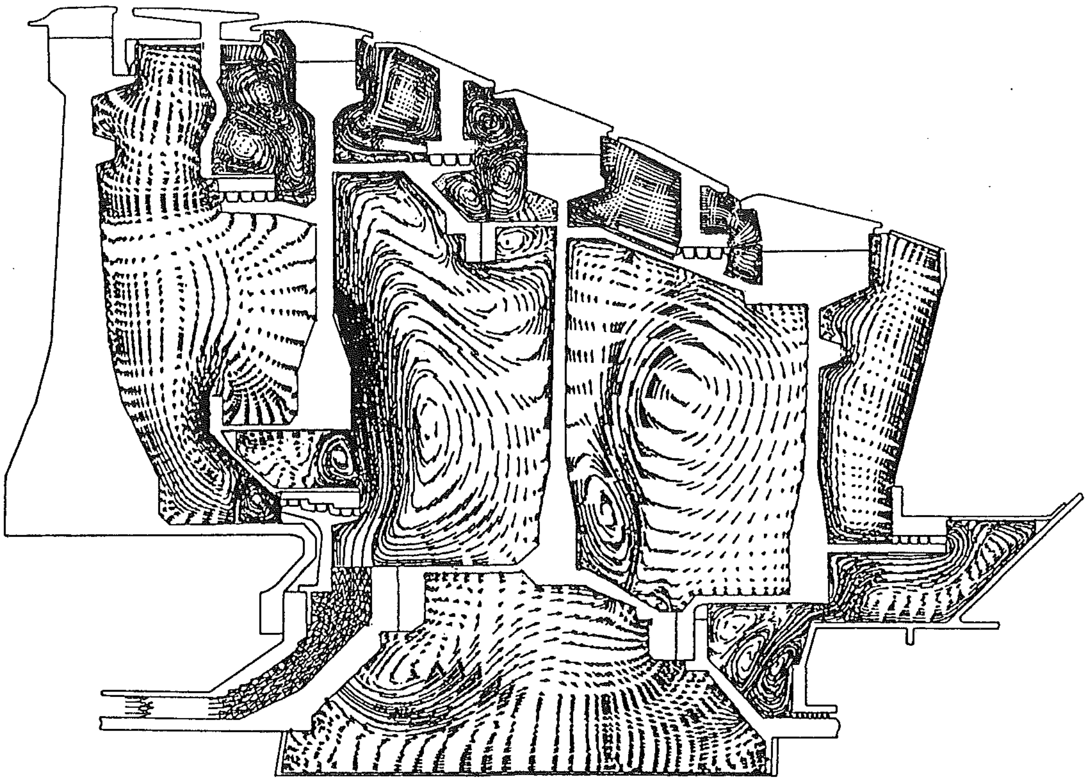

Fig. 8 Typical engine application

The demonstrated geometric capabilities of the code clearly enable a wide variety of engine cavities to be examined. This study, and earlier work, has shown that typical turbine cavities can be successfully calculated and important design information obtained. The validity of the method for some classes of disk flow is, however, unproven. A good example of this is the cavity between corotating disks with no imposed radial throughflow, as is often found in compressors. In these cavities, the convective flows are driven by buoyancy effects in the centripetal force field. Clearly, care is needed both in identifying which flows are suitable for this type of analysis and in obtaining accurate results.

Conclusions

The benefits of applying CFD methods to calculate flow and heat transfer in gas turbine engines are now being realized. Careful numerical testing and evaluation against experimental data enables predictions to be made with some confidence. Wider use of CFD is expected in the future with three-dimensional flows and integration of CFD methods in the disk thermal analysis receiving more attention.

Two near-wall turbulence model treatments have been compared in this study. Conventional wall functions were found to give acceptable results for velocity, moment, and heat transfer predictions, provided the Reynolds number was sufficiently high, and care was taken in specifying the near-wall mesh spacing. For heat transfer, care should also be taken to ensure correct treatment of frictional effects in the stagnation enthalpy wall function. The one-equation near-wall model has greater generality than wall functions with the disadvantage that it requires more mesh points. Note, however, that the one-equation treatment requires less near-wall mesh points than the low Reynolds number k–ϵ models used by several other workers.

Present results for the sealed rotor–stator and cobbed disk examples are consistent with expectations from earlier studies. Comparison with Millward and Robinson's (1989) heat transfer measurements for a rotor–stator system with radial outflow gives further confidence in the use of CFD. Although these experiments are not ideal for CFD validation, they are more representative of engine conditions than most of the available data.

Acknowledgments

The assistance of our colleagues John Millward and Peter Robinson in supplying and interpreting their experimental data is gratefully acknowledged.

References

Bayley, F. J., and Owen, J. M., 1970, "The Fluid Dynamics of a Shrouded-Disk System With Radial Outflow of Coolant," *ASME Journal of Engineering for Power*, Vol. 92, pp. 335–341.

Chew, J. W., 1984, "Prediction of Flow in Rotating Disc Systems Using the k–ϵ Turbulence Model," ASME Paper No. 84-GT-229.

Chew, J. W., 1985a, "Prediction of Flow in a Rotating Cavity With Radial Outflow Using a Mixing Length Turbulence Model," *Proceedings, International Conference on Laminar and Turbulent Flow*, Swansea, Pineridge Press, pp. 318–329.

Chew, J. W., 1985b, "Effect of Frictional Heating and Compressive Work in Rotating Axisymmetric Flow," ASME *Journal of Heat Transfer*, Vol. 107, pp. 984–986.

Chew, J. W., and Vaughan, C. M., 1988, "Numerical Predictions for the Flow Induced by an Enclosed Rotating Disc," ASME Paper No. 88-GT-127.

Chew, J. W., 1990, "Prediction of Rotating Disc Flow and Heat Transfer in Gas Turbine Engines," *Proceedings, 3rd International Symposium on Transport Phenomena and Dynamics of Rotating Machinery*, J. H. Kim and W. J. Yang, eds., Hemisphere, pp. 145–160.

Coupland, J., Fry, P., and King, R. A., 1991, "Application of 3D CFD Techniques to Gas Turbine Combustor Metal Temperature Predictions," *Proceedings, 10th International Symposium on Air Breathing Engines*, pp. 1026–1034.

Daily, J. W., and Nece, R. E., 1960, "Chamber Dimension Effects on Induced Flow and Frictional Resistance of Enclosed Rotating Disks," ASME *Journal of Basic Engineering*, Vol. 82, pp. 217–232.

Daily, J. W., Ernst, W. D., and Asbedian, V. V., 1964, "Enclosed Rotating Disks With Superposed Throughflow," Report No. 64, Hydrodynamics Laboratory, Massachusetts Institute of Technology, Cambridge, MA.

Farthing, P. R., 1988, "The Effect of Geometry on Flow and Heat Transfer in a Rotating Cavity," D.Phil. Thesis, University of Sussex, United Kingdom.

Farthing, P. R., and Owen, J. M., 1988, "The Effect of Disk Geometry on Heat Transfer in a Rotating Cavity With Radial Outflow of Fluid," ASME *Journal of Engineering for Gas Turbines and Power*, Vol. 110, pp. 70–77.

Gosman, A. D., Koosinlin, M. L., Lockwood, F. C., and Spalding, D. B., 1976a, "Transfer of Heat in Rotating Systems," ASME Paper No. 76-GT-25.

Gosman, A. D., Lockwood, F. C., and Loughhead, J. N., 1976b, "Prediction of Recirculating, Swirling, Turbulent Flow in Rotating Disc Systems," *Journal of Mechanical Engineering Science*, Vol. 18, pp. 142–148.

Howell, L. H., and Trefethen, L. N., 1990, "A Modified Schwarz-Christoffel Transformation for Elongated Regions," *SIAM Journal of Science, Statistics and Computing*, Vol. 11, No. 5, pp. 928–949.

Iacovides, H., and Theofanopoulos, I. P., 1991, "Turbulence Modelling of Axisymmetric Flow Inside Rotating Cavities," *International Journal of Heat and Fluid Flow*, Vol. 12, pp. 2–11.

Iacovides, H., and Chew, J. W., 1993, "The Computation of Convective Heat Transfer in Rotating Cavities," *International Journal of Heat and Fluid Flow*, Vol. 14, No. 2, pp. 146–154.

Koosinlin, M. L., Launder, B. E., and Sharma, B. I., 1974, "Prediction of Momentum, Heat and Mass Transfer in Swirling Turbulent Boundary Layers," ASME *Journal of Heat Transfer*, Vol. 96, pp. 204–209.

Lapworth, B. L., and Chew, J. W., 1992, "A Numerical Study of the Influence of Disk Geometry on the Flow and Heat Transfer in a Rotating Cavity," ASME Journal of Turbomachinery, Vol. 114, pp. 256–263.

Launder, B. E., 1988, "On the Computation of Convective Heat Transfer in Complex Turbulent Flows," ASME *Journal of Heat Transfer*, Vol. 110, pp. 1112–1128.

Launder, B. E., and Spalding, D. B., 1974, "The Numerical Computation of Turbulent Flows," *Comp. Meth. Appl. Mech. Eng.*, Vol. 3, pp. 269–289.

Manners, A. P., 1988, "The Calculation of Flows in Gas Turbine Combustion Systems," Ph.D. thesis, University of London, United Kingdom.

Millward, J. A., and Robinson, P. H., 1989, "Experimental Investigation Into the Effects of Rotating and Static Bolts on Both Windage Heating and Local Heat Transfer Coefficients in a Rotor/Stator Cavity," ASME Paper No. 89-GT-196.

Morse, A. P., 1988, "Numerical Prediction of Turbulent Flow in Rotating Cavities," ASME Journal of Turbomachinery, Vol. 110, pp. 202–212.

Morse, A. P., 1991a, "Application of a Low Reynolds Number k-ϵ Turbulence Model to High-Speed Rotating Cavity Flows," ASME Journal of Turbomachinery, Vol. 113, pp. 98–105.

Morse, A. P., 1991b, "Assessment of Laminar-Turbulent Transition in Closed Disk Geometries," ASME Journal of Turbomachinery, Vol. 113, pp. 131–138.

Morse, A. P., and Ong, C. L., 1992, "Computation of Heat Transfer in Rotating Cavities Using a Two-Equation Model of Turbulence," ASME Journal of Turbomachinery, Vol. 114, pp. 247–255.

Northrop, A., and Owen, J. M., 1988, "Heat Transfer Measurements in Rotating Disc Systems. Part 2: The Rotating Cavity With Radial Outflow of Cooling Air," *International Journal of Heat and Fluid Flow*, Vol. 9, pp. 27–36.

Pincombe, J. R., 1983, "Optical Measurements of the Flow Inside a Rotating Cylinder," D.Phil. Thesis, University of Sussex, United Kingdom.

Priddin, C. H., and Coupland, J., 1987, "Modelling the Flow and Combustion in a Production Gas Turbine Combustor," *Turbulent Shear Flows*, Springer-Verlag, New York, pp. 310–323.

Roscoe, D. V., Buggeln, R. C., Foster, J. A., and McDonald, H., 1988, "A Numerical Investigation of Fluid Flow for Disk Pumping Applications," ASME Paper No. 88-GT-299.

Spalding, D. B., and Patankar, S. V., 1967, *Heat & Mass Transfer in Boundary Layers*, Morgan-Grampian, London, United Kingdom.

Staub, F. W., 1992, "Rotor Cavity Flow and Heat Transfer With Inlet Swirl and Radial Outflow of Cooling Air," ASME Paper No. 92-GT-378.

Van Driest, E. R., 1956, "On Turbulent Flow Near a Wall," *Journal of the Aeronautical Society*, Vol. 23, pp. 1007–1011, 1036.

Williams, M., Chen, W. C., Baché, G., and Eastland, A., 1991, "An Analysis Methodology for Internal Swirling Flow Systems With a Rotating Wall," ASME Journal of Turbomachinery, Vol. 113, pp. 83–90.

Effects of Embedded Vortices on Injectant From Film Cooling Holes With Large Spanwise Spacing and Compound Angle Orientations in a Turbulent Boundary Layer

P. M. Ligrani
Associate Professor,
Department of Mechanical Engineering,
University of Utah,
Salt Lake City, UT

S. W. Mitchell
Graduate Student,
Department of Mechanical Engineering,
Naval Postgraduate School,
Monterey, CA

Experimental results are presented that describe the effects of embedded, longitudinal vortices on heat transfer and film injectant downstream of a single row of film cooling holes with compound angle orientations. Holes are spaced 7.8 hole diameters apart in the spanwise direction so that information is obtained on the interactions between the vortices and the injectant from a single hole. The compound angle holes are oriented so that their angles with respect to the test surface are 30 deg in a spanwise/normal plane projection, and 35 deg in a streamwise/normal plane projection. A blowing ratio of 0.5 is employed and the ratio of vortex core diameter to hole diameter is 1.6–1.67 just downstream of the injection holes ($x/d = 10.2$). At the same location, vortex circulation magnitudes range from 0.15 m^2/s to 0.18 m^2/s. The most important conclusion is that local heat transfer and injectant distributions are strongly affected by the longitudinal embedded vortices, including their directions of rotation and their spanwise positions with respect to film injection holes. To obtain information on the latter, clockwise rotating vortices R0–R4 and counterclockwise rotating vortices L0–L4 are placed at different spanwise locations with respect to the central injection hole located on the spanwise centerline. With vortices R0–R4, the greatest disruption to the film is produced by the vortex whose downwash passes over the central hole (R0). With vortices L0–L4, the greatest disruption is produced by the vortices whose cores pass over the central hole (L1 and L2). To minimize such disruptions, vortex centers must pass at least 1.5 vortex core diameters away from an injection hole on the upwash sides of the vortices and 2.9 vortex core diameters away on the downwash sides of the vortices. Differences resulting from vortex rotation are due to secondary flow vectors, especially beneath vortex cores, which are in different directions with respect to the spanwise velocity components of injectant after it exits the holes. When secondary flow vectors near the wall are in the same direction as the spanwise components of the injectant velocity (vortices R0–R4), the film injectant is more readily swept beneath vortex cores and into vortex upwash regions than for the opposite situation in which near-wall secondary flow vectors are opposite to the spanwise components of the injectant velocity (vortices L0–L4). Consequently, higher Stanton numbers are generally present over larger portions of the test surface with vortices R0–R4 than with vortices L0–L4.

Introduction

In recent years, film holes with compound angle orientations are employed extensively on components of gas turbine engines because they are believed to produce injectant distributions over surfaces that give better protection and higher film effectiveness values than injectant from holes with simple angle orientations. Holes with compound angle orientations inject the film with a spanwise velocity component relative to the mainstream flow when viewed in the streamwise/spanwise plane. Simple angle holes, on the other hand, are oriented so that injectant is issued approximately in the direction of the mainstream flow when viewed in the streamwise/spanwise plane.

A number of studies (Goldstein and Chen, 1985, 1987; Lig-

Contributed by the International Gas Turbine Institute and presented at the 38th International Gas Turbine and Aeroengine Congress and Exposition, Cincinnati, Ohio, May 24–27, 1993. Manuscript received at ASME Headquarters March 3, 1993. Paper No. 93-GT-211. Associate Technical Editor: H. Lukas.

rani and Williams, 1990; Ligrani et al., 1991) show that the film cooling protection provdied by simple angle injection holes may be disrupted by embedded longitudinal vortices, which, unfortunately, are abundant in the turbine passages of gas turbine engines. According to Ligrani and Mitchell (1994), such disruptions are even more complex if holes with compound angle orientations are employed because of the interactions between spanwise injectant velocities and vortex secondary flows near the wall. Ligrani and Mitchell (1994) provide information on the importance of the direction of vortex rotation in regard to these interactions, as well as information on the changes that occur if compound angle rather than simple angle holes are employed. However, because the investigators employ two staggered rows of holes with a spanwise distance between adjacent holes of only 3.9*d*, no information is presented on the interactions between the vortices and the injectant from a single compound angle hole. Such information is important because it allows a designer to determine the distances required between the vortices and the film holes to keep disruptions to film cooling small.

The present study is designed to remedy this deficiency and also provide new physical understanding of the interactions between embedded vortices and film injection from holes with compound angles. Like the study of Ligrani and Mitchell (1994), it is different from Ligrani et al. (1991) and Ligrani and Williams (1990) because interactions between the vortices and injectant from film holes with compound angle configurations, instead of simple angle configurations, are considered. The present study is different from Ligrani and Mitchell (1994) because the spanwise spacing between holes is 7.8*d*, instead of 3.9*d*, which allows information to be obtained on the interactions between a vortex and the injectant from a single compound angle hole. This is made possible by the large spanwise hole spacing since interactions with injectant from holes located at $Z = -7.8d$ are minimal when the vortex encounters injectant from the hole at $Z = 0d$. As this occurs, particular attention is paid to the different magnitudes of disruptions that occur as vortex strength is maintained constant and the spanwise position of the vortex is changed with respect to the hole at $Z = 0d$.

The importance of similar perturbations from embedded vortices downstream of simple angle holes is illustrated by a number of recent studies. These include investigations of the interactions of embedded vortices with film injection from slots (Blair, 1974), with film injection from rows of holes (Goldstein and Chen, 1985, 1987), as well as with film injectant from a single hole (Ligrani and Williams, 1990; Ligrani et al., 1991). According to Ligrani et al. (1991), the complicated nature of these physical situations results because of the dependence of local heat transfer and injection distributions on vortex strength, vortex size, and vortex location relative to a vast array of film cooling injection rates, hole sizes, and configurations.

Of the earlier studies, Blair (1974) reports heat transfer distributions measured on an endwall film-cooled using a slot inclined at a 30 deg angle. The large vortex located in the corner between the endwall and the suction surface of their cascade is believed to cause significant variations of measured heat transfer and film cooling effectiveness. Nicolas and LeMeur (1974), Folayan and Whitelaw (1976), and Mayle et al. (1977) all focus on the effects of wall curvature, as well as the resulting arrays of vortex pairs, on the performance of film cooling over turbine blades. Goldstein and Chen (1985, 1987) describe results from a study on the influence of flows originating near the endwall on blade film cooling from one and two rows of holes. A triangular region is described on the convex side of the blade where coolant is swept away from the surface by the passage vortex.

To clarify further the interactions between vortices and wall jets, Ligrani and Williams (1990) examine the effects of an embedded vortex on injectant from a single film cooling hole in a turbulent boundary layer. In this case, the hole is inclined at an angle of 30 deg with respect to the test surface. Attention is focused on the effects of spanwise vortex position with respect to the film injection hole. The main conclusion is that injection hole centerlines must be at least 2.9–3.4 vortex core diameters away from the vortex center in the lateral direction to avoid significant alterations to wall heat transfer and distributions of film coolant. When vortex centers are closer to the injection hole, the film coolant is often greatly disturbed and local Stanton numbers are often altered significantly by the secondary flows within the vortices. Ligrani et al. (1991) consider the influences of vortex strength on heat transfer and injectant distributions downstream of a single hole having the same geometry employed by Ligrani and Williams (1990). In Ligrani et al. (1991), a variety of vortex strengths are considered, with circulation magnitudes as large as 0.150 m^2/s. One of the most important conclusions from this study is that magnitudes of perturbations to injectant distributions are dependent upon the ratio of vortex circulation to injection velocity times hole diameter ($S = \Gamma/U_c d$), and the ratio of vortex circulation to injection velocity times vortex core diameter ($S1 = \Gamma/U_c 2c$).

In the present study, heat transfer, mean velocity components, and injection distributions are measured downstream of a single row of injection holes with compound angle geometry. Spanwise hole spacing is 7.8*d* and a blowing ratio of 0.5 is employed. Both clockwise rotating vortices and counterclockwise rotating vortices are employed, where these rotation directions are given from downstream-looking views of vortex secondary flow vectors in spanwise/normal planes. The direction of rotation of the vortices is important because changes result in sign changes to the direction of secondary flow vectors near the wall beneath vortex cores. These are then opposed to or coincident with the spanwise velocity components of the injectant. Vortices are generated using half-delta wings placed on the wind tunnel test surface. The direction of vortex rotation is changed by altering the angle of delta wings

Nomenclature

A = vortex generator delta wing angle of attack
c = average vortex core radius
C_p = specific heat
d = injection hole diameter
m = blowing ratio $= \rho_c U_c / \rho_\infty U_\infty$
S = nondimensional circulation $= \Gamma / U_c d$
$S1$ = nondimensional circulation $= \Gamma / U_c 2c$
St = Stanton number with vortex and film injection
St_o = baseline Stanton number, no vortex, no film injection
St_f = Stanton number with film injection and no vortex
T = static temperature
U = mean velocity
X, x = streamwise distance
Y = distance normal to the surface
Z = spanwise distance from test surface centerline
Γ = circulation of streamwise vorticity
θ = nondimensional injection temperature $= (T_{r,c} - T_{r,\infty}) / (T_w - T_{r,\infty})$
ξ = unheated starting length
ρ = density

Subscripts

c = injectant at exits of injection holes
r = recovery condition
w = wall
∞ = free stream

with respect to the streamwise direction, and vortex spanwise positions with respect to the film injection holes are altered by changing the spanwise positions of the vortex generators.

Experimental Apparatus, Procedures, and Approach

Experimental Approach. The present experiment was planned to provide information on the disruptions to the protection provided by film cooling from compound angle oriented holes due to the passage of embedded longitudinal vortices. Thus, the study focuses on the interactions between three different flow fields: embedded vortices, film injection, and a boundary layer. In order to match the experimental conditions found in many practical applications, all three types of flow are turbulent. Because of the considerable complexity of the interactions between these three turbulent flow fields, the present experiment was designed to be as simple as possible without additional physical effects that may obscure and complicate the interactions of interest. The interactions between film injectant and the vortices embedded in turbulent boundary layers are thus isolated so that they may be better understood. This is accomplished by performing all measurements on a flat plate in a zero pressure gradient. Wind tunnel speed is 10 m/s, and temperature differences are maintained at levels less than 30°C so that viscous dissipation is negligible and fluid properties are maintained approximately constant. Thus, the present experiment does not include many of the effects present in high-temperature engines (curvature, high free-stream turbulence, variable properties, stator/blade wake interactions, shock waves, compressibility, rotation, etc.) because these would increase the difficulty of interpreting the results.

To simplify the experiment further, the film injection holes are arranged in a row with spanwise spacing of $7.8d$ between adjacent holes. This large spacing is equivalent to 4.7–4.9 vortex core diameters, where core diameters, in this case, are deduced from measurements at $x/d = 10.2$ (procedures employed to determine vortex core sizes are discussed later in the paper). In most cases, spanwise extents of the vortices are about two vortex core diameters from the vortex centers. Thus, interactions between the vortex and the injectant from an individual hole may be observed with minimal interactions with injectant from neighboring holes. This is true even as the spanwise position of the vortex is changed by small amounts with respect to the film injection hole, which is important because the spacings and relative positions resulting in the maximum disruptions are then apparent. Such information is required if designers are to minimize the disruptions to film protection resulting from embedded vortices, and to optimize the use of compressor air for cooling the turbine.

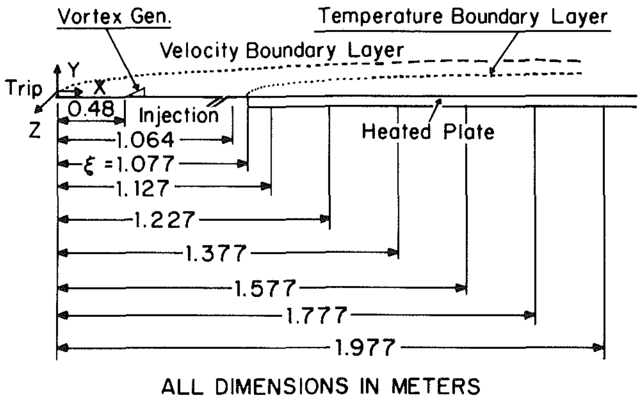

Fig. 1 Coordinate system and schematic of wind tunnel test section

Wind Tunnel and Coordinate System. The wind tunnel is the same one used in the experiments of Ligrani and Williams (1990) and Ligrani and Mitchell (1994). The facility is open-circuit, subsonic, and located in the laboratories of the Department of Mechanical Engineering of the Naval Postgraduate School. A schematic showing the test section and coordinate system is presented in Fig. 1. The test section is a rectangular duct 3.05 m long and 0.61 m wide, with a top wall whose height is adjusted to produce a zero streamwise pressure gradient when no film cooling and no vortices are present. When present, the vortices are produced using a single half-delta wing attached to a base plate, which is mounted on the floor of the test section. Figure 1 shows that this base plate is located 0.48 m downstream of the boundary layer trip. The left edge of this base plate (looking downstream) is the base edge referred to in Table 1 as a location reference line. The downstream edge of the injection holes is then 0.584 m farther downstream from this base plate. The surface used for heat transfer measurement is then located a short distance farther downstream. With this surface at elevated temperature, an unheated starting length of 1.077 m exists, and the direction of heat transfer is then from the wall to the gas. Thermocouple row locations along the test surface are also labeled in Fig. 1. In regard to the coordinate system, Z is the spanwise coordinate measured from the test section centerline, X is measured from the upstream edge of the boundary layer trip, and Y is measured normal to the test surface. x is measured from the downstream edge of the injection holes and generally presented as x/d.

Injection System. The injection system is described by Ligrani and Mitchell (1994). Air for the injection system originates in a 1.5 hp DR513 Rotron Blower capable of producing 30 cfm at 2.5 psig. From the blower, air flows through a regulating valve, a Fisher and Porter rotometer, a diffuser, and finally into the injection heat exchanger and plenum chamber. The exchanger provides means to heat the injectant above ambient

Table 1 Spanwise positions of the vortices and vortex generators. *Determined from vorticity survey measurements.

Vortex Label	Spanwise location of the vortex generator baseplate reference line, a (cm)	a/s	Centerline injection hole location with respect to the vortices	Vortex center z spanwise locations at x/d=10.2 (cm)
R0	0.0	0.00	Beneath downwash	-3.05 (-3.05*)
R1	1.8	0.24	Beneath downwash & core	-1.25
R2	3.6	0.49	Beneath upwash & core	0.55
R3	5.4	0.73	Beneath upwash	2.35
R4	7.2	0.98	Beneath side of upwash	4.15(4.06*)
L0	0.0	0.00	Beneath downwash	2.54(2.54*)
L1	-1.8	-0.24	Beneath downwash & core	0.74
L2	-3.6	-0.49	Beneath upwash & core	-1.06
L3	-5.4	-0.73	Beneath upwash	-2.86
L4	-7.2	-0.98	Beneath side of upwash	-4.66(-5.08*)

temperature. With this system and test plate heating, the nondimensional injection temperature parameter θ was maintained at about 1.5 for all tests to maintain conditions similar to ones existing in gas turibne components. The plenum connects to 13 plexiglass tubes, each 8 cm long with a length/diameter ratio of 8.4. Injection system performance was checked by measuring discharge coefficients that compared favorably with earlier measurements (Ligrani and Mitchell, 1994). With no vortex present, boundary layer displacement thickness at the injection location is $0.28d$.

Mean Velocity Components. Three mean velocity components are measured using a five-hole pressure probe with a conical tip manufactured by United Sensors Corporation. To obtain surveys of secondary flow vectors over spanwise/normal planes, the five-hole probe is mounted on the same automated traverse used for injectant surveys. Celesco transducers and Carrier Demodulators are used to sense pressures when connected to probe output ports. Following Ligrani et al. (1989a, 1989b), corrections were made to account for spatial resolution and downwash velocity effects. Ligrani and Mitchell (1994) provide additional details on these devices, the measurement procedures employed, as well as the data acquisition equipment and procedures used.

Stanton Number Measurements. Details on measurement of local Stanton numbers, including qualification tests of the test surface, are given by Ortiz (1987), and Bishop (1990). An overview of these procedures is repeated here for completeness.

The heat transfer surface is designed to provide a constant heat flux over its area. The surface next to the airstream is stainless steel foil painted flat black. Immediately beneath this is a liner containing 126 thermocouples, which is just above an Electrofilm Corp. etched foil heater rated at 120 volts and 1500 watts. Located below the heater are several layers of insulating materials including Lexan sheets, foam insulation, styrofoam, and balsa wood. Surface temperature levels and convective heat transfer rates are controlled by adjusting power into the heater using a Standard Electric Co. Variac, type 3000B. To determine the heat loss by conduction, an energy balance is performed. Radiation losses from the top of the test surface are analytically estimated. The thermal contact resistance between thermocouples and the foil top surface is estimated on the basis of outputs of the thermocouples and measurements from calibrated liquid crystals on the surface of the foil. This difference is then correlated as a function of heat flux through the foil. The convective heat flux q and surface temperature T_w are then used to determine Stanton numbers using $\mathrm{St}=q/((T_w-T_{r\infty})\rho_\infty U_\infty C_p)$.

Mean Temperature Measurements. Copper-constantan thermocouples are used to measure temperatures along the surface of the test plate, the free-stream temperature, as well as temperature distributions, which are correlated to injection distributions. For the distributions, a thermocouple is traversed over spanwise/normal planes (800 probe locations) using an automated two-dimensional traversing system that can be placed at different streamwise locations. For each measurement of temperature using a thermocouple and for each measurement of pressure using the five-hole probe, 50 samples of data are obtained at a sampling frequency of approximately 5 Hz.

Baseline Data Checks. Baseline data with no film injection show good agreement (maximum deviation is 5 percent) with the correlation from Kays and Crawford (1980) for turbulent heat transfer to a flat plate with unheated starting length and constant heat flux boundary condition. Local and spanwise-averaged Stanton numbers with injection at a blowing ratio of 0.5 (and no vortex) also show agreement with earlier results (see Ligrani and Williams, 1990, and Ligrani and Mitchell, 1994). Further checks on measurement apparatus and procedures were made by measuring spatial variations of Stanton numbers along the test surface with different strength vortices (and no injection). These data are also consistent with other results in the literature (Ligrani and Williams, 1990).

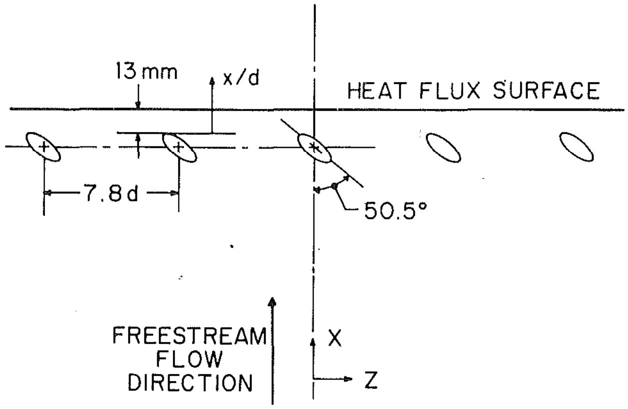

Fig. 2 Injection hole arrangement along the test surface to show compound angle film cooling hole spacing and geometry

Experimental Uncertainties. Uncertainty analysis details are given by Ligrani and Mitchell (1994). Uncertainty estimates are based upon 95 percent confidence levels, and determined following procedures described by Kline and McClintock (1953) and Moffat (1982). Typical nominal values of free-stream recovery temperature and wall temperature are 18.0 and 40.0°C, with respective uncertainties of 0.13 and 0.21°C. The free-stream density, free-stream velocity, and specific heat uncertainties are 0.009 kg/m^3 (1.23 kg/m^3), 0.06 m/s (10.0 m/s) and 1 J/kgK (1006 J/kgK), where typical nominal values are given in parentheses. For convective heat transfer, heat transfer coefficient, and heat transfer area, 10.5 W (270 W), 1.03 W/m^2 K (24.2 W/m^{2}K), and 0.0065 m^2 (0.558 m^2) are typical uncertainties. The uncertainties of St, St/St$_o$, m, and x/d are 0.000086 (0.00196), 0.058 (1.05), 0.025 (0.50), and 0.36 (41.9).

Injection Hole Arrangement

A schematic showing the compound angle film hole geometry along the test surface is shown in Fig. 2. Here, holes are arranged into a single row, with the spanwise spacing between adjacent holes denoted s, and equal to $7.8d$. As mentioned earlier, this spanwise spacing is chosen to allow sufficient space between adjacent injection holes as the spanwise locations of vortices are changed. The row of holes contains five injection cooling holes with a nominal inside diameter of 0.945 cm. The centerline of the middle hole is located on the spanwise centerline ($Z=0.0$ cm) of the test surface. The compound angle holes are employed with $\Omega=35$ deg and $\beta=30$ deg, where Ω is the angle of the injection holes with respect to the test surface as projected into the streamwise/normal plane, and β is the angle of the injection holes with respect to the test surface as projected into the spanwise/normal plane. The plane of each injection hole is angled at 50.5 deg from the streamwise/normal (X–Y) plane. Within the plane of each hole, hole centerlines are oriented at angles of 24 deg from the plane of the test surface (X–Z).

Generation and Control of Vortex Characteristics

The devices used to generate the vortices are shown in Fig. 3. In the present study, vortices are generated that rotate clockwise and counterclockwise when viewed looking downstream in spanwise/normal planes. In each case, each vortex generator is a half-delta wing with 3.2 cm height and 7.6 cm base. Each

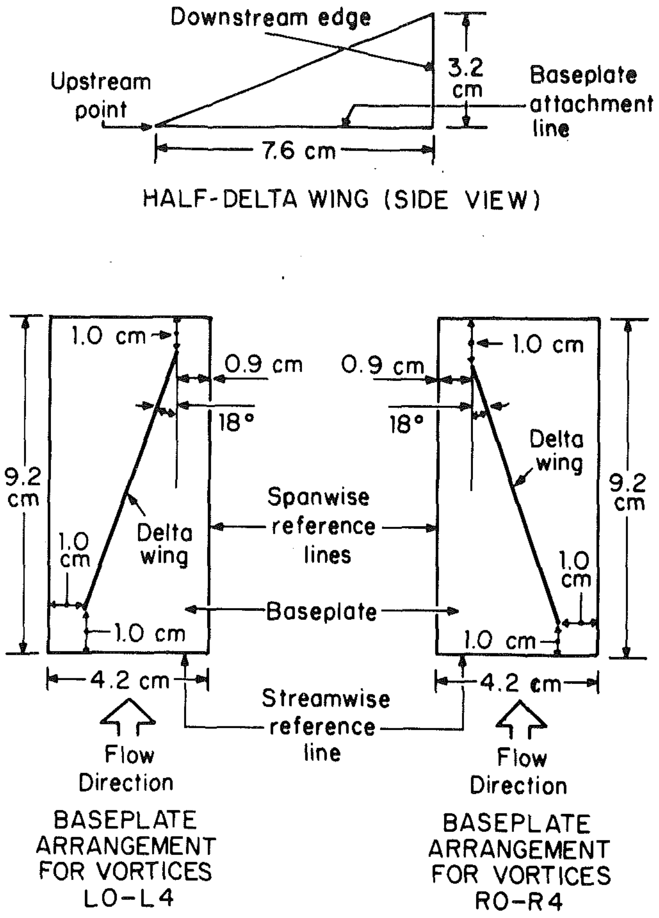

Fig. 3 Vortex generator geometry and orientations to produce clockwise and counterclockwise vortices (as viewed in spanwise/normal planes). Also shown are the dimensions of the vortex generator delta wing.

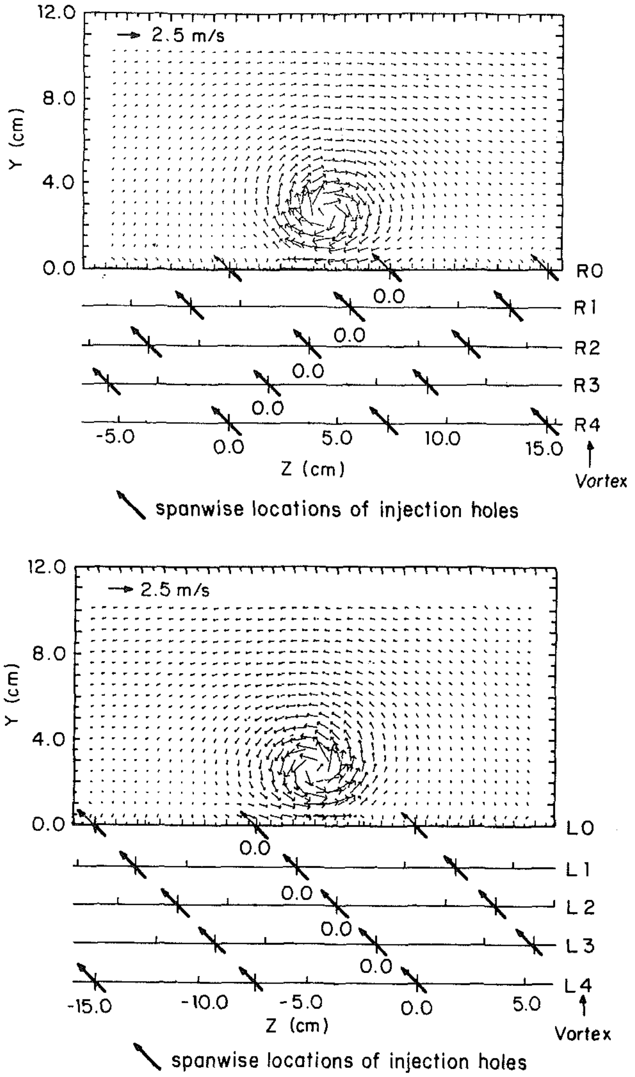

Fig. 4 Film cooling injection locations with respect to vortex center and secondary flow vectors ($x/d = 10.2$) (a) for vortices $R0$-$R4$, and (b) for vortices $L0$-$L4$. Each horizontal scale corresponds to a different vortex and different spanwise vortex position where $Z = 0$ corresponds to the centerline of the injection hole located on the wind tunnel centerline.

wing is attached to a base plate, which is moved in the spanwise direction to produce vortices with different spanwise locations with respect to the centerline film cooling hole (hereafter referred to as the central hole). Delta wing arrangements used to produce clockwise-rotating vortices $R0$-$R4$, and counterclockwise rotating vortices $L0$-$L4$, are shown in Fig. 3. The differences in the direction of vortex rotation result due to different delta wing placement on the baseplates relative to the mainstream flow direction.

With half-delta wing generators, vortices are produced with secondary flow vectors such as the ones shown in Figs. 4(a) and 4(b). In the first of these figures, the positions of the clockwise-rotating vortices $R0$-$R4$ are shown with respect to the film cooling hole locations. In the second figure, the positions of the counterclockwise-rotating vortices $L0$-$L4$ are shown with respect to the film cooling hole locations. The arrows along the abscissa of the plots denote the spanwise locations of the film cooling holes. As mentioned earlier, the centerline of the central hole is located at $Z = 0.0$ cm. Secondary flow vectors in Figs. 4(a) and 4(b) were measured within vortices $R0$ and $L0$, respectively, just downstream of the injection holes at $x/d = 10.2$. The horizontal axis is then shifted in these figures so that the centerline of the central hole is appropriately oriented with respect to vortex centers for all vortices.

Table 1 provides a tabulation of the spanwise positions of vortices $R0$-$R4$ and vortices $L0$-$L4$, as well as the vortex generators used to produce them. This includes information on the spanwise locations of vortex generator baseplates, and the locations of the central hole with respect to the vortices. The spanwise spacing between vortices $R0$ and $R1$ (as well as between vortices $R1$ and $R2$, $R2$ and $R3$, $L0$ and $L1$, $L1$ and $L2$, etc.) is 1.8 cm or 24 percent of the spanwise spacing between two adjacent holes ($s = 7.8d$). This is 1.14-1.18 times $2c$, or just greater than the size of one vortex core diameter, where vortex core radius is denoted c. The spanwise spacings between vortices $R0$ and $R4$ and between vortices $L0$ and $L4$ are both 0.98 times s, or just less than the spanwise spacing between two injection holes. Table 1 also includes estimated vortex center spanwise locations. These locations were also measured (at the locations of peak streamwise vorticity) for vortices $R0$, $R4$, $L0$, and $L4$. Good agreement between measured and estimated positions is evident for all four cases, with maximum deviation of 0.42 cm for vortex $L4$.

At $x/d = 10.2$, vortex core radii, c, of vortices $R0$-$R4$ and vortices $L0$-$L4$ are equal to 0.76-0.79 cm. c is determined as one half of the sum of average core radii in the Y and Z directions (as measured from vortex centers). These radii are determined for the area that encompasses all vorticity values greater than or equal to 40 percent of peak vorticity (at the center) for a particular vortex. The choice of 40 percent was made to give a good match to core radii determined at the locations of maximum secondary flow vectors (Ligrani and Mitchell, 1994). The area enclosed by secondary flow maxima is important, because for ideal Rankine vortices, it corresponds to the ideal core, which contains all vorticity. Secondary flow vector maxima are not used to determine core size as this gives results that are less accurate than the 40 percent threshold approach. $2c/d$ then gives the ratio of vortex core diameter to injection hole diameter. At $x/d = 10.2$, this quantity is then about 1.6–1.67 for vortices $R0$–$R4$ as well as for vortices $L0$–$L4$.

Referring to Fig. 4(*a*) and Table 1, with vortex $R0$, the central hole is located beneath the vortex downwash. With vortex $R1$, the central hole is located beneath the vortex core near the downwash. Upwash regions of vortices $R2$ and $R3$ are located above the central hole, whereas vortex $R4$ passes injection locations such that the central hole lies to the side of the upwash. Vortices $R0$ and $R4$ are displaced a spanwise distance from each other that about equals the spanwise spacing between two injection holes in the upstream row ($7.8d$). Thus, even though these two vortices are at different positions with respect to the central hole, they are at about the same positions relative to the overall hole pattern because of the spanwise periodicity of the injection hole locations. Consequently, spanwise variations of local heat transfer distributions are expected to be about the same for vortices $R0$ and $R4$ except for spanwise displacement of just less than $7.8d = 7.37$ cm.

In Fig. 4(*b*) it is evident that vortex $L0$ is located so that its downwash passes above the central hole as it passes $x/d = 0.0$. With vortex $L1$, the central hole is located beneath the vortex core near the downwash. Upwash regions of vortices $L2$ and $L3$ are located above the central hole, whereas vortex $L4$ passes injection locations such that the central hole lies to the side of the upwash. Compared to vortices $R0$–$R4$, vortices $L0$–$L4$ form a mirror image with respect to the Z axis. Just as for vortices $R0$ and $R4$, vortices $L0$ and $L4$ are displaced a spanwise distance from each other that is just less than the spanwise spacing between two injection holes in the upstream row ($7.8d$). Thus, even though vortices $L0$ and $L4$ are at different positions with respect to the central hole, they are at about the same positions relative to the overall hole pattern. Consequently, local heat transfer distributions are expected to be about the same for vortices $L0$ and $L4$ except for spanwise displacement of just less than $7.8d = 7.37$ cm.

Circulation magnitudes are calculated assuming that all vorticity values less than a threshold are equal to zero. The same numerical threshold of 100. (1/s) is used throughout this paper, chosen arbitrarily. It is about equal to 11 percent of the maximum vorticity of vortex $R0$ at $x/d = 10.2$ with no injection (909.8 1/s). At $x/d = 10.2$, circulation magnitudes (with no film cooling) range from 0.171 m^2/s to 0.177 m^2/s for vortices $R0$–$R4$, and from 0.149 m^2/s to 0.156 m^2/s for vortices $L0$–$L4$. Higher levels of vorticity evidence larger gradients of secondary flow vectors as one moves away from the vortex center. As vortex circulation becomes larger, secondary flow velocities between the main vortex center and wall increase, and amounts of spanwise vortex drift increase as the vortices are convected downstream.

With film injection at a blowing ratio of 0.5, the parameter S $(= \Gamma/U_c d)$ ranges from 3.62 to 3.75 for vortices $R0$–$R4$, and from 3.15 to 3.30 for vortices $L0$–$L4$. The parameter $S1$ $(= \Gamma/U_c 2c)$ ranges from 2.19 to 2.24 for vortices $R0$–$R4$, and from 1.96 to 1.99 for vortices $L0$–$L4$. These two parameters give measures of vortex strength relative to the injection velocity at $x/d = 10.2$ (Mitchell, 1990). According to Ligrani et al. (1991), S values higher than 1–1.5 and $S1$ values higher than 0.7–1.0 produce situations with simple angle film cooling in which injectant is swept into the vortex upwash and above the vortex core by secondary flows, and local heat transfer measurements show evidence of injectant beneath vortex cores and downwash regions near the wall only for x/d up to 17.4.

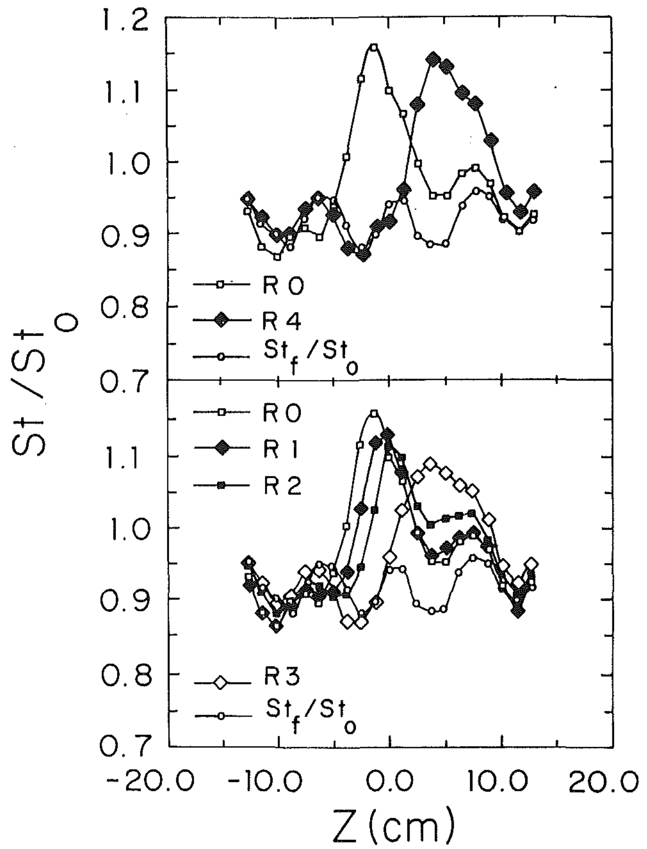

Fig. 5 Spanwise variations of local Stanton number ratios at $x/d = 33.1$ with $m = 0.5$ film cooling both with and without clockwise-rotating vortices $R0$–$R4$. Free-stream velocity = 10 m/s. Vortex spanwise positions and locations with respect to film injection holes are given in Table 1.

Heat Transfer and Injectant Distributions

In the discussion that follows, results with vortices $R0$–$R4$ are presented in Fig. 5 and 6, and results with vortices $L0$–$L4$ are presented in Figs. 7 and 8. Information on the streamwise development of local Stanton numbers with film cooling at a blowing ratio of 0.5 are presented in Fig. 9 for vortex $R0$ and in Fig. 10 for vortex $L0$.

Heat Transfer and Injectant Distributions With Vortices $R0$–$R4$. Distributions of St/St$_o$ as dependent upon spanwise coordinate Z are presented in Fig. 5. These data were measured at $x/d = 33.1$ ($X = 1.377$ m) downstream of the injection holes with a blowing ratio m of 0.5 both with and without longitudinal vortices $R0$–$R4$ embedded in the turbulent boundary layer.

In the top portion of Fig. 5, St/St_o distributions are presented for vortices $R0$ and $R4$ along with St_f/St_o data obtained when no vortices are present in the flow. Spanwise periodicity is evident in the St_f/St_o distribution, and in the St/St_o distributions where the influences of the vortices are minimal. This is due to the fact that the discrete film holes are spaced $7.8d$ apart resulting in spanwise separation between injectant concentrations at this x/d. Within the periodicity, lower St_f/St_o correspond to locations where injectant is more abundant, and higher St_f/St_o correspond to locations where less injectant is present.

Aside from the spanwise periodicity, the most apparent features on the top portion of Fig. 5 are the disturbances to local St/St_o distributions, which result from the proximity of vortex downwash regions to certain portions of the test surface. This is apparent where $St/St_o > St_f St_o$, which occurs for $Z > -5$ cm for vortex $R0$ and for $Z > 2$ cm for vortex $R4$. Here, St/St_o values are as high as 1.16 compared to St_f/St_o values from

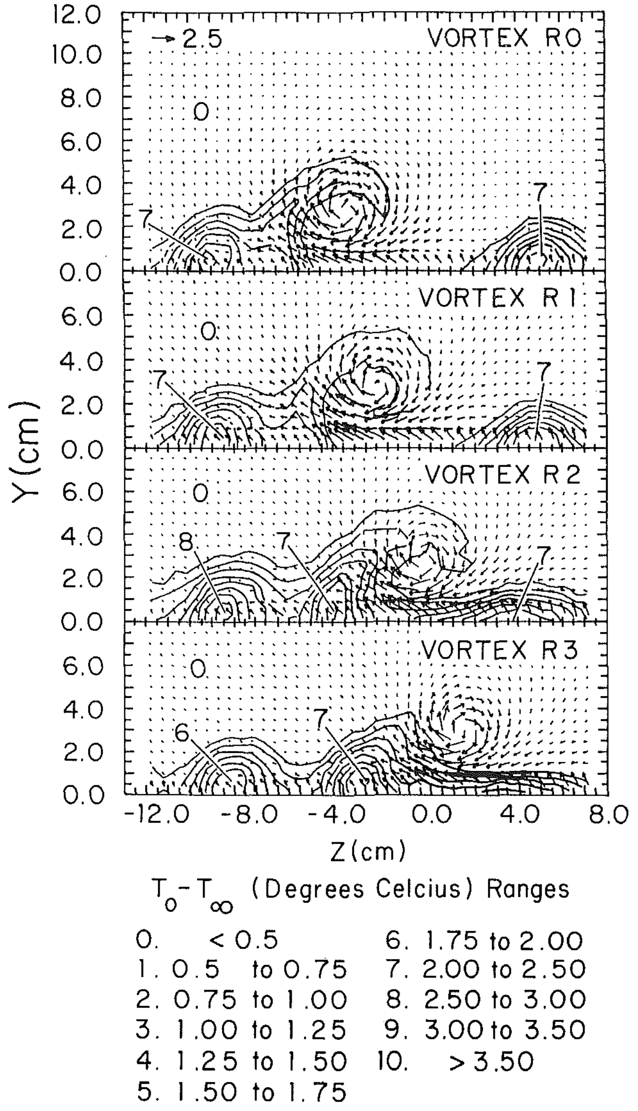

Fig. 6 Mean temperature field showing distributions of film injectant with secondary flow vectors at $x/d = 45.8$ with $m = 0.5$ film cooling and a free-stream velocity of 10 m/s. Data are given for clockwise-rotating vortices $R0$–$R3$. Vortex spanwise positions and locations with respect to film injection holes are given in Table 1.

0.87 to 0.95, where the latter are measured when no vortices are present. Test surface locations beneath vortex upwash regions correspond to $Z < -5$ cm for vortex $R0$ and to $Z < 2$ cm for vortex $R4$. Here, St/St$_o$ values may be slightly lower than the St$_f$/St$_o$ distribution, especially for vortex $R0$.

The spanwise variations of local heat transfer are about the same for vortices $R0$ and $R4$ except for spanwise displacement with respect to each other a distance of about 7.2 cm. This validates the measurement apparatus and procedures employed to obtain local heat transfer distributions. The small quantitative differences between the two curves that occur locally result because of the strong dependence of local heat transfer distributions on the positions of the embedded longitudinal vortices as they pass the injection holes, and the fact that the spanwise displacement between the two vortices is slightly less than s, the spanwise spacing between two adjacent injection holes. In this case the vortices are displaced from each other a distance of 7.2 cm or 98 percent of s (Table 1).

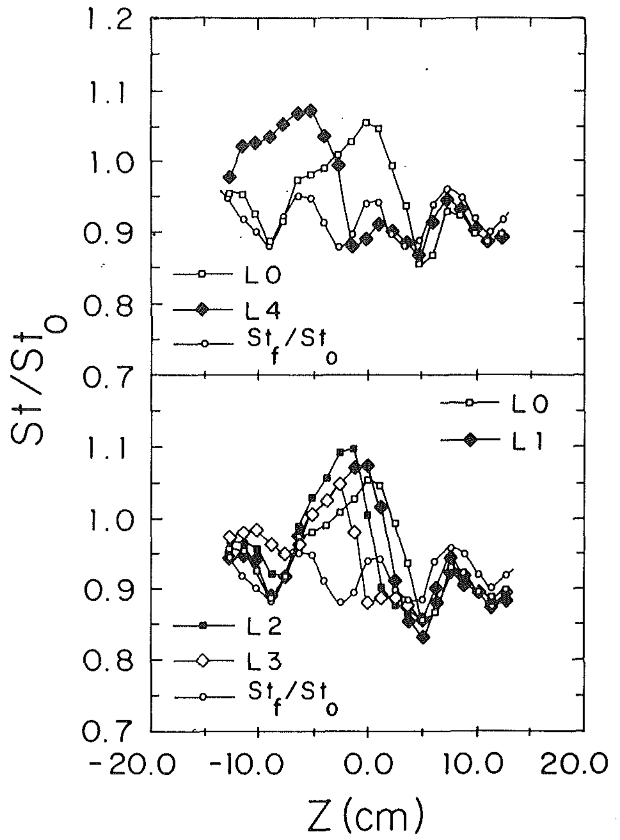

Fig. 7 Spanwise variations of local Stanton number ratios at $x/d = 33.1$ with $m = 0.5$ film cooling both with and without counterclockwise-rotating vortices $L0$–$L4$. Free-stream velocity = 10 m/s. Vortex spanwise positions and locations with respect to film injection holes are given in Table 1.

St/St$_o$ distributions with vortices $R0$, $R1$, $R2$, and $R3$ are presented in the bottom portion of Fig. 5. Here, significant quantitative and qualitative variations are seen as the spanwise locations of the vortices are changed. When the St/St$_o$ distributions are compared to each other, significant changes to the shapes of local maxima as well as to surrounding heat transfer distributions are apparent. Such variations evidence complicated interactions as different portions of an individual vortex interact with the injectant from the central hole. One important similarity caused by all four vortices is the sharp spanwise gradient of St/St$_o$, which is apparent at Z from -5 cm to 2 cm. As expected, this gradient moves in the $+Z$ direction as the spanwise locations of the vortices move in the $+Z$ direction. Away from this gradient, St/St$_o$ values approach St$_f$/St$_o$ both at large Z and at small Z at locations where the influences of the embedded vortices become less important.

The highest local St/St$_o$ value occurs with vortex $R0$, which convects downstream so that its downwash region passes over the central hole at $Z = 0$ cm. The other vortices are located at larger Z values as they are convected by the central hole, which causes their downwash regions to be located slightly farther away from the central hole. As this occurs, the bottom portion of Fig. 5 shows that magnitudes of local St/St$_o$ maxima continue to be significant for vortices $R1$, $R2$, and $R3$ even though their local St/St$_o$ maxima decrease in magnitude. Of these vortices, vortex $R3$ passes between two injectant holes and produces the broadest and lowest local St/St$_o$ maximum.

Such behavior is consistent with results obtained downstream of holes with simple angle orientations because both situations produce the least significant perturbations to the injectant (and to corresponding St/St$_o$) when the vortex core passes between two injection holes. If one consideres the interactions between an embedded vortex and the injectant from a single simple angle hole, Ligrani and Williams (1990) indicate that significant perturbations to injectant distributions result

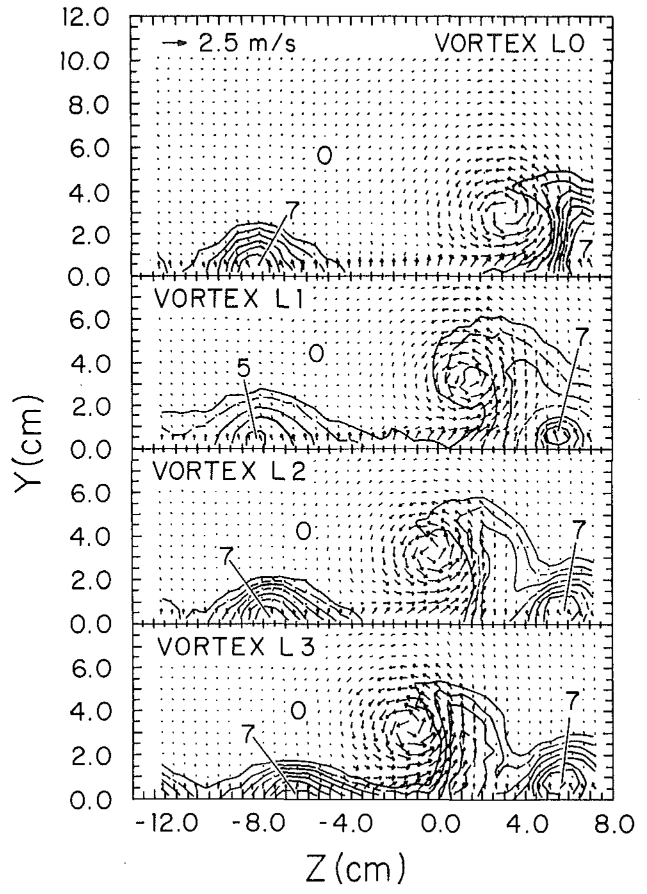

Fig. 8 Mean temperature field showing distributions of film injectant with secondary flow vectors at $x/d = 45.8$, with $m = 0.5$ film cooling and a free-stream velocity of 10 m/s. Data are given for counterclockwise-rotating vortices $L0$–$L3$. Vortex spanwise positions and locations with respect to film injection holes are given in Table 1.

when vortex cores pass within 1.67 core diameters on the downwash side, and 0.87 core diameters on the upwash side. The only vortices in the present study that meet this criteria with respect to the central hole are $R1$ and $R2$. Thus, because significant injectant disruptions result for all four vortices $R0$, $R1$, $R2$, and $R3$, evidence is provided that the interactions between the vortices and film change significantly if: (1) a row of holes rather than a single hole is employed, or (2) a row of holes with compound angle orientations rather than simple angle orientations is employed. The most significant differences for the latter comparison are a result of spanwise injectant velocity components with compound angle injection (which are not present with simple angle injection), which result in complex vortex interactions depending strongly upon the direction of vortex secondary flows near the wall (Ligrani and Mitchell, 1994).

Figure 6 quantifies the distortion and rearrangement of injectant by vortices $R0$–$R3$. These data are given for a blowing ratio m of 0.5 at $x/d = 45.8$. As mentioned earlier, the spanwise locations of vortices $R0$–$R3$ with respect to the film cooling holes are given in Fig. 4(a) and Table 1. From these two sources, it is evident that either downwash regions (vortices $R0$ and $R1$), core regions (vortices $R1$ and $R2$), or upwash regions (vortices $R2$ and $R3$) pass over the central injection hole as the vortices are convected downstream.

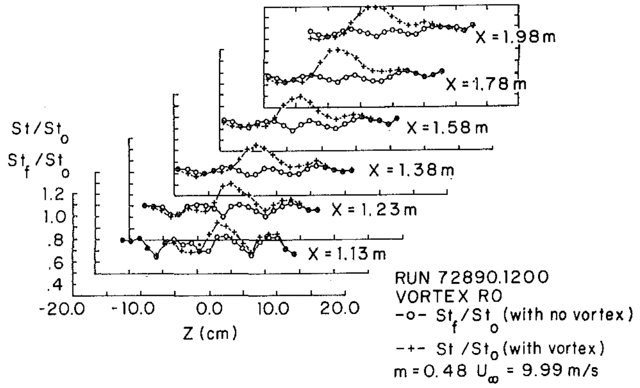

Fig. 9 Streamwise development of Stanton number ratios with $m = 0.5$ film cooling both with and without vortex $R0$. With this clockwise-rotating vortex, the downwash region passes over the central film cooling hole. Free-stream velocity = 10 m/s.

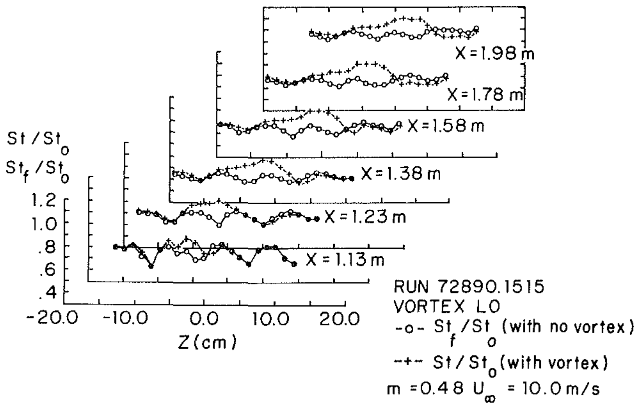

Fig. 10 Streamwise development of Stanton number ratios with $m = 0.5$ film cooling both with and without vortex $L0$. With this counterclockwise-rotating vortex, the downwash region passes over the central film cooling hole. Free-stream velocity = 10 m/s.

Measured secondary flow vectors are superimposed on each part of Fig. 6 to illustrate how their magnitudes and distributions relate to the reorganization of injectant by the different vortices. The same scaling for secondary flow vectors is used throughout all parts of Fig. 6. Similar procedures to determine injectant distributions are used by Ligrani and Williams (1990) and Ligrani and Mitchell (1994). In these studies and the present one, injectant distributions are qualitatively correlated to mean temperature distributions. To do this, injectant is heated to 50 °C without providing any heat to the test plate. Thus, because the injectant is the only source of thermal energy (relative to free-stream flow), higher temperatures (relative to free-stream temperature) generally indicate greater amounts of injectant. The temperature field is therefore given as $(T_o - T_\infty)$, and as such, shows how injectant accumulates and is rearranged mostly as a result of convective processes from the boundary layer and vortex secondary flows. Diffusion of injectant heat accounts for some of the temperature variations observed between injection hole exits and measuring stations, but compared to convection, this is of secondary importance.

If no vortex is present, concentrations of injectant are present in the boundary layer near the wall spaced about 7.4 cm apart in the spanwise direction at the same interval as the injection hole spacing. In Fig. 6, it is evident that all four vortices $R0$–$R3$ result in significant disturbances to the injectant because the distributions shown are different from the ones that would exist if no vortices were present. In each case, injectant is swept beneath the vortex centers in the negative Z direction, and then into vortex upwash regions. For vortices $R0$, $R1$, and $R2$, the injectant is also swept above the vortex centers. The spanwise locations of the centers of vortices $R0$, $R1$, $R2$, and $R3$ at $x/d = 45.8$ are at Z equal to -4.06 cm, -2.54 cm, -0.51 cm, and 1.52 cm, respectively. The Y coordinate of vortex centers is 2.5–3.0 cm. Centers are located at the point of maximum streamwise vorticity and are apparent in Fig. 6 at locations around which secondary flow vectors swirl.

Even though injectant distributions for vortices $R0$, $R1$, and $R2$ in Fig. 6 are displaced from each other in the spanwise direction, they are qualitatively similar. In each case, significant injectant deficits are evident beneath vortex cores and vortex downwash regions because of the influences of vortex secondary flows. For vortex $R0$, the deficit extends along the wall at Z from -5.5 cm to 1.5 mm. With vortex $R1$, the deficit extends over a smaller portion of the surface, and with vortex $R2$, the injectant deficit is even less in extent. This behavior is consistent with the $\mathrm{St}/\mathrm{St}_o$ distributions in the bottom portion of Fig. 5, since extents and magnitudes of local maxima regions decrease from vortex $R0$ to vortex $R1$ to vortex $R2$. The locations of the injectant deficits in Fig. 6 also correspond closely with the $\mathrm{St}/\mathrm{St}_o$ local maxima in Fig. 5 after accounting for the spanwise convection of the vortices between the two streamwise locations ($x/d=33.1$ for Fig. 5 and $x/d=45.8$ for Fig. 6).

The disruption to the injectant by vortex $R3$ is less severe than for vortices $R0$, $R1$, and $R2$. In particular, only small amounts of injectant seem to be depleted beneath vortex $R3$, and less injectant is swept into the vortex upwash region and above the vortex core compared to the other three vortices. The broad $\mathrm{St}/\mathrm{St}_o$ local maximum in the bottom portion of Fig. 5 is consistent since it is smaller in magnitude than the local maxima for the other three vortices, as mentioned earlier.

The results in Figs. 5 and 6 represent the situation in which vortex secondary flows beneath vortex centers are in the same direction as the spanwise velocity component of the injectant (Fig. 4*a*). The results in these figures indicate that disruptions to the protection provided by film cooling are minimized when the center of vortex $R3$ is convected between two injection holes. In this case, this amounts to a distance between the vortex center and the adjacent injection holes of 1.52 core diameters on the upwash side of the vortex, and 3.23 vortex core diameters on the downwash side of the vortex. Clearly, disruptions to film protection are more severe when vortex centers are in closer proximity to injection holes.

Just to the left of the injectant deficits (i.e., at smaller Z), extra accumulations of injectant are sometimes apparent in Fig. 6 as a consequence of convection by secondary flows within upwash regions of vortices $R0$, $R1$, $R2$, and $R3$. In some cases, such extra accumulations of injectant result in local increases of film protection where values of $\mathrm{St}/\mathrm{St}_o$ are locally lower than values of $\mathrm{St}_f/\mathrm{St}_o$, which would exist if no vortex were present. Such a region is apparent in Fig. 6 for vortex $R0$ at Z from -9 cm to -6 cm, and in Fig. 5 at Z from -10 cm to -5 cm.

Heat Transfer and Injectant Distributions With Vortices *L*0–*L*4. In the discussion that follows, surface heat transfer results with vortices $L0$ and $L4$ are discussed first. This is followed by discussions of $\mathrm{St}/\mathrm{St}_o$ results obtained with vortices $L0$, $L1$, $L2$, $L3$, and $L4$, and then by comparisons of these results with ones for vortices $R0$–$R4$. Injectant distributions for vortices $L0$–$L4$ are then discussed last.

Spanwise distributions of $\mathrm{St}/\mathrm{St}_o$ measured both with and without longitudinal vortices $L0$–$L4$ embedded in the turbulent boundary layer are shown in Fig. 7. As for the results shown in Fig. 5, the data in Fig. 7 were measured at $x/d=33.1$ ($X=1.377$ m) with film injection at a blowing ratio m of 0.5. In the top portion of Fig. 7, $\mathrm{St}/\mathrm{St}_o$ distributions are presented for vortices $L0$ and $L4$ along with $\mathrm{St}_f/\mathrm{St}_o$ data obtained when no artificially induced vortices are present in the flow. As for the results in the top of Fig. 5, the ones in the top of Fig. 7 illustrate significant disturbances to local $\mathrm{St}/\mathrm{St}_o$ distributions because of the vortices. This is particularly apparent in Fig. 7 for $-7\ \mathrm{cm}<Z<5$ cm for vortex $L0$, and for $Z<-2$ cm for vortex $L4$ if the $\mathrm{St}/\mathrm{St}_o$ distributions are compared to the $\mathrm{St}_f/\mathrm{St}_o$ distribution obtained with no vortices in the flow. $\mathrm{St}/\mathrm{St}_o$ are higher than $\mathrm{St}_f/\mathrm{St}_o$ over these areas as a consequence of the proximity of vortex downwash regions to these portions of the test surface. Vortex secondary flow within downwash regions and beneath vortex cores first sweep injectant in the spanwise direction along the wall and then into upwash regions. Deficits of injectant then result beneath downwash regions, which give decreased protection, and increased $\mathrm{St}/\mathrm{St}_o$ relative to $\mathrm{St}_f/\mathrm{St}_o$. The top potion of Fig. 7 also shows that $\mathrm{St}/\mathrm{St}_o$ values for each vortex are somewhat lower than the $\mathrm{St}_f/\mathrm{St}_o$ distribution for Z larger than 5 cm for vortex $L0$ and Z from -2 cm to 3 cm for vortex $L4$. These locations correspond to regions beneath vortex upwash regions where extra injectant accumulates, resulting in local increases of protection by the film.

The spanwise variations of local heat transfer are about the same for vortices $L0$ and $L4$ except for spanwise displacement with respect to each other a distance of about 7.2 cm, which is equivalent to 98 percent of s (Table 1). This provides validation of the measurement apparatus and procedures employed to obtain local heat transfer distributions in addition to that given by results in the top of Fig. 5. The small quantitative differences between the curves for vortices $L0$ and $L4$ in the top of Fig. 7 occur locally for the same reasons that data for vortices $R0$ and $R4$ in the top of Fig. 5 are locally different.

$\mathrm{St}/\mathrm{St}_o$ distributions with vortices $L0$, $L1$, $L2$, and $L3$ are presented in the bottom portion of Fig. 7. Here, significant quantitative and qualitative variations are seen as the spanwise locations of the vortices are changed. When the $\mathrm{St}/\mathrm{St}_o$ distributions are compared to each other, changes to the shapes of local maxima as well as to surrounding heat transfer distributions are apparent. Just like the results in Fig. 5, such variations evidence complicated interactions as different portions of individual vortices interact with the injectant from the central hole. In addition, vortices $L0$–$L4$ also result in sharp spanwise gradients of $\mathrm{St}/\mathrm{St}_o$. In Fig. 7, these gradients are apparent at Z from -3 cm to 4 cm, and move in the $-Z$ direction as the spanwise locations of the vortices move in the $-Z$ direction. The highest local $\mathrm{St}/\mathrm{St}_o$ value just to the left of one such gradient (i.e., at smaller Z) occurs with vortex $L2$. This particular vortex convects downstream so that its core and upwash region pass over the central injection hole at $Z=0$ cm (i.e., Fig. 4*b* and Table 1).

Vortices $L0$–$L4$ are different from vortices $R0$–$R4$ because of different directions of rotation (counterclockwise versus clockwise) when viewed looking downstream in spanwise/normal planes. This is important because secondary flow vectors, especially beneath vortex cores, are in different directions with respect to the spanwise coordinate Z as well as with respect to spanwise velocity components of injectant. Figure 2, which shows the orientations of the film cooling holes with respect to streamwise and spanwise coordinate directions, indicates the latter coordinate to be oriented so that the spanwise component of the injectant emerges in the $-Z$ direction. In Fig. 4(*a*), secondary flow vectors near the wall for vortices $R0$–$R4$ are then in the same direction as the spanwise components of the injectant velocity. The opposite is true in Fig. 4(*b*), where the near-wall secondary flow vectors for vortices $L0$–$L4$ have directions that are opposite to the direction of the spanwise components of the injectant velocity.

These differences between vortices $R0$–$R4$ and vortices $L0$–$L4$ are important because they result in significantly different local $\mathrm{St}/\mathrm{St}_o$ distributions as the vortices interact with the film injectant. This is evident if $\mathrm{St}/\mathrm{St}_o$ for vortices $R0$–$R4$ in Fig. 5 are compared to ones in Fig. 7 for vortices $L0$–$L4$. This comparison can be made for the same locations of vortex centers with respect to the central hole with the only changes due to the direction of rotation of the vortices. It is evident from Figs. 4(*a*) and 4(*b*) and Table 1 that this is done by comparing results for vortices having the same numbers in their name labels (i.e., comparing results for vortex *R*0 with results for vortex *L*0, comparing results for vortex *R*1 with results for vortex *L*1, *R*2 with *L*2, etc.). Because they are the same in all parts of Figs. 5 and 7, $\mathrm{St}_f/\mathrm{St}_o$ distributions (with film injection and no vortices) are appropriate to use as a reference to distributions measured with vortices *R*0–*R*4 as well as with vortices *L*0–*L*4.

With each comparison, the same overall qualitative differences between the clockwise and counterclockwise vortices are evident. $\mathrm{St}/\mathrm{St}_o$ distributions with the clockwise-rotating vortices *R*0–*R*4 always show regions greater than $\mathrm{St}_f/\mathrm{St}_o$ over larger portions of the test surface than the $\mathrm{St}/\mathrm{St}_o$ distributions associated with counterclockwise rotating vortices *L*0–*L*4. In addition, $\mathrm{St}/\mathrm{St}_o$ distributions with vortices *R*0–*R*4 show higher local maxima compared to $\mathrm{St}/\mathrm{St}_o$ measured beneath vortices *L*0–*L*4. Such differences evidence different interactions between injectant and the two types of vortices. Higher $\mathrm{St}/\mathrm{St}_o$ are present with vortices *R*0–*R*4 because the injectant is swept away from the wall (which results in decreased protection) more efficiently than with vortices *L*0–*L*4. The more efficient decimation of the injectant occurs since near-wall vortex secondary flows are in the same direction as the spanwise velocity components of the injectant. With vortices *L*0–*L*4, the opposite situation is present. Here, near-wall vortex secondary flows oppose the spanwise components of the film injectant resulting in greater resistance to injectant rearrangement by the vortices.

Figure 8 quantifies the distortion and rearrangement of injectant by vortices *L*0–*L*3. These data were obtained for a blowing ratio *m* of 0.5 at $x/d = 45.8$ using the same procedures employed to obtain the injectant distributions and secondary flow vectors given in Fig. 6. The spanwise locations of vortices *L*0–*L*3 with respect to the film cooling holes are given in Fig. 4(*b*) and Table 1. From these two sources, it is evident that either downwash regions (vortices *L*0 and *L*1), core regions (vortices *L*1 and *L*2), or upwash regions (vortices *L*2 and *L*3) pass over the central injection hole as the vortices are convected downstream. At $x/d = 45.8$, the spanwise locations of the centers of vortices *L*0, *L*1, *L*2, and *L*3 are at *Z* equal to 3.05 cm, 1.52 cm, −0.51 cm, and −1.52 cm, respectively. The *Y* coordinate of vortex centers in Fig. 8 vary from 3.0 cm to 3.5 cm.

Like the results presented in Fig. 6, the injectant distributions in Fig. 8 show that all four vortices *L*0–*L*3 produce significant disturbances to the injectant relative to distributions present if no vortices are present. In fact, individual distributions of injectant in Fig. 8 show some qualitative similarity to each other, accounting for the spanwise displacement between distributions. The distributions in Fig. 8 also show some qualitative similarity to the distributions presented in Fig. 6, accounting for the different directions of vortex rotation for the two figures. In Fig. 8, all four vortices sweep injectant beneath the vortex centers in the positive *Z* direction, and then into vortex upwash regions. As a result, all of the counterclockwise rotating vortices *L*0–*L*4 produce injectant deficits near the wall beneath vortex cores and near vortex cores beneath downwash regions. Of these, vortices *L*1 and *L*2 also sweep the injectant above the vortex centers at $x/d = 45.8$ and cause the highest local maxima of $\mathrm{St}/\mathrm{St}_o$ at $x/d = 33.1$ shown in Fig. 7. These occur at *Z* locations from −7 cm to 3 cm for vortex *L*1, and from −7 cm to 1 cm for vortex *L*2. Corresponding injectant deficits near the wall in Fig. 8 are evident over similar ranges of *Z*.

In comparing Figs. 6 and 8 (as well as Figs. 5 and 7), it is evident that vortex *R*0 produces the most significant injectant disruptions of the clockwise-rotating vortices, whereas vortices *L*1 and *L*2 produce the most significant injectant disruptions of the counterclockwise rotating vortices. These differences exist because of the different interactions that occur due to different directions of vortex rotation, and the fact that secondary flows beneath the vortex centers are aligned with the spanwise component of the injectant velocity for vortices *R*0–*R*4, and oppose the spanwise component of the injectant velocity for vortices *L*0–*L*4.

The counterclockwise-rotating vortex that produces the least significant injectant rearrangement and the lowest $\mathrm{St}/\mathrm{St}_o$ maximum is *L*3. Like vortex *R*3, vortex *L*3 is convected between injection holes as it passes $x/d = 0.0$. The spacing between the center of vortex *L*3 and the adjacent injection holes at this streamwise location is approximately 1.85 core diameters on the upwash side of the vortex, and 2.91 vortex core diameters on the downwash side of the vortex. Clearly, disruptions to film protection are more severe when vortex centers are in closer proximity to injection holes.

Streamwise Development of Heat Transfer Distributions With Film Cooling Both With and Without Vortex *R*0. Local $\mathrm{St}/\mathrm{St}_o$ values measured beneath longitudinal vortex *R*0 are presented in Fig. 9 for a blowing ratio *m* of 0.5 and a freestream velocity of 10 m/s. Also included on this figure are distributions of $\mathrm{St}_f/\mathrm{St}_o$ obtained with film cooling only and no vortices embedded in the boundary layers. $\mathrm{St}/\mathrm{St}_o$ and $\mathrm{St}/\mathrm{St}_f$ results are presented together so that disturbances caused by the vortices to surface heat transfer in the film cooled boundary layers are apparent.

In examining results on Fig. 9, it is apparent that the disturbances caused by the vortices persist to the end of the test plate. The same conclusion is reached if results from vortices *R*1–*R*4 are examined. In Fig. 9, this is evident since $\mathrm{St}/\mathrm{St}_o$ values are higher than $\mathrm{St}_f/\mathrm{St}_o$ at $X = 1.98$ m or $x/d = 96.6$. In fact, differences between $\mathrm{St}/\mathrm{St}_o$ and $\mathrm{St}_f/\mathrm{St}_o$ generally become greater with streamwise development, which illustrates the coherence of the vortices as they are convected downstream. Differences are quite small just downstream of the injection holes at $X = 1.13$ m or $x/d = 6.7$, which indicates that the film, rather than the vortices, is most affecting local heat transfer behavior at this location. According to Ligrani and Mitchell (1994), such behavior probably results because the vortices are lifted off of the test surface by the film injectant. In addition, vortex secondary flows have not had enough time to rearrange the injectant at this streamwise station since it is just downstream of film hole exit locations, where the vortices initially interact with the injectant.

The $\mathrm{St}/\mathrm{St}_o$ distribution for vortex *R*0 in Fig.9 is quantitatively and qualitatively similar to the distribution for vortex *R*4 at all six *x*/*d* where measurements are made, accounting for their relative displacement from each other in the spanwise direction (Mitchell, 1990). Such behavior is expected considering the similarity of the $\mathrm{St}/\mathrm{St}_o$ distributions for vortices *R*0 and *R*4 in the top of Fig. 5, which were discussed earlier. Of the $\mathrm{St}/\mathrm{St}_o$ distributions for the other clockwise-rotating vortices, the ones for vortices *R*1 and *R*2 also show important similarity to the distributions for vortices *R*0 and *R*4 (Mitchell, 1990). Each of these four vortices produces $\mathrm{St}/\mathrm{St}_o$ significantly greater than $\mathrm{St}_f/\mathrm{St}_o$ for $X \geq 1.23$ m ($x/d \geq 17.2$) at test surface locations where injectant is redistributed away from vortex core and downwash regions. Such significant disruptions of film cooling protection occur because vortex secondary flows and the spanwise component of the injectant are the same direction near the wall. This results in efficient secondary convection of injectant even though a different portion of each vortex (*R*0, *R*1, and *R*2) passes over the central hole at $x/d = 0$. The distribution for vortex *R*3, on the other hand, is considerably different from distributions for vortices *R*0–*R*2 and *R*4, especially for $X = 1.13$ m, 1.23 m, and 1.38 m ($x/d = 6.7$, 17.2, and 33.1) (Mitchell, 1990). In particular, $\mathrm{St}/\mathrm{St}_o$ for vortex *R*3 are closer to $\mathrm{St}_f/\mathrm{St}_o$ at these locations mostly because upwash and downwash regions are positioned so that they do not cause significant injectant disruptions as the vortex is convected past $x/d=0$.

Streamwise Development of Heat Transfer Distributions With Film Cooling Both With and Without Vortex *L*0. Local St/St_o values measured beneath longitudinal vortex $L0$ are presented in Fig. 10. Except for the different vortex employed, the data in this figure are presented for the same experimental conditions as the data for vortex $R0$ in Fig. 9. The data are also arranged and plotted in the same manner.

As for the St/St_o distributions for vortices $R0$ and $R4$, the St/St_o distributions for vortices $L0$ and $L4$ are quantitatively and qualitatively similar to each other in the spanwise direction (Mitchell, 1990). Such behavior is expected considering the similarity of the St/St_o distributions for vortices $L0$ and $L4$ in the top of Fig. 7, which were discussed earlier. Of the St/St_o distributions for the other vortices, the one for vortex $L3$ is similar to the distributions for vortices $L0$ and $L4$, especially in regard to the differences between local St/St_o maxima and local St_f/St_o values at the same x/d and Z (Mitchell, 1990).

St/St_o distributions for vortices $L1$ and $L2$ are similar to each other and higher than the ones for the other counterclockwise rotating vortices ($L0$, $L3$, and $L4$), especially for $X=1.13$ m, 1.23 m, and 1.38 m ($x/d=6.7$, 17.2, and 33.1) (Mitchell, 1990). The larger differences between St/St_o and St_f/St_o for vortices $L1$ and $L2$ are most apparent at $x/d=6.7$, the measurement station closest to the injection holes. They occur because the cores of vortices $L1$ and $L2$ pass directly over the central hole at $x/d=0$. In the case of vortex $L1$, the side of the core nearest the downwash region passes over the central hole, and in the case of vortex $L2$, the side of the core nearest the upwash region passes over the central hole as the vortex convects past $x/d=0$ (i.e., Fig. 4(*b*)). This causes the injectant to be disrupted by the most intense portions of the near-wall secondary flows of vortices $L1$ and $L2$. In contract, the secondary flows produced by the other counterclockwise-rotating vortices are significantly less intense just above the central hole since their cores pass significantly farther from the central hole as they are convected downstream (Mitchell, 1990).

With vortices $R0$–$R4$, regions where St/St_o are higher than St_f/St_o are at larger Z, and regions where St/St_o are lower than $St_f St_o$ are at smaller Z. The opposite trend is present with vortices $L0$–$L4$ since they rotate in directions opposite to vortices, $R0$–$R4$. However, in spite of these differences, both vortices $R0$–$R4$ and $L0$–$L4$ produce $St/St_o > St_f/St_o$ beneath downwash regions, and $St/St_o < St_f/St_o$ beneath upwash regions. If oppositely rotating vortices with the same center locations with respect to the central holes are compared (i.e., $R0$ and $L0$, $R1$ and $L1$, etc.), then greater disturbances and higher St/St_o are present beneath the downwash regions of vortices $R0$–$R4$ at most x/d. In addition, vortices $R0$–$R4$ produce regions where St/St_o are greater than St_f/St_o over larger spanwise portions of the test plate at x/d from 6.7 to 96.6 since they sweep injectant away from the wall more efficiently than vortices $L0$–$L4$. This is because the near-wall secondary flows of vortices $R0$–$R4$ are coincident with the spanwise velocity component of the film injectant.

Summary and Conclusions

Experimental results are presented that describe the effects of embedded, longitudinal vortices on heat transfer and film injectant downstream of a single row of film cooling holes spaced $7.8d$ apart in the spanwise direction. Each hole is oriented so that the injectant emerges with spanwise and streamwise velocity components. This compound angle arrangement gives hole angles with respect to the test surface of 30 deg in a spanwise/normal plane projection, and 35 deg in a streamwise/normal plane projection. A blowing ratio of 0.5, nondimensional injection temperature parameter θ of about 1.5, and free-stream velocity of 10 m/s are employed. Injection hole diameter is 0.945 cm to give a ratio of vortex core diameter to hole diameter of 1.6–1.67 just downstream of the injection holes ($x/d=10.2$). At the same location, vortex circulation magnitudes range from 0.15 m^2/s to 0.18 m^2/s. With film injection at a blowing ratio of 0.5, the ratio of vortex circulation to injection velocity times hole diameter ($S=\Gamma/U_c d$) then ranges from 3.2 to 3.8, and the ratio of vortex circulation to injection velocity times vortex core diameter ($S1=\Gamma/U_c 2c$) ranges from 2.0 to 2.2.

The most important conclusion is that local heat transfer and injectant distributions are strongly affected by the longitudinal embedded vortices, including their directions of rotation and their spanwise positions with respect to film injection holes. Vortices are generated using half-delta wings attached to the test surface of the wind tunnel at 18 deg angles of attack with respect to the mainstream flow direction. By changing the sign of the angle of attack, vortices are produced that rotate either clockwise or counterclockwise when viewed looking downstream in spanwise/normal planes. By moving the delta wings in the spanwise direction, the spanwise locations of the vortices with respect to the film cooling holes are also changed.

If one considers either the clockwise vortices or the counterclockwise vortices by themselves, St/St_o variations due to spanwise location result because different portions of an individual vortex interact with injectant from the central hole as each vortex passes $x/d=0$. Alterations resulting from different spanwise vortex positions include changes to local St/St_o maxima and to surrounding heat transfer distributions, as well as changes to injectant distributions measured in spanwise/normal planes. When near-wall vortex secondary flow vectors are coincident with the spanwise component of the injectant (clockwise-rotating vortices $R0$–$R4$), local St/St_o maxima are highest when a vortex downwash region passes over the central hole at $x/d=0$ and $Z=0$ cm (vortex $R0$). Injectant deficits and local St/St_o maxima then decrease in magnitude and spanwise extent as vortex downwash regions are located farther away from the central hole. When near-wall vortex secondary flow vectors oppose the spanwise component of the injectant (counterclockwise rotating vortices $L0$–L), local St/St_o maxima are highest when the core regions of individual vortices pass directly over the central hole. Vortices $L1$ and $L2$, which produce this behavior, also result in greater disruptions to the injectant than the other counterclockwise rotating vortices since they also sweep the injectant above the vortex centers at $x/d=45.8$.

However, in spite of these quantitative variations, many overall qualitative features remain the same as the spanwise position of a vortex is changed. These include significant deficits of injectant beneath vortex cores, as well as near vortex cores beneath downwash regions, which always correspond to locally higher St/St_o values, compared to St_f/St_o values at the same x/d and Z locations. Such variations persist as far as 97 hole diameters downstream of the injection holes ($x/d=96.6$) as a consequence of vortex secondary flows, which first sweep injectant in the spanwise direction along the wall and then into upwash regions. St/St_o values are generally lower than St_f/St_o beneath vortex upwash regions since extra injectant accumulates, resulting in local increases of protection by the film. In contrast, vortex disruptions are sometimes quite small just downstream of the injection holes at $x/d=6.7$, which indicates that the film, rather than the vortices, is most affecting local heat transfer behavior at this streamwise location.

The smallest disruptions produced both by the clockwise-rotating vortices ($R0$–$R4$) and the counterclockwise-rotating vortices ($L0$–$L4$) occur when the cores of individual vortices are convected between two adjacent holes. Of the clockwise-rotating vortices, $R3$ produces the smallest injectant disturbance (and the lowest St/St_o relative to St_f/St_o), and of the counterclockwise-rotating vortices, $L3$ produces the smallest injectant disturbance. These two vortices are similar in that they both have the same spacing between their centers and the central hole at $x/d = 0$. At $x/d = 10.2$, distances between vortex centers and adjacent holes are as small as 1.5 vortex core diameters on the upwash sides of the vortices and 2.9 vortex core diameters on the downwash sides of the vortices. This suggests that vortices located farther than these distances from individual film holes produce disruptions to film protection that are less than the ones observed in this study.

Differences resulting from vortex rotation are due to secondary flow vectors, especially beneath vortex cores, which are in different directions with respect to the spanwise velocity components of injectant after it exits the holes. When secondary flow vectors near the wall are in the same direction as the spanwise components of the injectant velocity (vortices $R0$-$R4$), the film injectant is readily swept beneath vortex cores and into vortex upwash regions. Consequently, the protection provided by the injectant is reduced significantly and $\mathrm{St}/\mathrm{St}_o$ may be as large as 1.16 at $x/d = 33.1$ compared to $\mathrm{St}_f/\mathrm{St}_o$ values with no vortex from 0.87 to 0.95. With the opposite situation (vortices $L0$-$L4$), $\mathrm{St}/\mathrm{St}_o$ are as high as 1.10 at $x/d = 33.1$. Secondary flow vectors near the wall are then directed opposite to the direction of the spanwise components of the injectant velocity, and the injectant is less likely to be rearranged by vortex secondary flows. $\mathrm{St}/\mathrm{St}_o$ thus generally show higher local maxima and higher magnitudes over larger portions of the test surface with vortices $R0$-$R4$ because the injectant is swept away from near wall regions (which results in decreased protection) more efficiently than with vortices $L0$-$L4$.

Acknowledgments

This study was supported, in part, by the Aero-Propulsion Laboratory of Wright Patterson Air Force Base, MIPR Number FY 1455-89-N0670. Dr. Bill Troha was program monitor.

References

Bishop, D. T., 1990, "Heat Transfer, Adiabatic Effectiveness and Injectant Distributions Downstream of Single and Double Rows of Film-Cooling Holes With Compound Angles," M. S. thesis, Department of Mechanical Engineering, Naval Postgraduate School, Monterey, CA.

Blair, M. F., 1974, "An Experimental Study of Heat Transfer and Film Cooling on Large-Scale Turbine Endwalls," ASME *Journal of Heat Transfer*, Vol. 96, pp. 524–529.

Eibeck, P. A., and Eaton, J. K., 1987, "Heat Transfer Effects of a Longitudinal Vortex Embedded in a Turbulent Boundary Layer," ASME *Journal of Heat Transfer*, Vol. 109, pp. 16–24.

Folayan, C. O., and Whitelaw, J. H., 1976, "The Effectiveness of Two-Dimensional Film-Cooling Over Curved Surfaces," ASME Paper No. 76-HT-31.

Goldstein, R. J., and Chen, H. P., 1985, "Film Cooling on a Gas Turbine Blade Near the Endwall," ASME *Journal of Engineering for Gas Turbines and Power*, Vol. 107, pp. 117–122.

Goldstein, R. J., and Chen, H. P., 1987, "Film Cooling of a Turbine Blade With Injection Through Two Rows of Holes in the Near-Endwall Region," ASME JOURNAL OF TURBOMACHINERY, Vol. 109, pp. 588–593.

Kays, W. M., and Crawford, M. E., 1980, *Convective Heat and Mass Transfer*, New York.

Kline, S. J., and McClintock, F. A., 1953, "Describing Uncertainties in Single-Sample Experiments," *Mechanical Engineering*, Jan., pp. 3–8.

Ligrani, P. M., Singer, B. A., and Baun, L. R., 1989a, "Spatial Resolution and Downwash Velocity Corrections for Multiple-Hole Pressure Probes in Complex Flows," *Experiments in Fluids*, Vol. 7, No. 6, pp. 424–426.

Ligrani, P. M., Singer, B. A., and Baun, L. R., 1989b, "Miniature Five-Hole Pressure Probe for Measurement of Mean Velocity Components in Low Speed Flows," *Journal of Physics E—Scientific Instruments*, Vol. 22, No. 10, pp. 868–876.

Ligrani, P. M., and Williams, W. W., 1990, "Effects of an Embedded Vortex on Injectant From a Single Film-Cooling Hole in a Turbulent Boundary Layer," ASME JOURNAL OF TURBOMACHINERY, Vol. 112, pp. 428–436.

Ligrani, P. M., Subramanian, C. S., Craig, D. W., and Kaisuwan, P., 1991, "Effects of Vortices With Different Circulations on Heat Transfer and Injectant Downstream of a Single Film-Cooling Hole in a Turbulent Boundary Layer," ASME JOURNAL OF TURBOMACHINERY, Vol. 113, No. 3, pp. 433–441.

Ligrani, P. M., and Mitchell, S. W., 1994, "Interactions Between Embedded Vortices and Injectant From Film Cooling Holes With Compound Angle Orientations in a Turbulent Boundary Layer," ASME JOURNAL OF TURBOMACHINERY, Vol. 116, pp. 80–91.

Mayle, R. E., Kopper, F. C., Blair, M. F., and Bailey, D. A., 1977, "Effect of Streamline Curvature on Film Cooling," ASME *Journal of Engineering for Power*, Vol. 99, pp. 77–82.

Mitchell, S. W., 1990, "The Effects of Embedded Vortices on Heat Transfer in a Turbulent Boundary Layer With Film Cooling From Holes With Compound Angles," M. S. Thesis, Department of Mechanical Engineering, Naval Postgraduate School, Monterey, CA.

Moffat, R. J., 1982, "Contributions to the Theory of Single-Sample Uncertainty Analysis," ASME *Journal of Fluids Engineering*, Vol. 104, pp. 250–260.

Nicolas, J., and Le Meur, A., 1974, "Curvature Effects on a Turbine Blade Cooling Film," ASME Paper No. 74-GT-156.

Ortiz, A., 1987, "The Thermal Behavior of Film Cooled Turbulent Boundary Layers as Affected by Longitudinal Vortices," M. S. Thesis, Department of Mechanical Engineering, Naval Postgraduate School, Monterey, CA.

Unsteady Wake Over a Linear Turbine Blade Cascade With Air and CO_2 Film Injection: Part I—Effect on Heat Transfer Coefficients

S. Ou[1]
Research Associate.

J.-C. Han
HTRI Professor.
Fellow ASME

A. B. Mehendale
Research Associate.

Department of Mechanical Engineering,
Turbine Heat Transfer Laboratory,
Texas A&M University,
College Station, TX 77843

C. P. Lee
Manager,
Turbine Aero & Cooling Design,
General Electric—Aircraft Engines,
Cincinnati, OH 45215
Mem. ASME

The effect of unsteady wake flow and air (D.R. = 1.0) or CO_2 (D.R. = 1.52) film injection on blade heat transfer coefficients was experimentally determined. A spoked wheel-type wake generator produced the unsteady wake. Experiments were performed on a five-airfoil linear cascade in a low-speed wind tunnel at the chord Reynolds number of 3×10^5 for the no-wake case and at the wake Strouhal numbers of 0.1 and 0.3. Results from a blade with three rows of film holes in the leading edge region and two rows each on the pressure and suction surfaces show that the Nusselt numbers are much higher than those for the blade without film holes. On a large portion of the blade, the Nusselt numbers "without wake but with film injection" are much higher than for "with wake but no film holes." An increase in wake Strouhal number causes an increase in pressure surface Nusselt numbers; but the increases are reduced at higher blowing ratios. As blowing ratio increases, the Nusselt numbers for both density ratio injectants (air and CO_2) increase over the entire blade except for the transition region where the effect is reversed. Higher density injectant (CO_2) produces lower Nusselt numbers on the pressure surface, but the numbers for air and CO_2 injections are very close on the suction surface except for the transition region where the numbers for CO_2 injection are higher. From this study, one may conclude that the additional increases in Nusselt numbers due to unsteady wake, blowing ratio, and density ratio are only secondary when compared to the dramatic increases in Nusselt numbers only due to film injection over the no film holes case.

Introduction

It is well known that gas turbine performance improves with an increase in turbine inlet temperature. This has caused a continuing trend toward higher gas turbine inlet temperatures and resulted in higher heat loads on turbine components. Hence, turbine blade external and internal cooling techniques must be employed in order to maintain the performance requirements.

There have been many studies to investigate the effect of unsteady wake on the downstream blade (without film holes) heat transfer coefficient distribution, which is caused by the relative motion between the upstream nozzle vanes and the downstream blades. It is clear from published results that this unsteady wake enhances the leading edge heat transfer and causes an earlier and longer laminar-turbulent transition on the suction surface. This elongated transition zone causes increased heat transfer over a larger area. Many investigations have been made to study the effect of unsteady wake and mainstream turbulence on the flow field and heat transfer coefficients of a downstream turbine blade. Abhari et al. (1992), Abhari and Epstein (1994), Blair et al. (1989a, 1989b), Blair (1994), Camci and Arts (1990), Dunn (1986), Dunn et al. (1986, 1989, 1994), and Nirmalan and Hylton (1990) conducted experiments in actual gas turbine engines, whereas Doorly (1988), Dullenkopf et al. (1991), Dullenkopf and Mayle (1994), Liu and Rodi (1989, 1992), O'Brien and Capp (1989), Priddy and Bayley (1988), Wittig et al. (1987, 1988), and Han et al. (1993) did laboratory simulations of upstream unsteady wake conditions. Two techniques to produce unsteady wake have been used in laboratory simulations. Liu and Rodi (1989, 1992), and Priddy and Bayley (1988) used a squirrel cage type wake generator, whereas Doorly (1988), Dullenkopf et al. (1991), Dullenkopf and Mayle (1994), O'Brien and Capp (1989), Wittig et al. (1987, 1988), and Han et al. (1993) used a spoked wheel type wake generator. Mayle and Dullenkopf (1990) and Mayle (1991) recently developed a theory to incorporate unsteady

---

[1] Current address: Aero Propulsion and Power Laboratory, Wright Patterson AFB, OH 45433.

Contributed by the International Gas Turbine Institute and presented at the 38th International Gas Turbine and Aeroengine Congress and Exposition, Cincinnati, Ohio, May 24–27, 1993. Manuscript received at ASME Headquarters March 3, 1993. Paper No. 93-GT-210. Associate Technical Editor: H. Lukas.

effect into a steady flow analysis by introducing a time-averaged intermittency factor.

Mick and Mayle (1988) studied the heat transfer coefficient distributions on a leading edge model with film injection. Mehendale and Han (1992), and Ou and Han (1992) studied the effect of high mainstream turbulence on a leading edge model with film injection. They reported that film injection alone enhances the "no film holes" surface heat transfer coefficients by 2–3 times. They noted that high mainstream turbulence increases surface heat transfer coefficients at all blowing ratios, but the increases reduce at higher blowing ratios.

Teekaram et al. (1989) studied the effect of secondary to mainstream density ratio on heat transfer coefficients over a flat plate with film injection. They used air and CO_2 at the same density for film injection. Densities of both injectants were made equal by controlling their temperatures. They reported that film-cooled heat transfer coefficients were independent of the gas used for injection (air or CO_2) as long as their densities were maintained the same. Ammari et al. (1990) studied the effect of density ratio on flat plate heat transfer coefficients with air or CO_2 film injection.

This study focuses on the effect of incident unsteady wake conditions on heat transfer coefficient distribution on a model turbine blade with air or CO_2 film injection through three rows of film holes in the leading edge region and two rows each on the pressure and suction surfaces. The objectives of this study are to determine: (1) the enhancement in blade heat transfer coefficients solely due to the upstream unsteady wake for the no film holes conditions, (2) the enhancement in blade heat transfer coefficients solely due to film injection for the no wake condition, (3) the effect of density ratio on blade heat transfer coefficients with air or CO_2 film injection, and (4) the combined effect of upstream unsteady wake and injectant density ratio on blade heat transfer coefficients.

A five-blade linear cascade with an instrumented blade at its center was used for this study. Two instrumented blades, one without film holes and the other with film holes, were used. The cascade was mounted in a low-speed wind tunnel at the Turbine Heat Transfer Laboratory of Texas A&M University. The upstream unsteady wake was produced by a spoked wheel type wake generator similar to the ones used by Dullenkopf et al. (1991), O'Brien and Capp (1989), Wittig et al. (1987), and Han et al. (1993). The blade with film holes was connected to air and CO_2 supply lines. Both test blades were instrumented with the thin foil-thermocouple technique similar to that used by Mehendale and Han (1992) and Han et al. (1993).

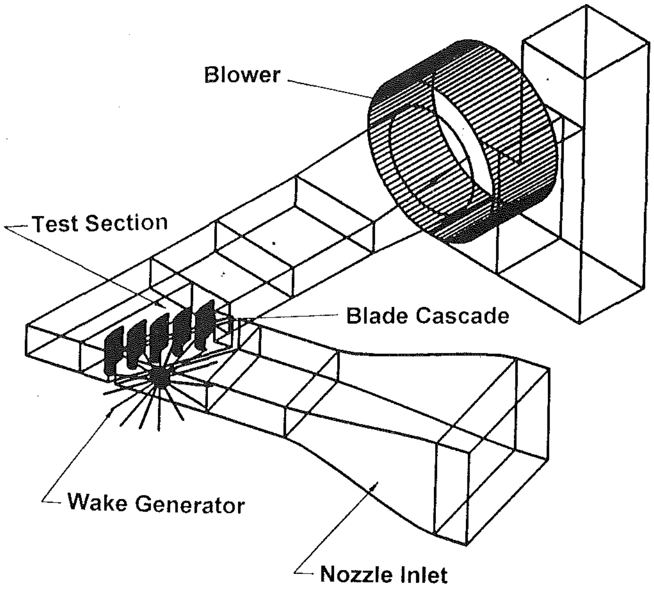

Fig. 1 Schematic of the linear turbine blade cascade with a spoked wheel type wake generator

Test Apparatus and Instrumentation

A schematic of the test apparatus is shown in Fig. 1. The test apparatus consisted of a low-speed, low-turbulence wind tunnel with an inlet nozzle, a spoked wheel type wake gen-

Nomenclature

C = blade chord
d = wake generator rod diameter
D = film hole diameter
D.R. = density ratio = ρ_s/ρ_∞
h = local heat transfer coefficient
H = blade radial (spanwise) length
I = momentum flux ratio = $(\rho V^2)_s/(\rho V^2)_\infty$
k = local thermal conductivity
M = blowing ratio (secondary to mainstream mass flux ratio) = $(\rho V)_s/(\rho V)_\infty$
n = number of rods in the wake generator
N = wake generator rotation speed, rpm
Nu = Nusselt number based on blade chord = hC/k
$\overline{\mathrm{Nu}}$ = spanwise-averaged Nusselt number
P = film hole pitch
q'' = net forced convection heat flux
q''_{cond} = local conduction heat loss flux
q''_{gen} = foil generated wall heat flux
q''_{loss} = local total heat loss flux
q''_{rad} = local radiation heat loss flux
r_m = distance between the wake generator shaft center and the cascade midspan
Re = Reynolds number based on the blade chord = V_1C/ν
S = wake Strouhal number = $2\pi Ndn/(60V_1)$
T_{aw} = local adiabatic wall temperature
T_s = secondary flow temperature within the injection cavity
T_w = local wall temperature
T_∞ = mainstream temperature at the cascade inlet
U_r = rotational velocity at the cascade midspan
V = local mainstream velocity
V_E = local mainstream velocity at the cascade exit
V_I = local mainstream velocity at the cascade inlet
V_1 = mean mainstream velocity at the cascade inlet
V_2 = mean mainstream velocity at the cascade exit
X = blade surface coordinate from stagnation in the streamwise direction
X/C = dimensionless blade surface coordinate in the streamwise direction
Y = blade radial (spanwise) coordinate
Y/H = dimensionless blade radial (spanwise) coordinate
ν = local kinematic viscosity
ρ_s = secondary density
ρ_∞ = mainstream density
$(\rho V)_s$ = local secondary mass flux
$(\rho V^2)_s$ = local secondary momentum flux
$(\rho V)_\infty$ = local mainstream mass flux
$(\rho V^2)_\infty$ = local mainstream momentum flux

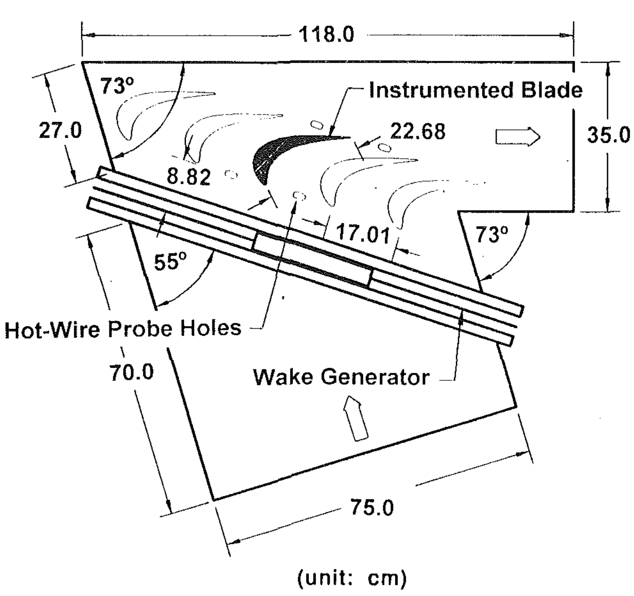

Fig. 2 Test apparatus and instrumentation location layout

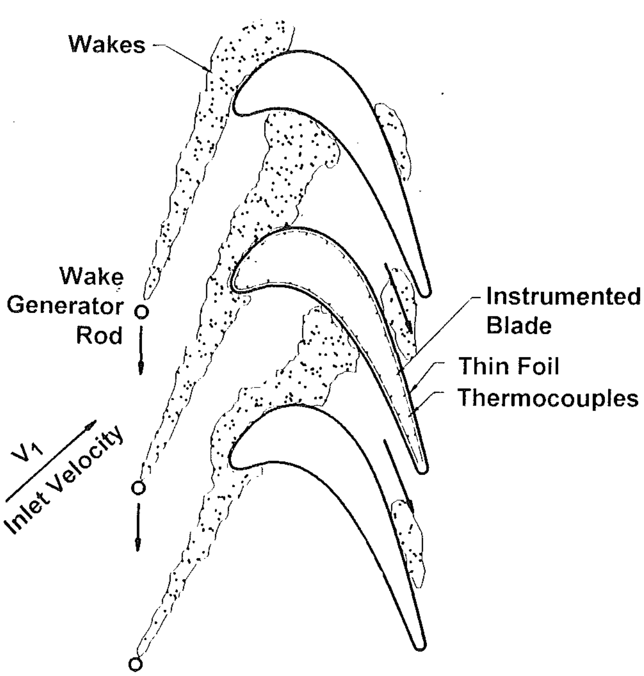

Fig. 3 Conceptual view of unsteady wake effect on a model heat transfer blade without film holes

erator, a linear turbine blade cascade with an instrumented blade at its center, and a suction type blower. The wind tunnel was designed for a blade turning angle of 107.49 deg. The nozzle had a contraction ratio of 3×1.5. The wake generator was covered with a casing to prevent leakage flow and its shaft was located below the bottom wall of the wind tunnel. The five blade cascade was installed downstream of the wake generator.

A detailed view of the cascade, wake generator, and hot wire locations is shown in Fig. 2. The cascade was designed for use in our low speed wind tunnel facility. The blade configuration was designed at General Electric—Aircraft Engine Division, to produce a similar velocity ratio distribution as in a typical advanced high pressure turbine blade row. The selected blade had a 107.49 deg turning with relative flow angles of 35 and -72.49 deg at the blade inlet and exit, respectively. A five times scaled-up model was used to simulate the engine Reynolds number. The cascade had five blades, each with a chord length of 22.68 cm and a radial span of 25.2 cm. The blade were spaced 17.01 cm apart at the cascade inlet. The cascade leading edge was 8.82 cm downstream of the wake generator. All blades were made of high quality model wood. Only the center blade was instrumented and was either the blade without film holes or the blade with film holes.

The spoked wheel type wake generator had 32 rods, each 0.63 cm in diameter to simulate trailing edge of an upstream blade. The wake generator was driven by a 2.2 kW (3 hp) DC motor. Its shaft was located 20 cm below the bottom wall of the wind tunnel. The wake Strouhal number was adjusted by controlling the motor speed. The wake generator rotation speed was accurately measured by a Pioneer DT-36M digital photo tachometer.

Using nonlinear rotating rods with a linear blade cascade causes the wakes at the top of the cascade to pass by the blades faster than the wakes at the bottom of the cascade. This error was small in the 7.6 cm midspan region where the thermocouples were located, as indicated by tests on a no film holes blade. Heat transfer coefficient tests for the no film holes blade indicate that for the 0.00378 cm thick foil, with negligible lateral conduction, spanwise thermocouple readings in the 7.6 cm midspan region were off by only about ± 0.5 percent.

Four slots were machined in the top wall of the wind tunnel, two near the leading edge and two near the trailing edge, in the middle of flow passages as shown in Fig. 2. Hot-wire probes were inserted through the leading edge slots to measure the oncoming flow velocities, wake profiles, turbulence fluctuations, and to check the flow periodicity between the two adjacent flow passages. The trailing edge slots were used to measure the exit flow velocities.

A calibrated single hot wire was used to measure the instantaneous velocity profile. It was connected to a three-channel TSI IFA 100 hot-wire anemometer. The analog signal from the anemometer was converted to digital by a DATA TRANSLATION 250 kHz A/D board in a 386SX 20 MHz machine. The anemometer output was also connected to a NICOLET 446A spectrum analyzer that displayed the instantaneous wake profile and frequency distribution.

A schematic of the top view of the blade without film holes is shown in Fig. 3. Twenty-six strips of stainless steel foil, each 25.4 cm long $\times$ 2 cm wide $\times$ 0.00378 cm thick, were cemented vertically on the test blade. They were separated by 0.8 mm gaps that were filled with wood putty and made flush with the foil surface. All foils were connected in series by copper bus bars. The foils produced an almost constant wall heat flux boundary condition when electrically heated. Thirty-six gage copper constantan thermocouples were cemented on the undersides of the foils. There were 11 rows of thermocouples on the pressure surface and 15 rows on the suction surface. Each row had three thermocouples spaced 2.52 cm apart in the radial midspan region of the blade.

A schematic of the top view of the blade with film holes is shown in Fig. 4. The first cavity supplied three rows of film holes: one near the leading edge, and one each on the pressure and suction surfaces. The second cavity supplies one row each on the pressure and suction surfaces. The third and fourth cavities supplied one row of film holes on the pressure and suction surfaces, respectively. Depending on its location, each row had 8 to 10 film holes between 30 and 70 percent of the radial blade span. Some of the film holes had a compound angle (radial and tangential) relative to the blade surface as seen in Fig. 4. Radial angle is defined as the angle between the film hole axis and the local radial (spanwise) direction. Tangential angle is defined as the angle between the film hole axis and the local streamwise tangential direction. Details of the film hole configuration (streamwise location, diameter, length, spanwise spacing, and compound angle) for this 5X model blade were specified by General Electric—Aircraft Engine Di-

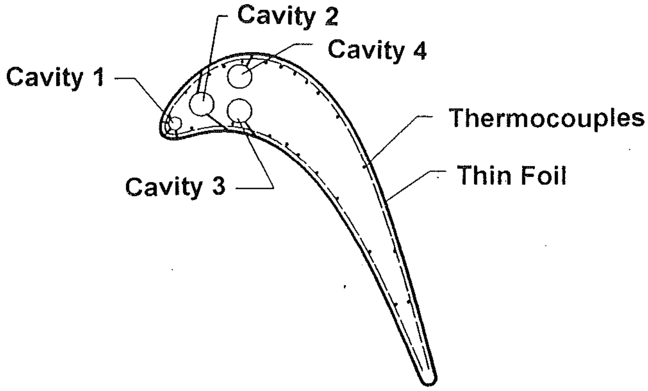

Film Hole Row Location	P/D	Axial Angle	Radial Angle	Tangential Angle
Leading Edge (All 3 Rows)	7.31	90°	27°	–
Cavity 2 Pressure Side	6.79	–	32°	55°
Cavity 2 Suction Side	4.13	–	90°	45°
Cavity 3 Pressure Side	5.00	–	35°	50°
Cavity 4 Suction Side	5.71	–	90°	30°

Fig. 4 Schematic of the model heat transfer blade with film holes

vision. Each cavity was supplied by an individually controlled injection (air or CO_2) flow rate. This blade was instrumented with thin foils and thermocouples similar to the blade without film holes, except that the foils did not cover the film hole region. Each thermocouple row had 4 thermocouples placed at strategic locations in the radial midspan region. Thermocouples were also mounted in the injection cavities to measure the secondary flow temperature. All thermocouples were connected to a 100-channel FLUKE 2280A datalogger interfaced with the 386SX machine. Input voltage and line current for both test blades were measured with FLUKE multimeter and current clamp.

Test Conditions and Data Analysis

The chord Reynolds number (Re) is defined as Re = V_1C/ν where V_1 is the mean mainstream velocity at the cascade inlet, C is the blade chord length, and ν is the local boundary layer kinematic viscosity. The chord Reynolds number was set at Re = 3×10^5 for all tests. This corresponds to an inlet velocity of 21 m/s.

According to O'Brien and Capp (1989), the wake Strouhal number (S) is defined as S = $2\pi Ndn/(60V_1)$ where N is the wake generator rotation speed (rpm), d is the wake generator rod diameter, n is the number of rods in the wake generator, and V_1 is the mean mainstream velocity at the cascade inlet. Three upstream unsteady wake conditions were studied: (1) the no wake condition where all rods from the wake generator were removed, (2) the medium wake Strouhal number of S = 0.1, which corresponded to N = 96 rpm, and (3) the high wake Strouhal number of S = 0.3, which corresponded to N = 287 rpm. The flow coefficients $V_1/U_r = dn/(r_m S)$ (O'Brien and Capp, 1989) at the Strouhal numbers of 0.1 and 0.3 were 5.7 and 1.9, respectively.

For the blade with film holes, the secondary (injectant) mass flux rate for a given row of injection holes was determined by knowing the local mainstream velocity at that location (as measured with a pressure tap instrumented blade: Han et al. 1993) and the desired blowing ratio. Tests were conducted a the blowing ratios of 0.4, 0.8, and 1.2. During the tests, the injectant temperature (air or CO_2) was maintained the same as the ambient mainstream temperature.

The mean velocity and turbulence intensity are time dependent and periodic in nature due to the periodic nature of wake shedding and passing. An analysis of the unsteady random signal indicates that the behavior cannot be characterized only by the time mean average. In order to calculate the time-dependent periodic mean velocity and turbulence intensity of the wake flow, the phase-averaged (ensemble-averaged) method suggested by O'Brien and Capp (1989), Dullenkopf et al. (1991), and Han et al. (1993) was adopted. Several wake passing periods were selected for data analysis. Each one of the selected wake passing periods was divided in the same number of bins. Data from the same bin in different periods were added. The phase-averaged mean velocity for that bin was then obtained by dividing the sum by the number of selected periods. This process was repeated for all other bins. The phase-averaged turbulence intensity of the wake flow was obtained in a similar manner. For higher accuracy in obtaining phase-averaged mean values, a digital record of 100 rod passing periods with 150 samples per period was made.

The local heat transfer coefficient with film injection is defined as

$$h = \frac{q''}{T_w - T_f} \tag{1}$$

where h is the local heat transfer coefficient, q'' is the net local convective heat flux, T_w is the local heated wall temperature, and T_f is the local film temperature due to the mixing of mainstream and secondary flows.

Since both mainstream and secondary flows (air or CO_2) are at the same ambient temperature (T_∞) and since Mach number $<< 1$ ($T_\infty \approx T_{aw}$), Eq. (1) can be modified to

$$h = \frac{q''}{T_w - T_\infty} = \frac{q''}{T_w - T_{aw}} \tag{2}$$

where T_∞ is the ambient temperature and T_{aw} is the local adiabatic wall temperature.

Since the foil heated blades experienced heat loss during tests, the local heat transfer coefficient was calculated as

$$h = \frac{q''_{\text{gen}} - q''_{\text{loss}}}{T_w - T_\infty} = \frac{q''_{\text{gen}} - (q''_{\text{cond}} + q''_{\text{rad}})}{T_w - T_{aw}} \tag{3}$$

where q''_{gen} is the generated surface heat flux, q''_{loss} is the local total heat loss flux, q''_{cond} is the local conduction heat loss flux, q''_{rad} is the local radiation heat loss flux, T_w is the local wall temperature with foil heat, T_∞ is the ambient mainstream temperature, and T_{aw} is the local adiabatic wall temperature without foil heat. Equation (3) was also used to calculate the local heat transfer coefficients for the blade without film holes. Heat loss tests were performed to estimate the total heat loss in Eq. (3) above.

During the heat transfer coefficient tests, T_w was in the 40-50°C range and T_{aw} was about 25°C. The measured total heat loss was about 10 percent of the foil generated heat. The conduction and radiation heat losses were 4 and 6 percent, respectively, of the heat generated. Heat loss through the tiny thermocouple wires was estimated to be very small (less than 0.1 percent), and axial and lateral conduction through the thin foil was also found to be negligible. The above-mentioned thin foil-thermocouple technique and the related data analysis method are the same as in Mehendale and Han (1992) and Han et al. (1993).

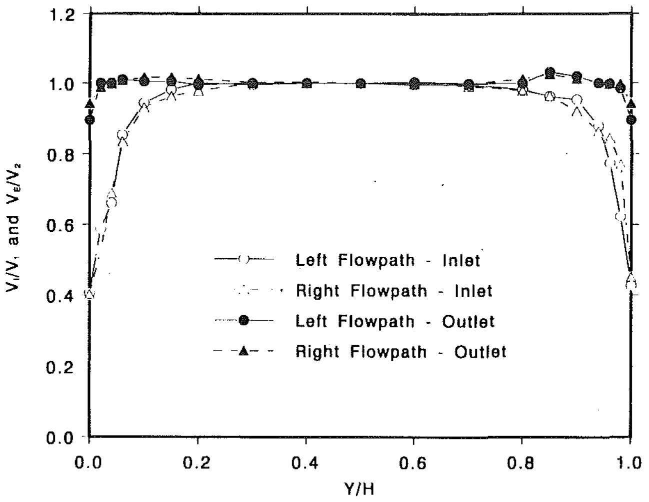

Fig. 5 Inlet and outlet velocity profiles for no wake and Re = 3 × 10^5

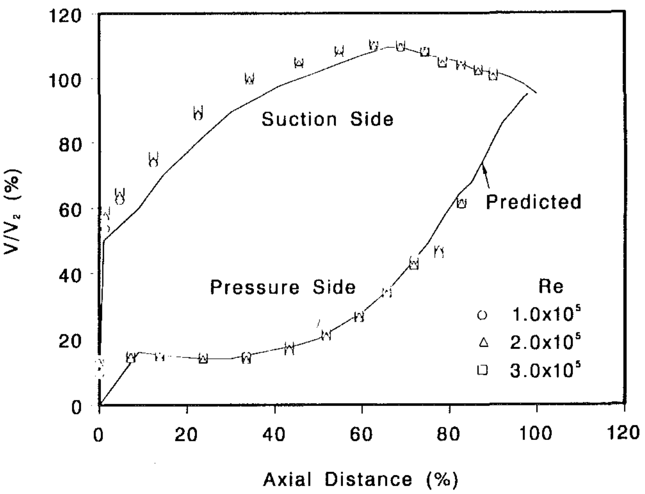

Fig. 6 Velocity distribution on the model blade for no wake and Re = 3 × 10^5

The local Nusselt number (Nu) was then calculated from Nu = hC/k where h is the local heat transfer coefficient, C is the blade chord length, and k is the local thermal conductivity. The local Nusselt numbers at a given streamwise location were averaged to obtain the spanwise-averaged Nusselt number ($\overline{Nu}$) at that location. An uncertainty analysis as in Kline and McClintock (1953) showed the uncertainty in Nusselt numbers to be ±5 percent based on 20:1 odds.

Results and Discussion

Flow Conditions. Velocity profiles in the radial direction at the inlet and outlet of the left and right flow paths were recorded. The dimensionless velocity profiles at the inlet and outlet of both the flow paths are shown in Fig. 5. The results indicate that the inlet and outlet velocity profiles in both the flow paths are essentially uniform in the 50 percent midspan region. Also, the flow direction at the inlet and outlet of both flow paths was uniform. Thus, the Nusselt numbers are free from the top and bottom wall boundary layer effects. The phase-averaged wake profiles in both the flow paths were found to be very similar.

A pressure tap instrumented blade was used to measure the surface static pressure distribution, which was converted to local mainstream velocity distribution around the blade (Han et al., 1993). The distribution of local to exit velocity ratio (V/V_2) around the blade is shown in Fig. 6. The solid line is a pretest prediction based on Re = 2×10^5 provided by General Electric—Aircraft Engine Division. The measured local mainstream velocity on the pressure surface is a good match, whereas on the suction surface, the measured local mainstream velocity is higher than the predicted value on the upstream side.

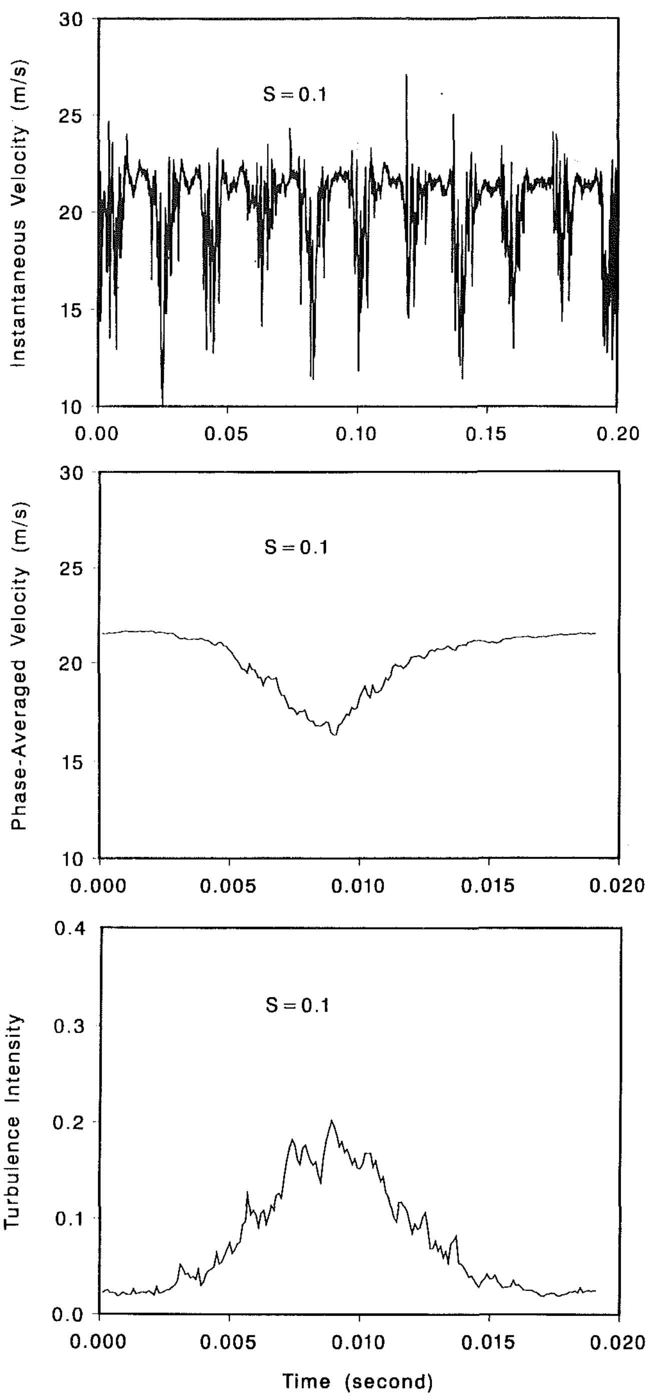

Fig. 7 Typical wake flow profiles for S = 0.1 at Re = 3 × 10^5

Typical instantaneous velocity profile, typical phase-averaged mean velocity profile, and typical phase-averaged turbulence intensity profile at the wake Strouhal number of S = 0.1 are shown in Fig. 7. The instantaneous velocity profile shows the periodic unsteady fluctuations caused by the upstream passing wake. The phase-averaged velocity profile shows the time-dependent mean velocity defect caused by the upstream passing wake. The phase-averaged turbulence intensity

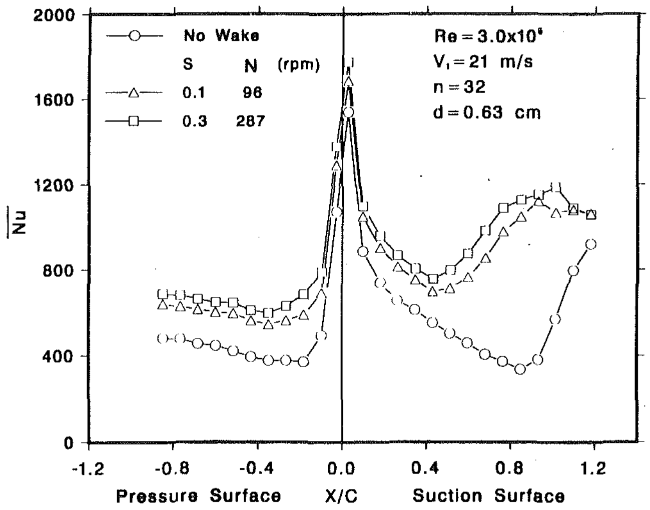

Fig. 8 Effect of unsteady wake on spanwise-averaged Nusselt numbers for the blade without film holes

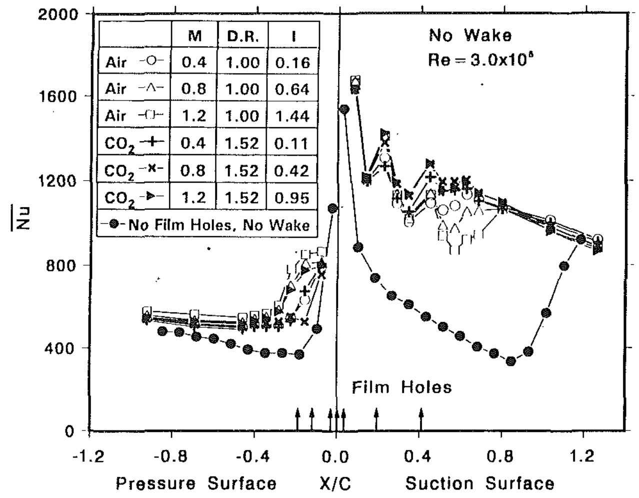

Fig. 9 Effect of air or CO_2 injection on spanwise-averaged Nusselt numbers for the no wake condition

reached as high as 20 percent inside the wake for S = 0.1. The time averaged turbulence intensities were about 8 and 13 percent for the wake Strouhal numbers of 0.1 and 0.3, respectively. The background turbulence intensity at the cascade inlet was only about 0.75 percent for the no wake condition.

Unsteady Wake Effect. The effect of wake Strouhal number on spanwise-averaged Nusselt number distribution for the blade without film holes is shown in Fig. 8. This figure depicts solely the effect of upstream unsteady wake. Results for the no wake base condition show that Nusselt number on the suction surface decreases monotonically with increasing streamwise distance from stagnation due to laminar boundary layer growth; but past $X/C = 0.85$ (i.e., 85 percent chord), the Nusselt number increases sharply due to boundary layer transition. Nusselt number on the pressure surface decreases sharply with increasing X/C for the same no wake condition, but starts gradually to increase from $X/C = -0.2$ due to strong acceleration as seen from Fig. 6. The effect of upstream unsteady wake is very similar to that presented by Dullenkopf et al. (1991) and Han et al. (1993). As wake Strouhal number increases, the increased flow unsteadiness disturbs the boundary layer and causes an increase in the heat transfer coefficient distribution over the entire test surface. This effect is more severe on the suction surface than on the pressure surface. The upstream unsteady flow conditions cause an earlier laminar to turbulent boundary layer transition on the suction surface (at only half the distance for the no wake case) and the transition length increases with increasing wake Strouhal number. These observations are consistent with those of Mayle (1991). The increases in heat transfer coefficients from the no wake case to S = 0.3 vary from 15 percent near the leading edge to as high as 235 percent at $X/C = 0.85$ on the suction surface, whereas the increases vary from 30 percent near the leading edge to 85 percent at $X/C = -0.2$ on the pressure surface. The increases in heat transfer coefficients from S = 0.1 to 0.3 vary from 0 to 15 percent over the entire test surface. Past the leading edge, the decrease in Nusselt number on the pressure surface is steeper than on the suction surface due to a much lower velocity on the pressure surface as seen from Fig. 6.

Film Injection Effect. The effect of film injection on spanwise-averaged Nusselt number distribution is shown in Fig. 9. This figure depicts solely the effect of film injection, i.e., for the no wake condition. The sharp increases in heat transfer coefficients immediately downstream of the film hole row locations on the suction surface are caused by the highly disturbed boundary layer due to the injection jet (secondary)-mainstream interaction. Following such peaks, the boundary layer growth and stabilization cause the heat transfer coefficients to decrease. Since the boundary layer on the pressure surface is thicker than on the suction surface, the increases in heat transfer coefficients caused by flow disturbances due to film injection are less prominent on the pressure surface.

Blowing Ratio Effect. In general, an increase in blowing ratio causes an increased injection jet-mainstream interaction and results in an increase in heat transfer coefficients on the pressure surface and most of the suction surface, except the region just downstream of the last row of film holes, for both the density ratios (Fig. 9). The effect of blowing ratio decreases farther downstream of the rows of film holes due to film dilution and a growing boundary layer. In the region just downstream of the last row of film holes on the suction surface, the heat transfer coefficients increase with a decreasing blowing ratio. This is because a lower blowing ratio with its lower momentum flux ratio, the accumulated effects of upstream film jets, and the significantly higher local mainstream velocity force an earlier and shorter boundary layer transition to a turbulent boundary layer. This earlier and shorter boundary layer transition results in higher heat transfer coefficients. An increase in blowing ratio causes an increase in penetration and lesser cumulative effects. This causes a lesser impact on the boundary layer and results in a delayed transition and hence lower heat transfer coefficients with increasing blowing ratio.

Density Ratio Effect. For a given blowing ratio, as the density ratio increases the momentum flux ratio decreases. Hence, at the same blowing ratio, the lower density injectant jet (air D.R. = 1.0) penetrates farther than the higher density injectant jet (CO_2, D.R. = 1.52). This causes a higher jet-mainstream interaction for the lower density ratio injectant and results in higher heat transfer coefficients. The effect of density ratio is more pronounced on the pressure surface, where the heat transfer coefficients for air injection are higher than for CO_2 injection (Fig. 9). On the suction surface, the heat transfer coefficients for both density ratios are very close except for the transition region where the higher density ratio injectant (CO_2) produces higher heat transfer coefficients. On the pressure surface, the momentum flux ratios for lower density ratio injectant (air) are higher than those for the higher density ratio injectant (CO_2). This results in higher jet-mainstream interaction and higher heat transfer coefficients for air injection. In the suction surface transition region, the lower momentum flux ratio CO_2 injection stays closer to the blade and causes an earlier transition to turbulent boundary layer. Hence, the

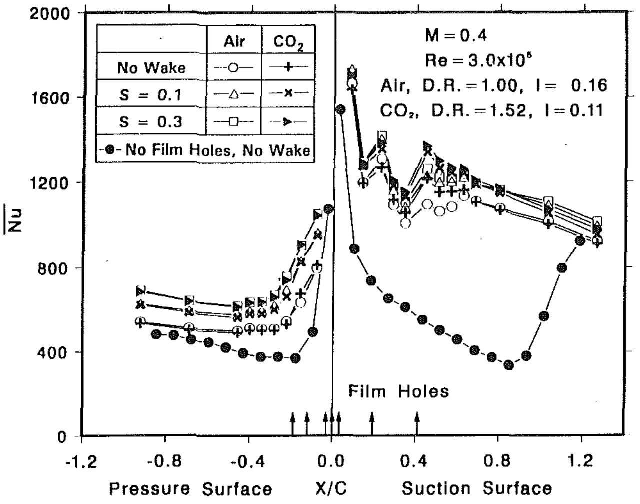

Fig. 10 Effect of unsteady wake and air or CO_2 injection on spanwise averaged Nusselt numbers for M = 0.4

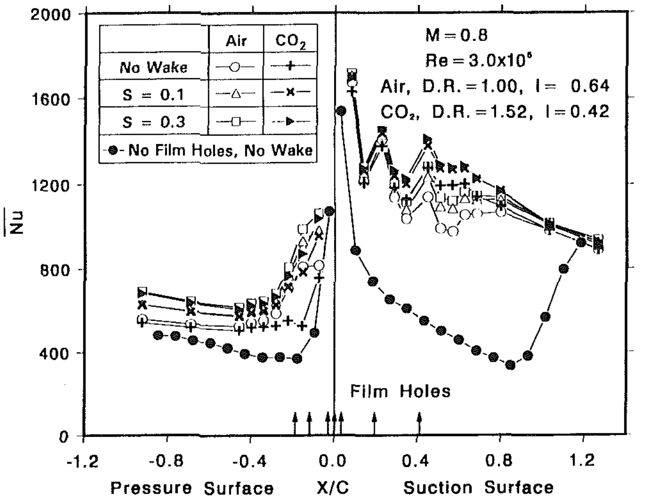

Fig. 11 Effect of unsteady wake and air or CO^2 injection on spanwise averaged Nusselt numbers for M = 0.8

higher density ratio injectant (CO_2) produces higher heat transfer coefficients than the lower density ratio injectant (air) in the transition region.

A comparison with Fig. 8 indicates that on the suction surface, the heat transfer coefficients for the "no wake but with film injection" case can be up to 1.7 times higher than those for the "no film holes but with strong wake" case in the $0 \leq X/C \leq 0.8$ region. This behavior is observed on a smaller scale near the film holes ($-0.2 \leq X/C \leq 0$) on the pressure surface.

Combined Unsteady Wake and Film Injection Effect. The effect of wake Strouhal number on spanwise-averaged Nusselt number distribution at the blowing ratios of 0.4, 0.8, and 1.2 is shown in Figs. 10, 11, and 12, respectively. The effect of unsteady wake in addition to film injection is depicted in these figures.

Pressure Surface. As the wake Strouhal number increases, the unsteady flow fluctuations disturb the boundary layer and cause higher heat transfer coefficients at all locations. As the blowing ratio increases, the heat transfer coefficients near the film hole row locations for both density ratios and for all wake Strouhal numbers increase due to increased interaction between injection jet and mainstream. Downstream of $X/C = -0.4$, the heat transfer coefficients for a given wake Strouhal number and a given injectant are almost exactly equal at all blowing ratios. This indicates that at these locations, the wake-generated boundary layer disturbance is stronger than the injectant jet generated one. The no wake heat transfer coefficients increase by up to 8 percent when the blowing ratio increases from 0.4 to 1.2. As blowing ratio increases, the boundary layer disturbance increases, and hence the increases in heat transfer coefficients due to unsteady wake (from the no wake case to S = 0.3) are reduced. The increases are reduced from a range of 42-24 percent at the blowing ratio of 0.4 to a range of only 23-14 percent at the blowing ratio of 1.2.

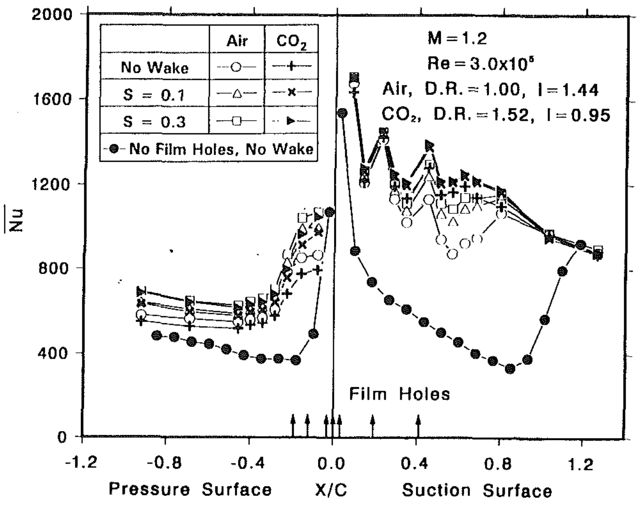

Fig. 12 Effect of unsteady wake and air or CO^2 injection on spanwise averaged Nusselt numbers for M = 1.2

At the lowest blowing ratio of 0.4, both density ratios show same levels of heat transfer coefficients because the amount of injectant coming out and the momentum flux ratios are very small. At higher blowing ratios, the differences between the two density ratios become more significant near the film injection locations, with low density ratio injectant (air) producing higher heat transfer coefficients for the reasons explained before. At farther downstream locations, the density ratio effect on heat transfer coefficients is very small due to film dilution.

Suction Surface (*Except Transition Region*). An increase in wake Strouhal number increases the unsteady flow fluctuations, thus disturbing the boundary layer and causing higher heat transfer coefficients for both injectants at all blowing ratios. As the blowing ratio increases, the heat transfer coefficients near the film hole row locations for both density ratios and for all wake Strouhal numbers increase slightly. The effect of unsteady wake is the greatest at the lowest blowing ratio of 0.4 where the jet is very weak. As blowing ratio increases, the boundary layer disturbance increases, and hence the increases in heat transfer coefficients due to unsteady wake (from the no wake to S = 0.3) reduce. The maximum increases in heat transfer coefficients due to the unsteady wake (from the no wake case to S = 0.3) are about 15 percent at all three blowing ratios. Both density ratio injectants (air and CO_2) show similar levels of heat transfer coefficients for all wake Strouhal numbers.

Suction Surface (*Transition Region*). In this transition region, as the blowing ratio decreases, the lower momentum flux ratio causes lesser penetration. This effect and such accumulated effects from the upstream film jets, in addition to high local mainstream velocities, promote an earlier and shorter boundary layer transition with higher heat transfer coefficients. For the higher density ratio injectant (CO_2), since the momentum flux ratios are lesser, the penetration is lesser. This results in earlier boundary layer transition and higher heat transfer coefficients than the lower density ratio injectant (air). The increases in heat transfer coefficients due to the unsteady wake (from the no wake case to S = 0.3) are more significant at the highest blowing ratio of 1.2 (the lowest heat transfer coefficients). This is because at higher blowing ratios, the transition is delayed and the unsteady wake flow disturbances easily affect the transitional boundary layer. The maximum increases in heat transfer coefficients (from the no wake case to S = 0.3) range from 15 percent at the blowing ratio of 0.4 to 31 percent at the blowing ratio of 1.2 for the low density ratio injectant (air). For the higher density ratio injectant (CO_2), an earlier transition makes the boundary layer highly disturbed and the effect of unsteady wake on heat transfer coefficients is not so severe but the trend remains the same as for the lower density ratio injectant (air).

Note

The effects of property differences between the higher density ratio injectant (CO_2) and the lower density ratio injectant (air) are discussed here.

The Prandtl numbers for both injectants are about the same. Since kinematic viscosity of CO_2 is only 53 percent that of air, the local Reynolds numbers for CO_2 injection can be as high as 89 percent over air injection, depending on the local CO_2 concentration in the boundary layer. But, the thermal conductivity of CO_2 is only 66 percent of air. If accounted for in the Nusselt number calculation, it will cause an increase of up to 51 percent in Nusselt numbers depending on the local CO_2 concentration in the boundary layer.

However, in this paper, the local values of air kinematic viscosity and air thermal conductivity were used for Reynolds number and Nusselt number calculations for both injectants (air and CO_2).

Concluding Remarks

The effect of upstream unsteady wake on surface heat transfer coefficients distribution of a test blade without film holes and a test blade with film injection in a linear cascade was investigated. A spoked wheel type wake generator was used. Tests were performed at the chord Reynolds number of 3×10^5 for the no wake, and at the wake Strouhal numbers of 0.1 and 0.3. For tests with film injection, air (D.R. = 1.0) and CO_2 (D.R. = 1.52) were used as injectants at the blowing ratios of 0.4, 0.8, and 1.2.

The main findings are:

1 The unsteady wake by itself, i.e., for the no film holes case, promotes an earlier boundary layer transition and increases the transition length on the suction surface. The heat transfer coefficients on both the pressure and the suction surfaces increase with increasing wake passing frequency. These increases over the "no wake no film holes" data are much higher on the suction surface (up to 235 percent) as compared to those on the pressure surface (up to 85 percent). Thus, by itself, the unsteady wake has a very dominant effect on heat transfer coefficients.

2 Film injection by itself, i.e., for the no wake condition, produces much higher heat transfer coefficients on the entire test surface; but the increases over the "no film holes" data are much higher on the suction surface than on the pressure surface. At some locations on the suction surface, the increases in heat transfer coefficients with only "film injection but no wake" are as high as 70 percent over those with "wake but no film holes." Thus, by itself, film injection has an even more dominant effect on heat transfer coefficients than by wake itself.

3 When unsteady wake condition is imposed on top of film injection, the effect is a further increase in heat transfer coefficients over the entire test surface. As blowing ratio increases, the increases in heat transfer coefficients due to the unsteady wake are reduced, except for the transition region, where they increase. The effect of unsteady wake is more pronounced on the pressure surface and in the transition region. On most of the suction surface (up to 80 percent chord length), however, the effect of unsteady wake in addition to film injection is secondary when compared with only the film injection effect.

4 In general, as blowing ratio increases, the surface heat transfer coefficients increase, except in the transition region where an increase in blowing ratio causes a decrease in heat transfer coefficients and an increase in the transition length. On most of the suction surface (up to 80 percent chord length), however, the effect of increasing blowing ratio is secondary when compared with the blowing ratio of 0.4.

5 At the lowest blowing ratio of 0.4, both density ratio injectants (air and CO_2) produce almost the same heat transfer coefficients, except in the transition region, where the values for the lower density ratio injection (air) are lower than those for the higher density ratio injectant (CO_2). At higher blowing ratios, air injection produces higher heat transfer coefficients than CO_2 injection on the pressure surface. On the suction surface, except for the transition region, air injection produces similar levels of heat transfer coefficients as CO_2 injection, at all blowing ratios. In the transition region, CO_2 injection produces higher heat transfer coefficients than air injection, at all blowing ratios. On most of the suction surface (up to 80 percent chord length), however, the effect of density ratio is secondary when compared with only the film injection effect.

The effect of several important parameters (unsteady wake, density ratio, and blowing ratio) on heat transfer coefficient for a turbine blade with film injection has been presented in this paper. The paper also indicates the relative strengths of these parameters. To the authors' knowledge, such information about combined effects of the parameters has not been presented elsewhere in the open literature. These results together with the adiabatic film effectiveness results in Part II (Mehendale et al., 1994) can be used in gas turbine blade design.

Acknowledgments

The project was sponsored by the U.S. Naval Air Warfare Center through General Electric Aircraft Engines. The project managers for the Naval Air Warfare Center were Mr. M. Sautner and Mr. R. Petruska. Their support is greatly appreciated. Very special thanks are due to Mr. T. Thomas of General Electric Aircraft Engines for his suggestions and discussions throughout the project investigation.

References

Abhari, R. S., Guenette, G. R., Epstein, A. H., and Giles, M. B., 1992, "Comparison of Time-Resolved Measurements and Numerical Calculations," ASME Journal of Turbomachinery, Vol. 114, pp. 818-827.

Abhari, R. S., and Epstein, A. H., 1994, "An Experimental Study of Film Cooling in a Rotating Transonic Turbine," ASME Journal of Turbomachinery, Vol. 116, pp. 63-70.

Ammari, H. D., Hay, N., and Lampard, D., 1990, "The Effect of Density Ratio on the Heat Transfer Coefficient From a Film Cooled Flat Plate," ASME Journal of Turbomachinery, Vol. 112, pp. 444-450.

Blair, M. F., Dring, R. P., and Joslyn, H. D., 1989a, "The Effects of Turbulence and Stator/Rotor Interactions on Turbine Heat Transfer: Part I—Design Operating Conditions," ASME Journal of Turbomachinery, Vol. 111, pp. 87-96.

Blair, M. F., Dring, R. P., and Joslyn, H. D., 1989b, "The Effects of Turbulence and Stator/Rotor Internations on Turbine Heat Transfer: Part II—Effects of Reynolds Number and Incidence," ASME Journal of Turbomachinery, Vol. 111, pp. 97-103.

Blair, M. F., 1994, "An Experimental Study of Heat Transfer in a Large-Scale Turbine Rotor Passage," ASME Journal of Turbomachinery, Vol. 116, pp. 1-13.

Camci, C., and Arts, T., 1990, "An Experimental Convective Heat Transfer Investigation Around a Film-Cooled Gas Turbine Blade," ASME Journal of Turbomachinery, Vol. 112, pp. 497-503.

Doorly, D. J., 1988, "Modeling the Unsteady Flow in a Turbine Rotor Passage," ASME Journal of Turbomachinery, Vol. 110, pp. 27-37.

Dullenkopf, K., Schulz, A., and Wittig, S., 1991, "The Effect of Incident

Wake Conditions on the Mean Heat Transfer of an Airfoil," ASME JOURNAL OF TURBOMACHINERY, Vol. 113, pp. 412–418.

Dullenkopf, K., and Mayle, R. E., 1994, "The Effects of Incident Turbulence and Moving Wakes on Laminar Heat Transfer in Gas Turbines," ASME JOURNAL OF TURBOMACHINERY, Vol. 116, pp. 23–28.

Dunn, M. G., 1986, "Heat Flux Measurements for the Rotor of a Full-Stage Turbine: Part I—Time-Averaged Results," ASME JOURNAL OF TURBOMACHINERY, Vol. 108, pp. 90–97.

Dunn, M. G., George, W. K., Rae, W. J., Woodward, S. H., Moller, J. C., and Seymour, J. P., 1986, "Heat Flux Measurements for the Rotor of a Full-Stage Turbine: Part II—Description of Analysis Technique and Typical Time-Resolved Measurements," ASME JOURNAL OF TURBOMACHINERY, Vol. 108, pp. 98–107.

Dunn, M. G., Seymour, P. J., Woodward, S. H., George, W. K., and Chupp, R. E., 1989, "Phase-Resolved Heat Flux Measurements on the Blade of a Full-Scale Rotating Turbine," ASME JOURNAL OF TURBOMACHINERY, Vol. 111, pp. 8–19.

Dunn, M. G., Kim, J., Civinskas, K. C., and Boyle, R. J., 1994, "Time-Averaged Heat Transfer and Pressure Measurements and Comparison With Prediction for a Two-Stage Turbine," ASME JOURNAL OF TURBOMACHINERY, Vol. 116, pp. 14–22.

Han, J. C., Zhang, L., and Ou, S., 1993, "Influence of Unsteady Wake on Heat Transfer Coefficient From a Gas Turbine Blade," ASME *Journal of Heat Transfer*, Vol. 115, pp. 904–911.

Kline, S. J., and McClintock, F. A., 1953, "Describing Uncertainties in Single-Sample Experiments," *Mechanical Engineering*, Vol. 75, Jan., pp. 3–8.

Liu, X., and Rodi, W., 1989, "Measurements of Unsteady Flow Over and Heat Transfer From a Flat Plate," ASME Paper No. 89-GT-2.

Liu, X., and Rodi, W., 1992, "Measurements of Unsteady Flow and Heat Transfer in a Linear Turbine Cascade," ASME Paper No. 92-GT-323.

Mayle, R. E., and Dullenkopf, K., 1990, "A Theory for Wake-Induced Transition," ASME JOURNAL OF TURBOMACHINERY, Vol. 112, pp. 188–195.

Mayle, R. E., 1991, "The Role of Laminar-Turbulent Transition in Gas Turbine Engines," ASME JOURNAL OF TURBOMACHINERY, Vol. 113, pp. 509–537.

Mehendale, A. B., and Han, J. C., 1992, "Influence of High Mainstream Turbulence on Leading Edge Film Cooling Heat Transfer," ASME JOURNAL OF TURBOMACHINERY, Vol. 114, pp. 707–715.

Mehendale, A. B., Han, J. C., Ou, S., and Lee, C. P., 1994, "Unsteady Wake Over a Linear Turbine Blade Cascade With Air and CO_2 Film Injection: Part II—Effect on Film Effectiveness and Heat Transfer Distributions," ASME JOURNAL OF TURBOMACHINERY, Vol. 116, this issue, pp. 730–737.

Mick, W. J., and Mayle, R. E., 1988, "Stagnation Film Cooling and Heat Transfer, Including Its Effect Within the Hole Pattern," ASME JOURNAL OF TURBOMACHINERY, Vol. 110, pp. 66–72.

Nirmalan, V., and Hylton, L. O., 1990, "An Experimental Study of Turbine Vane Heat Transfer With Leading Edge and Downstream Film Cooling," ASME JOURNAL OF TURBOMACHINERY, Vol. 112, pp. 477–487.

O'Brien, J. E., and Capp, S. P., 1989, "Two-Component Phase-Averaged Turbulence Statistics Downstream of a Rotating Spoked-Wheel Wake Generator," ASME JOURNAL OF TURBOMACHINERY, Vol. 111, pp. 475–482.

Ou, S., and Han, J. C., 1992, "Influence of Mainstream Turbulence on Leading Edge Film Cooling Heat Transfer Through Two Rows of Inclined Film Slots," ASME JOURNAL OF TURBOMACHINERY, Vol. 114, pp. 724–733.

Priddy, W. J., and Bayley, F. J., 1988, "Turbulence Measurements in Turbine Blade Passages and Implications for Heat Transfer," ASME JOURNAL OF TURBOMACHINERY, Vol. 110, pp. 73–79.

Teekaram, A. J. H., Forth, C. J. P., and Jones, T. V., 1989, "The Use of Foreign Gas to Simulate the Effect of Density Ratios in Film Cooling," ASME JOURNAL OF TURBOMACHINERY, Vol. 111, pp. 57–62.

Wittig, S., Dullenkopf, K., Schulz, A., and Hestermann, R., 1987, "Laser-Dopper Studies of the Wake-Effected Flow Field in a Turbine Cascade," ASME JOURNAL OF TURBOMACHINERY, Vol. 109, pp. 170–176.

Wittig, S., Schultz, A., Dullenkopf, K., and Fairbank, J., 1988, "Effects of Free-Stream Turbulence and Wake Characteristics on the Heat Transfer Along a Cooled Gas Turbine Blade," ASME Paper No. 88-GT-179.

Unsteady Wake Over a Linear Turbine Blade Cascade With Air and CO$_2$ Film Injection: Part II—Effect on Film Effectiveness and Heat Transfer Distributions

A. B. Mehendale
Research Associate.

J.-C. Han
HTRI Professor.
Fellow ASME

S. Ou[1]
Research Associate.

Department of Mechanical Engineering,
Turbine Heat Transfer Laboratory,
Texas A&M University,
College Station, TX 77843

C. P. Lee
Manager,
Turbine Aero & Cooling Design,
General Electric—Aircraft Engines,
Cincinnati, OH 45215
Mem. ASME

The effect of unsteady wake flow and air ($D.R. = 0.97$) or CO$_2$ ($D.R. = 1.48$) film injection on blade film effectiveness and heat transfer distributions was experimentally determined. A spoked wheel type wake generator produced the unsteady wake. Experiments were performed on a five-airfoil linear cascade in a low-speed wind tunnel at the chord Reynolds number of 3×10^5 for the no wake case and at the wake Strouhal numbers of 0.1 and 0.3. A model turbine blade with several rows of film holes on its leading edge, and pressure and suction surfaces ($-0.2 < X/C < 0.4$) was used. Results show that the blowing ratios of 1.2 and 0.8 provide the best film effectiveness over most of the blade surface for CO$_2$ and air injections, respectively. An increase in the wake Strouhal number causes a decrease in film effectiveness over most of the blade surface for both density ratio injectants and at all blowing ratios. On the pressure surface, CO$_2$ injection provides higher film effectiveness than air injection at the blowing ratio of 1.2; however, this trend is reversed at the blowing ratio of 0.8. On the suction surface, CO$_2$ injection provides higher film effectiveness than air injection at the blowing ratio of 1.2; however, this trend is reversed at the blowing ratio of 0.4. Co$_2$ injection provides lower heat loads than air injection at the blowing ratio of 1.2; however, this trend is reversed at the blowing ratio of 0.4. Heat load ratios under unsteady wake conditions are lower than the no wake case. For an actual gas turbine blade, since the blowing ratios can be greater than 1.2 and the density ratios can be up to 2.0, a higher density ratio coolant may provide lower heat load ratios under unsteady wake conditions.

Introduction

There have been many investigations to study the effect of film injection on flat or curved surfaces for low mainstream turbulence intensities. The effects of various blowing ratios, injection geometries, and film coolants have been investigated by Goldstein (1971), Eriksen and Goldstein (1974), Muska et al. (1976), Jabbari and Goldstein (1978), Ko et al. (1984), Han and Mehendale (1986), and Schwarz et al. (1991). Schönung and Rodi (1987) developed a two-dimensional boundary layer procedure to calculate film cooling parameters for film injection over a flat plate. Mick and Mayle (1988) studied the film effectiveness distributions for a low mainstream turbulence flow on a leading edge model.

Mehendale and Han (1992) and Ou and Han (1992) studied the effect of high mainstream turbulence on film effectiveness on a leading edge model with circular hole and slot injections. They reported that for 3-d hole and 3-ℓ slot injections, blowing ratios of 0.4 and 0.8, respectively, provide the best film effectiveness. They also reported that an increase in mainstream turbulence causes a reduction in film effectiveness; however, these decreases reduce as blowing ratio increases.

The effect of density ratio on film effectiveness for film injection on a flat plate has been studied by Goldstein et al. (1974), Pedersen et al. (1977), Afejuku et al. (1980), and Foster and Lampard (1980). Most of these studies were done at low mainstream turbulence with a heat-mass transfer analogy. Sinha et al. (1991) used a thermocouple instrumented flat plate to study the effect of density ratio on film effectiveness at low mainstream turbulence intensities. They reported that the film

---

[1] Current address: Aero Propulsion and Power Laboratory, Wright Patterson AFB, OH 45433.

Contributed by the International Gas Turbine Institute and presented at the 38th International Gas Turbine and Aeroengine Congress and Exposition, Cincinnati, Ohio, May 24–27, 1993. Manuscript received at ASME Headquarters March 1, 1993. Paper No. 93-GT-134. Associate Technical Editor: H. Lukas.

effectiveness increases with increasing coolant-to-mainstream density ratio.

Ito et al. (1978) studied the effect of density ratio on film effectiveness of a gas turbine blade model at low mainstream turbulence intensities. They found that on the suction surface, an increase in density ratio causes a decrease in film effectiveness at the blowing ratio of 0.5, whereas the trend is reversed on the pressure surface. They also found that at the blowing ratio 1.0, an increase in density ratio causes an increase in film effectiveness on both pressure and suction surfaces. Haas et al. (1992) reported the film effectiveness data under no wake condition for flow over a model turbine blade with suction side film coverage. They too found that at the low blowing ratio of 0.5, an increase in density ratio causes a decrease in suction side film effectiveness, and at higher blowing ratios, an increase in density ratio causes an increase in suction side film effectiveness.

Abhari and Epstein (1994) studied heat transfer on a film-cooled rotor blade, under simulated engine nondimensional conditions, with time-resolved measurements. They reported that film cooling reduced the time-averaged heat transfer by as much as 60 percent on the suction side, but the effect on the pressure side is relatively little. Takeishi et al. (1992) compared the film effectiveness values for a stationary cascade under 4 percent mainstream turbulence intensity and a rotor blade using the heat-mass transfer analogy. They reported that in the leading edge region and on the suction surface, the film effectiveness values for the cascade and rotor blade match well; whereas, on the pressure surface, the cascade film effectiveness values are higher.

Sautner et al. (1992) studied the effect of upstream unsteady wake on the film effectiveness distribution on a model turbine blade with several rows of film holes on its leading edge, and pressure and suction surfaces. They studied "film cooling" with air injection at a density ratio of 1.05 and reported that an increase in the unsteady wake passing frequency results in a reduction in film effectiveness at all blowing ratios.

Teekaram et al. (1989) studied the effect of secondary to mainstream density ratio on heat transfer coefficients over a flat plate with film injection. They used air and CO_2 at the same density for film injection. The densities of both injectants were made equal by controlling their temperatures. They reported that the film cooled heat transfer coefficients were independent of the gas used for injection (air or CO_2) as long as their densities were maintained the same.

This study focuses on the effect of incident unsteady wake conditions on film effectiveness and heat transfer distributions on a model turbine blade with air or CO_2 film injection through three rows of film holes in the leading edge region and two rows each on the pressure and suction surfaces. In order to investigate the overall effect of film injection on blade heat transfer (heat load), it is necessary to obtain the blade heat transfer coefficient distributions. The heat transfer coefficient distributions have been reported in Part I (Ou et al., 1994).

The objectives of this study are to determine: (1) the effect of film injection on blade film effectiveness and heat transfer distributions for the no wake condition, (2) the effect of density ratio on blade film effectiveness and heat transfer distributions with air or CO_2 film injection, and (3) the combined effect of upstream unsteady wake and injectant density ratio on blade film effectiveness and heat transfer distributions.

Test Apparatus and Instrumentation

A schematic of the test apparatus is shown in Fig. 1 of Part I (Ou et al., 1994). The test apparatus consisted of a low-speed, low-turbulence wind tunnel with an inlet nozzle, a spoked wheel type wake generator, a linear turbine blade cascade with an instrumented blade at its center, and a suction type blower. The test apparatus is described in detail in Part I.

A detailed view of the cascade, wake generator, and hot wire locations is shown in Fig. 2 of Part I. The cascade was designed for use in our low-speed wind tunnel facility. The blade configuration was designed at General Electric—Aircraft Engine Division to produce a similar velocity ratio distribution as in a typical advanced high pressure turbine blade row. The selected blade had a 107.49 deg turning with relative flow angles of 35 and −72.49 deg at the blade inlet and exit, respectively. A five times scaled-up model was used to simulate the engine Reynolds number. The cascade had five blades, each with a

Nomenclature

C = blade chord
d = wake generator rod diameter
D.R. = density ratio $= \rho_s/\rho_\infty$
h = local heat transfer coefficient with film injection
h_o = local heat transfer coefficient for the no film holes case
I = momentum flux ratio $= (\rho V^2)_s/(\rho V^2)_\infty$
M = blowing ratio (secondary to mainstream mass flux ratio) $= (\rho V)_s/(\rho V)_\infty$
n = number of rods in the wake generator
N = wake generator rotation speed, rpm
q'' = local forced convection heat flux with film injection
$\bar{q}''$ = spanwise averaged forced convection heat flux with film injection
q''_o = local forced convection heat flux for the no film holes case
$\bar{q}''_o$ = spanwise averaged forced convection heat flux for the no film holes case
q''_{cond} = local conduction heat loss flux
$q''_{\text{cond, g}}$ = local conduction heat gain flux from within the model blade
q''_{rad} = local radiation heat loss flux
Re = Reynolds number based on the blade chord $= V_1C/\nu$
S = wake Strouhal number $= 2\pi Ndn/(60V_1)$
T_{aw} = local adiabatic wall temperature
T_f = local film temperature
T_s = secondary flow temperature within injection cavity
T_w = local wall temperature
T_∞ = mainstream temperature at the cascade inlet
U_r = rotational velocity at cascade midspan
V = local mainstream velocity
V_1 = mean mainstream velocity at the cascade inlet
X = blade surface coordinate from stagnation in the streamwise direction
X/C = dimensionless blade surface coordinate in the streamwise direction
z = blade radial (spanwise) dimension
η = local film effectiveness
$\bar{\eta}$ = spanwise-averaged film effectiveness
ν = local kinematic viscosity
ρ_s = secondary density
ρ_∞ = mainstream density
$(\rho V)_s$ = local secondary mass flux
$(\rho V^2)_s$ = local secondary momentum flux
$(\rho V)_\infty$ = local mainstream mass flux
$(\rho V^2)_\infty$ = local mainstream momentum flux

chord length of 22.68 cm and a radial span of 25.2 cm. The blades were spaced 17.01 cm apart. The cascade leading edge was 8.82 cm downstream of the wake generator. All blades were made of high-quality model wood. Only the center blade had film holes and was instrumented.

The spoked wheel type wake generator had 32 rods, each 0.63 cm in diameter to simulate trailing edge of an upstream blade. Its shaft was located 20 cm below the bottom wall of the wind tunnel. The wake Strouhal number was adjusted by controlling the motor speed. The wake generator rotation speed was accurately measured by a digital photo tachometer.

A schematic of the top view of the model turbine blade is shown in Fig. 1. The blade had four injection cavities. The first cavity supplied three rows of film holes: one near the leading edge, and one each on the pressure and suction surfaces. The second cavity supplied one row each on the pressure and suction surfaces. The third and fourth cavities supplied one row of film holes on the pressure and suction surfaces, respectively. Depending on its location, each row had 8 to 10 film holes between 30 and 70 percent of the blade radial span. Some of the film holes had a compound angle (radial and tangential) relative to the blade surface as seen from Fig. 4 in Part I. Radial angle is defined as the angle between the film hole axis and the local radial (spanwise) direction. Tangential angle is defined as the angle between the film hole axis and the local streamwise tangential direction. Details of the film hole configuration (streamwise location, diameter, length, spanwise spacing, and compound angle) for this 5X model blade were specified by General Electric—Aircraft Engine Division. Each cavity was supplied by individually controlled injection (air or CO_2) flow rate. A heater with a temperature controller was used to heat the injectant. Twenty-six strips of stainless steel foil, each 25.4 cm long × 2 cm wide × 0.00378 cm thick, were cemented vertically on the test blade except in the film hole region. They were separated by 0.8 mm gaps that were filled with wood putty and made flush with the foil surface. Each thermocouple row had four thermocouples placed at strategic locations in the radial midspan region. Thermocouples were mounted in the injection cavities to measure the secondary flow temperature. All thermocouples were connected to a datalogger. This is the same model turbine blade used in Part I (Ou et al., 1994) to evaluate the heat transfer coefficients with film injection.

Test Conditions and Data Analysis

The chord Reynolds number (Re) is defined as $\mathrm{Re} = V_1 C/\nu$, where V_1 is the mean mainstream velocity at the cascade inlet, C is the blade chord length, and ν is the local boundary layer kinematic viscosity. The chord Reynolds number was set at $\mathrm{Re} = 3 \times 10^5$ for all tests. This corresponded to an inlet velocity of 21 m/s.

O'Brien and Capp (1989) have defined the wake Strouhal number (S) as $S = 2\pi N d n/(60 V_1)$, where N is the wake generator rotation speed (rpm), d is the wake generator rod diameter, n is the number of rods in the wake generator, and V_1 is the mean mainstream velocity at the cascade inlet. Three upstream unsteady wake conditions were studied: (1) the no wake condition where all rods from the wake generator were removed, (2) the medium wake Strouhal number of $S = 0.1$, which corresponded to $N = 96$ rpm, and (3) the high wake Strouhal number of $S = 0.3$, which corresponded to $N = 287$ rpm. The flow coefficients $V_1/U_r = dn/(r_m S)$ (O'Brien and Capp, 1989) at the Strouhal numbers of 0.1 and 0.3 were 5.7 and 1.9, respectively.

As described in Part I, the time-averaged turbulence intensity is about 8 and 13 percent for $S = 0.1$ and 0.3, respectively. For the no wake condition, the background turbulence intensity at the cascade inlet was only about 0.75 percent.

The secondary mass flux rate for a given row of injection holes was determined by knowing the local mainstream velocity at that location (as measured with a pressure tap instrumented blade—Han et al., 1993) and the desired blowing ratio. Tests were conducted at blowing ratios of 0.4, 0.8, and 1.2. During the tests the injectant temperatures (air or CO_2) within the injection chambers were maintained at about 45°C.

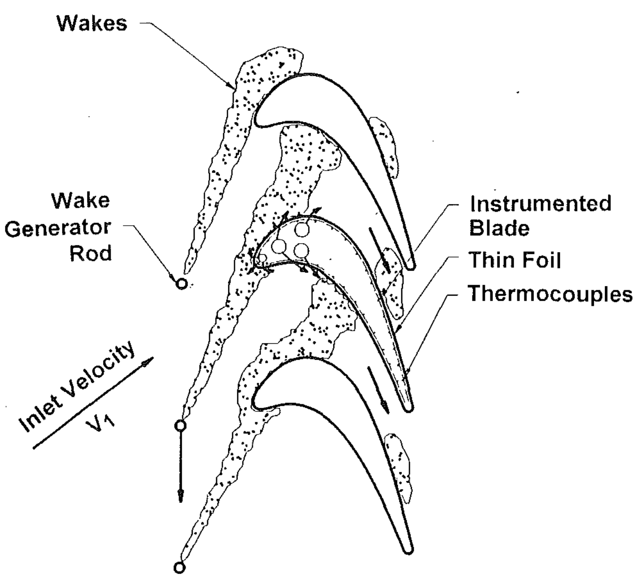

Fig. 1 Conceptual view of unsteady wake effect on a model blade with film holes

The local film effectiveness is defined as

$$\eta = \frac{T_f - T_\infty}{T_s - T_\infty} \tag{1}$$

where η is the local film effectiveness, T_f is the local film temperature due to the mixing of the injection flow with the mainstream flow, T_∞ is the mainstream temperature, and T_s is the injectant temperature in the injection cavity.

Since it is very difficult to determine the local film temperature, the test surface is initially assumed to be adiabatic. Under this assumption there is no heat transfer at the surface and the local film temperature must be equal to the local adiabatic wall temperature. Hence, for an adiabatic surface, Eq. (1) is modified to

$$\eta = \frac{T_{aw} - T_\infty}{T_s - T_\infty} \tag{2}$$

where η is the local adiabatic wall film effectiveness and T_{aw} is the local adiabatic wall temperature.

Since the blade surface was not perfectly adiabatic, heat losses and gains had to be accounted for. Because the injectant was hotter than the mainstream, there was a conduction gain from within the model blade, which resulted in higher wall temperatures at locations near injection cavities. However, heat loss from the surface due to conduction and radiation resulted in lower wall temperatures. These gains and losses were accounted for by dividing their local fluxes by the local heat transfer coefficient to yield an "equivalent corrective wall to mainstream temperature difference." The corrective temperature difference was positive or negative depending on the relative strengths of these fluxes. The film effectiveness was then calculated as

$$\eta = \frac{T_w - T_\infty}{T_s - T_\infty} + \frac{(q''_{\mathrm{cond}} + q''_{\mathrm{rad}}) - q''_{\mathrm{cond,\,g}}}{h(T_s - T_\infty)} \tag{3}$$

where η is the local film effectiveness, T_w is the local wall temperature as a result of the mixing of the hotter injectant with the ambient mainstream, T_∞ is the ambient mainstream

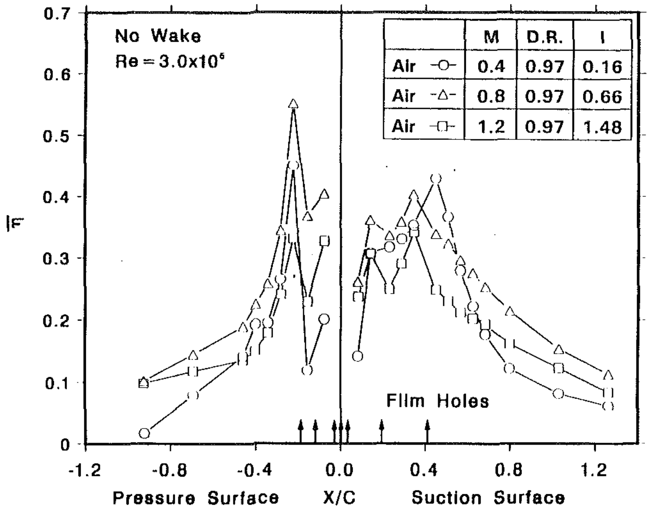

Fig. 2 Effect of air injection on spanwise-averaged film effectiveness for the no wake condition

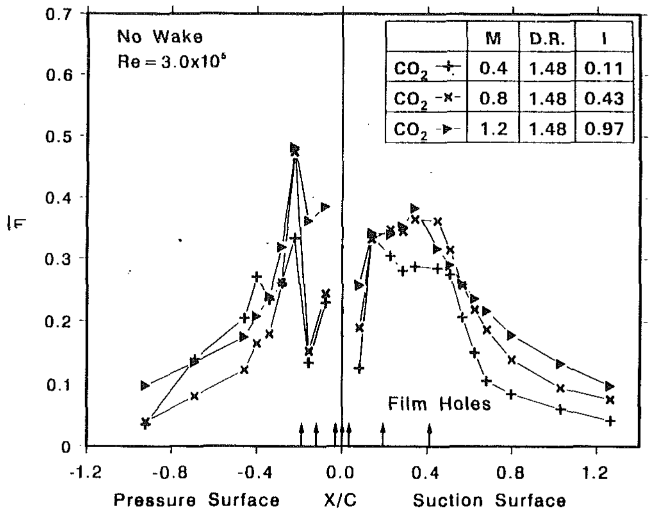

Fig. 3 Effect of CO_2 injection on spanwise-averaged film effectiveness for the no wake condition

temperature, q''_{cond} is the local conduction heat loss flux, q''_{rad} is the local radiation heat loss flux, $q''_{\text{cond,g}}$ is the local conduction heat gain flux, and h is the local heat transfer coefficient for the corresponding test conditions from Part I.

The above-mentioned thin foil-thermocouple technique and the related data analysis method are the same as in Mehendale and Han (1992).

The local film effectiveness values at a given streamwise location were averaged to obtain the spanwise-averaged film effectiveness ($\bar{\eta}$) at that location.An uncertainty analysis as in Kline and McClintock (1953) showed the uncertainty in film effectiveness and heat load ratio to be ±5 percent based on 20:1 odds.

Results and Discussion

Flow Conditions. Velocity profiles in the radial direction at the inlet and outlet of the left and right flow paths were recorded. The results indicate that the inlet and outlet velocity profiles in both flow paths are essentially uniform in the 50 percent midspan region as seen from Fig. 5 in Part I. Also, the flow direction at the inlet and outlet of both flow paths was uniform. Thus, the film effectiveness values are free from the top and bottom wall boundary layer effects. The phase-averaged wake profiles in both flow paths were found to be very similar.

The distribution of local to exit velocity ratio (V/V_2) around the blade is shown in Fig. 6 of Part I. The solid line is a pretest prediction based on $\text{Re} = 2 \times 10^5$ provided by General Electric—Aircraft Engine Division. The measured local mainstream velocity on the pressure surface is a good match; however, the measured local mainstream velocity on the suction surface is higher than the predicted value on the upstream side.

Transition Region. There exists a laminar to turbulent boundary layer transition region downstream of the last row of film holes on the suction surface ($0.4 \leq X/C \leq 0.6$). The effect of test parameters like blowing ratio, density ratio, and Strouhal number in this region is not the same as on the rest of the suction surface. This region has been described in detail in Part I.

Film Effectiveness

Film Injection Effect. The effect of film injection on spanwise-averaged film effectiveness distribution for air and CO_2 injections is shown in Figs. 2 and 3, respectively. These figures depict only the effect of film injection, i.e., for the no wake condition. In general, as seen from these figures, film effectiveness increases downstream of film holes for both air and CO_2 injections. These peaks in film effectiveness are due to better film coverage downstream of film holes. Following such peaks, the film effectiveness decreases due to injectant dilution and the values are very small far downstream of the film holes. For air injection, as seen from Fig. 2, the blowing ratio of 0.8 (with a medium momentum flux ratio and a medium mass flow rate) provides the best film effectiveness over most of the blade surface. At the higher blowing ratio of 1.2, a significantly higher momentum flux ratio causes more injectant penetration into the mainstream which results in lower film effectiveness values. At the lower blowing ratio of 0.4, only small amount of injectant comes out of the film holes which results in lower film effectiveness values. For CO_2 injection, as seen from Fig. 3, the blowing ratio of 1.2 provides the base film effectiveness over most of the blade surface. Since CO_2 is about 1.5 times as dense as air, its momentum flux ratio at the blowing ratio of 1.2 is only 66 percent that of air injection at the same blowing ratio, which results in a lesser jet penetration. This lesser jet penetration combined with the highest mass flow rate at the blowing ratio of 1.2 results in the best film coverage.

Pressure Surface. For air injection, the film effectiveness values at the blowing ratio of 0.8 are the highest as previously explained. At the lowest blowing ratio of 0.4, the film effectiveness values near the leading edge are very small but they increase farther downstream and subsequently decrease due to film dilution. Far downstream of film holes, the blowing ratio of 1.2 shows better film effectiveness than 0.4. Since the local mainstream velocities near the leading edge are very small, a very small amount of injectant comes out of the film holes at the lowest blowing ratio of 0.4. Hence, it produces lower film effectiveness than the blowing ratio of 1.2 (in spite of higher jet penetration at the blowing ratio of 1.2) near the leading edge. However, since its momentum flux ratio is small, the injectant at the blowing ratio of 0.4 gets trapped in the boundary layer. This effect accumulates with injections from the downstream rows and results in higher film effectiveness than the blowing ratio of 1.2. Film dilution causes the film effectiveness to decrease farther downstream of the last row of film holes, with the blowing ratios of 0.8 and 1.2 providing higher film effectiveness due to the higher amount of injectant mass flow rate. Another reason for this behavior is the spreading

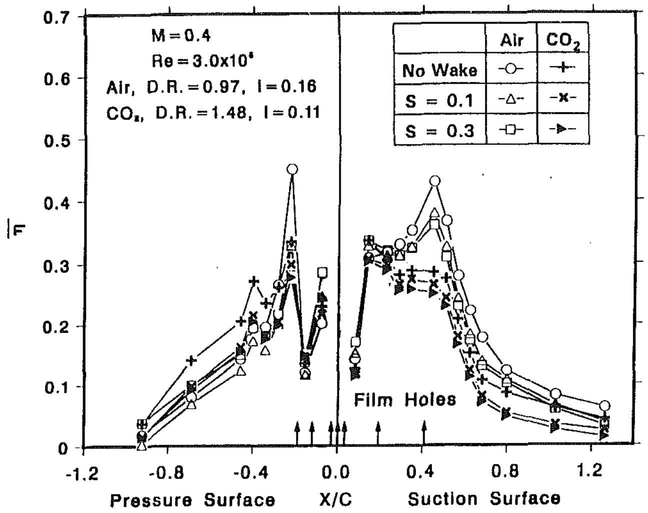

Fig. 4 Effect of unsteady wake and air or CO_2 injection on spanwise-averaged film effectiveness for M = 0.4

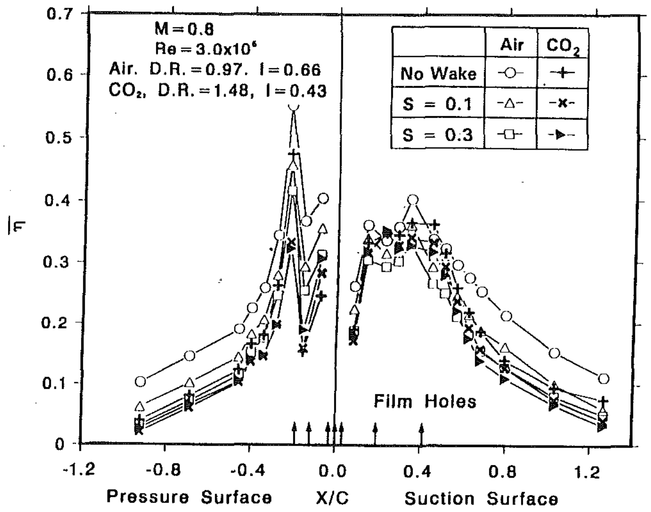

Fig. 5 Effect of unsteady wake and air or CO_2 injection on spanwise-averaged film effectiveness for M = 0.8

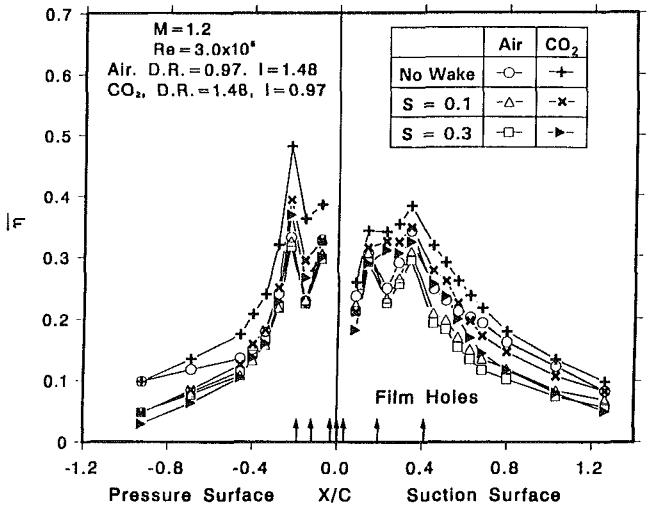

Fig. 6 Effect of unsteady wake and air or CO_2 injection on spanwise-averaged film effectiveness for M = 1.2

of the jet, which causes the jet to come in contact with the far downstream surface and results in higher film effectiveness, even though the jet may have previously penetrated the boundary layer. For CO_2 injection, the film effectiveness values at the blowing ratio of 1.2 are the highest as explained before. At the lowest blowing ratio of 0.4, the film effectiveness values near the leading edge are very small but increase farther downstream and subsequently decrease due to film dilution. Downstream of the last row of film holes, the results are not as consistent as for air injection.

Suction Surface (*Except Transition Region*). Film effectiveness values for air injection at the blowing ratio of 0.8 are the highest as explained before. Film effectiveness values near the leading edge are very small at the lowest blowing ratio of 0.4, but they increase farther downstream and subsequently decrease (as explained for the pressure surface). Far downstream of film holes, the blowing ratio of 1.2 shows better film effectiveness than 0.4 (as explained for the pressure surface). Film effectiveness values for CO_2 injection at the blowing ratio of 1.2 are the highest as explained before. Film effectiveness values near the leading edge at the lowest blowing ratio of 0.4, are very small but increase farther downstream and subsequently decrease (as explained for the pressure surface). Downstream of the transition region, a decrease in blowing ratio (a decrease in injectant mass flow rate) provides a poorer film coverage, which results in lower film effectiveness values.

Suction Surface (*Transition Region*). The blowing ratio of 0.4 provides the best film coverage for air injection, followed by 0.8 and 1.2. This is because the blowing ratio of 0.4 produces the earliest and shortest transition (see Fig. 9 in Part I) which results in more mixing within the boundary layer. This results in the highest film effectiveness for the blowing ratio in the transition region. As for the heat transfer coefficient case, an increase in blowing ratio results in a decrease in film effectiveness. The blowing ratio of 0.8 provides the best film coverage for CO_2 injection, followed by 1.2 and 0.4. This is because the blowing ratio of 0.8 produces the most mixing within the boundary layer and hence the highest heat transfer coefficients (see Fig. 9 in Part I). This results in the highest film effectiveness at the blowing ratio of 0.8 in the transition region. As seen from Fig. 9 in Part I, the blowing ratio of 0.4 produces the least mixing and hence least film effectiveness.

Combined Unsteady Wake and Film Injection Effect. The effect of wake Strouhal number on spanwise-averaged film effectiveness distribution for air and CO_2 injections at the blowing ratios of 0.4, 0.8, and 1.2 is shown in Figs. 4, 5, and 6, respectively. The effect of unsteady wake, in addition to film injection is depicted in these figures.

Pressure Surface. In general, as the wake Strouhal number increases, the unsteady flow fluctuations disrupt the film coverage, which results in lower film effectiveness values. For CO_2 and air injections, the decreases in film effectiveness from the no wake case, due to unsteady wake, are more at the blowing ratios of 1.2 and 0.8, respectively. Since the blowing ratio of 1.2 provides the best film coverage for CO_2 injection under the no wake condition, any boundary layer disturbance results in much lower film effectiveness values. For the same reason, the effect of unsteady wake is more at the blowing ratio of 0.8 for air injection. For reasons previously explained, CO_2 injection provides higher film effectiveness than air injection at the blowing ratio of 1.2; however, the effect is reversed at the blowing ratio of 0.8 for air injection. CO_2 injection seems to provide slightly higher film effectiveness values than air injection at the blowing ratio of 0.4.

Suction Surface (*Except Transition Region*). In general, as the wake Strouhal number increases, the unsteady flow fluctuations disrupt the film coverage, which results in lower film effectiveness values. The decreases in film effectiveness due to unsteady wake (from the no wake case) are more at the blowing ratios of 1.2 and 0.8 for CO_2 and air injections, respectively. This behavior is the same as that observed on the pressure surface for similar reasons. CO_2 injection provides higher film effectiveness than air injection at the blowing ratio of 1.2; however, the effect is reversed at the blowing ratio of 0.4. Because CO_2 provides optimum film coverage at the blowing ratio of 1.2, and since the momentum flux ratio for air injection at that blowing ratio is very high, the above-mentioned effect is observed. At the low blowing ratio of 0.4, the injection jet for CO_2 injection has a very small momentum flux ratio making the jet very weak. Hence, air injection at the blowing ratio of 0.4 provides higher film effectiveness values than CO_2 injection. This is consistent with the observations of Ito et al. (1978) and Haas et al. (1992).

Suction Surface (Transition Region). In general, as the wake Strouhal number increases, the unsteady flow fluctuations disrupt the film coverage, which results in lower film effectiveness values. CO_2 injection provides higher film effectiveness values than air injection at the blowing ratio of 1.2; however, the effect is reversed at the blowing ratio of 0.4. These trends are the same as on the rest of the suction surface.

Heat Transfer

Since the objective of film injection is to reduce the heat transfer (heat load) to a gas turbine component, heat loads with film injection and for no film holes case should be compared. The required analysis is explained below.

For a heated model blade without film holes, the local forced convection heat flux is given by

$$g''_o = h_o(T_w - T_\infty) \tag{4}$$

where q''_o is the local forced convective heat flux (heat load) for the no film holes case, h_o is the local forced convection heat transfer coefficient for the no film holes case, T_w is the local heated wall temperature, and T_∞ is the ambient mainstream temperature.

For a model blade with film injection, the local forced convection heat flux is given by

$$q'' = h(T_w - T_f) \tag{5}$$

where q'' is the local forced convective heat flux (heat load) with film injection, h is the local forced convection heat transfer coefficient with film injection, T_w is the local heated wall temperature, and T_f is the local film temperature due to the mixing of injection jet and mainstream.

The local heat flux ratio (heat load ratio) is then given by

$$\frac{q''}{q''_o} = \frac{h}{h_o}\,\frac{(T_w - T_f)}{(T_w - T_\infty)} \tag{6}$$

where a heat flux ratio of less than unity indicates that film injection reduces the surface heat load over the no film holes case.

Since it is very difficult to determine the local film temperature for a real gas turbine blade, Eq. (1) can be used to substitute for the film temperature. Equation (6) can then be rewritten as

$$\frac{q''}{q''_o} = \frac{h}{h_o}\left(1 - \frac{\eta(x, z)}{\phi}\right) \tag{7}$$

where η is the local film effectiveness, and ϕ is the overall cooling effectiveness given by $\phi = (T_w - T_\infty)/(T_s - T_\infty)$. For gas turbine blades, the value of ϕ usually ranges from 0.5 to 0.7.

Spanwise-averaged heat flux ratio was then obtained from

$$\frac{\overline{q}''}{\overline{q}''_o} = \frac{1}{n}\sum_{i=1}^{n}\frac{h(x, z_i)}{h_o(x, z_i)}\left(1 - \frac{\eta(x, z_i)}{\phi}\right) \tag{8}$$

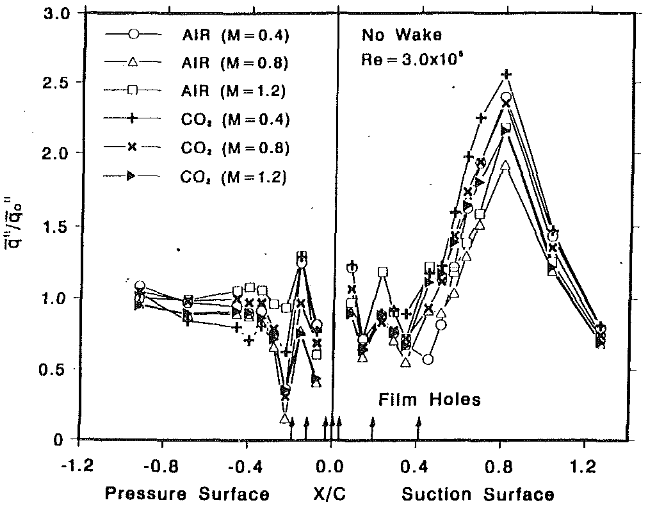

Fig. 7 Effect of air or CO_2 injection on spanwise-averaged heat transfer for the no wake condition

where $\overline{q}''$ is the spanwise-averaged forced convective heat flux with film injection at any streamwise location x, $\overline{q}''_o$ is the spanwise-averaged forced convective heat flux for the no film holes case at the same streamwise location x, n is the number of thermocouples in the row at the same streamwise location x, z is the spanwise dimension, and ϕ is the overall cooling effectiveness. A typical value of 0.6 was chosen for ϕ. This analysis is the same as in Mick and Mayle (1988) and Mehendale and Han (1992).

Film Injection Effect. The effect of film injection on spanwise-averaged heat transfer distribution ($\overline{q}''/\overline{q}''_o$) for air and CO_2 injections is shown in Fig. 7. This figure depicts only the effect of blowing ratio, i.e., for the no wake condition. From definition, it appears that film injection would be counterproductive if the heat load ratio is greater than unity. Although this may be true near the film holes, it is not necessarily true on the suction surface where transition occurs earlier due to film injection compared to without film holes case. Heat load near the film holes is higher by about 25 percent over the no film holes case. Downstream of the transition region, heat load ratios are much higher than unity. This trend is seen for both density ratio injectants at all blowing ratios. This is because (as observed in Part I) film injection by itself is capable of considerably increasing the heat transfer coefficients at some locations, while the film effectiveness values there are not that high as observed earlier in this paper. In general, the blowing ratios of 1.2 and 0.8 provide relatively lower heat load ratios over most of the blade surface for CO_2 and air injections, respectively.

Pressure Surface. Film injection provides lower heat loads than the no film holes case over most of the surface, except downstream of the film holes where they can be up to 25 percent higher than the no film holes case. Heat load ratios immediately downstream of the film holes are high because the heat transfer coefficients immediately downstream of the film holes are high (as seen from Part I), but film effectiveness values are higher a little farther downstream of the film holes. In general, the blowing ratios of 1.2 and 0.8 seem to provide the lowest heat load ratios for CO_2 and air injections, respectively. This is because, for the CO_2 and air injections, the blowing ratios of 1.2 and 0.8, respectively, provide the best film effectiveness values.

Suction Surface (Except Transition Region). The blowing ratios of 1.2 and 0.8 provide the lowest heat load ratios over most of the surface for air and CO_2 injections, respectively.

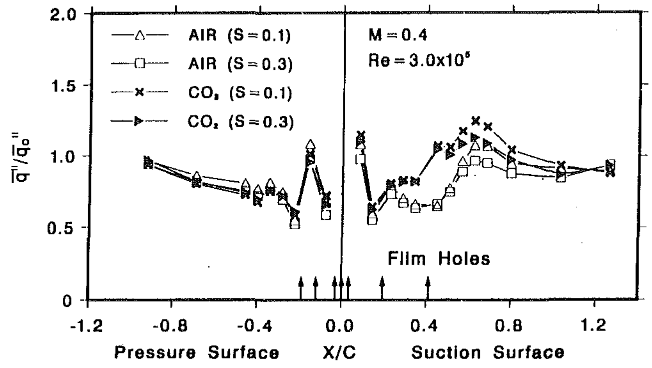

Fig. 8 Effect of unsteady wake and air or CO_2 injection on spanwise-averaged heat transfer for $M = 0.4$

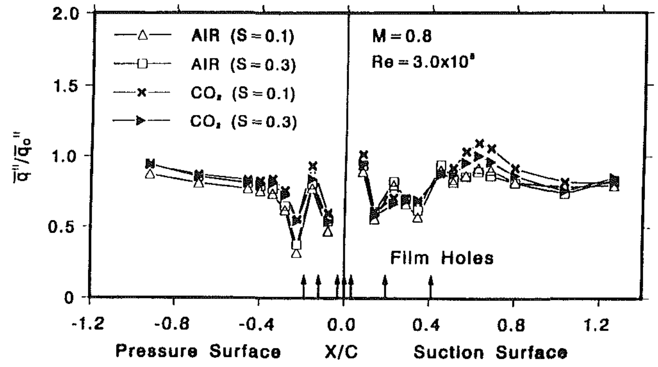

Fig. 9 Effect of unsteady wake and air or CO_2 injection on spanwise-averaged heat transfer for $M = 0.8$

Heat loads over 40 percent of the surface are reduced below those for the no film holes case. Heat loads increase just downstream of the film holes for the same reasons given before. Heat loads downstream of the transition region are substantially high as previously discussed.

Suction Surface (*Transition Region*). For CO_2 injection, the blowing ratio of 0.8 provides the lowest heat load ratios followed by 1.2, whereas, for air injection, the blowing ratio of 0.4 provides the lowest heat load ratios followed by 0.8. This is because, as seen from Fig. 9 of Part I, the heat transfer coefficients for CO_2 injection are almost equal but the blowing ratio of 0.8 provides the best film effectiveness in this region.

Combined Unsteady Wake and Film Injection Effect. The effect of wake Strouhal number on spanwise-averaged heat transfer distribution ($\bar{q}''/\bar{q}_o''$) at the blowing ratios of 0.4, 0.8, and 1.2 is shown in Figs. 8, 9, and 10, respectively. The effect of unsteady wake, in addition to film injection, is depicted in these figures. Since the no wake data are of lesser importance they have been omitted from these figures. It should be kept in mind that a heat load ratio of greater than unity is counterproductive. An increase in the wake Strouhal number actually causes lower heat load ratios. This is because the heat load ratio is defined as q''/q_o'', and as the wake Strouhal number increases, the denominator increases more than the numerator. (It was pointed out in Part I that the effect of increased unsteady wake is severe on the no film holes case but is only secondary on the film injection case.)

Pressure Surface. Heat load ratios at the blowing ratio of 0.4 are less than unity over most of the surface. Similar trends are seen at the other two blowing ratios of 0.8 and 1.2, except the heat load ratios are less than unity over the entire surface.

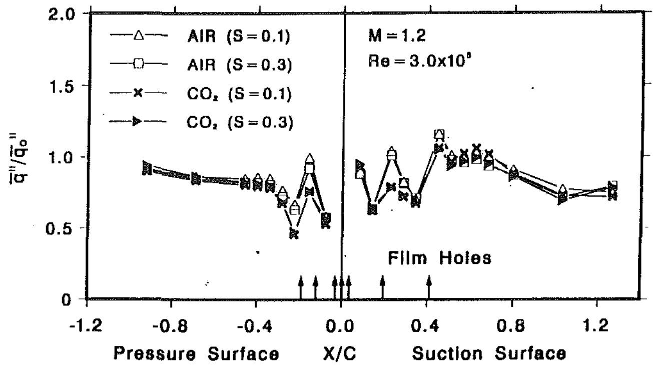

Fig. 10 Effect of unsteady wake and air or CO_2 injection on spanwise-averaged heat transfer for $M = 1.2$

Both air and CO_2 injections show similar values of heat load ratios at the blowing ratio of 0.4. At the blowing ratio of 0.8, air injection shows slightly lower heat load ratios than CO_2 injection. At the blowing ratio of 1.2, CO_2 injection provides lower heat load ratios than air injection.

Suction Surface (*Except Transition Region*). Heat load ratios at the blowing ratio of 0.4 are less than unity over most of the surface, except in the leading edge region where the heat transfer coefficients are very high but the film effectiveness values are very low. Similar trends are observed at higher blowing ratios. CO_2 injection provides lower heat load ratios than air injection at the blowing ratio of 1.2; however, the effect is reversed at the blowing ratio of 0.4.

Suction Surface (*Transition Region*). The effect of wake Strouhal number is more prominent at the low blowing ratio of 0.4. This effect reduces for both injectants as the blowing ratio increases. CO_2 injection provides lower heat load ratios than air injection at the blowing ratio of 1.2. An increase in blowing ratio causes a reduction in heat load ratios for CO_2 injection. At the blowing ratio of 0.4, air injection provides lower heat load ratios than CO_2 injection. This is due to CO_2 injection having much lower film effectiveness than air injection at that blowing ratio.

Note

The effect of property difference between the higher density ratio injectant (CO_2) and the lower density ratio injectant (air) are considered here. The specific heat of CO_2 is 14 percent lower than that of air. As shown by Han and Mehendale (1986), this can make the film effectiveness values for CO_2 injection as much as 14 percent lower depending on the local CO_2 concentration in the boundary layer. Hence, the film effectiveness values reported in this paper are conservative. In reality, for the same density ratio injectant as CO_2 but without other property effects, higher values of film effectiveness and lower heat load ratios are expected.

Concluding Remarks

The effect of upstream unsteady wake on film effectiveness and heat transfer distributions of a model turbine blade in a liner cascade was investigated. A spoked wheel type wake generator was used. Tests were performed at the chord Reynolds number of 3×10^5 for the no wake case, and at the wake Strouhal numbers of 0.1 and 0.3. Air (D.R. = 0.97) and CO_2 (D.R. = 1.48) were used as injectants at the blowing ratios of 0.4, 0.8, and 1.2.

The main findings are:

1 For the no wake condition, the blowing ratios of 1.2 and

0.8 provide the best film effectiveness over most of the blade surface for CO_2 and air injections, respectively. In the transition region on the suction surface, the blowing ratios of 0.8 and 0.4 provide the best film effectiveness for CO_2 and air injections, respectively.

2 When unsteady wake condition is imposed on top of film injection, the boundary layer is disturbed. An increase in wake Strouhal number causes a decrease in film effectiveness values over most of the blade surface for both density ratio injectants and at all blowing ratios.

3 On the pressure surface, CO_2 injection provides better film effectiveness than air injection at the blowing ratio of 1.2; however, the effect is reversed at the blowing ratio of 0.8. On the suction surface, CO_2 injection provides better film effectiveness than air injection at the blowing ratio of 1.2; however, the effect is reversed at the blowing ratio of 0.4.

4 For the no wake condition, both density ratio injectants at all blowing ratios produce heat load ratios much higher than unity downstream of the transition region on the suction surface. For CO_2 and air injections, the blowing ratios of 1.2 and 0.8, respectively, produce relatively lower heat loads.

5 When unsteady wake condition is imposed on top of film injection, a further reduction in heat load ratio (less than unity) is obtained over most of the blade surface. Downstream of the transition region heat loads are dramatically reduced to almost unity. CO_2 injection provides lower heat loads than air injection at the blowing ratio of 1.2; however, the effect is reversed at the blowing ratio of 0.4.

Under unsteady wake conditions, heat transfer on both suction and pressure surfaces with film injection is lower than that for without film holes. This agrees with Abhari and Epstein (1994), except they found the film cooling effect on pressure surface heat transfer is relatively small as compared to that on the suction surface.

Acknowledgments

The project was sponsored by the U.S. Naval Air Warfare Center through General Electric Aircraft Engines. The project managers for the Naval Air Warfare Center were Mr. M. Sautner and Mr. R. Petruska. Their support is greatly appreciated. Very special thanks are due to Mr. T. Thomas of General Electric Aircraft Engines for his suggestions and discussions throughout the project investigation.

References

Abhari, R. S., and Epstein, A. H., 1994, "An Experimental Study of Film Cooling in a Rotating Transonic Turbine," ASME Journal of Turbomachinery, Vol. 116, pp. 63-70.

Afejuku, W. O., Hay, N., and Lampard, D., 1980, "The Film Cooling Effectiveness of Double Rows of Holes," ASME *Journal of Engineering for Power*, Vol. 102, pp. 601-606.

Eriksen, V. L., and Goldstein, R. J., 1974, "Heat Transfer and Film Cooling Following Injection Through Inclined Circular Tubes," ASME *Journal of Heat Transfer*, Vol. 96, pp. 239-245.

Foster, N. W., and Lampard, D., 1980, "The Flow and Film Cooling Effectiveness Following Injection Through a Row of Holes," ASME *Journal of Engineering for Power*, Vol. 102, pp. 584-588.

Goldstein, R. J., 1971, "Film Cooling," *Advances in Heat Transfer*, Academic Press, New York.

Goldstein, R. J., Eckert, E. R. G., and Burggraf, F., 1974, "Effects of Hole Geometry and Density on Three-Dimensional Film Cooling," *International Journal of Heat and Mass Transfer*, Vol. 17, pp. 595-605.

Haas, W., Rodi, W., and Schönung, B., 1992, "The Influence of Density Difference Between Hot and Coolant Gas on Film Cooling by a Row of Holes: Predictions and Experiments," ASME Journal of Turbomachinery, Vol. 114, pp. 747-755.

Han, J. C., and Mehendale, A. B., 1986, "Flat Plate Film Cooling With Steam Injection Through One Row and Two Rows of Inclined Holes," ASME Journal of Turbomachinery, Vol. 108, pp. 137-144.

Han, J. C., Zhang, L., and Ou, S., 1993, "Influence of Unsteady Wake on Heat Transfer Coefficient From a Gas Turbine Blade," ASME *Journal of Heat Transfer*, Vol. 115, pp. 904-911.

Ito, S., Goldstein, R. J., and Eckert, E. R. G., 1978, "Film Cooling of a Gas Turbine Blade," ASME *Journal of Engineering for Power*, Vol. 100, pp. 476-481.

Jabbari, M. Y., and Goldstein, R. J., 1978, "Adiabatic Wall Temperature and Heat Transfer Downstream of Injection Through Two Rows of Holes," ASME *Journal of Engineering for Power*, Vol. 100, pp. 303-307.

Kine, S. J., and McClintock, F. A., 1953, "Describing Uncertainties in Single-Sample Experiments," *Mechanical Engineering*, Vol. 75, Jan., pp. 3-8.

Ko, S. Y., Xu, Y. Z., Yao, Y. Q., and Tsou, F. K., 1984, "Film Cooling Effectiveness and Turbulence Distribution of Discrete Holes on a Convex Surface," *International Journal of Heat and Mass Transfer*, Vol. 27, pp. 1551-1557.

Mehendale, A. B., and Han, J. C., 1992, "Influence of High Mainstream Turbulence on Leading Edge Film Cooling Heat Transfer," ASME Journal of Turbomachinery, Vol. 114, pp. 707-715.

Mick, W. J., and Mayle, R. E., 1988, "Stagnation Film Cooling and Heat Transfer, Including Its Effect Within the Hole Pattern," ASME Journal of Turbomachinery, Vol. 110, pp. 66-72.

Muska, J. F., Fish, R. W., and Suo, M., 1976, "The Additive Nature of Film Cooling From Rows of Holes," ASME *Journal of Engineering for Power*, Vol. 98, pp. 457-464.

O'Brien, J. E., and Capp, S. P., 1989, "Two-Component Phase-Averaged Turbulence Statistics Downstream of a Rotating Spoked-Wheel Wake Generator," ASME Journal of Turbomachinery, Vol. 111, pp. 475-482.

Ou, S., and Han, J. C., 1992, "Influence of Mainstream Turbulence on Leading Edge Film Cooling Heat Transfer Through Two Rows of Inclined Film Slots," ASME Journal of Turbomachinery, Vol. 114, pp. 724-733.

Ou, S., Han, J. C., Mehendale, A. B., and Lee, C. P., 1994, "Unsteady Wake Over a Linear Turbine Blade Cascade With Air and CO_2 Film Injection: Part I—Effect on Heat Transfer Coefficients," ASME Journal of Turbomachinery, Vol. 116, this issue, pp. 721-729.

Pedersen, D. R., Eckert, E. R. G., and Goldstein, R. J., 1977, "Film Cooling With Large Density Differences Between the Mainstream and the Secondary Fluid Measured by the Heat-Mass Transfer Analogy," ASME *Journal of Heat Transfer*, Vol. 99, pp. 620-627.

Sautner, M., Clouser, S., and Han, J. C., 1992, "Determination of Turbine Blade Heat Transfer and Film Cooling Effectiveness in Unsteady Wake Flow Conditions," presented at AGARD 80th Symposium, Heat Transfer and Cooling in Gas Turbines, Oct., Anatalya, Turkey, Paper No. 6.

Schönung, B., and Rodi, W., 1987, "Prediction of Film Cooling by a Row of Holes With a Two-Dimensional Procedure," ASME Journal of Turbomachinery, Vol. 109, pp. 579-587.

Schwarz, S. G., Goldstein, R. J., and Eckert, E. R. G., 1991, "The Influence of Curvature on Film Cooling Performance," ASME Journal of Turbomachinery, Vol. 113, pp. 472-478.

Sinha, A. K., Bogard, D. G., and Crawford, M. E., 1991, "Film-Cooling Effectiveness Downstream of a Single Row of Holes With Variable Density Ratio," ASME Journal of Turbomachinery, Vol. 113, pp. 442-449.

Takeishi, K., Aoki, S., Sato, T., and Tsukagoshi, K., 1992, "Film Cooling on a Gas Turbine Rotor Blade," ASME Journal of Turbomachinery, Vol. 114, pp. 828-834.

Teekaram, A. J. H., Forth, C. J. P., and Jones, T. V., 1989, "The Use of Foreign Gas to Simulate the Effect of Density Ratios in Film Cooling," ASME Journal of Turbomachinery, Vol. 111, pp. 57-62.

Heat Transfer in Rotating Serpentine Passages With Selected Model Orientations for Smooth or Skewed Trip Walls

B. V. Johnson

J. H. Wagner

United Technologies Research Center,
East Hartford, CT 06108

G. D. Steuber

Pratt & Whitney,
East Hartford, CT 06108

F. C. Yeh

Lewis Research Center,
National Aeronautics and
Space Administration,
Cleveland, OH 44135

Experiments were conducted to determine the effects of model orientation as well as buoyancy and Coriolis forces on heat transfer in turbine blade internal coolant passages. Turbine blades have internal coolant passage surfaces at the leading and trailing edges of the airfoil with surfaces at angles that are as large as ±50 to 60 deg to the axis of rotation. Most of the previously presented, multiple-passage, rotating heat transfer experiments have focused on radial passages aligned with the axis of rotation. The present work compares results from serpentine passages with orientations 0 and 45 deg to the axis of rotation, which simulate the coolant passages for the midchord and trailing edge regions of the rotating airfoil. The experiments were conducted with rotation in both directions to simulate serpentine coolant passages with the rearward flow of coolant or with the forward flow of coolant. The experiments were conducted for passages with smooth surfaces and with 45 deg trips adjacent to airfoil surfaces for the radial portion of the serpentine passages. At a typical flow condition, the heat transfer on the leading surfaces for flow outward in the first passage with smooth walls was twice as much for the model at 45 deg compared to the model at 0 deg. However, the differences for the other passages and with trips were less. In addition, the effects of buoyancy and Coriolis forces on heat transfer in the rotating passage were decreased with the model at 45 deg, compared to the results at 0 deg. The heat transfer in the turn regions and immediately downstream of the turns in the second passage with flow inward and in the third passage with flow outward was also a function of model orientation with differences as large as 40 to 50 percent occurring between the model orientations with forward flow and rearward flow of coolant.

Introduction

Advanced gas turbine airfoils are subjected to high heat loads that require escalating cooling requirements to satisfy airfoil life goals. The efficient management of cooling air dictates detailed knowledge of local heat load and cooling air flow distribution for temperature and life predictions. However, predictions of heat transfer and pressure loss in airfoil coolant passages currently rely primarily on correlations derived from the results of stationary experiments. Adjustment factors are usually applied to these correlations to bring them into nominal correspondence with engine experience. This is unsatisfactory when blade cooling conditions for new designs lie outside the range of previous experience.

Rotation of turbine blade cooling passages gives rise to Coriolis and buoyancy forces, which can significantly alter the local heat transfer in the internal coolant passages due to the development of cross-stream (Coriolis) as well as radial (buoyant) secondary flows. Buoyancy forces in gas turbine blades are substantial because of the high rotational speeds and coolant temperature gradients. Earlier investigations (Eckert et al., 1953) with stationary, single pass, co- and counterflowing coolant passages indicated that there can also be substantial differences in the heat transfer when the buoyancy forces are aligned with or counter to the forced convection direction. A better understanding of Coriolis and buoyancy effects and the capability to predict the heat transfer response to these effects will allow the turbine blade designer to achieve cooling configurations that utilize less flow and reduce thermal stresses in the airfoil.

An extensive analytical and experimental program was originated and sponsored by NASA at the Lewis Research Center as part of the Hot Section Technology (HOST) program. The objectives of this program were (1) to gain insight regarding the effect of rotation on heat transfer in turbine blade passages, (2) to develop a broad data base for heat transfer and pressure drop in rotating coolant passages, and (3) to improve computational techniques and develop correlations that can be

---

Contributed by the International Gas Turbine Institute and presented at the 38th International Gas Turbine and Aeroengine Congress and Exposition, Cincinnati, Ohio, May 24–27, 1993. Manuscript received at ASME Headquarters March 12, 1993. Paper No. 93-GT-305. Associate Technical Editor: H. Lukas.

useful to the gas turbine industry for turbine blade design. The attainment of these objectives became even more critical with the advent of the Integrated High Performance Turbine Engine Technology (IHPTET) initiative. As part of the IHPTET goal, the turbine would operate at near stoichiometric, i.e., 2200–2500 K (3500–4000°F) inlet temperatures, maintain efficiencies in the 88–94 percent range, and require total coolant flows of only 4 to 6 percent of the engine air flow rate (Ref. IHPTET Brochure, Circa 1984). To attain these ambitious goals, a thorough understanding of the rotational effects of heat transfer and flow in turbine blade coolant passages is mandatory.

Previous Studies. Heat transfer in rotating radial internal coolant passages, typical of turbine airfoils of large gas turbine aircraft engines, has been investigated experimentally and analytically for the past ten to fifteen years. The experimental studies have been sponsored by national and private laboratories (e.g., USA/NASA, USSR, UK/RAE, France, Germany/DLR, Japan, Taiwan, and USA/EPRI) and the large gas turbine manufacturers (e.g., PW, GE, and RR). The pioneering studies were reported by Morris (1981). More recent studies up to 1991, with a wider range of flow and geometric parameters, are reported in the authors' previous papers (Wagner et al., 1991a, b; Johnson et al., 1992), and in NASA contractors reports (Hajek et al., 1991; Johnson et al., 1993). Other recent references include Han et al. 1994), El-Husayni et al. (1994), and Mochizuki et al. (1994) and contain most references from the studies sponsored by GE, EPRI, and RAE. The results from these studies are bringing an understanding to the turbine blade durability designer of the many phenomena in rotating radial coolant passages including the flow parameters: Reynolds number, rotation wall-to-bulk density ratio, buoyancy parameter and the many geometric parameters including trip geometry, passage aspect ratio and inward or outward flow direction. One important aspect of flow and heat transfer that has not been explored is the effect of multiple coolant passage orientations with respect to the axis of rotation.

Objectives. Under the NASA Host program, a comprehensive experimental project was formulated to identify and separate effects of Coriolis and buoyancy forces for the range of dimensionless flow parameters encountered in axial flow, aircraft gas turbines. The specific objective of this experimental project was to acquire and correlate benchmark-quality heat transfer data for a multipass, coolant passage under conditions similar to those experienced in the blades of advanced aircraft gas turbines. A comprehensive test matrix was formulated, encompassing the range of Reynolds numbers, rotation numbers, and density ratios expected in modern gas turbine engines.

The results presented in this paper were obtained during the first and third phases of a three-phase program directed at studying the effects of rotation on a multipass model with smooth and rough wall configurations. The first phase utilized the smooth wall configuration. Initial results for outward flow in the first passage were previously presented by Wagner et al. (1991a). The effects of flow direction and buoyancy with smooth walls were presented by Wagner et al. (1991b). The second phase utilized a configuration with normal trips on the leading and trailing surfaces of the straight passages and was presented by Wagner et al. (1992). Results from the third phase had skewed surface roughness elements oriented at 45 deg to the flow direction (Johnson et al., 1992). Only a cursory discussion of the effects of rotating the plane of the serpentine passages was included in one previous paper.

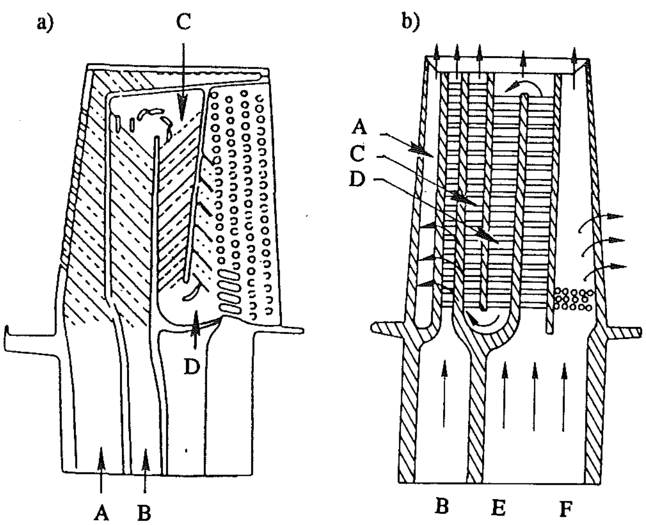

Fig. 1 Typical turbine blade internal coolant configurations: (*a*) rearward flow of coolant (Johnson et al., 1992), (*b*) forward flow of coolant (Han et al., 1986)

The present work is focused on the effects of the orientation of the plane of model passages on heat transfer in rotating, near-radial coolant passages. The results in this paper will be related to previous results from the NASA HOST/UTC experiments and to design consideration for the internal cooling passages at the leading or trailing regions of rotating blades.

Model

Sketches of two multiple-pass coolant passage configurations for turbine blades (Han et al., 1986; Johnson et al., 1994) are shown in Fig. 1. In the Fig. 1(*a*) configuration, the coolant flows radially outward through the center passage (*B*) and radially inward through the third passage (*C*), discharging through a fourth partial passage (*D*) and an array of pedestals. In the Fig. 1(*b*) configuration the colant in the multiple pass portion of the blade flows radially outward in passage *E*,

Nomenclature

A = area of passage cross section
d = hydraulic diameter
e = trip height
h = heat transfer coefficient
k = thermal conductivity
m = mass flow rate
Nu = Nusselt number = hd/k
N_∞ = Nusselt number for fully developed flow in smooth tube with $\mathrm{Pr}=0.72$; $\mathrm{Nu}_\infty=0.0176\ \mathrm{Re}^{0.8}$

R = local radius
Re = Reynolds number = $(md)/(\mu A)$
Ro = rotation number = $\Omega d/V$
V = mean coolant velocity
X = streamwise distance from inlet
μ = absolute viscosity
ρ = coolant density
$\Delta\rho/\rho$ = density ratio = $(\rho_b-\rho_w)/\rho_b$

Subscripts

b = bulk property
f = film property
i = inlet to model
w = heated surface location

Superscripts

$\bar{}$ = average
$'$ = distance from beginning of second passage
$''$ = distance from beginning of third passage

a) Blade With Foward Flowing Coolant

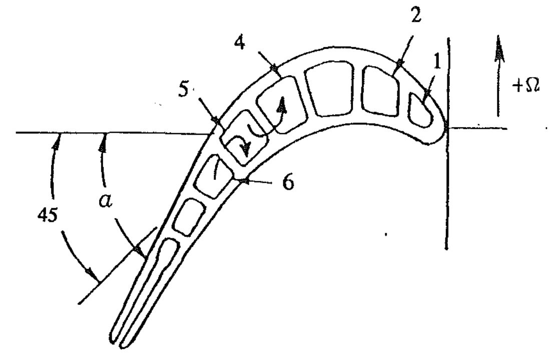

b) Heat Transfer Model

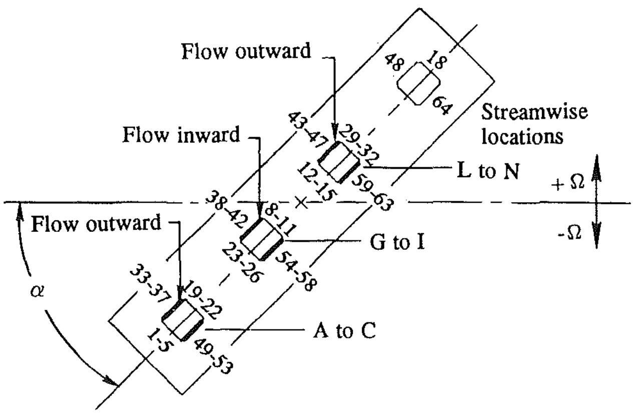

c) Blade With Rearward Flowing Coolant

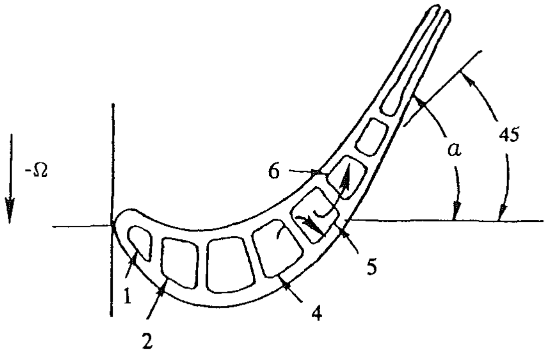

Fig. 2 Sketches of model and blade coolant passage cross sections viewed from root of blades and models; coolant passages superimposed upon UTRC LSRR turbine blade (Dring et al., 1981)

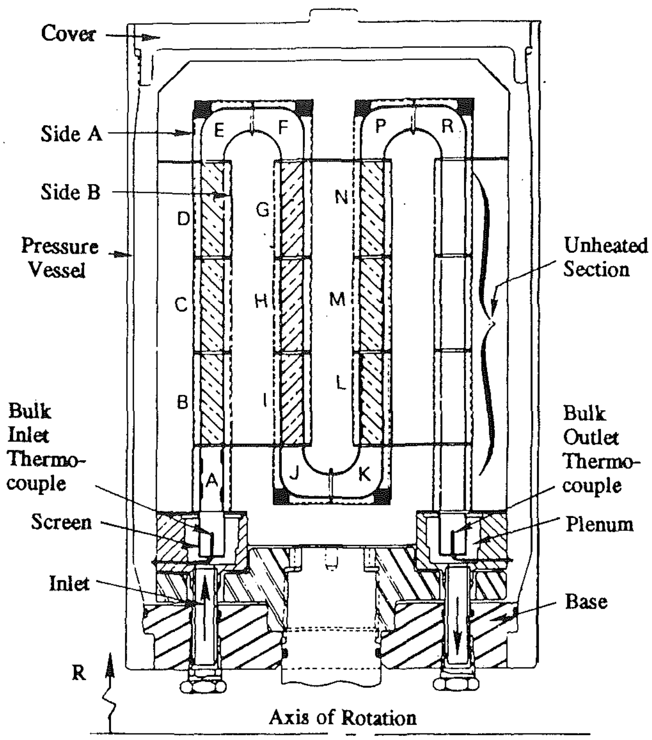

Fig. 3 Cross-sectional view of coolant passage heat transfer model assembly with skewed trip rough walls: view through center of model toward leading surfaces with $\Omega > 0$; dotted ribs show locations on the trailing surfaces

forward toward the leading portion of the blade and radially inward in passage *D* and further forward and radially outward in passage *C*. In the Fig. 1(*b*) configuration, the coolant from the multipass array leaves the blade through the tip. The coolant could also be discharged from passage *C* through film cooling holes.

Experiments were conducted with the plane of the coolant passage centerlines through the axis of rotation ($\alpha = 0$) and with the plane at a 45 deg angle to the axis of rotation ($\alpha = 45$ deg) as shown in Fig. 2(*b*). The model was rotated forward ($+\Omega$) and backward ($-\Omega$) as shown in Fig. 2(*b*). When the model is rotated forward with $\alpha = 45$ deg, the model passages correspond to the blade coolant passages shown in Fig. 2(*a*). Passages 6, 5, and 4 (Fig. 2*a*) form a three-legged serpentine coolant path in the blade. The coolant flows outward in Passage 6, inward in Passage 5, and outward in Passage 4. This set of passages corresponds to the forward flow of coolant in Passages *E*, *D*, and *C* (Fig. 1*b*) and the first, second, and third legs of the serpentine heat transfer model shown in Figs. 2(*b*) and 3. When the model is rotated backward ($-\Omega$) with $\alpha = 45$ deg, the model passages correspond to the blade coolant passage shown in Fig. 2(*c*). Passages 4, 5, and 6 (Fig. 2*c*) form a rearward-flowing coolant path in the blade corresponding to Passages *B*, *C*, and *D* of Fig. 1(*a*). Although the flow and heat transfer in the developed portions of each coolant passage (Locations *D*, *I*, and *N* of Fig. 3) are not expected to be affected by the change in the direction of model rotation, the flow and heat transfer in the turn regions (Locations *E*, *F*, *J*, and *K* of Fig. 3) and the regions immediately downstream of the turns (Locations *G* and *L* of Fig. 3) will be affected to some degree.

The smooth wall and skewed trip heat transfer models employed in the study were those described by Wagner et al. (1991a,b) and Johnson et al. (1994), respectively. The model consisted of 0.5 in. square (with 0.045 in. chamfers in the corners) coolant passages with straight sections 6.0 in. long (e.g. combination of sections *B*, *C*, and *D*) as shown in Fig. 3. Each test surface section (64 total for each model) was machined from a copper bar, was heated with an individually controlled and metered power supply, and had two thermocouples installed. The test surfaces were thermally isolated from each other with 0.064 in. rigid fiberglass strips. The test section streamwise identification *A* through *R* (Fig. 3) and the wall and test section wall identification (Fig. 2*b*) will be used to identify the location of each heat transfer test section. Note that the heat transfer results from each copper test section segment are the average values over the identified test region.

The experimental procedures and uncertainties for the models with smooth walls and with skewed trips are the same as described by Wagner et al. (1991a,b) and Johnson et al. (1994).

Results

Baseline Flow Conditions. A set of parametric experiments

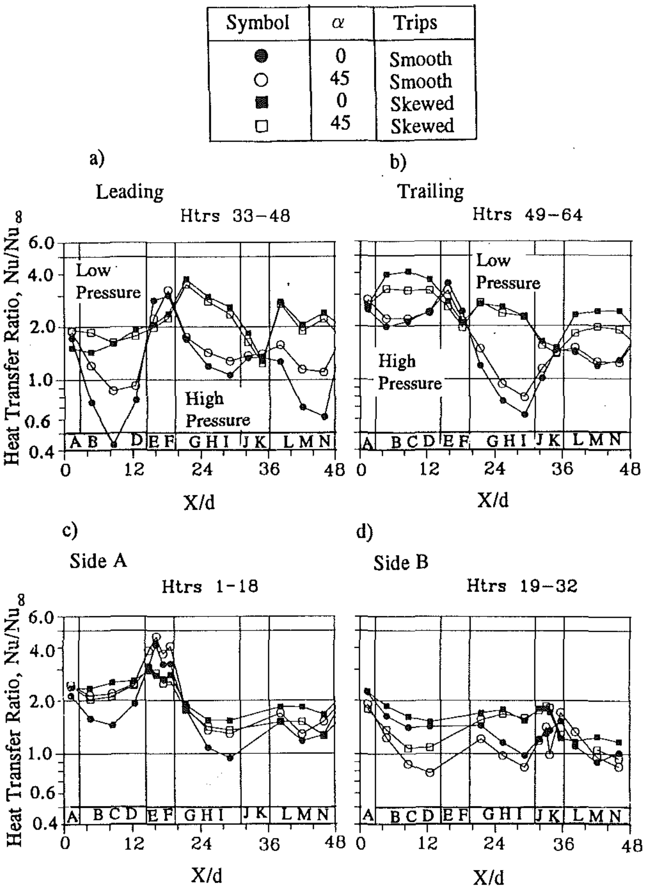

Symbol	α	Trips
●	0	Smooth
○	45	Smooth
■	0	Skewed
□	45	Skewed

Fig. 4 Comparison of heat transfer results for smooth and skewed trip walls at $\alpha = 0$ and 45 deg for baseline flow conditions; Re = 25,000, $Ro = 0.24$, $(\Delta\rho/\rho)_i = 0.13$, $R/d = 49$

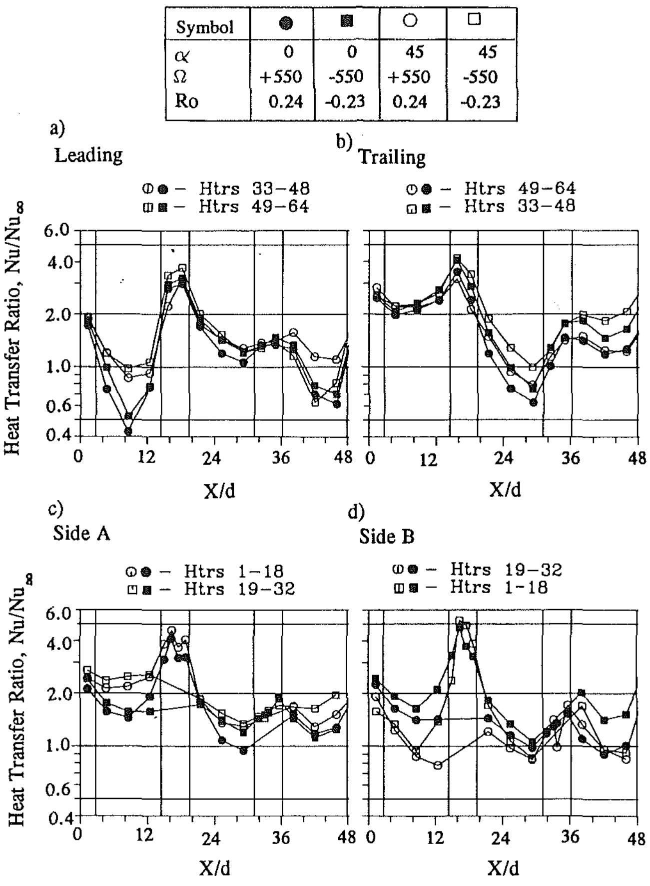

Symbol	●	■	○	□
α	0	0	45	45
Ω	+550	-550	+550	-550
Ro	0.24	-0.23	0.24	-0.23

Fig. 5 Effects of orientation and rotation direction on heat transfer ratio for smooth wall model; Re = 25,000, $\Delta T = 80°F$, $(\Delta\rho/\rho)_i = 0.13$

were conducted with the models described by Wagner et al. (1991a, 1992), and Johnson et al. (1994). The rotating baseline flow condition for all three models included a Reynolds number of 25,000, a rotation number of 0.24, a density ratio of 0.13, a geometric ratio ($\bar{R}/d$) of 52, and model orientation, α, of 0 deg. In our previous experiments, the use of a heat transfer ratio, Nu/Nu_∞, showed excellent correlation of the Reynolds number effects for Re = 25,000 and higher. Consequently, most of the previous parametric studies were conducted with Re = 25,000 and focused on the effects of the remaining flow parameters, i.e., Ro, $(\Delta\rho/\rho_b)_i$, and flow direction. The test conditions for the baseline flow condition were: $\Omega = 550$ rpm; $P_{in} = 148.5$ psia; $m = 0.013$ lb/sec; $T_{in} = 80°F$; $T_{wall} = 160°F$.

For the present study of the effects of model orientation, the Reynolds number was fixed at 25,000. The study was conducted with the smooth wall and skewed trip models at two orientations, $\alpha = 0$ and 45 deg. The model was rotated in the forward $(+\Omega)$ and backward $(-\Omega)$ direction with the smooth wall model and in the forward direction with the skewed trip model. The radius ratio had a constant value, $\bar{R}/d = 49$ with $d = 0.52$ in. (due to chamfered corners), for this study. The rotation number and the inlet density ratio were varied and the effects of flow direction were observed.

Comparisons for $\alpha = 0$ and 45 deg. A comparison of the heat transfer ratios for the smooth and skewed trip models and $\alpha = 0$ and +45 deg (Fig. 4) shows the differences for the two model orientations. For the smooth wall model, the largest differences occur in the first leg where the flow patterns are governed by Coriolis and buoyancy forces and less by the secondary flow from the turn regions. Note that for the leading segment defined for $\alpha = 0$ as "adjacent to the turbine blade airfoil suction surface," the minimum heat transfer ratio increased from 0.42 to 0.9 by a factor of two. When the $\alpha = 0$ side wall (Side *B*; Htr 19-32) is rotated and becomes a coleading surface (Fig. 4*b*), the heat transfer ratio decreases from 1.5 to 0.8, a factor of almost two. For the smooth wall model, the effects of model orientation are less severe in the second and third legs after the turn regions.

The absolute changes in the heat transfer ratio, i.e., $\Delta Nu/Nu_\infty$, for the skewed trip model are as large as for the smooth model. However, the percentage change is considerably less due to the higher values of heat transfer for $\alpha = 0$. The heat transfer ratio on the $(\alpha = 0)$ trailing surfaces of the first leg decreases from 4 to 3.2, approximately 20 percent. The same percentage decrease occurs in the third leg with flow also outward. The effect of model orientation has little effect in the second leg where the flow is inward. The absence of effects due to model orientation in the second leg is compatible with the previous studies for $\alpha = 0$ where the heat transfer in the second leg was also relatively insensitive to rotation and buoyancy effects.

Effects of Model Orientation and Rotation Direction for Smooth Wall Model. Experiments were conducted with the smooth wall model at $\alpha = 0$ and 45 deg to determine the model symmetry and the effects of the serpentine model orientation (Fig. 2). As expected, the differences in the heat transfer (Fig. 5) in the first leg for a constant α between $\Omega = +550$ and -550 rpm are small, of order 10 percent, because the flow has not developed asymmetries due to the turn regions and the model is essentially symmetric. The differences, both for $\alpha = 0$, $\Omega = \pm 550$ rpm and for $\alpha = 45$, $\Omega = \pm 550$ rpm, grow to 20 to 30 percent on the trailing side of the second leg and to 40 to 50 percent on both the leading and trailing side of the third

Symbol	○	□	▽	△	◇
Ro	0.00	0.12	0.18	0.24	0.35

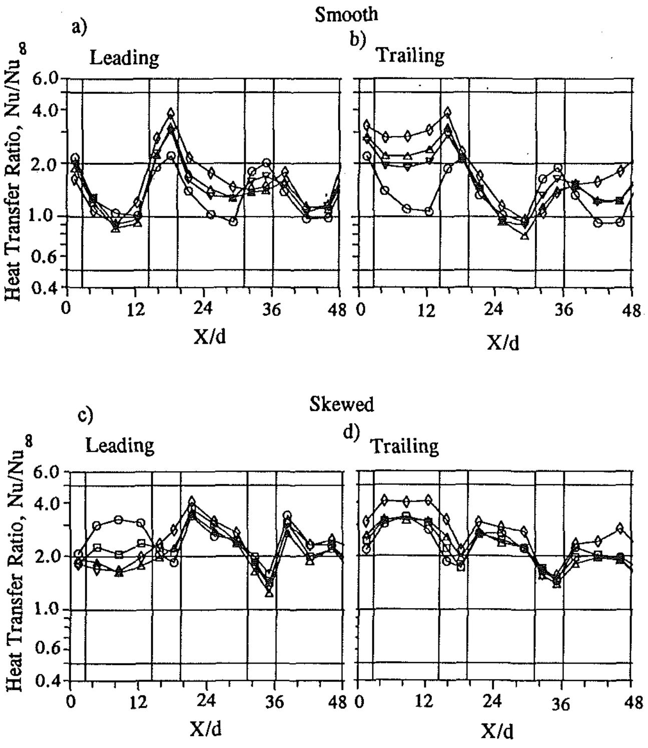

Fig. 6 Effects of rotation number on heat transfer of nominal leading and trailing surfaces for smooth and skewed trip walls for alpha equal $\alpha = 45$ deg; Re = 25,000, $\Delta T = 80°F$, $(\Delta\rho/\rho)_i = 0.13$

All test conditions standard except for α and $\Omega d/V$

Symbol	○	●	□	■	△	▲
α	0	45	0	45	0	45
$\Omega d/V$	0		0.24 std		0.36	

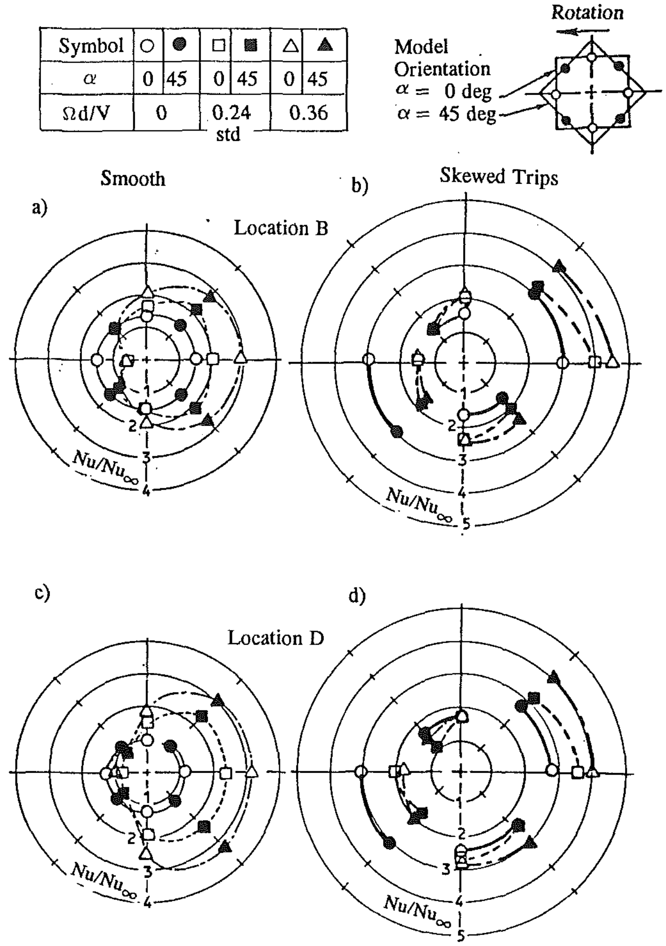

Fig. 7 Comparison of heat transfer results from first leg of smooth and rough wall models; $\Delta T = 80°F$, $(\Delta\rho/\rho)_i = 0.13$, Re = 25,000

legs. these differences are attributed to the differences in the secondary flow interactions through the first turn (outer turn) at $12 < x/D < 19$ and the second (inside turn) at $31 < x/D < 36$.

Effects of Rotation Number. The effects of rotation on heat transfer from the surfaces that would be adjacent to the leading and trailing surfaces of the airfoil for $\alpha = 45$ are presented in Fig. 6. For the smooth wall model (Figs. 6*a*, *b*), the largest effects occur on the high-pressure side of the coolant passage, i.e., trailing side for flow outward in the first and third legs and leading surface with flow inward in the second passage. For the skewed trip model (Figs. 6*c*, *d*), the largest effects of rotation occur on the leading side in the first passage. Note that for the highest value of the rotation number, $Ro = 0.35$, the heat transfer ratio is increased in all three legs on the trailing surface. These larger effects could be due to the increased influence of the buoyancy parameter, which tended to dominate at higher values of rotation for the skewed wall model compared to the smooth wall model (e.g., Johnson et al., 1994).

The results from the first leg of the smooth model at three rotation numbers (Figs. 7*a*, *c*) show symmetry as expected. Note that the heat transfer on the $\alpha = 0$ deg trailing surface or the $\alpha = 45$ deg trailing or trailing side wall surfaces is approximately the same and symmetric on either side of the $\alpha = 0$ results. Additionally, the average leading and leading-side-wall surfaces for $\alpha = 45$ deg have average heat transfer coefficients approximately the same as the $Ro = 0$ value.

The results from the first leg of the skewed trip model (Figs. 7*b*, *d*) are connected as shown because smooth ($\alpha = 0$ sidewalls) and skewed trip walls ($\alpha = 0$ leading and trailing walls) are adjacent to each other. The heat transfer on the leading surface ($\alpha = 0$) is decreased by a factor of two due to rotation (Johnson et al., 1994) for both the $\alpha = 0$ and 45 orientation. The heat transfer from the leading surface does not increase appreciably for the $\alpha = 45$ orientation as did the smooth wall model. At this time it is not known if an alternate skewed trip strip orientation (i.e., skewed the other direction) would alter this result.

Effects of Rotation and Inlet Density Ratio. The heat transfer ratio from the nominal leading and trailing downstream heat transfer surfaces are shown in Fig. 8 as a function of local rotation number with the inlet density ratio for each symbol noted. With the smooth wall model, the heat transfer ratio shows less effect of inlet density ratio for $\alpha = +45$ deg than for $\alpha = 0$ on the low-pressure surfaces (leading surface for flow out; trailing surface for flow in; Figs. 8*a*, *c*, *e*). As previously discussed for the smooth wall model, the most noticeable effects in terms of percentage change due to changes in rotation numbers for $\alpha = 0$ occur on the low pressure surfaces.

In previous papers from this series of NASA/HOST/UTC experiments, the results were also as correlated as a function of a buoyancy parameter. In the present study, the effects of buoyancy are less noticable and the presentation does not appear warranted.

Concluding Comments

Experimental results for smooth wall and skewed trip models with the plane through the center of the serpentine coolant passages orientated at 45 deg to the axis of rotation were related

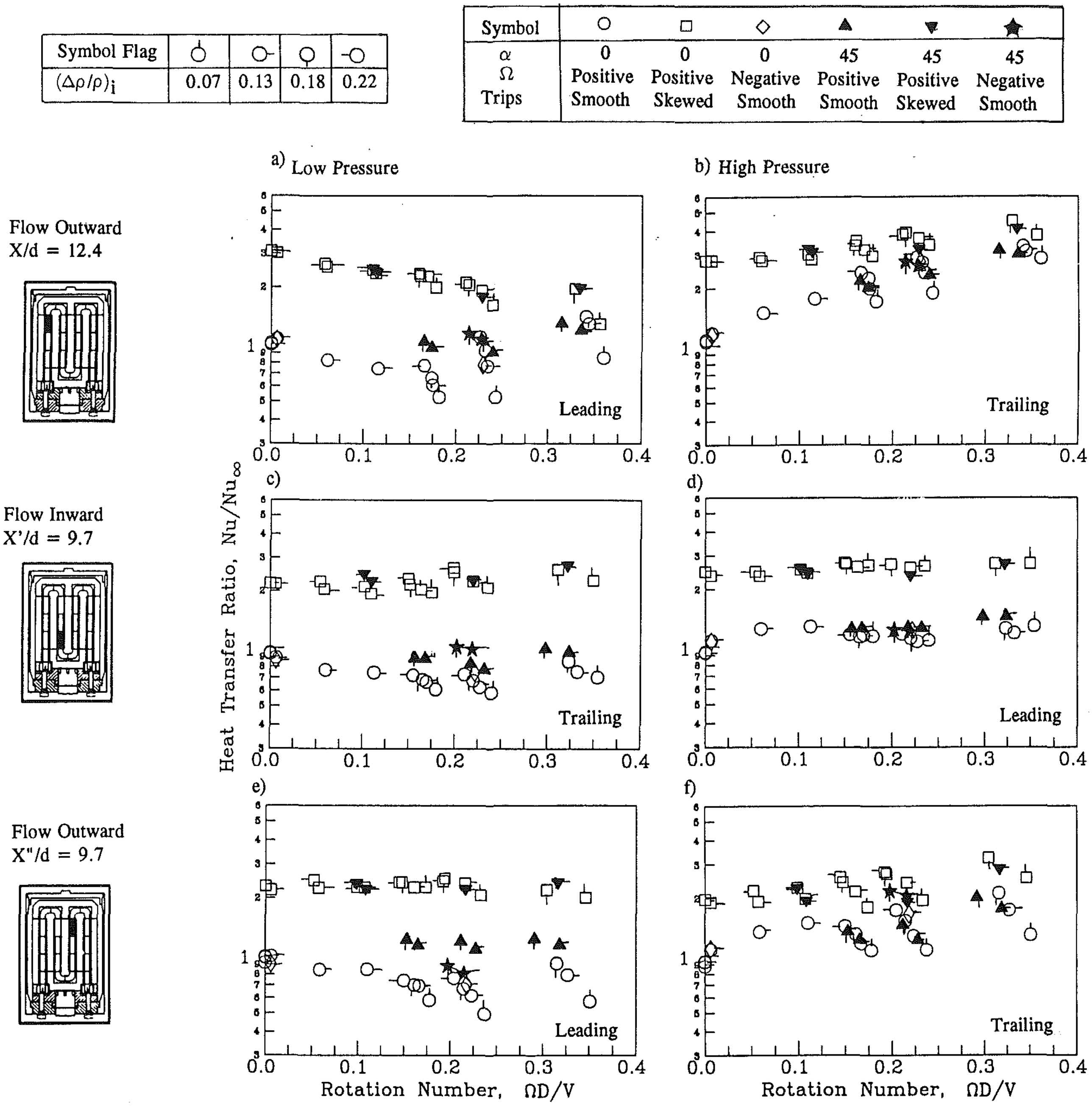

Symbol Flag	ȯ	○-	ọ	-○
$(\Delta\rho/\rho)_i$	0.07	0.13	0.18	0.22

Symbol	○	□	◇	▲	▼	★
α	0	0	0	45	45	45
Ω	Positive	Positive	Negative	Positive	Positive	Negative
Trips	Smooth	Skewed	Smooth	Smooth	Skewed	Smooth

Fig. 8 Effects of rotation number and inlet density ratio on heat transfer ratio; Re = 25,000, $R/d = 49$

to previous results (Wagner et al., 1991*a*, *b*; Johnson et al., 1994). These results are directly applicable to airfoil coolant passage geometries where the coolant passages walls adjacent to the airfoil surface are not parallel to the axis of rotation (Figs. 1 and 2).

The following are principal results and conclusions from this study:

- The largest fractional change in the heat transfer ratio due to model orientation occurred on the low-pressure side of the smooth wall model where the average heat transfer coefficient for each section was less sensitive to rotation at $\alpha = 45$ deg.
- The average heat transfer ratios for the developed-flow sections with skewed trips at $\alpha = +45$ deg were within 15 percent of those for the $\alpha = 0$ orientation.
- Variations of 20 to 50 percent in the heat transfer ratio were noted due to $\alpha = 45$ or 0 or to $+\Omega$ or $-\Omega$ orientations downstream of the turns before the flow became developed
- The effect of model orientation has little effect in the second leg where flow is inward.

Acknowledgments

The work published in this paper was supported by the NASA/Lewis Research Center under the HOST Program, Contract No. NAS3-23691 to the Pratt and Whitney Commercial Engine Business/Engineering Division and by the United Technology Corporation's independent research program. The authors gratefully acknowledge the assistance of Ms. S. Orr (UTRC) in the performance of this program. The authors are appreciative of the support and guidance by the HOST management team at NASA/Lewis Research Center and by their colleagues at P&W and UTRC.

References

Dring, R. P., Joslyn, H. D., Hardin, L. W., and Wagner, J. H., 1981, "Turbine Rotor Stator Interaction," ASME *Journal of Engineering for Power*, Vol. 106, pp. 729-742.

Eckert, E. R. G., Diaguila, A. J., and Curren, A. N., 1953, "Experiments on Mixed-Free and Forced-Convective Heat Transfer Connected With Turbulent Flow Through a Short Tube," NACA Technical Note 2973.

El-Husayni, H., A., Taslim, M. E., and Kercher, D. M., 1994, "Experimental Heat Transfer Investigation of Stationary and Orthoganally Rotating Asymmetric and Symmetric Heated Smooth and Turbulated Channels," ASME JOURNAL OF TURBOMACHINERY, Vol. 116, pp. 124-132.

Guidez, J., 1989, "Study of the Convective Heat Transfer in Rotating Coolant Channel," ASME JOURNAL OF TURBOMACHINERY, Vol. 111, pp. 43-50.

Hajek, T. J., Wagner, J. H., Johnson, B. V., Higgens, A. W., and Steuber, G. D., 1991, "Effects of Rotation on Coolant Passage Heat Transfer: Vol. I—Coolant Passages with Smooth Walls," NASA Contractor's Report 4396.

Han, J. C., Park, J. S., and Ibrahim, M. Y., 1986, "Measurement of Heat Transfer and Pressure Drop in Rectangular Channels With Turbulence Promoters," NASA Contractors Report 4015.

Han, J. C., Zhang, Y. M., and Lee, C. P., 1994, "Influence of Surface Heating Condition on Local Heat Transfer in a Rotating Square Channel With Smooth Walls and Radial Outward Flow," ASME JOURNAL OF TURBOMACHINERY, Vol. 116, pp. 149-158.

Johnson, B. V., Wagner, J. H., and Steuber, G. D., 1993, "Effect of Rotation on Coolant Passage Heat Transfer: Vol. II—Coolant Passages With Trips Normal and Skew to the Flow," NASA Contractor's Report 4396.

Johnson, B. V., Wagner, J. H., Steuber, G. D., and Yeh, F. C., 1994, "Heat Transfer in Rotating Serpentine Passages With Trips Skewed to the Flow," ASME JOURNAL OF TURBOMACHINERY, Vol. 116, pp. 113-123.

Mochizuki, S., Takamura, J., Yamawaki, S., and Yang, W.-J., 1994, "Heat Transfer in Serpentine Flow Passages With Rotation," ASME JOURNAL OF TURBOMACHINERY, Vol. 116, pp. 133-140.

Morris, W. D., 1981, *Heat Transfer and Fluid Flow in Rotating Coolant Channels*, Research Studies Press.

Wagner, J. H., Johnson, B. V., and Hajek, T. J., 1991a, "Heat Transfer in Rotating Passages With Smooth Walls and Radial Outward Flow," ASME JOURNAL OF TURBOMACHINERY, Vol. 113, No. 1, pp. 42-51.

Wagner, J. H., Johnson, B. V., and Kopper, F. C., 1991b, "Heat Transfer in Rotating Serpentine Passages With Smooth Walls," ASME JOURNAL OF TURBOMACHINERY, Vol. 113, pp. 321-330.

Wagner, J. H., Johnson, B. V., Graziani, R. A., and Yeh, F. C., 1992, "Heat Transfer in Rotating Serpentine Passages With Trips Normal to the Flow," ASME JOURNAL OF TURBOMACHINERY, Vol. 114, pp. 847-856; also issued as NASA TM 103758.

Prediction of Surface Roughness and Incidence Effects on Turbine Performance

R. J. Boyle
NASA Lewis Research Center,
Cleveland, OH 44135

The use of a Navier-Stokes analysis to predict the change in turbine efficiency resulting from changes in blade surface roughness or incidence flow angles is discussed. The results of a midspan Navier-Stokes analysis are combined with those from a quasi-three-dimensional flow analysis code to predict turbine performance. A quasi-three-dimensional flow analysis code was used to determine turbine performance over a range of incidence flow angles. This analysis was done for a number of incidence loss models. The change in loss due to changes in incidence flow computed from the Navier-Stokes analysis is compared with the results obtained using the empirical loss models. The Navier-Stokes analysis was also used to determine the effects of surface roughness using a mixing length turbulence model, which incorporated the roughness height. The validity of the approach used was verified by comparisons with experimental data for a turbine with both smooth and rough blades tested over a wide range of blade incidence flow angles.

Introduction

There is a need for accurate and relatively quick means of estimating turbine performance. The approach taken to estimate turbine performance should be capable of predicting the performance of existing designs, as well as for proposed applications that may lie outside of existing experimental databases. At an early stage in the design process the turbine performance will often be calculated using an inviscid analysis coupled to boundary layer analysis. Empirical correlations are used to account for incidence, clearance, and secondary flow losses. Navier-Stokes analyses, unlike boundary layer analyses, can accurately predict loss over a range of incidence angles because they do not break down when separation occurs. It is also desirable to determine the effect of blade surface roughness on turbine performance, since experiments by Roelke and Haas (1983) and Boynton et al. (1993) showed that polishing rough surface blades improved turbine efficiency by nearly two points. Both Navier-Stokes and boundary layer analyses can be modified to accommodate the effect of blade surface roughness. Davis et al. (1988) showed that a large number of grid points, and thus relatively long CPU times, were needed to obtain accurate loss predictions for a compressor cascade. The long CPU times for an accurate Navier-Stokes loss prediction analysis reduce its desirability for use in a preliminary design analysis. However, Navier-Stokes analyses can be used to correlate the loss due to incidence or surface roughness, and the correlations could be then used in a preliminary design analysis. In principle, a carefully done Navier-Stokes analysis of a proposed design would not need to be calibrated against data for existing designs. Consequently, evaluations of new blade designs would not be biased by correlations based on past designs.

The work reported herein presents the results of an analytic investigation to improve performance prediction methodology using the results of a midspan Navier-Stokes analysis. The Navier-Stokes analysis was used to determine the effects of surface roughness on turbine performance, and to illustrate how a correlation for the effect of incidence on turbine performance is obtained. The Navier-Stokes analysis used a computer code developed by Chima (1987). The Cebeci-Chang (1978) model for the effect of surface roughness was incorporated into the computer code. Verification of this approach was done by comparing the results with the experimental data of Boynton et al. (1993). The experimental results showed turbine efficiency for smooth and rough rotor blades over a wide range of operating conditions for a two-stage turbine. These results were obtained at the Marshall Space Flight Center turbine test facility. Additionally, the calculated effect of off-design incidence flows on turbine performance is compared with experimentally derived incidence loss calculations. When the Navier-Stokes analysis was done to determine the effects of either off-design incidence flows or surface roughness the primary interest was to determine if the analysis would predict the relative change in efficiency due to changes in flow angles or surface roughness. So long as the Navier-Stokes analysis predicted the correct change in efficiency, the results would be accurate, even if the Navier-Stokes analysis did not precisely predict the level of efficiency.

Description of Analysis

The analysis was begun using a quasi-three-dimensional inviscid flow analysis coupled to boundary layer analyses to determine turbine performance for smooth blades. This anal-

---

Contributed by the International Gas Turbine Institute and presented at the 38th International Gas Turbine and Aeroengine Congress and Exposition, Cincinnati, Ohio, May 24-27, 1993. Manuscript received at ASME Headquarters March 10, 1993. Paper No. 93-GT-280. Associate Technical Editor: H. Lukas.

ysis, referred to as MTSB, is described by Boyle et al. (1986), and consists of the coupling of two two-dimensional stream function flow analysis codes with a boundary layer analysis to calculate turbine performance. A midchannel hub-to-shroud analysis (Katsanis and McNally, 1977) is used to determine the stream tube thickness variation for a series of blade-to-blade analysis (Katsanis, 1969), for each blade row. The resulting flow distributions are used as input to a series of boundary layer analyses (McNally, 1970) to determine profile and endwall losses due to boundary layer growth. Empirical correlations are used to calculate incidence, secondary flow, rotor tip clearance, and disc windage losses. Each blade row is analyzed in sequence to determine the overall turbine performance. The analysis was done for the two-stage turbine tested by Boynton et al. (1992). The efficiency of the two-stage turbine was calculated over a wide range of operating conditions using the MTSB analysis. The overall loss in efficiency is broken down into its component parts, so as to identify the change in efficiency due to profile loss, endwall loss, secondary flow loss, rotor tip clearance loss, as well as incidence loss.

Incidence Loss. The original analysis used the correlation developed by Glassman (1973), in which the loss in available kinetic energy is given by:

$$L_I = \frac{W_{\mathrm{IN}}^2}{2}\left(1 - \cos^n(\alpha_{\mathrm{IN}} - \beta_{\mathrm{LE}} - i_{\mathrm{OPT}})\right)$$

where $n = 2$ for negative incidence, and $n = 3$ for positive incidence. The incidence angle for minimum loss, i_{OPT}, is given as between -4 and -8 deg, and was taken as -6 deg when Glassman's loss model was used. Additional incidence loss correlations were incorporated into the analysis. The correlation of Tran et al. (1992) is similar to Glassman's. The correlation for positive incidence is the same, but for negative incidence $n = 0.35$, and $i_{\mathrm{OPT}} = 0$.

The third correlation was that of Moustapha et al. (1990), in which the change in the kinetic energy loss coefficient, $\Delta\bar{e}_I$, is given as a function of geometric and flow parameters:

$$\Delta\bar{e}_I = \sum_{n=1}^{6} a_n \chi^n$$

The coefficients a_n are different depending on whether the incidence is positive or negative. χ is given by:

$$\chi = \left(\frac{d_{\mathrm{LE}}}{P}\right)^{-1.6}\left(\frac{\cos\beta_{\mathrm{TE}}}{\cos\beta_{\mathrm{LE}}}\right)^{2}(\alpha_{\mathrm{IN}} - \alpha_{\mathrm{DES}})$$

When the design flow angle, α_{DES}, is not known, as was the case for the comparisons made here, the design flow angle was assumed equal to the blade mean chamber leading edge angle.

The change in kinetic energy loss coefficient, $\Delta\bar{e}_I$, and the incidence loss, L_I, are related by:

$$\frac{2L_I}{W_{\mathrm{IN}}^2} = \Delta\bar{e}_I\,\frac{[1 - (p_2/p_1')^{(\gamma-1)/\gamma}]}{[1 - (p_1/p_1')^{(\gamma-1)/\gamma}]}$$

After the quasi three-dimensional turbine performance prediction analysis was done, a midspan Navier–Stokes analysis was done for a range of incidence flow angles. This analysis was done to determine if the changes in predicted efficiency were consistent with the changes in efficiency due to incidence flows determined by the loss correlation that gave best agreement with the experimental data. The midspan Navier–Stokes analysis was done using a computer code developed by Chima (1987), for a thin-layer Navier–Stokes analysis with a variable thickness stream tube. A four-stage Runge–Kutta time-marching algorithm is used, and implicit residual smoothing is employed to improve convergence. For the geometry analyzed the stream tube variation at midspan was very small. Consequently, the quasi-three-dimensional Navier–Stokes analysis was done as a two-dimensional analysis. Since the incidence loss correlations were based on two-dimensional results, it was felt to be appropriate to use a two-dimensional Navier–Stokes analysis. The Navier–Stokes analysis did not rely on experimental data, and therefore could be used to predict changes in turbine efficiency for blade geometries and flow conditions outside the range of the experimental correlations. C-type grids were used in the Navier–Stokes code, and they were generated using the GRAPE code developed by Sorenson (1980). Since the boundary layers are likely to be fully turbulent near the trailing edge, the boundary layers were assumed fully turbulent in the MTSB and Navier–Stokes analyses.

For consistency with the incidence loss correlation, the incidence loss at a specified flow angle was taken as the difference between the profile loss at α and the profile loss when $\alpha = \beta_{\mathrm{LE}}$, where β_{LE} is the angle of the mean chamber line at the leading edge:

$$\Delta\bar{e}_I = \bar{e}(\alpha) - \bar{e}(\beta_{\mathrm{LE}})$$

The choice of β_{LE} as a reference angle is arbitrary, and another angle, offset from this angle, could also be chosen as the reference angle. Since the choice of reference angle is arbitrary, the optimum incidence angle can be other than at the reference angle. Therefore, $\Delta\bar{e}_I$ can be less than zero. However, if the loss is negative, it is expected to be small relative to other losses.

Surface Roughness. The surface roughness model incorporated into the Navier–Stokes analysis was the model of Ce-

Nomenclature

A^+ = coefficient for near wall damping
a = coefficient in incidence loss model
d = diameter of leading edge
$\bar{e}$ = kinetic energy loss coefficient
h = roughness height
i = incidence angle
K = ratio of h_{EQ} to actual roughness height
l = mixing length
L = incidence loss
p = pressure
P = pitch
R = gas constant
s = span
T = temperature
U = wheel speed
u_τ = friction velocity
V = absolute velocity
W = relative velocity
y = distance from surface
Δy = increase in mixing length
α = flow angle
β = blade angle
γ = specific heat ratio
η = turbine efficiency
κ = mixing length constant
ν = viscosity
χ = incidence loss parameter

Subscripts

0 = inlet to turbine
1 = inlet to blade row
2 = exit of blade row
4 = exit of turbine second rotor
Abs = absolute frame
DES = design inlet angle
EQ = equivalent height
EXIT = blade row exit
I = incidence
IDEAL = based on overall pressure ratio
IN = blade row inlet
LE = blade leading edge
m = mean radius
OPT = optimum incidence angle
Rel = relative frame
TE = blade trailing edge

Superscripts

+ = normalized
′ = total

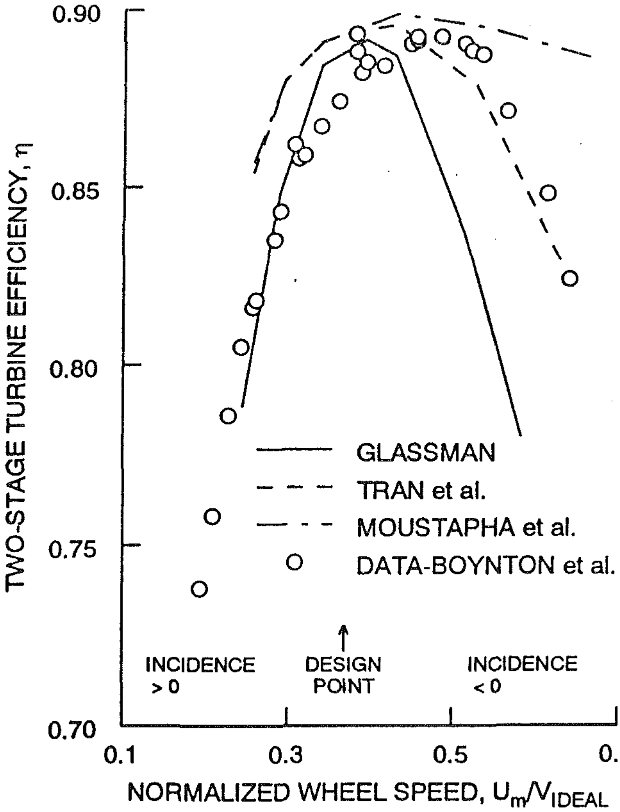

Fig. 1 Smooth blade predicted and measured efficiency

beci and Chang (1978). This is a mixing length model in which the mixing length is augmented to account for surface roughness. For a smooth surface the length scale, l, is given by:

$$l = \kappa y(1 - e^{-y^+/A^+})$$

where $y^+ = y\nu/u_\tau$ and $A^+ = 26$. All length quantities are normalized in the same manner as y.

For rough surfaces Cebeci and Chang use an offset distance, Δy, which is added to the physical normal distance. This was implemented by replacing y by $y^+\Delta y$ in the equations above. The mixing length when the surface is rough becomes:

$$l = \kappa(y + \Delta y)(1 - e^{-(y^+ + \Delta y^+)/A^+})$$

The mixing length offset, Δy, is a function of the actual roughness height, h, as well as the roughness geometry, and is expressed in terms of an equivalent height, h_{EQ}. The parameter K is the ratio of equivalent to actual roughness height. Δy and h_{EQ} are normalized in the same manner as y. Cebeci and Chang give Δy^+ as:

$$\Delta y^+ = 0.9(\sqrt{h_{\mathrm{EQ}}^+} - h_{\mathrm{EQ}}^+ e^{-h_{\mathrm{EQ}}^+/6})$$

Cebeci and Chang state that the equation above is valid in the range $4.535 < h_{\mathrm{EQ}}^+ < 2000$. When the equivalent roughness height, h_{EQ}^+, equals 4.535, Δy^+ is zero. This automatically accounts for the fact that small roughnesses, ($h^+ < 5$), are hydraulically smooth. Further details of the implementation of this roughness model are found in Boyle and Civinskas (1991), where the model was used to predict turbine blade heat transfer.

Results and Discussion

Incidence Effects. Figure 1 shows a comparison of the predicted and measured turbine efficiency for the smooth blade experimental data of Boynton et al. (1993). The test were conducted using the Space Shuttle Main Engine two-stage high-pressure fuel turbine in a cold flow test rig at the Marshall Space Flight Center. Additional information regarding the tests was given by Hudson et al. (1991). Table 1 lists some of the flow and relevant geometric characteristics of this turbine at the design point. Further details of the geometry are given by Civinskas et al. (1990). The analysis was done using the mass flow at the design point pressure ratio for various wheel speeds. The Reynolds number computed using the inlet velocity and first stage stator axial chord was 5.2×10^5.

Table 1 Geometry and design point flow conditions

	Turbine Stage			
	First		Second	
	Stator	Rotor	Stator	Rotor
P/d_{LE}	7.86	8.27	9.12	9.56
P/c	0.749	0.695	0.785	0.721
s/c	0.845	1.206	0.938	1.300
β_{LE}	14.8	43.6	34.5	42.5
α_{LE} – Rel	0.0	37.8	11.9	29.7
α_{LE} – Abs	0.0	69.9	11.9	67.7

The efficiency over a wide range of experimental test conditions was shown by Boynton et al. (1992) to be primarily a function of the ratio of mean wheel speed to the ideal isentropic velocity, U_m/V_{IDEAL}, where:

$$V_{\mathrm{IDEAL}} = \sqrt{\gamma R T_0'}\left(1 - \left(\frac{p_4'}{p_0'}\right)^{(\gamma-1)/\gamma}\right)\frac{\gamma+1}{\gamma-1}$$

Three predictions of the overall efficiency are given. They differ only in the calculation of incidence loss. The model of Tran et al. (1992), labeled TC, differed from Glassman's (1973), labeled G, model only for negative incidence, where U_m/V_{IDEAL} is greater than design. However, for illustration purposes, the incidence loss was calculated assuming that $n = 0.35$ for the entire range of U_m/V_{IDEAL}. The third incidence loss model is that of Moustapha et al. (1990), labeled MKT. At the design operating point, $U_m/V_{\mathrm{IDEAL}} = 0.37$, incidence is not a factor, and the analysis agrees well with the experimental data. Where incidence is important, the incidence correlation of Tran et al. agrees well with the data. That is to say that the curve labeled G agrees well with the data for U_m/V_{IDEAL} less than design, and the correlation labeled TC agrees well with the data for U_m/V_{IDEAL} greater than design. This is to be expected, since this incidence correlation was developed using these data. The MKT model predicts the smallest incidence penalty.

Table 2 gives a breakdown of the loss by type at three values of U_m/V_{IDEAL}. The loss breakdown is given for each of the loss correlations to illustrate the importance of using an accurate incidence loss model. As expected, near the design point incidence loss is low. However, off-design the incidence loss using Glassman's (1973) correlation is of the same order as the clearance loss. Changing U_m/V_{IDEAL} from 0.39 to 0.29 results in smaller changes in $\bar{e}_l$ than changing U_m/V_{IDEAL} from 0.39 to 0.52 because of the nonlinearity in incidence angle with respect to wheel speed. The first-stage rotor midspan incidence angle decreased by 31 deg when U_m/V_{IDEAL} increased to 0.52, and increased by 14 deg when U_m/V_{IDEAL} decreased to 0.29. The data in Fig. 1 are for a larger range of U_m/V_{IDEAL} than between 0.29 and 0.52, indicating even larger incidence angle variations. The maximum positive inlet flow angle to the rotor is the stator exit angle, while at $U_m/V_{\mathrm{IDEAL}} = 0.60$ the incidence angle decreased by nearly 55 deg to give an incidence angle less than -60 deg. This table also shows that at the lower speed ratio the change in efficiency due to a change in loss coefficient, $\Delta\eta/\Delta\bar{e}$, is greater than at the higher speed ratio. Consequently, a given loss coefficient results in lower efficiencies as the wheel speed is reduced. Figure 1 shows a decrease in efficiency as the wheel speed is reduced. The variation of profile loss with wheel speed does not show a consistent trend,

Table 2 Loss breakdown from MTSB analysis

	U_m/V_{IDEAL}								
	0.29			0.39			0.52		
	Incidence Loss Model								
	G	TC	MKT	G	TC	MKT	G	TC	MKT
Stator 1									
$\bar{e}_{TOTAL}$	0.049	0.048	0.047	0.051	0.050	0.049	0.049	0.048	0.047
$\bar{e}_I$	0.002	0.001	0.000	0.003	0.001	0.000	0.002	0.001	0.000
$\Delta\eta/\Delta\bar{e}$	0.778	0.778	0.778	0.672	0.672	0.672	0.658	0.658	0.658
Rotor 1									
$\bar{e}_{TOTAL}$	0.167	0.1337	0.132	0.150	0.149	0.148	0.203	0.163	0.154
$\bar{e}_{PROF}$	0.035	0.035	0.035	0.040	0.040	0.040	0.050	0.050	0.050
$\bar{e}_{ENDW}$	0.007	0.007	0.007	0.006	0.006	0.006	0.005	0.005	0.005
$\bar{e}_{CLEAR}$	0.061	0.063	0.063	0.081	0.081	0.081	0.078	0.081	0.083
$\bar{e}_{SEC}$	0.025	0.020	0.026	0.020	0.020	0.020	0.013	0.013	0.013
$\bar{e}_I$	0.039	0.002	0.001	0.003	0.002	0.001	0.058	0.018	0.004
$\Delta\eta/\Delta\bar{e}$	0.673	0.673	0.673	0.556	0.556	0.556	0.544	0.544	0.544
Stage 1									
η	0.850	0.874	0.875	0.883	0.884	0.885	0.855	0.877	0.885
Stator 2									
$\bar{e}_{TOTAL}$	0.079	0.053	0.053	0.055	0.050	0.048	0.137	0.080	0.051
$\bar{e}_{PROF}$	0.029	0.029	0.029	0.027	0.027	0.027	0.029	0.029	0.029
$\bar{e}_{ENDW}$	0.014	0.014	0.014	0.014	0.014	0.014	0.013	0.013	0.013
$\bar{e}_{SEC}$	0.009	0.009	0.009	0.006	0.006	0.006	0.004	0.004	0.004
$\bar{e}_I$	0.028	0.002	0.001	0.008	0.003	0.001	0.091	0.033	0.005
$\Delta\eta/\Delta\bar{e}$	0.821	0.821	0.821	0.686	0.686	0.686	0.671	0.671	0.671
Rotor 2									
$\bar{e}_{TOTAL}$	0.157	0.123	0.123	0.121	0.119	0.118	0.178	0.133	0.119
$\bar{e}_{PROF}$	0.036	0.035	0.035	0.030	0.030	0.030	0.035	0.034	0.034
$\bar{e}_{ENDW}$	0.006	0.006	0.006	0.004	0.004	0.004	0.002	0.002	0.002
$\bar{e}_{CLEAR}$	0.050	0.052	0.052	0.063	0.063	0.063	0.060	0.063	0.064
$\bar{e}_{SEC}$	0.027	0.027	0.027	0.020	0.020	0.020	0.012	0.012	0.012
$\bar{e}_I$	0.038	0.002	0.002	0.004	0.002	0.001	0.069	0.021	0.006
$\Delta\eta/\Delta\bar{e}$	0.601	0.601	0.601	0.550	0.550	0.550	0.547	0.547	0.547
Stage 2									
η	0.840	0.881	0.881	0.895	0.900	0.901	0.812	0.873	0.899
Overall									
η	0.848	0.880	0.880	0.891	0.894	0.895	0.837	0.878	0.895
p'_0/p'_4	1.395	1.378	1.377	1.422	1.420	1.420	1.530	1.497	1.486
Exp.									
η	0.843			0.883			0.888		

Table 3 Sensitivity of rotor loss to grid parameters

Grid	y_1^+	$\bar{e}$
145×54	0.6	0.0509
291×54	0.6	0.0423
291×70	0.6	0.0438
291×54	1.2	0.0375
291×54	0.3	0.0321
291×70	0.3	0.0441
MTSB		0.0351

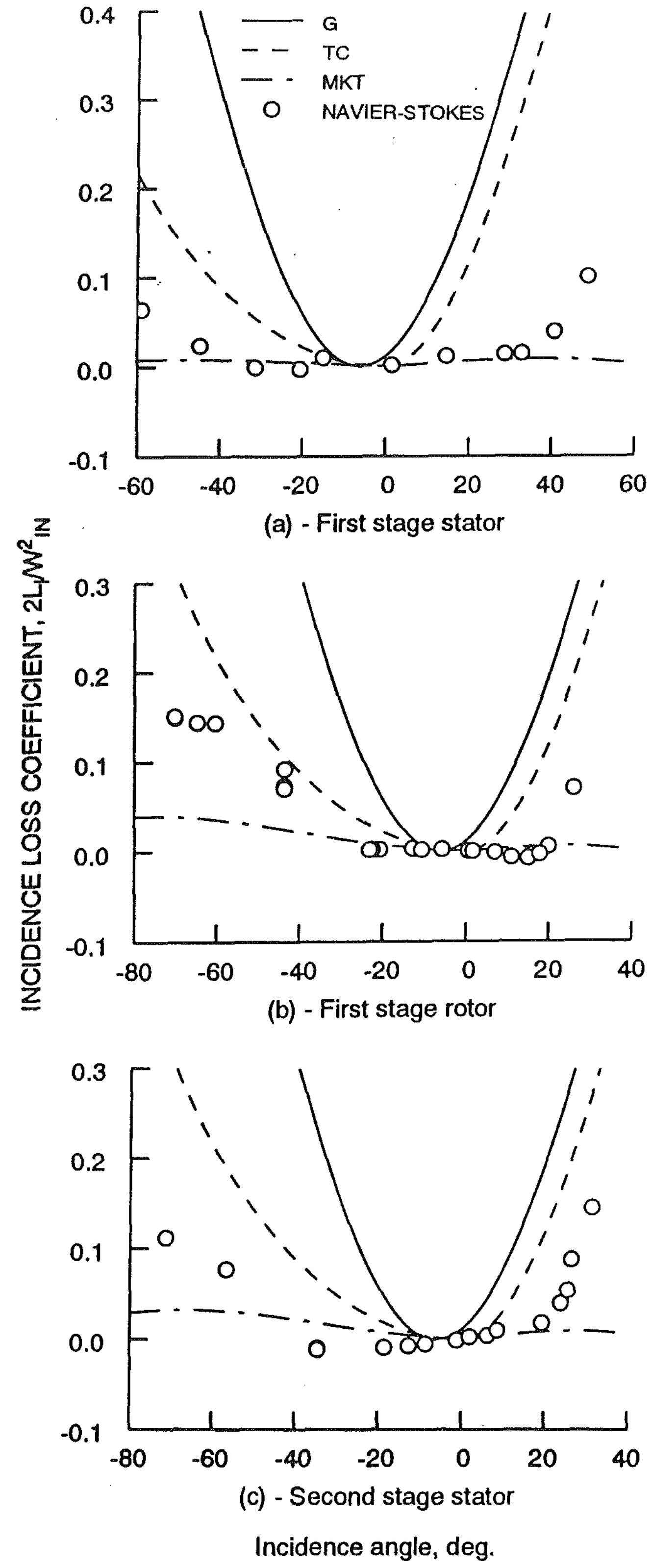

(a) - First stage stator

(b) - First stage rotor

(c) - Second stage stator

Fig. 2 Navier-Stokes and correlation incidence loss

and does not appear to account for the increased loss due to off-design incidence flows. This is the result of modifications made to the edge velocities in the boundary layer analysis when separation is indicated. If separation occurred near the leading edge, the peak velocities in this region were reduced until separation no longer occurred. If the actual boundary layer reattached on the forward part of the blade surface, the modification to the boundary layer free-stream edge velocities would not significantly affect the final boundary layer thickness. However, if the boundary layer did not reattach, the losses would be underpredicted.

The desired result of using the Navier-Stokes analysis was to obtain an incidence loss correlation that would result in good agreement with the experimental data. Because the correlation of Tran et al. was developed using these experimental data it was hoped that the Navier-Stokes results would agree with this correlation. The first step in applying the Navier-Stokes analysis was to determine the appropriate grid parameters needed to obtain accurate estimates of the change in loss due to incidence. Table 3 gives the calculated loss at design flow of the first-stage rotor midspan section for different grid parameters. In this table y_1^+ is a representative value for the distance of the first node from the blade surface. The table shows that very dense grids are needed for minimum loss. These results are consistent with those of Davis et al. (1988), where they show the effect of grid parameters on calculated loss for a compressor blade row. Their results showed that the calculated loss decreased with increasing grid lines in the circumferential direction, and that increasing the grid lines in the blade-to-blade direction at first resulted in decreased loss, but further increases resulted in increased loss. The profile loss from the MTSB analysis in Table 3 differs from the value in Table 2, because the value in Table 2 is the spanwise average, and not the midspan value. The profile loss from the MTSB analysis agrees reasonably well with the Navier-Stokes analysis. While the boundary layer analysis was expected to be accurate at the design point, the accuracy of the boundary layer analysis decreases once separation occurs. The Navier-Stokes analysis, however, should be accurate whether or not there is separation.

Figure 2 shows the incidence loss factor, $2L_I/W_{\mathrm{IN}}^2$, versus incidence angle for three of the four blade rows. Both rotors had similar geometries, while the first and second-stage stators had somewhat different geometries. The symbols are the calculated incidence loss from the Navier-Stokes analysis, and the incidence loss is zero by definition at zero incidence angle. The Navier-Stokes results generally lie between the correlation of Tran et al. and the correlation of Moustapha et al. The Navier-Stokes results reproduce the same trend as the correlation of Tran et al., where there is a rapid increase in loss at extreme incidence values. However, the Navier-Stokes results show the same loss level at larger magnitudes of incidence than the correlation of Tran et al. For the first-stage stator there was no experimental variation in incidence angle, and to apply the correlation of Tran et al. would be somewhat of an extrapolation. For this blade row the Navier-Stokes results are in better agreement with the correlation of Moustapha et al., thus indicating the applicability of the Navier-Stokes approach to determine incidence loss for blade rows outside the experimental data base. The analysis was done for each of the blade rows for a range of Reynolds numbers, near-wall spacings, and blade row pressure ratios. In general, variations in these parameters produced the same trend in the calculated incidence loss. For some cases the results were inconsistent with those shown in the figure. No specific cause for this behavior was identified, and it is speculated that the cause of the inconsistencies was incomplete convergence. The most consistent results were obtained with a minimum value of artificial viscosity, and when the first grid line wall spacing, y_1^+, was approximately unity.

Moustapha et al. (1990) compared their results with those of Mukhtarov and Krichakin (1969). It was found that the correlation of Mukhtarov and Krichakin gave results almost identical to that of Glassman. Glassman's model predicts the largest incidence penalty, while the MKT correlation shows the smallest incidence penalty. The Navier-Stokes incidence loss is calculated as the change in profile loss from the loss at an arbitrary angle. The Navier-Stokes incidence loss goes slightly negative, indicating that the optimum flow angle is other than the inlet blade angle. The Navier-Stokes results show a minimum loss around -20 deg of incidence, which is somewhat less than the expected value of -6 deg. The change in loss between -6 and -20 deg is small.

For all three blade rows the agreement between the Navier-Stokes analysis and a particular correlation is strongly influenced by the choice of zero loss incidence flow angle used in the correlation. This is illustrated in Fig. 3, where the comparisons are made with different zero loss angles. For each blade row comparisons are made for optimum incidence angles of 0 and -20 deg. The different symbols refer to the Navier-Stokes incidence loss based on different optimum incidence angles. The change in optimum incidence angle from 0 to -20 deg resulted in almost no change in the incidence loss distribution for the first-stage stator and rotor. These results show that for all three blade rows the correlations are more sensitive to the assumed zero loss incidence angle than the Navier-Stokes results. The Navier-Stokes analysis gives the total loss at each incidence angle, and does not rely on an a priori knowledge of the zero incidence loss angle. At large positive incidence angles there is a rapid rise in incidence loss. This rise occurs for the rotor Navier-Stokes results between 20 and 30 deg of incidence. The correlation of Moustapha et al. also gives a rapid rise in loss, but at incidence angles greater than shown on the plot.

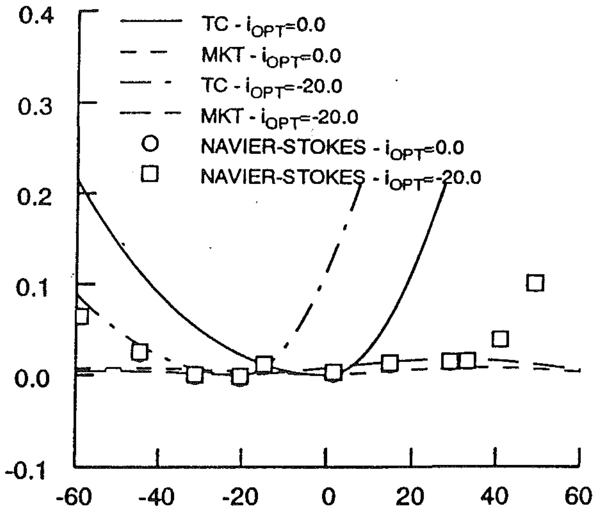

(a) - First stage stator

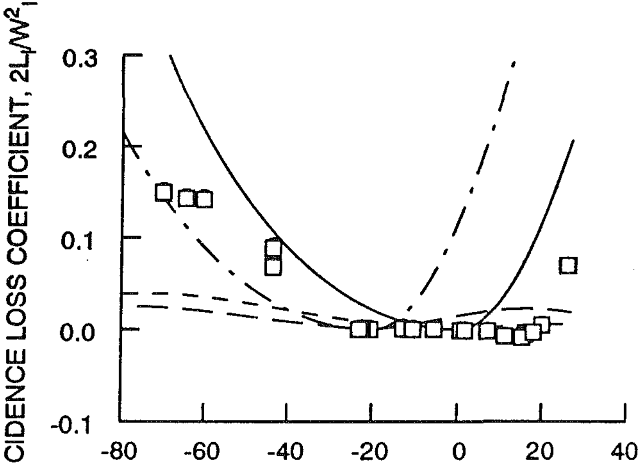

(b) - First stage rotor

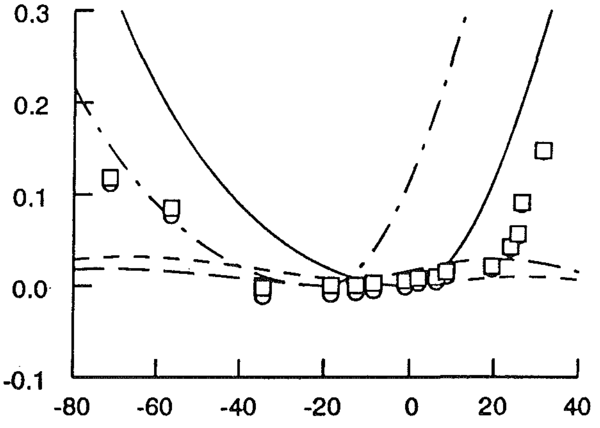

(c) - Second stage stator

Fig. 3 Effect of optimum incidence angle on loss

Figure 4 shows a comparison of the turbine efficiency using

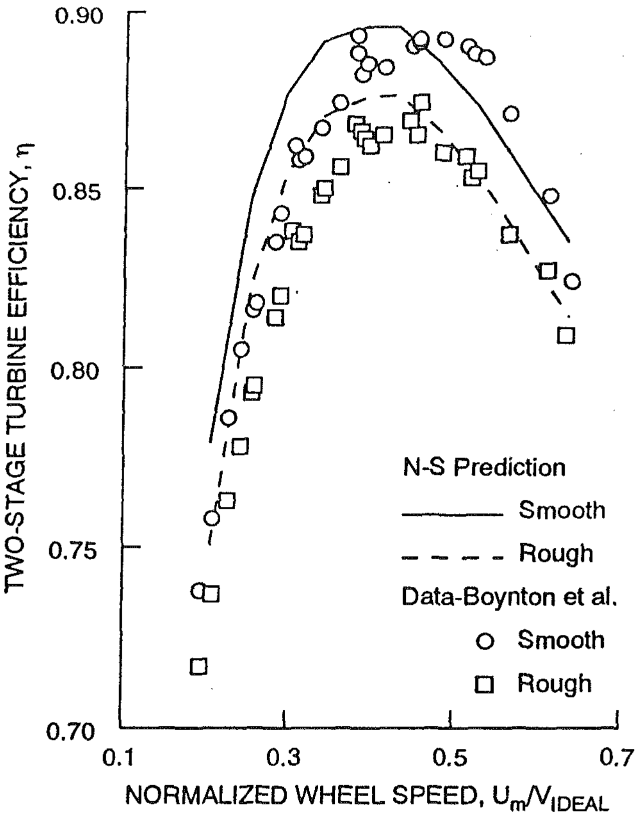

Fig. 4 Efficiency for smooth and rough blades

a curve fit of the Navier-Stokes results for the smooth blades. The curve fit was of the same form as used by Moustapha et al.

$$2L_I/W_{\mathrm{IN}}^2=\sum_{n=1}^{3} a_n\chi^n$$

The design angle is taken as the blade leading edge angle, so that χ is given by:

$$\chi=\left(\frac{d_{\mathrm{LE}}}{P}\right)^{-1.6}\left(\frac{\cos\beta_{\mathrm{TE}}}{\cos\beta_{\mathrm{LE}}}\right)^{2}(\alpha_{\mathrm{IN}}-\beta_{\mathrm{LE}})$$

For $\chi<0$, $a_1=8.0766\times10^{-5}$, $a_2=-5.4780\times10^{-7}$, and $a_3=5.4843\times10^{-9}$. For $\chi>0$, $a_1=6.8752\times10^{-5}$, $a_2=5.9368\times10^{-7}$, and $a_3=3.0534\times10^{-10}$.

The Navier-Stokes results that were used for the curve fits had minimum and maximum values of χ of -950 and 290. The corresponding values in the correlation of Moustapha et al. were -800 and 800, respectively.

The MTSB analysis was rerun over the wheel speed range using the Navier-Stokes derived incidence loss model. Close to the design point, $U_m/V_{\mathrm{IDEAL}}=0.39$, the predicted efficiency is 0.895 compared with the experimental value of 0.883. As expected, based on the results in the previous figures, the analysis overpredicts the efficiency at positive incidences, but is in reasonably good agreement with the experimental data for negative incidences. It is not expected that the correlation based on the Navier-Stokes analysis will be universally applicable. Rather, these results are shown to illustrate the use of the Navier-Stokes analysis to predicting turbine performance over a wide range of incidences.

Surface Roughness. As discussed by Boynton et al. (1993), the smooth blade results were obtained by polishing rotor blades that had a rough NiCrAlY coating. The purpose of the coating was to prevent airfoil cracks during engine start transient. The thickness of this coating was 10.2 μm. Dunn et al. (1994) tested a similar blade, which had a coating thickness of 15 μm. Table 4 gives the calculated profile loss for both smooth and rough blades. Results are shown for different grids to indicate the level of uncertainty in the calculation of the increment in loss due to surface roughness. For each grid, results are shown for different values of the equivalent height ratio, K, and for the damping coefficient, A^+. For given values of K and A^+ the variation in the increment in loss among the different grids is very small. The equivalent height ratio is not known with certainty, and was estimated to be 0.3 for the blades tested by Dunn et al. (1994). However, it could be that a value of 1.0, or even larger, would be appropriate for use in the rough surface mixing length model. Since $h_{\mathrm{EQ}}=hK$, $K=0.7$ for a roughness height of 15 μm has the same effect as $K=1.0$ for a roughness height of 10.2 μm.

Table 4 Grid and surface roughness assumptions effects; $h=15$ μm

Grid	y_1^+	K	A^+	$\overline{e}_{2D}$	$\Delta\eta$
291×54	0.3	0.0	26.0	0.0321	
		0.0	1.0	0.0483	0.011
		0.3	26.0	0.0348	0.002
		0.3	1.0	0.0550	0.015
		0.7	1.0	0.0656	0.022
		1.0	26.0	0.0455	0.009
		1.0	1.0	0.0703	0.025
291×54	0.6	0.0	26.0	0.0423	
		0.0	1.0	0.0570	0.010
		0.3	26.0	0.0449	0.002
		0.3	1.0	0.0654	0.015
		0.7	1.0	0.0726	0.020
		1.0	26.0	0.0546	0.008
		1.0	1.0	0.0767	0.023
291×54	1.2	0.0	26.0	0.0375	
		0.0	1.0	0.0531	0.010
		0.3	26.0	0.0402	0.002
		0.3	1.0	0.0586	0.014
		0.7	1.0	0.0686	0.021
		1.0	26.0	0.0502	0.008
		1.0	1.0	0.0730	0.024
291×70	0.3	0.0	26.0	0.0441	
		0.0	1.0	0.0564	0.008
		0.3	26.0	0.0462	0.001
		0.3	1.0	0.0623	0.012
		0.7	1.0	0.0720	0.019
		1.0	26.0	0.0581	0.009
		1.0	1.0	0.0760	0.021
Experimental					0.021

When the damping coefficient, A^+, was left at the smooth surface value of 26.0, the effect of surface roughness on profile loss was small. It was necessary to reduce A^+ to a small value in order to get good agreement with the experimental data for the loss in efficiency due to blade surface roughness. A small value of A^+ results in mixing lengths that are consistent with those given by Han and Delpassand (1990) for rough surfaces. Table 4 shows that just reducing A^+ and maintaining K at 0.0 does not sufficiently decrease efficiency to account for the measured efficiency change due to surface roughness. Also, Blair (1994) decreased the near-wall damping for his prediction of the effect of surface roughness on turbine blade heat transfer. However, when the turbulence model that was used in the present work was used to predict the heat transfer for the rough blade tests of Dunn et al. (1994), good agreement was achieved using an A^+ of 26. When an A^+ of 1.0 was used to calculate the heat transfer, the calculations gave heat transfer rates much larger than the experimental data.

The coating that resulted in rough surface blades was applied to both the blade surfaces and to the hub platform. Consequently, both the profile and endwall losses were affected by polishing the rotor blades. The effective change in loss due to roughness is given by:

$$(\Delta\bar{e})_{3D} = (\Delta\bar{e})_{2D}\left[\frac{(\bar{e}_{\mathrm{PROFILE}} + \bar{e}_{\mathrm{ENDWALL}})_{3D-\mathrm{SMOOTH}}}{(\bar{e}_{\mathrm{PROFILE}})_{2D-\mathrm{SMOOTH}}}\right]$$

The ratio of three-dimensional to two-dimensional effects was calculated to be 1.2. As seen in Table 2 the average value of $\Delta\eta/\Delta\bar{e}$ for the two rotors was 0.553.

Boynton et al. (1993) stated that when the rough blades were polished, the trailing edge thickness decreased by 18 percent. The method of Stewart (1955) was used to estimate the change in efficiency due to a change in trailing edge thickness. The thinner trailing edge thickness for the smooth blades was calculated to improve the efficiency by less than 0.1 of a point. The data in Table 4 were generated using the design point flow conditions. These data show that, for a roughness height of 15 μm, assuming an equivalent height ratio of 1.0 results in an average decrease in efficiency of 0.9 of a point compared to a height ratio of 0.3. Calculations were done in which the incidence flow angle was varied. The change in profile loss due to roughness for the off-design flow cases was within 10 percent of the change in profile loss due to roughness for the design flow case.

In addition to the smooth surface results, Fig. 4 shows a comparison of predicted and measured efficiencies for the rough blades. The blades with a rough surface were about two points lower in efficiency at design. The efficiency prediction assumed an equivalent roughness height ratio, K, of 1.0, a roughness height of 10.2 μm, and $A^+ = 1.0$. The change in rotor $\bar{e}$ due to surface roughness, and the sensitivity of blade row efficiency, $\Delta\eta/\Delta\bar{e}$, were used to determine overall efficiency for the rough surface blades. This approach predicts the change in efficiency over the speed range with reasonable accuracy.

Conclusions

The results of this work showed that a Navier–Stokes analysis was useful in predicting the change in turbine efficiency due to off-design incidence flows as well as the surface roughness. At the design point, where incidence is not a factor, the MTSB analysis predicted the efficiency of the two-stage turbine within 1.2 points. For the specific turbine with which comparisons were made, the Navier–Stokes analysis was in reasonably good agreement with an incidence loss correlation of Tran et al., which was derived from the experimental data. The results of the Navier–Stokes analysis were in reasonably good agreement with the incidence loss correlation of Moustapha et al. for the one blade row, the first-stage stator, which was not included in the correlation of Tran et al. For the other two blade rows the correlation of Tran et al. predicted higher incidence loss penalties than the correlation of Moustapha et al., and for negative incidence angles, lower incidence loss penalties than the correlation of Glassman. The Navier–Stokes results also showed this same behavior. Because the Navier–Stokes analysis is performed for the actual blade row, the analysis accounts for factors that might not be accounted for in the incidence loss correlations. Thus the Navier–Stokes analysis provides a method of predicting the performance of turbine blading that is not in an existing database.

The results of the investigation to determine the effects of blade surface roughness showed that the Navier–Stokes analysis accurately predicted these effects using the Cebeci–Chang roughness model. An investigation into the effect of grid size on predicted loss showed that dense grids, on the order of 15,000 points, were required to obtain accurate loss levels. While the level of loss was sensitive to the choice of grid parameters, the relative effects of surface roughness were much less sensitive to the grid parameters. The predicted effect of surface roughness on turbine efficiency was strongly affected by the choice of parameters in the rough surface turbulent eddy viscosity model. If the damping coefficient, A^+, was not made small, the increase in the mixing length due to roughness was insufficient to account for the effect of surface roughness on turbine efficiency. The inconsistencies in the value of A^+ between the value of unity needed to obtain accurate loss predictions and the value of 26 needed to obtain accurate heat transfer predictions shows the desirability of improving the turbulence model for rough surfaces.

References

Blair, M. F., 1994, "An Experimental Study of Heat Transfer in a Large-Scale Turbine Rotor Passage," ASME JOURNAL OF TURBOMACHINERY, Vol. 116, pp. 1–13.

Boyle, R. J., Haas, J. E., and Katsanis, T., 1986, "Predicted Turbine Stage Performance Using Quasi-Three-Dimensional and Boundary Layer Analyses," *AIAA Journal of Propulsion and Power*, Vol. 1, No. 3, pp. 242–251.

Boyle, R. J., and Civinskas, K. C., 1991, "Two-Dimensional Navier–Stokes Heat Transfer Analysis for Rough Turbine Blades," AIAA Paper No. 91-2129.

Boynton, J. L., Tabibzadeh, R., and Hudson, S. T., 1993, "Investigation of Rotor Blade Roughness Effects on Turbine Performance," ASME JOURNAL OF TURBOMACHINERY, Vol. 115, pp. 614–620.

Cebeci, T., and Chang, K. C., 1978, "Calculation of Incompressible Rough-Wall Boundary Layer Flows," *AIAA Journal*, Vol. 16, No.7, pp. 730–735.

Chima, R. V., 1987, "Explicit Multigrid Algorithm for Quasi-Three-Dimensional Flows in Turbomachinery," *AIAA Journal of Propulsion and Power*, Vol. 3, No. 5, pp. 397–405.

Civinskas, K. C., Boyle, R. J., and McConnaughey, H. V., 1990, "Turbine Blading Designed for High Heat Load Space Propulsion Applications," *AIAA Journal of Propulsion and Power*, Vol. 6, No. 5, pp. 598–611.

Davis, R. L., Hobbs, D. E., and Weingold, H. D., 1988, "Prediction of Compressor Cascade Performance Using Navier–Stokes Techniques," ASME JOURNAL OF TURBOMACHINERY, Vol. 110, pp. 520–531.

Dunn, M. G., Kim, J., Civinskas, K. C., and Boyle, R. J., 1994, "Time-Averaged Heat Transfer and Pressure Measurements, and Comparison With Prediction for a Two-Stage Turbine," ASME JOURNAL OF TURBOMACHINERY, Vol. 116, pp. 14–22.

Glassman, A. J., 1973, "Turbine Design and Application," NASA SP-290, Vol. II, pp. 143–146.

Han, L. S., and Delpassand, M., 1990, "A Heat Transfer Analysis for Rough Turbine Airfoils," WRDC-TR-89-2135, Final Contractor Report, The Ohio State University.

Hudson, S. T., Gaddis, S. W., Johnson, P. D., and Boynton, J. L., 1991, "Cold Flow Testing of the Space Shuttle Main Engine High Pressure Fuel Turbine Model," AIAA Paper No. 91-2503.

Katsanis, T., 1969, "Fortran Program for Calculating Transonic Velocities on a Blade-to-Blade Stream Surface of a Turbomachine," NASA TN D-5427.

Katsanis, T., and McNally, W. D., 1977, "Revised Fortran Program for Calculating Velocities and Streamlines on the Hub-Shroud Midchannel Stream Surface of an Axial-, Radial-, or Mixed Flow Turbomachine or Annular Duct, Vol. I—User's Manual," NASA TN D-8430.

McNally, W. D., 1970, "Fortran Program for Calculating Compressible Laminar or Turbulent Boundary Layers in Arbitrary Pressure Gradients," NASA TN D-5681.

Moustapha, S. H., Kacker, S. C., and Tremblay, B., 1990, "An Improved Incidence Loss Prediction Method for Turbine Airfoils," ASME JOURNAL OF TURBOMACHINERY, Vol. 112, pp. 267–276.

Mukhtarov, M. Kh., and Krichakin, V. I., 1969, "Procedure of Estimating Flow Section Losses in Axial Flow Turbines When Calculating Their Characteristics," *Teploenergotika*, Vol. 16, No. 7, pp. 76–79.

Roelke, R. J., and Haas, J. E., 1983, "The Effect of Rotor Blade Thickness and Surface Finish on the Performance of a Small Axial Flow Turbine," ASME *Journal of Engineering for Power*, Vol. 105, pp. 377–382.

Sorenson, R. L., 1980, "A Computer Program to Generate Two-Dimensional Grids about Airfoils and Other Shapes by the Use of Poisson's Equation," NASA TM 81198.

Stewart, W. L., 1955, "Analysis of Two-Dimensional Compressible-Flow Loss Characteristics Downstream of Turbomachine Blade Rows in Terms of Basic Boundary-Layer Characteristics," NACA TN-3515.

Tran, K., Chan, D. C., Hudson, S. T., and Gaddis, S. W., 1992, "Numerical Analysis of a Rocket Engine Turbine and Comparison With Air Test Data," ASME Paper No. 92-GT-12.

An Application of Octant Analysis to Turbulent and Transitional Flow Data

R. J. Volino

T. W. Simon

Department of Mechanical Engineering,
Heat Transfer Laboratory,
University of Minnesota,
Minneapolis, MN 55455

A technique called "octant analysis" was used to examine the eddy structure of turbulent and transitional heated boundary layers on flat and curved surfaces. The intent was to identify important physical processes that play a role in boundary layer transition on flat and concave surfaces. Octant processsing involves the partitioning of flow signals into octants based on the instantaneous signs of the fluctuating temperature, t', streamwise velocity, u', and cross-stream velocity, v'. Each octant is associated with a particular eddy motion. For example, $u' < 0$, $v' > 0$, $t' > 0$ is associated with an ejection or "burst" of warm fluid away from a heated wall. Within each octant, the contribution to various quantities of interest (such as the turbulent shear stress, $-u'v'$, or the turbulent heat flux, $v't'$) can be computed. By comparing and contrasting the relative contributions from each octant, the importance of particular types of motion can be determined. If the data within each octant are further segregated based on the magnitudes of the fluctuating components so that minor events are eliminated, the relative importance of particular types of motion to the events that are important can also be discussed. In fully developed, turbulent boundary layers along flat plates, trends previously reported in the literature were confirmed. A fundamental difference was observed in the octant distribution between the transitional and fully turbulent boundary layers, however, showing incomplete mixing and a lesser importance of small scales in the transitional boundary layer. Such observations were true on both flat and concave walls. The differences are attributed to incomplete development of the turbulent kinetic energy cascade in transitional flows. The findings have potential application to modeling, suggesting the utility of incorporating multiple length scales in transition models.

Introduction

Turbulent flow has long been known to contain considerable structure. Flow visualization shows the presence of turbulent eddies, near-wall "streaks" and "bursts," turbulent spots in transitional flow, and other structures. More recently, full Navier–Stokes solutions have reproduced these structures computationally. The structure plays an important role in the overall flow behavior. Turbulent eddies, for example, are responsible for the high level of mixing (eddy transport) in turbulence, which would not be present if the turbulent fluctuations were completely uncorrelated.

Most efforts to document turbulent structure have concentrated on mean transport quantities, such as the turbulent shear stress, $-u'v'$, and the turbulent heat flux, $v't'$. These quantities provide important information about effective mixing within particular flows, but they offer only limited information about the actual eddy structure that produces the effective mixing. Turbulence models derived from mean transport measurements in one flow should be applicable only to flows with similar eddy structure. If a model derived from one flow were applied to a flow with a fundamentally different structure, there is good reason to expect a poorer prediction of the mean transport quantities and, thus, poor prediction of the overall flow behavior. Fortunately, there appears to be considerable similarity in the structure of many turbulent flows. This has allowed development of rather robust turbulence models. There are, however, some important situations such as transitional flows where conventional models seem to be lacking important physics, as documented by Schmidt and Patankar (1991) and Rodi and Scheuerer (1985). In at least some of these cases the reason for the poor performance may be a difference in the flow structure. There is, therefore, a need for a more detailed study of flow structure in transitional flow. A better understanding of the flow will help provide explanations for some of the unexpected behavior seen in experiments and point the way toward development of better computational models.

Quadrant and Octant Analyses

One means of investigating flow structure is the quadrant

Contributed by the International Gas Turbine Institute and presented at the 38th International Gas Turbine and Aeroengine Congress and Exposition, Cincinnati, Ohio, May 24–27, 1993. Manuscript received at ASME Headquarters February 18, 1993. Paper No. 93-GT-72. Associate Technical Editor: H. Lukas.

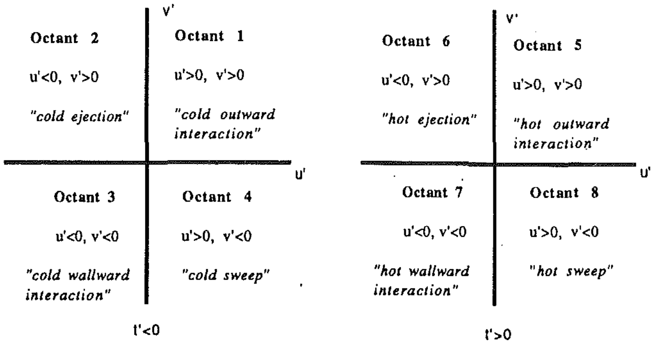

Fig. 1 Octant names

analysis. It was first used approximately twenty years ago by researchers such as Wallace et al. (1972) and Willmarth and Lu (1972). The technique involves partitioning of the flow signal into four quadrants, based on the instantaneous signs of the fluctuating velocity components u' and v'. Each quadrant is associated with a particular eddy motion. In quadrant 2, for example, low streamwise momentum (relative to the mean) fluid is moving with high cross-stream momentum (relative to the mean). In a turbulent boundary layer, this motion is attributed to turbulent "bursts" originating near the wall. The contribution to a quantity of interest (e.g., $-\overline{u'v'}$) is then calculated for each quadrant based on the data points that lie within it:

$$\overline{(u'v')}_1 = \frac{1}{N}\left[\sum_{1}^{N} I u'v'\right]_1 \tag{1}$$

where $I = 1$ if the point is within quadrant 1 (zero otherwise) and N is the total number of points (all quadrants). A data point refers to an instantaneous u-v pair. The relative contributions from the four quadrants can then be compared to show which eddy motions are more important. The turbulent shear stress is the sum of the contributions from the four quadrants.

The quadrant data can be further partitioned, based on strength of the entries. One method of doing this uses the following filter function given by Willmarth and Lu (1972):

$$\overline{u'v'}_i = \frac{\sum_{j=1}^{N} I u'v'_i}{N} \quad \text{where } I = \begin{bmatrix} 1 \text{ if } u'v' \text{ lies in quadrant } i \\ \text{and } |u'v'| > |H'\overline{u'v'}| \\ 0 \text{ otherwise} \end{bmatrix} \tag{2}$$

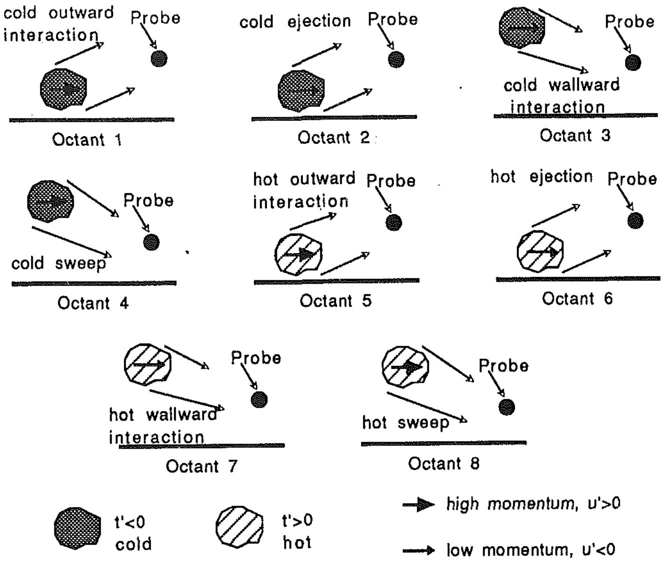

Fig. 2 Conceptual drawing of eddies in each octant

H' is termed the hole size parameter, and $\overline{u'v'}_i$ is the contribution to $\overline{u'v'}$ from that portion of quadrant i outside the hole described by the parameter H'. When $H' = 0$ Eq. (2) becomes Eq. (1). For large H', only the strongest eddies are considered, as shown in the I function definition of Eq. (2). Quadrant analyses can be extended in heated flows by inclusion of the temperature fluctuations, t'. If both positive and negative values of u', v', and t' are considered, eight possible combinations arise. The eight-way partitioning will be referred to as octant analysis. The octants are identified using names assigned by Kawaguchi et al. (1984) as shown in Fig. 1. Figure 2 is a conceptual drawing of the eddies responsible for the motion in each octant.

In a fully developed turbulent boundary layer on a heated flat plate, octants 4 and 6 should be the most significant. A turbulent "parcel" of fluid moving away from the wall ($v'>0$)[1] would most likely be of relatively low velocity ($u'<0$) and high temperature ($t'>0$), when the wall is heated. Such a motion would be characteristic of a turbulent burst and would

---

[1] $\overline{V} \approx 0$ is assumed when stating that $v'>0$ indicates motion away from the wall. This is satisfactory for discussing boundary layers. It must be remembered, however, that u', v', and t' are given relative to the mean quantities at the probe location.

Nomenclature

C_μ = empirical constant
C_f = skin friction coefficient
c_p = specific heat
FSTI = free-stream turbulence intensity
f_μ = empirical function
H = shape factor = δ^*/θ
H' = hole size parameter (Eq. (2))
I = indicator function (Eq. (1))
k = turbulence intensity
N = number of points in sample
q = wall heat flux per unit area
St = Stanton number
T = instantaneous temperature
T_w = wall temperature
T_∞ = free-stream temperature
t' = fluctuating component of temperature
U = instantaneous streamwise velocity
U_∞ = free-stream velocity
u' = fluctuating component of streamwise velocity
u_τ = friction velocity
$-\overline{u'v'}$ = turbulent shear stress
V = instantaneous cross-stream velocity
v' = fluctuating component of cross-stream velocity
$\overline{v't'}$ = normal component of turbulent heat flux
x = streamwise distance from leading edge
y = cross-stream distance from the wall
γ = intermittency (fraction of time flow is turbulent)
$\Delta_{99.5}$ = thermal boundary layer thickness
$\delta_{99.5}$ = boundary layer thickness
δ^* = displacement thickness
ϵ = turbulence dissipation
θ = momentum thickness
ν_T = eddy viscosity
ρ = density
$\overline{}$ = time-averaged

be classified as a hot ejection (octant 6). Similarly, a fluid packet moving toward the wall ($v' < 0$) would most likely have originated in the faster ($u' > 0$), cooler ($t' < 0$) fluid away from the wall. Such a motion, a cold sweep (octant 4), would be expected after a hot ejection as fluid moves in to replace that which had left. Motions in all eight octants would be present, but on the average the hot ejections and cold sweeps should be the largest contributors to quantities of interest. This is confirmed by the measurements of Suzuki et al. (1988) and those of the present study.

The simple representation given above of turbulent flows, depicting them as a series of predominantly ejections and sweeps, agrees with the assumptions used in most turbulence models. The arguments are basically those of the Prandtl mixing length model. In many cases they provide an adequate description of the eddy structure. In cases where they do not, differences become apparent in the octant analysis. Suzuki et al. (1988), for example, placed a heated horizontal cylinder normal to the flow direction above a heated flat wall. The thermal boundary conditions at the cylinder surface and on the wall were the same. Given the similarity in the heat and momentum boundary conditions, one might expect the presence of the cylinder to have similar effects on the wall heat transfer and skin friction. Surprisingly, the wall heat transfer was augmented, but the skin friction was not. An octant analysis showed a jump in the significance of octant 5, the hot outward interaction, when the cylinder was added. The increased significance of this octant agrees with the wall heat transfer and skin friction behavior and explains the dissimilarity between the near-wall heat and momentum transport rates.

In the present study the flow structures of two-dimensional heated boundary layers with zero streamwise pressure gradients are considered. The data used for this study include both new data and data taken in earlier studies: Kim (1986), Kim et al. (1989, 1992) and Kim and Simon (1991) using triple wire probes. The three wires of the probes were used to measure instantaneous U, V, and T. Details of the wind tunnel, probes, measurement techniques and flow conditions, as well as presentations of the processed data, including profiles of mean velocities, temperatures, and transport quantities, are available in those references. New measurements taken for this study were acquired using the same probe and essentially the same techniques as used by Kim and Simon (1991).

In this study, data were processed in terms of the octant analysis. The correlations $u'v'$, $v't'$, $u't'$, $u'v'^2$, and v'^2t' were calculated. The hole size, H', as used in Eq. (2), was varied from 0 to 10. In total, seven separate cases of differing curvature, boundary layer maturity, and free-stream turbulence intensity (FSTI) were considered. On a flat wall, Kim and Simon (1991) studied boundary layers subject to FSTI values of 0.3, 1.5, and 8.3 percent. The flow underwent natural transition in each case, and, at the upstream stations of the 0.3 and 1.5 percent FSTI cases, transitional profiles were obtained. The boundary layers at the other stations were fully turbulent. On a convex wall, with a radius of curvature of 90 cm, Kim (1986) acquired fully turbulent boundary layer data at 0.68 and 2.0 percent FSTI. On a concave wall, with a radius of curvature of -97 cm, Kim and Simon (1991) acquired fully turbulent boundary layer data at FSTI levels of 0.6 and 8.3 percent. Additional transitional boundary layer data, not previously reported, were acquired for the present study at an upstream location in the 0.6 percent FSTI concave-wall case. The FSTI values for the flat wall cases are based on the full spectra of the u', v' and w' fluctuations. For the curved wall cases, the FSTI are based on the full spectra of the u' and v' fluctuations. Because the data are extensive, only a sample is presented herein to demonstrate the utility of the octant technique and to show the most important effects of streamwise wall curvature, free-stream turbulence level, and transition, as revealed by octant decomposition. Emphasis is placed on the turbulent shear stress, $-u'v'$, and the normal component of the turbulent heat flux, $v't'$. Table 1 gives pertinent information regarding the six profiles presented.

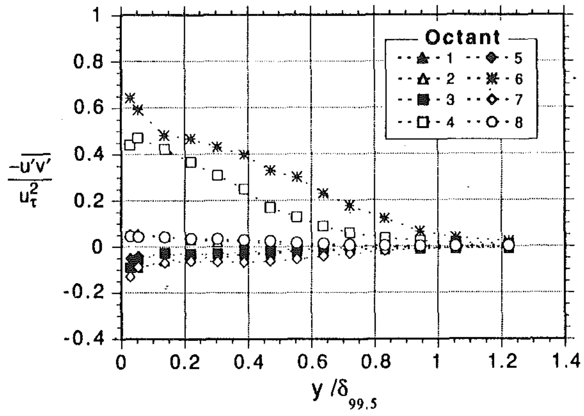

Fig. 3 Turbulent shear stress profiles, 1.5 percent FSTI flat-wall case, fully turbulent flow

Results and Discussion

Base Case: The Fully Turbulent, Flat-Wall Boundary Layer With Low-to-Moderate Free-Stream Turbulence Intensity Levels. Figure 3 shows profiles of the octants of the turbulent shear stress from the 1.5 percent FSTI, fully turbulent, flat-wall case, normalized on the friction velocity, u_τ. All data are shown with $H' = 0$, unless otherwise specified. As expected, octants 4 and 6 are the major contributors, with the other octants remaining near zero over the entire profile. Octant 6 is larger than octant 4 and its effects persist farther toward the edge of the boundary layer. Near the wall, the total $-u'v'/u_\tau^2$, found by summing the contributions from all the octants, approaches 1, as expected. The peak in all octants is near the wall, dropping toward zero at the freestream. Figure 4 shows similar results for the normal component of the turbulent heat flux, normalized as $v't'/(q/(\rho c_p))$.

Figures 5 and 6 show the effect of the hole size parameter at $y/\delta_{99.5} = 0.387$. The data at this position are typical of the distributions at other y locations. In Fig. 5, the normalized shear stress contributions of the octants are plotted versus H'. Figure 6 shows the number of points in each octant normalized

Table 1 Cases considered

No.	Ref.	Geometry	FSTI	x [m]	U_∞ [m/s]	q [W/m^2]	T_w-T_∞ [°C]	θ [cm]	H	$\delta_{99.5}$ [cm]	$\Delta_{99.5}$ [cm]	C_f ×10^3	St ×10^3	γ
1	†	flat	1.5%	1.029	16.86	154.8	3.56	0.154	1.361	1.749	2.025	4.05	2.201	100%
2	†	concave	0.6%	0.876	17.13	147.6	3.78	0.182	1.367	1.603	1.868	4.20	1.946	100%
3	‡	convex	0.68%	0.528	15.10	160.7	6.87	0.493	1.54	3.572	3.590	2.61	1.330	100%
4	†	flat	8.3%	0.800	9.19	181.9	6.07	0.191	1.364	2.451	3.012	4.70	2.528	100%
5	†	flat	1.5%	0.343	16.86	137.3	6.56	0.038	2.256	0.318	0.355	1.70	1.086	9.8%
6	*	concave	0.6%	0.610	9.58	170.9	4.12	-	-	0.788	0.813	3.00	3.686	56%

† Kim and Simon (1991); ‡Kim (1986); *present study

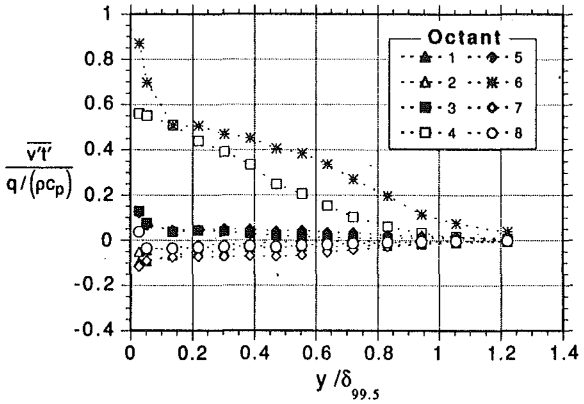

Fig. 4 Normal component of turbulent heat flux profiles, 1.5 percent FSTI flat-wall case, fully turbulent flow

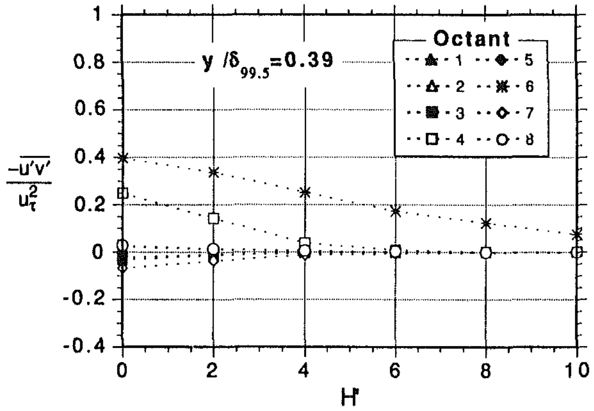

Fig. 5 Turbulent shear stress versus hole size at $y/\delta_{99.5}$ = 0.39, 1.5 percent FSTI flat-wall case, fully turbulent flow

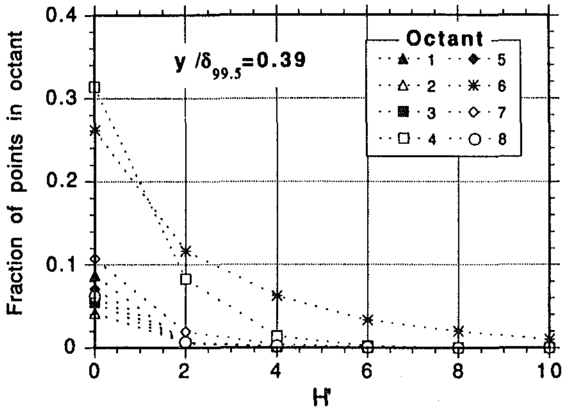

Fig. 6 Fraction of points in octant versus hole size at $y/\delta_{99.5}$ = 0.39, 1.5 percent FSTI flat-wall case, fully turbulent flow

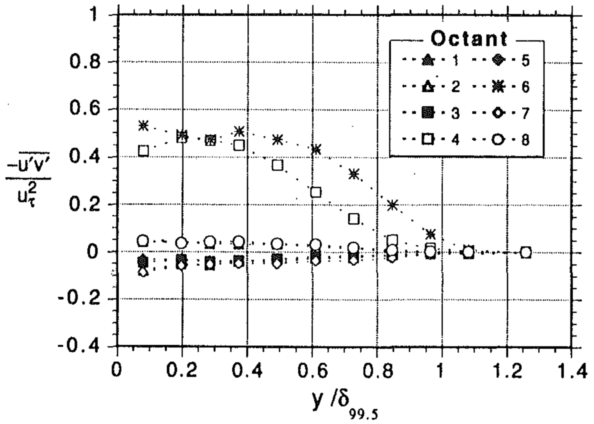

Fig. 7 Turbulent shear stress profiles, 0.6 percent FSTI concave-wall case, fully turbulent flow

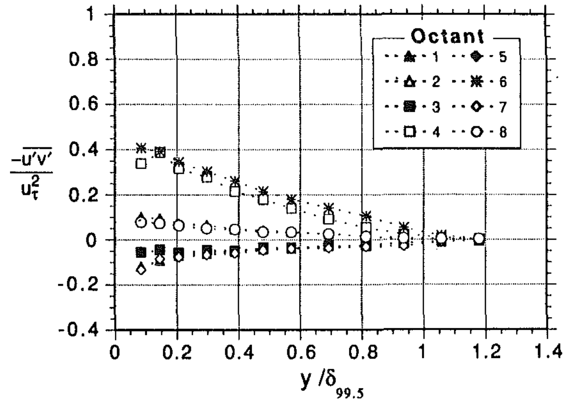

Fig. 8 Turbulent shear stress profiles, 0.68 percent FSTI convex-wall case, fully turbulent flow

on the total number of points in the sample and plotted versus H'. Well over half the events are in octants 4 and 6. Octant 4 contains the most points, but the eddies in octant 6 are stronger. Octant 7 is a distant third in importance. For $H' > 4$, only octant 6 makes a significant contribution.

Clearly, the hot ejection, which is associated with turbulent bursting, is the dominant structure in the turbulent boundary layer. Over one quarter of the data fall in this octant, and within these data lie the strongest eddies. The effects of the bursts extend farther toward the edge of the boundary layer than do the effects of the other octants. The cold sweep also makes an important contribution, occupying as much of the total time as does the hot ejection, but consisting mainly of somewhat weaker eddies. Octants 1 and 7, the cold outward interaction and hot wallward interaction, are next in importance, but appear to be of little significance. These octants are believed to result from the remnants of hot ejections and cold sweeps, which reverse direction normal to the wall. More discussion on this subject will be given below in conjunction with the transitional flow data, where these octants, particularly 7, play a more important role.

The Effects of Curvature on the Fully Turbulent Boundary Layer. Figures 7 and 8 show octant decomposition of shear stress for the 0.6 percent FSTI concave-wall and the 0.68 percent FSTI convex-wall, fully turbulent cases, respectively. Concave curvature leads to increased instability and, hence, enhanced mixing in the boundary layer. Additionally, stable, streamwise (Görtler) vortices were observed in this flow. The profile shown here was taken at the upwash location of a pair of these vortices. The increased scale of mixing is evidenced by the fuller profiles in Fig. 7 compared to those of Figs. 3 and 8. Convex curvature tends to increase stability, thereby reducing mixing and leading to less full profiles, as a comparison of Figs. 8 and 3 shows. The influence of curvature was evident in the mean $-u'v'$ profiles and is supported by the octant decomposition. There appears to be little reordering of the importance of the octants when curvature is introduced to the low-FSTI fully turbulent boundary layer, however. Octants 4 and 6 continue to play essentially the same relative roles in the flat-wall and curved-wall cases.

Effects of High Free-Stream Turbulence Intensity. Figure 9 shows shear stress profiles from the 8.3 percent FSTI, flat-wall case. The stated FSTI is the nominal value. At the point of this profile, the FSTI has decayed to 5.4 percent. The results

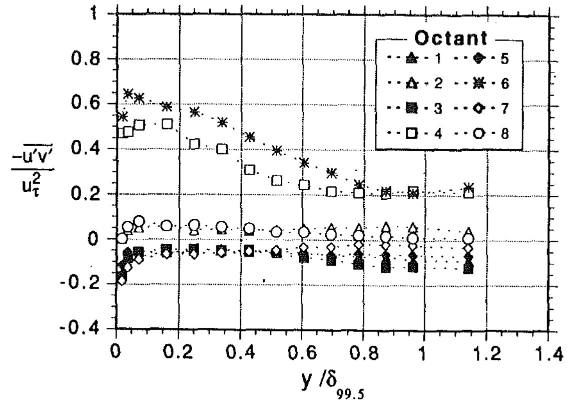

Fig. 9 Turbulent shear stress profiles, 8.3 percent FSTI flat-wall case, fully turbulent flow

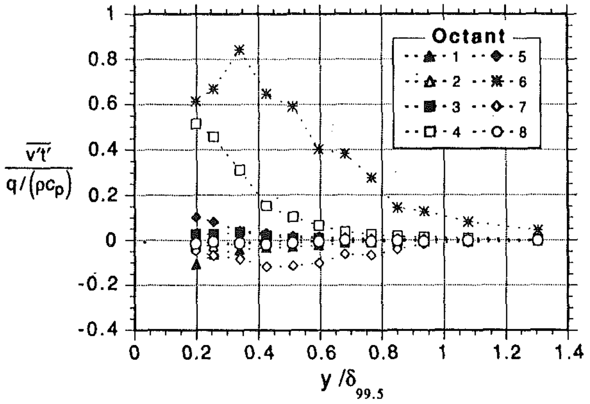

Fig. 12 Normal component of turbulent heat flux profiles, 1.5 percent FSTI flat-wall case, transitional flow

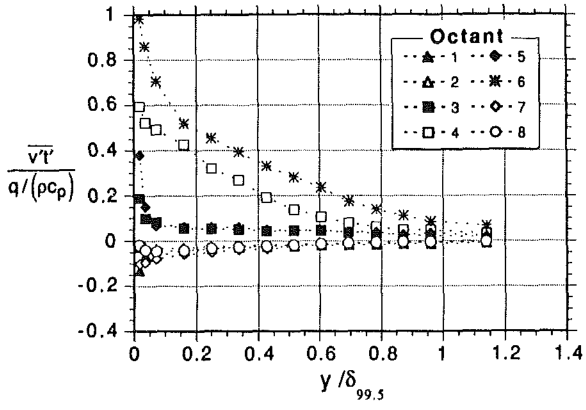

Fig. 10 Normal component of turbulent heat flux profiles, 8.3 percent FSTI flat-wall case, fully turbulent flow

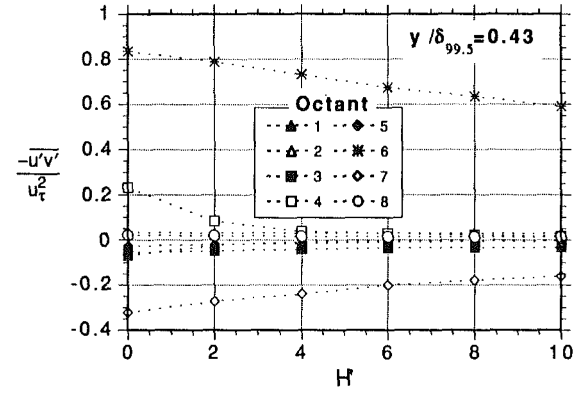

Fig. 13 Turbulent shear stress versus hole size at $y/\delta_{99.5}$ = 0.43, 1.5 percent FSTI flat-wall case, transitional flow

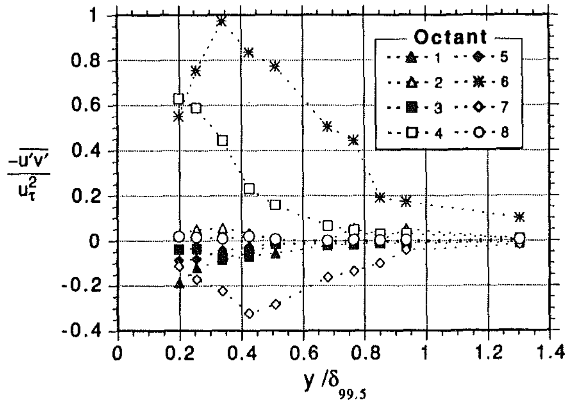

Fig. 11 Turbulent shear stress profiles, 1.5 percent FSTI flat-wall case, transitional flow

appear similar to the low FSTI cases (Fig. 3) in that octants 4 and 6 dominate. The main differences are observed near the edge of the boundary layer. The free-stream velocity fluctuations do not approach zero in the high-turbulence case, so $u'v'$ remains significant in octants 4 and 6 well beyond $\delta_{99.5}$. The other octants also show an increase in activity in the freestream, indicating a higher level of uncorrelated fluctuations there than in the low FSTI case. The sum of the octants goes to zero at $y/\delta \approx 1.2$; the free-stream $\overline{u'v'} = 0$. The octants of the $v't'$ decomposition, shown in Fig. 10, each go to zero at the edge of the boundary layer since free-stream temperature is uniform and, thus, t' goes to zero. A high FSTI concave-wall profile, not shown here, displayed the expected combination of larger uncorrelated fluctuations near the edge of the boundary layer along with the generally fuller profiles seen in the low-FSTI, concave-wall case.

Transitional Flow. Figure 11 shows the shear stress distribution in a transitional flow from the 1.5 percent FSTI, flat-wall case. At this point, transition is 9.8 percent complete. Figure 12 shows $\overline{v't'}$ for this case. The transitional profiles are quite different from the fully turbulent cases shown above. Octants 4 and 6 are still significant in transition, but they are joined in importance by other octants, particularly octant 7, the hot wallward interaction. Octant 6 gives the largest contribution, and the difference between 4 and 6 is larger than in the fully turbulent cases. At some locations, octant 7 has a larger magnitude than octant 4. Octants 1 and 7 also make contributions in the fully turbulent cases, as mentioned above, but they are much less important in those cases. Octants 1 and 7 are of opposite sign to octants 4 and 6, for both $\overline{u'v'}$ and $\overline{v't'}$. They therefore act to decrease the total turbulent shear stress and normal component of turbulent heat flux. Figures 13 and 14 show the shear stress data at $y/\delta_{99.5} = 0.425$ plotted versus H'. Octants 6 and 7 dominate. There are many data points in octant 4, but they are associated with weaker eddies and only make a minor contribution to $-\overline{u'v'}$. The contributions to octants 6 and 7 persist even at $H' = 10$, indicating that large eddies constitute the major contribution to $-\overline{u'v'}$. This contrasts with the fully turbulent flow shown in Fig. 6, where $-\overline{u'v'}$ drops more steeply with H'. This indicates that a wider range of scales is contributing to the shear stress in the fully turbulent flow.

The transitional flow on the concave wall is similar to that on the flat wall. In Fig. 15, the octant decomposition of $\overline{v't'}$ is shown with $H' = 0$. The data were acquired at the downwash location of a Görtler vortex pair at a point where transition

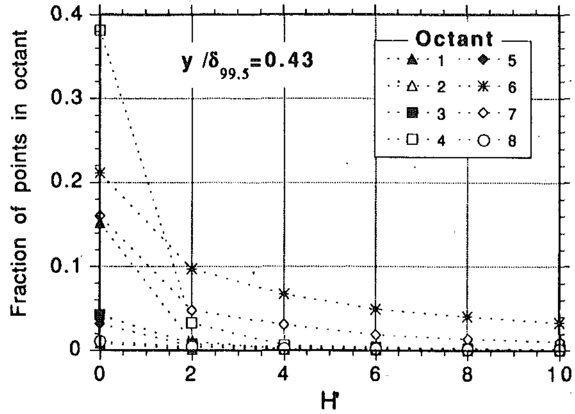

Fig. 14 Fraction of points in octant versus hole size at $y/\delta_{99.5} = 0.43$, 1.5 percent FSTI flat-wall case, transitional flow

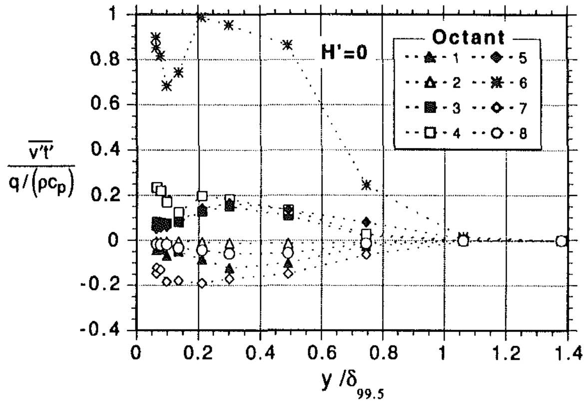

Fig. 15 Normal component of turbulent heat flux profiles, 0.6 percent FSTI concave-wall case, transitional flow, $H' = 0$

was 56 percent complete. The hot ejection (octant 6) dominates with the hot wallward interaction (octant 7) making a secondary contribution. In Fig. 16 the same profiles of $v't'$ are shown again with $H' = 10$. Comparing Figs. 15 and 16 shows that there is little change in octants 6 or 7 with a change of H', indicating the importance of large-scale eddies for these two octants.

The octant analysis shows a fundamental difference between transitional and fully turbulent flow structures. The differences are believed to be caused by incomplete development of the turbulence in the transitional region. In particular, the transitional flow is dominated by large-scale eddies since the cascade of energy from large scales to small is not yet established and the small scales have not had a chance to develop. The consequence is an incomplete mixing. An illustration of the proposed difference in mechanisms is given in Fig. 17. In fully turbulent flow, a parcel of low-speed, warm fluid is ejected from the wall in a relatively large-scale motion. Upon reaching the outer part of the boundary layer, the parcel is immediately acted upon by small-scale eddies, which disperse it by way of eddy straining and "turbulent diffusion." Mixing is fairly complete. A parcel of fluid moving with a cold sweep would be similarly dispersed. In transitional flow, the behavior is different. A burst still transports a parcel of warm, low-speed fluid to the outer part of the boundary layer, but there are few small scales present to act upon it. The parcel tends to remain intact for some time as a warm, low-speed entity. If it is next carried toward the wall, the parcel would be involved in a hot wallward interaction (octant 7). Similarly a parcel from a previous cold sweep might be thrown away from the wall as a cold outward interaction (octant 1). If the small-scale mixing were sufficiently poor, one could conceive of octants

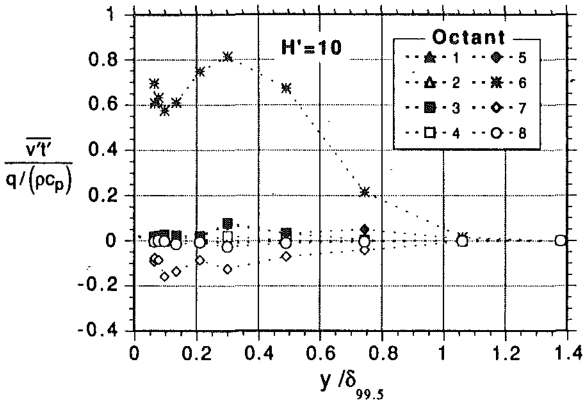

Fig. 16 Normal component of turbulent heat flux profiles, 0.6 percent FSTI concave-wall case, transitional flow, $H' = 10$

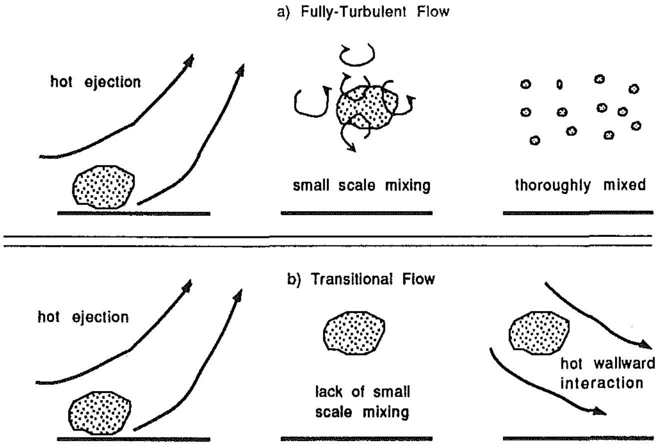

Fig. 17 Proposed differences between fully turbulent and transitional flow structures

1 and 7 approaching the levels of octants 4 and 6 with a net of zero turbulent mixing. In general, 1 and 7 do follow 4 and 6, but are of lesser importance.

Another feature in transitional flows is the larger difference between octants 4 and 6. Transition starts with near-wall bursting, so octant 6 should become dominant early in transition. Figure 14 supports this by showing that, although the total number of events in octants 4 and 6 are similar, the number in octant 4 drops more quickly as H' is increased.

Modeling Implications. The results given above suggest a potential benefit of incorporating an additional length scale or scales into existing transition models. A standard k-ϵ model bases the effective eddy viscosity on the turbulence intensity using a relation of the form $\nu_T = C_\mu f_\mu k^2/\epsilon$. The coefficient C_μ is an empirical constant and f_μ is an empirical function. If this relationship were employed for prediction of the transport by turbulent eddies in a transitional flow, it would predict excessive eddy viscosity even if k and ϵ were accurate, since C_μ and f_μ are based on fully turbulent flow where only octants 4 and 6 are important. Also, because of a falsely large contribution by turbulent eddies, the streamwise distance within which the boundary layer is transitional would be predicted to be too short. This is typical of existing models. The octant analysis results suggest that the standard k-ϵ modeling cannot fully capture the physics of the transitional flow structure. It suggests that an improvement to the situation would be a model that properly accommodates the larger-scale eddies in the transitional flow. Such a model may be an expansion of the standard k-ϵ model to two k equations with one k for the large scales and the other for the small scales. Turbulent energy would be mainly produced in the large scales by the standard production terms and would be transferred from the large scales to the small scales through a cascade model. Energy would be dissipated at the small scales. Contributions to $-\overline{u'v'}$ or eddy viscosity would come from both the large- and small-scale k, but the large scale contribution would be dominant. Since the small-scale energy would depend on transfer from the large scales, the turbulent kinetic energy in the small scales would lag that in the large scales as the boundary layer passes through transition. These measurements indicate that this lag would represent an improvement in predicting transition.

Conclusions and Recommendations

Octant analysis was applied to transitional and fully turbulent boundary layer data from both flat and curved walls.

The following conclusions can be drawn:

1 In fully turbulent flow, hot ejections and cold sweeps are the dominant flow structures. Eddies over a range of sizes contribute to quantities of interest, as evidenced by the sensitivity of these quantities to the hole size parameter, H'.

2 Curvature has an effect on the boundary layer, but does not appear to have a significant effect on the relative importance of the octants.

3 Octant decomposition in cases subject to high free-stream disturbances shows the difference between the uncorrelated fluctuations associated with free-stream "turbulence" and the highly correlated turbulence of the boundary layer. At, and beyond, the edge of the boundary layer, for the high free-stream turbulence case, the octant contributions do not approach zero, though their sum does.

4 Transitional flow is dominated by large scales, particularly hot ejections, and is characterized by incomplete mixing due to the incomplete development of small scale eddies. The octant analysis shows a decreased importance of the cold sweep and an increased importance of the hot wallward interaction in transitional flow. The hot wallward interaction is believed to follow directly from the hot ejection and acts to counteract the effects of ejections on the transport terms $-\overline{u'v'}$ and $\overline{v't'}$.

5 The differences between transitional and fully turbulent flows suggest the utility of multiple length scales in turbulence models that may be used to compute through transition.

6 Octant analysis has proven sufficiently useful that the present researchers will continue to employ it in future work. The authors are currently applying the technique to data from cases with accelerated boundary layers.

Acknowledgments

This work was sponsored by the Lewis Research Center of NASA under grant number NASA/NAG3-881. The contract monitor is Fred Simon. Some data used in this study were taken under sponsorship by the Air Force Office of Scientific Research under grant number AF/F49620-89-C-0060. The project monitor is Maj. Daniel Fant.

References

Kawaguchi, Y., Matsumori, Y., and Suzuki, K., 1984, "Structural Study of Momentum and Heat Transport in the Near Wall Region of a Disturbed Boundary Layer," presented at the 9th Biennial Symposium on Turbulence.

Kim, J., 1986, "The Development of a Turbulent Heat Flux Probe and Its Use in a 2-D Boundary Layer Over a Convex Surface," MSME Thesis, Dept. of Mech. Eng., U. of Minnesota.

Kim, J., and Simon, T. W., 1991, "Free-Stream Turbulence and Concave Curvature on Heated, Transitional Boundary Layers, Vol. 1—Final Report," NASA CR 187150, "Vol. II—Program Listings and Tabulated Data," NASA CR 187151.

Kim, J., Simon, T. W., and Kestoras, M., 1989, "Fluid Mechanics and Heat Transfer Measurements in Transitional Boundary Layers Conditionally Sampled on Intermittency," *Heat Transfer in Convective Flows*, ASME HTD-Vol. 107, pp. 69–81.

Kim, J., Simon, T. W., and Russ, S., 1992, "Free-Stream Turbulence and Concave Curvature Effects on Heated Transitional Boundary Layers," ASME *Journal of Heat Transfer*, Vol. 114, pp. 338–347.

Rodi, W., and Scheuerer, G., 1985, "Calculation of Laminar-Turbulent Boundary Layer Transition of Turbine Blades," *Heat Transfer and Cooling in Gas Turbines*, AGARD-CP-390, pp. 18-1 through 18-13.

Schmidt, R. C., and Patankar, S. V., 1991, "Simulating Boundary Layer Transition With Low-Reynolds Number $k-\epsilon$ Turbulence Models, Part 1—An Evaluation of Prediction Characteristics; Part 2—An Approach to Improving the Predictions," ASME JOURNAL OF TURBOMACHINERY, Vol. 113, pp. 10–26.

Suzuki, H., Suzuki, K., and Sato, T., 1988, "Dissimilarity Between Heat and Momentum Transfer in a Turbulent Boundary Layer Disturbed by a Cylinder," *Int. J. Heat Mass Transfer*, Vol. 31, No. 2, pp. 259–265.

Wallace, J. M., Eckelmann, H., and Brodkey, R. S., 1972, "The Wall Region in Turbulent Shear Flow," *J. Fluid Mech.*, Vol. 54, Part 1, pp. 39–48.

Willmarth, W. W., and Lu, S. S., 1972, "Structure of the Reynolds Stress Near the Wall," *J. Fluid Mech.*, Vol. 55, Part 1, pp. 65–92.

A Bypass Transition Model for Boundary Layers

M. W. Johnson
Department of Mechanical Engineering,
Turbomachinery Group,
University of Liverpool,
Liverpool, United Kingdom

Experimental data for laminar boundary layers developing below a turbulent free stream show that the fluctuation velocities within the boundary layer increase in amplitude until some critical level is reached, which initiates transition. In the near-wall region, a simple model, containing a single empirical parameter, which depends only on the turbulence level and length scale, is derived to predict the development of the velocity fluctuations in laminar boundary layers with favorable, zero, or adverse pressure gradients. A simple bypass transition model, which considers the streamline distortion in the near-wall region brought about by the velocity fluctuations, suggests that transition will commence when the local turbulence level reaches approximately 23 percent. This value is consistent with experimental findings. This critical local turbulence level is used to derive a bypass transition prediction formula, which compares reasonably with start of transition experimental data for a range of pressure gradients ($\lambda_\theta = -0.01$ to 0.01) and turbulence levels ($Tu = 0.2$ to 5 percent). Further improvement to the model is proposed through prediction of the boundary layer distortion, which occurs due to Reynolds stresses generated within the boundary layer at high free-stream turbulence levels and also through inclusion of the effect of turbulent length scale as well as turbulence level.

Introduction

The accurate prediction of boundary layer transition on a gas turbine blade is important because of the large increase in heat transfer rate that occurs once the boundary layer is turbulent. Additional blade cooling therefore needs to be provided downstream of the transition region.

Current transition prediction techniques rely almost entirely on empirical correlations (e.g., Abu Ghannam and Shaw, 1980, and Gostelow et al., 1994). Transition has been shown to depend on many parameters, such as free-stream turbulence level, pressure gradient, turbulent length scale, blade curvature, and blade leading edge geometry. Experiments are usually limited to the variation of only two or three of these parameters and it is often impossible to vary each parameter independently of the others. This has meant that correlations based on data from different laboratories frequently differ by 20 percent or more.

Theoretical models for transition prediction based on the Orr-Sommerfeld equation can be used to determine the growth in Tollmien-Schlichting waves, which precede transition. However, these models are based on linearized theory and are therefore only applicable to low free-stream turbulence levels. Moreover, there is little experimental evidence that Tollmien-Schlichting waves develop within laminar boundary layers in which the free-stream turbulence level exceeds about 1 percent. Under these conditions a bypass mode of transition (Mayle, 1991) is believed to exist. Theoretical predictions of transition through this bypass mode have not been particularly successful (Savill, 1991), except through direct numerical simulation using the full three-dimensional unsteady Navier-Stokes equations. Simulations of this type take large amounts of computer time and are, therefore, unsuitable for general design work, although they are likely to improve our understanding of the mechanisms of transition in that they can provide continuous histories of all flow properties through the boundary layer, which cannot be achieved by laboratory measurement.

The objective of the current study was to determine how free-stream turbulence influences the laminar boundary layer and hence to construct a semi-empirical model for predicting transition.

Experimental Data

A description of the experimental techniques used to obtain the data used in the current study is given by Fasihfar and Johnson (1992) and Fasihfar (1992). Laminar, transitional, and turbulent boundary layer profiles were measured on a flat plate for favorable, adverse, and zero pressure gradients for five turbulent grids, which gave nominal free stream turbulence levels of 0.2, 0.5, 1, 2.5, and 5 percent. Measurements were made using a single hot wire whose signal was processed digitally to obtain mean and rms velocities and turbulent intermittency.

The Influence of Free-Stream Turbulence on the Boundary Layer

The primary effect of the turbulent free stream on a laminar boundary layer is to induce significant fluctuation velocities,

---

Contributed by the International Gas Turbine Institute and presented at the 38th International Gas Turbine and Aeroengine Congress and Exposition, Cincinnati, Ohio, May 24-27, 1993. Manuscript received at ASME Headquarters February 19, 1993. Paper No. 93-GT-90. Associate Technical Editor: H. Lukas.

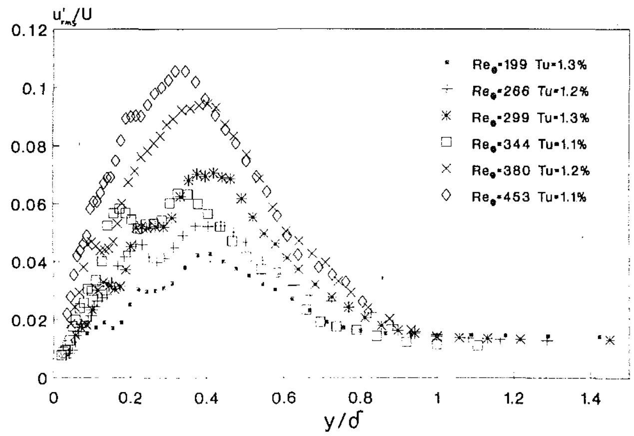

Fig. 1 Velocity fluctuation profiles in a developing zero pressure gradient laminar boundary layer; *Tu* = 1 percent

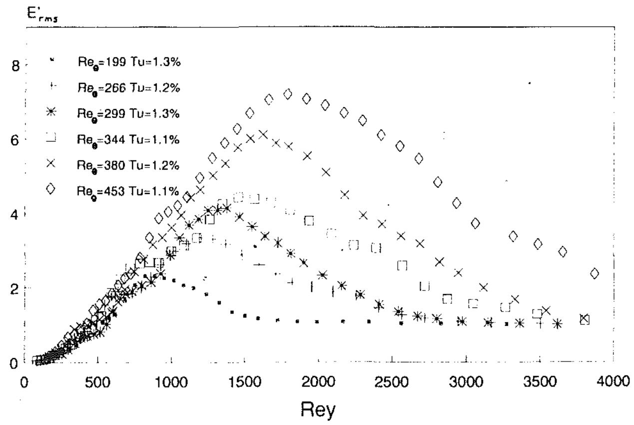

Fig. 2 Pressure fluctuation function *E*′ profiles for a developing zero pressure gradient laminar boundary layer

which can be many times larger in the boundary layer than in the free stream. Fluctuation profiles for a developing laminar boundary layer are shown for $Tu = 1$ percent in Fig. 1. Consider now the pressure fluctuations that lead to these measured velocity fluctuations. The instantaneous total pressure of an incompressible fluid is given by

$$P = \overline{P} + P' = \overline{p} + p' + \frac{1}{2}\rho(\overline{u} + u')^2 \tag{1}$$

and by subtracting the time mean of this equation and nondimensionalizing

$$E' = \frac{p' - P'}{\rho U'_{\mathrm{rms}}\overline{U}} = -\frac{u'\overline{u}}{U'_{\mathrm{rms}}\overline{U}} + \frac{\overline{u'^2} - u'^2}{U'_{\mathrm{rms}}\overline{U}} \tag{2}$$

where E' is defined by this equation.

The fluctuation velocity therefore depends on the difference *between the total and static pressure fluctuations.* Figure 2 shows E'_{rms} plotted against Reynolds number based on distance from the wall (Re_y) calculated from the experimental data presented in Fig. 1 using Eq. (2). It should be noted that Re_y nondimensionalizes distance y with free-stream properties and hence does not depend on the boundary layer thickness. Thus, in the near-wall region, where a common curve for E'_{rms} reasonably represents all stages of boundary layer development, E'_{rms} is independent of boundary layer thickness. In order to explain why E'_{rms} should correlate in this way in the near-wall region but not elsewhere, consider the static and total pressure fluctuations that contribute to E' in Eq. (2). Total pressure fluctuations are not only convected along streamlines from upstream, but also result through work done by both pressure fluctuations and viscous stresses. In the near-wall region, the strong shear of the flow will result in a rapid change, with streamwise distance, in the phase of the total pressure fluctuations on neighboring streamlines. This will result in high levels of fluctuating viscous stress, which will rapidly damp out the convected total pressure fluctuations. Thus the total pressure fluctuations on streamlines close to the wall will depend primarily on the work done locally by the static pressure fluctuations. The static pressure fluctuations depend on the instantaneous streamline curvature, which is induced by the free-stream turbulent eddies. Thus they will be largely independent of the boundary layer properties and will not experience significant changes in phase across the boundary layer. Figure 2 does show however that E'_{rms} depends on the boundary layer thickness in the outer part of the boundary layer where the shear in convection velocity is small and hence the convected total pressure fluctuations are only slowly dissipated. The variation in E'_{rms} may not be due so much to dependence of the amplitude of P' and p' as to the dependence of their phase on boundary layer thickness. When P' and p' are in phase, which is likely to occur in the free stream, the amplitude of E'_{rms} will be a minimum. However, in the outer parts of the boundary layer, P' and p' will move out of phase due to the differing convection velocities and the amplitude of E' will thus rise. This phase change will depend directly on the fluctuation frequency spectra, which were not determined by Fasihfar (1992) and therefore no attempt will be made here to predict E' in the outer part of the boundary layer. For prediction of the start of transition this is not important as the origin of turbulent bursts is within the near wall region.

Figure 3 shows that when a streamwise pressure gradient is imposed on the boundary layer, a common experimental curve for E'_{rms} is still obtained in the near wall region. Thus, as both u and u' vary linearly for at least a short distance from the wall. E'_{rms} can be approximated by

$$E'_{\mathrm{rms}} = \beta \mathrm{Re}_\delta^2 Y^2 \tag{3}$$

Nomenclature

C_f = skin friction
E' = pressure fluctuation function
H = δ^*/θ = shape factor
p = pressure
P = total pressure
Re = Reynolds number
Re_y = Uy/ν = Reynolds number based on normal distance from the plate
Tu = $U'_{\mathrm{rms}}/\overline{U}$ = free-stream turbulence level
u = streamwise velocity component
U = free-stream velocity
y = coordinate normal to plate
Y = y/δ = nondimensional coordinate normal to plate
δ = boundary layer thickness = 0.99 U
θ = boundary layer momentum thickness
λ = $(\delta^2/\nu)\,(dU/dx)$ = Pohlhausen parameter
λ_θ = $(\theta^2/\nu)\,(du/dx)$ = pressure gradient parameter
ν = kinematic viscosity
ρ = density

Superscripts and Subscripts

$\overline{}$ = time mean
$'$ = fluctuating component
rms = root mean square
S = value on a streamline

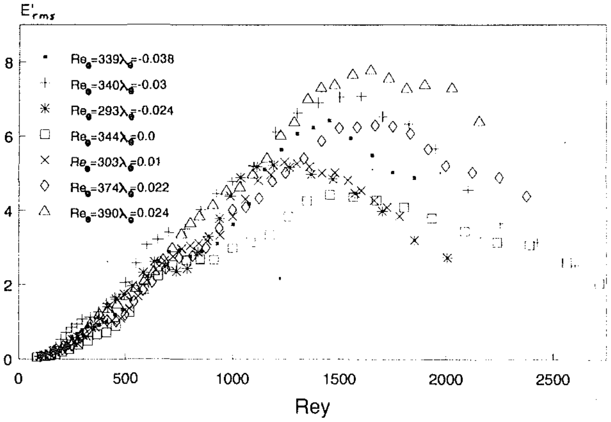

Fig. 3 Pressure fluctuation function E' profiles for nonzero pressure gradient laminar boundary layers; $Tu = 1$ percent

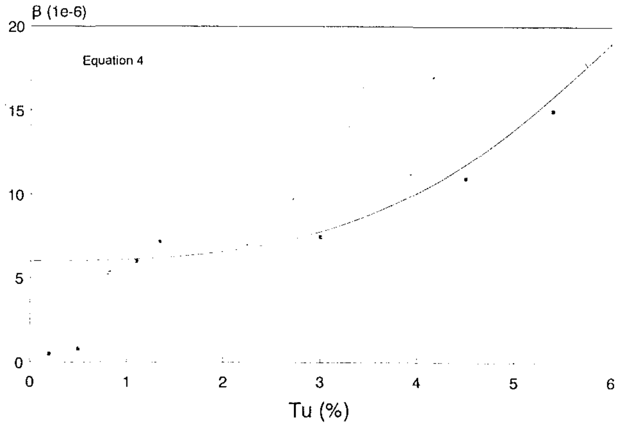

Fig. 5 The dependence of β on free-stream turbulence level

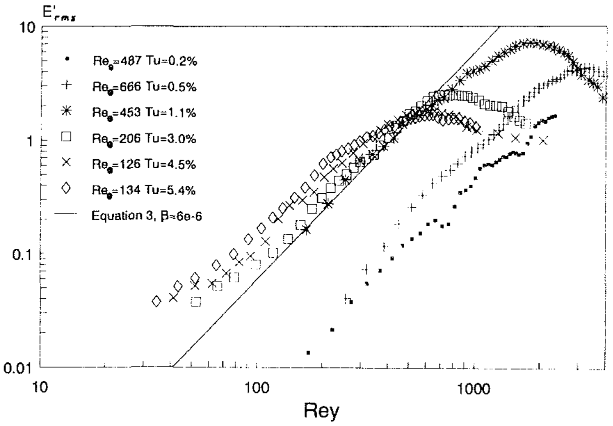

Fig. 4 Pressure fluctuation function E' profiles for zero pressure gradient laminar boundary layers for various turbulence grids

where β is a constant for all stages of laminar boundary layer development and all pressure gradients.

Figure 4 shows however that although β can be taken as a constant for a particular turbulence grid, its value alters from grid to grid. It seems likely therefore that β may vary with both turbulence level and length scale. The values of β obtained from Fig. 4 are presented in Fig. 5. It is clear that further data are required to determine a reliable functional relationship for β in terms of both turbulence level and length scale; however, the relationship

$$\beta = 6\times 10^{-6} + 6\times 10^{-2} Tu^3 \tag{4}$$

is a reasonable fit to the data in the region ($Tu > 1$ percent) where transition might be expected to occur through the bypass mode.

Criterion for Start of Transition

Consider Eq. (1) along a streamline within the boundary layer

$$\overline{P}_S + P'_S = \overline{p}_S + p'_S + \frac{1}{2}\rho u_S^2 \tag{5}$$

If the mean static pressure is constant across the boundary layer and substituting from Eq. (2) for the fluctuating pressures

$$\frac{1}{2}\left(\frac{u}{\overline{U}}\right)^2 = E' Tu + \frac{1}{2}\left(\frac{u_S}{\overline{U}}\right)^2 \tag{6}$$

Now if the wavelength of E' is large compared with the distance from the wall it may be assumed that the velocity fluctuations remain in phase. Therefore from continuity assuming spanwise velocity fluctuations are small

$$\int_0^Y \frac{\overline{u}}{\overline{U}}\,dy = \int_0^{Y_S} \frac{u_S}{\overline{U}}\,dY_S \tag{7}$$

and so assuming linear profiles for both mean and fluctuating velocities in the near-wall region

$$\frac{\overline{u}}{\overline{U}}\frac{Y}{2} = \frac{u_S}{\overline{U}}\frac{Y_S}{2} \tag{8}$$

and

$$\frac{u}{Y} = \frac{u_S}{Y_S} \tag{9}$$

Now, substituting into Eq. (6) and substituting for E'_{rms} from Eq. (3), assuming E' varies sinusoidally with time

$$\left(\frac{u}{\overline{U}}\right)^2 - \left(\frac{\overline{u}}{\overline{U}}\right)\frac{u}{\overline{U}} - 2\sqrt{2}\beta Tu \mathrm{Re}_\delta^2 Y^2 \sin\omega t = 0 \tag{10}$$

Thus,

$$\left(\frac{u}{\overline{U}}\right) = \frac{1}{2}\left\{\left(\frac{u}{\overline{U}}\right) + \left[\left(\frac{\overline{u}}{\overline{U}}\right)^2 + 8\sqrt{2}\beta Tu \mathrm{Re}_\delta^2 Y^2 \sin\omega t\right]^{1/2}\right\} \tag{11}$$

This equation describes how the velocity profile near the wall varies with time for various boundary layer Reynolds numbers and free-stream turbulence levels. However, the solution fails when the square bracketed term becomes negative, at the point in the cycle where $\sin \omega t = -1$. When the bracketed term is equal to zero, the pressure fluctuation term E' results in a minimum velocity of $1/2\overline{u}$; any further retardation of the flow leads to a situation where the flow stalls and separates instantaneously from the wall. This process would produce significant normal velocities and pressure gradients, which have been neglected in this very simple analysis; however, this mechanism is consistent with the appearance of hairpin vortices, which erupt from the wall at the onset of transition. The condition at which the square bracket in Eq. (11) goes to zero is therefore also taken as the condition for the start of transition. At this critical condition

$$\frac{u}{\overline{u}} = \frac{1 + (1 + \sin\omega t)^{1/2}}{2} \tag{12}$$

and so

$$\frac{u'_{\mathrm{rms}}}{\overline{u}} = \left(\frac{2\Pi}{2\sqrt{2} + \Pi} - 1\right)^{1/2} = 0.23 \tag{13}$$

Figures 6 and 7 show that this value of $u'_{\mathrm{rms}}/\overline{u}$ is consistent with the experimental values found close to the wall at start

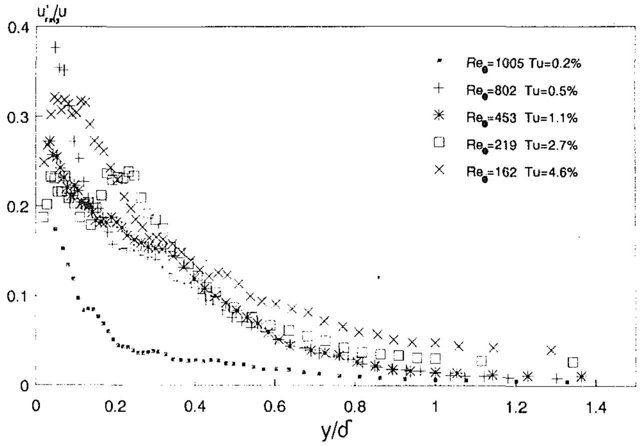

Fig. 6 Local turbulence level profiles at start of transition for zero pressure gradient and various turbulence grids

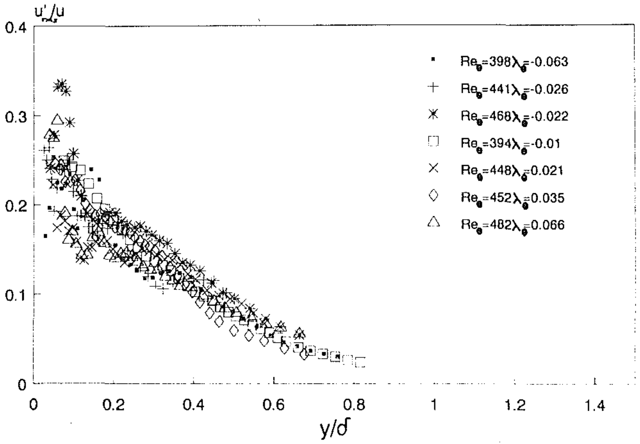

Fig. 7 Local turbulence level profiles at start of transition for adverse and favorable pressure gradients; Tu = 1 percent

of transition for a range of turbulence levels and pressure gradients. The preceding analysis has made some major assumptions, for example spanwise variations have been neglected and the fluctuations in E' are assumed to have a single sinusoidal frequency. The real situation is of course far more complex; however, the local turbulence level $u'_{\mathrm{rms}}/\bar{u}$ is essentially a measure of the degree of streamline distortion and therefore a local turbulence level of approximately 23 percent can be considered to represent the amount of streamline distortion that can be tolerated prior to laminar breakdown and the emergence of hairpin vortices and turbulent spots. It is also interesting to note that the local turbulence level near the wall in a turbulent boundary layer has a similar value of about 26 percent (Klebanoff, 1954).

From Eqs. (2) and (3)

$$\left(\frac{u'_{\mathrm{rms}}}{\bar{U}}\right)=\beta \mathrm{Re}_\delta^2 Y^2 Tu \bigg/ \left(\frac{\bar{u}}{\bar{U}}\right)^2 \tag{14}$$

and so assuming a Pohlhausen profile such that near the wall

$$\frac{\bar{u}}{\bar{U}}=\left(2+\frac{\lambda}{6}\right)Y \tag{15}$$

$$\mathrm{Re}_{\delta\mathrm{START}}=2\left(1+\frac{\lambda}{12}\right)\left(\frac{u'_{\mathrm{rms}}}{\bar{u}}\right)^{1/2}_{\mathrm{START}}\beta^{-1/2}Tu^{-1/2} \tag{16}$$

or

$$\mathrm{Re}_{\theta\mathrm{START}}=2\left(1+\frac{\lambda}{12}\right)\left(\frac{u'_{\mathrm{rms}}}{\bar{u}}\right)^{1/2}_{\mathrm{START}}\beta^{-1/2}\left(\frac{\theta}{\delta}\right)Tu^{-1/2} \tag{17}$$

where

$$\frac{\theta}{\delta}=\frac{37}{315}-\frac{\lambda}{945}-\frac{\lambda^2}{9072} \tag{18}$$

This equation can also be written in terms of the skin friction coefficient C_f at start of transition

$$C_{f\mathrm{START}}=2\beta^{1/2}Tu^{1/2}\left(\frac{u'_{\mathrm{rms}}}{\bar{u}}\right)^{-1/2}_{\mathrm{START}} \tag{19}$$

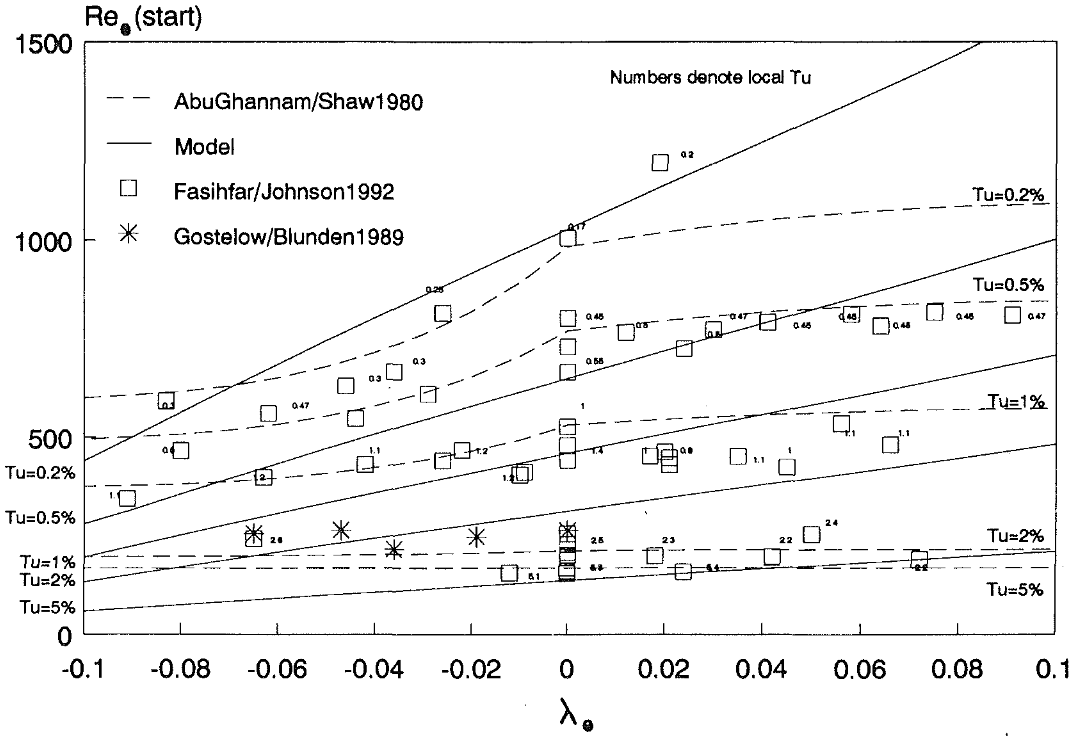

Fig. 8 Start of transition Reynolds number as a function of pressure gradient and free-stream turbulence level

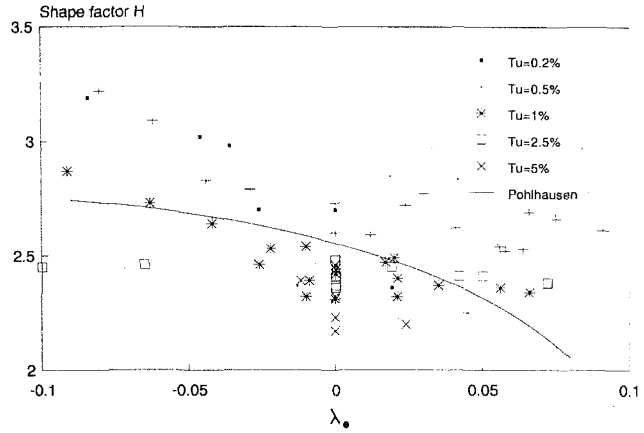

Fig. 9 Start of transition shape factor as a function of pressure gradient and free-stream turbulence level

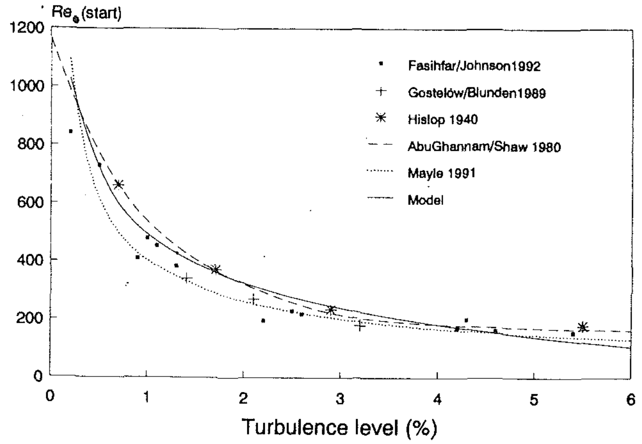

Fig. 10 Start of transition Reynolds number dependence on free-stream turbulence

Start of Transition Prediction

A prediction formula for start of transition is obtained by substituting for β, from the empirical Eq. (4) and for $(u'_{\rm rms}/\bar{u})_{\rm START}$ from Eq. (13) into Eq. (17)

$$\mathrm{Re}_\theta = 0.96\left(1+\frac{\lambda}{12}\right)\frac{\theta}{\delta}(6\times10^{-6}Tu+6\times10^{-2}Tu^4)^{-1/2} \quad (20)$$

This prediction formula is shown in Fig. 8 along with experimental start of transition data (typically 2 percent intermittency) for a range of free-stream turbulence levels and pressure gradients. The frequently used correlation of Abu Ghannam and Shaw (1980) is also shown for comparison. Abu Ghannam and Shaw chose to correlate their results based on the mean of the turbulence levels at the blade leading edge and the measurement location with the intention of accounting for the development history of the boundary layer. The current model predictions do not depend on this history and so Fig. 8 is presented in terms of local *Tu*.

The experimental data suggest that the effect of pressure gradient is greatest at low turbulence levels and is negligible for $Tu > 3$ percent as concluded by Mayle (1991). This is not, however, reflected by the model, because at high turbulence levels, the boundary layer profile is distorted significantly and the Pohlhausen representation for the velocity gradient at the wall (Eq. (15)) is no longer reliable. The degree of boundary layer distortion for the data of Fig. 8 is illustrated when the shape factors, *H*, are plotted in Fig. 9. At low turbulence levels the rate of decrease in shape factor with increasing λ_θ is close to the Pohlhausen relationship, although the experimental values are rather higher, suggesting a lower C_f and hence that the use of Pohlhausen profiles in the model will predict transition late. Apparently, although significant fluctuation velocities and hence Reynolds stresses are generated within the boundary layer, they are limited to the near-wall region and hence do not induce significant boundary layer distortion. At higher turbulence levels the variation of shape factor with pressure gradient is less marked than the Pohlhausen curve suggests and at $Tu = 2.5$ percent, *H* is virtually constant. This is because high free-stream turbulence levels create significant fluctuation velocities and Reynolds stresses throughout the boundary layer and these distort the boundary layer with an increase in C_f. Increases of up to 60 percent in skin friction coefficient due to elevated free-stream turbulence levels have been reported by Dyban et al. (1976).

The values for β for $Tu = 0.2$ and 0.5 percent from Eq. (4) used for the predictions in Fig. 8 are much higher than the values plotted in Fig. 5. If the lower β values had been used for $Tu < 1$ percent transition would have been predicted late. It would therefore appear that Tollmien–Schlichting instability triggers transition at low turbulence levels prior to the fluctuations generated through the bypass mechanism reaching a critical level. This finding is in accordance with those of Gostelow et al. (1994) who found that the amplification of Tollmien–Schlichting waves resulted in early transition inception for $Tu < 1$ percent under adverse pressure gradients. The local turbulence level does increase nevertheless to 23 percent even for $Tu < 1$ percent at start of transition as shown in Fig. 6.

For zero pressure gradients, Eq. (20) can be simplified to

$$\mathrm{Re}_{\theta\mathrm{START}} = 46(Tu+10^4Tu^4)^{-1/2} \quad (21)$$

This equation is shown in Fig. 10 together with experimental data and the correlations of Abu Ghannam and Shaw (1980) and Mayle (1991). Although the three curves differ by up to 20 percent for turbulence levels around 1 percent, they all fit the experimental data acceptably as considerable scatter is exhibited. This scatter is probably due to differing turbulent length scales as demonstrated by Mayle (1991).

Conclusions

1 A pressure fluctuation function E' has been defined, which in the near-wall region of a laminar boundary layer, depends only on the free-stream properties and hence is independent of boundary layer profile or thickness. The velocity fluctuations within the near-wall region of laminar boundary layers, with or without pressure gradient, can thus be determined from a single parameter β which varies only with the free-stream turbulent properties.

2 The local turbulence level close to the wall increases as a laminar boundary layer develops until it reaches approximately 23 percent at which point transition commences. The value of 23 percent can be determined analytically using a simple approximate model.

3 A semi-empirical start of transition prediction formula results from combining the findings outlined in conclusions 1 and 2. Transition is modeled fairly accurately for the bypass regime ($Tu > 1$ percent). For low turbulence levels, fluctuation velocities due to Tollmien–Schlichting instability induce transition sooner than the bypass mode.

4 The empirical relationship between β and *Tu* given in Eq. (4) is based on very limited data; furthermore, β undoubtedly depends on turbulent length scale as well as turbulence level. Additional data for a wide variety of turbulence-generating grids are required therefore to establish a general relationship for β.

5 The laminar boundary layer is very significantly distorted by high free-stream turbulence levels and this tends, in general, to stabilize the boundary layer, although it may be destabilized

in strong favorable pressure gradients. Again the degree of distortion will depend not only on turbulence level, but also length scale.

References

Abu Ghannam, B. J., and Shaw, R., 1980, "Natural Transition of Boundary Layers—The Effects of Turbulence, Pressure Gradient and Flow History," *J. Mech. Engng. Sci.*, Vol. 22, pp. 213-228.

Dyban, Y. P., Epik, E. Y., and Suprun, T. T., 1976, "Characteristics of the Laminar Boundary Layer in the Presence of Elevated Free-Stream Turbulence," *Fluid Mechanics—Soviet Research*, Vol. 5(4), pp. 30-36.

Fasihfar, A., and Johnson, M. W., 1992, "An Improved Boundary Layer Transition Correlation," ASME Paper No. 92-GT-245.

Fasihfar, A., 1992, "Mechanisms of Boundary Layer Transition," Ph.D. Thesis, University of Liverpool, United Kingdom.

Gostelow, J. P., and Blunden, A. R., 1989, "Investigations of Boundary Layer Transition in Adverse Pressure Gradient," ASME JOURNAL OF TURBOMACHINERY, Vol. 111, pp. 366-375.

Gostelow, J. P., Blunden, A. R., and Walker, G. J., 1994, "Effects of Free-Stream Turbulence and Adverse Pressure Gradients on Boundary Layer Transition," ASME JOURNAL OF TURBOMACHINERY, Vol. 116, pp. 392-404.

Hislop, G. S., 1940, "The Transition of a Laminar Boundary Layer in a Wind Tunnel," Ph.D. Thesis, Cambridge University, United Kingdom.

Klebanoff, P. S., 1954, "Characteristics of Turbulence in Boundary Layers With Zero Pressure Gradient," National Bureau of Standards, NACA TN 3178.

Mayle, R. E., 1991, "The Role of Laminar-Turbulent Transition in Gas Turbine Engines," ASME JOURNAL OF TURBOMACHINERY, Vol. 113, pp. 509-537.

Savill, A. M., 1991, "A Synthesis of T3 Test Case Predictions," *Proc. 1st ERCOFTAC Workshop*, Cambridge University Press, United Kingdom.

Walker, G. J., and Gostelow, J. P., 1990, "Effects of Adverse Pressure Gradients on the Nature and Length of Boundary Layer Transition," ASME JOURNAL OF TURBOMACHINERY, Vol. 12, pp. 198-205.

Calculation of Transitional Boundary Layers With an Improved Low-Reynolds-Number Version of the k-ϵ Turbulence Model

D. Biswas

Y. Fukuyama

Research and Development Center,
Toshiba Corporation,
Kawasaki, Japan

Several well-known low-Reynolds-number versions of the k-ϵ models are analyzed critically for laminar to turbulent transitional flows as well as near-wall turbulent flows from a theoretical and numerical standpoint. After examining apparent problems associated with the modeling of low-Reynolds-number wall damping functions used in these models, an improved version of the k-ϵ model is proposed by defining the wall damping factors as a function of some quantity (turbulence Reynolds number Re_t) that is only a rather general indicator of the degree of turbulent activity at any location in the flow rather than a specific function of the location itself, and by considering the wall limiting behavior, the free-stream asymptotic behavior, and the balance between production and destruction of turbulence. This new model is applied to the prediction of (1) transitional boundary layers influenced by the free-stream turbulence, pressure gradient, and heat transfer; (2) external heat transfer distribution on the gas turbine rotor and stator blade under different inlet Reynolds number and free-stream turbulence conditions. It is demonstrated that the present model yields improved predictions.

1 Introduction

The boundary layer developing on a turbomachinery blade usually starts as a laminar layer, but in most situations it inevitably becomes turbulent. The transition from laminar to turbulent in the boundary layer, which often causes a significant change in operational performance of the machinery, is generally influenced by the free-stream turbulence and also by the pressure gradients.

A very well-known approach for calculating the transition: boundary layers is to carry out boundary layer analysis using the low-Reynolds-number version of the k-ϵ turbulence model, which involves the low-Reynolds-number functions for simulating the turbulent transport of the free-stream turbulence into the laminar boundary layers. The low-Reynolds-number functions of the existing two-equation models have been successfully applied to the near-wall low-Reynolds-number flows (Patel et al., 1985), but few models have been tested for calculating the laminar to turbulent transition of boundary layers (Biswas et al., 1989). In the present work first of all, some of the well-known existing models are tested for their ability to calculate laminar to turbulent transition of boundary layers and the reasons for their deficiency have been examined carefully. Then an improved version of this model is proposed to reproduce the wall limiting behavior of turbulence, the correct streamwise blending between a pretransitional pseudolaminar boundary layer and the posttransitional fully turbulent boundary layer under the experimental effect of free-stream turbulence and pressure gradient. The validity of the new model along with the other models considered is then tested by applying to the prediction of: (1) transitional boundary layers influenced by free-stream turbulence, pressure gradient, and heat transfer; (2) external heat transfer distribution on a gas turbine stator and rotor blade, where the flow is very complicated, with strong acceleration on the blade pressure surface and acceleration followed by a region of deceleration on the suction surface, under different inlet Reynolds number and free-stream turbulence conditions.

2 Mathematical Models

2.1 Governing Equations. The basic equations used in the present study are the usual continuity, momentum, and stagnation enthalpy equations for two-dimensional boundary layers given below:

$$\frac{\partial(\rho U)}{\partial x}+\frac{\partial(\rho V)}{\partial y}=0 \tag{1}$$

$$\rho U\frac{\partial U}{\partial x}+\rho V\frac{\partial V}{\partial y}=-\frac{dP}{dx}+\frac{\partial}{\partial y}\left(\mu\frac{\partial U}{\partial y}-\rho\overline{uv}\right) \tag{2}$$

Contributed by the International Gas Turbine Institute and presented at the 38th International Gas Turbine and Aeroengine Congress and Exposition, Cincinnati, Ohio, May 24-27, 1993. Manuscript received at ASME Headquarters February 18, 1993. Paper No. 93-GT-73. Associate Technical Editor: H. Lukas.

$$\rho U\frac{\partial I^*}{\partial x}+\rho V\frac{\partial I^*}{\partial y}=\frac{\partial}{\partial y}\left\{-\frac{K}{C}\frac{\partial I^*}{\partial y}-\rho\overline{i^*v}+\mu\frac{\partial}{\partial y}\left(\frac{U^2}{2}\right)\right\} \tag{3}$$

where I^* is the stagnation enthalpy of the fluid, defined as $I^*=I+U^2/2$, and I is the static enthalpy. U and V are the x and y component of velocity, respectively. u, v, and i are the fluctuating velocities and enthalpy, respectively. ρ and μ are the density and viscosity of fluid, respectively and the overbar denotes the time averaging of the variables.

With the aid of Boussinesq assumption the turbulent shear stress ($\rho\overline{uv}$) and heat flux ($-\rho\overline{iv}$) are modeled as follows:

$$-\rho\overline{uv}=\mu_t\frac{\partial U}{\partial y} \tag{4}$$

$$-\rho\overline{iv}=\frac{\mu_t}{\mathrm{Pr}_t}\frac{\partial I^*}{\partial y} \tag{5}$$

where Pr_t is the turbulent Prandtl number and the eddy-viscosity μ_t is related to the turbulent kinetic energy k and to its dissipation rate ϵ as follows:

$$\mu_t=\rho C_\mu f_\mu\frac{k^2}{\tilde{\epsilon}} \tag{6}$$

$$\epsilon=\tilde{\epsilon}-D \tag{7}$$

where the local values of k and ϵ are evaluated from the following semi-empirical equations:

$$\rho U\frac{\partial k}{\partial x}+\rho V\frac{\partial k}{\partial y}=\frac{\partial}{\partial y}\left\{\left(\mu+\frac{\mu_t}{\sigma_k}\right)\frac{\partial k}{\partial y}\right\}+PK-\rho\epsilon \tag{8}$$

$$\begin{aligned}\rho U\frac{\partial\tilde{\epsilon}}{\partial x}+\rho V\frac{\partial\tilde{\epsilon}}{\partial y}&\\ =\frac{\partial}{\partial y}\left\{\left(\mu+\frac{\mu_t}{\sigma_\epsilon}\right)\frac{\partial\tilde{\epsilon}}{\partial y}\right\}+\frac{\tilde{\epsilon}}{k}\left(C_{\epsilon1}f_1PK-\rho C_{\epsilon2}f_2\tilde{\epsilon}\right)+E&\end{aligned} \tag{9}$$

where PK is the production of turbulence, defined as $PK=\mu_t(\partial U/\partial y)^2$. The terms D and E in Eqs. (7) and (9) are used in the Launder–Sharma model. The term D is used to satisfy the boundary condition $\tilde{\epsilon}=0$ at the wall and the term E is used to increase the dissipation rate in the buffer region, which resulted in a lower peak of k.

The turbulence models considered here are those of Launder-Sharma (L-S) (Launder and Sharma, 1979), Lam-Bremhorst (L-B) (Lam and Bremhorst, 1981), Nagano–Tagawa (N-T) (Nagano and Tagawa, 1990), and Kasagi-Sikasono (K-S) (Kasagi, 1992). These models are chosen for closer evaluation in the present work, because, when compared with other existing low Reynolds-number k-ϵ models, tests have shown these models to be among the best in predicting characteristics of fully turbulent flows (Patel et al., 1985; Nagano and Tagawa, 1990). Empirical constants C_μ, $C_{\epsilon1}$, $C_{\epsilon2}$, σ_k, and σ_ϵ used in these models are presented in Table 1. In order to incorporate the near-wall effects into the standard k-ϵ model, some low-Reynolds-number damping factors are introduced. The purpose of these functions f_μ, f_1, and f_2 in different models is to provide a somewhat similar kind of modifying influence on the standard k-ϵ model. These functions and the additional terms E and D, together with the wall boundary condition for ϵ, are summarized in Table 1.

2.2 Numerical Details. The calculations have been carried out with a forward marching two-dimensional semi-implicit finite volume boundary layer procedure based on Patankar-Spalding (Crawford and Kays, 1976), which employs a grid system adopting automatically to fit the growth of the boundary layer. Grid dependency of the results is verified by changing the number of cross-stream grid points. Grid-independent solutions are obtained by using about 100 grid points in the cross-stream directions. In order to resolve the streamwise changes in the viscous sublayer sufficiently, the maximum streamwise step size is restricted to the viscous sublayer thickness, i.e., $\Delta x<\nu/U_\tau$.

3 Modeling of Limiting Behavior of Wall Turbulence

The application of different k-ϵ models to predicting a flat plate transitional boundary layer led to the understanding that the existing k-ϵ models have some deficiencies in terms of modeling the low-Reynolds-number damping functions. Some of the models assumed that the approximations that have been devised to handle near-wall low-Reynolds-number flows are equally valid for low-Reynolds-number transitional flows. This is because these models could produce the correct blending between the (essentially laminar) viscous sublayer and fully turbulent outer boundary layer region (Nagano and Tagawa, 1990), but failed to provide the correct streamwise (x) blending between the pretransitional pseudolaminar boundary layer and the posttransitional fully turbulent boundary layer flow. This study indicated that the models in which low-Reynolds-number damping factors are defined as an explicit y dependence are less likely to predict accurate transition process, a fact that was observed by Fujisawa (1990) also. Physically, anywhere near correct predictions of transitional boundary layer can be

Nomenclature

C = specific heat (Eq. (3))
C_f = skin friction factor
$C_{\epsilon1}$, $C_{\epsilon2}$, C_μ = empirical constants in Eqs. (9) and (6) and listed in Table 1
f_1, f_2, f_μ = empirical functions in Eqs. (9) and (6) and listed in Table 1
I = static enthalpy
I^* = stagnation enthalpy
i = fluctuating static enthalpy
k = turbulent kinetic energy
K = thermal conductivity in Eq. (3)
l_{dh} = length scale for large scale eddies
l_{d1} = Taylor microscale
Pr = Prandtl number
Re_c = Reynolds number based on blade chord
Re_x = Reynolds number based on axial distance
Re_t, Re_g = turbulence Reynolds number defined in Eqs. (17), (21)
T_u = free-stream turbulence intensity
U = local mean velocity parallel to wall
V = local mean velocity normal to wall
u = fluctuating velocity parallel to wall
v = fluctuating velocity normal to wall
x = streamwise cartesian coordinate
y = Cartesian coordinate normal to the wall
y^+ = dimensionless value of y: $U_\tau y/\nu$
ϵ = dissipation rate of turbulent kinetic energy
$\tilde{\epsilon}$ = isotropic dissipation rate of turbulent kinetic energy
κ = von Karman mixing length constant
μ = dynamic viscosity
ν = kinematic viscosity
σ = Schmidt number
τ = shear stress
ρ = density

Subscripts

1 = inlet station
e = free-stream
w = wall

Table 1 Constants and functions for the k-ϵ group of models

Model	C_u	$C_{\epsilon 1}$	$C_{\epsilon 2}$	σ_k	σ_ϵ	f_μ	f_1	f_2	D	E	ϵ_w - B.C.
L-S	0.09	1.44	1.92	1.0	1.3	$\exp[\frac{-3.4}{(1+R_t/50)^2}]$	1.0	$1-0.3\exp(-R_t^2)$	$2\nu(\frac{\partial\sqrt{k}}{\partial y})^2$	$2\nu\nu_t(\frac{\partial^2 U}{\partial y^2})^2$	0
L-B	0.09	1.44	1.92	1.0	1.3	$[1-\exp(-0.016R_y)]^2$ $\times(1+\frac{19.5}{R_y})$	$1+(0.05/f_\mu)^3$	$1-\exp(-R_t^2)$	0	0	$\frac{\partial\epsilon}{\partial y}=0$
N-T	0.09	1.45	1.90	1.4	1.3	$[1-\exp(-\frac{y+}{26})]^2$ $\times(1+\frac{4.1}{R_t^{0.75}})$	1.0	$[1-0.3\exp\{-(\frac{R_t}{6.5})^2\}]$ $\times\{1-\exp(-\frac{y+}{6})\}^2$	0	0	$\nu\frac{\partial^2 k}{\partial y^2}$
K-S	0.09	1.32	1.80	1.4	1.3	$\{1+(\frac{13.5}{R_t})\exp(-R_t^{0.25})\}$ $\times[1-\exp\{-\frac{R_\epsilon}{150}-(\frac{R_\epsilon}{25})^2\}]$	1.0	$[1-2/9\exp\{-(\frac{R_t}{6})^2\}]$ $\times\{1-\exp(-\frac{R_\epsilon}{3.7})\}^2$	0	0	$\nu\frac{\partial^2 k}{\partial y^2}$
Present	0.09	1.46	1.90	1.4	1.3	$[1-\exp(-\frac{R_t}{150})]$ $\times(1+\frac{18.5}{R_t})$	$1+0.3\exp[-(\frac{R_t}{50})^2]$	$[1-0.3\exp\{-(\frac{R_t}{6.5})^2\}]$ $\times[1-\exp(-\frac{R_y}{10})]$	0	0	$\frac{\partial\epsilon}{\partial y}=0$

$R_t = \frac{k^2}{\nu\epsilon}$; $R_y = \frac{\sqrt{k}\,y}{\nu}$; $y^+ = \frac{U_\tau y}{\nu}$; $R_\epsilon = y/(\nu^3/\epsilon)^{0.25}$

achieved by defining the low-Reynolds-number damping factors as a function of some quantity (for example turbulence Reynolds number Re_t), which is only a rather general indicator of the degree of turbulent activity at any x or y location in the flow rather than a specific function of location itself. Based on the understanding of characteristics of different low-Reynolds-number functions, the present paper proposes an improved model in which these functions satisfy both the wall limiting effect and the asymptotic behavior in the region away from the wall.

3.1 Model Constants. Table 1 contains five empirical constants, C_μ, $C_{\epsilon 1}$, $C_{\epsilon 2}$, σ_k, and σ_ϵ, used in different models. Away from the wall, the functions f_μ, f_1, and f_2 multiplying the first three constants tend to unity; therefore, the model behavior depends only on the values of the five constants.

The constant C_μ is determined from experimental data in the near-wall region and has a value of 0.09. Table 1 shows a deversity in the values of $C_{\epsilon 1}$, $C_{\epsilon 2}$, σ_k, and σ_ϵ. In the present model, the constants $C_{\epsilon 1}$ and $C_{\epsilon 2}$ are chosen on the basis of the limiting behavior of free turbulence. This limiting behavior demands that the decay law of the final period of homogeneous turbulence be given by:

$$k \propto x^{-n} \tag{10}$$

where x is the streamwise distance. The experiment takes the value of n as $1 \sim 1.25$ during the initial period and 2.5 during the final period, respectively (Patel et al., 1985). In a homogeneous decaying turbulent flow, Eqs. (8) and (9) become simply:

$$U\frac{dk}{dx} = -\tilde{\epsilon} \tag{11}$$

$$U\frac{d\tilde{\epsilon}}{dx} = -C_{\epsilon 2}f_2\frac{\tilde{\epsilon}^2}{k} \tag{12}$$

Combining Eqs. (10), (11), and (12), we have:

$$C_{\epsilon 2}f_2 = (n+1)/n \tag{13}$$

Taking $n=1.1$ for the initial period ($f_2=1$), the model constant $C_{\epsilon 2}$ becomes 1.9. Also, the set of constants $C_{\epsilon 1}$ and $C_{\epsilon 2}$ must satisfy the relation:

$$C_{\epsilon 1} = C_{\epsilon 2} - \left(\frac{k^2}{\sigma_\epsilon\sqrt{C_\mu}}\right) \tag{14}$$

to which the ϵ equation reduces in local equilibrium flows with a logarithmic velocity distribution. Using $C_{\epsilon 2}=1.9$, $\kappa=0.41$, $\sigma_\epsilon=1.3$, and $C_\mu=0.09$, Eq. (14) gives $C_{\epsilon 1}=1.46$, which is used in the present model.

In general, the constants σ_k and σ_ϵ are given values of 1.0 and 1.3, respectively. However, if these model constants are set as $\sigma_k<\sigma_\epsilon$, the turbulent diffusion of k from the wall region overwhelms that of ϵ. Therefore, based on the results of the Reynold's stress equation modeling ($\sigma_k/\sigma_\epsilon=1.09$) by Hanjalic and Launder (1976) using $\sigma_k=1.3$, σ_ϵ is given a value of 1.4.

3.2 Reynolds Shear Stress and the Function f_μ. The function f_μ multiplies the eddy viscosity relation Eq. (6) and is introduced to mimic the direct effect of molecular viscosity on the shear stress. This function attempts to model both the viscous and pressure strain effects. In the immediate vicinity of the wall, the relations $U^+=y^+$, $u \propto y$, $v \propto y^2$, and $w \propto y$ hold, as does $\epsilon \rightarrow \epsilon_w$ for $y \rightarrow 0$. Consequently, the limiting behavior of wall turbulence is represented by the following relations: $k \propto y^2$, $-\overline{uv} \propto y^3$; however, according to Van Driest mixing length formula the shear stress $-\overline{uv} \propto y^4$. Using this relation in Eq. (4), $\nu_t \propto y^n$, where $n=3$ or 4. From Eq. (6) we have $f_\mu \propto y^n$ where n lies between 0 and -1.

In the present study in modeling f_μ, the relationship between two length scales, one very near the wall, which is the Taylor microscale, and the other in the fully turbulent region (large-scale energy containing eddies) is considered first; the length scale for large-scale eddies is defined as:

$$l_{dh} = C_d k^{1.5}/\epsilon \tag{15}$$

However, near the wall, where the dissipation of turbulent kinetic energy is very large, the length scale is represented by the Taylor microscale defined as:

$$l_{d1} = C_1\sqrt{\nu k/\epsilon}; \quad C_1 = \sqrt{2} \tag{16}$$

These two length scales can be related as:

$$l_{dh}/l_{d1} \propto \sqrt{\mathrm{Re}_t}; \quad \mathrm{Re}_t = k^2/(\nu\epsilon) \tag{17}$$

This Eq. (17) means that near the wall where, $\mathrm{Re}_t \rightarrow 0$, l_{d1} becomes larger than l_{dh} and away from the wall where Re_t becomes very large, l_{dh} dominates. Thus Re_t serves as a link between these two length scales of dissipation and in the present model f_μ is defined as a function of Re_t by the following relation:

$$f_\mu = \left\{1-\exp\left(-\frac{\mathrm{Re}_t}{150}\right)\right\} \times \left\{1+\frac{18.5}{\mathrm{Re}_t}\right\} \tag{18}$$

Table 2 Exponents of the near-wall variation of the turbulence quantities

Model	L - S	L - B	N - T	K - S	Present
$\tilde{\epsilon}$	1	0	0	0	0
$k^2/\tilde{\epsilon}$	3	4	4	4	4
f_μ	0	0	-1	-1	0
$-\overline{uv}$	3	4	3	3	4
$k^{3/2}/\tilde{\epsilon}$	2	3	3	3	3

The physical meaning of Eq. (18) is clear from Eq. (6). Thus, away from the wall (where Re_t becomes large), the relation $\nu_t \propto k^{0.5} l_{dh}$, holds and the eddy viscosity is thereby determined by the comparatively large-scale energy-containing eddies, on the other hand as the wall is approached it is the small-scale eddies dominating mainly the dissipation process. This corresponds closely to the fact that the energy conservation law is maintained by dissipating almost all the energy, which is diffusively transported from the region away from the wall. Also, by a series expansion of f_μ (Eq. (18)) we obtain $f_\mu \propto y^0$, and using f_μ, from Eqs. (4) and (6), we obtain $-\overline{uv} \propto y^4$, which satisfies the Van Driest mixing length formula. However, further research will be performed to study the wall near behavior of shear stress. The exponents of different variables for different models are compiled in Table 2. Also, the numerical values of 150 and 18.5 in Eq. (18) are decided on the basis of algebraic stress model (So et al., 1991) and numerical experiment, respectively.

3.3 The Function f_2. The function f_2 is introduced primarily to incorporate low-Reynolds-number effects in the destruction term of the ϵ equation. To satisfy the limiting behavior of free turbulence, f_2 can be written in the form

$$f_2 = 1 - 0.3 \exp\left\{-\left(\frac{\mathrm{Re}_t}{6.5}\right)^2\right\} \tag{19}$$

On the other hand, the ϵ equation (Eq. (5)) at the wall becomes

$$\nu \frac{\partial^2 \epsilon}{\partial y^2} = C_{\epsilon 2} f_2 \frac{\epsilon^2}{k} \tag{20}$$

Considering the limiting behavior of wall turbulence, $f_2 \propto y^2$ is required to satisfy Eq. (20). However, near the wall the Eq. (19) reaches y^0. Therefore, in the present model, in order to satisfy the limiting behavior at the wall $f_2 \propto y^2$ and free turbulence as well, the following equation is proposed:

$$f_2 = \left[1 - 0.3 \exp\left\{-\left(\frac{\mathrm{Re}_t}{6.5}\right)^2\right\}\right]\left\{1 - \exp\left(\frac{-\mathrm{Re}_y}{10}\right)\right\} \tag{21}$$

Near the wall we have $\mathrm{Re}_y = \sqrt{k}\,(y/\nu) \propto y^2$ and a series expansion of f_2 (Eq. (21)), results in $f_2 \propto y^2$. In the present work Re_y is used in the equations of f_2; however, in future work this would be replaced with Re_t-dependence. The numerical value of 10 in Eq. (21) is decided on the basis of numerical experiment.

3.4 The Function f_1. In the calculation of transitional flow by taking into account the correct effect of near-wall low-Reynolds-number flow, proper balance between production and destruction of turbulence in this region needs to be considered. In the present model in order to have this balance, the magnitude of ϵ is increased in this region by defining f_1 as follows:

$$f_1 = 1 + 0.3 \exp\left\{-\left(\frac{\mathrm{Re}_t}{50}\right)^2\right\} \tag{22}$$

Near the wall, the Eq. (22) reaches y^0 and satisfies the limiting behavior of wall turbulence $f_1 \propto y^0$. The numerical value of 50 in Eq. (22) is decided on the basis of the algebraic stress model (So et al., 1991).

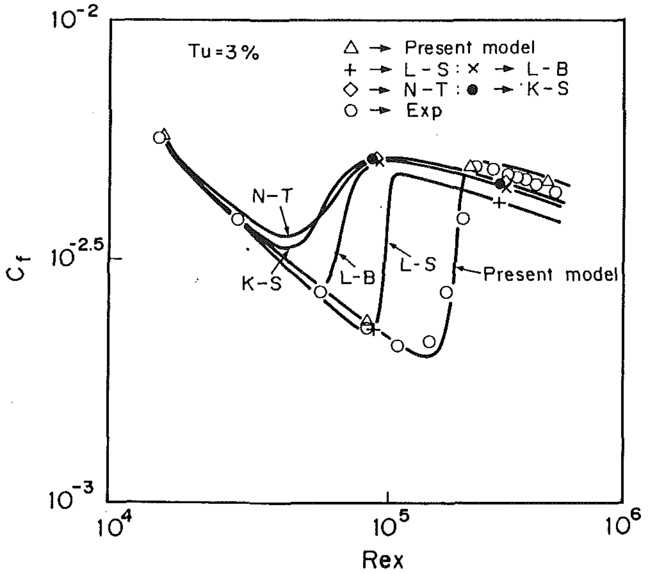

Fig. 1(*a*) Variation of friction coefficient in a transitional boundary layer (turbulence intensity = 3 percent)

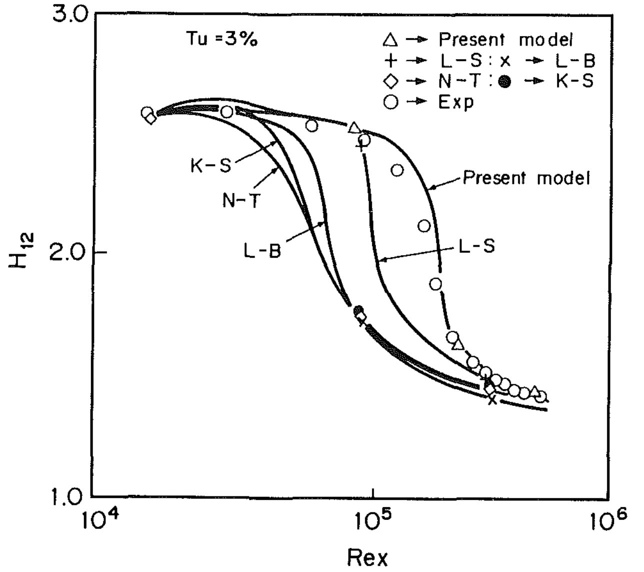

Fig. 1(*b*) Variation of shape factor H_{12} in a transitional boundary layer (turbulence intensity = 3 percent)

4 Results and Discussion

First of all the validity of the models is tested by comparing the results of calculations with the experimental data on flat plate transitional boundary layers presented in the ERCOFTAC (European Research Community On Flow Turbulence and Combustion) Workshop '91 (Savill, 1991). The object is to predict the initial effect of two different levels of isotropic free-stream turbulence on a laminar boundary layer, and the subsequent transition, in zero pressure gradient.

In the case of computations, the experimental initial profile for the mean velocity and turbulent kinetic energy is specified at the starting location. The initial profile of ϵ is given by $\epsilon = Ak(\partial U/\partial y)$, where A is chosen as 0.3, which is the value for the local equilibrium flow conditions. The experimental value of free-stream turbulence length scale at the starting location of calculation is used to obtain free-stream ϵ. The experimental free-stream distribution of mean velocity and turbulence intensity are specified and serve as boundary con-

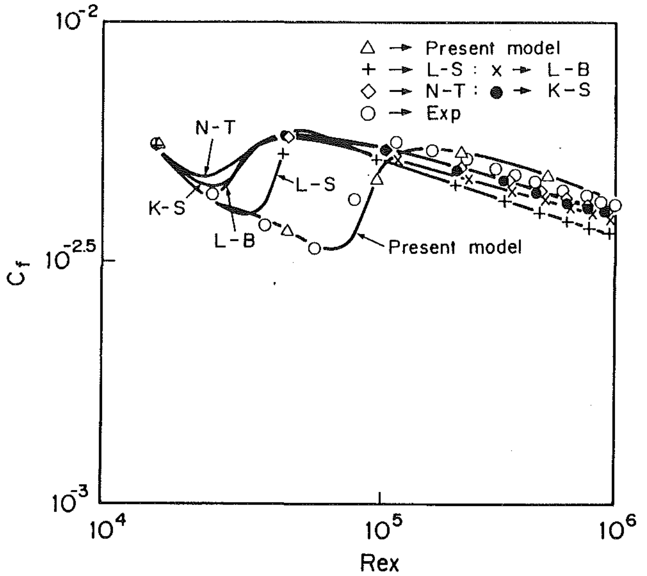

Fig. 2(*a*) Variation of friction coefficient in a transitional boundary layer (turbulence intensity = 6 percent)

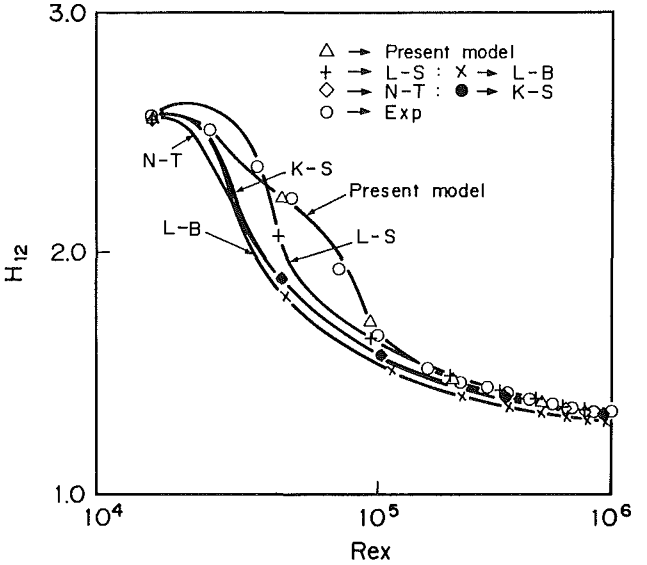

Fig. 2(*b*) Variation of shape factor H_{12} in a transitional boundary layer (turbulence intensity = 6 percent)

ditions. The free-stream distribution of ϵ is given by $U(dU/dx) = -\epsilon$.

In Fig. 1(*a*, *b*) and 2(*a*, *b*) are plotted the calculated variation of friction coefficient C_f and shape factor H with flow Reynolds number along with the experimental data for initial turbulence intensities of 3 and 6 percent, respectively. The symbols Δ, +, ×, ◇, and • represent the results of calculation by the present model, L-S, L-B, N-T, and K-S model, respectively, and the symbol ○ represents the experimental data. It can be observed from these figures that there is a wide variation of flow Reynolds number in the predicted location of transition. N-T and K-S models predict transition far too early as compared to experiment for both 3 and 6 percent turbulence intensity. For turbulence intensity of 3 percent, L-B model predicted transition slightly early. The L-S model produced better prediction of transition for 3 percent turbulence intensity; however, the fully turbulent C_f is slightly underpredicted. In the ERCOFTAC Report (Savill, 1991), some groups have showed better agreement between experimental data and prediction by using the modified L-S model for the case of 3 percent turbulence intensity. For 6 percent turbulence intensity the L-S and L-B models also predicted transition far too early. However, all the models predicted well the experimental fact that the location of transition moves upstream with the increase of free-stream turbulence intensity. More significantly, it is observed from this study that all the models are a little too sensitive to increasing turbulence intensity. The present model showed very good predictions of transition and the fully turbulent C_f level for both the turbulence intensity levels and hence reproduced the experimental effect of free-stream turbulence quite satisfactorily. Also, the present model predicted the variation of H right through transition quite accurately. For a higher turbulence level of 6 percent, the effect of the diffusion of turbulent kinetic energy from the free stream into the laminar boundary layer is expected to reproduce the initial drop in H prior to transition onset.

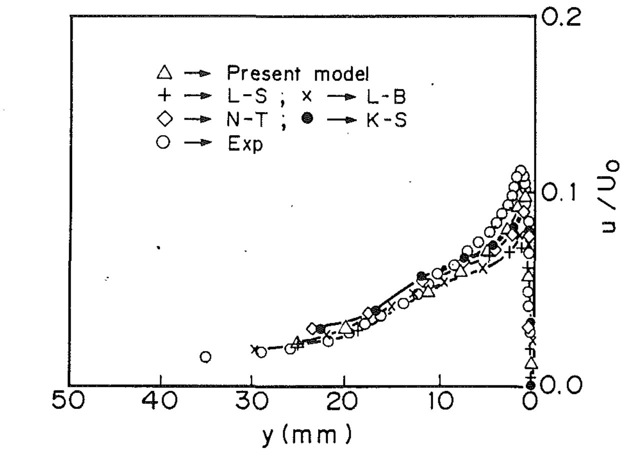

Fig. 3(*a*) Boundary layer turbulence velocity u/U_0 profile at $x = 0.995$ m and turbulence intensity of 3 percent

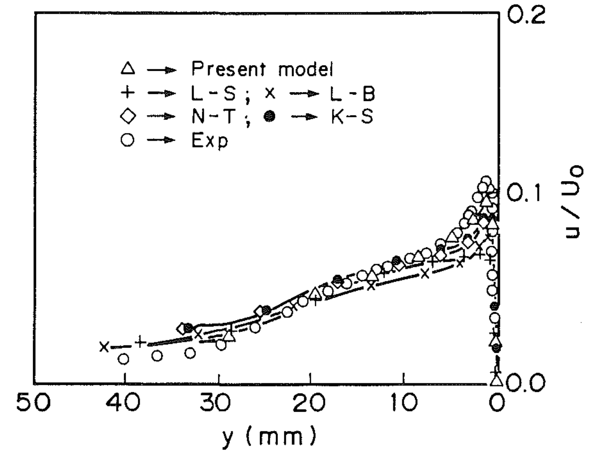

Fig. 3(*b*) Boundary layer turbulence velocity u/U_0 profile at $x = 1.495$ m and turbulence intensity of 3 percent

In Fig. 3(*a*, *b*) and 4(*a*, *b*) are plotted the calculated boundary layer turbulent velocity u/U_e profiles along with the experimental data at axial locations $x = 0.995$ m ($\mathrm{Re}_x = 3.35 \times 10^5$) and 1.495 m ($\mathrm{Re}_x = 5.04 \times 10^5$) for turbulence intensity of 3 percent and at $x = 0.895$ m ($\mathrm{Re}_x = 5.5 \times 10^5$) and 1.495 m ($\mathrm{Re}_x = 9.1 \times 10^5$) for turbulence intensity of 6 percent, respectively. The symbols have the same meaning as mentioned in the earlier figures. The turbulence velocity is calculated on the basis of the following relation (Myong, 1990);

$$u^2 = \frac{2}{3}k + \frac{1}{3}(2C_1 - C_3)\nu_t \frac{k}{\epsilon}\left(\frac{\partial U}{\partial y}\right)^2 \tag{23}$$

where $C_1 = 0.8$ and $C_3 = -0.15$.

It can be observed from these figures that N-T and K-S models predicted the boundary layer turbulence velocity quite

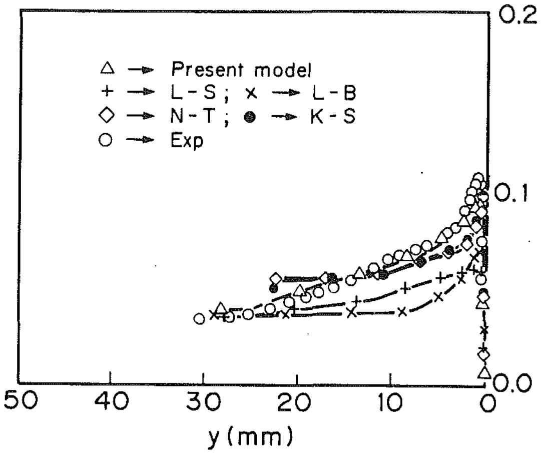

Fig. 4(*a*) Boundary layer turbulence velocity u/U_o profile at $x = 0.895$ m and turbulence intensity of 6 percent

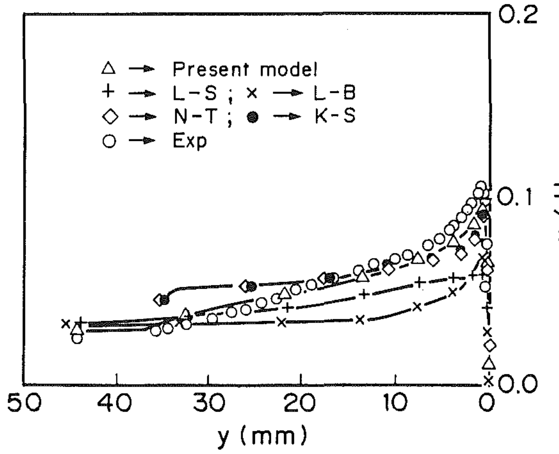

Fig. 4(*b*) Boundary layer turbulence velocity u/U_o profile at $x = 1.495$ m and turbulence intensity of 6 percent

satisfactorily, because of the fact that these two models predicted the transition far too early and the turbulence had sufficient time to develop. The L-B model underpredicted the experimental data. The L-S model, which gave nearly correct prediction of transition for 3 percent turbulence intensity, considerably underpredicted the fullness of the profiles. The present model predicted the experimental profile quite satisfactorily and lead to the understanding that in the present model the correct blending between viscous sublayer and fully turbulent outer boundary layer is devised quite satisfactorily.

Secondly, low-Reynolds-number flow limiting behavior turbulence quantities such as k, ϵ, $\overline{uv}$, f_μ, etc., as the wall is approached in the case of fully turbulent flow is tested by comparing with the experimental data presented by Patel et al. (1985). In Fig. 5(*a*, *b*, *c*) are plotted the computed turbulent kinetic energy k^+, dissipation rate ϵ^+, and shear stress $-uv^+$ profiles in the fully turbulent region along with the experimental data (Patel et al., 1985), (momentum thickness Reynolds number $\mathrm{Re}_\theta = 5000$):

$$k^+ = \frac{k}{U_\tau^2};\quad \epsilon^+ = \frac{\epsilon\nu}{U_\tau^4};\quad -uv^+ = \frac{-\overline{uv}}{U_\tau^2} \tag{24}$$

and $U_\tau = (\tau_w/\rho_w)$ is the friction velocity.

In these figures the symbols have the same meaning as before. The original experimental data scattered over a range and the average value are plotted here; however, a fair agreement with the location of maximum turbulent kinetic energy k^+ and magnitude of ϵ^+ is observed for all the models. Also all the models predicted the experimental shear stress profile quite satisfactorily.

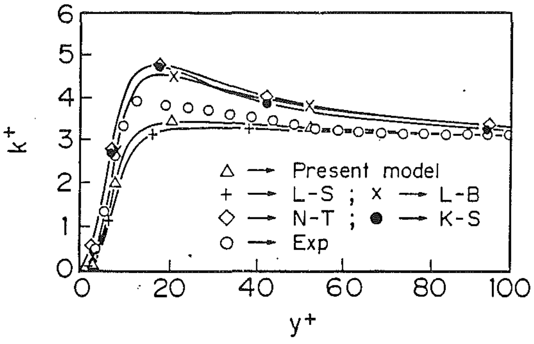

Fig. 5(*a*) Measured and calculated boundary layer turbulence kinetic energy profile

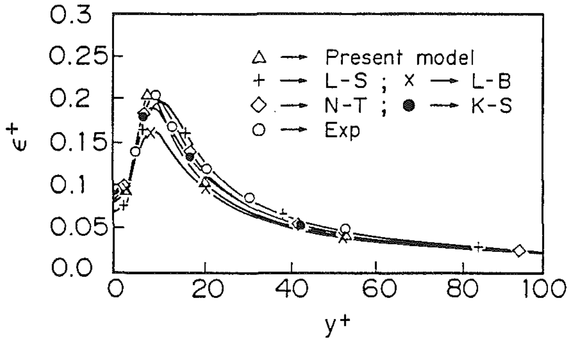

Fig. 5(*b*) Measured and calculated boundary layer dissipation rate profile

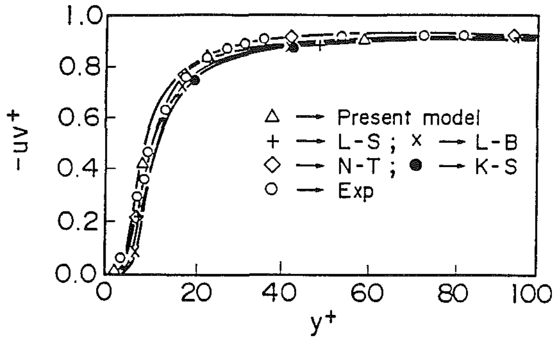

Fig. 5(*c*) Measured and calculated boundary layer Reynolds stress profile

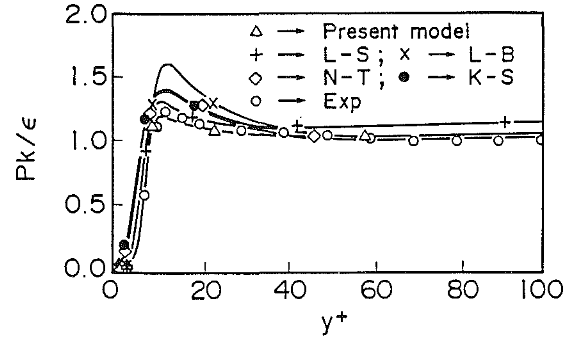

Fig. 5(*d*) Boundary layer *Pk*/ϵ profile

In Fig. 5(*d*) are plotted the computed turbulent boundary layer PK/ϵ profile (where $PK = -\overline{uv}(\partial U/\partial y)$. The symbols have the same meaning as above. The experimental results (Patel et al., 1985) indicate that in the vicinity of the wall the dissipation of turbulence is very large as compared to its production and production of turbulence dominates over dissipation in the buffer region (gives a peak of PK/ϵ of about 1.2); finally, in the log law region $40 < y^+ < 100$, say, PK roughly equals ϵ. The present model predicted the experimental fact

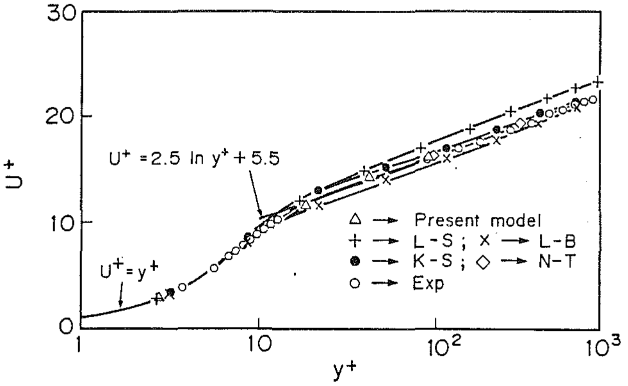

Fig. 6 Boundary layer mean velocity profile

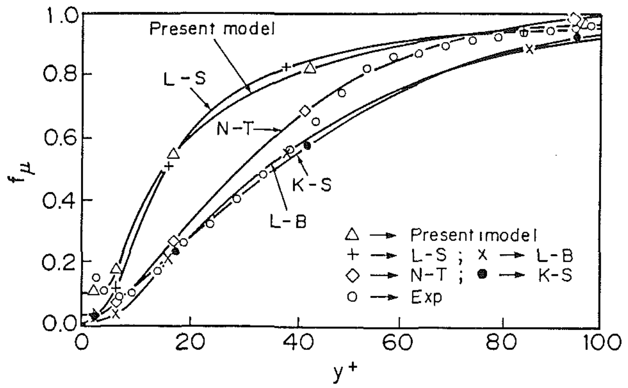

Fig. 7 Boundary layer f_μ profile

very well. The L-B, N-T, and K-S model gave a little higher peak value, and the L-S model predicted a little bit higher production of turbulence in the logarithmic region.

In Fig. 6 are plotted the computed turbulent boundary layer mean velocity profiles along with experimental data ($Re_\theta = 5000$), and universal velocity profile law given by $U^+ = 2.5 \ln y^+ + 5.5$).

The symbols have the same meaning as above. The L-S model slightly overpredicted the experimental data, which is the reason behind the underestimation of turbulent C_f level as is observed in Fig. 1(*a*) and 2(*a*). The present model and the other models predicted the experimental data and universal velocity profile quite satisfactorily.

Another important criterion of the appropriateness of a model, as emphasized by Patel et al. (1985), is the estimation of model damping function f_μ. In Fig. 7 are plotted the computed f_μ along with the experimental data (Patel et al., 1985). This figure indicates that the N-T model follows closely the distribution suggested by the data over the whole range of y^+. The L-B and K-S models are a good approximation in the viscous zone ($y^+ < -40$); but give a slightly lower value in the log law region away from the wall, while L-S and the present model yield high values there, but showed very good agreement with the experimental curve in the logarithmic region ($y^+ > 40$). It is mentioned by Patel that the viscous effect becomes negligible for $y^+ > 60$, and f_μ should reach an asymptotic value of unit in this region. This criterion is satisfied very well by the present model; however, further study needs to be carried out to have a better approximation in the viscous zone.

Next the validity of these models is tested by applying them to the flow problem with favorable pressure gradient and heat transfer (Blair and Werle, 1981). The experiment was performed under a flow condition of constant acceleration parameter of 0.2×10^{-6}. The free-stream velocity distribution is given by the following equation:

$$U_o = 89.9144 \times (5.08 \times x)^{-1.066} \tag{25}$$

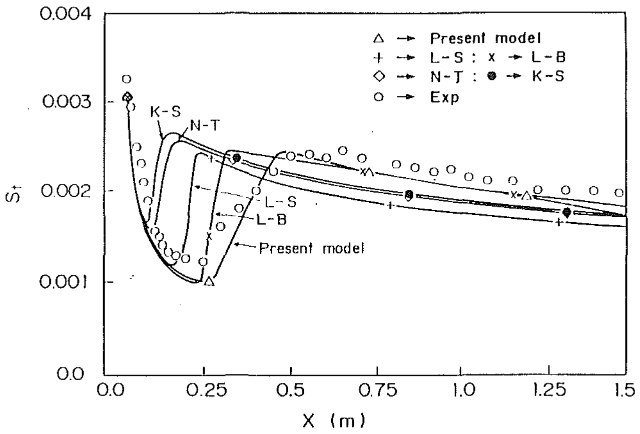

Fig. 8 Variation of Stanton number with the axial distance

Table 3 Flow conditions used in the simulation of blade heat transfer coefficient

Data	Case	M_1	M_2	P_O (Mpa)	T_O (K)	T_w (k)	R_{ec}	Tu (%)
Daniels	1	0.35	0.94	0.292	432	288	6.7×10^5	4 %
Daniels	2	0.33	0.94	0.581	432	288	1.3×10^6	4 %
NASA	1	0.17	0.92	0.245	795	644	3.9×10^5	6.5 %
NASA	2	0.16	0.91	0.395	792	642	6.4×10^5	6.5 %
Toshiba	1	0.14	0.80	0.370	1686	1123	1.8×10^5	6 %

M_1 : Inlet Mach Number ; M_2 : Outlet Mach Number ;

P_O : Inlet Total Pressure ; T_O : Inlet Total Temperature ;

T_w : Wall Temperature ; R_{ec} : Inlet Reynolds number ($U_1 \rho_1 C / \mu_1$)

The index "1" represents the value at the inlet.

Tu : Turbulence Intensity

where *x* represents the axial distance. The free-stream velocity and turbulence intensity at $x = 0$ are considered to be 15.9 m/s and 2.1 percent, respectively. The ratio of wall temperature and free-stream temperature T_w/T_e and T_e are specified as 1.03 and 297 K, respectively.

In Fig. 8 are plotted the calculated variations of Stanton number with axial distance along with the experimental data. This figure shows that here also N-T and K-S models predicted the transition far too early. The L-S and L-B models showed closer prediction of transition. Also, the L-S, N-T, and K-S models underpredicted the experimental turbulent Stanton number. In this flow condition also, the present model not only predicted the transition well, but also the fully turbulent Stanton number is reproduced satisfactorily.

Next these models are applied to a gas turbine rotor blade cascade and NASA C3X gas turbine vane cascade for which Daniels and Browne (1981) and Hylton et al. (1983), respectively, performed experiments on heat transfer. Two test cases are selected for each of the cases for simulation. For Daniels' blade these test cases are characterized by chord Reynolds numbers Re_c of 6.7×10^5 and 1.3×10^6, and for NASA C3X these cases are characterized by chord Reynolds number Re_c of 3.9×10^5 and 6.4×10^5, respectively, where

$$Re_c = U_1 C \frac{\rho_1}{\mu_1} \tag{26}$$

Here, $U_1 \rightarrow$ inlet mean velocity; $c \rightarrow$ axial chord length; $\rho_1 \rightarrow$ inlet density; $\mu_1 \rightarrow$ inlet viscosity. The flow conditions are summarized in Table 3.

In Figs. 9 and 10 are plotted the calculated distribution of heat transfer on the pressure and suction surface of the blade along with the experimental results of Daniel and Browne (1981) for Re_c of 6.7×10^5 and 1.3×10^6, respectively. Figure 9 shows that on the suction surface N-T and K-S models predicted the transition far too early, L-S and L-B models

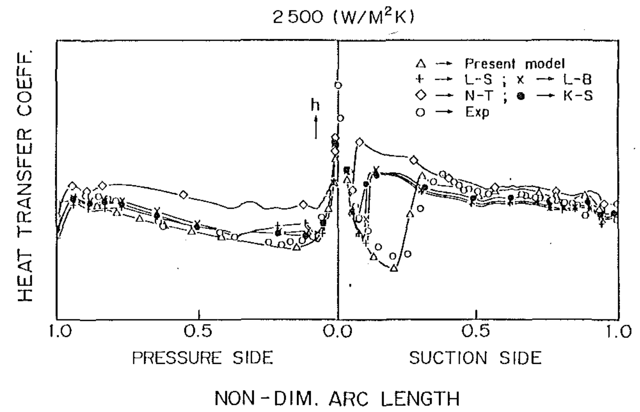

Fig. 9 Distribution of heat transfer coefficient on Daniels blade surface ($Re_c = 6.7 \times 10^5$)

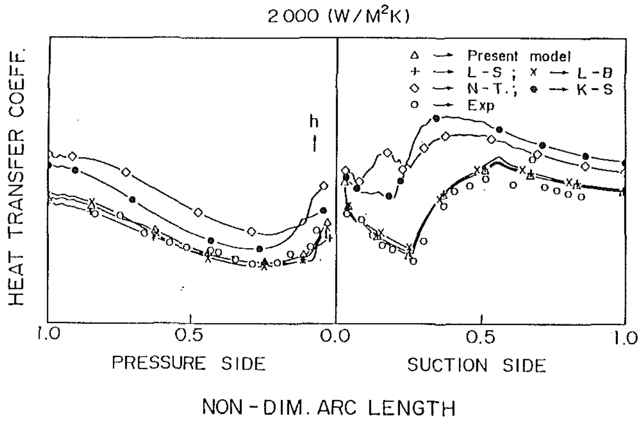

Fig. 11 Distribution of heat transfer coefficient on C3X vane surface ($Re_c = 3.9 \times 10^5$)

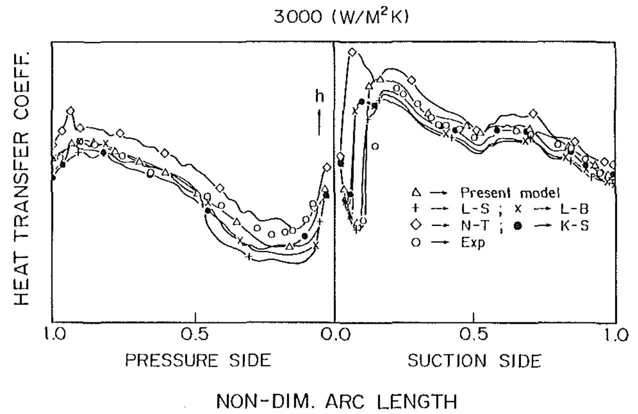

Fig. 10 Distribution of heat transfer coefficient on Daniels blade surface ($Re_c = 1.3 \times 10^6$)

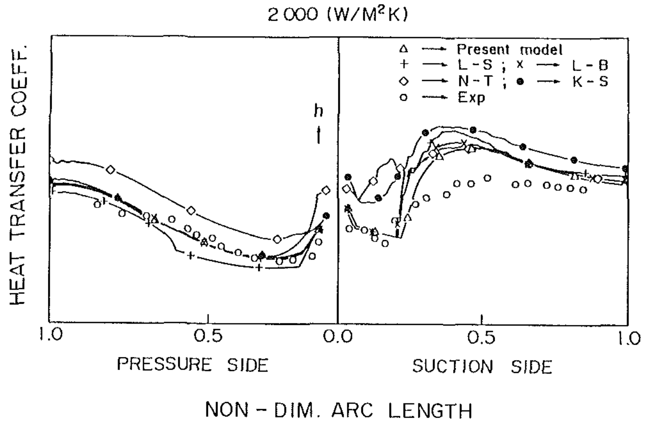

Fig. 12 Distribution of heat transfer coefficient on C3X vane surface ($Re_c = 6.4 \times 10^5$)

predicted the transition early too, and the present model predicted the transition best. However, all the models predicted the turbulent heat transfer level quite satisfactorily. This figure also indicates that on the pressure surface where the flow is transitional in the whole region because of high acceleration, all the models predicted the experimental heat transfer quite satisfactorily, except the N-T model, which overpredicted the experimental value. In the case of higher Re_c, it can be observed from Fig. 10 that the N-T model did not show any transition at all, the K-S model predicted the transition a bit too early, the L-B and L-S models showed closer prediction of transition, but the present model showed the best overall agreement. This figure also indicates that on the pressure surface, the N-T model overpredicted the experimental heat transfer, the L-S, L-B and K-S models gave slightly lower values of heat transfer as compared to the experimental data near the leading edge region, but the present model showed best overall agreement. Also it is observed from this study that as compared to other models, which are a little too sensitive to increasing Reynolds number, the present model reproduced the experimental effect of flow Reynolds number quite satisfactorily.

In Figs. 11 and 12 are plotted the calculated distribution of heat transfer on the pressure and suction surfaces of NASA C3X vane along with the experimental results (Hylton et al., 1983) for Re_c equal to 3.9×10^5 and 6.4×10^5, respectively. Figure 11 shows that N-T and K-S models not only predicted the transition too early, but also the laminar and turbulent heat transfer are overpredicted. Not much difference in terms of prediction by the present model, L-S and L-B models is observed and all these three models predicted the experimental data quite satisfactorily. This figure also indicates that on the pressure surface the N-T and K-S models overpredicted the experimental data and good agreement between the experimental data and results of calculation by the present model, L-S and L-B models is observed. In the case of higher Re_c, it can be observed from Fig. 12 that here also the N-T and K-S models predicted the suction surface transition early and slightly overpredicted the laminar heat transfer. In this case although the present model, L-S and L-B models predicted the suction surface transition quite satisfactorily, the turbulent heat transfer in the midchord region is slightly overpredicted. This figure also indicates that on the pressure surface the N-T model overpredicted the experimental heat transfer, the L-S model slightly underpredicted the heat transfer in the midchord region, and a good agreement between experimental data and results of calculations by the present model, L-B and K-S models is observed.

Additionally, numerical simulation using L-S, L-B, and the present models are carried out in the case of a high-temperature gas turbine vane (steam cooled and air cooled trailing edge) cascade (Amagasa et al., 1992) for which we performed experiments to obtain the surface temperature distribution under flow conditions, characterized by chord Reynolds number Re_c of 1.8×10^5. The flow conditions are summarized in Table 3 and the profile of the vane is shown in Fig. 13. The free-stream velocity distribution obtained by solving the Euler equations for this cascade flow condition is used as the boundary condition for external heat transfer calculation. Calculated external heat transfer distribution is specified as the boundary condition for the computation of the surface temperature distribution by taking into account the internal heat transfer effect. In Fig. 14 are plotted the calculated surface temperature distributions on the suction and pressure surface of the vane along with the experimental data. This figure showed not much difference in prediction of data by different models. All the models predicted the suction surface location of transition

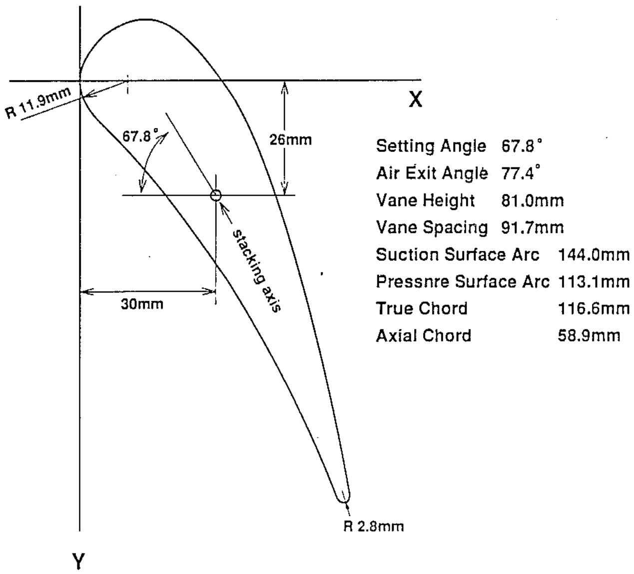

Fig. 13 Toshiba vane profile

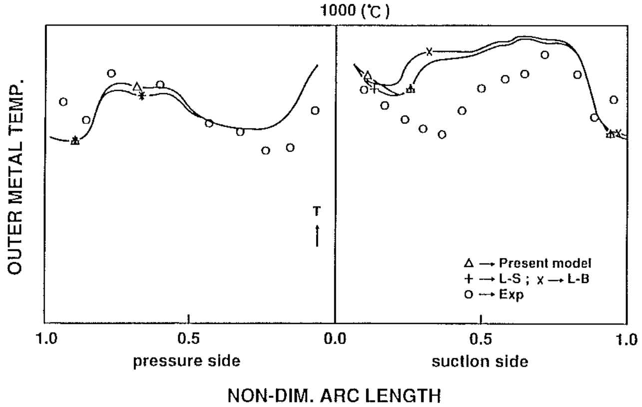

Fig. 14 Distribution of temperature on Toshiba vane surface ($\mathrm{Re}_c = 1.8 \times 10^5$)

slightly upstream as compared to the experimental data. However, the temperature in the fully turbulent flow region and sudden temperature drop in the trailing edge region of the suction surface is well predicted by all the models. The pressure surface temperature distribution including the temperature drop in the trailing edge region is predicted quite satisfactorily by all the models. The difference between measured and predicted suction surface transition location is expected to be due to the errors associated with the measurement of turbulence intensity in the cascade experiment and also due to the experimental uncertainty associated with the measurement of transition location.

5 Conclusions

The performance of different low-Reynolds-number versions of the k-ϵ turbulence model in predicting transitional boundary layers have been tested and low-Reynolds-number functions are evaluated based on experimental data with different free-stream turbulence levels. Comparative studies of the existing models showed that the models that defined the damping factors as a function of a specific location like y^+ or y are less likely to predict transition, although they can provide the correct blending between near-wall viscous sublayer and fully turbulent outer boundary layer. Physically, in order to obtain anywhere near correct prediction of transitions it is desirable to define damping factors as a function of some quantity (like the turbulence Reynolds number Re_t), which is only a rather general indicator of the degree of turbulence activity at any x or y location in the flow, rather than a specific function of the location itself.

The improved model proposed in the present work defines the damping factors as a function of turbulence Reynolds number. It satisfies the exponents of the near-wall variation of turbulence quantities such as k, ϵ, $-\overline{uv}$, and f_μ (Van Driest mixing length), and by modeling the proper balance between production and dissipation of turbulence in the near-wall and far-wall region, can reproduce both the linkage between the pretransitional pseudolaminar boundary layer and the post-transitional fully turbulent boundary layer and the near-wall low-Reynolds-number flow behavior quite satisfactorily.

The present model could also reproduce the experimental effect of flow Reynolds number and free-stream turbulence intensity over a range on the transitional boundary layer heat transfer in the case of a gas turbine blade and vane cascade quite satisfactorily.

Acknowledgments

We would like to thank Prof. Kasagi and Mr. Sikasono for their useful discussions and for providing their model for comparison in this work.

References

Amagasa, S., Ohtomo, F., et al., 1992, "Testing of a Steam Cooling Gas Turbine Nozzle," *The 69th JSME Spring Annual Meeting*, Vol. B, pp. 408-410.

Biswas, D., Fukuyama, Y., and Araki, T., 1989, "Computation of Transitional Boundary Layer in Gas Turbine Blade Cascade," *Journal of Gas Turbine Society of Japan*, Vol. 17, No. 66, pp. 11-18.

Blair, M. F., and Werle, M. J., 1981, "Combined Influence of Free-Stream Turbulence and Favorable Pressure Gradients on Boundary Layer Transition," UTRC Report R81-914388-17.

Crawford, M. E., and Kays, W. M., 1976, "STAN5—A Program for Numerical Computation of Two-Dimensional Internal and External Boundary-Layer Flows," NASA CR-2742.

Daniels, L. C., and Browne, W. B., 1981, "Short Duration Measurements of Heat Transfer Rate to a Gas Turbine Rotor Blade," *International Journal of Heat and Mass Transfer*, Vol. 24, pp. 871-879.

Fujisawa, N., 1990, "Calculations of Transitional Boundary Layers With a Refined Low-Reynolds-Number Version of a k-ϵ Model of Turbulence," *Engineering Turbulence Modeling and Experiments*, Elsevier Science Publishing Co., pp. 23-32.

Hanjalic, K., and Launder, B. E., 1976, "Contribution Towards a Reynolds-Stress Closure for Low-Reynolds-Number Turbulence," *Journal of Fluid Mechanics*, Vol. 74, pp. 593-610.

Hylton, L. D., Mihlec, M. S., et al., 1983, "Analytical and Experimental Evaluation of the Heat Transfer Distribution Over the Surface of Turbine Vane," NASA CR-168015.

Kasagi, N., 1992, Tokyo University, private communication.

Lam, C. K. G., and Bremhorst, K., 1981, "A Modified Form of the k-ϵ Model for Predicting Wall Turbulence," ASME *Journal of Fluids Engineering*, Vol. 103, pp. 456-460.

Launder, B. E., and Sharma, B. I., 1979, "Application of the Energy-Dissipation Model of Turbulence to the Calculation of Flow Near a Spinning Disc," *Letters in Heat and Mass Transfer*, Vol. 1, pp. 131-138.

Myong, H. K., and Kasagi, N., 1990, "Toward an Anisotropic k-ϵ Turbulence Model Taking into Account the Wall-Limiting Behavior of Turbulence," *International Symposium on Computational Fluid Dynamics*, Japan, pp. 269-274.

Nagano, Y., and Tagawa, M., 1990, "An Improved k-ϵ Model for Boundary Layer Flows," ASME *Journal of Fluids Engineering*, Vol. 112, pp. 33-39.

Patel, V. C., Rodi, W., and Scheuerer, G., 1985, "Turbulence Models for Near-Wall and Low-Reynolds Number Flow—A Review," *AIAA Journal*, Vol. 23, No. 9, pp. 1308-1319.

Savill, A. M., 1991, "A Synthesis of T3 Test Case Prediction," Research Report of ERCOFTAC Workshop.

So, R. M. C., Lai, Y. G., and Hwang, B. C., 1991, "Near-Wall Turbulence Closure for Curved Flows," *AIAA Journal*, Vol. 29, pp. 1202-1213.